University of Rochester
Laboratory for Laser Energetics

DOE/NA/28302-923
January 2010

LLE 2009 Annual Report

October 2008 – September 2009

Cover Photos

Top left: Two of the targets used for an OMEGA NLUF experiment carried out by a team from MIT's Plasma Science and Fusion Center to study jet formation using proton radiography. The large, 20-mm-diam conical structures shield the diagnostic systems from x-ray radiation generated by the laser beams that are used to form the jet in the foam cylinder behind the cones.

Middle left: Participants at the first Omega Laser Users Group Workshop held at LLE from 29 April–1 May 2009. The workshop attracted 110 researchers from 29 universities and laboratories and 4 countries. The purpose of the workshop was to facilitate communication and exchanges among the individual users and between the users and LLE. Almost 50 presentations highlighting ongoing and proposed research experiments were given, most of which were presented by the 32 students and postdoctoral candidates in attendance.

Bottom left: A new type of detector comprised of (Cd,Mn)Te (CMT). It is being investigated as a viable material for radiation detection because it can be used for x-ray energies of up to 100 keV and is relatively easy to grow as large, high-quality (homogeneous) single crystals.

Top right: A photograph of the gold-plated copper components for the moving-cryostat upgrade. They have highly polished surfaces to create a low surface emissivity. This reduces both the radiation heat load to the cold head and the need for multilayer insulation.

Middle right: Colorful spectral dispersion observed through diffraction from a multilayer-dielectric grating. Several large-aperture diffraction gratings are used to compress the pulse width of the OMEGA EP short-pulse laser beams. LLE is investigating high-damage-threshold grating designs and manufacturing processes to increase the energy delivered to target.

Bottom right: A view of the OMEGA EP Laser Bay during a four-beam laser shot. The beamline structures are illuminated by the flash of light that energizes the laser amplifiers. The grating compressor chamber can be seen in the shadows at the right.

Prepared for
U.S. Department of Energy
San Francisco Operations Office
DOE/SF/19460-798

Distribution Category
October 2007–September 2008

Printed in the United States of America
Available from
National Technical Information Services
U.S. Department of Commerce
5285 Port Royal Road
Springfield, VA 22161
Price codes: Printed Copy A12
Microfiche A01

The work described in this volume includes current research at the Laboratory for Laser Energetics, which is supported by New York State Energy Research and Development Authority, the University of Rochester, the U.S. Department of Energy Office of Inertial Confinement Fusion under Cooperative Agreement No. DE-FC52-08NA28302, and other agencies.

For questions or comments, Laboratory for Laser Energetics,
250 East River Road, Rochester, NY 14623-1299, (585) 275-5286.
Worldwide-Web Home Page: http://www.lle.rochester.edu/

University of Rochester
Laboratory for Laser Energetics

DOE/NA/28302-923
January 2010

LLE 2009 Annual Report

UR LLE

October 2008 – September 2009

Inertial Fusion Program and National Laser Users' Facility Program

Contents

Executive Summary

The fiscal year ending September 2009 (FY2009) concluded the second year of the third five-year renewal of Cooperative Agreement DE-FC52-08NA28302 with the U.S. Department of Energy (DOE). This annual report summarizes progress in inertial fusion research at the Laboratory for Laser Energetics (LLE) during the past fiscal year. It also reports on LLE's progress on laboratory basic science research; laser, optical materials, and advanced technology development; operation of OMEGA and OMEGA EP for the National Laser Users' Facility (NLUF), and other external users; and programs focusing on the education of high school, undergraduate, and graduate students during the year.

Progress in Inertial Confinement Fusion (ICF) Research

The science research program at the University of Rochester's Laboratory for Laser Energetics (LLE) focuses on inertial confinement fusion (ICF) research supporting the goal of achieving ignition on the National Ignition Facility (NIF). This program includes the full use of the OMEGA 60-beam UV laser as well as the OMEGA EP high-energy, short-pulse laser system. During FY09, OMEGA EP was operated on target at an energy level of 2.1 kJ at 10 to 12 ps, making the laser the world's highest-energy short-pulse laser system. Within the National Ignition Campaign (NIC), LLE is the lead laboratory for the validation of the performance of cryogenic target implosions, essential to all forms of ICF ignition. LLE has taken responsibility for a number of critical elements within the Integrated Experimental Teams (IET's) supporting the demonstration of indirect-drive ignition on the NIF and is the lead laboratory for the validation of the polar-drive approach to ignition on the NIF. LLE is also developing, testing, and building a number of diagnostics that are being deployed on the NIF for the NIC. During this past year, progress in the inertial fusion research program was made in three principal areas: NIC experiments; development of diagnostics for experiments on OMEGA, OMEGA EP, and the NIF; and theoretical analysis and design efforts aimed at improving direct-drive-ignition capsule designs and advanced ignition concepts such as fast ignition and shock ignition.

1. National Ignition Campaign Experiments

In FY09, LLE, in collaboration with Lawrence Livermore National Laboratory (LLNL) and Sandia National Laboratories (SNL), demonstrated a key shock-timing technique for ignition targets at the NIF. The article beginning on p. 1 reports on this technique to measure the velocity and timing of shock waves in a capsule contained within hohlraum targets. This technique is critical for optimizing the drive profiles for high-performance ICF capsules, which are compressed by multiple precisely timed shock waves. The shock-timing technique was demonstrated on OMEGA using surrogate hohlraum targets heated to a radiation temperature of 180 eV and fitted with a re-entrant cone and quartz window to facilitate velocity measurements using velocity interferometry. Cryogenic experiments using targets filled with liquid deuterium further demonstrated the entire timing technique in a hohlraum environment. Direct-drive cryogenic targets with multiple spherical shocks were also used to validate this technique, including convergence effects at relevant pressures (velocities) and sizes. These results provide confidence that shock velocity and timing can be measured in NIF ignition targets, thereby optimizing these critical parameters.

Recent progress in high-density implosions of direct-drive cryogenic capsules based on a collaboration including scientists from LLE, NRC (Israel), and the Plasma Science and Fusion Center–MIT (PSFC–MIT) is reviewed beginning on p. 12. Ignition-relevant areal densities of ~200 mg/cm^2 in cryogenic D_2 implosions with peak laser-drive intensities of $\sim 5 \times 10^{14}$ W/cm^2 were previously reported. The laser intensity is being increased to $\sim 10^{15}$ W/cm^2 to demonstrate ignition-relevant implosion velocities of 3 to 4×10^7 cm/s, providing an understanding of the relevant target physics. Planar-target acceleration experiments show the importance of the non-local electron-thermal-transport effects for modeling the laser drive. Nonlocal, hot-electron preheat is observed to stabilize the Rayleigh–Taylor growth at the peak drive intensity of $\sim 10^{15}$ W/cm^2. The shell preheat caused by the hot electrons generated by two-plasmon-decay (TPD) instability was reduced

by using Si-doped ablators. The measured compressibility of planar plastic targets driven with high-compression, shaped pulses agrees well with 1-D simulations at these intensities. Shock mistiming has contributed to compression degradation of recent cryogenic implosions driven with continuous pulses. Multiple-picket (shock-wave) target designs make it possible for a more robust tuning of the shock-wave arrival times. Cryogenic implosions driven with double-picket pulses demonstrate improved compression performance at a peak drive intensity of $\sim 10^{15}$ W/cm^2.

Experiments (p.178) on the OMEGA Laser System (in collaboration with LLNL and SNL) using laser-driven vacuum hohlraum targets show distinct differences between cryogenic (<20 K) and warm targets. Warm hohlraum targets coated with 2 μm of CH replicate the behavior of cryogenic targets. This indicates that cryogenic hohlraums are affected by the condensation of background gases on the cold hohlraum surface. The introduction of low-Z material into the hohlraums significantly reduces the x-ray conversion efficiency, resulting in lower hohlraum radiation temperature. The coatings (both CH and condensates) produce long-scale-length, low-Z plasmas that reduce the absorption of laser light in the hohlraums. This causes higher reflectivity and produces hot electrons that generate hard x rays ($h\nu > 20$ keV), both of which are detrimental to the performance of hohlraum-driven inertial confinement fusion targets. These finding are important to some non-ignition hohlraums that use low-Z liners (or layers) on the inside hohlraum walls to tamp or resist the expansion of the laser-ablated wall material. In contrast, ignition hohlraums will be filled with a low-Z gas to keep the laser entrance hole open. Windows are placed on the laser entrance holes to retain the gas; these windows also serve to protect the inside of the hohlraum from the deposition of condensates. Moreover, the NIF cryogenic targets are housed inside shrouds to minimize condensation until they open a few seconds before the shot. These OMEGA experiments confirm that eliminating condensation on cryogenic targets is crucial for optimal hohlraum performance.

Scientists from PSFC–MIT, LLE, and LLNL present recent experiments using proton backlighting of laser–foil interactions to provide a unique opportunity for studying magnetized plasma instabilities in laser-produced, high-energy-density plasmas (p. 74). Time-gated proton radiograph images indicate that the outer structure of a magnetic field entrained in a hemispherical plasma bubble becomes distinctly asymmetric after the laser turns off. It is shown that this asymmetry is a consequence of pressure-driven, resistive magnetohydrodynamic (MHD) interchange instabilities. In contrast to the predictions made by ideal MHD theory, the increasing plasma resistivity after the laser turns off allows for greater low-mode destabilization (mode number $m > 1$) from reduced stabilization by field-line bending. For laser-generated plasmas presented herein, a mode-number cutoff for stabilization of perturbations with $m > \sim\sqrt{8\pi\beta\left(1 + D_m k_\perp^2 \gamma_{\max}^{-1}\right)}$, is found in the linear growth regime. The growth is measured and is found to be in reasonable agreement with model predictions.

2. Cryogenic Target Fabrication

Scientists from the University of Rochester's (UR's) Department of Electrical Engineering and LLE present a method by which the ponderomotive force, exerted on all dielectric liquids by a nonuniform electric field, can be used for the remote, voltage-controlled manipulation of 10- to 100-nl volumes of cryogenic liquids (p. 101). This liquid dielectrophoretic (DEP) effect, imposed by specially designed electrodes, combines with capillarity to influence the hydrostatic equilibria of liquid deuterium. A simple, 1-D model accurately predicts the measured meniscus rise of D_2 against gravity for sufficiently wide, parallel electrodes. For narrow electrodes, where the sidewalls influence the equilibrium, a finite-element solution using the Surface Evolver software correctly predicts the behavior. A bifurcation phenomenon previously observed for room-temperature dielectrics is also observed in liquid deuterium. This effect could possibly be used in the future to meter cryogenic deuterium when fueling targets for laser fusion.

Scientists from LLE, the Power Photonic Corporation, and the State University of New York at Stony Brook describe the spectral and output-power stability of a 3-nm-wavelength, GaSb-based diode laser operated at room temperature (p. 111). More than 50 mW of output power has been achieved at 14°C with high spectral and output-power stability. This diode laser has a direct application for layering cryogenic targets for ICF implosions on the OMEGA laser.

3. Target Diagnostics for OMEGA, OMEGA EP, and the NIF

Beginning on p. 20 we describe a new method (developed in collaboration with PSFC–MIT) for analyzing the spectrum of knock-on deuterons (KOd's) elastically scattered by primary DT neutrons, from which a fuel ρR can be inferred for values up to ~200 mg/cm^2. This new analysis method, which used Monte Carlo modeling of a cryogenic DT implosion, significantly improves the previous analysis method in two fundamental ways: First, it is not affected by significant spatial-yield variations, which degrade the diagnosis of fuel ρR (spatial-yield variations of about ±20% are typically observed), and second, it does not break down when the fuel ρR exceeds 70 mg/cm^2.

Based on a joint effort involving LLE, PSFC–MIT, and the University of Nevada–Reno, we describe a method from which the cold fuel layer's density is inferred from framed x-ray radiographs of a laser-driven spherical implosion (p. 26). The density distribution is determined by using Abel inversion to compute the radial distribution of the opacity κ from the observed optical depth τ. With the additional assumption of the mass of the remaining cold fuel, the absolute density distribution can be determined. This is demonstrated at the Omega Laser Facility with two x-ray backlighters of different mean energies that lead to the same inferred density distribution independent of backlighter energy.

The article beginning on p. 55, co-authored by scientists from LLE, LLNL, the University of Nevada–Reno, and the University of California at San Diego, highlights the diagnosis of high-energy-density plasmas created in laser-fusion experiments with x-ray spectroscopy. Over the last three decades, x-ray spectroscopy has been used to record the remarkable progress made in ICF research. Four areas of x-ray spectroscopy for laser-fusion experiments are highlighted in this article: K_α emission spectroscopy to diagnose target preheat by suprathermal electrons, Stark-broadened K-shell emissions of mid-Z elements to diagnose compressed densities and temperatures of implosion cores, K- and L-shell absorption spectroscopy to diagnose the relatively cold imploding shell (the "piston") that does not emit x rays, and multispectral monochromatic imaging of implosions to diagnose core temperature and density profiles. A large portion of the seminal research in these areas has been carried out by LLE and is discussed in this report.

A report beginning on p. 68 authored by scientists from LLE and the UR's Institute of Optics discusses high-resolution coherent transition radiation (CTR) imaging for diagnosing electrons accelerated in laser–solid interactions with intensities of $\sim 10^{19}$ W/cm^2. The CTR images indicate electron-beam filamentation and annular propagation. The beam temperature and half-angle divergence are inferred to be ~1.4 MeV and ~16°, respectively. Three-dimensional hybrid-particle-in-cell code simulations reproduce the details of the CTR images, assuming an initial half-angle divergence of 56°. Self-generated resistive magnetic fields are responsible for the difference between the initial and the measured divergences.

A team from LLE and Ad-Value Photonics report (p. 51) on work that experimentally validates the concept of effective Verdet constant to describe the Faraday rotation characteristics of optical fiber. The effective Verdet constant of light propagation in fiber includes contributions from the materials in both the core and the cladding. This article presents a measured Verdet constant in 25-wt% terbium-doped–core phosphate fiber to be –6.2±0.4 rad/Tm at a wavelength of 1053 nm, which is 6× larger than in silica fiber. The result agrees well with the Faraday rotation theory for optical fiber.

This same team reports (p. 206) on an all-fiber optical magnetic field sensor. The sensor consists of a fiber Faraday rotator and a fiber polarizer. The fiber Faraday rotator uses a 2-cm-long section of 56-wt%-terbium-oxide–doped silica fiber, and the fiber polarizer is a Corning SP1060 single-polarization fiber. The all-fiber optical magnetic field sensor has a sensitivity of 0.45 rad/T and can measure a magnetic field up to 3.5 T.

4. Theoretical Analysis and Design

Beginning on p. 31 we report on integrated simulations of implosion, electron transport, and heating for direct-drive fast-ignition targets. A thorough understanding of future integrated fast-ignition experiments combining compression and heating for high-density thermonuclear fuel requires hybrid (fluid + particle) simulations of the implosion and ignition process. Different spatial and temporal scales need to be resolved to model the entire fast-ignition experiment. The 2-D axisymmetric hydrocode *DRACO* and the 2-D/3-D hybrid-PIC code *LSP* have been integrated to simulate the implosion and heating of direct-drive, fast-ignition targets. *DRACO* includes the physics required to simulate compression, ignition, and burn of fast-ignition targets. *LSP* simulates the transport of hot electrons from their generation site to the dense fuel core, where their energy is absorbed. The results from integrated simulations of cone-in-shell CD targets designed for fast-ignition experiments on the OMEGA/OMEGA EP Laser System are presented. Target heating and neutron yields are computed. The results from *LSP* simulations of electron transport in solid-density plastic targets are also presented. They confirm an increase in the electron-divergence angle with the laser intensity in the current experiments. The self-generated resistive magnetic field is found to collimate the hot-electron beam and increase the coupling efficiency of hot electrons with the target. Resistive filamentation of the hot-electron beam is also observed.

Lasers, Optical Materials, and Advanced Technology

A report co-authored by scientists from LLE and the UR's Department of Mechanical Engineering discusses *in-situ*, simultaneous measurements of both drag and normal forces in magnetorheological optical finishing (MRF) using a spot-taking machine (STM) as a test bed to take MRF spots on stationary optical parts (p. 42). The force measurements are carried out over the entire removal area, produced by the

projected area of the MRF removal function/spot on the part surface, using a dual-force sensor. This approach experimentally addresses the mechanisms governing material removal in MRF for optical glasses in terms of the hydrodynamic pressure and shear stress, applied by the hydrodynamic flow of magnetorheological (MR) fluid at the gap between the part surface and the STM wheel. This work demonstrates that the volumetric removal rate shows a positive linear dependence on shear stress. Shear stress exhibits a positive linear dependence on a material figure of merit that depends on Young's modulus, fracture toughness, and hardness. A modified Preston's equation is proposed that will better estimate MRF material removal rate for optical glasses by incorporating mechanical properties, shear stress, and velocity.

A team from LLE and the UR's Departments of Mechanical Engineering and Chemical Engineering reports on MRF spotting experiments performed on glasses and ceramics using a zirconia-coated-carbonyl-iron-particle–based MR fluid (p. 190). The coating layer was ~50 to 100 nm thick, faceted in surface structure, and well adhered. Coated particles showed long-term stability against aqueous corrosion. A viable MR fluid was prepared simply by adding water. Spot-polishing tests were performed on a variety of optical glasses and ceramics over a period of nearly three weeks with no signs of MR fluid degradation or corrosion. Stable material-removal rates and smooth surfaces inside spots were obtained.

Scientists from the UR's Department of Mechanical Engineering discuss crack growth in brittle glass plates using known finite element modeling to determine the maximum allowable initial crack size in plates undergoing radiative cooling (p. 145). In these simulations both BK7 borosilicate crown and LHG8 phosphate glass were slowly cooled in vacuum from 200°C down to room temperature. The authors used finite elements and incorporated available experimental results on crack growth in BK7 and LHG8. Numerical simulation showed that the heaviest stressed locations were the midpoints of the plate's long edges, where any crack growth was likely to originate. This article outlines a procedure to estimate the deepest-allowable surface flaw to prevent fracture. Fracture is analyzed in terms of strength, fracture toughness, or slow crack growth. Merits of these approaches are discussed, and an extensive comparison of cracking in BK7 versus the laser glass LHG8 is presented.

Scientists from LLE; the UR's Department of Electrical Engineering; the Institute of Bio- and Nanosystems, Research Centre of Jülich; and the Institute of Electrical Engineering, Slovak Academy of Sciences applied finite element analysis to ultrafast photoconductive switches of the metal–semiconductor–metal (MSM) type to explain why MSM devices with alloyed electrodes show improved photoresponse efficiency compared to devices with surface contact electrodes (p. 154). The alloyed device, despite having a somewhat larger capacitance, has an active region of lower resistance with a more-uniform and deeper-penetrating electric field and carrier transport current. The authors use the latter to explain the experimentally observed faster response of the alloyed device in terms of the equivalent lumped parameters. They also use the model to predict improved responsivity, based on electrode spacing and antireflective coating.

Scientists from LLE and the UR's Department of Mechanical Engineering describe an extension of the theory governing motion of polymer cholesteric liquid crystal flakes in the presence of ac electric fields by introducing the effect of gravity acting on flakes, an important term when the flake density differs from the density of the suspending host fluid (p. 80). Gravity becomes the driving force for flake relaxation when the electric field is removed, and it is now possible to predict relaxation times. Experimental results are compared with predictions from the extended theoretical model.

Beginning on p. 86, an article by scientists from LLE and the UR's Department of Mechanical Engineering presents a method for modeling the effect of microencapsulation on the electro-optical behavior of polymer cholesteric liquid crystal (PCLC) flakes suspended in a host fluid. Several microencapsulation configurations in an applied ac electric field are investigated using Comsol Multiphysics software in combination with an analytical model. The field acting on the flakes is significantly altered as various encapsulant materials and boundary conditions are explored. The modeling predicts that a test cell with multiple materials in the electric-field path can have a wide range of electro-optic responses in ac electric fields. Both theoretical predictions and experimental evidence show that for PCLC flake reorientation to occur as a result of Maxwell–Wagner polarization, a reasonably strong electric field must be present along with at least moderately dissimilar PCLC flake and host fluid material dielectric constants and conductivities. For materials with low dielectric constants, electrophoretic behavior is observed under dc drive conditions at high field strengths for all evaluated microencapsulation configurations. The modeling method is shown to be a useful predictive tool for developing switchable particle devices that use microencapsulated dielectric particles in a host fluid medium.

A spatially resolved spectral interferometry technique, known as S^2 imaging, has been used for the first time to measure the higher-order-mode content of a large-mode-area amplifier at full power (p. 134). The technique was adapted for the short-fiber amplifier at full power and revealed a small amount of a co-polarized LP_{11} mode. This mode's power, relative to the fundamental LP_{01} mode, depended on the alignment of the input signal at injection to the rod amplifier, and ranged from –18 dB, for optimized alignment, to –13 dB when the injection alignment was offset along the LP_{11} axis by 15 μm (30% of the 55-μm mode-field diameter). The increase in LP_{11} contributed to the M^2 degradation that was measured when the injection was misaligned.

Optical differentiation in a regenerative amplifier (RA) with temperature-tuned volume Bragg grating (VBG) as an intracavity spectral filter has been demonstrated for the first time (p. 141). The VBG as a spectrally selective resonator mirror works as an optical differentiator when the VBG reflection peak is detuned from the central laser wavelength. A simple, reliable laser system that produces multimillijoule ~150-ps pulses without mode-locking, using an RA with VBG as an optical differentiator, is described.

Scientists from the UR's Department of Electrical and Computer Engineering and the Laboratory for Solid State Physics, ETH Zurich, report on their experimental studies on the time-resolved carrier dynamics in high-quality $Al_{0.86}Ga_{0.14}N$ single crystals, grown using a solution technique in a high-nitrogen-gas-pressure system (p. 210). Optical measurements were performed using two-color, femtosecond pump–probe spectroscopy. By studying the correlation signal amplitude's dependence on both the pump light's absorbed power and wavelength, they obtained a two-photon-absorption coefficient $b = 0.442 \pm 0.02$ cm/GW, as well as its spectral dependence, and confirmed that within the tuning range of the laser, the latter was in very good agreement with the Sheik–Bahae theory for wide, direct-bandgap semiconductors. The optical bandgap of the $Al_{0.86}Ga_{0.14}N$ crystal was determined to be 5.81 ± 0.01 eV.

National Laser Users' Facility and External Users' Programs

Under the governance plan implemented in FY08 to formalize the scheduling of the Omega Laser Facility as a National Nuclear Security Agency (NNSA) facility, OMEGA shots are allocated by campaign. The majority of the FY09 target shots (~56.7%) were allocated to the National Ignition Campaign (NIC), and integrated experimental teams from LLNL, LANL, SNL, and LLE conducted a variety of NIC-related experiments on both the OMEGA and OMEGA EP Laser Systems. Twenty percent (20%) of the FY09 shots were allocated to high-energy-density stewardship experiments (HEDSE) from LLNL and LANL. Under this governance plan, 25% of the facility shots were allocated to basic science experiments. Roughly half of these were dedicated to university basic science, i.e., the National Laser Users' Facility (NLUF) Program, and the remaining shots were allotted to the Laboratory Basic Science (LBS) Program, comprising peer-reviewed basic science experiments conducted by the national laboratories and LLE/FSC. The Omega Facility is also being used for experiments by teams from the Commissariat à l'Énergie Atomique (CEA) of France and the Atomic Weapons Establishment (AWE) of the United Kingdom. These programs are conducted on the basis of special agreements put in place by DOE/NNSA and the participating institutions.

The external users during this year included a record 11 collaborative teams that participated in the NLUF Program as shown in Table I. Ten teams from LLNL, LANL, and LLE were allotted shots under the LBS Program (Table II). Integrated experimental teams from the national laboratories and LLE conducted 851 shots for the NIC, and investigators from LLNL, LANL, and LLE conducted over 232 shots for the HEDSE programs. A total of 56 shots were conducted by scientists from CEA and 35 shots were carried out by scientists from AWE.

1. NLUF Programs

FY09 was the first of a two-year period of performance for the NLUF projects approved for the FY09–FY10 funding and OMEGA shots. Eleven NLUF projects were allotted OMEGA and OMEGA EP shot time and received a total of 165 shots on OMEGA and 43 shots on OMEGA EP in FY09. Some of this work is summarized beginning on p. 218. A new solicitation will be issued by DOE in FY10 for NLUF grants for the period FY11–FY12.

A detailed article on Lorenz mapping of magnetic fields in hot, dense plasma, one of the NLUF experiments carried out by a collaborative team led by the Plasma Science and Fusion Center–MIT, is presented beginning on p. 129. The authors show that monoenergetic proton radiography combined with Lorentz mapping can be used to uniquely detect and discriminate magnetic and electric fields. Protons were used to image two identical expanding plasma bubbles, formed on opposite sides of a 5-μm-thick plastic (CH) foil by two 1-ns-long laser-interaction beams. The second bubble reversed the sign of any magnetic fields relative to the first bubble by the protons, while keeping the electric fields the same. Field-induced deflections of the monoenergetic, 14.9-MeV probe protons passing through

Table I: FY09–FY10 NLUF Projects.

Principal Investigator	Affiliation	Proposal Title
F. Beg	University of California, San Diego	Systematic Study of Fast-Electron Transport and Magnetic Collimation in Hot Plasmas
R. P. Drake	University of Michigan	Experimental Astrophysics on the OMEGA Laser
R. Falcone	University of California, Berkeley	Detailed *In-Situ* Diagnostics of Multiple Shocks
U. Feldman	ARTEP, Inc.	OMEGA EP–Generated X-Ray Source for High-Resolution 100- to 200-keV Point-Projection Radiography
Y. Gupta	Washington State University	Ramp Compression Experiments for Measuring Structural Phase Transformation Kinetics on OMEGA
P. Hartigan	Rice University	Dynamics of Shock Waves in Clumpy Media
R. Jeanloz	University of California, Berkeley	Recreating Planetary Core Conditions on OMEGA, Techniques to Produce Dense States of Matter
K. Krushelnick	University of Michigan	Intense Laser Interactions with Low-Density Plasmas Using OMEGA EP
R. Mancini	University of Nevada, Reno	Three-Dimensional Studies of Low-Adiabat Direct-Drive Implosions on OMEGA
M. Meyers	University of California, San Diego	Response of BCC Metals to Ultrahigh Strain Rate Compression
R. D. Petrasso	Massachusetts Institute of Technology	Monoenergetic Proton and Alpha Radiography of Laser-Plasma-Generated Fields and of ICF Implosions

Table II: Approved FY09 LBS Experiments.

Principal Investigator	Affiliation	Proposal Title	Facility Required
R. Betti	LLE/FSC	Ultra-Strong Shock and Shock-Ignition Experiments on OMEGA EP	OMEGA EP long pulse/short pulse
H. Chen	LLNL	Electron–Positron Jets	OMEGA EP short pulse/2 beams
J. H. Eggert	LLNL	Powder X-Ray Diffraction on OMEGA: Phase Transitions in Tin	OMEGA
M. B. Hegelich	LANL	Proton and Light Ion Production for Fast Ignition and Warm Dense Matter Applications	OMEGA EP short pulse
D. G. Hicks	LLNL	A New Technique for Efficient Shockless Compression to Several Mbar: Studies Using X-Ray Absorption Spectroscopy	OMEGA 40 beams
A. J. MacKinnon	LLNL	Fast Electron Transport in Hot Dense Matter	OMEGA EP long pulse
H.-S. Park	LLNL	Study of High-Z Material Properties Under Compression Using High Energy Backlighter Diffraction	OMEGA EP long pulse/short pulse
P. K. Patel	LLNL	Fundamental Benchmarking of Relativistic Laser–Matter Interaction Physics	OMEGA EP short pulse
S. P. Regan	LLE	Probing Hydrogen–Helium Warm Dense Matter (WDM) with Inelastic X-Ray Scattering: Toward the Equation of State of Jupiter's Core	OMEGA
W. Theobald	LLE	Integrated Core Heating for Fast Ignition	OMEGA and OMEGA EP

the two bubbles, measured quantitatively with proton radiography, were combined with Lorentz mapping to provide separate measurements of magnetic and electric fields. The authors' results provided absolute identification and measurement of a toroidal magnetic field around each bubble and determined that any electric field component parallel to the foil was below measurement uncertainties.

2. FY09 LLNL Omega Facility Programs

In FY09, LLNL led 238 target shots on the OMEGA Laser System. Approximately half of these shots supported the National Ignition Campaign (NIC). The remainder were dedicated to experiments for the high-energy-density stewardship experiments (HEDSE). Objectives of the LLNL-led NIC campaigns on OMEGA included

- *Laser–plasma interaction studies in physical conditions relevant for the National Ignition Facility (NIF) ignition targets*
- *Demonstration of* T_r *= 100-eV foot-symmetry tuning using a re-emission sphere*
- *X-ray scattering in support of conductivity measurements of solid-density Be plasmas*
- *Experiments to study the physical properties (thermal conductivity) of shocked fusion fuels*
- *High-resolution measurements of velocity nonuniformities created by microscopic perturbations in NIF ablator materials*
- *Development of a novel Compton radiography diagnostic platform for ICF experiments*
- *Precision validation of the equation of state for quartz*

The LLNL HEDSE campaigns included the following:

- *Quasi-isentropic (ICE) drive used to study material properties such as strength, equation of state, phase, and phase-transition kinetics under high pressure*
- *Development of a high-energy backlighter for radiography in support of material strength experiments using OMEGA EP and the joint OMEGA/OMEGA EP configuration*
- *Debris characterization from long-duration, point-apertured, point-projection x-ray backlighters for NIF radiation transport experiments*
- *Demonstration of ultrafast temperature and density measurements with x-ray Thomson scattering from short-pulse-laser–heated matter*
- *Development of an experimental platform to study non-local thermodynamic equilibrium (NLTE) physics using direct-drive implosions*
- *Opacity studies of high-temperature plasmas under LTE conditions*
- *Characterization of copper (Cu) foams for HEDSE experiments*

A summary of experiments carried out by LLNL at the Omega Laser Facility in FY09 begins on p. 235.

3. FY09 LANL Omega Facility Programs

Los Alamos National Laboratory (LANL) successfully fielded a range of experiments on the OMEGA laser during FY09 in support of the national program. LANL conducted a total of 104 target shots: 93 on OMEGA and 11 on OMEGA EP. Collaborations with LLNL, LLE, LULI, NRL, MIT, NSTec, UCSD, and AWE remain an important component of LANL's program on OMEGA. The LANL programs executed on OMEGA in FY09 included the following:

- *NIF 5*
- *High Z*
- *OMEGA EP ions*
- *Gamma-reaction history diagnostic*
- *Defect implosion experiment (DIME)*
- *High-energy backlighting on OMEGA EP*
- *Neutron imaging*

The LANL experiments are summarized beginning on p. 246.

4. FY09 AWE Omega Facility Programs

The AWE conducted 35 OMEGA laser target shots and joined CEA on 5 shots on OMEGA EP. AWE-led experiments on OMEGA in FY09 continued to test radiation–hydrodynamic simulations of hohlraum drive and capsule implosion under

conditions where a hohlraum target was driven in a deliberately asymmetric manner. The FY09 experiments are summarized beginning on p. 254.

5. FY09 CEA Omega Facility Programs

CEA conducted 56 OMEGA shots in FY09 (51 on OMEGA and 5 on OMEGA EP (jointly with AWE). The CEA efforts included the following:

- *CEA copper activation diagnostic for DT neutron-yield measurements*
- *MeV photon x-ray sources produced by OMEGA EP*
- *Two new neutron imaging systems on OMEGA*
- *Ablative Rayleigh–Taylor stabilization mechanism experiment*

A summary of the FY09 CEA programs on OMEGA begins on p. 256.

Laboratory Basic Science (LBS) Experiments

Ten proposals were approved and were allocated 25 shot days on OMEGA in FY09 under the Laboratory Basic Science Program (six proposals from LLNL, three from LLE, and one from LANL as shown on Table II).

Unfortunately, because of the DOE funding shortfall in FY09, only 17 days (109 shots) of LBS experiments were actually funded and carried out during this fiscal year. The FY10 solicitation for the LBS Program resulted in 25 proposals with shot requests totaling 63.5 shot days. After peer review by an independent committee, 13 LBS proposals have been recommended for 29 shot days in FY10. Three additional shot days were recommended and approved for FY09 make-up shots. The approved FY10 LBS proposals are listed in Table III.

Table III: Approved FY10 LBS Experiments.

Principal Investigator	Affiliation	Proposal Title	Facility Required
R. Betti	LLE/FSC	Integrated Shock-Ignition Experiments on OMEGA	OMEGA
P. M. Celliers	LLNL	Measurement of the Viscosity of Shock-Compressed Fluids: Studies of Water and Silica	OMEGA
H. Chen	LLNL	Producing Pair Plasma and Gamma-Ray Burst Using OMEGA EP	OMEGA EP
D. E. Fratanduono	LLE	Optical Properties of Compressed LiF	OMEGA and OMEGA EP
D. H. Froula/J. S. Ross	LLNL	First Observations of Relativistic Plasma Effects on Collective Thomson Scattering	OMEGA
S. H. Glenzer	LLNL	Capsules Adiabat Measurements with X-Ray Thomson Scattering	OMEGA
D. G. Hicks	LLNL	Ramp and Multi-Shock Compression of Iron to Several Megabars: Studies Using Extended and Near Edge X-Ray Absorption Spectroscopy	OMEGA
H.-S. Park	LLNL	Study of High-*Z* Material Properties under Compression Using High-Energy Backlighter Diffraction	OMEGA EP
P. K. Patel	LLNL	Benchmarking Laser-Electron Coupling at Fast Ignition–Relevant Conditions	OMEGA EP
S. P. Regan	LLE	Validating Inelastic X-Ray Scattering from H and H/He Warm Dense Matter with Shock Velocity Measurements: Toward the Equation of State of Jupiter's Core	OMEGA
R. Smith/J. H. Eggert/ S. M. Pollaine	LLNL	Phase Transformation Kinetics	OMEGA
C. Stoeckl/ W. Theobald/W. Seka	LLE	Channeling in Long-Scale-Length Plasmas	OMEGA EP
W. Theobald	LLE	Integrated Core Heating for Fast Ignition	OMEGA and OMEGA EP

One of the LBS experiments is focused on studies of shock ignition and is based on a collaboration including LLE, the Fusion Science Center for Extreme States of Matter and Fast Ignition Studies, and PSFC–MIT. An article beginning on p. 117 discusses shock-ignition experiments that have been performed on OMEGA with peak shock-generating laser intensities of $\sim 1 \times 10^{16}$ W/cm^2. Shock ignition is a two-step ICF concept in which a strong shock wave is launched at the end of the laser-drive pulse to ignite the compressed core, relaxing the driver requirements and promising high gains. In the experiments described in this article, room-temperature plastic shells filled with D_2 gas were compressed on a low adiabat by 40 beams of the 60-beam OMEGA Laser System. The remaining 20 beams were delayed and tightly focused onto the target to drive a strong shock into the compressed core. Good coupling of the shock-beam energy was observed in these experiments, leading up to an ~20× increase in neutron yield compared to a similar implosion without the high-intensity pulse. The authors observed significant stimulated Raman backscattering of laser energy; however, fast-electron measurements showed a relatively cold energy distribution. These fast electrons are actually beneficial for shock ignition since they have short mean free paths and are stopped in the thin outer layer of the imploding target, augmenting the strong hydrodynamic shock.

Laser-driven magnetic-flux compression in high-energy-density plasma experiments (p. 123) is an LBS program that is based on a collaboration involving LLE, FSC, MIT, and LLNL. During FY09, this team demonstrated for the first time magnetic-field compression to many tens of megagauss (MG) in cylindrical implosions of inertial confinement fusion targets. The very high magnetic-flux compression was achieved using the ablative pressure of the OMEGA laser to drive a cylindrical shell at high implosion velocity, trapping and compressing an embedded external field to tens of MG, high enough to magnetize the hot-spot plasma. The magnetic fields in the compressed core were probed via proton deflectrometry using the fusion products from an imploding D^3He target. Line-averaged magnetic fields between 30 and 40 MG were observed.

An LBS experiment based on a collaboration involving LLNL, LLE, and Rice University demonstrated the highest positron production rate ever achieved in the laboratory (Fig. 1).

FY09 Laser Facility Report

During FY09 the Omega Laser Facility conducted 1153 target shots on OMEGA and 349 target shots on OMEGA EP for a total of 1502 combined target shots (see Table IV). Twenty-four DT and 24 D_2 low-adiabat spherical cryogenic target implosions were conducted on OMEGA. Triple-picket pulse-shaping developments highlighted the ongoing development of

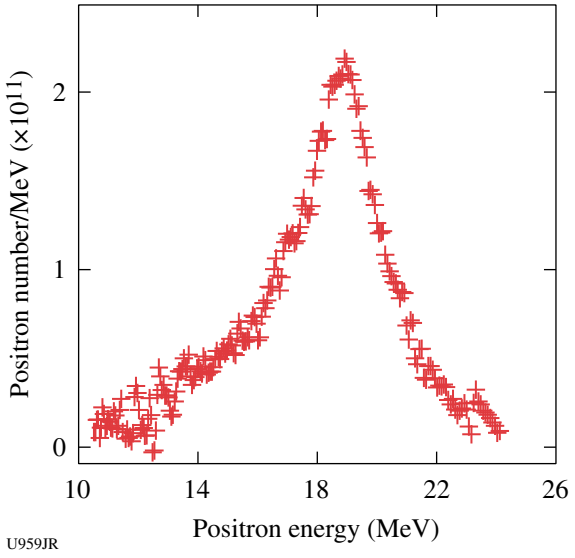

Figure 1
Positron spectrum measured on the OMEGA EP laser.

Table IV: OMEGA Facility target shot summary for FY09.

OMEGA Target Shot Summary					
Laboratory	Planned Number of Target Shots	Actual Number of Target Shots	NIC	Shots in Support of NIC	Non-NIC
LLE	476	488	68	420	0
LLNL	200	230	125	0	105
NLUF	145	165	0	0	165
LANL	85	93	3	0	90
LBS	70	73	0	0	73
CEA	45	51	0	0	51
AWE	30	35	0	0	35
U. Mich.	10	11	0	0	11
SNL	5	7	7	0	0
Total	1066	1153	203	420	530

OMEGA EP Target Shot Summary					
Laboratory	Planned Number of Target Shots	Actual Number of Target Shots	NIC	Shots in Support of NIC	Non-NIC
LLE	215	212	0	212	0
LLNL	40	42	16	0	26
NLUF	40	43	0	0	43
LBS	45	36	0	0	36
LANL	10	11	0	0	11
CEA/AWE	5	5	0	0	5
Total	355	349	16	212	121

direct-drive cryogenic implosion capability. A planar cryogenic platform to measure spherical shock timing was validated and used extensively to support spherical cryogenic experiments. A total of 31 planar cryogenic target shots were taken. The OMEGA Availability and Experimental Effectiveness averages for FY09 were 93% and 96%, respectively.

OMEGA EP was operated extensively in FY09 for a variety of internal and external users. A total of 298 short-pulse IR target shots were conducted. Of these, 212 target shots were taken on the OMEGA EP target chamber and 86 joint target shots were taken on the OMEGA target chamber. Beams 1 and 2 were activated to target in the UV, and the first four-beam UV target shots were conducted. A total of 76 OMEGA EP target shots included UV beams. OMEGA EP averaged 4.7 target shots per day with Availability and Experimental Effectiveness averages for FY09 of 90% and 97%, respectively.

Education

As the only major university participant in the National ICF Program, education continues to be an important mission for the Laboratory. Laboratory education programs span the range of high school (p. 214) to graduate education.

1. High School Student Program

During the summer of 2009, 16 students from Rochester-area high schools participated in the Laboratory for Laser Energetics' Summer High School Research Program. The goal of this program is to excite a group of high school students about careers in the areas of science and technology by exposing them to research in a state-of-the-art environment. Too often, students are exposed to "research" only through classroom laboratories, which have prescribed procedures and predictable results. In LLE's summer program, the students experience many of the trials, tribulations, and rewards of scientific research. By participating in research in a real environment, the students often become more excited about careers in science and technology. In addition, LLE gains from the contributions of the many highly talented students who are attracted to the program.

The program culminated on 26 August with the "High School Student Summer Research Symposium," at which the students presented the results of their research to an audience including parents, teachers, and LLE staff. The students' written reports will be made available on the LLE Web site.

Two hundred and forty-nine high school students have now participated in the program since it began in 1989.This year's students were selected from a record 80 applicants.

At the symposium LLE presented its 13th annual William D. Ryan Inspirational Teacher Award to Mr. Jeffrey Klus, a mathematics teacher at Fairport High School. This award is presented to a teacher who motivated one of the participants in LLE's Summer High School Research Program to study science, mathematics, or technology and includes a $1000 cash prize.

2. Undergraduate Student Programs

Approximately 60 undergraduate students participated in work or research projects at LLE this past year. Student projects include operational maintenance of the Omega Laser Facility; work in laser development, materials, and optical-thin-film–coating laboratories; computer programming; image processing; and diagnostics development. This is a unique opportunity for students, many of whom will go on to pursue a higher degree in the area in which they gained experience at the Laboratory.

3. Graduate Student Programs

Graduate students are using the Omega Facility as well as other LLE facilities for fusion and high-energy-density physics research and technology development activities. These students are making significant contributions to LLE's research program. Twenty-five faculty from the five University academic departments collaborate with LLE scientists and engineers. Presently, 88 graduate students are involved in research projects at LLE, and LLE directly sponsors 37 students pursuing Ph.D. degrees via the NNSA-supported Frank Horton Fellowship Program in Laser Energetics. Their research includes theoretical and experimental plasma physics, high-energy-density physics, x-ray and atomic physics, nuclear fusion, ultrafast optoelectronics, high-power-laser development and applications, nonlinear optics, optical materials and optical fabrication technology, and target fabrication.

In addition, LLE directly funds research programs within PSFC–MIT, the State University of New York (SUNY) at Geneseo, the University of Nevada, Reno, and the University of Wisconsin. These programs involve a total of approximately 16 graduate students, 27 undergraduate students, and 7 faculty members.

Robert L. McCrory
Director, Laboratory for Laser Energetics
Vice Provost, University of Rochester

Demonstration of the Shock-Timing Technique for Ignition Targets at the National Ignition Facility

Introduction

Ignition experiments at the National Ignition Facility (NIF) will use x rays in indirect-drive (hohlraum) targets to drive implosions of capsules containing deuterium–tritium (DT) fuel.[1] These inertial confinement fusion (ICF) targets use three shock waves to quasi-isentropically compress the capsule before the main compression wave drives the implosion of the fuel assembly.[2] The goal is to minimize the required drive energy by minimizing the entropy imparted to the capsule as it is imploded. To achieve ignition, both the strength and timing of the shock and compression waves must be accurately set.

The National Ignition Campaign (NIC) is a multi-laboratory program[3] that designed and will perform experiments that lead to ignition on the NIF. The campaign includes various tuning experiments that iteratively optimize the laser and target parameters to achieve specified conditions and maximize target performance. To achieve optimal shock conditions, experiments using optical diagnostics will detect the shock-velocity temporal profiles, providing both the strength and timing of the various shocks within the capsule fuel.[4] The tuning campaign will use these data to adjust the laser (and, therefore, x-ray) drive until the shock strengths and timings meet design specifications. These experiments require surrogate targets that make it possible to diagnostically access the inside of the capsule but closely mimic the behavior of the ignition targets. The ignition capsule in these targets has a re-entrant Au cone filled with liquid deuterium and extends out beyond the hohlraum wall.[5] With these targets, optical diagnostics can detect spherically converging shock waves within the deuterium-filled capsule.

Optical diagnostics can readily measure both shock velocity and timing to the precision and accuracy required for ignition target designs. These measurements, taken in a cryogenic capsule embedded in a hohlraum and driven to radiation temperatures in excess of 150 eV, present considerable challenges. To demonstrate that this is a viable technique for the NIF, experiments were performed at the Omega Laser Facility.[6] This article discusses the resolution of several issues associated with this approach and demonstrates that this technique is a valid method to time shocks in ignition targets on the NIF.

Shock Timing

ICF targets are spherical shells that have a layer of solid (cryogenic) DT fuel that must be compressed to 1000 g/cc on a low adiabat and then heated to ~5 keV to initiate ignition and burn.[1] This compression is produced by the ablation process that can be driven either directly or indirectly by laser beams. In the indirect case, the capsule is contained in a cylindrical hohlraum that is irradiated by many high-power laser beams that produce up to a 1×10^{15} W/cm^2 flux of thermal x rays that drive an ablative implosion of the capsule. Target design is a delicate optimization of maximizing fuel compression while minimizing the internal energy imparted to the pusher and fuel. The primary approach is to approximate an isentropic compression using a series of three shock waves of increasing strength, followed by a compression wave that drives the compressed shell of fuel to implode at velocities of $\sim 3.6 \times 10^7$ cm/s. Shock waves provide discrete "markers" that will be used to diagnose the compression history. The steps in drive pressure (that produce the shocks) are controllable parameters that make it possible for the compression to be optimized while controlling entropy increases. Shock waves are also desirable for ablators that may have a spatial structure that can be smoothed out by the melting produced by a first shock.[7]

In its simplest form, an ICF target is a two-layer system—an ablator surrounding a layer of DT ice. (Actual ablators have internal layers of varied composition to enhance the absorption and ablation processes.[8]) For optimal target performance each shock must have the correct strength. Specification requires that the velocity be set to a precision of 1%. The shocks must arrive at the inner DT-fuel surface in a tight sequence, with their launch times known to a precision of 50 ps (Ref. 4). The assembled mass is swept inward by the compression wave that must be timed to a precision of 100 ps. When properly tuned in strength and timing, the shocks minimize the adiabat (internal energy) of the DT fuel, keeping it on a low isentrope. By

arriving at the inner surface of the ice in a tightly controlled sequence, most of the fuel has been shocked and re-shocked along a low adiabat.

If the later, stronger shocks overtake the first shock too early, a large portion of the fuel is heated by this strong shock and will be on a higher adiabat and be harder to compress. Late coalescence means that previous shocks have time to unload significant material from the inner surface of the ice, creating a low-density blowoff that would be significantly heated by the subsequent shocks, again placing the fuel on a higher isentrope.

Temporal profiles of the laser and resultant radiation temperature need to produce the desired shock strengths and timing. The residual uncertainties in the calculated hohlraum drive and the opacity and equation of state (EOS) of the ablator and fuel require full-scale tuning experiments to achieve the precision required for ignition. The NIC includes experiments that will iteratively "fine tune" the drive to optimize shock timing. Critical to this effort are precise measurements of shock timing in surrogate targets that are equivalent to ignition targets.

Figure 117.1(a) depicts the Lagrangian trajectories of four shocks through the ablator and DT ice. For optimal performance, these shocks should arrive at the inner DT-ice surface in a tight temporal sequence.[4] The laser pulse shape for ignition targets is shown schematically in Fig. 117.1(b), along with the expected radiation temperature in the hohlraum. The steps in the radiation temperature launch three successive shocks with pressures of approximately 0.8, 4, and 12 Mb in the DT fuel. The main compression wave begins with pressures greater than 40 Mb. (Individual designs vary these values slightly.)

Since the EOS of deuterium is known,[9] a measurement of the shock velocity provides all the pertinent information about the shock wave. The NIC shock-timing campaign will use shock-velocity measurements to iteratively adjust the level and timing of each "step" in power to produce the desired shock velocity (pressure) and timing. Knowledge of the temporal velocity profiles provides, through integration, the positions of shock coalescence.

The velocity interferometry system for any reflector (VISAR)[10] probe beam is reflected off the leading shock front (the one closest to VISAR). At these pressures, shock-compressed deuterium is a metal-like reflector that is opaque to visible light.[11] The following shock fronts cannot be viewed inside the opaque medium; instead, they are detected only when they overtake or coalesce with the leading shock front.

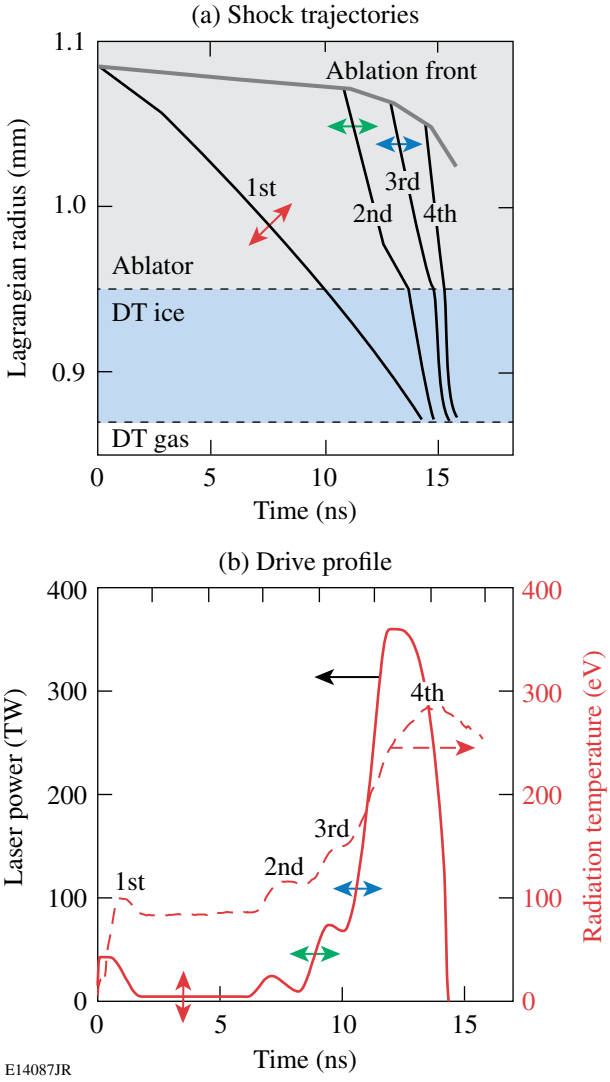

Figure 117.1
(a) Lagrangian trajectories of shocks in an ignition target showing optimal timing with shocks arriving at the inner DT-ice surface in a tight sequence. (b) Temporal history of laser intensity and resulting radiation temperature for an ignition target on the NIF. A shock-timing tuning campaign will iteratively adjust (arrows) the laser pulse shape to optimize shock timing.

The single-shock velocities corresponding to the pressures of the first three steps in the drive pulse (i.e., following coalescence) are approximately 20, 36, and 57 km/s, respectively. (Again, there are several designs and the specified velocities range by ~5% from those values, depending on how the implosion optimization is performed.) For a given design the velocity can have a 2% shot-to-shot variation, but to ensure proper timing, the shock velocities will be measured with a precision of 1% and the coalescence times to less than 30 ps. For the 75-μm-thick DT layer the transit time of the first shock is

~3.75 ns. By integrating the first shock velocity (known to 1%) up to the coalescence time (known to 30 ps), one can determine the coalescence position to a precision of <2 μm. The precision of the VISAR diagnostic is more than adequate to determine this position. The error budget for shock-strength and timing experiments is readily met if the velocity is measured to 1% and shock timing is measured to 30 ps.

A DT ignition capsule has a specific drive profile needed to achieve optimal performance. To guide the ignition-tuning campaign, that optimal drive profile is applied (in simulations) to a capsule containing liquid deuterium–deuterium (DD). The resultant shock structure (velocity profiles and timing) in that simulation then serves as the metric to which shock-timing experiments are gauged. The optimal shock strengths (velocities) in liquid DD are obtained from this simulation. Because the shock velocities (but not the shock pressures) are nearly the same in liquid DD as in solid DT, the optimal coalescence position for the shock-timing experiments is very close to that in the solid-DT layer of an ignition capsule. This simulation procedure introduces a surrogacy error that is estimated to be less than 1% in shock velocity.

Experimental Technique

1. VISAR Windows

VISAR has been extensively used to detect and measure laser-driven shock waves in transparent media and has a demonstrated shock-speed precision of 1%–2% and temporal accuracy of <30 ps (Refs. 12–14). Shock waves with pressures above ~0.2 Mb transform liquid deuterium (normally transparent) into a conducting medium;[11] as a result, the steep shock front (a conducting surface) readily reflects the VISAR probe beam at a wavelength of 532 nm (and similarly at 590 nm for the NIF VISAR). The arms of a VISAR interferometer have unequal optical paths and produce an output phase that is proportional to the Doppler shift of the reflected probe beam and to the difference in the unequal paths (usually expressed as a time delay). The time delay determines the velocity sensitivity of the interferometer and is adjustable (proportional to the thickness of a glass delay element placed in one arm of the interferometer). For these experiments, the VISAR on OMEGA had a velocity error of ~1.7%. The NIF VISAR is designed to achieve 1% velocity measurements.

Cryogenic targets require a closed volume to retain the deuterium gas. In a standard target, the spherical shell is the boundary of that volume. In shock-timing experiments a line of sight is needed for VISAR to probe the shock-velocity profile. Various target configurations were considered, but the stringent performance tolerances dictated that shock-timing surrogate targets mimic ignition targets with high fidelity. For the NIC tuning experiments, spherical targets will be fitted with a re-entrant cone that extends through the hohlraum wall and is capped by a 20-μm-thick quartz window that confines the DD fuel. This target configuration is shown in Fig. 117.2. Integrated 3-D simulations of this target show that perturbations to the radiation temperature and hohlraum symmetry are minimal.[15] By design, the change in the albedo caused by the portion of the cone traversing the hohlraum-capsule space is offset by that of the sections of ablator surface and hohlraum wall displaced by that cone. It is expected that on the hohlraum wall, where shock timing is measured, the radiation flux will mimic a full ignition target to ~4% (1% in T_{rad}) (Ref. 5).

It has been shown that for direct-drive targets at high intensities the normally transparent material ahead of the shock wave can absorb the VISAR probe laser.[16] This is caused by high-energy x rays produced in the laser-plasma corona.[17] The x rays photoionize the unshocked material, creating free electrons that interact with and absorb the probe light, causing a "blanking" of the probe beam in the material. This could compromise the VISAR data. This is not expected to be a problem in the deuterium (which has a low x-ray-absorption cross section), but the diagnostic window that retains the DD

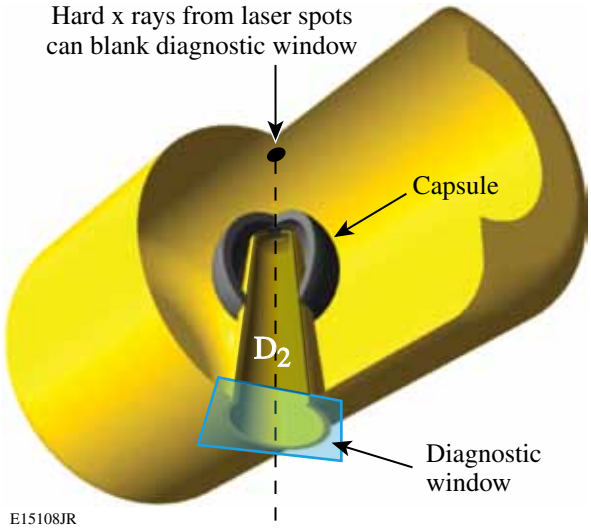

Figure 117.2
NIC shock-timing tuning experiments will use ignition-style targets that have a re-entrant cone in the capsule. The capsule and cone are filled with liquid deuterium. Optical diagnostics probe the inside of the capsule through the window and aperture in the cone.

in the NIF shock-timing targets (Fig. 117.2) can experience this ionization blanking.

Single-sided [one laser entry hole (LEH)] hohlraum experiments with cryogenic and warm targets were used to study this effect and to select a window material. Windows made of silicon nitride, diamond, sapphire, and quartz were tested. Quartz (20 μm thick) was chosen because of its resistance to blanking (band gap of ~15 eV), optical quality, and ease of fabrication. Though quite resilient, quartz, nevertheless, blanks if exposed to sufficient x-ray flux.

In NIF shock-timing targets, the VISAR window has a line of sight through the ablator material to the hohlraum wall that is directly irradiated by laser beams (Fig. 117.2). Since the ablator absorbs most of the radiation below ~1.5 keV, ionization blanking in these targets results primarily from the Au M-band (2 to 4 keV) emission produced by the laser spots. The VISAR cone has a 260-μm hole at the end through which shock timing is measured. The aperture size has been chosen to limit the extent of the hohlraum wall with a "view" of the VISAR window without limiting the area over which a VISAR signal can be collected for NIC-scale capsules. Figure 117.3(a) is a map of beam placement on the interior of a NIF ignition hohlraum. While the capsule is driven by *thermal* radiation from many beams, the VISAR window is irradiated by M-band emission ($h\nu > 2$ keV) that originates only from beam spots in the line of sight through the cone aperture. The region on the hohlraum wall that can irradiate the VISAR window is shown as the black dot in Fig. 117.3(a). Two NIF quad beam spots overlap at that point.

A series of experiments were performed on the OMEGA laser using planar targets to investigate the effect of x-ray emission from laser spots on the optical transmission of quartz windows. The configuration is shown in Fig. 117.3(b). A gold foil was placed 1.5 mm from a Be−Cu−Be sandwich (75, 0.5, and 75 μm thick, respectively) that mimics the opacity of a typical NIC ablator design. An aperture was placed directly behind the ablator and a window was placed 3.5 mm from the Au foil. VISAR probed the rear surface of the aperture and ablator (through the aperture). Nine OMEGA beams without beam smoothing were focused onto the gold foil to replicate the wall intensity of a NIF target at the relevant incidence angle (60°). The window transmission was observed, and the intensity at which x rays from the laser spots would blank the window was determined. The energy and pulse widths available on OMEGA dictate that the test be done in two steps,

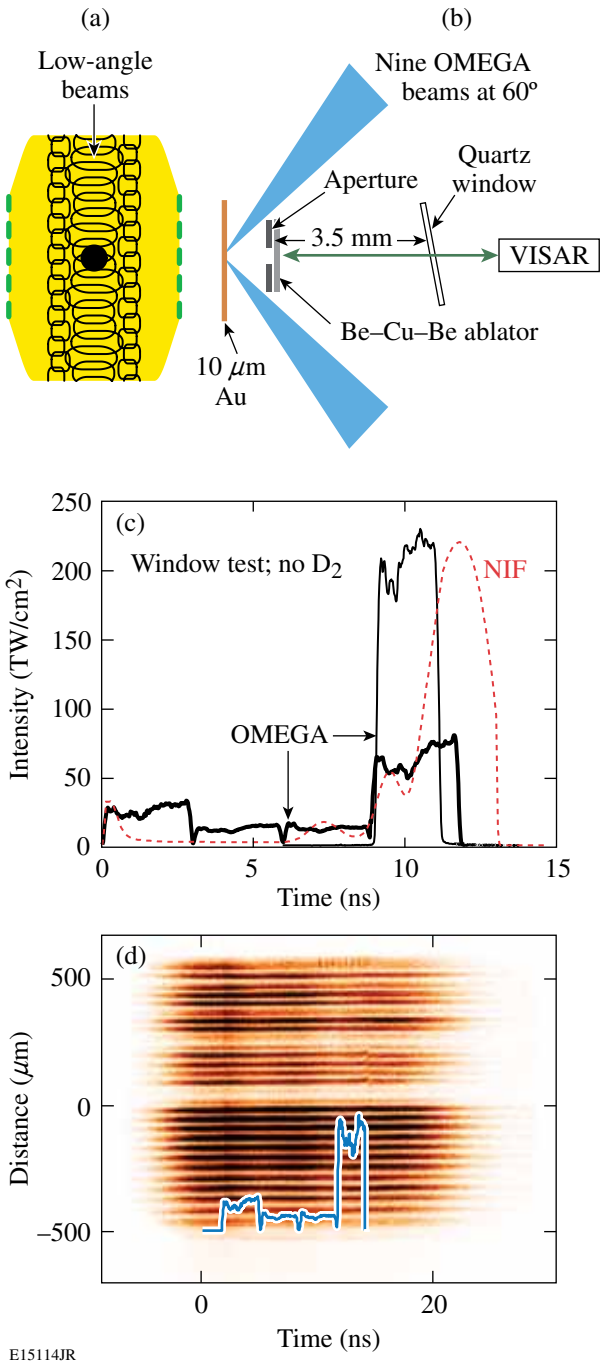

Figure 117.3
(a) The pattern of beam spots in an ignition hohlraum. (b) Target configuration to study effects of M-band emission on windows. (c) NIF laser intensity at the hohlraum equator wall (dashed curve); laser intensity for OMEGA experiments with stacked pulses (solid curves). (d) VISAR data from a stacked-pulse OMEGA experiment showing continuous fringes. The quartz window remains transparent throughout irradiation history, indicating that M-band emission from the laser spot does not "blank" (photoionize) the quartz.

separately measuring peak and integrated fluences associated with ignition-target conditions up to the breakout time of the third shock. Figure 117.3(c) (dashed curve) shows the incident intensity at the NIF hohlraum wall at the VISAR window line of sight [Fig. 117.3(a)]. The intensity profile for the OMEGA experiment with nine beams having temporally square pulses staggered to approximate the NIF wall intensity up to 12 ns is also shown (thick curve). Figure 117.3(d) shows a VISAR record with fringes that have continuous intensity throughout that experiment, indicating that the window remains transparent. Similar results were obtained for nine beams overlapped [thin solid curve in Fig. 117.3(c)] to replicate the intensity at the fourth rise. To investigate the limiting flux for this configuration, a third experiment was performed with a 1-ns pulse at 500 TW cm^2. At this fluence the quartz window blanked, but this is 2.5× higher than required for the NIF.

These results indicate that the quartz windows remained transparent when exposed to both the instantaneous flux and the integrated flux (up to the third shock) required for shock timing. These tests are conservative in that the NIF beams have high angles of incidence and will traverse considerable plasma en route to the hohlraum wall, reducing the actual intensity at the wall. Also, the Au foil was 1.5 mm from the aperture and 3.5 mm from the window; in the NIF targets those distances will be ≈2 mm and ≈8 mm, respectively.

2. Hohlraum Experiments

The radiation environment in a laser-driven hohlraum is different than that of an open-geometry planar-target laser plasma: the laser beams overlap and are tightly focused at the LEH and the plasma scale lengths are changed by the closed geometry. VISAR measurements were performed with hohlraum targets to investigate if they could cause window blanking or other deleterious effects.

For these tests, NIF-sized Au re-entrant cones were inserted into OMEGA-scale hohlraums (2.55 mm long, 1.6 mm in diameter with 1.2-mm laser entrance holes). The cones were 5 mm long and had an 11° opening angle (to accommodate the *f*/3 VISAR focal cone). The NIF tip has a 10-μm wall formed into a spherical shape that will be ultimately placed within ~200 μm of the spherical-ablator inside surface. That tip has a 260-μm-diam aperture through which shocks are viewed. Inside the shell the cone wall is 50 μm thick and the rest of the cone is 100-μm-thick Au. The hohlraums were empty: no gas fill, no LEH windows. Figure 117.4(a) shows three views of these targets.

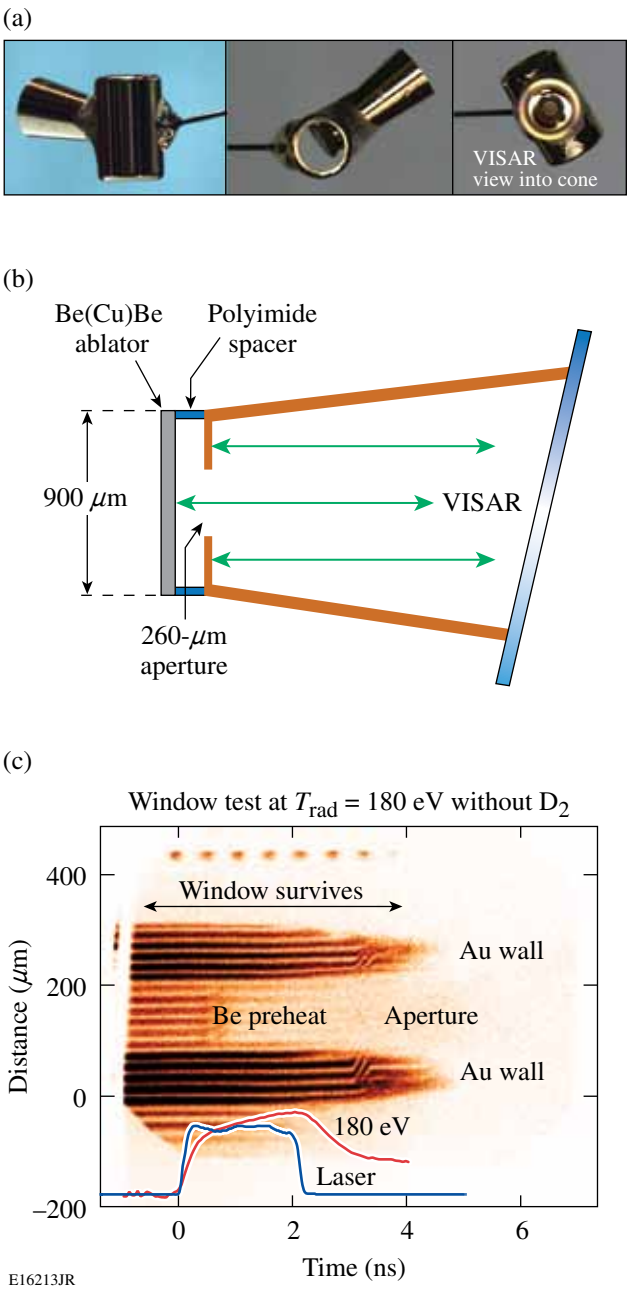

Figure 117.4
(a) The OMEGA targets have NIF-sized diagnostic cones inserted into the OMEGA scale-1 hohlraums. (b) The ablator and cone tip assembly for the OMEGA shock-timing tests in hohlraum targets. The Be−Cu sandwich replicates the opacity of a NIF ablator. (c) VISAR data for a warm, empty hohlraum heated to 180 eV. The probe beam reflects off the cone face and the ablator (through cone aperture). These data show the Be ablator unloading because of preheat and window transparency persisting throughout the experiment, thereby proving viability of this technique.

The OMEGA experiments used planar ablators, so those cones had a 10-μm-thick, 260-μm-aperture planar tip. The rest of the cone was identical to the NIF cone design. The ablators were sandwiches of Be and Cu to simulate the x-ray opacity of the Cu-doped Be ablators[2] for the NIF. They were comprised of two 75-μm Be foils with a 0.5-μm Cu foil in between and were "brazed" to form a glueless bond. The ablators were mounted 190 μm from the cone tip to replicate the shell-to-cone-tip distance in the NIF targets.

One concern was that M-band x rays entering the aperture at high angles could heat the inner cone wall sufficiently to create a secondary hohlraum that would re-radiate and blank the window. To mimic the spherical-capsule geometry, which allows these high-angle rays to enter the aperture, the ring that held the planar ablator away from the cone tip was made of 60-μm polyimide. This ring has similar opacity to the Be−Cu ablator. The ablator and cone geometry are shown in Fig. 117.4(b).

The VISAR diagnostic is not perpendicular to any convenient and symmetric hohlraum axes in the OMEGA chamber. Rather than perturb the irradiation pattern and line of sight for radiation-temperature measurements (Dante), the VISAR cones were inserted 79.2° from the hohlraum axis to accommodate this offset [Fig. 117.5(a)]. This deviation from the NIF geometry is considered conservative since, at this angle, the cone views the region irradiated by beams with lower angles of incidence and are, therefore, of higher intensity than those at the equator. The cones were inserted so the ablators were on the central axis of the hohlraum. The ablators were ~0.8 mm from the hohlraum wall, less than half the distance of the NIF targets to the hohlraum wall.

The hohlraums were irradiated by 38 OMEGA beams with no beam smoothing and having 2-ns-long, temporally square pulses to produce radiation temperatures of >180 eV. VISAR measurements of the rear side of the ablator (i.e., made through the window and cone aperture) are shown in Fig. 117.4(c). The VISAR data comprise a series of interferometer fringes[13,16] whose vertical position is proportional to the velocity of the reflecting surface (shock wave or ablator surface). Figure 117.4(c) shows two regions of the target probed by the VISAR: the inner surface of the aperture, and the rear surface of the ablator, viewed through the aperture. Prior to the drive pulse and subsequent thermal radiation (graphs shown in plot), the fringes are horizontal and of constant intensity. As the drive temperature rises, the ablator is heated and, at ~1 ns, the expanded rear-surface material absorbs the VISAR probe beam, causing the signal to diminish. It is important to note that the signal from the Au aperture surface (above and below the ablator signal) that is well shielded and, therefore, not preheated and does not expand, persists throughout the drive pulse. This indicates that the window remains transparent and survives the radiation from the hohlraum.

Experiments with hohlraums driven to $T_{rad} > 200$ eV produced blanking in the quartz window. This is consistent with the open experiments described in **VISAR Windows** (p. 3) and

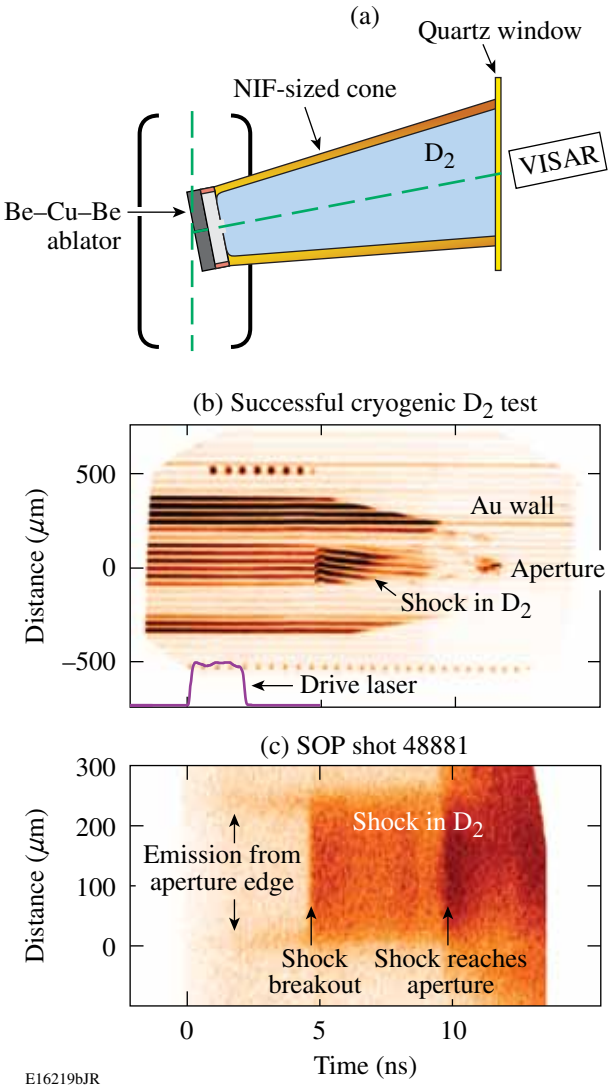

Figure 117.5
(a) The cryogenic target is identical to that in Fig. 117.4(a), except that the cone is filled with liquid deuterium and the assembly is mounted on a cryostat. (b) VISAR data show again that the window remains transparent and that the shock in deuterium is observed. (c) Streaked optical pyrometer (SOP) data showing temporal features (in self-emitted light) that confirm the behavior in the VISAR data (b).

ultimately limit the conditions under which windows can be used. In the **Fourth Shock Timing** section below a windowless target is proposed for timing the fourth "shock."

During these experiments it was found that scattered light from the incident drive beams could blank the VISAR window from the outside. To prevent this, the diagnostic cones were fitted with shields to block all scattered light from irradiating the window. This is an important aspect of the NIF target design because a significant amount of unconverted light passes within a 3- to 10-mm annulus around NIF targets. As a further precaution, some cones were coated on the inside with CH to minimize any secondary-hohlraum effect by reabsorbing any low-energy photons re-emitted by the cone wall upon irradiation by M-band emission. As expected, these experiments also showed no window blanking and CH overcoats are not expected to be required at the NIF.

3. Cryogenic Experiments

Experiments were performed using cryogenic targets filled with liquid deuterium. The hohlraums were empty while the cones were filled with liquid deuterium between the ablator and the VISAR window [Fig. 117.5(a)]. Figure 117.5(b) shows the VISAR data from such an experiment driven at 135 eV. These data clearly show that the window survives throughout the drive pulse and the shock in the deuterium is observed. The self-emission data [Fig. 117.5(c)] from the streaked optical pyrometer (SOP)[18] exhibit identical temporal features that confirm the timing of the shock breakout (arrival at rear surface) and arrival time at the aperture after transiting the ablator–cone gap. Additionally, the heating of the aperture edge, as evidenced by its self-emission, is seen early in time. While this heating is unavoidable, it is not expected to present a problem with the measurements or their precision.

These data at 135 eV confirm that the proposed shock-timing technique is viable for the NIF targets driven by higher radiation temperatures because the OMEGA experiments produce more M band than is expected on the NIF. Figure 117.6 shows the predicted M-band flux from the NIF experiments at 165 eV, compared to the OMEGA emission from the 135-eV hohlraums. Note that the OMEGA hohlraums produce significantly more x-ray flux above 2 keV than expected from the NIF targets. This is because the OMEGA hohlraums have a smaller fraction of wall irradiated by beams and have lower time-dependent albedo and, therefore, require a higher beam intensity to reach a given radiation temperature. This higher intensity leads to more M band, which is produced primarily in the laser-spot regions.

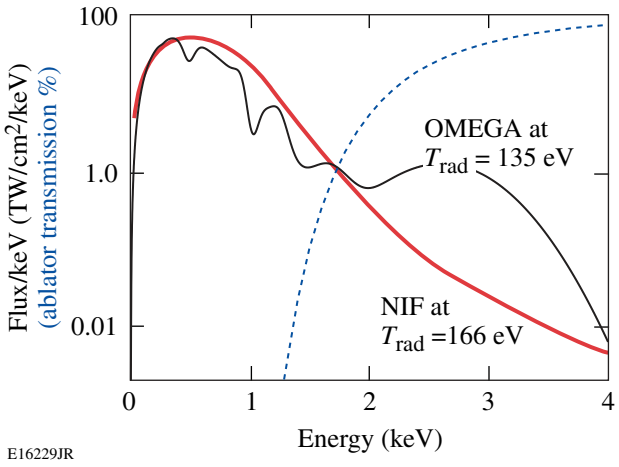

Figure 117.6
Radiation spectrum expected on the NIF (thick solid curve) for conditions of the third shock (165 eV) and that for the OMEGA experiments at 135 eV (thin solid curve). Note that above 2 keV, the OMEGA experiments have higher fluxes. The ablator transmits (dashed curve) this region of the spectrum.

4. Fourth Shock Timing

The tuning experiments for NIF shock timing must also time the compression wave (or fourth shock) that is driven by radiation temperatures above 250 eV. The fluxes from these drives are expected to blank the VISAR window; therefore, a windowless target was designed. These targets have a re-entrant cone with no aperture, confining the deuterium only to the capsule. The compression wave will be detected by the arrival of the shock at the inner surface of the cone tip. This will be detected as either movement or cessation of the fringes. If the released material remains solid when the shock arrives at a solid/vacuum interface, this material can continue to reflect the VISAR probe beam and the free surface velocity can be detected. If, however, the material is sufficiently heated to melt and then expand, it typically produces a density gradient that absorbs the probe beam at the rear surface and the signal then vanishes.

This concept was tested on OMEGA with the hohlraum driven to much higher temperatures. Figure 117.7(a) shows the target design that comprised a standard NIF cone and [in Fig. 117.7(b)] the Be–Cu–Be ablator sandwich. The cone tip had an Au step assembly (16 μm and 36 μm thick) facing the ablator. VISAR and SOP probed the rear surface of that assembly. In these experiments, for simplicity, there was no deuterium in the gap between the ablator and the Au step. The gap was filled with 1 atm of air during fabrication and well sealed. There was no need for a VISAR window, so none was used at the end of the cone. The VISAR data [Fig. 117.7(c)] show continuous

fringes until the arrival (at 3.5 and 4 ns) of shocks at the rear of the two steps.

The radiation temperature in this experiment was 220 eV, and as was the case seen in Fig. 117.6, the M-band emission was significantly (12×) higher than that expected for a 250-eV NIF hohlraum. As a result, the shock that first breaks out of the two steps was driven by the M-band emission incident on the cone face. The subsequent arrival of the shock driven by the thermal spectra is seen as a brief increase of intensity that occurs at the thin step [upper portion in Fig. 117.7(c)] at ~5.7 ns. These features are confirmed by 1-D simulations using the experimental drive including the M-band emission. Simulations

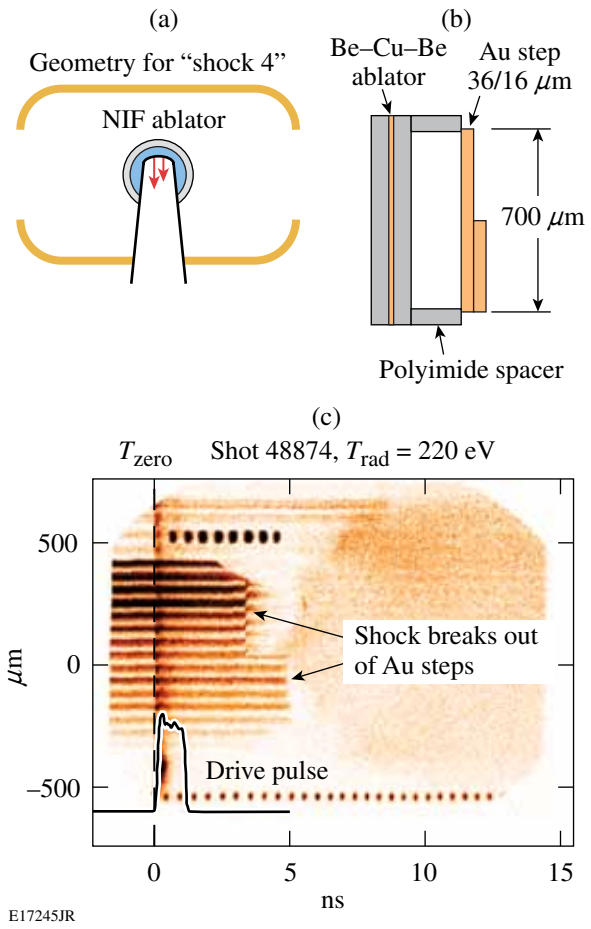

Figure 117.7
(a) The NIF target configuration used to measure the timing of the compression wave. It is similar to the design in Fig. 117.2, except there is no aperture in the cone and no diagnostic window. (b) The OMEGA cone-tip design used to test the compression-wave timing technique. (c) VISAR results for a target driven to 220 eV, showing persistence of VISAR fringes until shock breakout. This breakout provides an unambiguous arrival time for the shock at the rear surface of the steps.

of NIF targets predict that the thermal shock breaks out well before any M-band–driven shocks.

The unambiguous breakout feature is the cessation of the fringes caused by the release of material absorbing the VISAR laser. This is a common observation in shock experiments using opaque samples. This technique is applicable to shock experiments over a wide range of shock pressures. At lower pressures, the breakout may not cause a cessation of fringes but, instead, the onset of motion. At very high drive intensities, the sample could be preheated, causing the rear-surface release. In this latter case, the VISAR signal could be lost, but experiments show that the arrival of the shock can still be observed [as in Fig. 117.7(c)] because it steepens the density gradient, producing a brief reflected VISAR signal and an unambiguous SOP signal. [The steepening occurs in times less than the resolution time of the VISAR (30 ps) and lasts a few hundred picoseconds, depending on the time it takes for that material to relax and once again form an absorbing profile.] This provides confidence that this technique can be used for a wide range of conditions on the NIF. It is expected that the shock-propagation time across the cone tip can be accounted for with precision sufficient to achieve the necessary shock timing on the NIF.

5. Spherically Convergent Shock Experiments

Previous experiments used planar ablators and single drive pulses for expediency. The NIF experiments will involve multiple, spherically converging shocks—conditions not attainable in OMEGA hohlraum experiments without resorting to quarter-scale spherical targets with insufficient reflecting surface area. To study these effects, larger-scale, direct-drive experiments were performed on cryogenic spherical targets. These targets were 900-μm-diam, 10-μm-thick CD shells fitted with the NIF-scale VISAR cones. The assemblies were filled with liquid deuterium and irradiated by 36 OMEGA beams in the hemisphere centered on the VISAR line of sight [Fig. 117.8(a)]. This produces spherical shocks that converge toward the cone aperture. Figure 117.8(b) shows the VISAR record for an experiment driven by the multiple laser pulses shown at the base of this figure.

These targets have a 1000-Å Al coating on their outer surface. Before time zero, the VISAR probe beam reflects off the inner surface of this layer. At time zero, the laser ablates the layer and the x rays from the laser plasma cause the CD shell to blank (absorb) the VISAR probe beam, causing the VISAR fringes to disappear. At about 0.5 ns, the shock emerges from the CD shell and enters the deuterium. The VISAR fringes return because the shocked deuterium is reflective (>50%) and

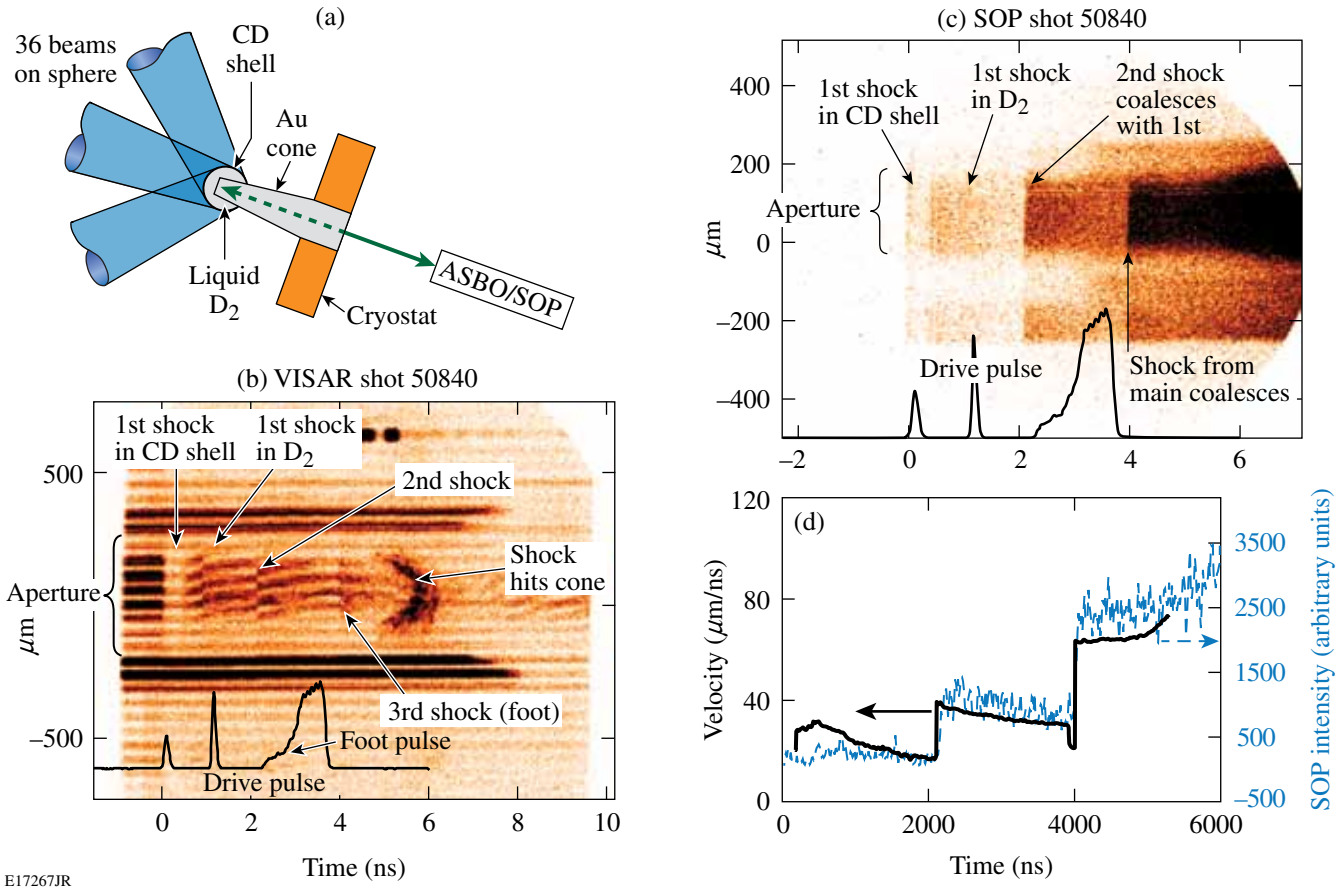

Figure 117.8
(a) Direct-drive cryogenic spherical targets used to study the timing of multiple convergent shocks on OMEGA. (b) VISAR record for three shocks in deuterium produced by the multiple pulses shown at the base of the figure. Evidence of shock coalescence (stronger shocks overtaking weaker ones) are evident at 2 and 4 ns; these indicate that multiple convergent shocks can be timed with this target and diagnostic configuration. (c) The SOP data show that the coalescence features observed in VISAR data are replicated in the self-emission intensity. (d) Shock velocities inferred from VISAR data and self-emission intensity histories for the data shown in (b) and (c).

the unshocked deuterium in front of it remains transparent. The curvature in the fringes from 0.5 to 2 ns results from deceleration of this first shock, which decays because it is unsupported: the first drive pulse has turned off. Just after 2 ns the shock produced by the second drive pulse (at 1.2 ns) overtakes the first shock. This is observed as a jump in fringe position produced by the jump to the new shock velocity. Since the first shock produces conduction electrons in the deuterium, the shocked material is reflective and opaque to the VISAR probe. As a result, VISAR cannot detect the second shock "through" the first shock, until the second overtakes the first shock.

At about 2.25 ns the "main" drive pulse begins at low intensity and ramps to higher intensity. At 4 ns, the shock from this pulse overtakes the combined first and second shocks, producing another jump in fringe position. About 1 ns later the shock hits the front surface of the Au cone. The bright feature that begins at ~5 ns is either reflection off of or self-emission from the hot material from the aperture that was heated by the shock. This material flows into the aperture, producing the converging feature from 5 to 6 ns. Ultimately the material cools, the shock passes it, and the decaying shock can again be observed at late times. It should be noted that in the NIF tuning campaign the pertinent shock-timing events are over before the shock reaches the cone face.

The self-emission from the shock was acquired simultaneously with VISAR data. Figure 117.8(c) depicts the intensity of light (590 to 850 nm) emitted by the shock and detected by the SOP. The features of the three shocks described above are plainly visible in Fig. 117.8(c). The material closing into the aperture is not observed (as in the VISAR data), but the arrival

of the shock at the aperture can be seen as a spatial broadening of the emission region. The slope of this growing edge can be traced back to the original diameter, intersecting at ~5 ns, which is the arrival time observed by VISAR. Figure 117.8(d) shows the shock velocity (deduced from VISAR) and the self-emission intensity histories measured for this shot. Note that these measured velocities span the range of shock velocities (20 to 57 km/s) that are prescribed for the first three shocks in a NIF ignition target, demonstrating this technique at applicable shock conditions.

These data confirm that VISAR and SOP can readily detect the velocities and the timing of spherically converging shocks that have traveled (and converged) by the ~200-μm distance from the shell to the cone tip. The lateral extent of the VISAR data is governed by the amount of probe light that is returned into the collection lens of the diagnostic and is proportional to the curvature of the spherical shell. The NIF capsules will be about twice the size of those used for the OMEGA experiments, so the detected region will be twice that of the OMEGA experiments while the radial distance traveled is the same. The OMEGA conditions are therefore more stringent (i.e., smaller curvatures) than the NIF experiments.

Conclusions

The National Ignition Campaign requires that multiple spherically convergent shock waves be timed to high precision. Targets with re-entrant cones will make it possible for optical diagnostics to probe the interior of the capsules *in situ*, with minimal interference to the x-ray-flux environment driving the probed capsule region. These targets also make possible the precise optical measurements of the velocity profiles (and therefore timing) of multiple shocks in the harsh radiation environment of an ignition hohlraum; this presents formidable challenges.

Experiments were performed on the OMEGA laser to assess the viability of the proposed techniques. These experiments used open and hohlraum geometries to select quartz as the material for the diagnostic window in the NIF targets. Hohlraum experiments showed that quartz remains transparent throughout experiments that were driven to radiation temperatures greater than 180 eV, and that produced M-band emission greater than that expected on ignition targets, up to the timing of the third shock. Cryogenic experiments confirmed that the column of liquid deuterium is not adversely affected by thermal and M-band x rays from the hohlraum. Direct-drive experiments on cryogenic spherical targets demonstrated that shock timing can be performed on multiple, spherically convergent shocks, and that shocks up to ~70 km/s can be detected optically.

Each of the OMEGA experiments had more adverse conditions than those expected on the NIF, i.e., higher M-band emission, less standoff distance to the window, and smaller radius of curvature. These experiments, therefore, provide high confidence that the NIC plan for shock timing is viable and will successfully time shocks to adequate precision for ignition targets.

ACKNOWLEDGMENT

This work was supported by the U.S. Department of Energy Office of Inertial Confinement Fusion under Cooperative Agreement No. DE-FC52-08NA28302 (LLE), DE-AC52-07NA27344 (Lawrence Livermore National Laboratory), the University of Rochester, and the New York State Energy Research and Development Authority. Sandia is a multiprogram laboratory operated by Sandia Corporation, a Lockheed Martin Company, for the United States Department of Energy's National Nuclear Security Administration under contract DE-AC04-94AL85000. The support of DOE does not constitute an endorsement by DOE of the views expressed in this article.

REFERENCES

1. J. D. Lindl, *Inertial Confinement Fusion: The Quest for Ignition and Energy Gain Using Indirect Drive* (Springer-Verlag, New York, 1998), Chap. 6, pp. 61–82.
2. T. R. Dittrich *et al.*, Phys. Plasmas **6**, 2164 (1999).
3. B. A. Hammel *et al.*, Plasma Phys. Control. Fusion **48**, B497 (2006).
4. D. H. Munro *et al.*, Phys. Plasmas **8**, 2245 (2001).
5. D. H. Munro, H. F. Robey, B. K. Spears, and T. R. Boehly, Bull. Am. Phys. Soc. **51**, 105 (2006).
6. T. R. Boehly, D. L. Brown, R. S. Craxton, R. L. Keck, J. P. Knauer, J. H. Kelly, T. J. Kessler, S. A. Kumpan, S. J. Loucks, S. A. Letzring, F. J. Marshall, R. L. McCrory, S. F. B. Morse, W. Seka, J. M. Soures, and C. P. Verdon, Opt. Commun. **133**, 495 (1997).
7. S. W. Haan *et al.*, Eur. Phys. J. D **44**, 249 (2007).
8. S. W. Haan *et al.*, Phys. Plasmas **12**, 056316 (2005).
9. D. G. Hicks, T. R. Boehly, P. M. Celliers, J. H. Eggert, S. J. Moon, D. D. Meyerhofer, and G. W. Collins, Phys. Rev. B **79**, 014112 (2009).
10. P. M. Celliers *et al.*, Phys. Rev. Lett. **84**, 5564 (2000).
11. L. M. Barker and R. E. Hollenbach, J. Appl. Phys. **43**, 4669 (1972).
12. P. M. Celliers *et al.*, Appl. Phys. Lett. **73**, 1320 (1998).
13. P. M. Celliers, D. K. Bradley, G. W. Collins, D. G. Hicks, T. R. Boehly, and W. J. Armstrong, Rev. Sci. Instrum. **75**, 4916 (2004).

14. T. R. Boehly, T. J. B. Collins, O. Gotchev, T. J. Kessler, J. P. Knauer, T. C. Sangster, and D. D. Meyerhofer, J. Appl. Phys. **92**, 1212 (2002).

15. H. F. Robey, D. H. Munro, B. K. Spears, M. M. Marinak, O. S. Jones, M. V. Patel, S. W. Haan, J. D. Salmonson, O. L. Landen, T. R. Boehly, and A. Nikroo, J. Phys., Conf. Ser. **112**, 022078 (2008).

16. T. R. Boehly, E. Vianello, J. E. Miller, R. S. Craxton, T. J. B. Collins, V. N. Goncharov, I. V. Igumenshchev, D. D. Meyerhofer, D. G. Hicks, P. M. Celliers, and G. W. Collins, Phys. Plasmas **13**, 056303 (2006).

17. W. Theobald, J. E. Miller, T. R. Boehly, E. Vianello, D. D. Meyerhofer, T. C. Sangster, J. Eggert, and P. M. Celliers, Phys. Plasmas **13**, 122702 (2006).

18. J. E. Miller, T. R. Boehly, A. Melchior, D. D. Meyerhofer, P. M. Celliers, J. H. Eggert, D. G. Hicks, C. M. Sorce, J. A. Oertel, and P. M. Emmel, Rev. Sci. Instrum. **78**, 034903 (2007).

Cryogenic Target Performance and Implosion Physics Studies on OMEGA

Introduction

The goal of inertial confinement fusion (ICF)[1,2] is to implode a spherical target to achieve high compression of the fuel and high temperature of the hot spot to trigger ignition and maximize the thermonuclear energy gain. Both direct- and indirect-drive concepts of ICF rely on targets with thick, cryogenic deuterium–tritium (DT) shells for ignition.[1–3] While target designs vary in their details, these concepts have common basic physics such as ablator and fuel compressibility, energy coupling and transport, hydrodynamic instabilities, shock tuning, and preheating. Recent OMEGA cryogenic D_2 experiments demonstrated ignition-relevant fuel compression with a neutron-averaged areal density of ~200 mg/cm^2 (Refs. 4 and 5). This corresponds to an estimated peak fuel density of ~100 g/cm^3, ~500× higher than initial cryogenic ice density. These experiments were conducted at peak drive intensities of $\sim 5 \times 10^{14}$ W/cm^2 using 10-μm-thick plastic ablators with an implosion velocity of $\sim 2.4 \times 10^7$ cm/s (Refs. 4 and 5). To achieve an ignition-relevant implosion velocity of $\sim 4 \times 10^7$ cm/s, the peak drive intensity must be increased to ~10^{15} W/cm^2 (Refs. 3 and 4). Recent direct-drive ICF research on OMEGA focused on understanding the physics of this high-intensity regime. Understanding the dynamics of target implosion is essential to all ignition target designs, whether directly or indirectly driven. This article reviews the results obtained over this past year in the physics of cryogenic target implosions, including energy coupling and transport, hydrodynamic instabilities, compressibility, shock timing, and preheating.

The following sections (1) show the importance of nonlocal electrons in modeling laser coupling and energy transport; (2) present recent results from experiments that show stabilization of hydrodynamic instabilities at peak intensities of ~10^{15} W/cm^2; and (3) describe compressibility experiments performed in plastic ablators, shock-timing experiments, compression results from cryogenic D_2 spherical implosions, and spherical experiments in Si-doped plastic ablators. The final section summarizes these results.

Energy Coupling and Transport

Acceleration experiments with planar plastic foils were conducted to study energy coupling and transport in plastic ablators.[6] In these experiments, 2.5-mm-diam, 20-μm-thick CH targets were driven with a 1-ns square pulse shape at a peak laser intensity of ~10^{15} W/cm^2. The targets were driven with 12 overlapped beams using all standard OMEGA beam-smoothing techniques, including distributed phase plates (DPP's),[7] polarization smoothing (PS),[8] and smoothing by spectral dispersion (SSD).[9] The target acceleration was measured using side-on radiography with a streak camera using ~2-keV x rays from a dysprosium sidelighter and compared with two-dimensional (2-D) *DRACO* simulations.[6] The simulations used a local model for electron transport[10] with a time-dependent flux limiter derived from a one-dimensional (1-D) nonlocal thermal-electron-transport model.[11] The nonlocal model solves the Boltzman equation with the Krook's collision operator and an appropriate electron-deposition length. It gives an effective time-dependent flux limiter, defined as the ratio of nonlocal heat flux to the free-stream heat flux.[11]

The measured target trajectory [Fig. 117.9(a)] is in good agreement with the simulated trajectory using the effective time-dependent flux limiter shown in Fig. 117.9(b). Reference 6 shows that the measured target trajectories are in good agreement with nonlocal model predictions over the broad range of intensities from $\sim 2 \times 10^{14}$ to 1×10^{15} W/cm^2. Predictions using a local model of thermal transport with a constant flux limiter of $f = 0.06$ (Ref. 10) (previous standard model for OMEGA experiments) are in good agreement with experiments at intensities below $\sim 5 \times 10^{14}$ W/cm^2, but break down at peak intensities ~10^{15} W/cm^2, as shown in Fig. 117.9(a). These results indicate that nonlocal effects are critical for modeling energy coupling and transport in direct-drive-ignition designs using high-intensity UV lasers. Experiments using green and IR lasers have shown that nonlocal effects were important even at much lower intensities of $\sim 1 \times 10^{14}$ W/cm^2 (Refs. 12 and 13).

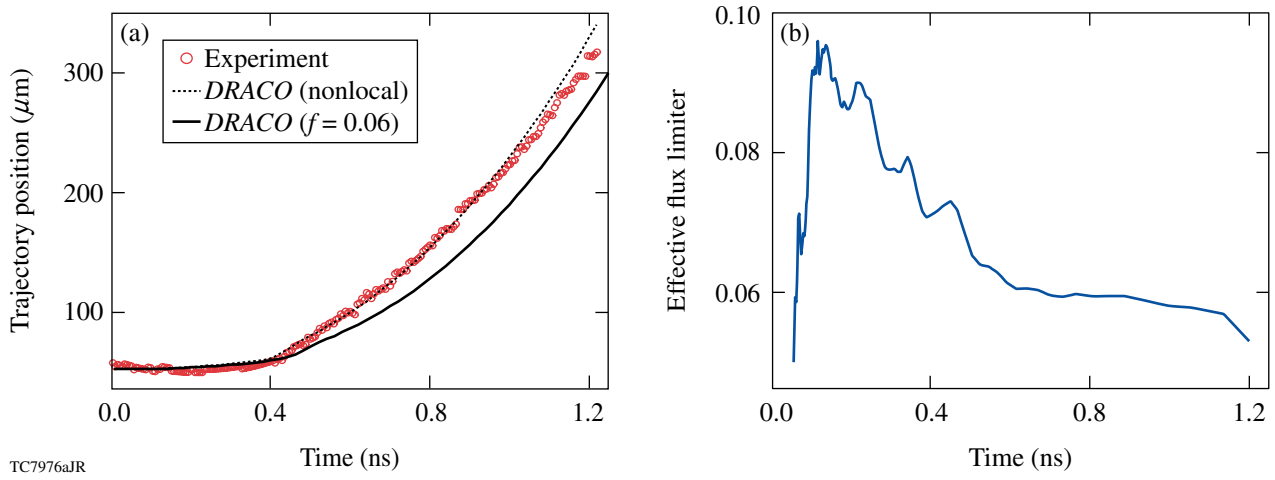

Figure 117.9
(a) Measured (circles) and simulated target trajectories using a flux limiter of $f = 0.06$ (solid line) and an effective flux limiter derived from the nonlocal model (dotted line), shown in (b).

Hydrodynamic Instability Experiments

The nonlocal model for electron thermal transport predicts target decompression at the ablation front[11] relative to prediction of the local model.[10] The decompression at the ablation front is caused by heating from the high-energy tail of the electron distribution. The decompression at the ablation surface reduces the growth rate of Rayleigh–Taylor (RT) instability.[12–15] In the linear stage of RT instability, the growth rate as a function of modulation wave number k in plastic targets is given by the dispersion relation[16]

$$\gamma(k) = 0.94\left[\mathrm{kg}/(1 + kL_n)\right]^{0.5} - 1.5\, kV_a, \qquad (1)$$

where g is the target acceleration, V_a is the ablation velocity, and L_n is the density scale length. The growth rate is proportional to the first acceleration term and is reduced by the second stabilizing term $-1.5\, kV_a$, caused by material ablation. When the target is decompressed, the ablation velocity increases, resulting in a reduced RT growth rate. This reduction is stronger for modulations with high wave numbers (shorter wavelengths). This was experimentally observed in 20-μm-thick, planar CH targets driven with various square drive pulses.[14,15]

In this work, 20-μm-thick CH targets were driven with 12 overlapped beams with full beam smoothing including DPP's,[7] PS,[8] and SSD.[9] The RT growth of preimposed 2-D modulations was measured with through-foil, x-ray radiography[14,15] using ~1.3-keV x rays from a uranium backlighter. In the RT experiments, the 2-D preimposed modulations had wavelengths of 20, 30, and 60 μm, with initial amplitudes of 0.05, 0.05, and 0.125 μm, respectively. Results of RT growth experiments are shown in Fig. 117.10 for a 1-ns drive at an intensity of $\sim 1 \times 10^{15}$ W/cm^2 [Figs. 117.10(a)–117.10(c)] and a 1.6-ns drive at an intensity of $\sim 5 \times 10^{14}$ W/cm^2 [Figs. 117.10(d)–117.10(f)]. The experimental data at a 60-μm wavelength are weakly affected by the stabilizing term $-1.5\, kV_a$ [Figs. 117.10(a) and 117.10(d)]. This modulation grows more rapidly at a drive intensity of $\sim 10^{15}$ W/cm^2 than at $\sim 5 \times 10^{14}$ W/cm^2. This indicates that the acceleration is higher at high intensity, as expected. At an intensity of $\sim 5 \times 10^{14}$ W/cm^2 the short-wavelength modulations (at wavelengths of 20 μm and 30 μm) grow faster than the long, 60-μm-wavelength modulation. At a high intensity of 1×10^{15} W/cm^2, this trend is reversed: the 60-μm-wavelength modulation grows faster than the 30-μm perturbation, with the 20-μm-wavelength perturbation completely stabilized.

This stabilization is consistent with the increased ablation velocity and density scale length at high intensity predicted by the nonlocal electron transport model.[11,14] The stabilization is also correlated with the hot-electron signal from two-plasmon-decay (TPD) instability.[14,17,18] This signal becomes detectable at intensities above $\sim 5 \times 10^{14}$ W/cm^2, similar to previous experiments.[4,19] The relationship between the x-ray emission and the target preheat is still under investigation. The strong measured RT growth stabilization reduces the requirements for mitigation of the hydro-instability growth in direct-drive-ignition capsules

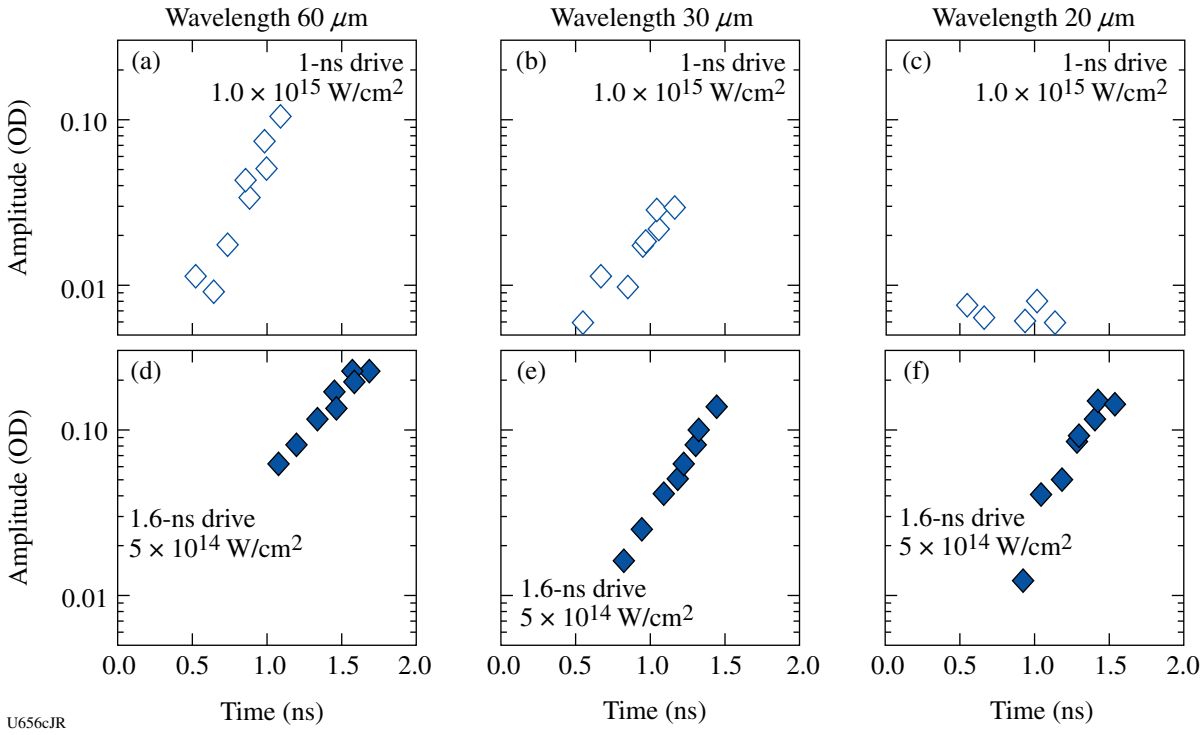

Figure 117.10
Optical-depth modulations versus time for a 1-ns square laser drive at an intensity of ~1×10^{15} W/cm^2 [(a), (b), and (c)], and with a 1.6-ns square laser drive at an intensity of ~5×10^{14} W/cm^2 [(d), (e), and (f)] with wavelengths of 60 μm, 30 μm, and 20 μm, respectively.

at the National Ignition Facility (NIF).[14] Future experiments will distinguish between nonlocal and hot-electron contributions to the ablation-surface preheating.

Plastic-Ablator Compressibility

Figure 117.11 shows a schematic of the plastic-ablator compressibility experiments[20] performed with ~125-μm-thick, ~280-μm-wide plastic planar targets driven with a high-compression, 3-ns-long shaped pulse at a peak drive intensity of ~1×10^{15} W/cm^2, as shown in Fig. 117.12(a). The targets were driven with 14 overlapped beams with full beam smoothing, including DPP's,[7] PS,[8] and SSD.[9] The target compression was measured with x-ray, side-on radiography using an ~6.4-keV iron sidelighter. The 2-ns-long foot of the pulse sends a shock wave that compresses the ablator by ~3×. The compression increases up to ~9× when the main shaped pulse sends a compression wave through the target. Figures 117.12(b) and 117.12(c) compare the measured and simulated optical-depth compression of the target. The shock and compression waves travel from right to left in these data. The predictions for (b) 2.3 ns and (c) 2.9 ns show good agreement with the experiment, confirming the compression of the plastic ablator by a shaped laser drive. These measurements validated

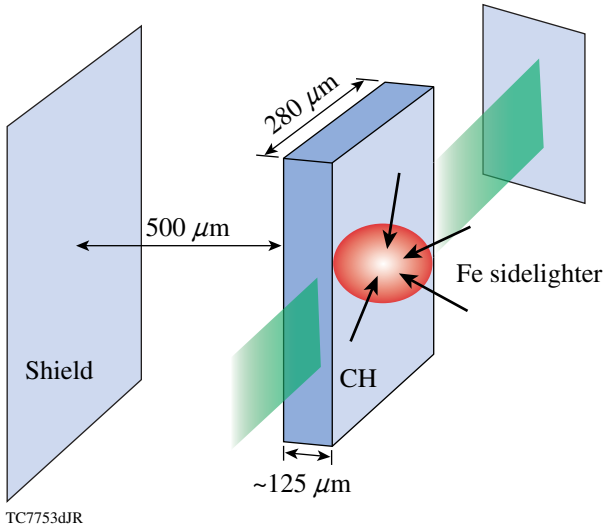

Figure 117.11
Experimental setup for plastic-ablator compressibility experiments performed with ~125-μm-thick, ~280-μm-wide plastic planar targets driven with 14 overlapped beams. The target compression was measured with x-ray, side-on radiography using an ~6.4-keV iron sidelighter.

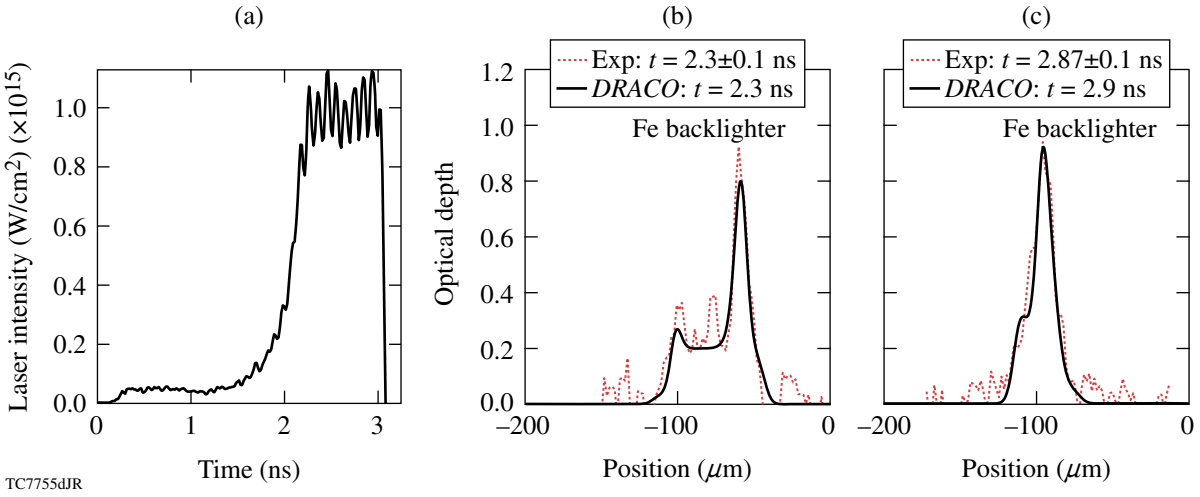

Figure 117.12
(a) High-compression, 3-ns-long laser pulse shape. The measured (dotted line) and simulated (solid line) optical-depth target compression at (b) 2.3 ns and (c) 2.9 ns. The shock and compression waves travel from right to left. The predictions show good agreement with measurements.

the hydrodynamics and equation of state (*SESAME*) of the shock and compression waves predicted by the 2-D hydrocode *DRACO*,[20] used to simulate the experiments. Similar experiments conducted at lower intensities of ~5 × 10^{14} W/cm^2 also showed agreement with hydro simulations, while experiments at an intensity of ~1.5 × 10^{15} W/cm^2 (higher than required for ignition on the NIF) showed target decompression that was correlated with the presence of hot electrons generated by TPD instability.[20]

Shock Timing

Figure 117.13 shows a schematic of the shock-timing experiments performed with spherical 10-μm-thick CD shells filled with cryogenic D_2 liquid.[21] The target cone makes it possible for the active shock breakout (ASBO)[22] system to probe the shock waves in liquid deuterium. The experiments were performed with 36 overlapped OMEGA beams using all standard OMEGA beam-smoothing techniques, including DPP's,[7] PS,[8] and SSD.[9] The diagnostics probed the central region of the target, which had the same illumination conditions as cryogenic spherical implosions. Figure 117.14(a) shows the pulse shape used during one of the experiments. The measured shock velocity as a function of time (solid curve) is shown in Fig. 117.14(b). The data are compared with the 1-D predictions, shown by the dotted curve. In the 1-D prediction, the picket pulse launches the first shock, which decays as it travels through the target. This is shown by the decreasing shock velocity as a function of time. As a compression wave is launched by the shaped laser pulse starting at ~1.2 ns, the shock velocity gradually decreases in the simulation. The measurements indicate that the

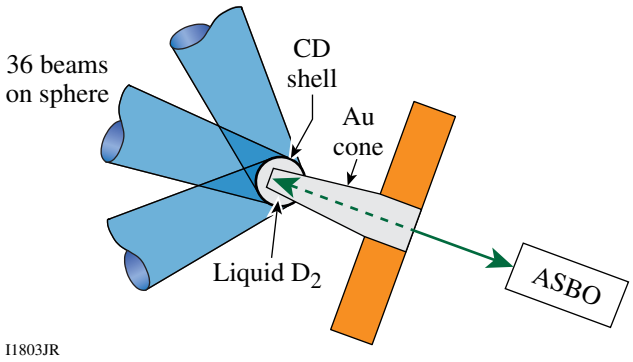

Figure 117.13
Schematic of shock-timing experiments consisting of spherical 10-μm-thick CD shells filled with liquid deuterium driven with 36 overlapped OMEGA beams. The targets have openings for active shock breakout (ASBO) diagnostics to probe shocks in liquid deuterium.

compression wave turns into a shock wave inside the target. The measured shock velocity from the first shock is smaller than predicted. This measurement suggests that energy coupling from the picket and low-intensity part of the pulse is reduced, compared to the simulation. The adiabat (the ratio of the plasma pressure to the Fermi pressure of a fully degenerate electron gas) of the CD shell and D_2 fuel is likely higher than simulated, leading to compression degradation in spherical implosions.

Since 1-D simulations incorrectly predict the shock timing, experimental measurements can be used to tune multiple hydrodynamic waves. Experimentally, it is easier to tune shock waves than compression waves because the multiple shock

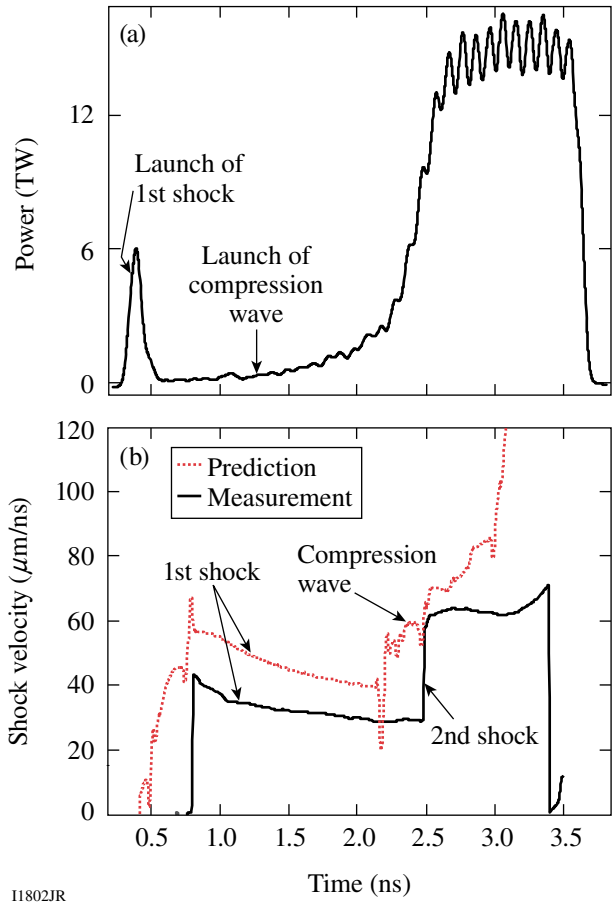

Figure 117.14
(a) The laser pulse shape for the continuous laser-pulse experiments. (b) The measured (solid line) and simulated (dotted line) shock velocities as a function of time.

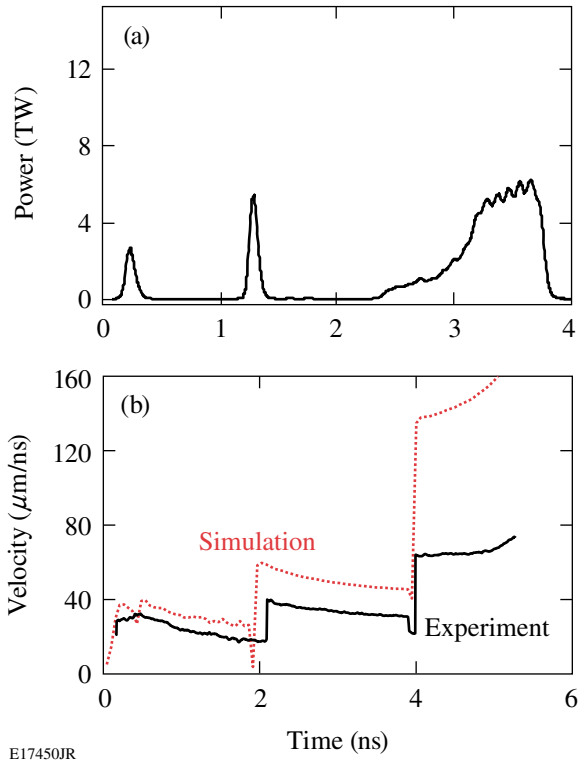

Figure 117.15
(a) The pulse shape for the double-picket, laser-pulse experiments. (b) The measured (solid line) and simulated (dotted line) shock velocities as a function of time.

waves are much easier to create and interpret. Figure 117.15(a) shows the double-picket pulse shape used for one such experiment and the measured shock velocity as a function of time [solid curve in Fig. 117.15(b)]. The data are compared with the 1-D prediction shown by the dotted curve. In the 1-D prediction, the first picket sends the first shock wave that decays as it travels through the target. The second picket sends a stronger second shock that travels faster and overtakes the first shock wave at ~2 ns. The main part of the pulse sends a third shock wave, which coalesces with the two earlier shocks at ~4 ns. The experiment shows that the shocks coalesce. The shock velocities are smaller, however, in the experiment, indicating that the shock coalescence events occur at different spatial locations than predicted. Future experiments will tune shock waves using triple-picket pulses with the square main pulse. This technique is similar to that used for shock tuning in indirect-drive-ignition designs.[1,2,21]

Cryogenic-Target Compression

Figure 117.16 shows compression results obtained in spherical implosions with outer 10-μm-thick CD ablators and inner 95-μm-thick cryogenic-D_2-ice fuel shells. Figure 117.16(a) shows three examples of continuous laser pulses at a peak intensity range from ~5×10^{14} W/cm^2 to ~8×10^{14} W/cm^2. Figure 117.16(b) shows an example of a double-picket pulse at a peak intensity range of ~9×10^{14} W/cm^2. Figure 117.16(c) shows a comparison of the compression results obtained with these two types of laser pulses in which the neutron-averaged areal density was predicted to be ~250 mg/cm^2 if the shock pulses were properly timed. The highest compression with measured areal density in the range of 180 to 200 mg/cm^2 was obtained at the peak intensity of ~5×10^{14} W/cm^2. Two of the four data points at this intensity were presented in Ref. 5, while the other two were obtained recently, showing a good repeatability of these results. The neutron yield varied by a factor of ~5 because of variations of the inner ice roughness in these implosions. While the yield varied, the areal density did not, showing that the areal density is a robust measure of target compression, as previously shown in plastic implosions.[23]

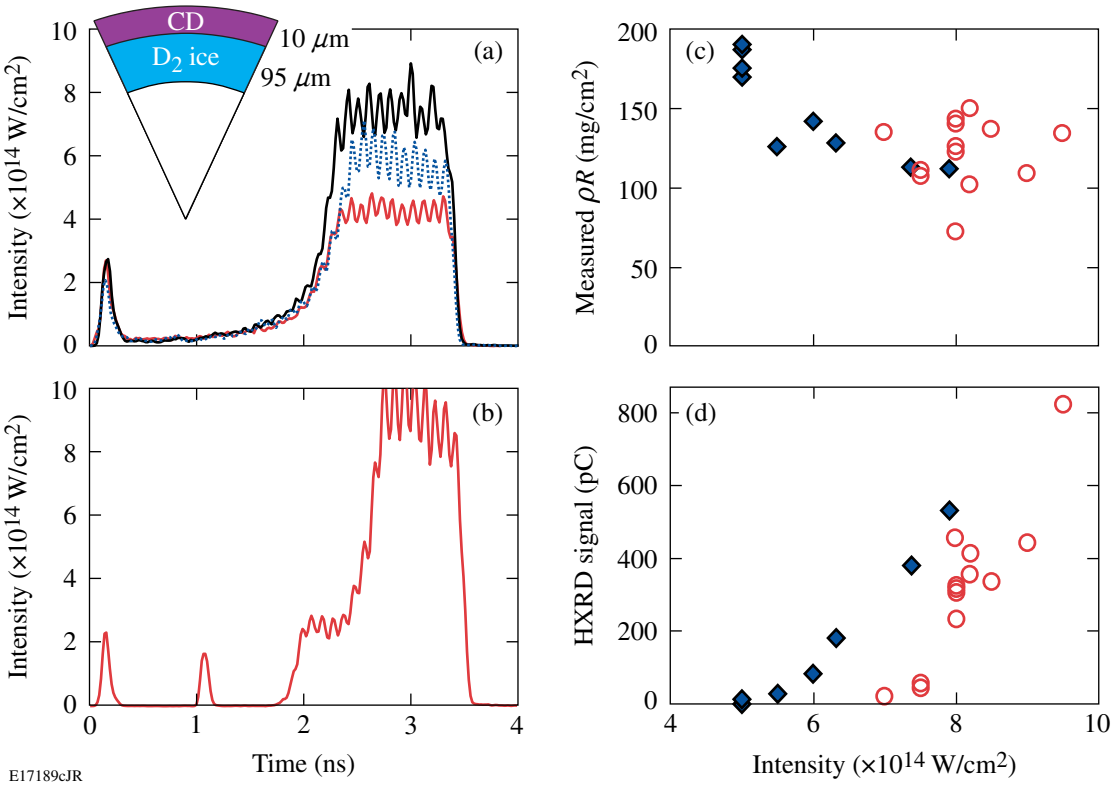

Figure 117.16
(a) Schematic of spherical targets used in implosions consisting of outer 10-μm-thick CD ablators and 95-μm-thick inner cryogenic-D_2-ice shells driven with continuous laser pulses at peak intensities ranging from ~5×10^{14} W/cm^2 to ~8×10^{14} W/cm^2. (b) An example of a double-picket laser pulse with a peak intensity of ~9×10^{14} W/cm^2. (c) Measured neutron-averaged areal density as a function of peak drive intensity with continuous (diamonds) and double-picket (circles) pulses. (d) Hard x-ray signal as a function of peak drive intensity with continuous (diamonds) and double-picket (circles) pulses.

By increasing the peak intensity in the continuous-pulse implosions, the areal density did not increase, shown by the diamonds in Fig. 117.16(c). As discussed in the previous section, the shocks were not properly timed in these implosions, resulting in a decrease of the measured compression. The better-timed, double-picket implosions produced higher compression with areal densities up to ~150 mg/cm^2 at high peak intensities, shown by the open circles [Fig. 117.16(c)]. Variations in these data are caused by variations in the picket energies and uncertainties for the shock-timing experiments. These multiple-picket designs are being optimized in current campaigns. Figure 117.16(d) presents the measured hard x-ray signal, produced by hot electrons from TPD instability, as a function of peak intensity for both types of drive pulses. The hard x-ray signal increases with peak intensity.[24] The preheat energy, which is estimated based on the measured hard x-ray signal, is of the order of ~20 J in the high-intensity implosions.[4] This corresponds to ~0.1% of the total laser energy.[4] With such levels of preheat, the areal density is expected to be reduced from ~250 mg/cm^2 to ~210 mg/cm^2, if shock timing is optimized. These levels of preheat should not preclude obtaining an ignition-relevant areal density of ~200 mg/cm^2 at peak intensities of ~1×10^{15} W/cm^2. The fact that the measured compression is below this level suggests that shock timing still must be improved and/or the hot-electron preheat is larger than previously estimated. Future experiments with both triple-picket pulse shapes and high-Z ablators will address the most important issues in the direct-drive program.

Preheat

An important source of compression degradation is the shell preheat caused by hot electrons generated by TPD instability.[4,18,19,24] This preheat was shown to be virulent in DT and D_2 ablators[4,24] and was reduced by using plastic ablators.[4,5] As a result, the highest, ignition-relevant areal densities with shell ρR of ~200 mg/cm^2 were achieved in cryogenic D_2-fuel implosions with plastic ablators when the hot-electron preheat was reduced to zero, at a moderate laser-drive peak intensity of

~5 × 10^{14} W/cm^2 (Ref. 5). By increasing the peak intensity to ~1 × 10^{15} W/cm^2, the implosion velocity can be raised to levels required for ignition, but hard x-ray signals, associated with TPD hot electrons, also increase,[24] as shown in Fig. 117.16(d). While current hot-electron preheat estimates in plastic-ablator OMEGA implosions (with the estimated cold-shell preheat-energy fraction approaching ~0.1% of the total laser energy) do not preclude achieving ignition-relevant compression (with shell ρR of ~200 mg/cm^2) at high peak intensities of ~1 × 10^{15} W/cm^2 and an initial shell adiabat of $\alpha \sim 2$ (Ref. 4), the longer plasma scale lengths in NIF targets make them potentially more vulnerable to hot-electron production than OMEGA targets.[24] While there are no reliable predictive capabilities for hot-electron preheat due to the very complex nature of nonlinear TPD instability, higher-Z ablators are expected to mitigate the hot-electron preheat compared to the plastic ablators. Plastic ablators with 5% by atom of Si dopant were used recently[25] for this purpose.

Figure 117.17 shows a comparison of the hard x-ray signals measured in plastic and Si-doped plastic implosions. The implosions were performed with shaped pulses in which the peak intensity varied from ~0.8 to ~1.1 × 10^{15} W/cm^2 and a drive energy from ~18 to ~27 kJ. Two representative pulse shapes are shown in Fig. 117.17(a). The plastic and Si-doped plastic shells were 27 μm thick, and the concentration of Si dopant in plastic shells was 5% by atom. The comparison of the measured hard x-ray signals in the >40-keV range [Fig. 117.17(b)] shows that the signals grow exponentially with the drive energy in CH implosions as drive energy increases. The signals were reduced in Si-doped CH shells at low drive energies; the reduction was ~1.5× at higher drive energies and peak intensities of ~1.1 × 10^{15} W/cm^2. Future experiments will use higher-Z ablators to further reduce hot-electron preheat.

Conclusions

This article has reviewed progress in cryogenic-implosion physics on OMEGA. After achieving ignition-relevant areal densities of ~200 mg/cm^2 in cryogenic-D_2 implosions at peak laser-drive intensities of ~5 × 10^{14} W/cm^2, the focus of the program has been on understanding the compression physics at peak laser-drive intensities of ~1 × 10^{15} W/cm^2 that are required to achieve ignition-relevant implosion velocities. Acceleration experiments showed the importance of the nonlocal electron-thermal-transport effects in modeling the laser drive. The nonlocal, hot-electron preheat was shown to stabilize Rayleigh–Taylor growth at a peak drive intensity of ~1 × 10^{15} W/cm^2. The measured compressibility of plastic targets driven with high-compression, shaped pulses agrees well with 1-D predictions. Shock mistiming has been shown to be an important mechanism in compression degradation of recent cryogenic implosions driven with continuous pulses. Cryogenic implosions driven with double-picket pulses, which are easier to tune than continuous pulses, demonstrate an improvement in compression performance at a peak drive intensity of ~1 × 10^{15} W/cm^2. The shell preheat caused by hot electrons generated by two-plasmon-decay instability was reduced by using Si-doped ablators. Future experiments will investigate higher-Z ablators (such as glass or Si) for further hot-electron preheat reduction. Significant progress in understanding ignition-relevant cryogenic target implosions has been made on OMEGA since the publication of Ref. 4.

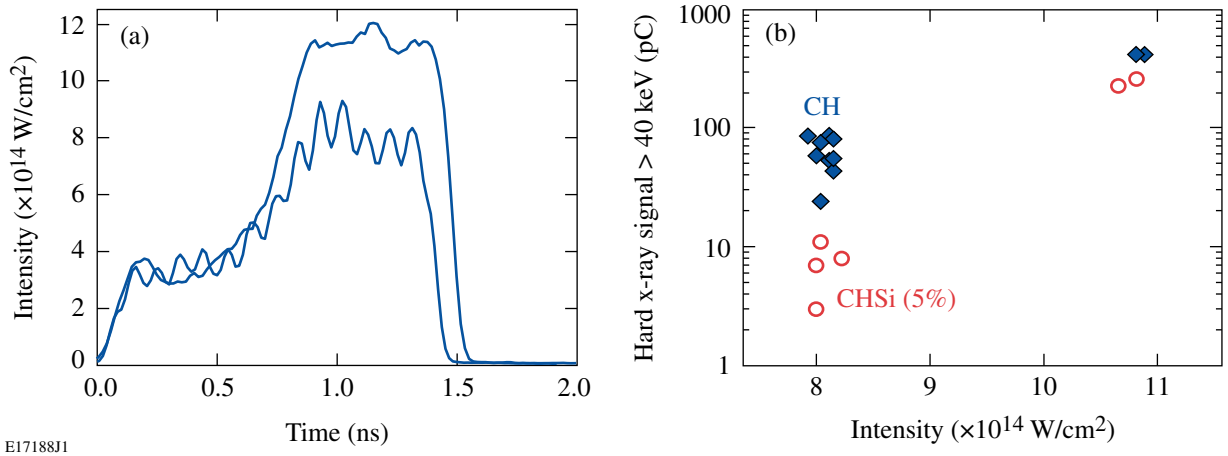

Figure 117.17
(a) Two representative pulse shapes used to implode 27-μm-thick plastic shells and Si-doped (5% by atom) plastic shells. (b) Hard x-ray signals measured in plastic (diamonds) and Si-doped (circles) implosions.

ACKNOWLEDGMENT

This work was supported by the U.S. Department of Energy Office of Inertial Confinement Fusion under Cooperative Agreement No. DE-FC52-08NA28302, the University of Rochester, and the New York State Energy Research and Development Authority. The support of DOE does not constitute an endorsement by DOE of the views expressed in this article.

REFERENCES

1. S. Atzeni and J. Meyer-ter-Vehn, *The Physics of Inertial Fusion: Beam Plasma Interaction, Hydrodynamics, Hot Dense Matter*, International Series of Monographs on Physics (Clarendon Press, Oxford, 2004).
2. J. D. Lindl, *Inertial Confinement Fusion: The Quest for Ignition and Energy Gain Using Indirect Drive* (Springer-Verlag, New York, 1998).
3. S. E. Bodner *et al.*, Phys. Plasmas **7**, 2298 (2000).
4. R. L. McCrory, D. D. Meyerhofer, R. Betti, R. S. Craxton, J. A. Delettrez, D. H. Edgell, V. Yu Glebov, V. N. Goncharov, D. R. Harding, D. W. Jacobs-Perkins, J. P. Knauer, F. J. Marshall, P. W. McKenty, P. B. Radha, S. P. Regan, T. C. Sangster, W. Seka, R. W. Short, S. Skupsky, V. A. Smalyuk, J. M. Soures, C. Stoeckl, B. Yaakobi, D. Shvarts, J. A. Frenje, C. K. Li, R. D. Petrasso, and F. H. Séguin, Phys. Plasmas **15**, 055503 (2008).
5. T. C. Sangster, V. N. Goncharov, P. B. Radha, V. A. Smalyuk, R. Betti, R. S. Craxton, J. A. Delettrez, D. H. Edgell, V. Yu. Glebov, D. R. Harding, D. Jacobs-Perkins, J. P. Knauer, F. J. Marshall, R. L. McCrory, P. W. McKenty, D. D. Meyerhofer, S. P. Regan, W. Seka, R. W. Short, S. Skupsky, J. M. Soures, C. Stoeckl, B. Yaakobi, D. Shvarts, J. A. Frenje, C. K. Li, R. D. Petrasso, and F. H. Séguin, Phys. Rev. Lett. **100**, 185006 (2008).
6. S. X. Hu, V. A. Smalyuk, V. N. Goncharov, S. Skupsky, T. C. Sangster, D. D. Meyerhofer, and D. Shvarts, Phys. Rev. Lett. **101**, 055002 (2008).
7. Y. Lin, T. J. Kessler, and G. N. Lawrence, Opt. Lett. **20**, 764 (1995).
8. T. R. Boehly, V. A. Smalyuk, D. D. Meyerhofer, J. P. Knauer, D. K. Bradley, R. S. Craxton, M. J. Guardalben, S. Skupsky, and T. J. Kessler, J. Appl. Phys. **85**, 3444 (1999).
9. S. P. Regan, J. A. Marozas, J. H. Kelly, T. R. Boehly, W. R. Donaldson, P. A. Jaanimagi, R. L. Keck, T. J. Kessler, D. D. Meyerhofer, W. Seka, S. Skupsky, and V. A. Smalyuk, J. Opt. Soc. Am. B **17**, 1483 (2000).
10. R. C. Malone, R. L. McCrory, and R. L. Morse, Phys. Rev. Lett. **34**, 721 (1975).
11. V. N. Goncharov, O. V. Gotchev, E. Vianello, T. R. Boehly, J. P. Knauer, P. W. McKenty, P. B. Radha, S. P. Regan, T. C. Sangster, S. Skupsky, V. A. Smalyuk, R. Betti, R. L. McCrory, D. D. Meyerhofer, and C. Cherfils-Clérouin, Phys. Plasmas **13**, 012702 (2006).
12. S. G. Glendinning, S. N. Dixit, B. A. Hammel, D. H. Kalantar, M. H. Key, J. D. Kilkenny, J. P. Knauer, D. M. Pennington, B. A. Remington, R. J. Wallace, and S. V. Weber, Phys. Rev. Lett. **78**, 3318 (1997).
13. H. Azechi *et al.*, Phys. Plasmas **4**, 4079 (1997).
14. V. A. Smalyuk, S. X. Hu, V. N. Goncharov, D. D. Meyerhofer, T. C. Sangster, D. Shvarts, C. Stoeckl, B. Yaakobi, J. A. Frenje, and R. D. Petrasso, Phys. Rev. Lett. **101**, 025002 (2008).
15. V. A. Smalyuk, S. X. Hu, V. N. Goncharov, D. D. Meyerhofer, T. C. Sangster, C. Stoeckl, and B. Yaakobi, Phys. Plasmas **15**, 082703 (2008).
16. R. Betti, V. N. Goncharov, R. L. McCrory, and C. P. Verdon, Phys. Plasmas **5**, 1446 (1998).
17. Y. C. Lee and P. K. Kaw, Phys. Rev. Lett. **32**, 135 (1974).
18. C. S. Liu and M. N. Rosenbluth, Phys. Fluids **19**, 967 (1976).
19. C. Stoeckl, R. E. Bahr, B. Yaakobi, W. Seka, S. P. Regan, R. S. Craxton, J. A. Delettrez, R. W. Short, J. Myatt, A. V. Maximov, and H. Baldis, Phys. Rev. Lett. **90**, 235002 (2003).
20. S. X. Hu, V. A. Smalyuk, V. N. Goncharov, J. P. Knauer, P. B. Radha, I. V. Igumenshchev, J. A. Marozas, C. Stoeckl, B. Yaakobi, D. Shvarts, T. C. Sangster, P. W. McKenty, D. D. Meyerhofer, S. Skupsky, and R. L. McCrory, Phys. Rev. Lett. **100**, 185003 (2008).
21. T. R. Boehly, D. H. Munro, P. M. Celliers, R. E. Olson, D. G. Hicks, V. N. Goncharov, G. W. Collins, H. F. Robey, S. X. Hu, J. A. Marozas, T. C. Sangster, O. L. Landen, and D. D. Meyerhofer, Phys. Plasmas **16**, 056302 (2008).
22. P. M. Celliers, D. K. Bradley, G. W. Collins, D. G. Hicks, T. R. Boehly, and W. J. Armstrong, Rev. Sci. Instrum. **75**, 4916 (2004).
23. V. A. Smalyuk, R. Betti, J. A. Delettrez, V. Yu. Glebov, V. N. Goncharov, D. Y. Li, D. D. Meyerhofer, S. P. Regan, S. Roberts, T. C. Sangster, C. Stoeckl, W. Seka, J. A. Frenje, C. K. Li, R. D. Petrasso, and F. H. Séguin, Phys. Plasmas **14**, 022702 (2007).
24. V. A. Smalyuk, D. Shvarts, R. Betti, J. A. Delettrez, D. H. Edgell, V. Yu. Glebov, V. N. Goncharov, R. L. McCrory, D. D. Meyerhofer, P. B. Radha, S. P. Regan, T. C. Sangster, W. Seka, S. Skupsky, C. Stoeckl, B. Yaakobi, J. A. Frenje, C. K. Li, R. D. Petrasso, and F. H. Séguin, Phys. Rev. Lett. **100**, 185005 (2008).
25. J. P. Knauer, P. B. Radha, V. N. Goncharov, I. V. Igumenshchev, R. Betti, R. Epstein, F. J. Marshall, S. P. Regan, V. A. Smalyuk, D. D. Meyerhofer, and S. Skupsky, Bull. Am. Phys. Soc. **52**, 233 (2007).

Diagnosing Fuel ρR and ρR Asymmetries in Cryogenic DT Implosions Using Charged-Particle Spectrometry on OMEGA

Introduction

Cryogenic deuterium–tritium (DT) capsules are routinely imploded on LLE's OMEGA Laser System.[1] These implosions are hydrodynamically equivalent to the baseline direct-drive-ignition design for the National Ignition Facility (NIF)[2] to allow for experimental validation of the design prior to the first ignition experiments at the NIF. The design consists of a cryogenic-DT-fuel layer inside a thin spherical ablator,[3] which is compressed quasi-isentropically to minimize the laser energy required to achieve ignition conditions. If the capsule is sufficiently compressed, the high areal density (ρR) of the cryogenic DT fuel can support a propagating thermonuclear burn wave due to local bootstrap heating by the DT-alpha particles. Maximizing ρR for a given on-capsule laser energy is therefore very important. Determining ρR is also important for assessing implosion performance during all stages of development from energy-scaled cryogenic DT implosions on OMEGA to cryogenic fizzles to ignited implosions on the NIF. Determining fuel ρR in moderate-ρR (100 to 200 mg/cm^2) cryogenic DT implosions has been challenging since it requires the development of new spectrometry techniques and analysis methods. A new type of neutron spectrometer, the magnetic recoil spectrometer (MRS),[4–6] has been built, installed, and calibrated on OMEGA to measure primarily the down-scattered DT neutron spectrum, from which ρR of the fuel can be directly inferred. Another MRS is currently being developed to diagnose high-ρR cryogenic DT-capsule implosions on the NIF.

This article describes a complementary method for analyzing the spectral shape of knock-on deuterons (KOd's), elastically scattered by primary DT neutrons, from which ρR can be inferred for values up to ~200 mg/cm^2. This new analysis method, which uses Monte Carlo modeling[7] of a cryogenic DT implosion, significantly improves, in two fundamental ways, the existing analysis method, which uses a relatively simple implosion model to relate the fuel ρR to the KOd yield in the high-energy peak.[8–10] First, it is not affected by significant spatial-yield variations, which degrade the diagnosis of fuel ρR (spatial-yield variations of about ±20% are typically observed). Secondly, it does not break down when the fuel ρR exceeds ~70 mg/cm^2. Modeling the actual shape of the KOd spectrum is therefore a more powerful method than the yield method for diagnosing the fuel ρR in cryogenic DT implosions.

The following sections describe the analysis method used to model the KOd spectrum, from which a ρR of the fuel can be inferred for a cryogenic DT implosion; present the experiments, data analysis, and results; and summarize the article.

Diagnosing Fuel ρR in Moderate-ρR Cryogenic DT Implosions Using Knock-On Deuterons

Fuel ρR in DT-filled CH-capsule implosions has been diagnosed routinely at the Omega Laser Facility for more than a decade.[8–10] In those experiments, two magnet-based charged-particle spectrometers (CPS's)[11] have been used to measure the KOd spectrum in two different directions. With the recent implementation of the MRS, a third measurement of the KOd spectrum is now possible (the MRS can be operated in a charged-particle mode, which involves removing the conversion foil near the implosion[5] and operating the system like a normal charged-particle spectrometer). Since both ρR and ρR symmetry are important measures of the performance of a cryogenic DT implosion, the MRS adds significantly to the existing ρR-diagnostic suite on OMEGA (Fig. 117.18).

For a fuel ρR around 100 mg/cm^2, about 1% of the primary DT neutrons elastically scatter off the deuterium, producing KOd's with energies up to 12.5 MeV as expressed by the reaction

$$\mathrm{n}(14.1\ \mathrm{MeV}) + \mathrm{D} \rightarrow \mathrm{n}' + \mathrm{D}'(\leq 12.5\ \mathrm{MeV}). \qquad (1)$$

At this neutron energy, the differential cross section for the nD-elastic scattering in the central-mass system is well known and represents the birth spectrum of the KOd's (see Fig. 117.19). As the KOd's pass through the high-density DT fuel, they lose energy in proportion to the amount of material through which they pass (ρR). A ρR value for the portion of the implosion

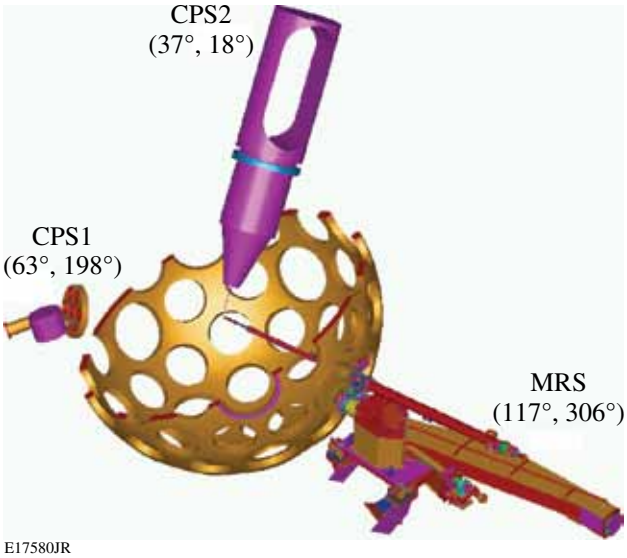

Figure 117.18
The magnetic recoil spectrometer (MRS) and the charged-particle spectrometers CPS1 and CPS2 on the OMEGA chamber. These spectrometers are used to simultaneously measure spectra of elastically scattered deuterons, so-called knock-on deuterons (KOd's), from which fuel ρR and ρR asymmetries in cryogenic DT implosions can be directly inferred. The MRS can operate in either charged-particle or down-scattered neutron mode; the latter mode allows one to measure the down-scattered neutron spectrum, from which the ρR of the fuel can be inferred as well.

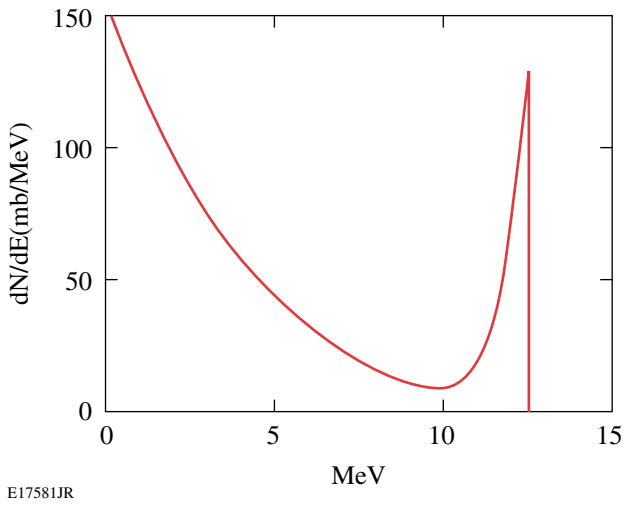

Figure 117.19
The birth spectrum of knock-on deuterons (KOd's), elastically scattered by primary 14.1-MeV neutrons. Due to kinematics, the KOd high-energy end point is at 12.5 MeV.

facing a given spectrometer can therefore be determined from the shape of the measured KOd spectrum by using theoretical formulation of the slowing down of deuteron energy in a plasma.[12] Previous work used a relatively simple model to relate the fuel ρR to the yield under the high-energy peak of the KOd spectrum.[8–10] That model, however, is subject to significant spatial-yield variations that degrade the diagnosis of the fuel ρR (spatial yield variations of about ±20% are typically observed). It also breaks down when the fuel ρR exceeds ~70 mg/cm^2 because the KOd spectrum becomes sufficiently distorted by the effects of energy slowing down that the measurement of the high-energy peak becomes ambiguous; an accurate determination of ρR must therefore rely on more-sophisticated modeling. Monte Carlo modeling of an implosion, similar to the modeling described in Ref. 7, was instead used to simulate the KOd spectrum from which a fuel ρR can be inferred. This made it possible to use more-realistic temperature and density profiles than those in the hot-spot and uniform models described in Refs. 8–10. From the Monte Carlo modeling, it was established that the shape of the KOd spectrum depends mainly on fuel ρR and that density and electron-temperature profile variations typically predicted in the high-density region play minor roles. This was concluded by studying how the spectral shape varied with varying temperature and density profiles for a fixed ρR. The variations were made to still meet a measured burn-averaged ion temperature of 2.0±0.5 keV, a radius of the high-density region of 30±10 μm, and a peak density of 10 to 160 g/cc (peak density varied less for a fixed ρR). The envelopes (represented by the standard deviation) in which the density and temperature profiles were varied are illustrated in Fig. 117.20 for a fuel ρR of 105 mg/cm^2. The resulting simulated birth profiles of the primary neutrons and KOd's are also shown in Fig. 117.20. Figure 117.21 shows how the simulated KOd spectrum varies with varying ρR. The error bars (standard deviation) shown in each spectrum represent the effect of varying density and temperature profiles, and as indicated by the error bars, the shape of the KOd spectrum depends weakly on any profile variations. In contrast, the spectral shape depends strongly on ρR. In addition, the modeling was constrained strictly by isobaric conditions at bang time, burn duration, DT-fuel composition, and a steady state during burn. As discussed in Ref. 13, the latter constraint is an adequate approximation for these types of measurements since the time evolution of the fuel ρR does not affect significantly the shape of the burn-averaged spectrum, which simplifies the ρR interpretation of the measured KOd spectrum. Multidimensional features could, on the other hand, affect the analysis and interpretation of the KOd spectrum since these effects would manifest themselves

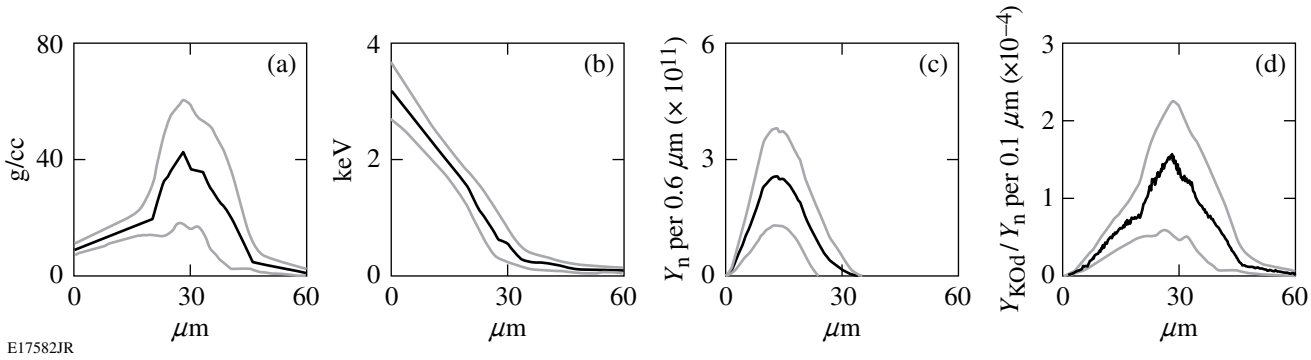

Figure 117.20
(a) Density and (b) temperature profiles used to model a cryogenic DT implosion with a ρR of 105 mg/cm^2. The black line represents the average, while the gray lines indicate the envelopes (represented by the standard deviation) in which the density and temperature profiles were varied. The variations were made to still meet the measured burn-averaged ion temperature of 2.0±0.5 keV and the position of the high-density region of 30±10 μm. Resulting birth profiles of the primary neutrons and KOd's are shown in (c) and (d). In addition, the modeling was constrained by isobaric conditions at bang time, burn duration, DT-fuel composition, and steady state during burn.

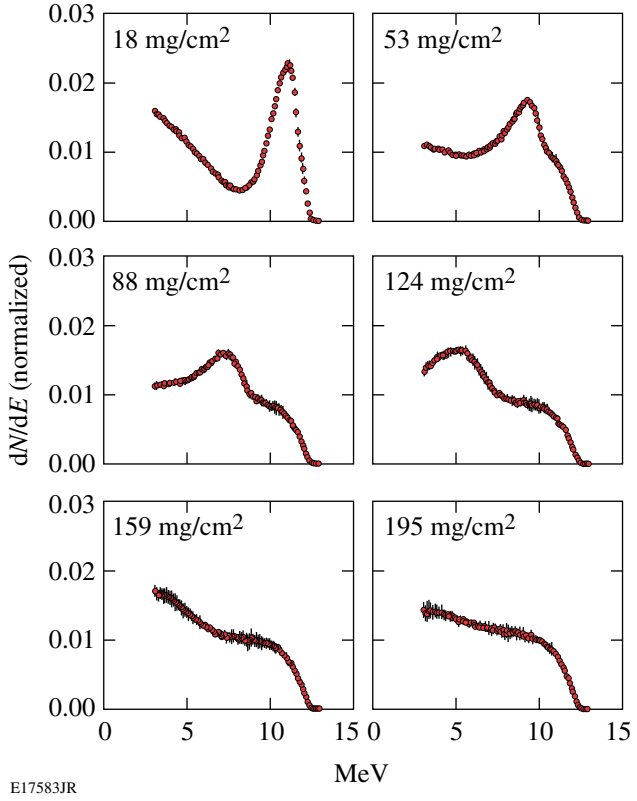

Figure 117.21
KOd spectra for different fuel ρR's. The error bars (standard deviation) shown in each spectrum represent the effect of varying density and temperature profiles. As illustrated, the shape of the KOd spectrum depends strongly on ρR, while density and temperature profile effects play minor roles as indicated by the error bars. The KOd spectra are normalized to unity.

by slightly smearing out the high-energy peak for low fuel ρR's (<100 mg/cm^2). For higher ρR's (>150 mg/cm^2), these effects should be less prominent since high-mode nonuniformities would not significantly alter the shape of the KOd spectrum.

Experiments, Data Analysis, and Results

The cryogenic DT-capsule implosions discussed in this article were driven with a laser pulse designed to keep the fuel on an adiabat α of approximately 1 to 3, where α is the ratio of the internal pressure to the Fermi-degenerate pressure.[14] The on-capsule laser energy varied from 12 to 25 kJ, and the laser intensity varied from 3×10^{14} to 10^{15} W/cm^2. Full single-beam smoothing was applied during all pulses by using distributed phase plates (DPP's),[15] polarization smoothing (PS) with birefringent wedges,[16] and 2-D, single-color-cycle, 1-THz smoothing by spectral dispersion (SSD).[17] The ablator was typically made of 5 to 10 μm of deuterated polyethylene (CD), which was permeation filled with an equimolar mixture of DT gas to 1000 atm. At this pressure, the shell and gas were slowly cooled to a few degrees below the DT triple point (19.8 K), typically producing a DT-ice layer of 90- to 100-μm thickness,[14] which is thicker than the OMEGA design energy scaled from the baseline direct-drive-ignition design for the NIF. The thicker DT ice was chosen to increase the shell stability during the acceleration phase of the implosion. In addition, by tailoring the adiabat in the shell and fuel, the expected imprint perturbation growth for such a thick shell is substantially reduced, further improving the implosion performance. Based on 1-D hydrocode simulations,[18] the burn-averaged fuel ρR is in excess of 200 mg/cm^2 for these types of implosions.

Figure 117.22 shows examples of measured and fitted simulated KOd spectra for four different low-adiabat cryogenic DT implosions. From the simulated fits to the measured spectra, ρR values ranging from 25 to 205 mg/cm^2 were inferred. The relatively low ρR's for shots 43070 and 43945 are primarily attributed to a nonoptimal-designed laser pulse shape that generated mistimed shocks. The performance of these implosions was also further degraded by the relatively large capsule offset of ~30 to 40 μm from target chamber center. Although the offset was about the same for shot 49035, the inferred ρR is significantly higher than for shots 43070 and 43945—a consequence of a better-designed laser pulse shape. The high ρR value for shot 48734 was achieved using the shock-ignition concept described in Refs. 19 and 20. The fact that the capsule was perfectly centered (11±15 μm) resulted in a determined ρR value close to the 1-D simulated value of about 200 mg/cm^2. In addition, it is notable that the high-energy endpoints are at the theoretical maximum of 12.5 MeV, demonstrating that KOd's are produced in the outermost parts of the implosion and the plastic ablator has been burnt away entirely.

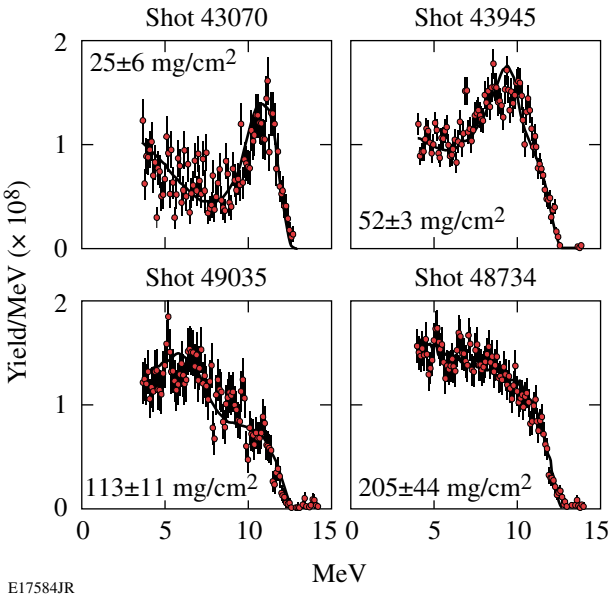

Figure 117.22
Examples of measured KOd spectra for four different low-adiabat, cryogenic DT implosions. Simulated fits (solid lines) to the measured spectra are also shown. From the fits, a fuel ρR of 25±6, 52±3, 113±11, and 205±44 mg/cm^2 was determined for shots 43070, 43945, 49035, and 48734, respectively. The errors of the inferred ρR values are due mainly to modeling uncertainties as discussed in this article and statistical uncertainties in the experimental data. See text for more detailed information about these implosions.

The ρR data obtained for hydrodynamically equivalent cryogenic D_2 implosions[14] were used to validate the ρR analysis of the KOd spectrum. Since a well-established ρR diagnostic technique exists for cryogenic D_2 implosions,[21] this comparison provides a good check of the analysis method described herein. The comparison is made in Fig. 117.23, which illustrates the experimental ρR as a function of 1-D predicted ρR [Fig. 117.23(a)] and the observed ρR_{asym} as a function of capsule offset [Fig. 117.23(b)] for low-adiabat DT and D_2 implosions driven at various intensities. Both sets of data show similar behavior, demonstrating that the ρR analysis of the KOd spectrum is accurate.

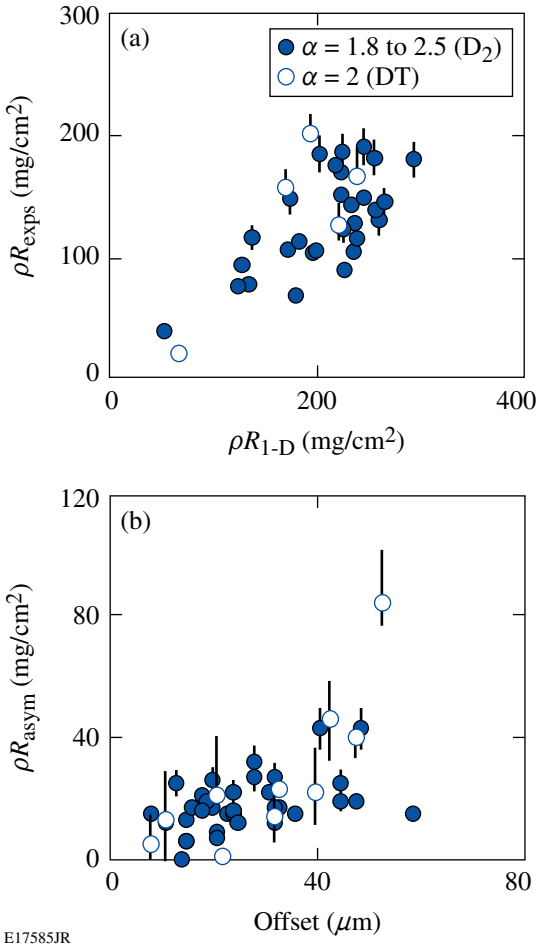

Figure 117.23
(a) Observed average ρR as a function of 1-D predicted ρR for implosions with a capsule offset of less than 40 μm to the target chamber center. (b) Observed ρR_{asym} as a function of capsule offset. These data sets are for low-adiabat DT (open data points) and D_2 (solid data points) implosions driven at various intensities. Similar performance relative to 1-D and similar ρR_{asym} as a function of capsule offset are observed for both the DT and D_2 implosions, indicating that the ρR analysis of the KOd spectrum is accurate.

Summary and Conclusions

Through Monte Carlo modeling of a cryogenic DT implosion it has been demonstrated that ρR's for moderate-ρR (<200 mg/cm^2) cryogenic DT implosions on OMEGA can be determined accurately from the shape of the measured KOd spectrum. Results from the Monte Carlo modeling of an implosion have provided a deeper understanding of the relationship between ρR, implosion structure, and KOd production. In particular, it was established that the shape of the KOd spectrum depends mainly on ρR, and that effects of spatially varying density and temperature profiles play minor roles. It should be pointed out that multidimensional features could have an effect on the analysis and interpretation of the KOd spectrum since these effects would manifest themselves by slightly smearing out the high-energy peak for low fuel ρR's (<100 mg/cm^2). For higher ρR's (>150 mg/cm^2), these effects should be less prominent since high-mode nonuniformities would not significantly alter the shape of the KOd spectrum. The ρR analysis of the KOd spectrum was also validated by comparing these results to ρR data obtained for hydrodynamically equivalent cryogenic D_2 implosions using a well-established ρR diagnostic technique. The good agreement observed between the two analysis methods indicates that the KOd analysis method described herein is accurate.

ACKNOWLEDGMENT

The work described here was supported in part by the U.S. Department of Energy (Grant No. DE-FG03-03SF22691), LLE (No. 412160-001G), LLNL (No. B504974), and GA under DOE (DE-AC52-06NA27279). This work was also supported by the U.S. Department of Energy Office of Inertial Confinement Fusion under Cooperative Agreement No. DE-FC52-08NA28302, the University of Rochester, and the New York State Energy Research and Development Authority. The support of DOE does not constitute an endorsement by DOE of the views expressed in this article.

REFERENCES

1. T. R. Boehly, D. L. Brown, R. S. Craxton, R. L. Keck, J. P. Knauer, J. H. Kelly, T. J. Kessler, S. A. Kumpan, S. J. Loucks, S. A. Letzring, F. J. Marshall, R. L. McCrory, S. F. B. Morse, W. Seka, J. M. Soures, and C. P. Verdon, Opt. Commun. **133**, 495 (1997).

2. G. H. Miller, E. I. Moses, and C. R. Wuest, Nucl. Fusion **44**, S228 (2004).

3. P. W. McKenty, V. N. Goncharov, R. P. J. Town, S. Skupsky, R. Betti, and R. L. McCrory, Phys. Plasmas **8**, 2315 (2001).

4. J. A. Frenje, K. M. Green, D. G. Hicks, C. K. Li, F. H. Séguin, R. D. Petrasso, T. C. Sangster, T. W. Phillips, V. Yu. Glebov, D. D. Meyerhofer, S. Roberts, J. M. Soures, C. Stoeckl, K. Fletcher, S. Padalino, and R. J. Leeper, Rev. Sci. Instrum. **72**, 854 (2001).

5. J. A. Frenje, D. T. Casey, C. K. Li, J. R. Rygg, F. H. Séguin, R. D. Petrasso, V. Yu. Glebov, D. D. Meyerhofer, T. C. Sangster, S. Hatchett, S. Haan, C. Cerjan, O. Landen, M. Moran, P. Song, D. C. Wilson, and R. J. Leeper, Rev. Sci. Instrum. **79**, 10E502 (2008).

6. V. Yu. Glebov, D. D. Meyerhofer, T. C. Sangster, C. Stoeckl, S. Roberts, C. A. Barrera, J. R. Celeste, C. J. Cerjan, L. S. Dauffy, D. C. Eder, R. L. Griffith, S. W. Haan, B. A. Hammel, S. P. Hatchett, N. Izumi, J. R. Kimbrough, J. A. Koch, O. L. Landen, R. A. Lerche, B. J. MacGowan, M. J. Moran, E. W. Ng, T. W. Phillips, P. M. Song, R. Tommasini, B. K. Young, S. E. Caldwell, G. P. Grim, S. C. Evans, J. M. Mack, T. Sedillo, M. D. Wilke, D. C. Wilson, C. S. Young, D. Casey, J. A. Frenje, C. K. Li, R. D. Petrasso, F. H. Séguin, J. L. Bourgade, L. Disdier, M. Houry, I. Lantuejoul, O. Landoas, G. A. Chandler, G. W. Cooper, R. J. Lepeer, R. E. Olson, C. L. Ruiz, M. A. Sweeney, S. P. Padalino, C. Horsfield, and B. A. Davis, Rev. Sci. Instrum. **77**, 10E715 (2006).

7. S. Kurebayashi, J. A. Frenje, F. H. Séguin, J. R. Rygg, C. K. Li, R. D. Petrasso, V. Yu. Glebov, J. A. Delettrez, T. C. Sangster, D. D. Meyerhofer, C. Stoeckl, J. M. Soures, P. A. Amendt, S. P. Hatchett, and R. E. Turner, Phys. Plasmas **12**, 032703 (2005).

8. S. Skupsky and S. Kacenjar, J. Appl. Phys. **52**, 2608 (1981).

9. S. Kacenjar, S. Skupsky, A. Entenberg, L. Goldman, and M. Richardson, Phys. Rev. Lett. **49**, 463 (1982).

10. C. K. Li, F. H. Séguin, D. G. Hicks, J. A. Frenje, K. M. Green, S. Kurebayashi, R. D. Petrasso, D. D. Meyerhofer, J. M. Soures, V. Yu. Glebov, R. L. Keck, P. B. Radha, S. Roberts, W. Seka, S. Skupsky, C. Stoeckl, and T. C. Sangster, Phys. Plasmas **8**, 4902 (2001).

11. F. H. Séguin, J. A. Frenje, C. K. Li, D. G. Hicks, S. Kurebayashi, J. R. Rygg, B.-E. Schwartz, R. D. Petrasso, S. Roberts, J. M. Soures, D. D. Meyerhofer, T. C. Sangster, J. P. Knauer, C. Sorce, V. Yu. Glebov, C. Stoeckl, T. W. Phillips, R. J. Leeper, K. Fletcher, and S. Padalino, Rev. Sci. Instrum. **74**, 975 (2003).

12. C. K. Li and R. D. Petrasso, Phys. Rev. Lett. **70**, 3059 (1993).

13. J. A. Frenje, C. K. Li, J. R. Rygg, F. H. Séguin, D. T. Casey, R. D. Petrasso, J. Delettrez, V. Yu. Glebov, T. C. Sangster, O. Landen, and S. Hatchett, Phys. Plasmas **16**, 022702 (2009).

14. T. C. Sangster, R. Betti, R. S. Craxton, J. A. Delettrez, D. H. Edgell, L. M. Elasky, V. Yu. Glebov, V. N. Goncharov, D. R. Harding, D. Jacobs-Perkins, R. Janezic, R. L. Keck, J. P. Knauer, S. J. Loucks, L. D. Lund, F. J. Marshall, R. L. McCrory, P. W. McKenty, D. D. Meyerhofer, P. B. Radha, S. P. Regan, W. Seka, W. T. Shmayda, S. Skupsky, V. A. Smalyuk, J. M. Soures, C. Stoeckl, B. Yaakobi, J. A. Frenje, C. K. Li, R. D. Petrasso, F. H. Séguin, J. D. Moody, J. A. Atherton, B. D. MacGowan, J. D. Kilkenny, T. P. Bernat, and D. S. Montgomery, Phys. Plasmas **14**, 058101 (2007).

15. Y. Lin, T. J. Kessler, and G. N. Lawrence, Opt. Lett. **20**, 764 (1995).

16. T. R. Boehly, V. A. Smalyuk, D. D. Meyerhofer, J. P. Knauer, D. K. Bradley, R. S. Craxton, M. J. Guardalben, S. Skupsky, and T. J. Kessler, J. Appl. Phys. **85**, 3444 (1999).

17. S. Skupsky, R. W. Short, T. Kessler, R. S. Craxton, S. Letzring, and J. M. Soures, J. Appl. Phys. **66**, 3456 (1989).

18. J. Delettrez, Can. J. Phys. **64**, 932 (1986).

19. R. Betti, C. D. Zhou, K. S. Anderson, L. J. Perkins, W. Theobald, and A. A. Solodov, Phys. Rev. Lett. **98**, 155001 (2007).

20. W. Theobald, R. Betti, C. Stoeckl, K. S. Anderson, J. A. Delettrez, V. Yu. Glebov, V. N. Goncharov, F. J. Marshall, D. N. Maywar, R. L. McCrory, D. D. Meyerhofer, P. B. Radha, T. C. Sangster, W. Seka, D. Shvarts, V. A. Smalyuk, A. A. Solodov, B. Yaakobi, C. D. Zhou, J. A. Frenje, C. K. Li, F. H. Séguin, R. D. Petrasso, and L. J. Perkins, Phys. Plasmas **15**, 056306 (2008).

21. F. H. Séguin, C. K. Li, J. A. Frenje, S. Kurebayashi, R. D. Petrasso, F. J. Marshall, D. D. Meyerhofer, J. M. Soures, T. C. Sangster, C. Stoeckl, J. A. Delettrez, P. B. Radha, V. A. Smalyuk, and S. Roberts, Phys. Plasmas **9**, 3558 (2002).

Plasma Density Determination from X-Ray Radiography of Laser-Driven Spherical Implosions

The fuel layer density of an imploding spherical shell is inferred from x-ray radiographs. The density distribution is determined by using Abel inversion to compute the radial distribution of the opacity κ from the observed optical depth τ. With the additional assumption of the mass of the remaining cold fuel, the absolute density distribution can be determined. This is demonstrated on the OMEGA Laser System with two x-ray backlighters of different mean energies that lead to the same inferred density distribution independent of backlighter energy.

Recent experiments on the OMEGA laser have successfully inferred the areal density of the imploding capsule at the time of fusion particle production[1–3] (hot-spot formation). At this time, the hot-spot temperature is at maximum, whereas the cold main fuel layer is still evolving. The integral areal density of the capsule is determined from the slowing down of protons resulting from D−^{3}He fusion reactions within the fuel. These can be either primary fusion reactions from a D^{3}He gas fill or secondary reactions from a D_2 gas fill. This method determines the total areal density ρR by associating proton energy loss with the amount of plasma traversal. This method is fairly insensitive to the assumptions about the conditions of the plasma but is restricted to sampling the areal density at the time of fusion particle production.

In non-igniting capsules, the cold main fuel layer produces negligible fusion yield; therefore it is difficult to diagnose. The problem is solved by the introduction of an outside source of radiation (backlighter) acting as a probe. Both x-ray[4] and proton backlighters[5] have been employed as plasma probes in laser-driven fusion experiments. X-ray backlighters have been extensively used for both planar experiments and spherical implosions on OMEGA.[6] X-ray backlighting of spherical implosions on OMEGA has been restricted to experiments using fewer than 60 beams to drive the target implosion, freeing up some of the beams to generate the x-ray backlighter emission. The recent completion of the Omega EP Facility[7] will make it possible to generate a backlighter while using all 60 OMEGA beams to drive the implosion.

In this work it is shown that the density distribution of the plasma can be inferred from framed x-ray radiographs. With x-ray backlighter emission available during and after core formation, the time history of the main fuel layer's density, and therefore the areal density, can be determined. The use of two-dimensional (2-D) imaging techniques such as pinhole imaging, Kirkpatrick–Baez microscopes, and Bragg crystal diffraction are preferred since there may be significant azimuthal variation of the plasma density.

In contrast to a previous treatment of this problem where only the relative density distribution was determined,[8] it is shown that with the application of Abel inversion and the further constraint of constant mass, the absolute plasma density distribution can be inferred from the framed x-ray radiographs. This is demonstrated using x-ray radiographs of polar-driven implosions[9] on the OMEGA Laser System[6] with simultaneous backlighters at a mean energy of ~2.3 keV (from broadband Au emission) and from ~4.7-keV x rays (from a Ti backlighter). Despite a significant difference in the magnitude of the plasma opacity resulting from these two backlighters, the method yields the same density distribution when simultaneous framed images are compared.

Absorption of backlighter x rays along a path L follows the relation

$$I = I_0 \times \exp\left[-\int \mu(E,r)\rho(r)\,\mathrm{d}L\right], \tag{1}$$

where I is the observed intensity, I_0 is the backlighter intensity, μ is the mass absorption coefficient at energy E in cm^2/g, and ρ is the density in g/cm^3. If the density distribution is spherically symmetric, the integral can be re-expressed as

$$\kappa_{\mathrm{A}}(E,y) = 2\int_y^{\infty} \frac{\mu(E,r)\rho(r)r\,\mathrm{d}r}{\sqrt{r^2-y^2}}, \tag{2}$$

where $\kappa_A(E,y)$ is the Abel transform[10] of the opacity $\kappa(E,r) = \mu(E,r)\,\rho(r)$ at the projected radial position y. The inverse Abel transform[10] gives the radially dependent opacity

$$\kappa(E,r) = -\frac{1}{\pi}\int_r^\infty \frac{d\kappa_A}{dy}\frac{dy}{\sqrt{y^2-r^2}}. \tag{3}$$

Normally applied to optically thin emission, Eq. (3), when combined with Eq. (1), determines the radial distribution of the opacity

$$\kappa(E,r) = \frac{1}{\pi}\int_r^\infty \frac{d}{dy}\left\{\ell n\left[\frac{I(y)}{I_0}\right]\right\}\frac{dy}{\sqrt{y^2-r^2}}. \tag{4}$$

If the mass absorption coefficient is approximately constant through the plasma, as is the case for bound-free absorption[11] by inner-shell electrons, then

$$\rho(r) = \kappa(E,r)/\mu_{\text{eff}}(E), \tag{5}$$

where $\mu_{\text{eff}}(E)$ is the mass absorption coefficient averaged over the effective energy band of the radiograph. Because of uncertainties in the instrumental response or an incomplete knowledge of the spectral shape, it is difficult to determine the exact value of $\mu_{\text{eff}}(E)$. If, however, the mass of the plasma shell M_{shell} is assumed or obtained from simulations, then $\mu_{\text{eff}}(E)$ can be determined as follows:

$$M_{\text{shell}} = \int \rho(r)\,dV = 4\pi\int \frac{\kappa(E,r)}{\mu_{\text{eff}}(E)} r^2\,dr, \tag{6}$$

$$\therefore\quad \mu_{\text{eff}}(E) = \frac{4\pi}{M_{\text{shell}}}\int \kappa(E,r)\times r^2\,dr. \tag{7}$$

By choosing M_{shell} to be the unablated mass, the absolute density is then determined. The applicability of this approximation has been previously explored[12] for deuterated polystyrene (CD) and shown to apply for absorption by the carbon atoms in the polystyrene when the temperature of the absorber is below ~100 eV and the density is below ~10 g/cm^3. If the plasma is isothermal, the temperature restriction is further relaxed. Fujioka *et al.*[13] have shown that absorption of x rays from a Ti backlighter (one of two used in this work) by polystyrene (CH) can indeed be characterized by an effective energy-band–dependent absorption coefficient.

If the absorber is fully stripped, as is the case for a pure-hydrogen fuel layer, and is at a sufficiently high temperature, as would be expected for a D or DT main fuel layer near stagnation, the opacity is $\propto \rho^2/T^{1/2}$, and, therefore, the optical depth is $\propto \rho^2 R/T^{1/2}$ (Refs. 14 and 15), where T is the temperature and R is the radius. If the temperature variation of the absorber is small, the radial variation of the opacity can be determined by Abel inversion from which a functional form of the density distribution can be determined. The assumption of constant mass allows one to calculate the absolute density distribution as a function of radius.

Experiments were performed using 40 beams of the OMEGA laser in the polar-drive illumination configuration,[9] emulating the conditions on the NIF (the National Ignition Facility)[16] when direct-drive implosions are performed with the beams in the indirect-drive configuration. The beam pointing used was described in Marshall *et al.*[9] (case 3, with offsets of rings 1, 2, and 3 of 90, 150, and 150 μm, respectively) on a target with an outer radius of 433 μm. The target consisted of a 24-μm-thick glow-discharge-polymer (GDP) (i.e., CH) shell filled with 15 atm of D_2 at room temperature. The main drive pulse consisted of a 1.5-ns pulse with a 1-to-3 (foot-to-main) intensity ratio, with the foot and main part of the pulse having approximately equal durations (~0.75 ns). A total of 13.2 kJ was incident on the target with 1-THz-bandwidth smoothing by spectral dispersion (SSD)[17] with polarization smoothing[18] used to minimize small-scale illumination nonuniformities. This pulse shape was used to keep the main fuel layer on a low adiabat $\left(E/E_{\text{Fermi}} \sim 3\right)$ (Ref. 19).

Two backlighter targets were employed opposite two x-ray framing cameras. One backlighter was a 25-μm-thick Au foil and the other a 25-μm-thick Ti foil, each with four OMEGA beams of ~350 J/beam, focused to diameters of 750 μm and 600 μm, respectively. Each framing camera was positioned behind a 4×4 array of 10-μm-diam pinholes producing four strips of framed images with a time-gated resolution of ~30 ps, 56 ps between images, and strip times independently set to the nearest 100 ps. Absolute frame times were determined by observing the backlighter onset on the first strip and from the measured delay from strip to strip determined from an electronically recorded monitor signal.

The images are recorded on film with an imposed step wedge, so that absolute intensity variations can be determined. The exposed images and step wedge are developed simultaneously to make possible the subsequent conversion to intensity

variation from scanned and digitized film. Variations of the backlighter intensity are removed by fitting the shape of the backlighter to a supergaussian-plus background outside the region of the target radiograph and then extending this fit to the region of the radiograph.[20]

Figure 117.24 shows a set of these corrected radiographs up to shell stagnation, which occurs at ~2.3 ns. The values are presented as $-\ell n\left(I/I_0\right)$ [i.e., the optical depth τ]; all values are >0 with the exception of the frames from 2.32 ns and on, where self-emission from the core exceeds emission from the backlighter in the central region of the images. Figure 117.25(a) shows the azimuthally averaged optical-depth variation for one nearly simultaneous pair (at the mean time of $t = 2.14$ ns) of Au- and Ti-backlit images. The magnitude of the optical depth is greater for the lower-energy backlighter, as expected. The dotted line in Fig. 117.25(a) is the Au-backlit profile divided by 1.7, showing that the optical depths differ by only a multiplicative constant. Applying Abel inversion and assuming the unablated shell mass (3.34×10^{-5} g) given by the one-dimensional (1-D) hydrodynamic code *LILAC*[21] determines the density distributions from the observed optical depths [Fig. 117.25(b)]. The inferred density distributions from the Au and Ti backlighters are nearly identical, with only small differences due to noise in the images.

Figure 117.26 shows the density distributions determined for a sample of these images. The densities inferred from one additional simultaneous pair of Au- and Ti-backlit images are included. The *LILAC*-simulated shell density is shown for comparison for the 2.20-ns case. Figure 117.27 shows the resulting calculated shell areal densities ρR_{shell} determined from all Au- and Ti-backlit images plotted as a function of frame time from the beginning of the main laser pulse ($t = 0$). For the two frames where the Au- and Ti-backlit images occurred at the same time, the areal density values are the same within errors. All times have an uncertainty of ±50 ps. The absolute densities, and therefore areal densities, are assumed to be uncertain by ±10% because of an uncertainty in the unablated mass. The time from ~2.3 to 2.6 ns corresponds to the time during which intense x-ray emission from the core as well as fusion production occurs. During peak emission, heat from the core moves out through the shell and absorption by the backlighter is momentarily obscured. Since an independent measurement of this emission is not available (image with no backlighter), it cannot be corrected for and no density profiles are determined during this time interval. Later in time, the shell cools and absorption of the backlighter reappears. Frames during this later time were recorded by the Ti-backlit framing camera (2.70 ns and later).

The mean neutron production time (bang time), as recorded by the neutron temporal diagnostic,[22] occurred at 2.43 ns during the time interval when x-ray emission from the core is evident. The areal density averaged over the time of fusion particle production was independently determined by a set of three filtered

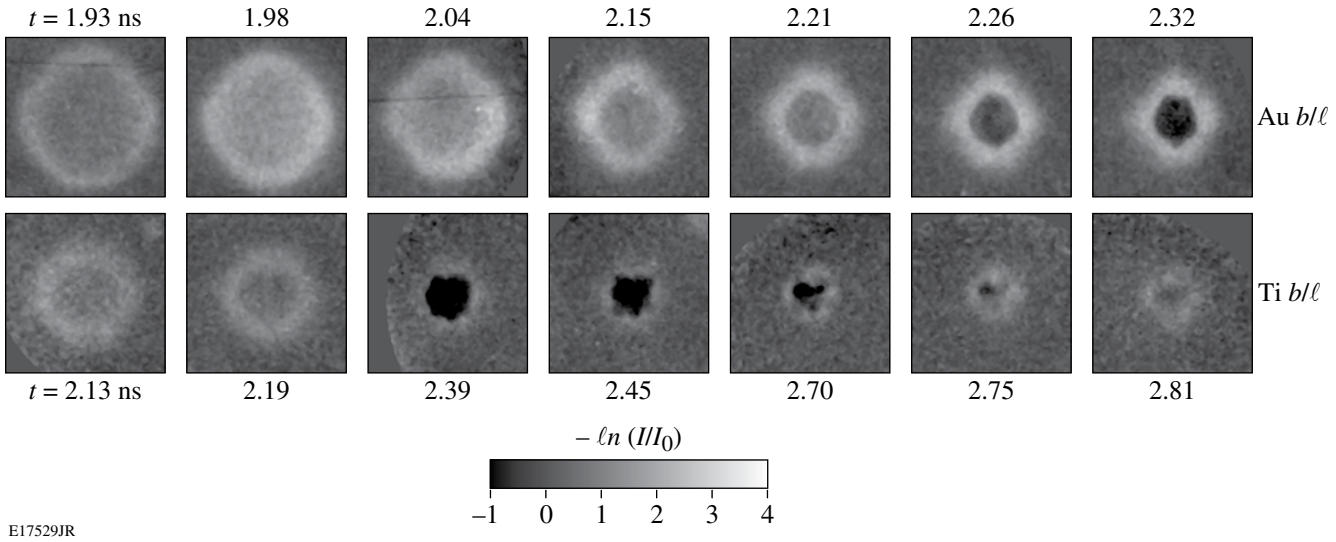

Figure 117.24
Intensity-corrected x-ray radiographs from OMEGA shot 49331 taken with two x-ray framing cameras, one backlit by an Au target and the other by a Ti target. Each image is a 400×400-μm region corrected for backlighter intensity variation as explained in the text.

CR39 packs measuring the slowing down of the D–^{3}He protons[1] and yields a value of $\langle \rho R \rangle_p$ = 58±5 mg/cm^2 (the error is one standard deviation of the three values). The value determined in this case is the sum of the areal densities of the fuel (gas fill) and the shell. An estimate of the fuel areal density ρR_{fuel} is determined from the size of the observed core emission at stagnation (~50 μm) and mass conservation, yielding ρR_{fuel} = 6±1 mg/cm^2. The proton inferred shell areal density is therefore $\langle \rho R_{shell} \rangle_p$ = 52±5 mg/cm^2 and is plotted as a single point in Fig. 117.27 at bang time. The value determined from the proton spectra falls closely on the trend of the x-ray measurements, giving additional credence to the results of this method. The *LILAC* simulation of this implosion was performed assuming flux-limited diffusion[23] with a flux limiter f = 0.06. The predicted areal density is shown as a solid line in Fig. 117.27. The areal density measurements are seen to closely follow this prediction until the time of stagnation, where significant departures from spherical symmetry can be seen in the framed images (Fig. 117.24).

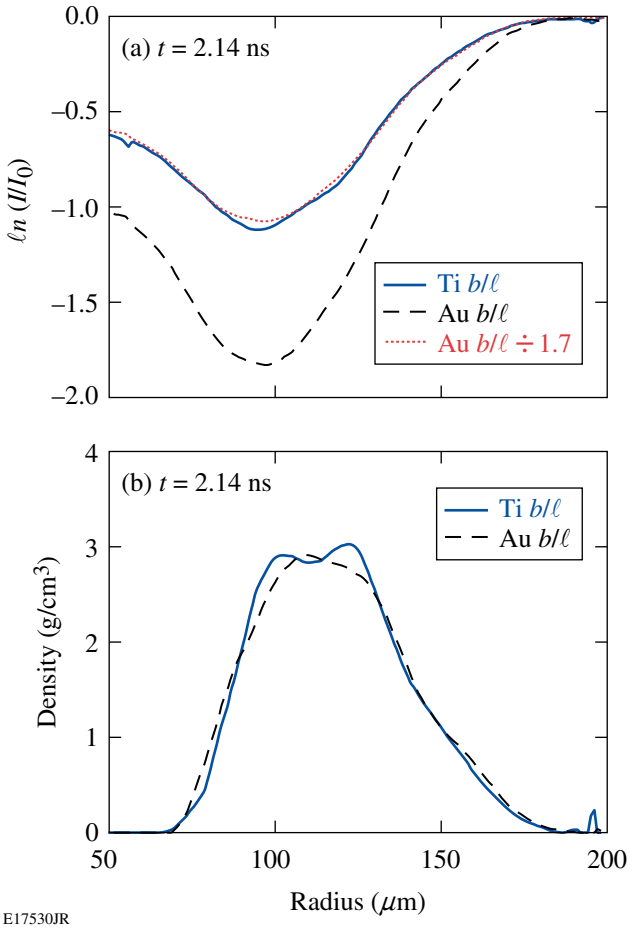

Figure 117.25
(a) The natural logarithm of the intensity variation as a function of projected radial distance in the image plane for a simultaneous pair of Au- and Ti-backlit images. The profiles are azimuthally averaged about the image centers. The dotted line is the Au profile normalized to the Ti profile, demonstrating that they differ only by a multiplicative constant (1.7). (b) The absolute density distributions were computed from the intensity profiles of (a) by Abel inversion with the additional constraint of constant mass as described in the text.

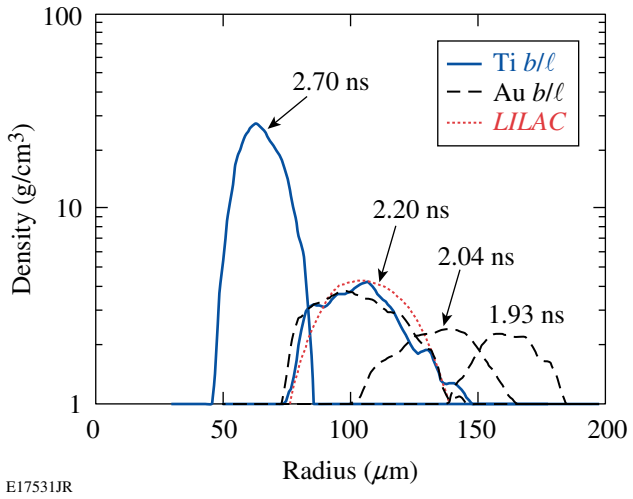

Figure 117.26
Density distributions computed from the x-ray radiographs showing the evolution of the shell density and position as a function of the indicated frame times.

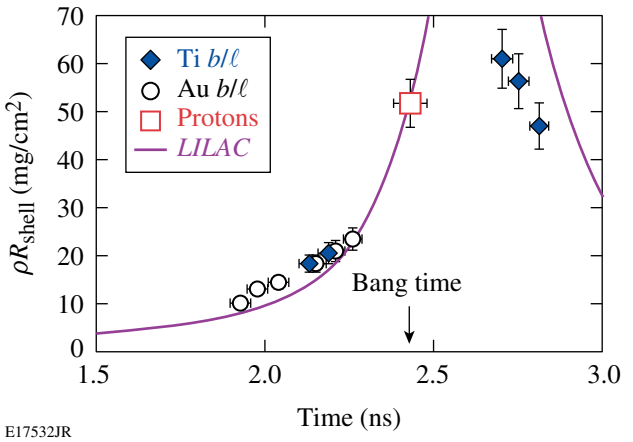

Figure 117.27
The shell areal densities computed from all available x-ray radiographs including those where the emission from the core is just starting (2.3 ns) to the tail end of the core emission (2.6 ns) and later. The value determined from the proton spectra is plotted at the time of peak neutron emission (2.43 ns). The *LILAC*-simulated shell areal density, shown as a solid curve, reached a peak of 110 mg/cm^2 at 2.64 ns (off scale).

This analysis demonstrates that with the application of an area x-ray backlighter, the time history of the shell areal density can be measured on a single implosion experiment from early in the implosion, up to stagnation, and again later in time after core emission has subsided. Such a determination is limited by the temporal extent of the backlighter and the requisite exclusion of target self-emission. A similar measurement of the areal-density time history using proton radiography[5] requires that the implosion be repeated, acquiring a single time measurement from each of a series of identical implosions. The x-ray radiography technique therefore offers a much less intensive use of the experimental facility, not requiring that the implosion be repeated multiple times to acquire the areal-density time history. The results of this technique support the conclusion that the direct-drive implosion exhibits near 1-D performance, in this case up to the time of core self-emission, with evolving nonuniformities affecting the performance thereafter.

ACKNOWLEDGMENT

This work was supported by the U.S. Department of Energy Office of Inertial Confinement Fusion under Cooperative Agreement No. DE-FC52-08NA28302, the University of Rochester, and the New York State Energy Research and Development Authority. The support of DOE does not constitute an endorsement by DOE of the views expressed in this article.

REFERENCES

1. F. H. Séguin, J. A. Frenje, C. K. Li, D. G. Hicks, S. Kurebayashi, J. R. Rygg, B.-E. Schwartz, R. D. Petrasso, S. Roberts, J. M. Soures, D. D. Meyerhofer, T. C. Sangster, J. P. Knauer, C. Sorce, V. Yu. Glebov, C. Stoeckl, T. W. Phillips, R. J. Leeper, K. Fletcher, and S. Padalino, Rev. Sci. Instrum. **74**, 975 (2003).

2. V. A. Smalyuk, P. B. Radha, J. A. Delettrez, V. Yu. Glebov, V. N. Goncharov, D. D. Meyerhofer, S. P. Regan, S. Roberts, T. C. Sangster, J. M. Soures, C. Stoeckl, J. A. Frenje, C. K. Li, R. D. Petrasso, and F. H. Séguin, Phys. Rev. Lett. **90**, 135002 (2003).

3. J. A. Frenje, C. K. Li, F. H. Séguin, J. Deciantis, S. Kurebayashi, J. R. Rygg, R. D. Petrasso, J. Delettrez, V. Yu. Glebov, C. Stoeckl, F. J. Marshall, D. D. Meyerhofer, T. C. Sangster, V. A. Smalyuk, and J. M. Soures, Phys. Plasmas **11**, 2798 (2003).

4. O. L. Landen *et al*., Rev. Sci. Instrum. **72**, 627 (2001).

5. C. K. Li, F. H. Séguin, J. A. Frenje, M. Manuel, R. D. Petrasso, V. A. Smalyuk, R. Betti, J. Delettrez, J. P. Knauer, F. Marshall, D. D. Meyerhofer, D. Shvarts, C. Stoeckl, W. Theobald, J. R. Rygg, O. L. Landen, R. P. J. Town, P. A. Amendt, C. A. Back, and J. D. Kilkenny, Plasma Phys. Control. Fusion **51**, 014003 (2009).

6. T. R. Boehly, D. L. Brown, R. S. Craxton, R. L. Keck, J. P. Knauer, J. H. Kelly, T. J. Kessler, S. A. Kumpan, S. J. Loucks, S. A. Letzring, F. J. Marshall, R. L. McCrory, S. F. B. Morse, W. Seka, J. M. Soures, and C. P. Verdon, Opt. Commun. **133**, 495 (1997).

7. C. Stoeckl, J. A. Delettrez, J. H. Kelly, T. J. Kessler, B. E. Kruschwitz, S. J. Loucks, R. L. McCrory, D. D. Meyerhofer, D. N. Maywar, S. F. B. Morse, J. Myatt, A. L. Rigatti, L. J. Waxer, J. D. Zuegel, and R. B. Stephens, Fusion Sci. Technol. **49**, 367 (2006).

8. D. H. Kalantar *et al*., Rev. Sci. Instrum. **68**, 814 (1997).

9. F. J. Marshall, R. S. Craxton, M. J. Bonino, R. Epstein, V. Yu. Glebov, D. Jacobs-Perkins, J. P. Knauer, J. A. Marozas, P. W. McKenty, S. G. Noyes, P. B. Radha, W. Seka, S. Skupsky, and V. A. Smalyuk, J. Phys. IV France **133**, 153 (2006).

10. R. N. Bracewell, *The Fourier Transform and Its Applications*, 3rd ed. (McGraw-Hill, Boston, 2000), pp. 351–356.

11. H. A. Bethe and E. E. Salpeter, *Quantum Mechanics of One- and Two-Electron Atoms* (Academic Press, New York, 1957), pp. 295–305.

12. F. J. Marshall, J. A. Delettrez, R. Epstein, and B. Yaakobi, Phys. Rev. E **49**, 4381 (1994).

13. S. Fujioka *et al*., Phys. Plasmas **10**, 4784 (2003).

14. Ya. B. Zel'dovich and Yu. P. Raĭzer, in *Physics of Shock Waves and High-Temperature Hydrodynamic Phenomena*, edited by W. D. Hayes and R. F. Probstein (Academic Press, New York, 1966), Chap. V, Vol. I, pp. 269–272.

15. B. Yaakobi, R. Epstein, and F. J. Marshall, Phys. Rev. A **44**, 8429 (1991).

16. W. J. Hogan, E. I. Moses, B. E. Warner, M. S. Sorem, and J. M. Soures, Nucl. Fusion **41**, 567 (2001).

17. S. Skupsky, R. W. Short, T. Kessler, R. S. Craxton, S. Letzring, and J. M. Soures, J. Appl. Phys. **66**, 3456 (1989).

18. T. R. Boehly, V. A. Smalyuk, D. D. Meyerhofer, J. P. Knauer, D. K. Bradley, R. S. Craxton, M. J. Guardalben, S. Skupsky, and T. J. Kessler, J. Appl. Phys. **85**, 3444 (1999).

19. J. D. Lindl, Phys. Plasmas **2**, 3933 (1995).

20. J. P. Knauer, R. Betti, D. K. Bradley, T. R. Boehly, T. J. B. Collins, V. N. Goncharov, P. W. McKenty, D. D. Meyerhofer, V. A. Smalyuk, C. P. Verdon, S. G. Glendinning, D. H. Kalantar, and R. G. Watt, Phys. Plasmas **7**, 338 (2000).

21. J. Delettrez, R. Epstein, M. C. Richardson, P. A. Jaanimagi, and B. L. Henke, Phys. Rev. A **36**, 3926 (1987).

22. R. A. Lerche, D. W. Phillion, and G. L. Tietbohl, Rev. Sci. Instrum. **66**, 933 (1995).

23. R. C. Malone, R. L. McCrory, and R. L. Morse, Phys. Rev. Lett. **34**, 721 (1975).

Integrated Simulations of Implosion, Electron Transport, and Heating for Direct-Drive Fast-Ignition Targets

Introduction

In fast-ignition[1] inertial confinement fusion (ICF), a cryogenic shell of deuterium and tritium (DT) is first imploded by a high-energy driver to produce an assembly of thermonuclear fuel with high densities and areal densities. Such a dense core is then ignited by the fast electrons (or protons) accelerated through the interaction of a high-power, ultra-intense laser pulse with either a coronal plasma or a solid cone-shaped target.[2,3] The separation of the target compression and ignition stages in fast ignition relaxes the requirements on the symmetry of the implosion and compression energy. By using massive cryogenic targets,[4] fast ignition has the potential for gains higher than the conventional ICF central hot-spot ignition scheme.

Fast ignition has shown significant promise in successful small-scale integrated experiments[2] that combine implosions of plastic cone-in-shell targets and heating by subpetawatt laser pulses. The next generation of integrated fast-ignition experiments will use more-massive plastic or cryogenic-DT cone-in-shell targets heated by more-powerful petawatt laser pulses. Such experiments have started at LLE and are planned at other facilities, such as ILE (Osaka University), NIF (LLNL), and the HiPER project. The success of those experiments depends crucially on the understanding of fast-ignition physics and its careful modeling using the best-available numerical codes. The rich physics of fast ignition includes processes having very different temporal and spatial scales, which must be studied using different types of codes. Target implosions are simulated using hydrocodes. Generation of hot electrons by a petawatt laser pulse is simulated using particle-in-cell (PIC) codes. Transport of hot electrons to the dense core is simulated using hybrid-PIC, Monte Carlo, or Fokker–Plank codes. Ignition and burn require simulations of fusion reactions, α-particle transport, and target hydrodynamics, which are done using hydrocodes.

At LLE a comprehensive theory and simulation program is being pursued to explore the physics of fast ignition. High-gain fast-ignition targets have been developed based on hydrodynamic simulations of implosion,[4] and performance of those targets has been investigated using hydrodynamic and hybrid simulations.[5,6] The capabilities of the radiation-hydrodynamic code *DRACO*,[7] developed at LLE to study the implosion physics, have been recently extended to simulate cone-in-shell targets.[8] *DRACO* has also been recently integrated with the hybrid-PIC code *LSP*[9] to simulate the hot-electron transport, target heating, and ignition.[6]

This article reports the latest results from integrated simulations of implosion, hot-electron transport, and heating, for direct-drive, cone-in-shell surrogate plastic targets used in the integrated fast-ignition experiments at LLE, performed using *DRACO* and *LSP*. *LSP* simulations of planar plastic targets are also presented. An important effect found in the simulations is the collimation of hot electrons by the self-generated resistive magnetic field. This effect appears to be highly beneficial for fast ignition because hot electrons are generated in the petawatt laser interaction with a solid-density plasma of the cone tip with an inevitable angular spread.[10,11] In the absence of collimation there is little hope to deliver the energy by hot electrons into a small volume of the target core with a radius of about 20 μm, located tens or even hundreds of μm away from the cone tip.[5,12,13] Magnetic collimation of hot electrons increases their coupling with the core and thus decreases the minimum energy required for ignition.

The following sections describe (1) *DRACO* and *LSP*, the two codes used in the simulations; (2) *LSP* simulations of hot-electron transport in solid-density and compressed plastic targets, providing a connection between the recent solid-target experiments and near-future integrated fast-ignition experiments using imploded plastic shells; and (3) the results from integrated simulations of realistic cone-in-shell plastic (CD) targets used in the integrated fast-ignition experiments at LLE, predicting target heating by hot electrons and neutron yields from deuterium–deuterium (D–D) nuclear reactions. The last section summarizes conclusions.

DRACO, *LSP*, and Integrated *DRACO–LSP* Simulation Toolkit

DRACO[7] is a two-dimensional (2-D) axisymmetric radiation-hydrodynamic code developed at LLE. It includes the physics required to simulate implosion, ignition, and burn of direct-drive ICF targets. It includes radiation transport and uses realistic equations of state. *LSP*[9] (large-scale plasma) is a 2-D/3-D (three-dimensional) implicit hybrid-PIC code. It uses an implicit solution for the electromagnetic fields and an implicit particle push, hybrid fluid-kinetic description for plasma electrons with dynamic reallocation, intra- and interspecies collisions based on Spitzer rates, and an ideal-gas equation of state. The hybrid fluid-kinetic description for plasma electrons is especially suited for modeling the hot-electron transport in the fast-ignition scheme. Fluid species can be used for background plasma electrons (and ions) while kinetic species are required to describe energetic electrons. The temperature equation solved for fluid species provides good energy conservation in the modeling of plasma heating by hot electrons. An implicit algorithm in *LSP* provides numerical stability even for very dense plasmas, when the numerical time step greatly exceeds the period of plasma oscillations (high-frequency phenomena, however, are not resolved).

The collisional model in *LSP* was modified to include relativistic and high-density plasma effects and extensively tested to reproduce the correct ranges, blooming, and straggling of hot electrons, as predicted by Refs. 14 and 15. The collisional model uses new recalculated transport scattering coefficients for hot electrons, obtained using the relativistic Rutherford-scattering cross section.[16] The transport coefficients for hot electrons are also modified to account for the electron energy loss caused by incoherent excitation of plasma waves.[14] The fluid electron−ion Spitzer collisional rate is modified to saturate at low electron temperatures to reproduce the appropriate maximum electrical resistivities.[17] For compressed materials, the fluid electron-ion Spitzer collisional rate is saturated below the Fermi-degenerate temperature $\left[\hbar^2\left(\pi^2 n_e\right)^{2/3}/3^{1/3}m_e\right]$, which can be hundreds of eV for compressed DT or plastic fast-ignition targets. The Coulomb logarithms in the Spitzer rates are modified to include ion strong-coupling and electron-degeneracy corrections as suggested in Ref. 18. Since, in the collisional model in *LSP*, each species is approximated by a single drifting (relativistic) Maxwellian distribution, simulations in this article use separate species for hot electrons in different energy ranges. This ensures that correct scattering and slowing-down rates are used for hot electrons at different energy levels.

The *DRACO* and *LSP* codes have been recently integrated and used to simulate electron transport and ignition for spherically symmetric cryogenic-DT, high-gain, fast-ignition targets.[6] In the integrated simulations, *LSP* generates the hot-electron source term in the temperature equation for background plasma electrons, solved in *DRACO*. In the simulations of Ref. 6, a self-generated resistive magnetic field was found to collimate the hot electrons and reduce the minimum energy required for ignition, in agreement with Ref. 19. The minimum hot-electron-beam energy of 43 kJ was found to be necessary for ignition using Gaussian electron beams with a mean electron energy of 2 MeV and a divergence half-angle of 20°. Collimation is less effective for electron beams with a larger divergence half-angle.

Simulations of Hot-Electron Transport in Solid-Density and Compressed Plastic Targets

In cone-guided fast ignition, hot electrons are generated by the petawatt laser pulse interacting with the tip of a gold cone about a hundred or more microns away from the dense target core. The transport of hot electrons to the dense core is possible if the beam current of about 1 GA, greatly exceeding the Alfvén limit, is compensated by the return current of plasma electrons. Most present experiments that study the transport of hot electrons in such conditions use solid-density metallic, plastic, or glass targets. The transport properties of hot electrons in those materials can be significantly different than in the compressed hydrogenic plasmas of fast-ignition targets, for instance, due to very different values of the electrical resistivities.

For a 300-g/cm^3 plasma, the hot-electron beam energy required for ignition is minimized when the beam radius on target is about 20 μm (Refs. 5, 12, and 13), approximately the minimum size of the laser spot on target. Since hot electrons are generated with an intrinsic angular spread, some collimation mechanism is necessary for the electron-beam radius to remain constant when it reaches the dense core. Collimation of hot electrons was observed in the plastic- and glass-target experiments using relatively low energy laser pulses of a few tens of joules.[20−22] More recent experiments (see Ref. 10 and references therein) using more-energetic laser pulses up to a few hundred joules and metallic (usually aluminum or copper) or plastic targets did not show collimation, with the divergence angle of hot electrons found to increase with the laser pulse intensity (see, for instance, Fig. 2 of Ref. 10). Hot-electron collimation in the experiments of Refs. 20−22 was explained by the presence of self-generated resistive magnetic fields.[23,24]

We have performed *LSP* simulations of hot-electron transport in solid-density plastic plasmas ($\rho \approx 1$ g/cm^3) containing hydrogen ions H^+ and four-times-ionized carbon ions C^{4+}. The Spitzer plasma resistivity[25] was saturated at low temperatures according to $\eta = 1\Big/\sqrt{\eta_{\max}^{-2} + \eta_{Sp}^{-2}}$, where[17] $\eta_{\max} = 3 \times 10^{-6}\,\Omega$m. Figures 117.28–117.30 show the results of 2-D planar geometry simulations performed for three different laser-pulse intensities. The laser pulses are Gaussian in space and in time with a focal-spot diameter of 10 μm, full width at half maximum (FWHM), and duration of 1 ps. The maximum intensities in the simulations of Figs. 117.28–117.30 are 5×10^{18} W/cm^2, 2×10^{19} W/cm^2, and 6×10^{19} W/cm^2, respectively. The laser wavelength is $\lambda_0 = 1.054$ μm. Hot electrons are promoted from the background of plasma electrons at the left-hand-side plasma boundary, having an exponential energy distribution $\left[\exp\left(-E\Big/\langle E\rangle\right)\right]$. The mean energy is given by the maximum of the ponderomotive[26] and Beg's[27] scaling

$$\langle E\rangle\,[\mathrm{MeV}] = \max\left\{0.511\left[\left(1 + I\lambda_0^2\Big/2.8 \times 10^{18}\right)^{1/2} - 1\right],\right.$$

$$\left. 0.1\left(I\lambda_0^2\Big/10^{17}\right)^{1/3}\right\},$$

where I is the local instantaneous value of the laser intensity in W/cm^2 and λ_0 is in μm. The energy-conversion efficiency to hot electrons is given by[28]

$$\eta_h = 1.75 \times 10^{-6} I^{0.2661}.$$

Hot electrons are injected in the plane of simulation at a random angle toward the beam axis, having a Gaussian distribution and a mean half-angle of 30°, half width at half maximum (HWHM). (Such a divergence half-angle is consistent with recent particle-in-cell simulations of hot-electron generation by a petawatt laser pulse.[10,11])

Snapshots of the hot-electron-beam density and magnetic field 700 fs after the peak of the laser pulse are shown in Figs. 117.28–117.30. It is seen that the hot-electron beam is sufficiently well collimated by the self-generated resistive magnetic field in the simulation of Fig. 117.28, while it is only partially collimated in the simulations of Figs. 117.29 and 117.30. The resistive filamentation[29] of electron beams is also observed in the simulations. Figures 117.31(a)–117.31(c) show the results of similar simulations in which the laser-spot diameter was increased to 20 μm. Figure 117.31 shows a similar trend as

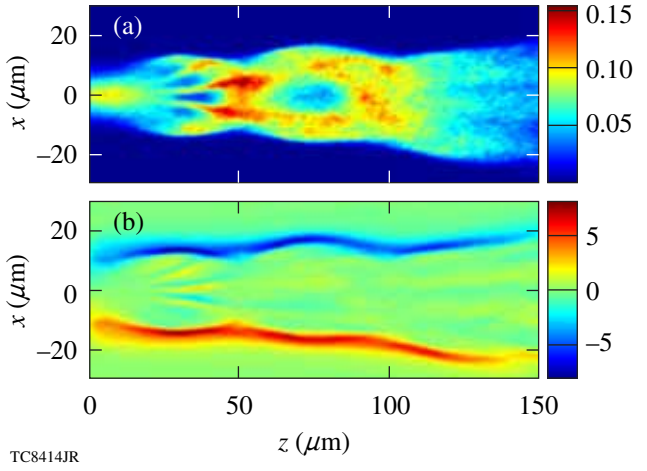

Figure 117.28
(a) Hot-electron density (in cm$^{-3} \times 10^{21}$) and (b) B_y component of magnetic field (in MG) 700 fs after the peak of the laser pulse in the simulation for a solid-density plastic target, and a laser pulse with a focal-spot diameter of 10 μm and a maximum intensity of 5×10^{18} W/cm^2.

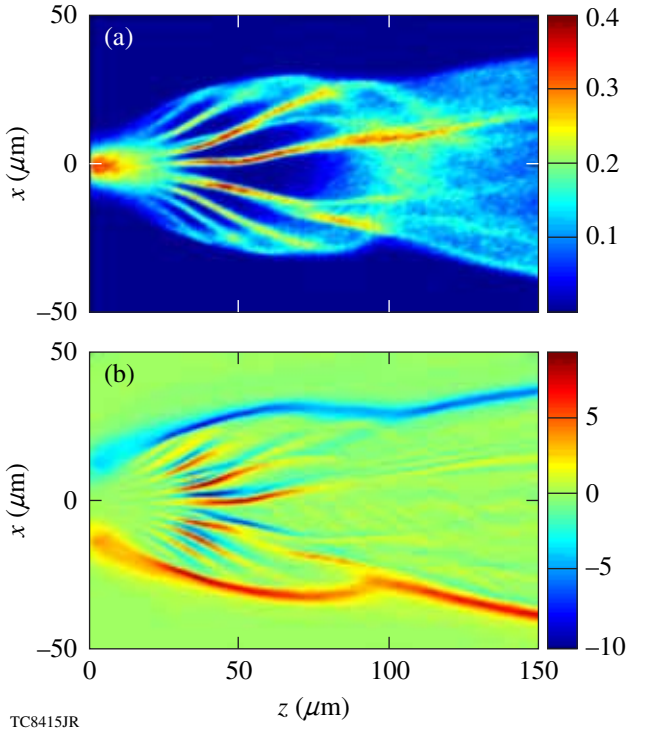

Figure 117.29
(a) Hot-electron density (in cm$^{-3} \times 10^{21}$) and (b) B_y component of magnetic field (in MG) 700 fs after the peak of the laser pulse in the simulation for a solid-density plastic target, and a laser pulse with a focal-spot diameter of 10 μm and a maximum intensity of 2×10^{19} W/cm^2.

Figs. 117.28–117.30—the electron collimation decreases when the laser intensity is increased. The same trend was observed in the solid-target electron-transport experiments. Electron collimation seems to be slightly weaker in the simulations with a larger spot size (Fig. 117.31), but the main dependence is on the laser intensity, in agreement with Ref. 10. Notice that more-sophisticated three-dimensional simulations are required for a better quantitative agreement of the electron-divergence half-angle in the experiments and simulations. The intensity dependence of the initial electron-divergence half-angle in the target, details of the resistivities for different target materials, and the ionization energy loss should also be accounted for. Such 3-D simulations are in progress.

The first integrated fast-ignition experiments on OMEGA will be performed on imploding plastic targets, leading to plasmas with densities exceeding the solid-state value. The simulation of Fig. 117.32 uses a $C^{4+}H^{+}$ uniform plasma with a density of 10× the solid density value ρ_{solid}, while in the simulation of Fig. 117.33, a Gaussian density distribution,

$$\rho = 100\,\rho_{solid} \times \exp\left(-\left\{\left[z(\mu\text{m}) - 90\right]^2 + x(\mu\text{m})^2\right\}\Big/ 42^2\right),$$

is used to mimic the profile of a compressed fast-ignition target. In the simulation of Fig. 117.33 the density grows from ρ_{solid} at

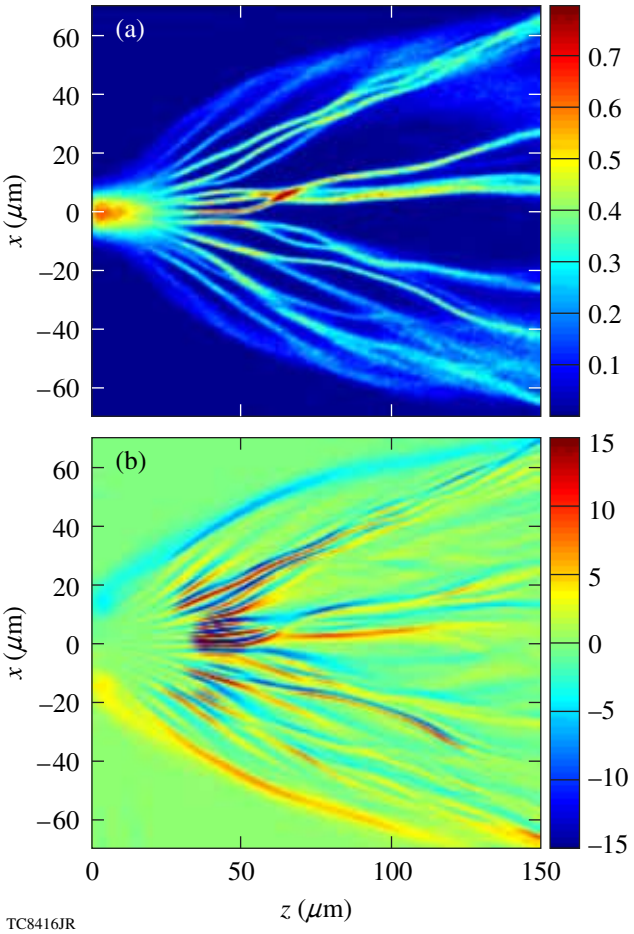

Figure 117.30
(a) Hot-electron density (in $\text{cm}^{-3} \times 10^{21}$) and (b) B_y component of magnetic field (in MG) 700 fs after the peak of the laser pulse in the simulation for a solid-density plastic target, and a laser pulse with a focal-spot diameter of 10 μm and a maximum intensity of 6×10^{19} W/cm^2

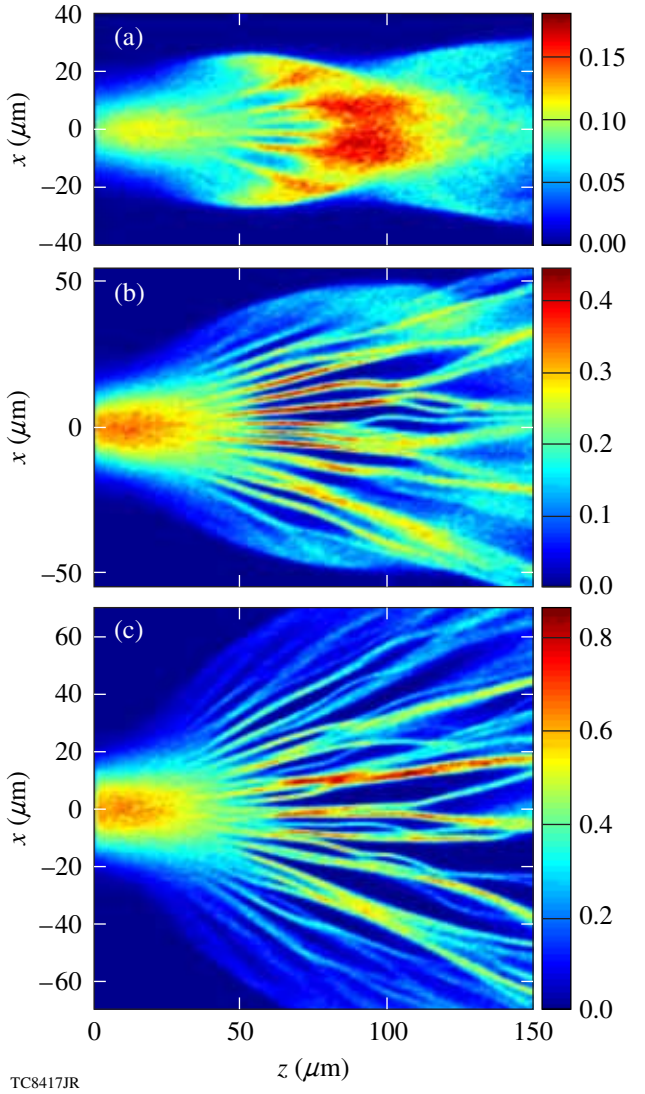

Figure 117.31
Hot-electron density (in $\text{cm}^{-3} \times 10^{21}$) 700 fs after the peak of the laser pulse in the simulations for a solid-density plastic target, and a laser pulse with a focal-spot diameter of 20 μm and maximum intensities of (a) 5×10^{18} W/cm^2, (b) 2×10^{19} W/cm^2, and (c) 6×10^{19} W/cm^2.

the left-hand-side plasma boundary where the electron beam enters the plasma to $100\times\rho_{\text{solid}}$ in the center of the target. The parameters of the laser pulse in both simulations are the same as in the simulation of Fig. 117.31(c): the spot diameter is 20 μm and the maximum intensity is 6×10^{19} W/cm^2.

In the simulation of Fig. 117.32 the hot-electron beam is well collimated over a length of 150 μm. The beam is also collimated in the simulation of Fig. 117.33, where it reaches the dense core and deposits its energy through collisions with plasma electrons and ions. The collimation is due to the generation of a large magnetic field on the electron-beam surface. These simulations show that magnetic collimation is effective at high laser intensities when the plasma is compressed above solid density as expected in fast-ignition targets.

Theoretical models of resistive collimation and filamentation were developed by Davies *et al.*[23] and Bell *et al.*[24] (collimation) and Gremillet *et al.*[29] (filamentation). The first estimate of the magnetic-field generation in fast-ignition plasmas was reported by Glinsky.[30] As the electron beam enters the plasma, it sets up an electrostatic and inductive ohmic electric field that opposes the hot-electron motion and drives a return current of background cold electrons,

$$\mathbf{E}=\eta\mathbf{j}_{\text{p}}\approx-\eta\mathbf{j}_{\text{h}}, \tag{1}$$

where $\mathbf{j}_{\text{p}}$ and $\mathbf{j}_{\text{h}}$ are the cold- and hot-electron current densities, respectively. Initially the two oppositely directed currents cancel each other and the magnetic field is absent. The resistive magnetic field grows in time according to Faraday's law,

$$\frac{\partial\mathbf{B}}{\partial t}=-c\nabla\times\mathbf{E}. \tag{2}$$

The net current density also grows according to Ampere's law $\mathbf{j}\approx(c/4\pi)\nabla\times\mathbf{B}$. The magnetic field of the beam pinches and collimates the hot electrons. A similar process occurs on local peaks of the current density leading to resistive filamentation. Since the plasma resistivity is a function of the electron temperature, the resistivity decreases as the plasma is heated by hot electrons. At sufficiently high temperatures, the electrical resistivity follows Spitzer's formula[25]

$$\eta=10^{-2}\,Zf(Z)\ln\Lambda T_{\text{e}}^{-3/2}\,\Omega\times\text{cm}, \tag{3}$$

where Z is the ion charge state, $\ln\Lambda$ is the Coulomb logarithm, T_{e} is the electron temperature in eV, and $f(Z)$ changes from 0.52 to 0.3 when Z increases from 1 to infinity. The main heating mechanism for the background plasma is joule heating,

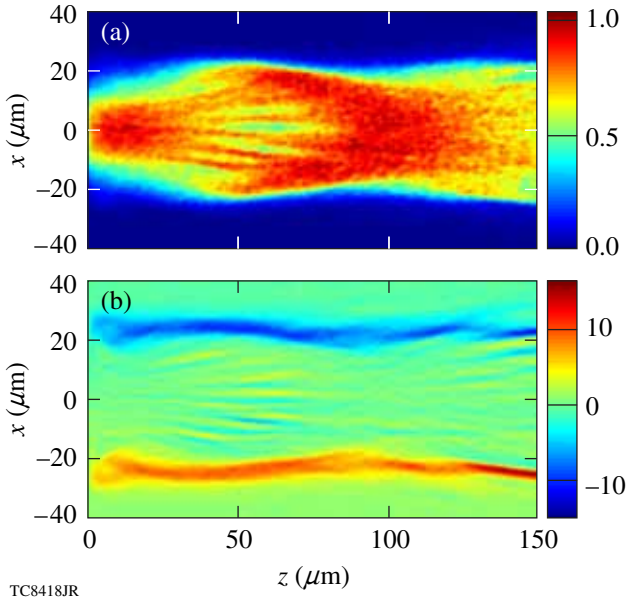

Figure 117.32
(a) Hot-electron density (in cm$^{-3}\times10^{21}$) and (b) magnetic field (in MG) 700 fs after the peak of the laser pulse in the simulation for a compressed uniform plastic target and a laser pulse with a focal-spot diameter of 20 μm and a maximum intensity of 6×10^{19} W/cm^2.

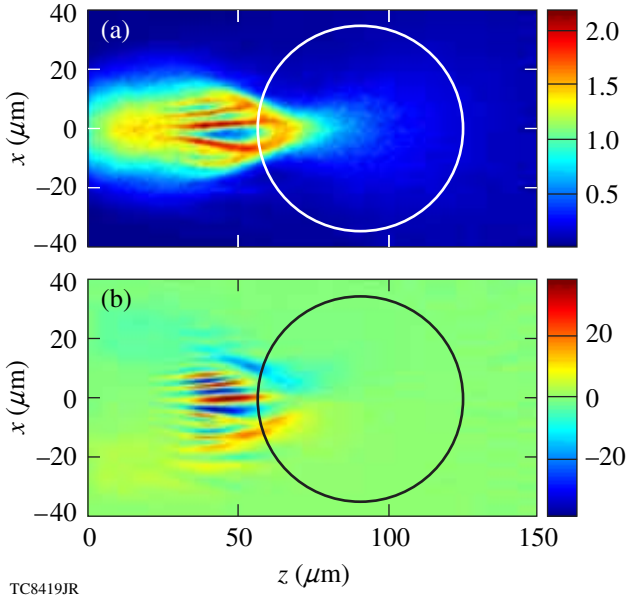

Figure 117.33
(a) Hot-electron density (in cm$^{-3}\times10^{21}$) and (b) magnetic field (in MG) 700 fs after the peak of the laser pulse in the simulation for a compressed plastic target with a Gaussian spatial density distribution, and a laser pulse with a focal-spot diameter of 20 μm and a maximum intensity of 6×10^{19} W/cm^2.

$$\frac{\partial T_e}{\partial t} = \frac{\eta j_p^2}{C}, \tag{4}$$

where $C = (3/2)n_e$ is the specific-heat capacity of an ideal electron gas and n_e is the electron density. Hot-electron collisions with cold plasma electrons become a dominant heating mechanism close to the dense core of the fast-ignition target (also suggested in Refs. 31 and 32). Plasma heating slows down the growth of the magnetic field and reduces the filamentation instability growth rate.

Magnetic collimation is not effective in the simulations of Figs. 117.29, 117.30, and 117.31(b)–117.31(c) because the plasma is heated too fast and the collimating magnetic field does not have enough time to grow before the resistivity decreases because of the high plasma temperature. On the other hand, in the simulations of Figs. 117.28 and 117.31(a), a strong magnetic field is generated as the plasma is heated slowly by the lower-intensity electron beam, thus keeping the resistivity low enough and allowing the field to grow. The mean energy of hot electrons in the simulations with a lower intensity is also smaller, according to the ponderomotive scaling[26]—a fact that facilitates the beam collimation. In the simulations of Figs. 117.32 and 117.33, the electron density is higher and the heating time is longer [see Eq. (4)]. Thus the collimating magnetic field has enough time to grow to a large enough strength to collimate high-energy electron beams. The resistive collimation of hot electrons can be induced more effectively if the laser pulse and the corresponding electron beam have a long rising front. In this case, a stronger collimating magnetic field can be generated during the rising pulse front, thus improving the collimation of the main beam.

In the next sections, the results of integrated *DRACO–LSP* simulations of cone-in-shell fast-ignition targets are presented. It is important to notice that many features of the electron-beam transport are similar to those obtained in the simplified simulations described in this section.

Integrated Simulations of Cone-in-Shell Plastic Targets for the Fast-Ignition Experiments at LLE

Integrated experiments on OMEGA using low-adiabat implosions of cone-in-shell plastic targets and petawatt heating pulses have begun at LLE. The targets are 40-μm-thick empty CD shells of ~870-μm outer diameter [Fig. 117.34(a)]. A hollow gold cone with an opening angle of 35° or 70° is inserted through a hole in the shell. The cone has a thickness of 10 μm inside the shell and ends in a 15-μm-thick flat tip, as shown in Fig. 117.34(b). The shell is compressed using a

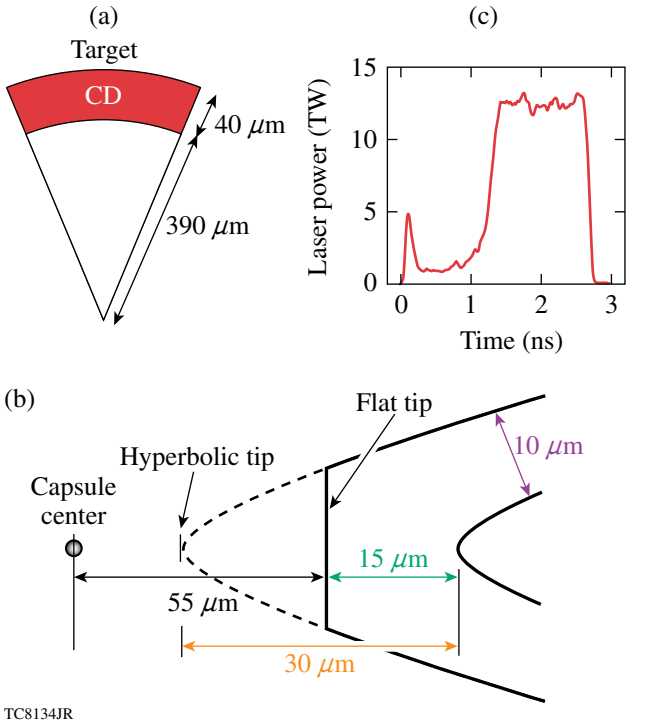

Figure 117.34
Fuel assembly in the integrated simulations for a cone-in-shell plastic target used in the fast-ignition experiments at LLE. Schematics of (a) a plastic shell and (b) a cone tip; (c) temporal profile of the laser pulse used for the target implosion.

351-nm-wavelength, highly shaped pulse of ~3-ns duration and ~20-kJ energy [Fig. 117.34(c)] designed to achieve high areal densities.[33] Previous implosion experiments using similar targets but without the OMEGA EP heating beam,[34] measured a neutron yield from D–D nuclear reactions of (2 to 3) × 10^7. The OMEGA EP petawatt laser delivers laser pulses with a 1.054-μm wavelength, energy up to 2.6 kJ, and a duration of about 10 ps.

We have carried out a set of integrated *DRACO–LSP* simulations of target heating for the OMEGA fast-ignition experiments. The simulations were performed for a 50° cone target. In the integrated simulations, *DRACO* was used to simulate the implosion of the plastic cone-in-shell target. *DRACO* and *LSP* were then integrated to simulate the target heating. Because of numerical difficulties related to the cone's gold opacities, the radiation transport was turned off in the *DRACO* simulations. Figure 117.35(a) shows the target density obtained in a *DRACO* simulation at $t = 3.54$ ns, close to the time of maximum areal density $\rho R \sim 0.8$ g/cm^2 (in the direction opposite to the cone). Figure 117.35(b) shows the density lineout through the z axis. The density in the compressed shell at this time was around 300 g/cm^3. The initial position of the cone is shown by the white

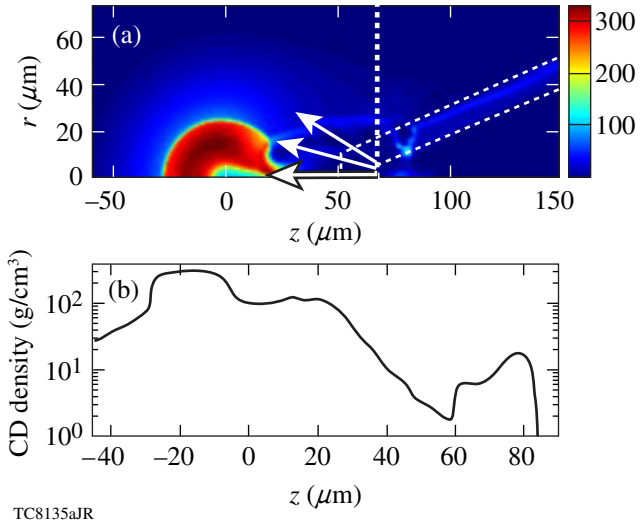

Figure 117.35
(a) Target-density profile at the time of maximum ρR in the integrated simulations for the fast-ignition experiments at LLE. The dashed lines show the initial position of the cone. Hot electrons are injected in the simulations 70 μm from target center. (b) Lineout of CD density through the z axis. The density increase at $z > 60$ μm is due to compression by a shock reflected from the cone tip.

dashed lines. At $t = 3.54$ ns the cone tip was displaced away from the target center by a jet of high-pressure CD gas escaping through the hole in the compressed shell. Despite the fact that the plastic shell was initially empty, plastic was ablated from the inner shell surface and formed a hot, low-density plasma inside the shell. The cone tip not only shifted at this time but was also crushed, and a plastic/gold plasma filled the interior of the cone. We are currently working on optimizing the cone-in-shell implosions,[8] by varying the cone-tip thickness and distance from the target center, to preserve the integrity of the cone tip at the time of maximum ρR. Here we focus solely on the hot-electron transport in the plastic plasma outside the cone tip. We assume that it is possible to optimize the cone-in-shell implosion and that the hot electrons penetrating through the cone tip reach the plastic plasma. These assumptions will be verified in future integrated simulations.

In the present simulations hot electrons were injected at the time of maximum ρR in the plastic plasma located past the cone tip, 70 μm away from the target center. The plastic plasma was assumed to be fully ionized in the simulations described in this section. The hot-electron beam had a square profile in time with a duration of 10 ps and a Gaussian radial profile with FWHM of 20 μm. We assume that the beam was generated by an OMEGA EP laser pulse with a similar profile, an energy of 2.6 kJ, on-axis intensity of 5.4×10^{19} W/cm^2, and energy conversion efficiency to hot electrons of 30%. For a given energy, the pulse intensity in the experiment can be varied by changing the pulse duration. According to the ponderomotive scaling,[26] the mean energy of hot electrons also changes. In the simulations hot electrons were generated with a relativistic Maxwellian energy-distribution function, and the mean energy was varied from 1.2 to 2.4 MeV to account for the intensity changes. The angular spread of hot electrons from the cone tip was estimated based on previous experimental results. Hot-electron divergence of about 20° (half-angle) has been reported in earlier cone-target experiments.[2,35] Hot-electron divergence could increase with an increasing thickness of the cone tip because of a strong electron scattering in the gold. The initial divergence was taken as a free parameter in the simulations and varied from 20° to 60° (HWHM, half-angle).

Figure 117.36 shows snapshots of the (a) plasma density, (b) electron-beam density, and (c) azimuthal magnetic field 6 ps after the beginning of the hot-electron beam in the simulation with a mean electron energy of 2 MeV and angular divergence of 20° (half-angle). Figure 117.36(d) shows the temperature of the plasma before the electron beam arrives and Fig. 117.36(e) shows the plasma temperature increase caused by the heating by hot electrons. Figure 117.36(b) shows that the electron beam is well collimated by the self-generated resistive magnetic field. Interestingly, the hot electrons at the axis are somewhat deflected in the $+r$ direction when they approach the core. This is due to the magnetic field (having a negative sign) generated in the hot gas escaping from the center of the target through the hole in the compressed shell. Indeed, the Spitzer plasma resistivity [Eq. (3)] is a decreasing function of temperature. According to Eqs. (1) and (2), in the region of a nonuniform resistivity, a magnetic field of such a sign is generated, deflecting the hot electrons to the region of a higher resistivity. The hot electrons are deflected from the low-density hot-gas region to the dense core, increasing the coupling of hot electrons with the core in the experiment.

Figure 117.36(e) shows that the maximum temperature increase due to hot electrons is about 2.5 keV. It is achieved, however, in the low-density part of the plasma [see the plasma density contours in Fig. 117.36(e)]. The maximum temperature increase in the dense core is about 1 keV in the right-hand side of the core.

Figure 117.37 shows the (a) electron-beam density and (b) azimuthal magnetic field 6 ps after the beginning of the hot-electron beam propagation. In this simulation the electron-beam divergence was increased to 60° (half-angle). The plasma temperature increase due to hot electrons is shown in

Fig. 117.37(c). Even for such a large angular divergence, a large fraction of hot electrons were still collimated by the resistive magnetic field and reached the dense core. (See also Fig. 117.39 showing the hot-electron-density lineouts near the dense core in the simulations of Figs. 117.36–117.38.) Some electrons, however, escape in the radial direction. The temperature increase in the dense core is about 500 eV maximum.

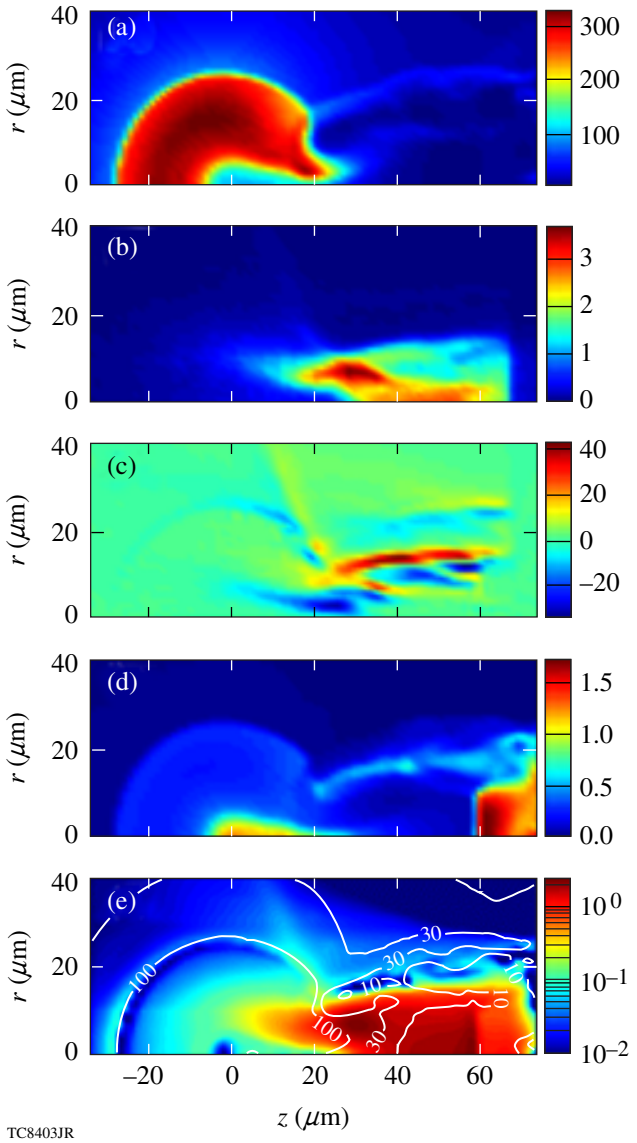

Figure 117.36
(a) Plasma density (in g/cm^3), (b) hot-electron density (in cm^{-3} × 10^{21}), and (c) azimuthal magnetic field (in MG) 6 ps after the beginning of the hot-electron beam with an initial divergence of 20° (half-angle). (d) Plasma temperature (in keV) before the electron-beam injection. (e) Ion-temperature increase (in keV) in the end of the hot-electron pulse; plasma density in g/cm^3 contours (white curves) are also shown.

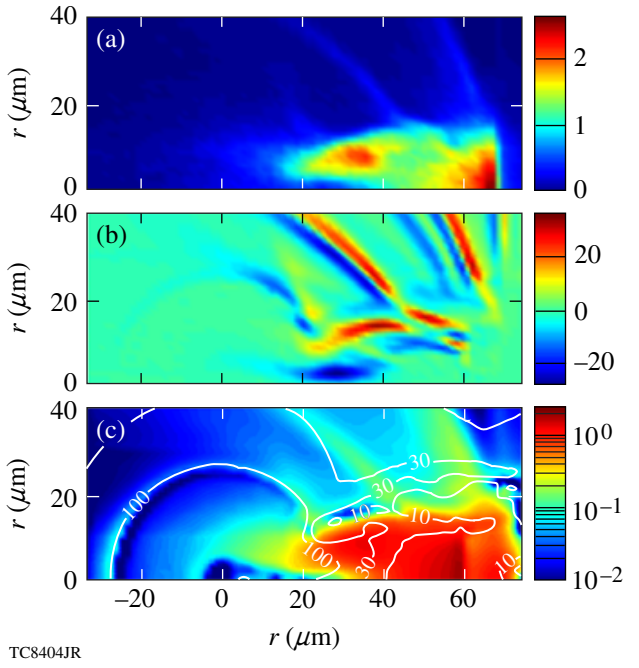

Figure 117.37
(a) Hot-electron density (in cm^{-3} × 10^{21}) and (b) azimuthal magnetic field (in MG) 6 ps after the beginning of the hot-electron beam with an initial divergence of 60° (half-angle). (c) Ion-temperature increase (in keV) in the end of the hot-electron pulse; plasma density in g/cm^3 contours (white curves) are also shown.

Figure 117.38 shows the results of a simulation in which the electron-beam parameters were kept the same as in the simulation of Fig. 117.36, but the electron beam was injected 60 ps earlier. At this time the core radius is smaller and the maximum density is higher [compare Figs. 117.36(a) and 117.38(a)] because the maximum ρR is reached when the target begins to expand. Figures 117.38(b) and 117.38(c) show that the electron beam was highly deflected by the magnetic field in the escaping hot gas, and many electrons missed the dense core. This happened because a strong defocusing magnetic field was generated and shifted in the $+r$ direction due to a larger opening in the shell at this time. The dense core outer radius was also smaller, so more hot electrons missed the core. If not for this effect, earlier injection of hot electrons could be beneficial since the cone tip's integrity can be preserved before it is crushed by the hot-gas jet from the compressed shell.

Figure 117.40 summarizes the results of our simulations by plotting the fraction of hot-electron-beam energy deposited in the dense core (in the region with density $\rho > 80$ g/cm^3) as a function of the mean electron energy and angular divergence. This fraction is a weak function of the mean electron energy and decreases from about 50% to 25% when the angular divergence is increased from 20° to 60° (half-angle).

The calculated neutron yield from D–D nuclear reactions was maximum for lower angular divergences. The yield increase caused by the hot-electron-beam heating was about 3 $\times 10^9$ neutrons for a divergence of 20° (half-angle).

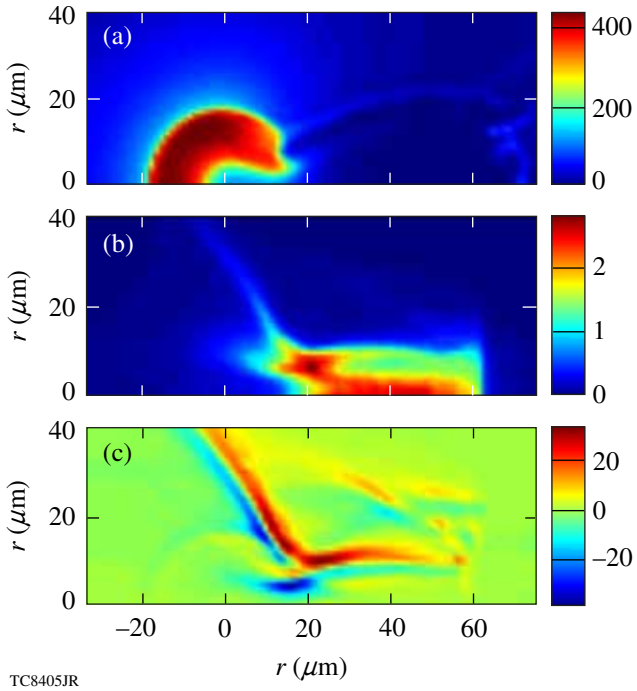

Figure 117.38
(a) Plasma density (in g/cm^3), (b) hot-electron density (in cm^{-3} $\times$ 10^{21}), and (c) azimuthal magnetic field (in MG) 6 ps after the beginning of the hot-electron beam with an initial divergence of 20° (half-angle), injected 60 ps earlier than in the simulation in Fig. 117.36.

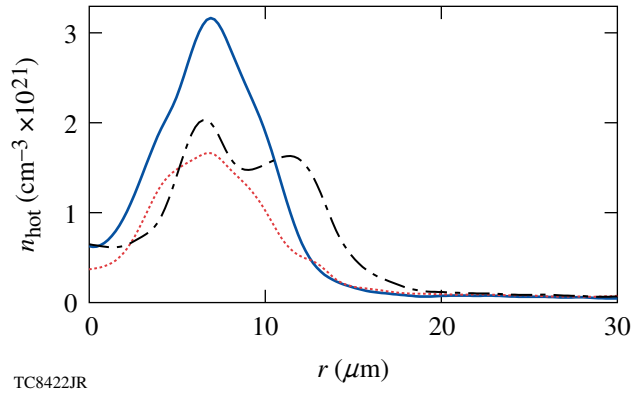

Figure 117.39
Radial lineouts of the hot-electron density near the dense core: at $z = 25$ μm in Figs. 117.36(b) (solid line) and 117.37(a) (dotted line), and at $z = 13$ μm in Fig. 117.38(b) (dashed–dotted line).

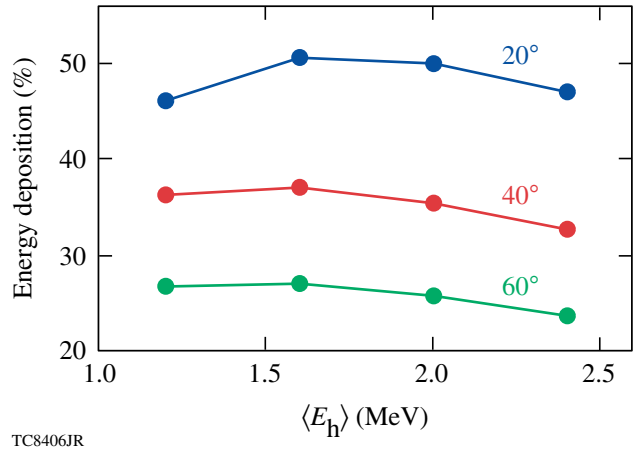

Figure 117.40
Fraction of the electron-beam energy deposited in the dense core (in the region with density $\rho > 80$ g/cm^3).

It is important to mention that more work is necessary to optimize cone-in-shell implosions to preserve the integrity of the cone tip. The transport of hot electrons through the cone tip also must be addressed through dedicated hybrid-PIC simulations. For this purpose *LSP* must be modified to model the ionization of the high-Z cone material, using the quantum equations of state.[36] We expect that the angular divergence of the hot electrons will increase due to the enhanced electron scattering in the gold. Tens- to hundreds-of-megagauss resistive magnetic fields are expected in the cone because of the high collisionality of the return current. In such fields, the Alfvén limit can be reached for the filaments or for the entire beam. Magnetic fields can develop at plasma discontinuities (inner cone surface or cone–plasma interface) and cause a surface transport and/or trapping of hot electrons. Finally, an inevitable laser prepulse can create extended regions of pre-plasma inside the cone, increasing the thickness of the high-Z cone material through which the hot electrons propagate.

Conclusion

This article has described the latest results from a set of integrated simulations of the implosion, hot-electron transport, and ignition of direct-drive, fast-ignition cone-in-shell plastic targets, using the hydrodynamic code *DRACO* and the hybrid-PIC code *LSP*. *LSP* simulations of electron transport in solid-density plastic targets have also been presented. These simulations show the importance of self-generated resistive magnetic fields to the transport of hot electrons. *LSP* simulations of solid-density plastic targets show that the effectiveness of magnetic collimation of laser-generated hot electrons decreases with an increase in the laser intensity, in agreement

with solid-target electron-transport experiments. It has also been shown that hot-electron collimation for high-intensity petawatt laser pulses is possible in compressed plastic targets with densities relevant to integrated fast-ignition experiments on OMEGA.

Performance of the cone-in-shell plastic targets developed for integrated fast-ignition experiments at LLE has been investigated using integrated simulations of implosion, hot-electron transport, and target heating. In the present simulations, only the hot-electron transport through the plastic plasma has been investigated. The hot-electron transport through the cone was not simulated. Resistive collimation of hot electrons was found to effectively reduce the hot-electron angular spread and increase the coupling efficiency of hot electrons to the core. Resistive collimation is effective even for electron beams with a large angular spread, up to 60° (half-angle). The coupling efficiency of hot electrons with the target core is about 50% for initial electron divergence of 20° (half-angle), decreasing to 25% for initial divergence of 60°. The integrated simulations predict a neutron-yield enhancement from D−D nuclear reactions of about 10^9 neutrons, which can be easily measured in the experiments. This is significantly more than the implosion neutron yield measured for such targets without a petawatt laser beam.

ACKNOWLEDGMENT

This work was supported by the U.S. Department of Energy under Cooperative Agreement DE-FC02-04ER54789 (Fusion Science Center, Office of Fusion Energy Science) and DE-FC52-08NA28302 (Office of Inertial Confinement Fusion), the University of Rochester, and the New York State Energy Research and Development Authority. The support of DOE does not constitute an endorsement by DOE of the views expressed in this article.

REFERENCES

1. M. Tabak *et al.*, Phys. Plasmas **1**, 1626 (1994).
2. R. Kodama *et al.*, Nature **412**, 798 (2001); R. Kodama *et al.*, Nature **418**, 933 (2002).
3. K. A. Tanaka *et al.*, Phys. Plasmas **10**, 1925 (2003); P. A. Norreys, K. L. Lancaster, C. D. Murphy, H. Habara, S. Karsch, R. J. Clarke, J. Collier, R. Heathcote, C. Hernandez-Gomez, S. Hawkes, D. Neely, M. H. R. Hutchinson, R. G. Evans, M. Borchesi, L. Romagnani, M. Zepf, K. Akli, J. A. King, B. Zhang, R. R. Freeman, A. J. MacKinnion, S. P. Hatchett, P. Patel, R. Snavely, M. H. Key, A. Nikroo, R. Stephens, C. Stoeckl, K. A. Tanaka, T. Norimatsu, Y. Toyama, and R. Kodama, Phys. Plasmas **11**, 2746 (2004).
4. R. Betti and C. Zhou, Phys. Plasmas **12**, 110702 (2005).
5. A. A. Solodov, R. Betti, J. A. Delettrez, and C. D. Zhou, Phys. Plasmas **14**, 062701 (2007).
6. A. A. Solodov, K. S. Anderson, R. Betti, V. Gotcheva, J. Myatt, J. A. Delettrez, S. Skupsky, W. Theobald, and C. Stoeckl, Phys. Plasmas **15**, 112702 (2008).
7. P. B. Radha, T. J. B. Collins, J. A. Delettrez, Y. Elbaz, R. Epstein, V. Yu. Glebov, V. N. Goncharov, R. L. Keck, J. P. Knauer, J. A. Marozas, F. J. Marshall, R. L. McCrory, P. W. McKenty, D. D. Meyerhofer, S. P. Regan, T. C. Sangster, W. Seka, D. Shvarts, S. Skupsky, Y. Srebro, and C. Stoeckl, Phys. Plasmas **12**, 056307 (2005).
8. K. S. Anderson, A. A. Solodov, R. Betti, and P. W. McKenty, Bull. Am. Phys. Soc. **53**, 53 (2008).
9. D. R. Welch *et al.*, Phys. Plasmas **13**, 063105 (2006).
10. J. S. Green, V. M. Ovchinnikov, R. G. Evans, K. U. Akli, H. Azechi, F. N. Beg, C. Bellei, R. R. Freeman, H. Habara, R. Heathcote, M. H. Key, J. A. King, K. L. Lancaster, N. C. Lopes, T. Ma, A. J. MacKinnon, K. Markey, A. McPhee, Z. Najmudin, P. Nilson, R. Onofrei, R. Stephens, K. Takeda, K. A. Tanaka, W. Theobald, T. Tanimoto, J. Waugh, L. Van Woerkom, N. C. Woolsey, M. Zepf, J. R. Davies, and P. A. Norreys, Phys. Rev. Lett. **100**, 015003 (2008).
11. J. C. Adam, A. Héron, and G. Laval, Phys. Rev. Lett. **97**, 205006 (2006).
12. S. Atzeni, Phys. Plasmas **6**, 3316 (1999).
13. S. Atzeni, A. Schiavi, and C. Bellei, Phys. Plasmas **14**, 052702 (2007).
14. A. A. Solodov and R. Betti, Phys. Plasmas **15**, 042707 (2008).
15. C. K. Li and R. D. Petrasso, Phys. Rev. E **70**, 067401 (2004); C. K. Li and R. D. Petrasso, Phys. Rev. E **73**, 016402 (2006).
16. E. M. Lifshitz and L. P. Pitaevskifi, *Physical Kinetics*, 1st ed., Course of Theoretical Physics, Vol. 10 (Pergamon Press, Oxford, 1981), Chap. 4.
17. R. R. Freeman *et al.*, Fusion Sci. Technol. **49**, 297 (2006); M. H. Key, Phys. Plasmas **14**, 055502 (2007).
18. Y. T. Lee and R. M. More, Phys. Fluids **27**, 1273 (1984).
19. J. J. Honrubia and J. Meyer-ter-Vehn, J. Phys., Conf. Ser. **112**, 022055 (2008); S. Atzeni *et al.*, Phys. Plasmas **15**, 056311 (2008).
20. M. Tatarakis *et al.*, Phys. Rev. Lett. **81**, 999 (1998).
21. M. Borghesi *et al.*, Phys. Rev. Lett. **83**, 4309 (1999).
22. L. Gremillet *et al.*, Phys. Rev. Lett. **83**, 5015 (1999).
23. J. R. Davies *et al.*, Phys. Rev. E **56**, 7193 (1997).
24. A. R. Bell and R. J. Kingham, Phys. Rev. Lett. **91**, 035003 (2003).
25. L. Spitzer Jr. and R. Härm, Phys. Rev. **89**, 977 (1953); L. Spitzer, *Physics of Fully Ionized Gases*, 2nd rev. ed., Interscience Tracts on Physics and Astronomy (Interscience, New York, 1962).
26. S. C. Wilks and W. L. Kruer, IEEE J. Quantum Electron. **33**, 1954 (1997).
27. F. N. Beg *et al.*, Phys. Plasmas **4**, 447 (1997).

28. R. P. J. Town *et al.*, Nucl. Instrum. Methods Phys. Res. A 544, **61** (2005).

29. L. Gremillet, G. Bonnaud, and F. Amiranoff, Phys. Plasmas **9**, 941 (2002).

30. M. E. Glinsky, Phys. Plasmas **2**, 2796 (1995).

31. B. Chrisman, Y. Sentoku, and A. J. Kemp, Phys. Plasmas **15**, 056309 (2008).

32. J. J. Honrubia and J. Meyer-ter-Vehn, Nucl. Fusion **46**, L25 (2006).

33. C. D. Zhou, W. Theobald, R. Betti, P. B. Radha, V. A. Smalyuk, D. Shvarts, V. Yu. Glebov, C. Stoeckl, K. S. Anderson, D. D. Meyerhofer, T. C. Sangster, C. K. Li, R. D. Petrasso, J. A. Frenje, and F. H. Séguin, Phys. Rev. Lett. **98**, 025004 (2007).

34. C. Stoeckl, T. R. Boehly, J. A. Delettrez, S. P. Hatchett, J. A. Frenje, V. Yu. Glebov, C. K. Li, J. E. Miller, R. D. Petrasso, F. H. Séguin, V. A. Smalyuk, R. B. Stephens, W. Theobald, B. Yaakobi, and T. C. Sangster, Phys. Plasmas **14**, 112702 (2007).

35. R. B. Stephens *et al*., Phys. Rev. Lett. **91**, 185001 (2003).

36. R. M. More *et al*., Phys. Fluids **31**, 3059 (1988).

Shear Stress in Magnetorheological Finishing for Glasses

Introduction

Magnetorheological finishing (MRF) is a sub-aperture polishing tool for fabrication of precision optics. The removal function of MRF is based on a magnetorheological (MR) fluid that consists of magnetic carbonyl iron (CI), non-magnetic polishing abrasives, and water or other non-aqueous carrier fluids and stabilizers. The MR fluid ribbon stiffens in the presence of a magnetic field to form a localized polisher, and spindle-mounted parts are moved through the polishing zone to polish the surface and to correct the figure.[1,2]

For conventional polishing processes, the material removal rate (MRR, $\Delta h/\Delta t$ where Δh is a representative height of removal averaged over the entire part area) is predicted by the traditional Preston relationship or Preston's equation:[3]

$$\text{MRR} = C_p PV = C_p \frac{F_n}{A_c} V, \tag{1}$$

where C_p is the Preston coefficient, which includes the effects of the process parameters affecting the interaction between the work piece and the tool (e.g., pH, slurry, type of abrasives, frictional forces, etc.), P is the normal pressure applied (i.e., normal force F_n divided by the contact area A_c between the polishing tool/pad and the substrate being polished), and V is the relative velocity between the part and the tool. The applicability of Preston's equation for material removal in MRF is a subject of study. Shorey[4] used the spot-taking machine (STM, described in detail on p. 44) to measure drag force on a sapphire part, using a drag force measuring device and aqueous MR fluids consisting of different types and concentrations of CI particles and abrasives. Shorey[4] found that there is a strong positive linear relationship between the material removal rate for sapphire and the drag force in MRF, predicting a similar result for fused silica (FS), although drag force values under the above conditions were not reported for FS. Shorey also calculated that the normal force acting on a single abrasive particle (within the MR fluid ribbon) and the part is approximately 1×10^{-7} N (Ref. 4). This is several orders of magnitude smaller than that for conventional polishing, 5 to 200×10^{-3} N (Ref. 5). Shorey concluded that there must be drag force to have removal in MRF.

To address MRF, first Kordonski[6] and later Shorey[4] proposed a modified Preston's coefficient $C'_{p,\text{MRF}(F_n)}$ in terms of the normal force F_n by introducing a coefficient of friction (COF, μ), correlating material removal rate for MRF (MRR_{MRF}, identified as $\Delta h/\Delta t$, where Δh is a representative height of removal averaged over the MRF spot area) with drag force. Equation (2) shows this transition as described by Shorey:

$$\text{MRR}_{\text{MRF}} = C'_{p,\text{MRF}(F_n)} \frac{\mu F_n}{A_s} V = C'_{p,\text{MRF}(F_d)} \frac{F_d}{A_s} V$$

$$= C'_{p,\text{MRF}(\tau)} \times \tau \times V, \tag{2}$$

where, for MRF, the normal force F_n is divided by the spot area A_s, instead of A_c [Eq. (1)]. A_s is the projected spot area over which polishing occurs (see **Characterization**, p. 46), i.e., the pressure applied by the hydrodynamic flow of MR fluid at the gap between the part surface and the STM wheel.[7] $C'_{p,\text{MRF}(F_d)}$ is a modified Preston's coefficient for MRF in terms of drag force. The drag force F_d divided by the spot area A_s equals the shear stress τ. $C'_{p,\text{MRF}(\tau)}$ is a modified Preston's coefficient in terms of shear stress [note that $C'_{p,\text{MRF}(\tau)} = C'_{p,\text{MRF}(F_d)}$]. Equation (2) predicts that material removal in MRF is proportional to the hydrodynamic pressure and shear stress. Although they did not report on shear stress, Shorey[4] and Shorey *et al.*[8] indicated that the normal force in MRF is relatively small compared to conventional polishing techniques, and therefore, material removal in MRF is governed by shear stress rather than the hydrostatic pressure. It is also important to note that this is the first time where the modified Preston's coefficient, as suggested by Kordonski[6] and Shorey,[4] is associated with respect to either normal force or drag force/shear stress.

DeGroote[9] incorporated Shorey's[4] modified Preston equation, specifically the proportionality between material removal

rate and shear stress, in an empirical model for characterizing MRF of optical glasses with nanodiamonds. Using a drag force sensor other than Shorey's,[4] DeGroote studied six optical glasses: three phosphates and three silicates. DeGroote[9] and DeGroote *et al.*[10] found that the peak removal rate (assuming a constant contact zone for all materials divided by the spotting time) increased (silicates) or decreased (phosphates) linearly with drag force. Drag force and peak removal rate did not show the same linear correlation across all six optical glasses since "chemistry and glass composition play a significant role in the MRF material removal process, *and removal rate cannot be characterized by drag force alone*."[10] It is also important to note that because the spot area was assumed to be constant for all glasses, drag force and shear stress were considered to be equivalent (within a constant of proportionality) when discussing the relationship between these two properties and material removal.

Using the same drag force sensor as DeGroote,[9] Miao *et al.*[11] calculated shear stress from MRF drag force measurements for a variety of materials including optical glasses, polycrystalline ceramics, and hard metals and found a positive linear dependence of peak removal rate with shear stress. They did not consider, however, how shear stress is correlated to material properties.

As reviewed above, previous work concentrated only on the contribution of drag force to material removal in MRF. Limited study was carried out on shear stress that is closely related to drag force, but incorporates the MRF spot area A_s. This article reports on the use of a dual force sensor for the real-time, simultaneous measurement of both drag force and normal force in MRF. We study how the measurable normal and drag forces, and calculated shear stress with respect to the measured projected spot area on the part surface, contribute to material removal in MRF for optical glasses based on their mechanical properties. The variability of the value for the Preston's coefficient in MRF over the three glass types is examined in terms of the normal force, drag force, shear stress, and a material figure of merit. We propose a new modification to the Preston's equation that predicts MRF material removal rate in terms of mechanical properties and shear stress for optical glasses.

The following sections (1) describe materials tested in this work, the STM experimental platform, data acquisition, and methodology used for characterizing experimental results; (2) present MRF spotting results including spot depth, area and volume, removal rate, and force measurement data; (3) discuss the dependence of drag and normal forces on material properties, the role of shear stress in MRF material removal, and the modified Preston's equation; and (4) present conclusions based on this work.

Experimental Details

1. Materials

Three types of optical glasses were chosen for this study based on their economic importance: phosphate (LHG8), borosilicate (BK7), and fused silica (FS). LHG8 is a phosphate laser glass that is widely used in high-peak-power laser systems. It is mechanically soft and has moderate chemical durability. BK7 and FS are optical glasses commonly used for visible and ultraviolet applications because of their excellent chemical, mechanical, and optical properties. The materials' mechanical properties, ranked in order by increasing Vickers hardness, are listed in Table 117.I. The figure of merit (FOM) shown in Table 117.I is defined as $E\big/K_c H_V^2$, where E is Young's modulus (resistance to elastic deformation), H_V is Vickers hardness (resistance to plastic deformation), and K_c is fracture toughness (resistance to fracture/crack growth). This figure of merit was originally used by Lambropoulos *et al.*[12] to evaluate volumetric removal in loose-abrasive lapping of optical glasses.

Table 117.I: Physical and mechanical properties of optical glasses rank in order by increasing Vickers hardness.[(a)]

Material	Mat. ID	Young's Modulus E (GPa)	Vickers Hardness H_V (GPa)	Fracture Toughness[(b)] K_c ($\text{MPa} \times \text{m}^{1/2}$)	Figure of Merit[(c)] $E\big/K_c H_V^2$ ($\times 10^{-3}\ \text{MPa}^{-2} \times \text{m}^{-1/2}$)	Source
Phosphate	LHG8	62	3.7	0.5	8.71	Hoya
Borosilicate	BK7	81	6.0	0.8	2.81	Schott
Fused Silica	FS	69	7.5	0.8	1.64	Corning

[(a)]Mechanical properties are from Ref. 9 where glass hardness was measured using a 100-gf load; errors for all values are less than ±25%.
[(b)]Fracture toughness numbers were calculated using the model of Evans.[13]
[(c)]Figures of merit (FOM) were calculated after Lambropoulos *et al.*[12]

The relationship between the FOM and the removal rate in MRF is discussed on p. 47.

Three pieces of each material were used in this work, except LHG8, for which only one piece was available. All substrates were flats, pitch polished in LLE's Optical Fabrication Shop to a surface flatness of less than 1 μm for all materials[14] and to a root-mean-square (rms) surface roughness of less than ~2 nm (Ref. 15). All substrates were round disks (~40 mm) with thicknesses varying from ~2 mm to ~10 mm.

2. Spot-Taking Machine

An MRF spot-taking machine (STM, see Fig. 117.41) was used as a test bed to take removal-rate data in the form of spots on part surfaces *without part rotation*. Unlike a commercial MRF machine, the STM has only z-axis motion and cannot be used to polish a surface. The MRF removal function from the STM is characterized with an MRF spot that is created by lowering a nonrotating part into the rotating MR fluid ribbon. Material is removed in a characteristic D-shaped spot, as shown in Fig. 117.42.

The STM operating settings were kept constant for all spots taken in this work. Fluid temperature was held at ~23°C. The mixing rate within the fluid confinement vessel was 1000 rpm,

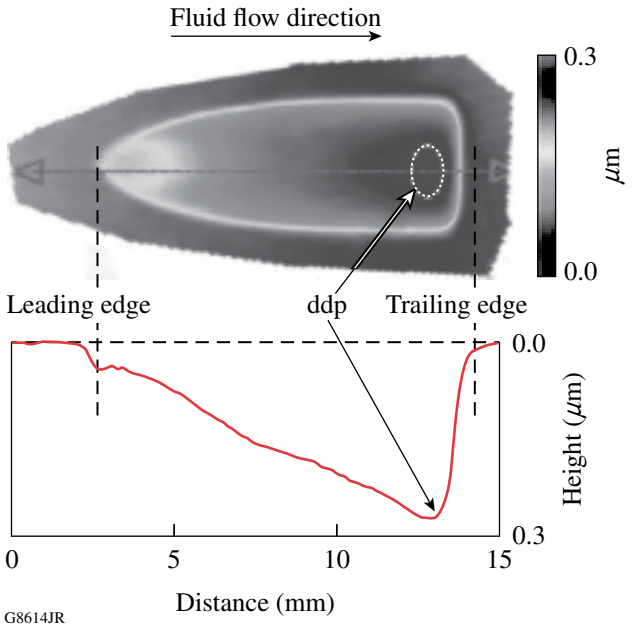

Figure 117.42
Interferometric image of an MRF spot on BK7 glass and its accompanying profile.[14] The dashed ellipse denotes the depth-of-deepest-penetration (ddp) region where a maximum amount of material is removed. Parallel dashed lines indicate the leading edge (where the MRF ribbon starts to contact the part) and the trailing edge (where the MRF fluid ribbon leaves the part). The MR fluid is flowing from left to right. The spot line profile is extracted through the center of the spot image; the distance from the leading edge to the trailing edge is ~12 mm and the spot depth is ~0.28 μm.

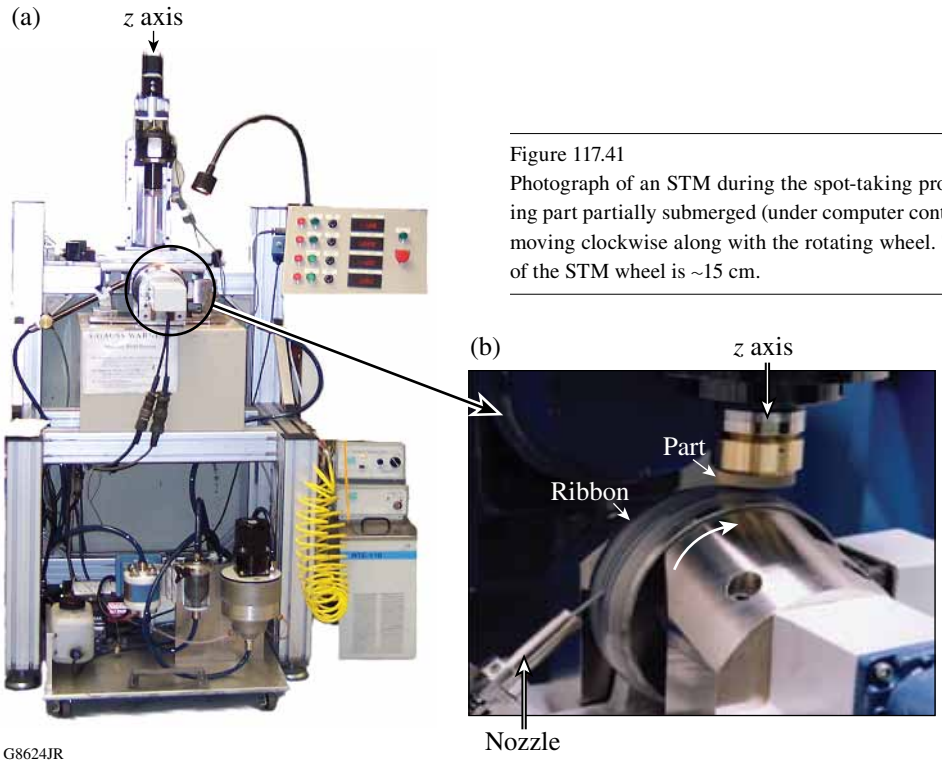

Figure 117.41
Photograph of an STM during the spot-taking process: (a) spot-taking machine; (b) the nonrotating part partially submerged (under computer control) into the stiffened MR fluid ribbon, which is moving clockwise along with the rotating wheel. The STM has only z-axis motion. The diameter of the STM wheel is ~15 cm.

the magnetic pole-piece current was 15 A (resulting in a magnetic field strength of 2 to 3 kG), the wheel speed was 200 rpm, and the out-of-field viscosity was 45 cP, as measured on the STM. The pump speed was adjusted to maintain a ribbon height of 1.6 mm, and the depth of the part immersed into the MR fluid ribbon, precisely controlled by computer, was kept constant at 0.3 mm. Spotting times (i.e., dwell times) varied from 1.17 s to 2.16 s in order to keep spot depths within the measurement range of a laser interferometer (see **Characterization**, p. 46).

A standard aqueous magnetorheological (MR) fluid was used in this experiment. This MR fluid consisted of carbonyl iron (CI) particles, nonmagnetic nanodiamond abrasives, deionized (DI) water, and stabilizers. The CI particles used in the MR fluid had a median particle size of ~4 μm. A small amount of nanodiamond particles, ~50-nm median size,[9] were used as polishing abrasives to enhance the material removal efficiency.

3. Dual-Force Sensor/Sample Mounting Device

A mounting device was developed for measuring both drag and normal forces acting on the part surface during MRF spotting, as shown in Fig. 117.43. The device consists of two dynamic piezoelectric force sensors,[16,17] mounted directly above the MR fluid ribbon and part surface contact zone. This ensures that both the sensors and the part align along the machine's z axis. This configuration limits the spotting experiment to one spot per part, except for LHG8 where only one part was available, requiring a small offset of the part itself. The sample mount portion of the device was modified to permit this adjustment.

The sensors are suitable for measuring relatively low forces (response threshold less than 0.1 and 0.01 N for the drag and normal force sensors, respectively),[16,17] which makes it possible to detect subtle changes in substrate type and surface condition, MR fluid composition, and STM machine settings. Special care was taken to keep the part's surface horizontal and perpendicular to the z axis for force measurements during spotting. System noise encountered in previous mounts was overcome by fabricating the force sensor/sample mounting device from aluminum to reduce its overall weight and by installing two 150-Hz filters (hardware) on both dual-mode amplifiers used for data acquisition.

Off-line calibration of the dual-force sensor assembly was performed on each material individually after each part was mounted. The normal-force sensor and drag-force sensor were calibrated separately. The calibration test showed that the vertical load applied for calibrating the normal-force sensor did not introduce a horizontal-force signal in the drag-force sensor, and a horizontal force applied for calibrating the drag-force sensor did not introduce a vertical-force signal in the normal-force sensor.

A LabVIEW interface was designed to record drag- and normal-force signals simultaneously.[18] Force was averaged over the spotting time for each individual measurement.

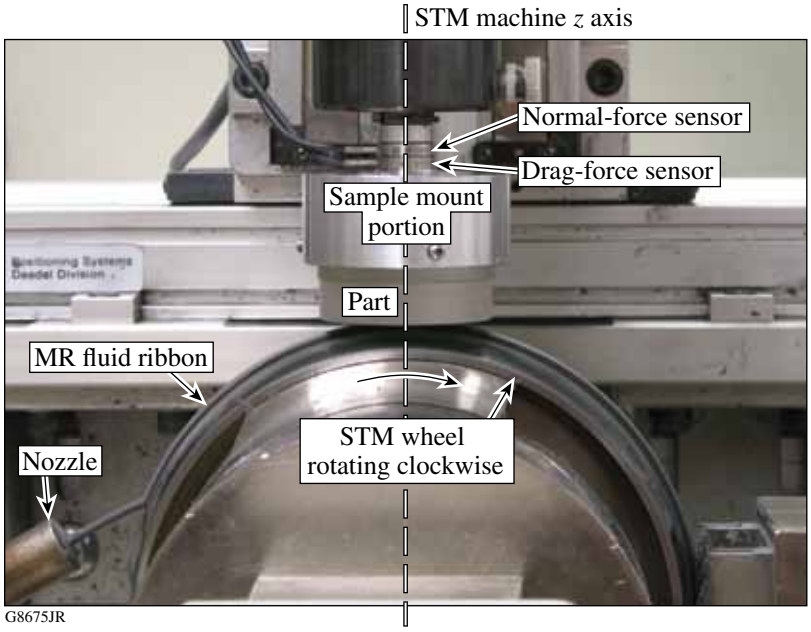

Figure 117.43
Photograph of the dual force sensor/sample mounting device, during spot taking on the STM, indicating the machine's z axis, the normal- and drag-force sensors, the sample mounting device, a part, the MR fluid ribbon, and the rotating wheel (diameter ~15 cm). The sensors are located directly above the contact zone between the MR fluid ribbon and the part for real-time *in-situ* measurements. The sample is waxed to a glass disk held by a set of screws against the aluminum housing of the sample mounting device.

4. Characterization

Removal rates for parts were obtained from MRF spots. The initial surface flatness was determined by a Zygo Mark IVxp interferometer (HeNe Fizeau interferometer),[14] which was also used to determine MRF-spot physical properties including spot profile, depth of deepest penetration (ddp), spot area, and spot volume. Spot volume (the volume of material removed in the spot) was measured using the laser interferometer by subtracting the original surface (before spotting) from the new surface that included the spot.[19] Volumetric removal rate was calculated as the spot volume divided by the spotting time. Spot area A_s was obtained by "drawing" a contour line on the spot periphery (light outline seen in the image in Fig. 117.42). Pressure was calculated by dividing normal force by spot area. Shear stress was calculated by dividing drag force by spot area.

It is important to note that in MRF, the contact area A_c and the spot area A_s are not the same. A_c represents the whole area of the part in contact with the MR fluid ribbon, while A_s is where the material removal effectively takes place during MRF spotting. The spot area, within the contact area, is normally slightly smaller, due to the fact that shear stress at the spot edge is almost zero, resulting in negligible material removal. Results from spotting experiments (not described here) demonstrate that A_c is the same for all materials when spotted under the same STM settings; A_s is, however, dependent on material type.

The peak-to-valley (p−v) and root-mean-square (rms) surface roughness within the spot ddp region for all materials was measured with a Zygo NewView 5000 noncontacting white-light interferometer.[15] Unfiltered areal ($350 \times 260\ \mu m^2$) surface roughness data were acquired at five randomly located sites within the spot ddp region for every spot taken.

Experimental Results

All spotting experiments were conducted under the same STM settings (except for the spotting time described in **Spot-Taking Machine**, p. 44) within a three-day period, approximately ten days after loading the MR fluid into the STM. Table 117.II summarizes the experimental results, including spot ddp, calculated peak removal rate ($\Delta h/\Delta t$), area (projected spot area), volume, calculated volumetric removal rate (VRR), drag force (F_d), normal force (F_n), and p−v and rms surface roughness. The rate of material removal is given in terms of volumetric removal rate. VRR is a practical measure of process efficiency providing a three-dimensional representation of material removal over the whole spot area (notice that the horizontal scale of Fig. 117.42 is in millimeters, whereas the vertical line, i.e., the spot depth, is in micrometers). Surface roughness data entered in Table 117.II for each material are averaged over 15 measurements, taken at five sites within the ddp region of each of three spots.

Drag force (F_d) is between ~4 to ~5 N, and normal force is between ~6 to ~9 N. These results fall within the range (2 to 20 N) of normal-force values reported by Schinhaerl *et al.*[20] using a three-axis dynamometer and a cerium-oxide MR fluid on BK7 glass over a range of operating conditions. Figure 117.44 plots both normal and drag forces versus the materials' Vickers hardness, where it is seen that only normal force has a positive linear dependence on material hardness.

Table 117.II: Experimental data for materials after spotting.

Material	Spotting time (s)	ddp (μm)	Peak removal rate (μm/min)	Spot area (mm^2)	Spot volume ($\times 10^6$ mm^3)	Volumetric removal rate (mm^3/min)	F_d (N)	F_n (N)	p−v (nm)	rms (nm)
LHG8	1.17	0.9±0.014	46±0.8	36±2	10.1±0.7	0.517±0.038	4.0±0.0	6.2±0.4	12±2	1.5±0.2
BK7	1.17	0.28±0.001	14±0.1	54±1	5.4±0.2	0.268±0.016	5.1±0.1	8.4±0.2	14±1	1.6±0.3
FS	2.16	0.28±0.016	8±0.4	50±0.1	3.4±0.1	0.102±0.012	4.1±0.1	9.3±0.3	9±1	1.0±0.1

Material	F_d/F_n	F_n/A_s (MPa)	F_d/A_s (MPa)
LH8	0.64±0.04	0.17±0.0157	0.11±0.0001
BK7	0.61±0.01	0.16±0.0052	0.09±0.00126
FS	0.44±0.01	0.19±0.0085	0.08±0.0028

The measured ratio of drag force to normal force $\left(F_d/F_n\right)$ falls between ~0.4 to ~0.6, which is in the typical range for the coefficient of friction (COF) reported for most materials in the sliding friction mode.[21] This is the first reported measurement of F_d/F_n for MRF.

The resultant p−v and rms surface roughness after the spotting process is expected since the sample piece is not rotated. These areal rms values of ~1 nm are typical of those previously reported for glass spotted on the STM.[8–10]

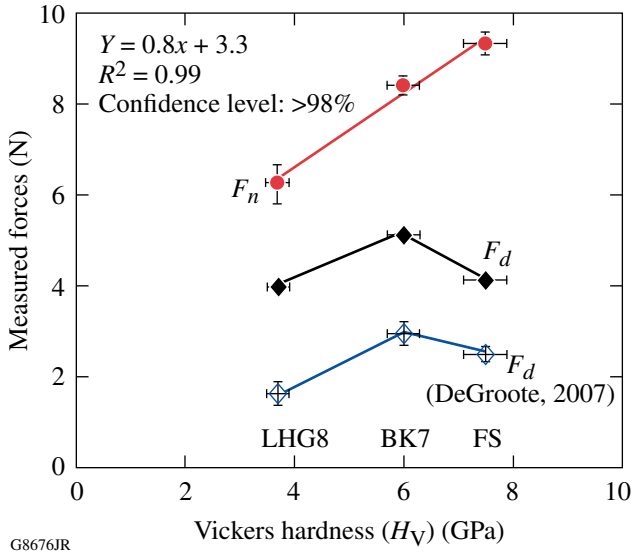

Figure 117.44
Normal force F_n and drag force F_d as a function of the material's Vickers hardness (GPa) for LHG8, BK7, and FS. (See text for a discussion of data taken by DeGroote.[9])

Discussion

1. From Normal Force to Hydrodynamic Pressure, from Drag Force to Shear Stress

For the first time, both drag force (F_d) and normal force (F_n) are measured simultaneously *in situ* for MRF. This section discusses how these measured forces correspond to the material removal model presented in the **Introduction** (p. 42) and its validity to MRF.

Normal force shows a positive linear dependence on material type (Fig. 117.44) under the conditions used in this experiment. Broadly speaking, material wear depends on its mechanical hardness, i.e., a soft material will wear more rapidly than a harder one. Our results show that the normal force is sensitive to the substrate surface hardness and, therefore, must have some, as yet undetermined, role to play in the motion/interaction between the MR fluid ribbon and the part. In addition, the volumetric removal rate decreases as normal force increases, as seen from the data in Table 117.II. However, when an attempt is made to plot and examine (not shown here) the ratio of F_n/A_s, i.e., the hydrodynamic pressure, to material Vickers hardness, no dependence is seen. Likewise, plotting the volumetric removal rate versus the hydrodynamic pressure (not shown here) reveals no dependence. (Note that the calculated hydrodynamic pressure range is from 0.1 to 0.3 MPa. This is comparable to literature values for pressure found in conventional chemical mechanical polishing processes.[22]) These results confirm experimentally that hydrodynamic pressure has negligible effect on material removal, and, contrary to previous reports,[4] the normal force is affected by the material hardness. The next section evaluates the different process parameters that affect the removal rate in MRF.

Figure 117.44 shows that the drag force alone does not depend on material type. This was originally reported by DeGroote[9] (see Fig. 117.44) on the STM, using a different force-sensor mounting device that included only a drag-force sensor. The current results are ~100%, 20%, and 60% higher for LHG8, BK7, and FS, respectively, compared to those measured previously. This increase in the measured drag force is attributed to improved alignment of the location of the drag-force sensor relative to the STM z axis and different MRF fluid/spotting conditions; otherwise, the results are similar.

It is not clear why drag force does not show an upward or downward trend with material hardness. As suggested by DeGroote[9] and DeGroote *et al.*,[10] the contribution of the glass-surface chemical dissolution to material removal in the MRF process is not explicitly represented by any terms in Eq. (2). The effect of chemistry on lowering the drag force experienced by the phosphate LHG8 could be considerable. A modification of Eq. (2) is offered in the next section, which provides a relatively simple prediction of material removal for MRF from that described by DeGroote[9] and DeGroote *et al.*,[10] without considering chemical contributions in the removal process.

Our results indicate that the hydrodynamic flow pressure in the converging gap, between the workpiece and MR fluid ribbon, depends on the composition of the upper gap surface. If pure no-slip boundary conditions held at the part surface, one would expect both normal and drag (shear) forces to be independent of part composition. We conclude, therefore, that the no-slip boundary condition must be violated to some extent on the part's surface. This is not surprising, given the fact that the MR fluid consists of a high concentration of solid abrasives in an aqueous medium.

Figure 117.45 plots the volumetric removal rate as a function of shear stress, F_d/A_s. It shows a strong dependence between material removal and shear stress, as predicted by Eq. (2), for shear stress values between ~0.08 to 0.15 MPa for the three glasses under the specific conditions of this experiment. It can also be extrapolated from these results that, for shear stresses less than about 0.08 MPa, the removal rate practically vanishes. This suggests a shear stress threshold below which material removal is very low; therefore the process efficiency is very low. As seen from Fig. 117.45, the volumetric removal rate does not depend on the hydrodynamic pressure F_n/A_s.

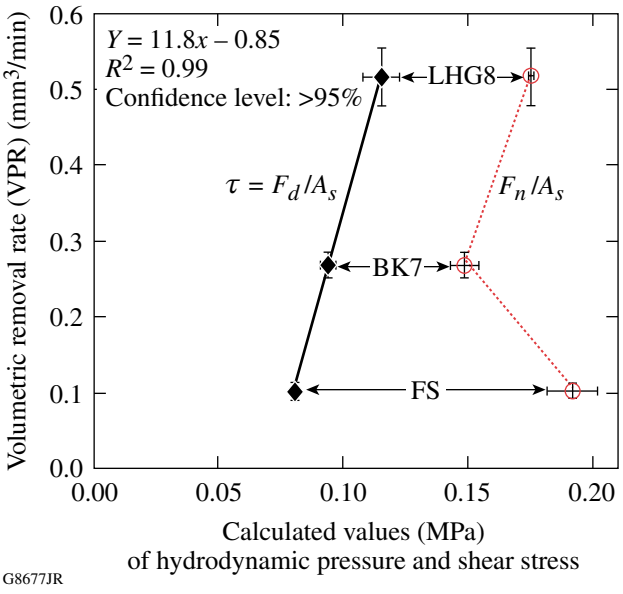

Figure 117.45
Volumetric removal rate (VRR) as a function of shear stress (τ), F_d/A_s, and as a function of the hydrodynamic pressure F_n/A_s.

2. Material Removal Rate Model

Lambropoulos *et al.*[23] found that the material removal rate is linearly proportional to both material mechanical properties (combined into a mechanical FOM) and pressure for loose-abrasive lapping of optical glasses. Their equation is now modified to describe material removal in MRF on the basis of the mechanical contributions to a FOM. Vickers hardness (H_V) is used in this analysis instead of Knoop hardness (H_K). The exponents of the mechanical property components are simplified as $E/K_cH_V^2$ (this term is designated as the mechanical FOM), similar to DeGroote's[9] and DeGroote *et al.*,[10] where near-surface Young's modulus and nanohardness were used instead of bulk values.

We next discuss the development of a coefficient to describe MRF removal similar to $C'_{p,\mathrm{MRF}(\tau)}$ in Eq. (2). To establish such a coefficient, we may use either pressure (as usually done in Preston analysis) or shear stress (as our current work indicates).

The effects of both shear stress (τ) and mechanical properties $\left(E/K_cH_V^2\right)$ can be incorporated into a predictive equation for material removal as shown in Eq. (3):

$$\mathrm{MRR_{MRF}} = C'_{p,\mathrm{MRF}(\tau,\mathrm{FOM})}\frac{E}{K_cH_V^2} \times \tau \times V, \qquad (3)$$

where $C'_{p,\mathrm{MRF}(\tau)}$ is a modification of Preston's coefficient in terms of shear stress τ and the material FOM. $\mathrm{MRR_{MRF}}$ could alternatively be written as the ratio $\mathrm{VRR_{MRF}}/A_s$, which is identified as $\Delta h/\Delta t$, where $\mathrm{VRR_{MRF}}$ is the volumetric removal rate for MRF and Δh is a representative height of removal averaged over the whole spot area.

For a linear velocity ~1.57 m/s at the wheel edge, assuming that the nanodiamond abrasives and the CI particles in the stiffened MR fluid ribbon are moving at the same speed as the rotating wheel, it is possible to estimate values for each of the three Preston's coefficients identified in Eqs. (2) and (3). Table 117.III shows the calculated values for $C'_{p,\mathrm{MRF}(F_n)}$, $C'_{p,\mathrm{MRF}(\tau)}$, and $C'_{p,\mathrm{MRF}(\tau,\mathrm{FOM})}$ for all materials spotted by MRF along with literature values for C_p from conventional loose-abrasive polishing on a polyurethane pad. The coefficients are calculated from $\mathrm{VRR_{MRF}}/A_s$, as discussed above. The calculated $C'_{p,\mathrm{MRF}(F_n)}$ varies from as low as 1.2×10^{-4} GPa^{-1} for FS to as high as 8.8×10^{-4} GPa^{-1} for LHG8, nearly an 8× increase. $C'_{p,\mathrm{MRF}(\tau)}$ has a smaller range, however, of about 5×, from 2.6×10^{-4} GPa^{-1} for FS to 1.4×10^{-3} GPa^{-1} for LHG8. Substituting shear stress for pressure narrows the range of Preston's coefficient; however, because of the absence of material properties, there is still a significant variance in $C'_{p,\mathrm{MRF}(\tau)}$. Combining shear stress with mechanical properties results in a much tighter range of the coefficient $C'_{p,\mathrm{MRF}(\tau,\mathrm{FOM})}$ from 1.6×10^{-4} GPa^{-1} for FS up to 2.0×10^{-4} GPa^{-1} for BK7, only a single variance in magnitude. The coefficient $C'_{p,\mathrm{MRF}(\tau,\mathrm{FOM})}$ varies by only ±12% among LHG8, BK7, and FS, which may be attributable to the particular surface condition and specific material composition.

Table 117.III: Preston's coefficient for conventional chemical mechanical polishing processes from literature and modified Preston's coefficients calculated for MRF from this work.

Material	C_p (GPa^{-1})	$C'_{p,\mathrm{MRF}(F_n)}$ (GPa^{-1})	$C'_{p,\mathrm{MRF}(\tau)}$ (GPa^{-1})	$C'_{p,\mathrm{MRF}(\tau,\mathrm{FOM})}$ (MPa)
LHG8	–	8.8×10^{-4}	1.4×10^{-3}	1.6×10^{-4}
BK7	8.3×10^{-4} (a) 10.7×10^{-4} (b)	3.4×10^{-4}	5.6×10^{-4}	2.0×10^{-4}
FS	1.7×10^{-4} (a) 3.3×10^{-4} (b)	1.2×10^{-4}	2.6×10^{-4}	1.6×10^{-4}
Variance in magnitude(c)	–	8×	5×	≪1×

(a)From Izumitani,[24,25] using conventional loose-abrasive lapping, CeO_2 abrasives and polyurethane pad, p = 20 KPa, V = 0.5 m/s.
(b)From Cumbo,[26] using conventional loose-abrasive lapping, CeO_2 abrasives and polyurethane pad, p = 5 KPa, V = 0.11 m/s.
(c)Variance in magnitude is defined by dividing the largest value in the column by the smallest value.

Conclusions

This work reports for the first time on *in-situ* measurements of drag and normal forces in MRF. Three optical glasses ranging in hardness and chemical composition were tested. A spot-taking machine (STM) was used as a test bed for MRF spotting experiments. We examined how the measurable drag and normal forces, and the calculated shear stress as a function of material mechanical properties, contribute to material removal in MRF. A modified Preston's equation, combining shear stress with material mechanical properties, is proposed, which suggests that material removal is dominated by the material mechanical properties. Our main observations are summarized as follows:

- Normal force was measured simultaneously with drag force in MRF for the first time. Normal force was within the range of 6 to 9 N, whereas drag force was within the range of 4 to 5 N. These results are in good agreement with the literature, where either one of these forces was measured individually, but not simultaneously.

- It was confirmed experimentally that the hydrostatic pressure [normal force divided by the projected spot area F_n/A_s, first term of Eq. (1) (see data in Table 117.II and Fig. 117.45)] does not predict the material removal rate in MRF. It was found for the first time that the measured normal force is dependent on material hardness.

- It was also demonstrated for the first time how the calculated shear stress (drag force divided by the projected spot area on the part) governs the volumetric removal rate, not drag force alone. This experimentally confirms Shorey's[4] predictions that material removal in MRF is dominated by shear.

- For the glasses tested under the STM geometry and conditions reported here, it was found that there is a threshold for shear stress below which a removal rate becomes negligible. In order to effectively remove material in MRF, shear stress should be kept above ~0.08 MPa by adjusting the process parameters. Additional work is required to identify what process parameters affect shear stress, such as the size of the projected spot area on the part. Our results show that drag force is within a range of ~4 to 5 N for a range of optical glass materials, ranging from relatively "soft" LHG8 to hard FS. Therefore, by keeping a spot area <50 mm^2 while keeping drag force in the range reported above, one should expect efficient material removal in MRF for glasses.

- Preston's coefficient was calculated for MRF in terms of the hydrostatic pressure, shear stress, and a combination of a material's figures of merit and shear stress. These calculated coefficients indicate a narrow range for our modified Preston's coefficient when both material figures of merit and shear stress are considered for a range of optical glasses, providing predictive capabilities for new glasses. Therefore, we conclude that material removal in MRF for optical glasses is governed by a material's mechanical properties and shear stress.

ACKNOWLEDGMENT

The authors thank Alex Maltsev and Mike Kaplun of the Laboratory for Laser Energetics (LLE) for their help with sample preparation. The authors also thank Scott Russell of the Department of Mechanical Engineering at the University of Rochester for his help with the LabVIEW software. The authors acknowledge the Laboratory for Laser Energetics (LLE) at the University of Rochester for continuing support. One of the authors (C. Miao) is an LLE Horton Fellow.

Research was sponsored by the U. S. Army Armament, Research, Development and Engineering Center (ARDEC) and was accomplished under Cooperative Agreement Number W15QKN-06-2-0104 and the U.S. Department of Energy Office of Inertial Confinement Fusion under Cooperative Agreement No. DE-FC52-08NA28302, the University of Rochester, and the New York State Energy Research and Development Authority. The views and conclusions contained in this document are those of the authors and should not be interpreted as representing the official policies, either expressed or implied, of U.S. Army ARDEC or the U.S Government. The support of DOE does not constitute an endorsement by DOE of the views expressed in this article. The U.S. Government is authorized to reproduce and distribute reprints for Government purposes notwithstanding any copyright notation hereon.

REFERENCES

1. S. D. Jacobs, D. Golini, Y. Hsu, B. E. Puchebner, D. Strafford, Wm. I. Kordonski, I. V. Prokhorov, E. Fess, D. Pietrowski, and V. W. Kordonski, in *Optical Fabrication and Testing*, edited by T. Kasai (SPIE, Bellingham, WA, 1995), Vol. 2576, pp. 372–382.

2. S. D. Jacobs, S. R. Arrasmith, I. A. Kozhinova, L. L. Gregg, A. B. Shorey, H. J. Romanofsky, D. Golini, W. I. Kordonski, P. Dumas, and S. Hogan, in *Finishing of Advanced Ceramics and Glasses*, edited by R. Sabia, V. A. Greenhut, and C. G. Pantano, Ceramic Transactions, Vol. 102 (The American Ceramic Society, Westerville, OH, 1999), pp. 185–199.

3. F. W. Preston, J. Soc. Glass Technol. **XI**, 214 (1927).

4. A. B. Shorey, "Mechanisms of Material Removal in Magnetorheological Finishing (MRF) of Glass," Ph.D. thesis, University of Rochester, 2000.

5. V. H. Bulsara *et al.*, Trans. ASME, J. Appl. Mech. **65**, 410 (1998).

6. V. W. Kordonski and D. Golini, in *Proceedings of the Sixth International Conference on Electro-Rheological Fluids, Magneto-Rheological Suspensions and Their Applications*, edited by M. Nakano and K. Koyama (World Scientific, Singapore, 1998), pp. 837–844.

7. D. Golini, H. Pollicove, G Platt, S. Jacobs, and W. Kordonsky, Laser Focus World **31**, 83 (1995).

8. A. B. Shorey, S. D. Jacobs, W. I. Kordonski, and R. F. Gans, Appl. Opt. **40**, 20 (2001).

9. J. E. DeGroote, "Surface Interactions Between Nanodiamonds and Glass in Magnetorheological Finishing (MRF)," Ph.D. thesis, University of Rochester, 2007.

10. J. E. DeGroote, A. E. Marino, J. P. Wilson, A. L. Bishop, J. C. Lambropoulos, and S. D. Jacobs, Appl. Opt. **46**, 7927 (2007).

11. C. Miao, S. N. Shafrir, H. Romanofsky, J. Mici, J. C. Lambropoulos, and S. D. Jacobs, in *Optical Fabrication and Testing*, OSA Technical Digest (CD) (Optical Society of America, Washington, DC, 2008), Paper OThB4.

12. J. C. Lambropoulos, S. D. Jacobs, and J. Ruckman, in *Finishing of Advanced Ceramics and Glasses*, edited by R. Sabia, V. A. Greenhut, and C. G. Pantano, Ceramic Transactions, Vol. 102 (The American Ceramic Society, Westerville, OH, 1999), pp. 113–128.

13. A. G. Evans, in *Fracture Mechanics Applied to Brittle Materials*, edited by S. W. Freiman (American Society for Testing and Materials, Philadelphia, 1979), Vol. ASTM STP 678, Part 2, pp. 112–135.

14. Zygo Mark IVxp™, Zygo Corporation, Middlefield, CT 06455. This instrument is a 4-in. HeNe Fizeau interferometer with a wavelength of 632.8 nm. Peak-to-valley (p–v) for surface flatness and depth of deepest penetration (ddp) of the spot was measured in microns.

15. Zygo NewView 5000 noncontact white light interferometer, Zygo Corporation, Middlefield, CT 06455. Average microroughness data (peak-to-valley, p–v, and root-mean-square, rms) were obtained under the following conditions: 20× Mirau objective; high FDA Res.; 20-μm bipolar scan length; Min/Mod: 5%, unfiltered. This instrument has a lateral resolution of ~1 μm and a vertical resolution of ~0.3 nm.

16. Single-axis slim-line compressive (K9133B21) force sensor measuring system, Kistler Instrument Corp., Amherst, NY 14228-2171.

17. Single-axis slim-line shear (K9143B21) force sensor measuring system, Kistler Instrument Corp., Amherst, NY 14228-2171.

18. The LabVIEW data-collecting program (National Instruments Corporation, Austin, TX 78759-3504) was written by S. Russell and S. N. Shafrir of the University of Rochester, Rochester, NY (2008).

19. MetroPro Reference Guide, OMP-0347, Zygo Corporation, Middlefield, CT 06455.

20. M. Schinhaerl *et al.*, in *Current Developments in Lens Design and Optical Engineering IX*, edited by P. Z. Mouroulis, W. J. Smith, and R. B. Johnson (SPIE, Bellingham, WA, 2008), Vol. 7060, p. 706006.

21. B. Bhushan and B. K. Gupta, in *Handbook of Tribology: Materials, Coatings, and Surface Treatments* (Krieger Publishing Company, Malabar, FL, 1997), Chap. 2, Table 2.1, p. 2.11.

22. J. Steigerwald, S. P. Murarka, and R. J. Gutmann, *Chemical Mechanical Planarization of Microelectronic Materials* (Wiley, New York, 1997).

23. J. C. Lambropoulos, S. Xu, and T. Fang, Appl. Opt. **36**, 1501 (1997).

24. T. S. Izumitani, in *Optical Fabrication and Testing*, OSA Technical Digest (Optical Society of America, Washington, DC, 1982), pp. 1–4.

25. T. S. Izumitani, in *Optical Fabrication and Testing Workshop*, OSA Technical Digest (Optical Society of America, Washington, DC, 1984), pp. TuB-A1-1–TuB-A1-3.

26. M. J. Cumbo, "Chemo-Mechanical Interactions in Optical Polishing (Glass Finishing)," Ph.D. thesis, University of Rochester, 1993.

Effective Verdet Constant in Terbium-Doped-Core Phosphate Fiber

Faraday rotators are widely used in optical isolators, circulators, Faraday mirrors, and magnetic/current field sensors. Traditional Faraday rotators are based on bulk optics, which require optical coupling for use with fiber-optic systems. Optical fibers continue to be the platform of choice in many optics fields, making the development of all-fiber Faraday rotation components highly desirable. This is particularly true for high-power fiber laser systems, where fiber termination and small free-space beams place restrictions on how much power can be transported through such components in order to avoid damage at optical interfaces.

Several standard silica-fiber Faraday rotators have been reported[1–4] but are relatively impractical because of long fiber lengths. The small Verdet constant in standard silica fiber, which translates to a long fiber length, makes it difficult to realize all-fiber Faraday rotators. The Verdet constant is only about 1 rad/Tm at 1064 nm in silica, compared with 40 rad/Tm in terbium gallium garnet (TGG) crystals often used in bulk optics.[5] As an example, if the magnetic field is 0.2 T, the silica fiber length required for a 45° rotation is around 4 m. To maintain a constant orientation of the magnetic field along the entire axial length, the fiber cannot be coiled. This creates an impractical requirement that the magnet structure be as long as the fiber.

To overcome this limitation, Shiraishi[6] reported the fabrication of a high-Verdet-constant (21× greater than silica fiber) optical fiber using Hoya FR-5 (terbium borosilicate) glass, where both the core and the cladding were doped with terbium (Tb). Ballato and Snitzer[7] also reported the fabrication of a 54-wt%-terbium–doped optical fiber, measuring the Verdet constant on bulk samples to be 20× higher than silica fiber.

Doping with high-Verdet-constant materials, such as terbium, can be an effective way to increase the total Verdet constant in optical fiber. The Verdet constant experienced by an optical field is different, however, from the material Verdet constants in the core and cladding when they are made of different materials. The results described above did not measure or predict this effect. The first experimental proof of the effective Verdet constant theory is presented in this article. The effective Verdet constant in a phosphate fiber that is terbium doped in the core only is measured. The experimental results agree well with theory and describe how the effective Verdet constant differs from the value measured from the bulk samples.

The Verdet constant experienced by light in an optical fiber is different from that in bulk glass. In bulk glass, the Verdet constant is normally uniform everywhere. In optical fiber, the core and cladding have different Verdet constants since they are typically made of different materials. Only a portion of the guided mode exists in the core of the fiber waveguide. Thus, the effective Verdet constant V_{eff} is defined as the Verdet constant experienced by the optical mode in the fiber,

$$V_{\text{eff}} = V_{\text{core}}\Gamma + V_{\text{clad}}(1-\Gamma), \tag{1}$$

where V_{core} and V_{clad} are the Verdet constants in the core and cladding, respectively, and the confinement factor $\Gamma = P_{\text{core}}/P_{\text{tot}}$ represents the ratio of the power contained in the core, P_{core}, to total power P_{tot}. The confinement factor Γ can be calculated directly by assuming that the fundamental mode profile is Gaussian, $\Gamma = 1 - \exp\left(-2/\xi^2\right)$. The ratio of beam-spot size to fiber radius ξ is usually approximated by

$$\xi \simeq 0.65 + 1.619\, v^{-3/2} + 2.879\, v^{-6}, \tag{2}$$

which is accurate to within 1% for $1.2 \le v \le 2.4$, where v is the normalized frequency (or V number).[8] Equation (1) for the effective Verdet constant has a straightforward physical meaning: the Verdet constant includes two parts contributing from the core and the cladding, weighted by the mode overlap in each region.

In recent theoretical work,[9] the rotation of an optical field in a fiber was derived using Maxwell's equations with a magnetic field applied along the axial direction of the fiber. An empirical equation, which has a relative error of 2% for $1 \le v \le 3$, was used to approximate the propagation constant. Using these results,

one can derive the effective Verdet constant directly from the circular birefringence of the propagation constant. After algebraic manipulation, this derivation produces an effective Verdet constant given by $V_{\text{eff}}^{\text{Yoshino}} = V_{\text{core}}\alpha + V_{\text{clad}}(1+\alpha)$, where the factor $\alpha = 1.306 - 1.138/v$ and is a dimensionless constant. Figure 117.46 shows the relative difference $\Delta = (\alpha - \Gamma)/\alpha$ between factors Γ and α as a function of normalized frequency v. In the region $2 < v < 2.4$, where most single-mode fibers are designed, Δ is less than 4%. Considering that both models use empirical equations during derivation, such a difference is reasonable. Therefore, although not indicated in Ref. 9, the factor α should have the same physical meaning as Γ, representing the light confinement in the core. This indicates that Eq. (1) can also be derived via rigorous electromagnetic calculations.

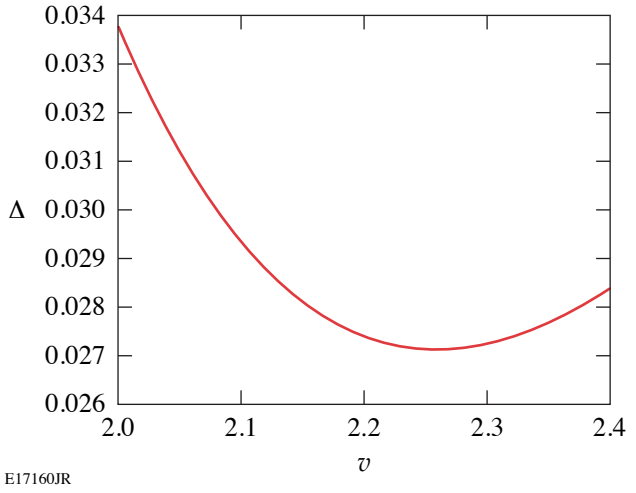

Figure 117.46
Normalized difference between factors Γ and α for a single-mode fiber as a function of normalized frequency v.

The phosphate optical fiber used in these experiments was fabricated at NP Photonics.[10] It is 25-wt% terbium doped in the single-mode core [numerical aperture (N.A.) = 0.147] and 6-wt% lanthanum doped in the cladding to provide the appropriate core N.A. Core and cladding diameters are 4.5 μm and 120 μm, respectively, and the propagation loss is 0.12 dB/cm at 980 nm. The Verdet constant is measured at 1053 nm and room temperature using the experimental configuration shown in Fig. 117.47. A 4-cm section of Tb-doped phosphate fiber, spliced between two polarization-maintaining (PM) fibers, goes through a magnet tube. Linearly polarized, 1053-nm light is launched into the fiber, and the polarization direction of the output light is monitored. The N48 NdFeB magnet tube is 4 cm long with inner and outer diameters of 5 mm and 6 cm, respectively. As the magnet is translated along the fiber, the magnetic field imposed on the Tb fiber is changed. By measuring the rotation angle as a function of the magnet's position on the fiber axis, V_{eff} can be extracted, provided the magnetic field is known.

Magnetic fields can be readily calculated by using the geometrical shape of the magnet.[11] The axial component of the magnetic-field distribution along the central axis of the magnet tube is derived to be

$$B_z(z) = \frac{B_r}{2}\left\{\frac{z+l/2}{\left[a_1^2+(z+l/2)^2\right]^{1/2}} - \frac{z+l/2}{\left[a_2^2+(z+l/2)^2\right]^{1/2}} - \frac{z-l/2}{\left[a_1^2+(z-l/2)^2\right]^{1/2}} + \frac{z-l/2}{\left[a_2^2+(z-l/2)^2\right]^{1/2}}\right\}, \quad (3)$$

where a_1 and a_2 are the inner and outer radii, respectively, l is the length of the magnet, and B_r is the residual magnetic flux density. Figure 117.48 shows the calculated $B_z(z)$ for the N48 magnet used in the experiment ($B_r = 1.35T$) along with the measured magnetic field outside the magnet. The physical ends of the magnet are also shown for reference. The magnetic field, measured only outside the magnet because the probe size is larger than a_1, agrees very well with the theoretical curve calculated from Eq. (3). The magnetic field has different directions inside and outside the magnet, such that the total integrated field along the z axis is zero, i.e., $\int_{-\infty}^{+\infty} B_z(z)\,dz = 0$, resulting from Ampère's law. This means that if a sufficiently long piece of fiber with axially uniform V_{eff} goes through the

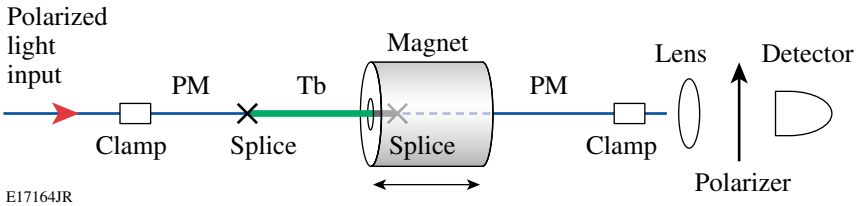

Figure 117.47
Experimental configuration of the Faraday rotation measurement.

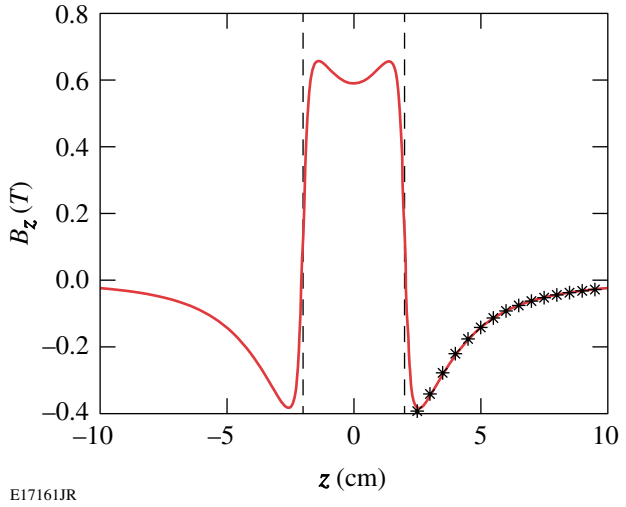

Figure 117.48
Theoretical (solid) and measured (star) magnetic density flux distribution B_z along the center axis z; dashed lines represent the magnet ends.

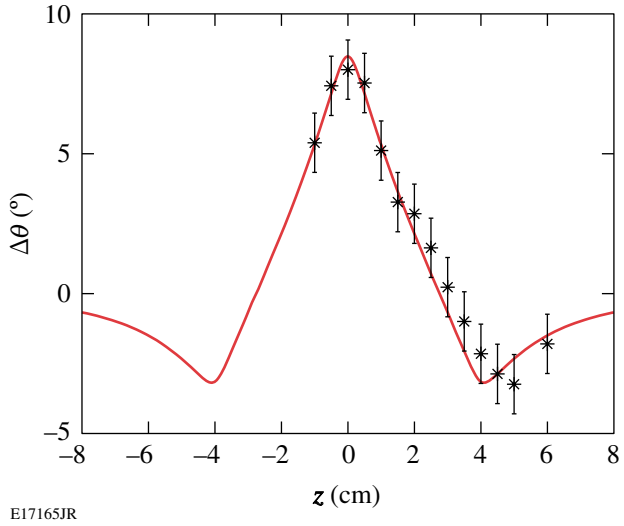

Figure 117.49
Measured (star) rotation angle and corresponding curve fit (solid) at 1053 nm along the center axis z.

magnet, the rotation angles inside and outside the magnet counteract each other and the total rotation angle is zero. If the fiber consists of i different sections of length L_i, the total rotation angle $\Delta\theta_{\text{tot}}$ can be written as a sum of the rotation in each section $\Delta\theta_i$, given by

$$\Delta\theta_{\text{tot}} = \sum_i \Delta\theta_i = \sum_i V_{\text{eff}}^i \int_{L_i} B_z(z)\mathrm{d}z, \tag{4}$$

where V_{eff}^i and $\int_{L_i} B_z(z)\mathrm{d}z$ are the effective Verdet constant and the line integral of the magnetic field in each section, respectively. For the experimental configuration shown in Fig. 117.47, Eq. (4) can be simplified as

$$\Delta\theta_{\text{tot}} = V_{\text{eff}}^{\text{Tb}} \int_{L_{\text{Tb}}} B_z(z)\mathrm{d}z + V_{\text{eff}}^{\text{PM}} \int_{L_{\text{PM}}} B_z(z)\mathrm{d}z, \tag{5}$$

where the two terms represent the Verdet constant of and the integration over the Tb-doped and PM fibers, respectively. $V_{\text{eff}}^{\text{PM}}$ can be neglected in our experiment because the large linear birefringence in PM fiber suppresses Faraday rotation.

In the experiment, the magnet is axially translated in 5-mm steps. At each step, the direction of the major polarization axis is measured; the power is measured as the polarizer in front of the detector is rotated, and the polarization direction is extracted by fitting this data to a cosine-squared function. Figure 117.49 shows the measured rotation angle and the corresponding curve fit at 1053 nm along the central axis. The error in the measured angle is primarily caused by air flow, and it is determined to be 1° by a polarization stability measurement. The curve fit is obtained by adjusting $V_{\text{eff}}^{\text{Tb}}$, yielding a measured Verdet constant of $V_{\text{measure}} = -6.2 \pm 0.4$ rad/Tm. This value is 6× higher than that of the silica and demonstrates the potential for compact all-fiber Faraday rotators.

The bulk value of the Tb-doped core is calculated from Ref. 7 to be $V_{\text{core}} = -9.3$ rad/Tm, assuming a linear dependence on the terbium ion concentration. Since no Verdet constant data are available in the near-infrared region for the lanthanum-doped phosphate glass used in the cladding, the value is approximated based on two observations: First, the Verdet constant dispersion curve of the lanthanum-doped phosphate glass is roughly 0.8 rad/Tm higher than the curve for SiO_2 in the visible region.[12,13] Assuming a similar trend in the near-infrared region, the Verdet constant of the lanthanum-doped phosphate glass should be 0.8 rad/Tm larger than that of the SiO_2. Second, the rare-earth element present in the host material is the dominating factor in determining the Verdet constant. For example, the Verdet constant of the terbium aluminosilicate is similar to that of the terbium phosphate.[13] Therefore, the Verdet constant of the crystal lanthanium fluoride (LaF_3) measured at 1064 nm (Ref. 12) should also be similar to that of lanthanum phosphate. Both of these observations lead to a value of $V_{\text{clad}} = 1.8$ rad/Tm. Using these values for the core and cladding Verdet constants, the theoretical models predict $V_{\text{eff}} = -6.0$ rad/Tm and $V_{\text{eff}}^{\text{Yoshino}} = -6.3\,\text{rad}/\text{Tm}$, the differ-

ence between the models resulting from the approximations contained in each. They both agree well with the experimental result, which differs substantially from the bulk core value of −9.3 rad/Tm due to the mode confinement properties of the fiber, as described above. This measurement validates the theory of the effective Verdet constant.

Several methods can be used to increase the effective Verdet constant for compact all-fiber Faraday rotators. For example, the same high-Verdet-constant material can be doped in both the core and the cladding. In this case, the V_{eff} will be equal to the material's Verdet constant. If the high-Verdet-constant material is doped only in the core, the N.A. and the core diameter can be increased (while maintaining a V number less than 2.405) to confine more light in the core, therefore increasing V_{eff}. Other rare-earth elements besides terbium can also be doped. For example, praseodymium and dysprosium also have Verdet constants much higher than silica.

In conclusion, the first experimental validation of the effective Verdet constant theory has been reported. The effective Verdet constant of light propagation in a fiber includes contributions from the materials in both the core and the cladding. It is measured in a 25-wt%-terbium-doped-core phosphate fiber to be −6.2±0.4 rad/Tm at 1053 nm, which is 6× larger than silica fiber. The result agrees well with the Faraday rotation theory in optical fibers.

ACKNOWLEDGMENT

This work was supported by the U.S. Department of Energy Office of Inertial Confinement Fusion under Cooperative Agreement No. DE-FC52-08NA28302, the University of Rochester, and the New York State Energy Research and Development Authority. The support of DOE does not constitute an endorsement by DOE of the views expressed in this article.

REFERENCES

1. E. H. Turner and R. H. Stolen, Opt. Lett. **6**, 322 (1981).
2. G. W. Day *et al*., Opt. Lett. **7**, 238 (1982).
3. J.-F. Lafortune and R. Vallée, Opt. Commun. **86**, 497 (1991).
4. V. Annovazzi-Lodi, S. Merlo, and A. Leona, J. Lightwave Technol. **13**, 2349 (1995).
5. E. Khazanov *et al*., Appl. Opt. **41**, 483 (2002).
6. K. Shiraishi, S. Sugaya, and S. Kawakami, Appl. Opt. **23**, 1103 (1984).
7. J. Ballato and E. Snitzer, Appl. Opt. **34**, 6848 (1995).
8. G. P. Agrawal, *Lightwave Technology: Components and Devices* (Wiley, Hoboken, NJ, 2004).
9. T. Yoshino, J. Opt. Soc. Am. B **22**, 1856 (2005).
10. NP Photonics, Inc., Tucson, AZ 85747, http://www.npphotonics.com.
11. M. McCaig and A. G. Clegg, *Permanent Magnets in Theory and Practice*, 2nd ed. (Wiley, New York, 1987).
12. D. R. Lide, *CRC Handbook of Chemistry and Physics*, 82nd ed. (CRC Press, Boca Raton, FL, 2001).
13. M. J. Weber ed., *CRC Handbook of Laser Science and Technology*, edited by M. J. Weber, Supplement 2: Optical Materials (CRC Press, Boca Raton, FL, 1995), Sec. 9.

Applied Plasma Spectroscopy: Laser-Fusion Experiments

Introduction

The remarkable progress of laser-fusion experiments [i.e., inertial confinement fusion (ICF) driven by high-intensity laser beams] has been charted with x-ray spectroscopy. Hans Griem, considered the father of plasma spectroscopy, provided an excellent foundation for this research.[1] Inertial confinement fusion occurs when a spherical-shell target containing thermonuclear fuel [i.e., deuterium and tritium (DT)] is imploded to produce energy gain.[2,3] The implosion is driven by the ablation of material from the outer shell surface with intense laser beams (direct drive)[2] or with x rays produced in a high-Z enclosure or hohlraum (indirect drive).[3] Both of these schemes rely on the solid-state Nd:glass laser invented by Elias Snitzer in 1961.[4] High-power Nd:glass laser beams were developed at LLE and Lawrence Livermore National Laboratory (LLNL) in the 1960s and 1970s, as well as in France, Japan, and Russia.[5] Historically, indirect-drive[3] ICF was pursued at LLNL, while direct-drive[2] implosions were the main focus of the LLE research program.

Four areas of x-ray spectroscopy for laser-fusion experiments are highlighted in this article: K_α emission spectroscopy to diagnose target preheat by suprathermal electrons,[6–10] Stark-broadened K-shell emissions of mid-Z elements to diagnose compressed densities and temperatures of implosion cores,[11–13] K- and L-shell absorption spectroscopy to diagnose the relatively cold imploding shell that does not emit x rays,[14–16] and multispectral monochromatic imaging of implosions to diagnose core temperature and density profiles.[17–20] The original x-ray-spectroscopy experiments in these areas will be discussed and compared to current state-of-the-art measurements. This article concentrates on direct-drive ICF[2] since laser ablation was used to create the high-energy-density plasmas probed with x-ray spectroscopy in the highlighted research. LLE Senior Scientist B. Yaakobi pioneered many of the x-ray-spectroscopy experiments in laser-fusion research.[6,8,9,11,12,14,18]

Over the last three decades, increasing amounts of energy have been delivered to target with multibeam Nd:glass laser systems.[5] At LLE, the four-beam DELTA laser,[21] operating at 1ω with 10 J in a 40-ps pulse, evolved into the OMEGA Laser System,[22] which consists of a 60-beam, 3ω, 30-kJ compression laser and the high-energy petawatt OMEGA EP laser.[23] The uniformity of direct-drive implosions steadily improved with scientific advancements in laser technology and target physics. Laser-irradiation nonuniformity levels approaching 1%–2% rms[24] were achieved using phase plates,[25] two-dimensional (2-D) smoothing by spectral dispersion (SSD),[26] polarization smoothing (PS),[27] and a large number of symmetrically arranged laser beams. The hydrodynamic efficiency of laser ablation was significantly improved by frequency tripling the fundamental 1ω laser wavelength.[28] The size of the gas-filled spherical-shell implosion targets increased more than an order of magnitude to ~1 mm. X-ray streak cameras[29] were developed to record time-resolved x-ray spectra. Significant theoretical advances in spectral line-shape calculations were made,[30–35] beginning with the realization by H. Griem that the distribution of electric microfields of the ions and electrons led to Stark broadening of spectral line shapes in plasmas.[1] Increases in computational power kept pace with Moore's law[36] and made it feasible to more accurately calculate complex spectra.[30–35] Progress on all these fronts paved the way to highly reproducible x-ray spectroscopic results for laser-fusion experiments, which complemented measurements of charged-particle spectroscopy and neutronics.[2,3] The next step of thermonuclear ignition on the soon-to-be-completed 192-beam, 1.8-MJ National Ignition Facility (NIF) laser system[37] at LLNL will greatly benefit from these results.

The following sections present a brief introduction to laser-fusion research, describe the plasma spectroscopy applications in laser-fusion experiments, and summarize our conclusions.

Inertial Confinement Fusion

Over the last three decades, x-ray spectroscopy has recorded the remarkable progress made in inertial confinement fusion. Hot-spot ignition involves the implosion of a thin-shell spherical target containing a cryogenic-DT layer.[2,3] For direct-drive ICF, a 3ω shaped laser pulse designed to achieve nearly isentropic compression initially irradiates the target with a low-intensity

foot (10^{13} to 10^{14} W/cm^2), followed by a high-intensity main drive (10^{15} W/cm^2) (Refs. 2 and 3). The laser irradiation breaks down the target surface and forms a coronal plasma. The laser energy is absorbed in the corona via inverse bremsstrahlung[2,3] and transported to the ablation surface via electron thermal conduction.[2,3] The ablated shell mass forms a coronal plasma that surrounds the target and accelerates the shell or pusher inward via the rocket effect.[2,3] The implosion can be divided into the following four stages (as illustrated in Fig. 118.1): shock propagation, acceleration phase, deceleration phase, and peak compression.[2,3]

Laser ablation launches hydrodynamic waves through the fuel layer and sets the target on the desired shell adiabat during the foot pulse. Shock heating is the main heating mechanism of the shell in an ablatively driven implosion.[2,3] The shell adiabat is defined as the ratio of shell pressure to the Fermi-degenerate pressure.[2,3] High compressibility requires that the DT fuel remains close to Fermi degenerate throughout the implosion. The dense, nearly Fermi degenerate matter or warm dense matter created by the shock waves is diagnosed with x-ray absorption spectroscopy using surrogate-planar, plastic-tamped Al targets.[15,16]

As the laser intensity rises during the main drive and the shock wave breaks out of the rear surface of the shell, the target begins to accelerate. Modulations at the ablation surface caused by mass perturbations and laser-irradiation nonuniformities are amplified by Rayleigh–Taylor (RT) hydrodynamic instability and feed through to the inner shell surface.[2,3] The corona evolves into a long-scale-length plasma and becomes susceptible to two-plasmon-decay (TPD) instability, which occurs near quarter-critical density when the phase-matching conditions are satisfied for the laser light to decay into two electron-plasma waves or plasmons.[38,39] Wave–particle interactions (e.g., Landau damping, trapping, and wave breaking) can generate suprathermal electrons with energies greater than 50 keV (Ref. 39). These hot electrons can preheat the fuel and adversely affect the target compressibility.[2,3] K_α emission spectroscopy of targets with buried mid-Z tracer layers is used to infer levels of target preheat.[6–9]

When the higher-density shell converges toward the target center and is decelerated by the lower-density fuel, a hot spot forms.[2,3] The hot dense matter created in the implosion core is diagnosed with x-ray emission spectroscopy.[11–13] The cold dense shell surrounding the hot spot is diagnosed with x-ray absorption spectroscopy.[14] The RT instability on the inner shell surface, seeded by feedthrough of nonuniformities from the ablation surface and by mass modulations on the inner surface, causes hydrodynamic mixing of the cold dense shell plasma with the hot-spot plasma. The radiative properties of hot dense matter with pressures of ~10 Gbar and the implosion dynamics of an Ar-doped-deuterium-gas–filled plastic-shell target are illustrated using the Stark-broadened spectral line shapes of Ar K-shell emission.[13] Levels of mixing of the plas-

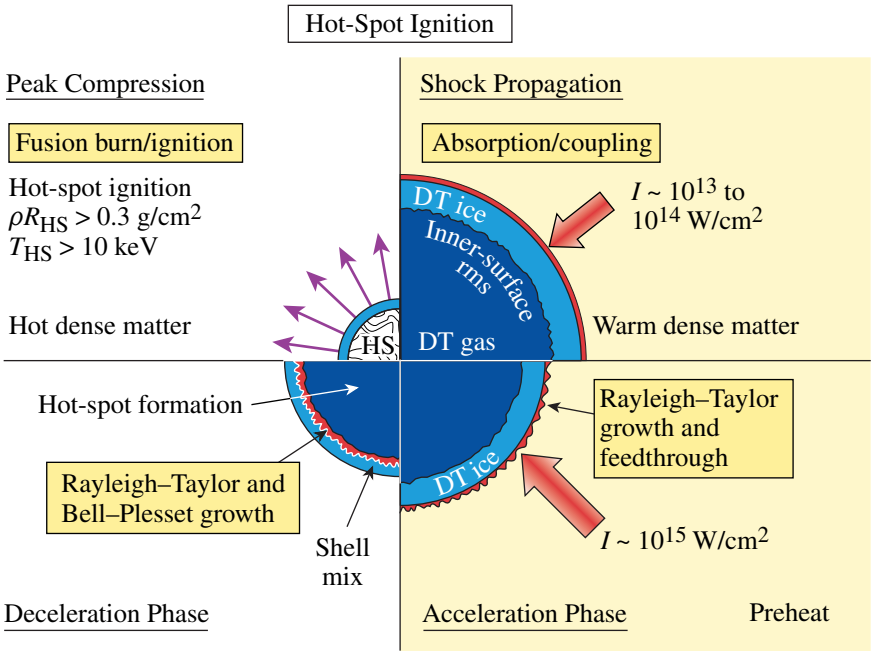

E14874bJR

Figure 118.1
Schematic illustrating the four stages—shock propagation, acceleration phase, deceleration phase, and peak compression—of a direct-drive implosion for hot-spot ignition.

tic shell with the deuterium fuel are estimated by combining x-ray spectroscopic results with fuel densities inferred from charged-particle spectroscopy.[40,41] The electron temperature and density profiles of the hot spot are inferred from multiple monochromatic x-ray imaging.[20]

Compression by the cold dense shell causes the pressure and DT fusion reaction rate of the hot spot to increase. It is predicted that the α-particle fusion products will deposit sufficient energy in the hot spot to launch a thermonuclear burn wave out through the cold dense fuel in the shell just prior to peak compression, when the areal density of the hot spot exceeds 0.3 g/cm^2 and the hot-spot temperature reaches 10 keV (Refs. 2 and 3). Energy gain with hot-spot ignition depends on the implosion velocity of the shell V_{imp}, the shell areal density ρR_{shell} at the time of burn, and the in-flight shell adiabat.[2,3,42–44] A complementary approach to hot-spot ignition is fast ignition, which uses a high-energy petawatt laser to generate a beam of electrons or ions to heat a compressed mass to thermonuclear conditions.[45] Fast ignition reduces the drive uniformity requirements of the compression laser.

Laser-Fusion Experiments

The four areas of x-ray spectroscopy for laser-fusion experiments are presented in the order in which the seminal papers were published to emphasize the pursuit of the research. More-sophisticated target-physics experiments have accompanied the advances in laser-driver development. K_α emission spectroscopy used to diagnose target preheat by suprathermal electrons was reported first,[6] followed by measurements of Stark-broadened K-shell emissions of mid-Z elements to diagnose compressed densities and temperatures of implosion cores.[11] These experiments were performed on the four-beam DELTA Laser System.[21] K- and L-shell absorption spectroscopy used to diagnose the relatively cold imploding shell on DELTA[14] was reported several years later, along with backlighting using multifrequency x rays to diagnose the temperature and areal density of the implosion core on the two-beam GEKKO II Laser System.[17] The concept of combining a pinhole aperture with a Bragg crystal spectrometer to achieve multiple monochromatic x-ray images was extended to hundreds of pinholes nearly two decades later on the 60-beam OMEGA Laser System.[18] The original x-ray-spectroscopy experiments in these areas are discussed in this section and compared to current state-of-the-art measurements.

1. K_α Emission Spectroscopy

K_α emission spectroscopy was first used by Yaakobi *et al.*[6] to infer preheat by fast electrons in laser-fusion experiments. The four-beam, 1ω, 0.8-TW DELTA Laser System irradiated thin (~1-μm-thick) 90-μm-diam spherical glass shells filled with 10 atm of Ne gas with peak intensities of 2 to 3 × 10^{15} W/cm^2 as shown in Fig. 118.2(a). The 1ω laser irradiation generates suprathermal electrons via resonance absorption with energies of ~10 keV (Ref. 39). Such energetic electrons deposit their energy throughout the target shown in Fig. 118.2(a), resulting in K_α emission from the Ne-gas fill. In contrast to the ablatively driven implosion where the shock wave is the dominant heating mechanism of the shell, the rapid heating of the thin glass shell by suprathermal electrons and x-ray radiation from the

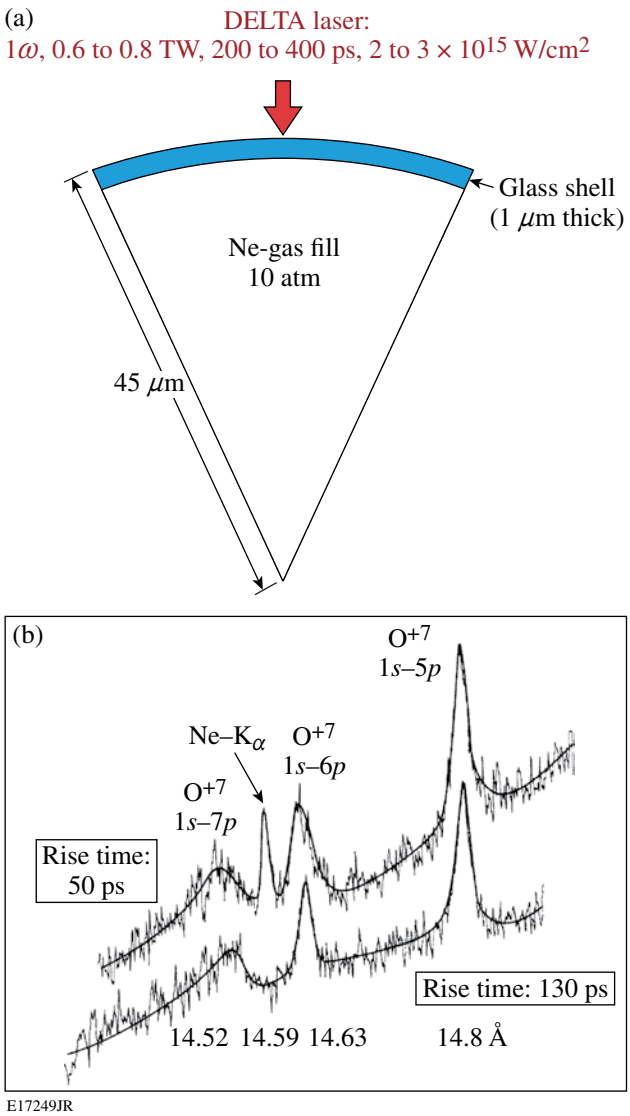

Figure 118.2
(a) Schematic of a direct-drive target, consisting of a thin glass shell filled with Ne gas, used in preheat experiments on the DELTA Laser System. (b) Measured, time-integrated x-ray spectrum showing Ne K_α emission.

corona causes the entire shell to explode. This type of implosion is called an exploding pusher: roughly half of the shell mass explodes outward and the remaining half inward, driving the implosion.[46] The number of fast electrons was estimated from the calibrated time-integrated x-ray spectrum of the Ne K_α emission shown in the upper trace in Fig. 118.2(b). This experiment did not shield the Ne gas from the coronal x-ray emission so the magnitude of the photopumping of the Ne K_α emission was estimated. Subsequent work by Hares *et al*. eliminated the effects of photopumping and saturation of K_α emission caused by ionization.[7] Multilayer planar targets composed of different elements, as shown in Fig. 118.3(a), shielded the K_α fluorescer from being photopumped by the x-ray radiation of the corona.[7] These planar targets were irradiated with conditions similar to the spherical targets in Yaakobi's experiment. The K_α emission characteristic of each layer, shown in Fig. 118.3(b), discriminates among the various excitation mechanisms and provides a higher-fidelity inference of the fast electrons.

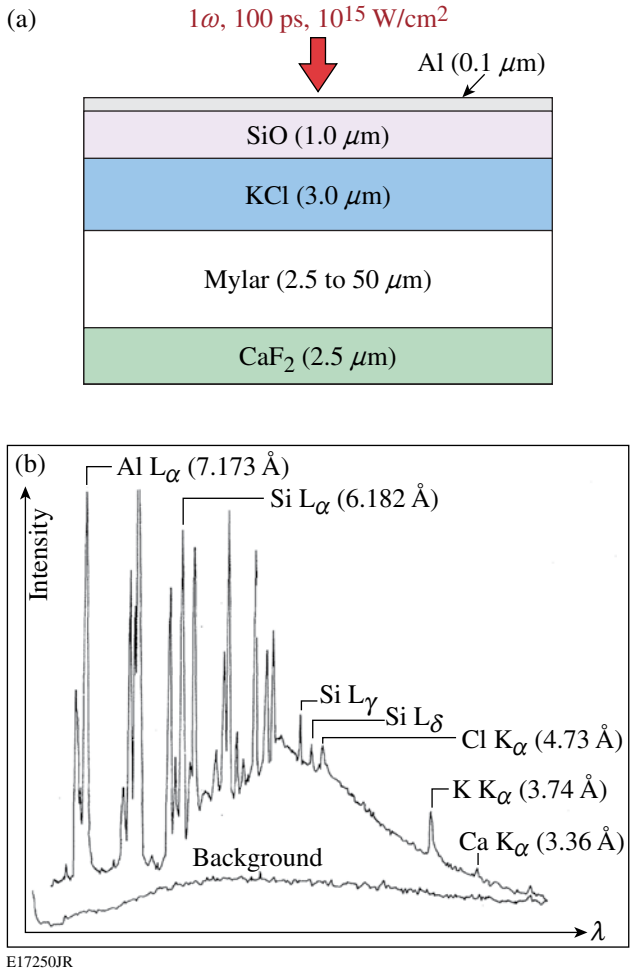

Figure 118.3
(a) Schematic of planar multilayer target used for preheat experiments and designed to discriminate between excitation mechanisms of photopumping from the coronal x-ray emission and fast electrons. (b) Measured, time-integrated x-ray spectrum showing K_α emission characteristic of each tracer layer.

Current state-of-the-art preheat measurements carried out on OMEGA for plastic-shell[8] and cryogenic-deuterium-shell[9] implosion targets rely on K_α emission spectroscopy to calibrate hard x-ray diagnostics[47] used to infer preheat. Similar experiments are also performed for fast ignition;[10,45] however, in stark contrast to hot-spot ignition, fast ignition must maximize the conversion of laser energy into hot electrons. Laser-to-hot-electron conversion-efficiency measurements were performed on the Nova 1ω, 400-J, 0.5- to 20-ps petawatt laser.[10] Planar Al/Mo/CH targets were irradiated with focused intensities of 0.02 to 3.0×10^{20} W/cm^2, and conversion efficiencies of ~50% were inferred at the highest intensity using Mo $K_{\alpha,\beta}$ spectroscopy.

2. X-Ray Emission Spectroscopy

The Stark-broadened spectral line shapes of the K-shell emission from mid-*Z* tracer elements provide a time-resolved measure of the electron temperature and density of the imploding core. Hans Griem showed that the distribution of the electric microfields of the ions and electrons led to Stark broadening of spectral line shapes in plasmas.[1] His former graduate student, Chuck Hooper, extended spectral-line-shape calculations to mid-*Z* elements with his research group at the University of Florida at Gainesville.[30] The hot dense matter created by spherical compression was diagnosed first by Yaakobi using the Stark-broadened K-shell emission of mid-*Z* tracer elements in the gas fill of spherical-shell implosion targets.[11] The four-beam, 1ω, 0.2-TW, 40-ps DELTA Laser System irradiated thin (~1-μm-thick), ~70-μm-diam spherical glass shells filled with 2 to 8.6 atm of Ne gas, as shown in Fig. 118.4(a). Compressed densities in the cores of exploding pusher implosions were diagnosed using Stark broadening of Ne K-shell emissions. As shown in Fig. 118.4(b), an electron density of 7×10^{22} cm^{-3} was inferred from Stark broadening of Ne Lyman-γ emission, which was calculated by Chuck Hooper's atomic physics group.[30] Yaakobi extended this work to the ZETA Laser System,[12] which was the first six-beam laser system of the 24-beam OMEGA Laser System.[48] The six-beam, 1ω, 100-J, 50-ps ZETA Laser System irradiated thin (~0.5- to 2-μm-thick) spherical glass shells with (1.5- to 4.2-μm-thick) plastic ablators ~50 μm in diameter and filled with 3 to 16 atm of Ar gas, as shown in Fig. 118.5(a). Increasing the thickness of the shell with the CH ablator changes the implosion from an exploding pusher[46] to an ablatively driven implosion. The compressed mass density and temperature were inferred from the He_β Stark-broadened, Ar K-shell spectral line shapes shown in Fig. 118.5(b). Again, the

predicted spectral line shapes were calculated by Hooper.[30] This x-ray spectroscopic observation demonstrated that symmetric illumination (six beam) with an ablatively driven implosion leads to high-volumetric convergence (>1000) (Ref. 12).

Laser-fusion experiments worldwide use Stark-broadened spectral line shapes to diagnose implosions.[11–13,30,31,34,49–54] The development of more-sophisticated codes to calculate the Stark-broadened spectral line shapes accompanied these experimental advances.[30–35] Hooper's atomic physics group developed the Multi-Electron Radiator Line Shape (MERL) code,[32] which uses the adjustable parameter exponential approximation (APEX)[33] for ion-microfield calculation, and a quantum-mechanical relaxation approximation for electron broadening.[34] The asymmetry of the Stark-broadened Ar K-shell emission was studied.[31] Kilkenny *et al.* performed a more-rigorous analysis of the spectral line shapes measured on a two-beam Ne:glass laser at the Rutherford Laboratory Cen-

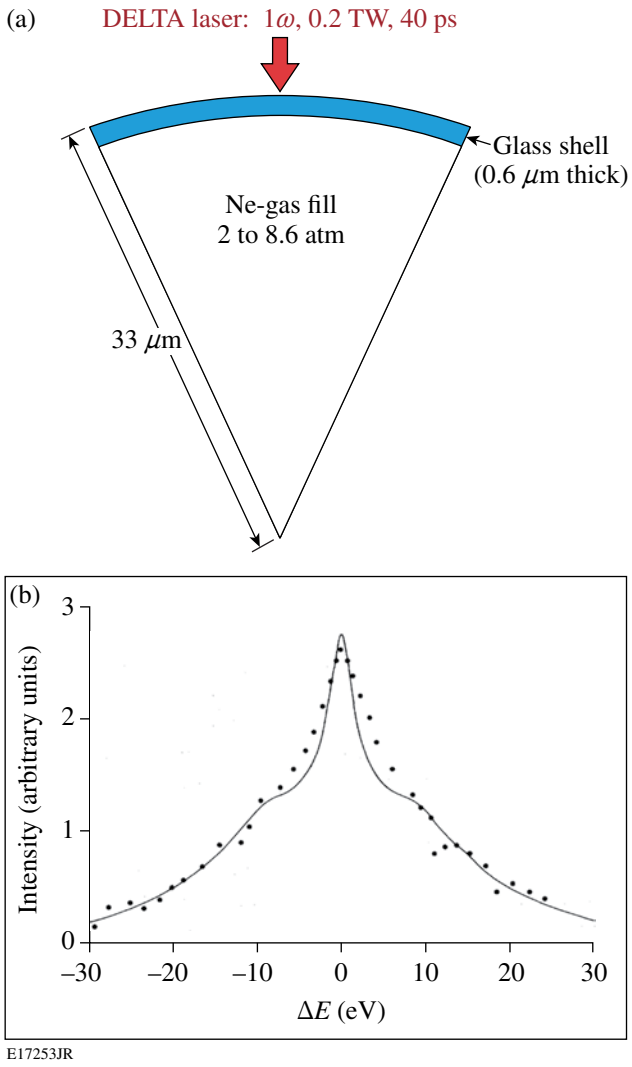

Figure 118.4
(a) Schematic of a direct-drive target, consisting of a thin glass shell filled with Ne gas, used in implosion compression experiments on the DELTA Laser System. (b) Measured, time-integrated x-ray spectrum of the Stark-broadened Ne Ly_γ emission (solid circles), compared to the predicted[30] spectral line shape (solid curve).

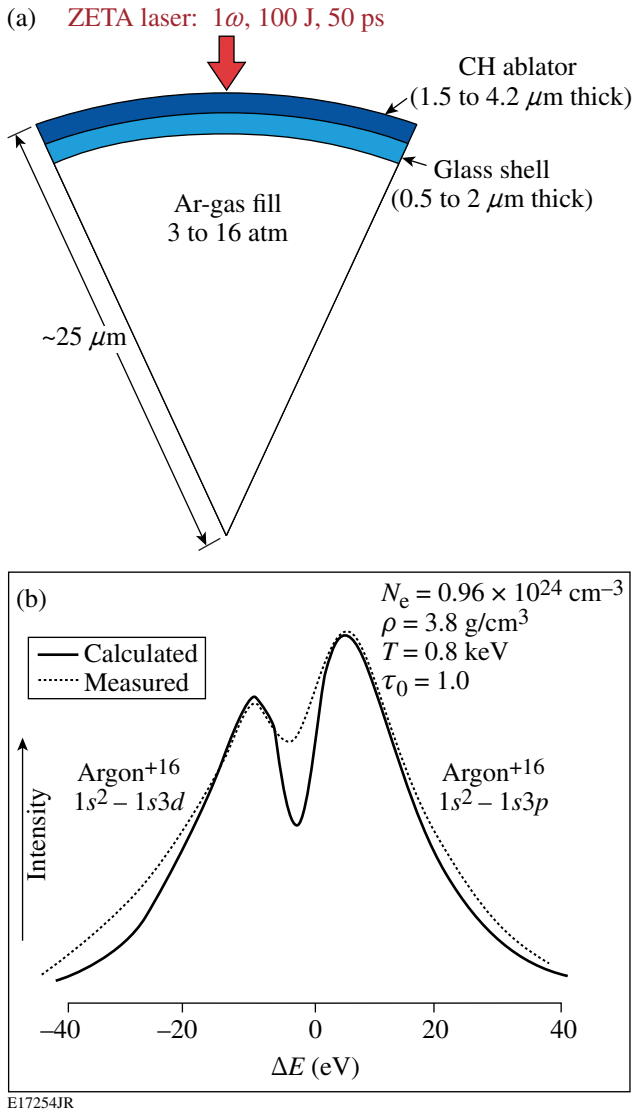

Figure 118.5
(a) Schematic of a direct-drive target, consisting of a thin glass shell with a plastic ablator filled with Ar gas, used in implosion compression experiments on the ZETA Laser System. (b) Measured, time-integrated x-ray spectrum of the Stark-broadened Ar He_β emission (dotted curve) compared to the predicted[30] spectral line shape (solid curve).

tral Laser Facility by self-consistently fitting all the observed lines of one state of ionization to diagnose electron density and opacity.[49] Hooper *et al.* used an x-ray streak camera to record time-resolved Stark-broadened Ar K-shell emission from direct-drive implosions on OMEGA.[50] Hammel *et al.* used Stark-broadened Ar K-shell emission to study indirect-drive implosions on Nova.[51] Nishimura *et al.* used similar x-ray spectroscopic techniques to study indirect-drive implosions on the GEKKO XII Laser System.[52] Keane *et al.* extended the research on Nova with indirect-drive implosions using Xe L-shell emission.[53] Woolsey *et al.* inferred the temporal evolution of electron temperature and density in indirectly driven spherical implosions on Nova.[54] Haynes *et al.* studied the effects of ion dynamics and opacity on Stark-broadened Ar K-shell emission on OMEGA.[34]

State-of-the-art measurements using Stark-broadened K-shell emission from implosion cores were performed on OMEGA.[13] As shown in Fig. 118.6(a), a plastic-shell target (20 μm thick and 860 μm in diameter) with an Ar-doped deu-

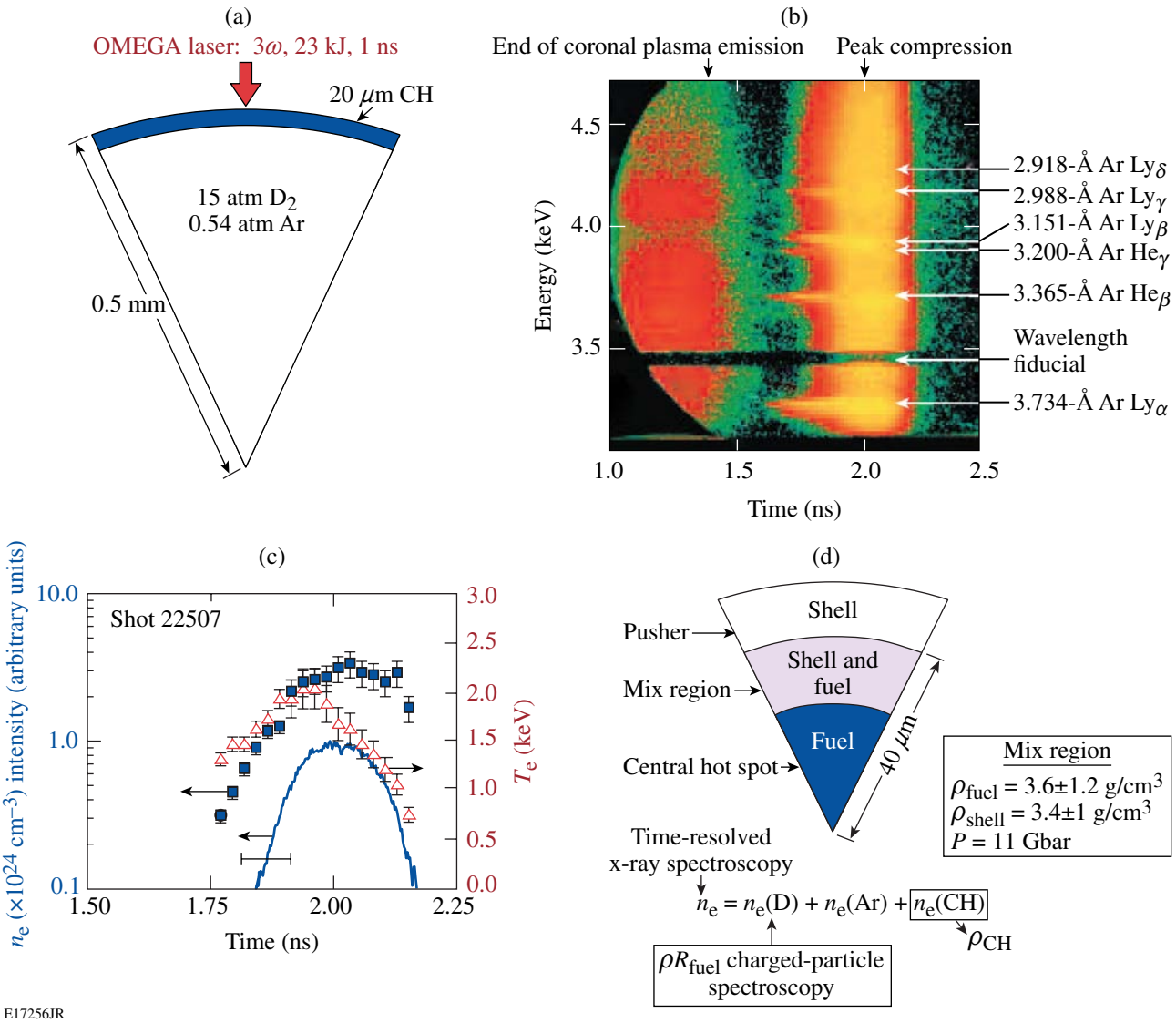

Figure 118.6

(a) Schematic of a direct-drive target, consisting of a 20-μm-thick plastic shell filled with deuterium gas doped with Ar, used in implosion compression experiments on the 60-beam OMEGA Laser System. (b) Measured, time-resolved Stark-broadened Ar K-shell emission. (c) Emissivity-averaged electron temperature (triangles) and density (squares) inferred from time-resolved Ar K-shell x-ray spectroscopy and ~3.5-keV x-ray continuum (solid curve) emitted from the implosion. (d) Schematic of the physical picture of the compressed core at peak neutron production showing an RT-induced mix region, consisting of shell and fuel, formed between the shell and the fuel.

terium fill gas was driven with a 23-kJ, 1-ns square laser pulse smoothed with phase plates,[25] 2-D SSD,[26] and PS.[27] Compared to the targets used for the seminal work on ZETA,[12] the gas-filled spherical-shell implosion targets on OMEGA were more than an order of magnitude larger than previously used. The time-resolved Ar K-shell emission dispersed with a Bragg crystal and recorded with an x-ray streak camera is shown in Fig. 118.6(b), with the prominent spectral features identified. The spectral line shapes were analyzed with the MERL code[32] to infer the time history of the emissivity-averaged electron temperature and density in the implosion core shown in Fig. 118.6(c). This diagnostic technique charts the evolution of the implosion dynamics. A strong rise in the electron temperature and density is observed as the shell decelerates. The peak in the electron temperature occurs at peak neutron production time, and peak compression occurs at stagnation when peak x-ray production is observed. The RT-induced fuel–shell mix in implosions was estimated[40] by combining the density inferred from Ar K-shell spectroscopy[13] and the areal density inferred from charged-particle spectroscopy.[41] The physical picture of the compressed core is shown schematically in Fig. 118.6(d). A mix region consisting of plastic shell and Ar-doped deuterium gas develops between the shell pusher and the fuel in the central hot spot. The electron density in the mix region is inferred from the Ar K-shell spectroscopy.[12,40] The deuterium fuel, Ar dopant, and any plastic shell material contribute to the electron density in the mix region. The contribution from the deuterium fuel was estimated from the fuel-areal-density measurement,[41] and the contribution from Ar was calculated to be small. A ratio of approximately 1:1 of plastic and fuel in the mix region was inferred.[40]

3. X-Ray Absorption Spectroscopy

Many of the high-energy-density plasmas created during the implosion are too cold to emit x rays. X-ray absorption spectroscopy effectively characterizes such matter. The relatively cold conditions in the imploding shell (the "piston") were first diagnosed by Yaakobi using x-ray absorption spectroscopy.[14] The four-beam, 1ω, 0.2-TW, 60- to 70-ps DELTA Laser System irradiated thin (~1-μm-thick) spherical glass shells or thick (~8-μm-thick) spherical plastic-coated glass shells, 60 to 110 μm in diameter and filled with either 7 to 20 atm of Ar gas or 18 atm of DT, as shown in Fig. 118.7(a). Figure 118.7(b) shows the time-integrated x-ray absorption spectra for two shots.[14] Both spectra show prominent Si K-shell emissions from the inner wall of the shell that is heated by heat conduction from the hot spot and by the shock wave reflected from the center of the target. The outgoing x-ray continuum emission from the hot spot and the inner wall of the imploding shell backlights the compressed shell. The lower spectrum in Fig. 118.7(b) showing Si 1s–2p absorption features from B-like Si (i.e., Si^{9+}) to He-like Si (i.e., Si^{12+}) ions indicates that a relatively cold (i.e.,

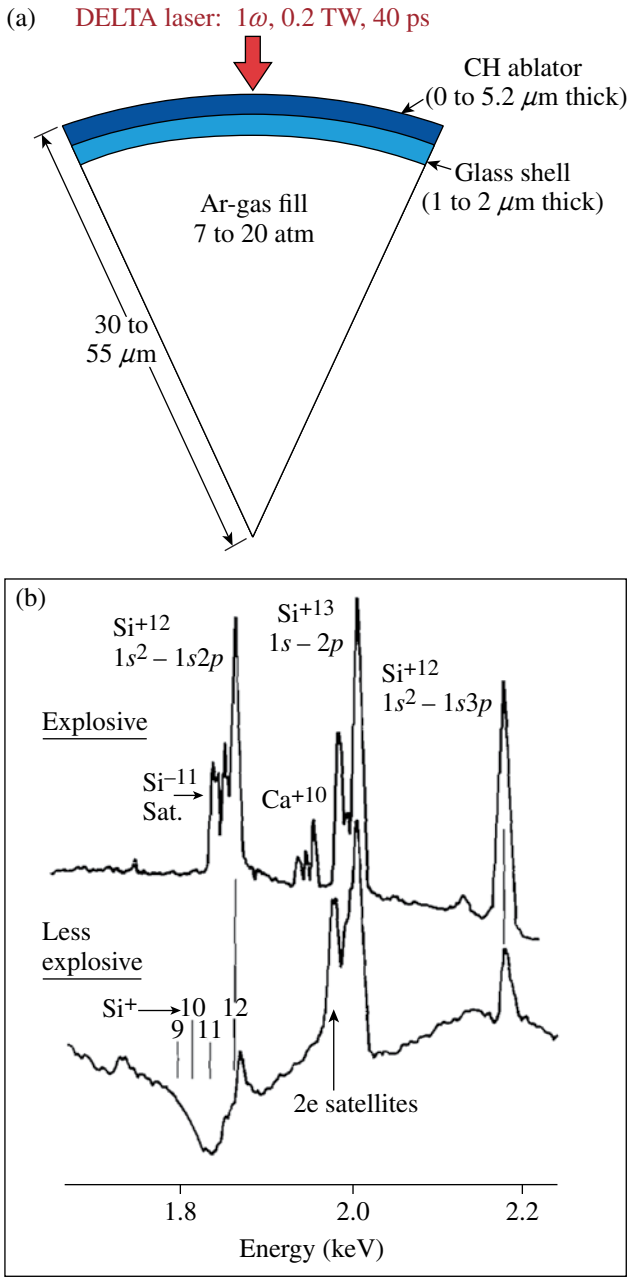

Figure 118.7
(a) Schematic of a direct-drive target, consisting of a thin glass shell with a plastic ablator filled with Ar gas, used in x-ray absorption spectroscopy experiments on the DELTA Laser System. (b) Measured, time-integrated x-ray spectrum of the Si K-shell spectrum taken for an explosive pusher (upper spectrum) and an ablatively driven implosion (lower trace). The Si 1s–2p absorption is observed in the latter case.

$T_e < 200$ eV) dense shell surrounds the hot spot,[14] which is characteristic of an ablatively driven implosion.[3,4] The absence of Si 1*s*–2*p* absorption features in the upper trace of Fig. 118.7(b) indicates that the glass shell material surrounding the hot spot is not cold (i.e., $T_e > 200$ eV); rather it is characteristic of an exploding pusher implosion.

Applications of x-ray absorption spectroscopy are not limited to compressed matter. Novel point-projection x-ray absorption spectroscopy experiments were performed using indirect drive[55] on Nova. X-ray–heated samples of Al were diagnosed using Al 1*s*–2*p* spectroscopy.[55]

State-of-the-art measurements using x-ray absorption spectroscopy have been performed on OMEGA to diagnose the shock-heated and compressed matter characteristic of the shock-propagation stage.[15,16] These results greatly benefit from earlier work by Hoarty *et al.*,[56] Boehly *et al.*,[57] and A. Ng.[58] As shown in Fig. 118.8(a), plastic planar-foil targets (50 μm thick) with a buried layer of Al (~1 μm thick) were shock heated and compressed by directly irradiating planar targets with high-intensity laser beams, generating 10- to 70-Mbar shock-wave pressures with on-target intensities in the range of 0.05 to 1.0×10^{15} W/cm^2 over a 0.5-mm diameter.[15] The buried depth was varied to probe the shock wave at different

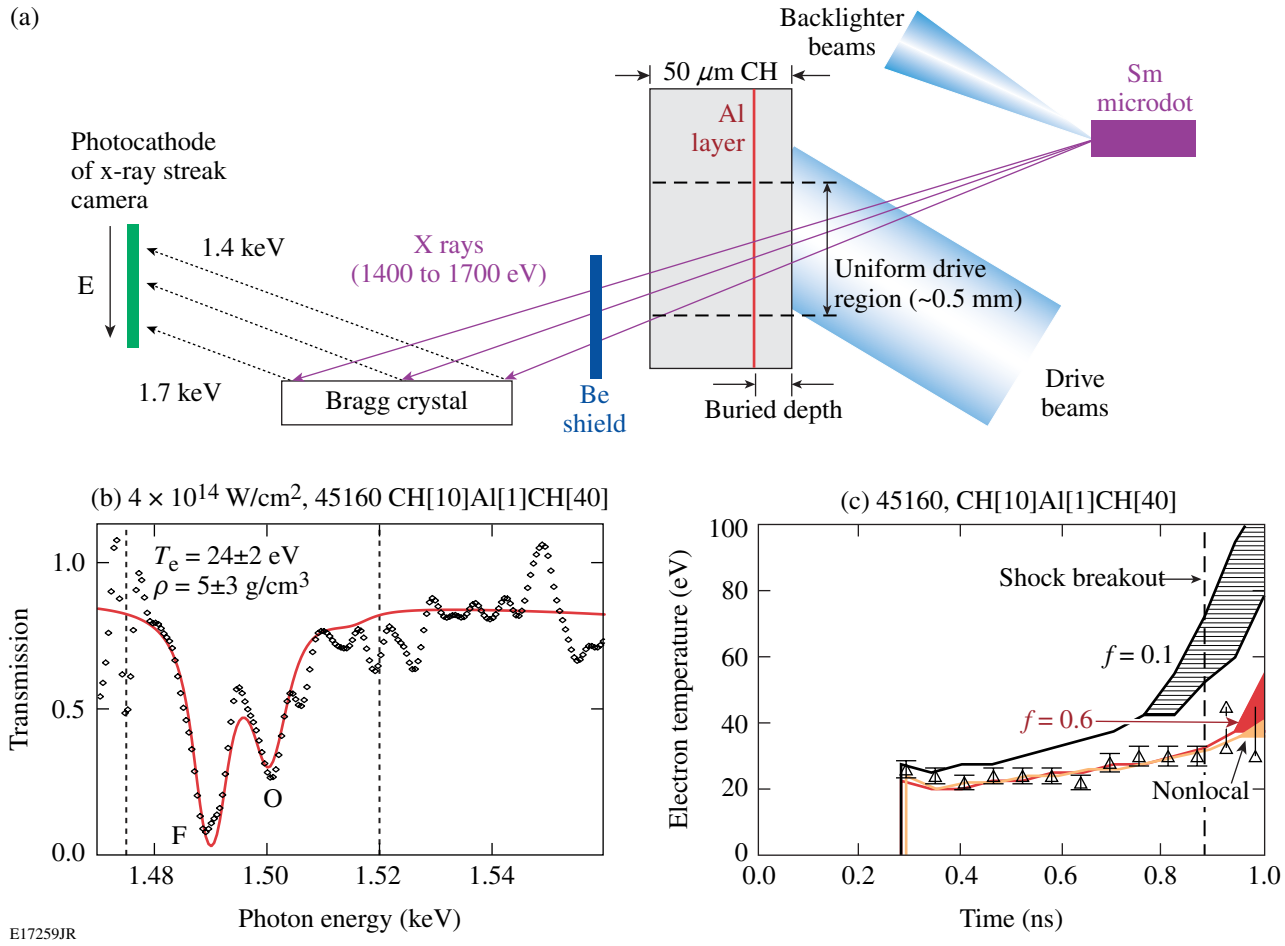

Figure 118.8
(a) Schematic of an experimental setup for a time-resolved x-ray absorption spectroscopy experiment on the 60-beam OMEGA laser to diagnose laser-ablation–driven shock heating and compression. (b) Time-resolved Al 1*s*–2*p* absorption spectrum recorded after the shock wave propagated through the buried Al layer. (c) Time history of the electron temperature in the Al layer compared with various 1-D hydrodynamic models. The shock wave passes through the buried Al layer just after 0.2 ns and breaks out of the rear surface of the target just after 0.8 ns.

times. The shock wave creates nearly uniform conditions in the Al layer. A separate group of tightly focused beams with an intensity of ~10^{16} W/cm^2 irradiated the Sm point-source (100-μm-diam) backlighter producing a pseudo-continuum of Sm M-shell emission in the 1400- to 1700-eV photon energy range.[15] The resulting warm dense matter was probed with time-resolved Al 1s–2p absorption spectroscopy, using a Bragg crystal spectrometer and an x-ray streak camera arranged as shown in Fig. 118.8(a), to infer temperature and density in the buried Al layer.[15] Al 1s–2p absorption provides the experimental signature of shock-wave ionization of the buried Al layer. The density is inferred from the Stark broadening of the spectral line shapes, and the temperature is inferred from the relative distribution of the various absorption charge states.[15,32,35] An Al 1s–2p absorption spectrum recorded after a single, strong laser-ablation–driven shock wave propagated through the buried Al layer is shown in Fig. 118.8(b). The drive intensity was 4×10^{14} W/cm^2. Prominent F-like and O-like Al 1s–2p features are observed.[15] Higher charge states of Al are ionized in succession and absorbed in 1s–2p transitions as the electron temperature increases. A time history of the inferred temperature in the buried Al layer is presented in Fig. 118.8(c) and compared with different models of electron thermal conduction.[15] The nonlocal model and the flux-limited model with $f = 0.06$ show good agreement with the experimental results for this drive condition.[15] Dense, Fermi-degenerate Al created using multiple shock waves was diagnosed with Al 1s–2p absorption spectroscopy to be compressed to 4× solid density (11±5 g/cm^3) and heated to 20±2 eV (Refs. 15 and 16).

4. Multispectral Monochromatic X-Ray Imaging

Azechi *et al.* obtained the first multiple monochromatic images of implosion cores by placing a pinhole array in front of a flat Bragg crystal.[17] Thin glass shells (1 μm thick and 60 μm in diameter) filled with 3.5 atm of Ne, as shown in Fig. 118.9(a), were imploded on the two-beam, 1ω, 45-J, 120-ps GEKKO II Laser System[5] and backlit with x rays to diagnose the temperature and areal density of the implosion core.[17] The experimental setup for the backlighting using multifrequency x rays (i.e., multiple monochromatic x-ray images) is shown in Fig. 118.9(b). The concept of combining a pinhole aperture with a Bragg crystal spectrometer to achieve multiple monochromatic x-ray images was extended to hundreds of pinholes nearly two decades later on OMEGA.[18] As shown in Fig. 118.10(a), a plastic shell target (28 μm thick and 920 μm in diameter) with an inner Ti-doped plastic layer and a 10-atm-deuterium-gas fill was driven with a 30-kJ, 1-ns square laser pulse. The time-integrated multiple monochromatic images recorded during the implosion are presented in Fig. 118.10(b), with the prominent Ti K-shell emission and Ti K_α emission identified.

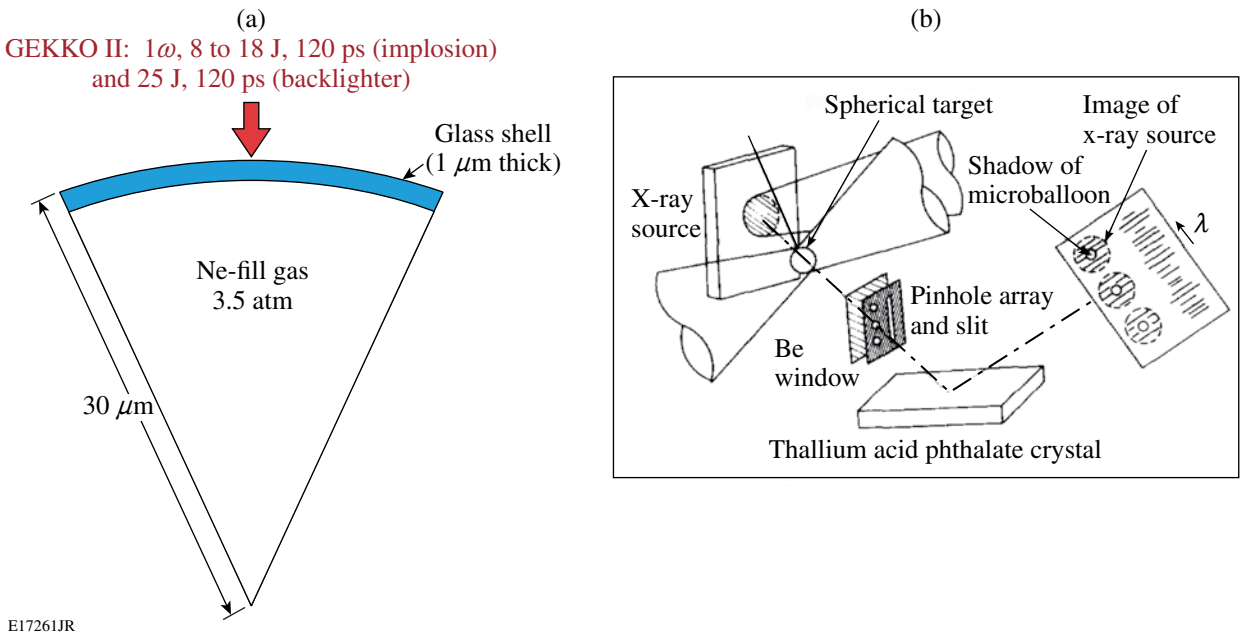

Figure 118.9
(a) Schematic of a direct-drive glass-shell-implosion target filled with Ne gas and used in multifrequency x-ray backlighting experiments on the GEKKO II Laser System. (b) Schematic of the experimental setup for multifrequency x-ray backlighting.

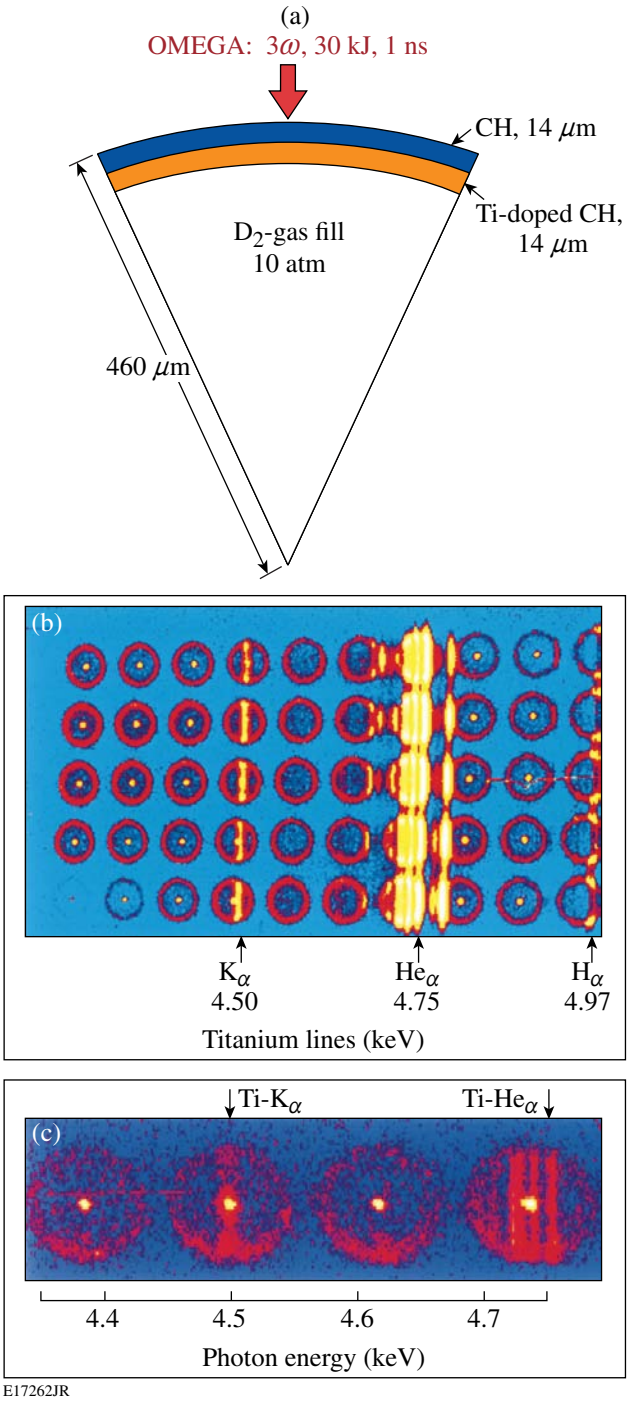

Figure 118.10
(a) Schematic of a direct-drive plastic-shell-implosion target used to demonstrate the pinhole-array x-ray spectrometer. The inner layer of the plastic shell is doped with trace amounts of Ti and the target is filled with deuterium gas. (b) A multiple monochromatic image recorded with a pinhole-array x-ray spectrometer with the prominent Ti K-shell emission identified. (c) Image highlighting the cold Ti-doped portion of the shell pumped by an x-ray continuum from the core emits Ti K_α emission.

The outermost ring of emission is from the coronal plasma and the bright central spot is emission from the hot spot. The cold Ti-doped portion of the shell pumped by an x-ray continuum from the core emits Ti K_α emission, as shown in Fig. 118.10(c). The vertical profile of the Ti K_α emission shows the true dimension of the cold shell at peak compression.[18]

Current state-of-the-art multiple monochromatic imaging involved synchronized, time-resolved images from multiple lines of sight for direct-drive implosions on OMEGA of Ar-doped-deuterium–filled plastic-shell targets recorded by Roberto Mancini's research group.[20] Multiple monochromatic images from three quasi-orthogonal lines of sight of the Ly_β emission profiles of a direct-drive implosion are shown in Fig. 118.11(a). Koch *et al*. designed a multiple monochromatic imager for Ar K-shell emission from indirect-drive-implosion cores.[59] Welser-Sherrill *et al*. used the images of the Ar K-shell emission lines to diagnose electron density and temperature spatial profiles in the cores of indirect-drive implosions.[19] Tommasini redesigned a multiple monochromatic imager for Ar K-shell emission for direct-drive-implosion cores,[60] which have better diagnostic access, simpler targets, and higher electron temperatures in the implosion core than indirect-drive implosions on OMEGA. The multiple monochromatic imaging using multiple lines of sight [see Fig. 118.11(a)] for the He_β and Ly_β emission profiles were used to infer the electron-temperature profile of the direct-drive-implosion core shown in Fig. 118.11(b).[61]

Conclusions

X-ray spectroscopy has been used to chart the remarkable progress of laser-fusion experiments over the last three decades. Hans Griem provided the foundation for this research. He studied the effect of plasma particles, in particular the fast-moving free electrons, on the Stark-broadening of spectral line shapes in plasmas. Four areas of x-ray spectroscopy for laser-fusion experiments were highlighted: K_α emission spectroscopy to diagnose target preheat by suprathermal electrons, Stark-broadened K-shell emissions of mid-Z elements to diagnose compressed densities and temperatures of implosion cores, K- and L-shell absorption spectroscopy to diagnose the relatively cold imploding shell that does not emit x rays, and multispectral monochromatic imaging of implosions to diagnose core temperature and density profiles. The seminal research leading to the original x-ray-spectroscopy experiments in these areas was discussed and compared to current state-of-the-art measurements.

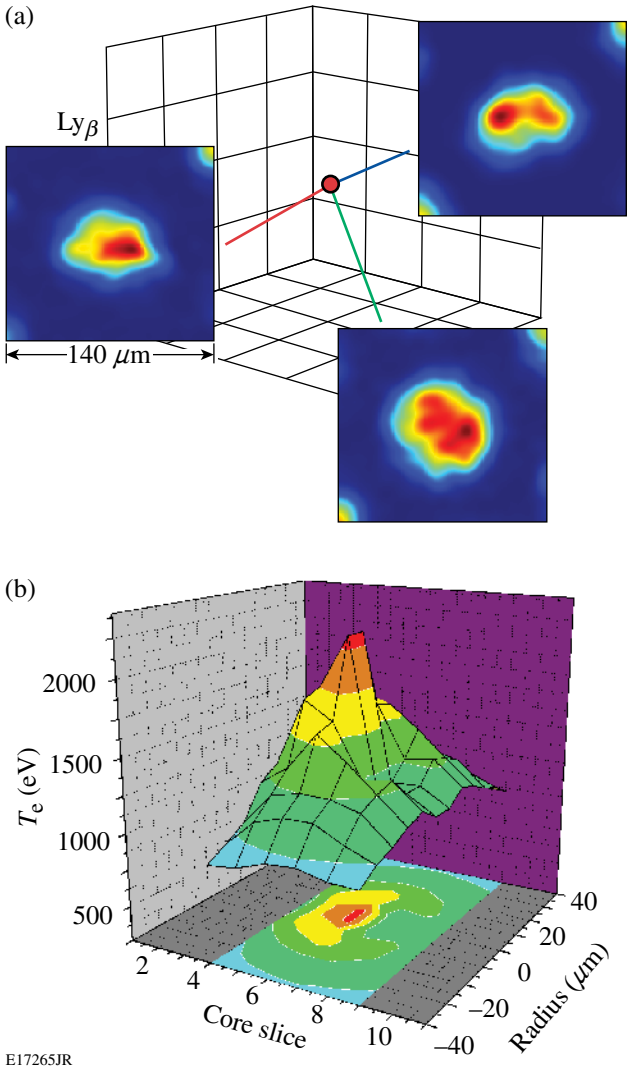

Figure 118.11
(a) Schematic of an experimental setup for time-resolved multiple monochromatic imaging of a direct-drive implosion in Ar Ly_β emission performed along three quasi-orthogonal views. (b) Temperature profile inferred from analyzing time-resolved multiple monochromatic imaging of a direct-drive implosion in Ar Ly_β and He_β emissions performed along three quasi-orthogonal views.

ACKNOWLEDGMENT

This work was supported by the U.S. Department of Energy Office of Inertial Confinement Fusion under Cooperative Agreement No. DE-FC52-08NA28302, the University of Rochester, and the New York State Energy Research and Development Authority. The support of DOE does not constitute an endorsement by DOE of the views expressed in this article.

REFERENCES

1. H. R. Griem, *Principles of Plasma Spectroscopy* (Cambridge University Press, Cambridge, England, 1997).
2. R. L. McCrory, D. D. Meyerhofer, R. Betti, R. S. Craxton, J. A. Delettrez, D. H. Edgell, V. Yu Glebov, V. N. Goncharov, D. R. Harding, D. W. Jacobs-Perkins, J. P. Knauer, F. J. Marshall, P. W. McKenty, P. B. Radha, S. P. Regan, T. C. Sangster, W. Seka, R. W. Short, S. Skupsky, V. A. Smalyuk, J. M. Soures, C. Stoeckl, B. Yaakobi, D. Shvarts, J. A. Frenje, C. K. Li, R. D. Petrasso, and F. H. Séguin, Phys. Plasmas **15**, 055503 (2008); P. W. McKenty, V. N. Goncharov, R. P. J. Town, S. Skupsky, R. Betti, and R. L. McCrory, Phys. Plasmas **8**, 2315 (2001).
3. J. D. Lindl, *Inertial Confinement Fusion: The Quest for Ignition and Energy Gain Using Indirect Drive* (Springer-Verlag, New York, 1998); J. D. Lindl *et al.*, Phys. Plasmas **11**, 339 (2004).
4. E. Snitzer, Phys. Rev. Lett. **7**, 444 (1961).
5. G. Verlarde and N. Carpintero–Santamaría, *Inertial Confinement Nuclear Fusion: A Historical Approach by Its Pioneers* [Foxwell & Davies (UK) Ltd., London, 2007].
6. B. Yaakobi, I. Pelah, and J. Hoose, Phys. Rev. Lett. **37**, 836 (1976).
7. J. D. Hares *et al.*, Phys. Rev. Lett. **42**, 1216 (1979).
8. B. Yaakobi, C. Stoeckl, T. Boehly, D. D. Meyerhofer, and W. Seka, Phys. Plasmas **7**, 3714 (2000).
9. B. Yaakobi, C. Stoeckl, W. Seka, J. A. Delettrez, T. C. Sangster, and D. D. Meyerhofer, Phys. Plasmas **12**, 062703 (2005); V. A. Smalyuk, D. Shvarts, R. Betti, J. A. Delettrez, D. H. Edgell, V. Yu. Glebov, V. N. Goncharov, R. L. McCrory, D. D. Meyerhofer, P. B. Radha, S. P. Regan, T. C. Sangster, W. Seka, S. Skupsky, C. Stoeckl, B. Yaakobi, J. A. Frenje, C. K. Li, R. D. Petrasso, and F. H. Séguin, Phys. Rev. Lett. **100**, 185005 (2008).
10. K. Yasuike *et al.*, Rev. Sci. Instrum. **72**, 1236 (2001).
11. B. Yaakobi, D. Steel, E. Thorsos, A. Hauer, and B. Perry, Phys. Rev. Lett. **39**, 1526 (1977).
12. B. Yaakobi, S. Skupsky, R. L. McCrory, C. F. Hooper, H. Deckman, P. Bourke, and J. M. Soures, Phys. Rev. Lett. **44**, 1072 (1980).
13. S. P. Regan, J. A. Delettrez, R. Epstein, P. A. Jaanimagi, B. Yaakobi, V. A. Smalyuk, F. J. Marshall, D. D. Meyerhofer, W. Seka, D. A. Haynes Jr., I. E. Golovkin, and C. F. Hooper Jr., Phys. Plasmas **9**, 1357 (2002).
14. B. Yaakobi, R. L. McCrory, S. Skupsky, J. A. Delettrez, P. Bourke, H. Deckman, C. F. Hooper, and J. M. Soures, Opt. Commun. **34**, 213 (1980).
15. H. Sawada, S. P. Regan, P. B. Radha, R. Epstein, D. Li, V. N. Goncharov, S. X. Hu, D. D. Meyerhofer, J. A. Delettrez, P. A. Jaanimagi, V. A. Smalyuk, T. R. Boehly, T. C. Sangster, B. Yaakobi, and R. C. Mancini, Phys. Plasmas **16**, 052702 (2009).

16. S. P. Regan, H. Sawada, V. N. Goncharov, D. Li, P. B. Radha, R. Epstein, J. A. Delettrez, S. X. Hu, V. A. Smalyuk, B. Yaakobi, T. C. Sangster, D. D. Meyerhofer, R. L. McCrory, and R. C. Mancini, "Spectroscopic Observations of Fermi-Degenerate Aluminum Compressed and Heated to Four Times Solid Density and 20 eV," submitted to Physical Review E.

17. H. Azechi *et al*., Appl. Phys. Lett. **37**, 998 (1980).

18. B. Yaakobi, F. J. Marshall, and D. K. Bradley, Appl. Opt. **37**, 8074 (1998).

19. L. Welser-Sherrill, R. C. Mancini, J. A. Koch, N. Izumi, R. Tommasini, S. W. Haan, D. A. Haynes, I. E. Golovkin, J. J. MacFarlane, J. A. Delettrez, F. J. Marshall, S. P. Regan, V. A. Smalyuk, and G. Kyrala, Phys. Rev. E **76**, 056403 (2007).

20. L. A. Welser, R. C. Mancini, J. A. Koch, N. Izumi, H. Dalhed, H. Scott, T. W. Barbee Jr., R. W. Lee, I. E. Golovkin, F. Marshall, J. Delettrez, and L. Klein, J. Quant. Spectrosc. Radiat. Transf. **81**, 487 (2003).

21. J. Soures, L. M. Goldman, and M. Lubin, Nucl. Fusion **13**, 829 (1973).

22. T. R. Boehly, D. L. Brown, R. S. Craxton, R. L. Keck, J. P. Knauer, J. H. Kelly, T. J. Kessler, S. A. Kumpan, S. J. Loucks, S. A. Letzring, F. J. Marshall, R. L. McCrory, S. F. B. Morse, W. Seka, J. M. Soures, and C. P. Verdon, Opt. Commun. **133**, 495 (1997).

23. L. J. Waxer, D. N. Maywar, J. H. Kelly, T. J. Kessler, B. E. Kruschwitz, S. J. Loucks, R. L. McCrory, D. D. Meyerhofer, S. F. B. Morse, C. Stoeckl, and J. D. Zuegel, Opt. Photonics News **16**, 30 (2005); C. Stoeckl, J. A. Delettrez, J. H. Kelly, T. J. Kessler, B. E. Kruschwitz, S. J. Loucks, R. L. McCrory, D. D. Meyerhofer, D. N. Maywar, S. F. B. Morse, J. Myatt, A. L. Rigatti, L. J. Waxer, J. D. Zuegel, and R. B. Stephens, Fusion Sci. Technol. **49**, 367 (2006).

24. S. P. Regan, J. A. Marozas, R. S. Craxton, J. H. Kelly, W. R. Donaldson, P. A. Jaanimagi, D. Jacobs-Perkins, R. L. Keck, T. J. Kessler, D. D. Meyerhofer, T. C. Sangster, W. Seka, V. A. Smalyuk, S. Skupsky, and J. D. Zuegel, J. Opt. Soc. Am. B **22**, 998 (2005).

25. T. J. Kessler, Y. Lin, J. J. Armstrong, and B. Velazquez, in *Laser Coherence Control: Technology and Applications*, edited by H. T. Powell and T. J. Kessler (SPIE, Bellingham, WA, 1993), Vol. 1870, pp. 95–104; Y. Lin, T. J. Kessler, and G. N. Lawrence, Opt. Lett. **21**, 1703 (1996).

26. S. Skupsky, R. W. Short, T. Kessler, R. S. Craxton, S. Letzring, and J. M. Soures, J. Appl. Phys. **66**, 3456 (1989); S. Skupsky and R. S. Craxton, Phys. Plasmas **6**, 2157 (1999).

27. Y. Kato, unpublished notes from work at LLE, 1984; K. Tsubakimoto *et al*., Opt. Commun. **103**, 185 (1993); *LLE Review Quarterly Report* **71**, 145, Laboratory for Laser Energetics, University of Rochester, Rochester, NY, LLE Document No. DOE/SF/19460-186, NTIS Order No. DE98000308 (1997); T. E. Gunderman, J.-C. Lee, T. J. Kessler, S. D. Jacobs, D. J. Smith, and S. Skupsky, in *Conference on Lasers and Electro-Optics*, Vol. 7, 1990 OSA Technical Digest Series (Optical Society of America, Washington, DC, 1990), p. 354; T. R. Boehly, V. A. Smalyuk, D. D. Meyerhofer, J. P. Knauer, D. K. Bradley, R. S. Craxton, M. J. Guardalben, S. Skupsky, and T. J. Kessler, J. Appl. Phys. **85**, 3444 (1999).

28. R. L McCrory and R. L. Morse, Phys. Rev. Lett. **38**, 544 (1977); R. S. Craxton, Opt. Commun. **34**, 474 (1980); R. S. Craxton, S. D. Jacobs, J. E. Rizzo, and R. Boni, IEEE J. Quantum Electron. **QE-17**, 1782 (1981); W. Seka, S. D. Jacobs, J. E. Rizzo, R. Boni, and R. S. Craxton, Opt. Commun. **34**, 469 (1980).

29. B. L. Henke and P. A. Jaanimagi, Rev. Sci. Instrum. **56**, 1537 (1985).

30. R. J. Tighe and C. F. Hooper Jr., Phys. Rev. A **14**, 1514 (1976).

31. R. F. Joyce, L. A. Woltz, and C. F. Hooper Jr., Phys. Rev. A **35**, 2228 (1987).

32. R. C. Mancini *et al*., Comput. Phys. Commun. **63**, 314 (1991).

33. C. A. Iglesias, J. L. Lebowitz, and D. MacGowan, Phys. Rev. A **28**, 1667 (1983).

34. D. A. Haynes Jr., D. T. Garber, C. F. Hooper Jr., R. C. Mancini, Y. T. Lee, D. K. Bradley, J. Delettrez, R. Epstein, and P. A. Jaanimagi, Phys. Rev. E **53**, 1042 (1996).

35. J. J. MacFarlane *et al*., High Energy Density Phys. **3**, 181 (2006).

36. G. E. Moore, Electronics **38**, 114 (1965).

37. J. A. Paisner, E. M. Campbell, and W. J. Hogan, Fusion Technol. **26**, 755 (1994); G. H. Miller, E. I. Moses, and C. R. Wuest, Opt. Eng. **43**, 2841 (2004).

38. D. W. Phillion *et al*., Phys. Rev. Lett. **49**, 1405 (1982); D. M. Villeneuve, R. L. Keck, B. B. Afeyan, W. Seka, and E. A. Williams, Phys. Fluids **27**, 721 (1984); C. Rousseaux *et al*., Phys. Fluids B **4**, 2589 (1992); W. Seka, R. E. Bahr, R. W. Short, A. Simon, R. S. Craxton, D. S. Montgomery, and A. E. Rubenchik, Phys. Fluids B **4**, 2232 (1992); C. S. Liu and M. N. Rosenbluth, Phys. Fluids **19**, 967 (1976); A. Simon, R. W. Short, E. A. Williams, and T. Dewandre, Phys. Fluids **26**, 3107 (1983); A. B. Langdon, B. F. Lasinski, and W. L. Kruer, Phys. Rev. Lett. **43**, 133 (1979); B. F. Lasinski and A. B. Langdon, Lawrence Livermore National Laboratory, Livermore, CA, Report UCRL-50021-77, 4-49 (1978); B. B. Afeyan and E. A. Williams, Phys. Plasmas **4**, 3827 (1997); C. Stoeckl, R. E. Bahr, B. Yaakobi, W. Seka, S. P. Regan, R. S. Craxton, J. A. Delettrez, R. W. Short, J. Myatt, A. V. Maximov, and H. Baldis, Phys. Rev. Lett. **90**, 235002 (2003).

39. W. L. Kruer, *The Physics of Laser–Plasma Interactions*, Frontiers in Physics, Vol. 73, edited by D. Pines (Addison-Wesley, Redwood City, CA, 1988), Chap. 4, pp. 37–43.

40. S. P. Regan, J. A. Delettrez, F. J. Marshall, J. M. Soures, V. A. Smalyuk, B. Yaakobi, V. Yu. Glebov, P. A. Jaanimagi, D. D. Meyerhofer, P. B. Radha, W. Seka, S. Skupsky, C. Stoeckl, R. P. J. Town, D. A. Haynes Jr., I. E. Golovkin, C. F. Hooper Jr., J. A. Frenje, C. K. Li, R. D. Petrasso, and F. H. Séguin, Phys. Rev. Lett. **89**, 085003 (2002).

41. C. K. Li, F. H. Séguin, D. G. Hicks, J. A. Frenje, K. M. Green, S. Kurebayashi, R. D. Petrasso, D. D. Meyerhofer, J. M. Soures, V. Yu. Glebov, R. L. Keck, P. B. Radha, S. Roberts, W. Seka, S. Skupsky, C. Stoeckl, and T. C. Sangster, Phys. Plasmas **8**, 4902 (2001).

42. C. D. Zhou and R. Betti, Phys. Plasmas **15**, 102707 (2008).

43. M. C. Herrmann, M. Tabak, and J. D. Lindl, Nucl. Fusion **41**, 99 (2001).

44. R. Betti, K. Anderson, V. N. Goncharov, R. L. McCrory, D. D. Meyerhofer, S. Skupsky, and R. P. J. Town, Phys. Plasmas **9**, 2277 (2002).

45. M. Tabak and D. Callahan-Miller, Phys. Plasmas **5**, 1895 (1998); S. Atzeni, Phys. Plasmas **6**, 3316 (1999); M. H. Key, Phys. Plasmas **14**, 055502 (2007).

46. M. D. Rosen and J. H. Nuckolls, Phys. Fluids **22**, 1393 (1979).

47. C. Stoeckl, V. Yu. Glebov, D. D. Meyerhofer, W. Seka, B. Yaakobi, R. P. J. Town, and J. D. Zuegel, Rev. Sci. Instrum. **72**, 1197 (2001).

48. J. M. Soures, T. C. Bristow, H. Deckman, J. Delettrez, A. Entenberg, W. Friedman, J. Forsyth, Y. Gazit, G. Halpern, F. Kalk, S. Letzring, R. McCrory, D. Peiffer, J. Rizzo, W. Seka, S. Skupsky, E. Thorsos, B. Yaakobi, and T. Yamanaka, in *Laser Interaction and Related Plasma Phenomena*, edited by H. J. Schwarz, H. Hora, M. J. Lubin, and B. Yaakobi (Plenum Press, New York, 1981), Vol. 5, pp. 463–481.

49. J. D. Kilkenny *et al*., Phys. Rev. A **22**, 2746 (1980).

50. C. F. Hooper Jr., D. P. Kilcrease, R. C. Mancini, L. A. Woltz, D. K. Bradley, P. A. Jaanimagi, and M. C. Richardson, Phys. Rev. Lett. **63**, 267 (1989).

51. B. A. Hammel *et al*., Phys. Rev. Lett. **70**, 1263 (1993).

52. H. Nishimura *et al*., Phys. Plasmas **2**, 2063 (1995).

53. C. J. Keane *et al*., Phys. Rev. Lett. **72**, 3029 (1994).

54. N. C. Woolsey *et al*., Phys. Rev. E **56**, 2314 (1997).

55. T. S. Perry *et al*., Phys. Rev. Lett. **67**, 3784 (1991).

56. D. Hoarty *et al*., Phys. Rev. Lett. **78**, 3322 (1997).

57. T. R. Boehly, J. A. Delettrez, J. P. Knauer, D. D. Meyerhofer, B. Yaakobi, R. P. J. Town, and D. Hoarty, Phys. Rev. Lett. **87**, 145003 (2001).

58. A. Ng, Lawrence Livermore National Laboratory, private communication (2006).

59. J. A. Koch, T. W. Barbee Jr., N. Izumi, R. Tommasini, R. C. Mancini, L. A. Welser, and F. J. Marshall, Rev. Sci. Instrum. **76**, 073708 (2005).

60. R. Tommasini, J. A. Koch, N. Izumi, L. A. Welser, R. C. Mancini, J. Delettrez, S. Regan, and V. Smalyuk, Rev. Sci. Instrum. **77**, 10E303 (2006).

61. T. Nagayama, R. C. Mancini, R. Florido, R. Tommasini, J. A. Koch, J. A. Delettrez, S. P. Regan, V. A. Smalyuk, L. A. Welser-Sherrill, and I. E. Golovkin, Rev. Sci. Instrum. **79**, 10E921 (2008).

Relativistic Electron-Beam Transport Studies Using High-Resolution, Coherent Transition Radiation Imaging

Laser-generated relativistic electron beams have applications in compact, high-brightness laser–plasma particle accelerators,[1] narrowband x-ray sources for medical applications,[2] x-ray sources for ignition-scale, high-density inertial confinement fusion (ICF) target backlighter radiography,[3] collimated electron beams for free-electron lasers,[4] and collimated electron beams for the fast-ignition approach to ICF.[5] The fast electrons are generated by focusing short-pulse, high-intensity, $I \sim 10^{19}$ W/cm^2 laser light onto the front surface of planar-foil targets.[6] An understanding of the fast-electron generation and subsequent transport is essential for these applications.

The properties of fast electrons generated in short-pulse, high-intensity laser–solid interactions are studied using spatially resolved coherent transition radiation (CTR) emitted from the rear surface of planar targets.[7] Experiments employing CTR imaging with the highest spatial resolution reported, ~1.4 μm, are described.[8] The images contain bright, small-scale structures suggestive of electron-beam filamentation.[9] The small-scale features are embedded in larger annular-like structures. Analysis of the images suggests a fast-electron temperature of ~1.4 MeV and a half-angle divergence of ~16°. Three-dimensional (3-D) simulations of the fast-electron transport in planar, solid-density targets, using the hybrid-particle-in-cell (PIC) code *LSP*,[10] reproduce the details of the CTR images for an initial half-angle divergence of ~56°. The initial divergence is reduced in the target by a self-generated resistive magnetic field.[11]

CTR is emitted when an electron beam, with longitudinal electron-density modulations, crosses a refractive-index boundary, such as the rear surface of a target.[12] The density modulations drive a radiating, time-dependent polarization with strong frequency components at the modulation periodicity. The radiated energy is proportional to the square of the modulation amplitude and is strongly peaked in narrow spectral bands centered on the modulation frequencies.[7] Electron acceleration mechanisms that are active in high-intensity laser–solid interactions generate fast-electron beams with the required modulations. Acceleration by the laser electric field[6] drives electrons into the target once per optical cycle, whereas acceleration by the $v \times B$ component of the Lorentz force[6] drives electrons into the target twice per optical cycle. These electrons propagate through the target as a train of bunches separated in space by λ and $\lambda/2$, respectively, where λ is the laser wavelength. The density modulations are smeared out by refluxing,[13] so the CTR signal is produced by the electron's first pass through the target.

The experiments were conducted at LLE's Multi-Terawatt (MTW) Laser Facility.[14] A single laser pulse of wavelength $\lambda_L = 1053$ nm, with an energy of $E_L \sim 5$ J and a duration of $\Delta t_L \sim 500$ fs, was focused at normal incidence to a 4-μm-radius spot, producing an intensity of $I \sim 10^{19}$ W/cm^2. The laser pulse's intensity contrast ratio was ~10^3 at 1 ps before the peak of the pulse and ~10^8 at 50 ps before the peak. The Al, Cu, Sn, and Au foil targets had transverse dimensions of 500 μm and thicknesses ranging from 5 to 100 μm. A CTR diagnostic was fielded to acquire images of the rear-side optical emission with a spatial resolution of $\Delta \sim 1.4$ μm (Ref. 8). The images were captured on a scientific-grade charge-coupled-device (CCD) camera with a dynamic range of 10^4.

Figure 118.12 shows three characteristic images of the rear-surface emission plotted in arbitrary units of intensity on both a linear (top row) and logarithmic scale (bottom row). From left to right the targets are 20-μm-thick Al, 30-μm-thick Al, and 50-μm-thick Cu. The emission contains small-scale structures, with a mean diameter of ~4.0 μm, superimposed on a larger annular feature whose diameter increases with target thickness. The images are produced by light emitted at the target's rear surface with a wavelength $\lambda \sim 527$ nm, corresponding to the second harmonic of the incident laser. Imaging of the rear surface in an adjacent spectral window, centered on $\lambda =$ 480 nm, produced no measurable signal. The signal strength at $\lambda \sim 527$ nm implies that the emission is produced by a coherently driven mechanism—the most likely candidate being CTR from a density-modulated, relativistic electron beam, accelerated by the $v \times B$ component of the Lorentz force. The spatial distribution of the CTR emission suggests the electron-beam filaments.[9] The larger annular patterns suggest electron-beam hollowing and annular propagation.[15]

Figure 118.13(a) shows the spatially integrated CTR energy from 60 laser shots using Al, Cu, Sn, and Au foils of various thicknesses. Each point represents the mean CTR energy for the number of shots (two to five) taken at that thickness; the error bars are standard deviations and arise from shot-to-shot fluctuations. The integrated CTR energy decreases as the target thickness increases: for Al the decrease is about three orders of magnitude from 6 to 60 μm; for Au the decrease is about four orders of

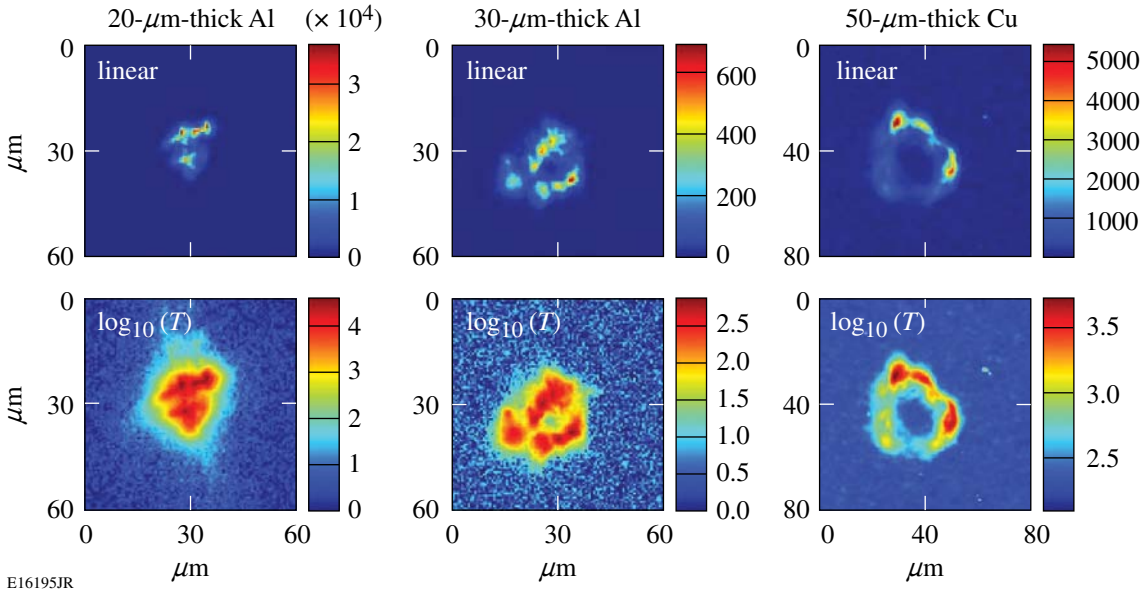

Figure 118.12
Images of the rear-surface optical emission, in arbitrary units of intensity, from thin foil targets illuminated at normal incidence with an intensity of $I \sim 10^{19}$ W/cm^2. The top row shows the emission on a linear scale while the bottom row uses a logarithmic scale. From right to left, the targets are 20-μm-thick Al, 30-μm-thick Al, and 50-μm-thick Cu. The images indicate the presence of bright small-scale structures that are embedded into a larger ringlike structure whose diameter increases with target thickness.

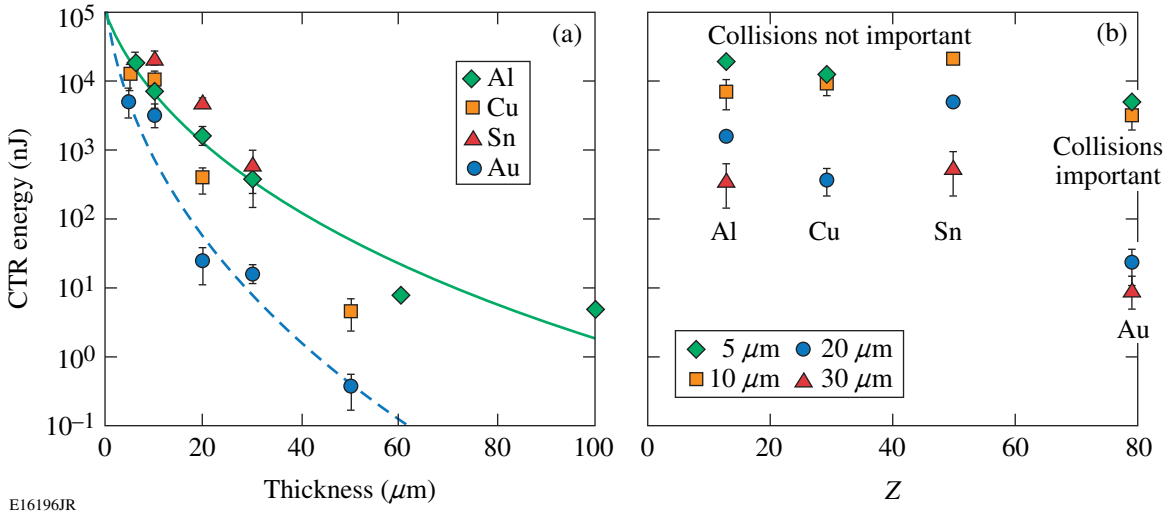

Figure 118.13
(a) The CTR signal decreases with increasing target thickness. The solid line is fitted to the Al data using the velocity dispersion model and is consistent with a fast-electron temperature of $T_{hot} \sim 1.4$ MeV. The dashed line is fitted to the Au data and is consistent with $T_{hot} \sim 0.9$ MeV. (b) The CTR energy's dependence on Z is weak for low- to mid-Z materials but significant for high-Z materials.

magnitude from 5 to 50 μm. The CTR energy's dependence on Z, at four different thicknesses, is shown in Fig. 118.13(b). Except for the highest-Z materials such as Au ($Z = 79$), the CTR energy does not depend on Z. For all thicknesses, the CTR signal is approximately constant from Al ($Z = 13$) to Sn ($Z = 50$). For the 5-μm targets, the CTR signal decreases by a factor of ~5 from Sn to Au, while for the 30-μm foils, the decrease from Sn to Au is approximately two orders of magnitude.

The CTR energy becomes dependent on target thickness because of fast-electron velocity dispersion. The velocity dispersion reduces the correlation between propagating bunches of electrons. This effect on the CTR signal has been quantified by Zheng *et al.*[12] The velocity dispersion model is used to estimate the fast-electron temperature T_{hot} from the variation of the CTR energy with target thickness. The solid line in Fig. 118.13(a) is fitted to the Al data; the variation in the CTR signal with increasing thickness is consistent with $T_{hot} = 1.4 \pm 0.1$ MeV. The dashed line shows that the corresponding fit to the Au data is consistent with $T_{hot} = 0.9 \pm 0.1$ MeV. The difference is attributed to collisional processes that also reduce the correlation between propagating electrons. The effect of fast-electron scattering from target atoms on the CTR signal has been estimated using the Monte Carlo code Geant4 (Ref. 16). A bunch of 1-MeV electrons were propagated along an electron-beam filament through 50 μm of Al or Au. The relative number of electrons remaining in the filament, as a function of distance, was used to estimate the variation in the CTR signal. The decrease in the CTR signal caused by scattering was found to be insignificant in Al. In Au, scattering's effect on the CTR signal became important after ~20 μm. This is seen in Fig. 118.13(b), where the measured CTR energy falls abruptly in Au targets for thicknesses ≥20 μm. Since it is not complicated by collisional effects, the result obtained from Al is taken to be the correct value for T_{hot}.

Figure 118.14 shows how the size of the rear-surface emission region grows with target thickness in the range from 5 to 100 μm; the values were determined by measuring the horizontal and vertical dimensions of the emission pattern. No dependence on the target material was observed, and each point represents the radial size averaged over all materials at each thickness. The half-angle electron-beam divergence was inferred to be $\theta_{1/2} \sim 16°$ using a least-squares linear fit. The linear fit intercepts the radial axis at ~4 μm, consistent with the laser focal spot being the source of the electron beam.

Due to the large range of spatial and temporal scales involved, the acceleration of electrons in high-intensity laser–solid interactions and their subsequent transport cannot be modeled simultaneously. The acceleration of electrons is modeled for short durations and small spatial scales using PIC codes with high temporal and spatial resolution.[17] Hybrid-PIC codes model the collisional transport of electrons over experimentally realistic spatial and temporal scales with restricted spatial and temporal resolution.[10] The details of the acceleration depend on the target's front-surface pre-plasma.[6,17] Behind the critical surface, the fast-electron beam is subject to the Weibel instability saturated by collisions as the electrons enter denser plasma.[17,18] State-of-the-art, 2-D PIC simulations resolve plasma densities up to 100× critical, while the electron density in the front of the target can be 10× higher.[17,18] Such simulations provide a large uncertainty in the initial angular divergence of electrons entering the target.

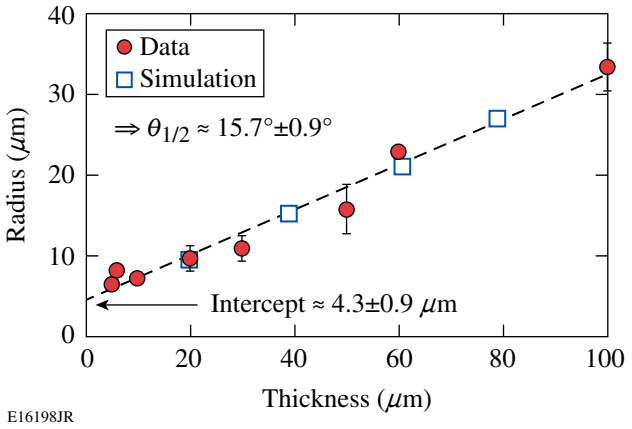

Figure 118.14
The transverse size of the rear-surface emission grows with target thickness. The dashed line shows a least squares fit to the experimental points and indicates a half-angle divergence of $\theta_{1/2} \sim 15.7° \pm 0.9°$. Numerical simulations of the electron transport reproduce the observed expansion.

The hybrid-PIC code *LSP*[10] modeled the 3-D transport of fast electrons in solid-density targets. In the target, fast electrons are collimated by a self-generated resistive magnetic field[19] and their angular divergence is reduced. The initial half-angle divergence was adjusted until the half-angle divergence in the target matched that observed in the experiments. This approach is different than that reported in Ref. 20, where the fast-electron acceleration was simulated but the electron transport in the target was not. The collimating effect of the resistive magnetic field in the target cannot be neglected. This approach predicts the initial fast-electron angular divergence, a quantity otherwise unavailable in absence of detailed 3-D PIC simulations. The *LSP* simulations predict a transverse fast-electron-density distribution that closely resembles the transverse distribution of CTR seen in the experiments.

In the simulations presented here, the fast electrons are injected (promoted from the background) with an exponential distribution, $\sim \exp\left(-E/\langle E_h \rangle\right)$, with a mean energy $\langle E_h \rangle$ given by the maximum of the ponderomotive[6] and Beg[21] scaling. The laser pulse was Gaussian in space and time with a duration of $\tau = 650$ fs, full width at half maximum (FWHM), a focal-spot size of 5.5 μm (FWHM), and a maximum intensity of $I = 1.45 \times 10^{19}$ W/cm^2, consistent with the parameters of the MTW laser. The laser-to-fast-electron energy conversion efficiency was 20% and independent of the laser intensity.[22] The initial electron-beam half-angle divergence is given by $\theta_{1/2} = \alpha \tan^{-1}\left[\sqrt{2/(\gamma-1)}\right]$, where $\gamma = \left(1 - v^2/c^2\right)^{-1/2}$, v is the fast-electron velocity, and c is the speed of light. Electrons with energy $E = (\gamma - 1)mc^2$, where m is the electron mass, are randomly injected in a cone of half-angle $\theta_{1/2}$, which for $\alpha = 1$ describes the angle at which electrons are ejected from a focused laser by the ponderomotive force.[23] Simulations were performed for 6×-, 8×-, and 10×-ionized Al targets with transverse dimensions of 120 μm and thicknesses of 20, 40, 60, and 80 μm. The plasma's Spitzer resistivity was saturated at low temperature according to $\eta = 1/\sqrt{\eta_{max}^{-2} + \eta_{sp}^{-2}}$, where $\eta_{max} = 1.6 \times 10^{-6}$ Ωm (Ref. 24) and $\eta_{sp} \propto Z/T^{3/2}$, where Z is the atomic number and T is the background temperature.[25] A broad vacuum region surrounded the target and the simulations used conducting boundaries. The spatial resolution was 1 μm in the longitudinal (z) and transversal (x and y) directions for $|x|, |y| < 30$ μm, with the transverse resolution gradually increased to 3 μm for $|x|, |y| > 30$ μm.

Simulations performed for $\alpha = 1$ in 8× ionized Al showed the half-angle divergence in the target to be $\theta_{1/2} \sim 16°$, as observed in the experiments. This result could be reproduced in the 6×- and 10×-ionized Al by varying α by 7%. Figure 118.15 shows the density distribution of fast electrons, with energy >250 keV, at the back of the target for $\alpha = 1$ and different target thicknesses. The density distributions are averaged in time using $\int n(\mathbf{r},t)dt/1.65\,\tau$, where $\mathbf{r}$ is the radial coordinate of the density. Although the distribution of CTR is not calculated, the spatial distribution of the fast-electron density at the rear surface, predicted by *LSP*, reproduces the details of the CTR emission pattern. The spot size in the simulations is also plotted as a function of the target thickness in Fig. 118.14.

The reduction in the half-angle divergence of the beam is caused by a collimating, azimuthal, self-generated resistive magnetic field. The field is generated at the transverse edge of the electron beam and is most intense in the first 20 μm, close to the front surface. Figure 118.16(a) shows cross sections through the azimuthal magnetic field for the 60-μm target, 350 fs after the peak of the laser pulse. The magnetic field partially collimates the beam. A beam with initial half-angle divergence of $\theta_{1/2} = 56°$ (mean angle = 37°), averaged inside the FWHM of the beam's spatial and temporal distribution, is reduced to a beam with an angular distribution peaked at 16°. The variation of the electron-density distribution with target thickness resembles an expanding annulus that breaks, along its circumference, into filaments generated by the resistive filamentation instability. Figure 118.16(b) shows the location of the fast-electron-density isosurface (solid surface) at 50% of the peak density in the 60-μm target, 350 fs after the peak of the laser pulse; the semitransparent surface corresponds to

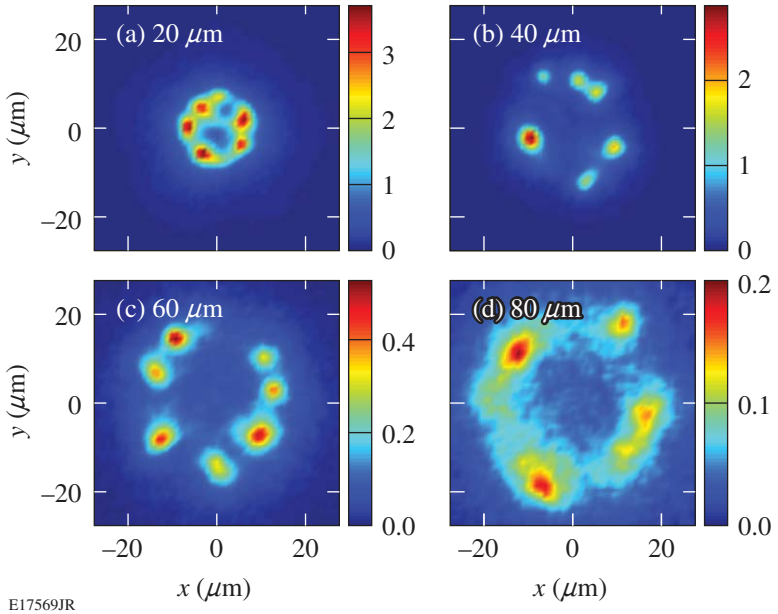

Figure 118.15
Predictions of the rear-surface, transverse density distribution of fast electrons for different thicknesses of Al (in units of 10^{20} cm^{-3}). The distributions closely resemble the measured rear-surface CTR distributions. The thickness for each target is specified on the figure.

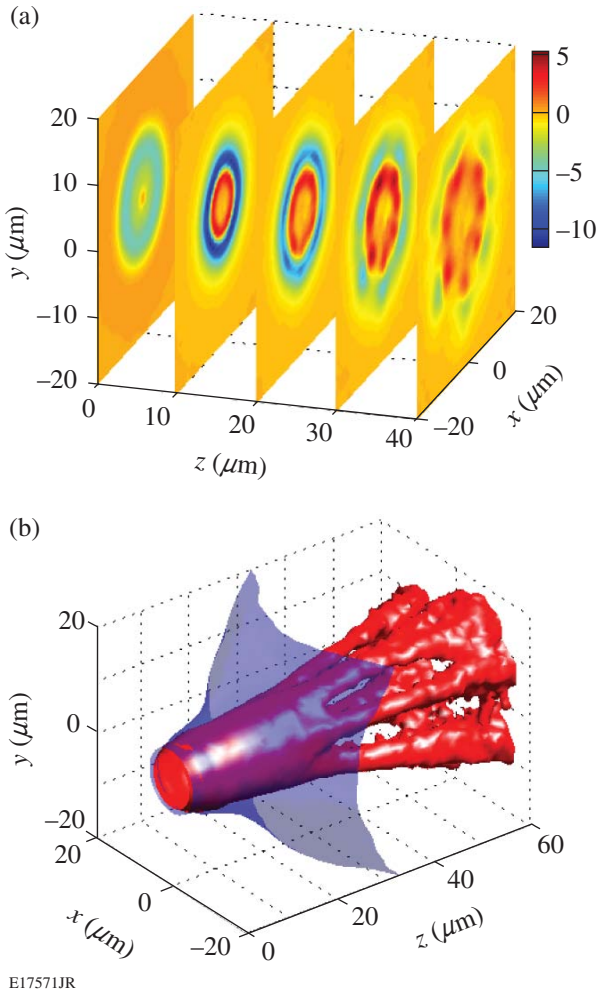

Figure 118.16
(a) Cross sections through the azimuthal magnetic field (in units of megaGauss) for the 60-μm target, 350 fs after the peak of the laser pulse. (b) The location of the fast-electron-density isosurface at 50% of the peak density (solid surface) and the equivalent isosurface with the magnetic field artificially suppressed (semitransparent surface).

the case with the magnetic field artificially suppressed. The expanding annulus forms because of a different mechanism than the one suggested by the simulations of Refs. 15 and 26, where an electron beam with initial half-angle divergence of 15° was used. The annular shape formed there because of excessive heating on-axis and magnetic field reversal just off-axis. The annulus did not expand radially because the magnetic field was still perfectly collimating at its outer side, resulting in simulations that did not reproduce the experimentally measured half-angle divergence of 20° (Ref. 15). In the simulations reported here, the plasma temperature maximizes in the annulus and has a minimum value on-axis in all transversal-beam cross sections except for the first ~6 μm, where the divergent beam maintains its maximum density on-axis. The formation of the annulus is not related to heating-induced field reversal as in the simulations of Refs. 15 and 26 but to partial collimation by the outside-edge field.

Comparison of the simulations with the experimental observations suggests the initial half-angle divergence of fast electrons approximately follows the ponderomotive law. It does not necessarily follow that the ponderomotive mechanism is dominant in determining the electron divergence because other mechanisms, such as the collisionless Weibel instability seen in the PIC simulations, can produce similar divergence angles.[18] More insight on this problem can be gained by applying the methodology developed in this article to the analysis of existing data obtained in other solid-target experiments (see, for instance, Ref. 20 and references therein).

In conclusion, experiments have been conducted to measure high-current, relativistic electron beams from high-intensity laser–solid interactions. High-resolution CTR imaging of the rear-side emission from metal targets reveals a structured pattern. Variations in the brightness of the emission with increasing target thickness were used to estimate a fast-electron temperature of $T_{hot} \sim 1.4$ MeV. The increase in the size of the emission region with increasing target thickness suggests a fast-electron half-angle divergence of $\theta_{1/2} \sim 16°$. Three-dimensional hybrid-PIC simulations model the details of the fast-electron transport inside the target. The spatial distribution of the fast-electron density at the rear surface reproduces the details of the CTR emission pattern by assuming an initial fast-electron half-angle divergence of $\theta_{1/2} \sim 56°$. The initial half-angle divergence is reduced in the target by the self-generated resistive magnetic field. The radially expanding annular pattern results from the partial collimation of an initially divergent fast-electron beam. Filamentation occurs in the annulus because of the resistive filamentation instability.

ACKNOWLEDGMENT

This work was supported by the U.S. Department of Energy Office of Inertial Confinement Fusion under Cooperative Agreement No. DE-FC52-08NA28302, the Office of Fusion Energy Science DE-FC02-04ER54789 (Fusion Science Center), the University of Rochester, and the New York State Energy Research and Development Authority. The support of DOE does not constitute an endorsement by DOE of the views expressed in this article.

REFERENCES

1. T. Katsouleas, Nature **444**, 688 (2006).
2. K. K. Kainz *et al*., Med. Phys. **31**, 2053 (2004).
3. W. Theobald, K. Akli, R. Clarke, J. Delettrez, R. R. Freeman, S. Glenzer, J. Green, G. Gregori, R. Heathcote, N. Izumi, J. A. King, J. A. Koch, J. Kuba, K. Lancaster, A. J. MacKinnon, M. Key, C. Mileham, J. Myatt, D. Neely, P. A. Norreys, H.-S. Park, J. Pasley, P. Patel, S. P. Regan, H. Sawada, R. Shepherd, R. Snavely, R. B. Stephens, C. Stoeckl, M. Storm, B. Zhang, and T. C. Sangster, Phys. Plasmas **13**, 043102 (2006).
4. C. A. Brau, Science **239**, 1115 (1988).
5. M. Tabak *et al*., Phys. Plasmas **1**, 1626 (1994).
6. S. C. Wilks and W. L. Kruer, IEEE J. Quantum Electron. **33**, 1954 (1997).
7. H. Popescu *et al*., Phys. Plasmas **12**, 063106 (2005).
8. M. Storm, I. A. Begishev, R. J. Brown, C. Guo, D. D. Meyerhofer, C. Mileham, J. F. Myatt, P. M. Nilson, T. C. Sangster, C. Stoeckl, W. Theobald, and J. D. Zuegel, Rev. Sci. Instrum. **79**, 10F503 (2008).
9. L. Gremillet, G. Bonnaud, and F. Amiranoff, Phys. Plasmas **9**, 941 (2002).
10. D. R. Welch *et al*., Phys. Plasmas **13**, 063105 (2006).
11. A. A. Solodov, K. S. Anderson, R. Betti, V. Gotcheva, J. F. Myatt, J. A. Delettrez, S. Skupsky, W. Theobald, and C. Stoeckl, Phys. Plasmas **16**, 056309 (2009).
12. J. Zheng *et al*., Phys. Plasmas **10**, 2994 (2003).
13. J. Myatt, W. Theobald, J. A. Delettrez, C. Stoeckl, M. Storm, T. C. Sangster, A. V. Maximov, and R. W. Short, Phys. Plasmas **14**, 056301 (2007).
14. V. Bagnoud, I. A. Begishev, M. J. Guardalben, J. Puth, and J. D. Zuegel, Opt. Lett. **30**, 1843 (2005).
15. P. A. Norreys *et al*., Plasma Phys. Control. Fusion **48**, L11 (2006).
16. S. Agostinelli *et al*., Nucl. Instrum. Methods Phys. Res. A **506**, 250 (2003).
17. B. Chrisman, Y. Sentoku, and A. J. Kemp, Phys. Plasmas **15**, 056309 (2008).
18. J. C. Adam, A. Héron, and G. Laval, Phys. Rev. Lett. **97**, 205006 (2006).
19. A. R. Bell and R. J. Kingham, Phys. Rev. Lett. **91**, 035003 (2003).
20. J. S. Green, V. M. Ovchinnikov, R. G. Evans, K. U. Akli, H. Azechi, F. N. Beg, C. Bellei, R. R. Freeman, H. Habara, R. Heathcote, M. H. Key, J. A. King, K. L. Lancaster, N. C. Lopes, T. Ma, A. J. MacKinnon, K. Markey, A. McPhee, Z. Najmudin, P. Nilson, R. Onofrei, R. Stephens, K. Takeda, K. A. Tanaka, W. Theobald, T. Tanimoto, J. Waugh, L. Van Woerkom, N. C. Woolsey, M. Zepf, J. R. Davies, and P. A. Norreys, Phys. Rev. Lett. **100**, 015003 (2008).
21. F. N. Beg *et al*., Phys. Plasmas **4**, 447 (1997).
22. P. M. Nilson, W. Theobald, J. Myatt, C. Stoeckl, M. Storm, O. V. Gotchev, J. D. Zuegel, R. Betti, D. D. Meyerhofer, and T. C. Sangster, Phys. Plasmas **15**, 056308 (2008).
23. C. I. Moore, J. P. Knauer, and D. D. Meyerhofer, Phys. Rev. Lett. **74**, 2439 (1995).
24. M. H. Key, Phys. Plasmas **14**, 055502 (2007).
25. S. I. Braginskii, in *Reviews of Plasma Physics*, edited by Acad. M. A. Leontovich (Consultants Bureau, New York, 1965), Vol. 1, p. 205.
26. J. R. Davies, J. S. Green, and P. A. Norreys, Plasma Phys. Control. Fusion **48**, 1181 (2006).

Pressure-Driven, Resistive Magnetohydrodynamic Interchange Instabilities in Laser-Produced, High-Energy-Density Plasmas

Introduction

Pressure-driven, resistive interchange modes are fundamental magnetohydrodynamic (MHD) instabilities in plasmas.[1–4] These convective instabilities occur under circumstances with unfavorable field curvature relative to the pressure gradient [$\boldsymbol{\kappa} \bullet \nabla P > 0$, where $\boldsymbol{\kappa} = \mathbf{B} \bullet \nabla \mathbf{B}/B^2$ is the line curvature of the magnetic (B) field and ∇P is the plasma pressure gradient]. In this configuration, field lines are concave toward the plasma and have tension that tends to make them shorten and collapse inward, while plasma pressure has a natural tendency to expand outward. Unstable perturbations that have short wavelengths perpendicular to the B field ($k_\perp L_p \gg 1$, where $L_p \equiv P/\nabla P$ is the pressure scale length) and long wavelengths parallel to the field ($k_\parallel$) grow and result in interchanges of field and their plasma content between the inside and outside of the plasma edge, leading to a state of lower internal energy. The instabilities evolve through a linear-growth phase, followed by a nonlinear one.[3,4] The basic behavior of these unstable modes is analogous to the Rayleigh–Taylor (RT) instabilities, which are driven by acceleration (equivalent to the pressure gradient for interchange instabilities) in plasmas.[3,4] Interchange instabilities have been widely studied in the magnetically confined, tenuous plasmas[1–4] but have not been explored, to our knowledge, in high-temperature, dense, high-energy-density (HED) plasmas.[5]

Laser-produced plasmas are typical HED plasmas with thermal and/or magnetic pressures >1 Mbar (Ref. 5). Generated by a circular laser beam interacting with a solid foil, a plasma bubble[6–9] is similar to those plasmas confined by a typical Z pinch. Ideal MHD theory,[3] which ignores plasma resistivity, predicts that the only unstable interchange modes are the $m = 0$ (sausage instability) and the $m = 1$ (kink instability), while the other $m > 1$ modes are stabilized because their growth is energetically unfavorable in overcoming the tension generated by the curvature of B-field lines ($\propto B^2/r$), where r is the curvature radius. The stabilizing field-line bending effect can be significantly reduced in resistive plasmas since the plasma resistivity results in field slipping and diffusion across the plasma boundary, making it possible for high-mode-number modes to be destabilized and to grow. This scenario is illustrated schematically in Fig. 118.17.

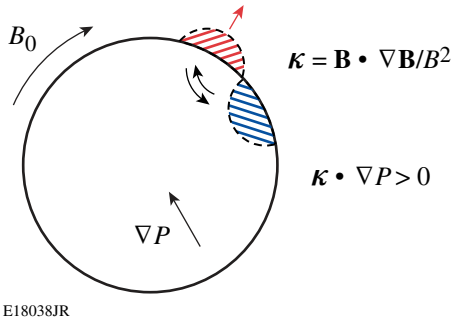

Figure 118.17
Top view (schematic) of a laser-generated plasma bubble, illustrating a high-mode-number ($m > 1$), pressure-driven, resistive MHD interchange instability resulting in an interchange of fields between the inside and outside of the bubble edge. The diffusion of the B field reduces the effect of field-line bending. B_0 represents the undisturbed B field.

The first observation of such an edge asymmetry in laser-produced plasmas by proton radiography of laser–foil interactions was recently reported.[6] Based largely on conceptual arguments and order-of-magnitude estimates, therein it was conjectured that this asymmetric structure was a consequence of pressure-driven, resistive MHD interchange instabilities. This hypothesis is made quantitative and more rigorous in this article. The generation of laser-produced spontaneous magnetic fields is outlined. A theoretical description of the features of interchange modes in HED plasmas is then presented. The theory is supported by experimental results and discussions are presented. The important findings are then summarized.

Laser-Produced, High-Energy-Density Plasmas and Spontaneous Magnetic Fields

Laser-generated plasmas are transient with durations of the order of a few nanoseconds. High plasma densities ($\sim 10^{18}$ cm^{-3}), high temperatures (~1 keV), intense self-generated B fields [~1 megagauss (MG)], and high ratios of thermal pressure to magnetic pressure ($\beta \gg 1$) distinguish this from the

tenuous plasmas of the order of $10^{14}/\text{cm}^3$ or lower, which are characteristics of most magnetic-confinement experiments. For long-pulse, low-intensity laser light, the dominant source for B-field generation is noncollinear electron-density and temperature gradients ($\nabla n_e \times \nabla T_e$), where n_e is the electron density and T_e is the temperature.[10–12] In the regime with a low-ionization-state Z and high temperature, where resistivity is low, B-field growth is linear in time and is balanced by convective transport[10–12] [$\nabla \times (\mathbf{v} \times \mathbf{B})$, where $\mathbf{v}$ is the plasma fluid velocity; i.e., the B field is "frozen in"]. When the laser is off and the cooling plasma becomes more resistive, field diffusion dominates convective transport[10–12] [$\nabla \times (D_m \nabla \times \mathbf{B})$, where D_m is the magnetic diffusion coefficient]. Under these circumstances, B-field generation and evolution are governed by[10–12]

$$\frac{\partial \mathbf{B}}{\partial t} \approx \nabla \times (\mathbf{v} \times \mathbf{B}) - \frac{1}{e n_e} \nabla n_e \times \nabla T_e - \nabla \times \left(D_m \nabla \times \mathbf{B}\right), \quad (1)$$

where e is the electron charge.

Figure 118.18 shows the spatial distributions of n_e, T_e, and B field in a plasma bubble caused by the interaction of a laser beam (wavelength = 0.351 nm, 1-ns pulse with a beam-spot size ~800 μm in diameter, and energy ~400 J), with a 5-μm-thick plastic (CH) foil at a time of 1.8 ns, simulated by the two-dimensional (2-D) radiation–hydrodynamics code LASNEX.[13,14] The maximum field strength occurs around the surface of the hemispherical plasma bubble because the largest temperature gradients occur around the bubble's edge. The relative importance of plasma convection to diffusion during field evolution is characterized by the magnetic Reynolds number

$$R_m = \frac{L_\perp \mathbf{v}}{D_m} \approx \left| \frac{\nabla \times (\mathbf{v} \times \mathbf{B})}{\nabla \times \left(D_m \nabla \times \mathbf{B}\right)} \right|, \quad (2)$$

where $L_\perp$ is the characteristic length scale.[3,4] When the laser is on, $R_m \gg 1$; therefore, the fields must be frozen in and move with the plasmas (for example, taking a characteristic scale length $L_\perp \approx T_e / \nabla T_e \sim 100$ μm , a bubble expansion velocity $v \sim 5 \times 10^7$ cm/s, and a diffusion $D_m \sim 4 \times 10^2$ cm^2/s, one has $R_m \sim 1000$). The flow is dominated by plasma fluid dynamics and is insignificantly affected by the fields despite their MG levels.[6–8,15] The bubble expansion in this regime can be approximated as "free-streaming" because the velocity is of the order of the ion sound velocity ($C_s \sim 2 \times 10^7$ cm/s). After the laser pulse turns off (the energy input is stopped), the plasma bubble continues to expand and begins to cool. The cooling plasma becomes more collisional and increasingly resistive. This makes it possible for the field to diffuse across the plasma boundary and eventually dissipate. At these post-driven times, the fluid behavior near the plasma edge is increasingly governed by the field and resistive effects (i.e., $R_m < 1$), and the local plasma β becomes of the order of 1 (Refs. 6–8,15). As will be shown, this gives rise to pressure-driven resistive instabilities. The large amplitudes of unstable modes, resulting from exponential growth around the plasma bubble edge, provide unique opportunities for the experimental study of such important instabilities in HED plasmas.

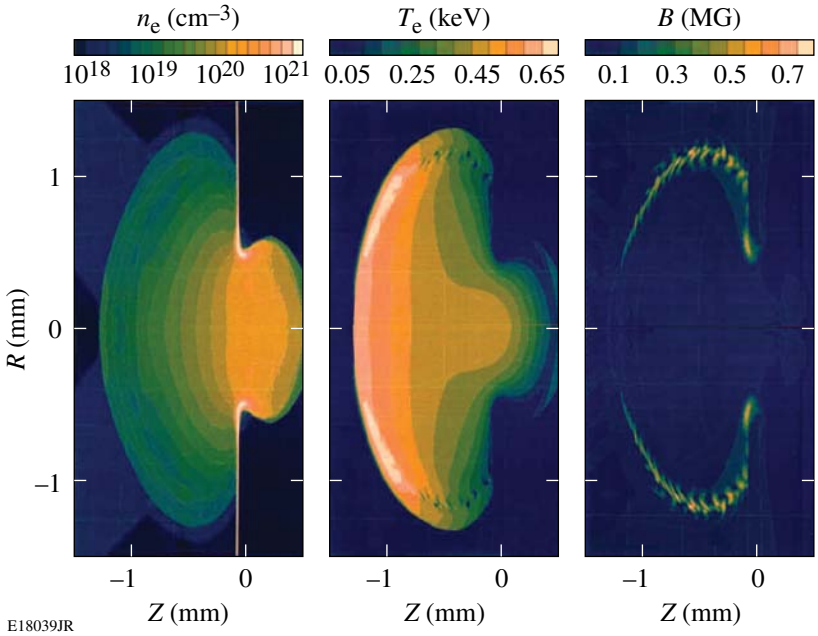

Figure 118.18
Side view of the distributions of n_e, T_e, and B-field amplitude in an isolated laser-generated plasma bubble at t = 1.8 ns for a 1-ns laser drive pulse with a beam-spot size ~800 μm in diameter, simulated with the 2-D code LASNEX. The surface of the foil is at position Z = 0.0 on the horizontal axes, and the laser is incident from the left. The field is always perpendicular to the plane of the image.

Pressure-Driven Resistive Instabilities

In analyzing the instabilities in the linear growth phase, it is assumed that the perturbations are small so that the linearized MHD equations can be used to elucidate the fundamental features of the instabilities. Considering the small-scale modes ($k_\perp L_p \gg 1$), linearizing the equations ($\partial/\partial t \longrightarrow \gamma$, where γ is the growth rate) and Fourier transforming the perturbations ($\nabla \longrightarrow ik$), a set of algebraic high-β-reduced MHD eigen-equations is obtained.[4] By solving for the eigenvalues, a dispersion relation for the mode growth rate is obtained:[4]

$$\gamma^2 \approx \frac{2(\mathbf{B}\cdot\nabla\mathbf{B})\nabla P}{\rho B^2} - \frac{k_\parallel^2 v_A^2}{1 + D_\mathrm{m} k_\perp^2 \gamma^{-1}}. \tag{3}$$

In this dispersion equation, the second term represents the mode stabilization caused by the field-line bending. Perturbations are stabilized when

$$\frac{2(\mathbf{B}\cdot\nabla\mathbf{B})\nabla P}{\rho B^2} \le \frac{k_\parallel^2 v_A^2}{1 + D_\mathrm{m} k_\perp^2 \gamma^{-1}}, \tag{4}$$

where

$$v_\mathrm{A} = \sqrt{\frac{B^2}{\rho}} \tag{5}$$

is the Alfvén speed, and the wave number along the toroidal B field is

$$k_\parallel = \frac{m}{2\pi R}, \tag{6}$$

where m is the mode number. As illustrated in Fig. 118.18, the scale length of the temperature is about 30% of the bubble radius (R), i.e., $L_T \sim 0.3 \times R$. The wave number perpendicular to the field line is given as approximately $k_\perp \sim L_B^{-1}$ $\left(L_B \equiv B/\nabla B \sim 0.1 \times R\right)$. Considering $\nabla \sim L_T^{-1}$, the field-line curvature is approximately

$$\left|\boldsymbol{\kappa}\right| = \left|\frac{\mathbf{B}\cdot\nabla\mathbf{B}}{B^2}\right| \sim \frac{1}{L_T}. \tag{7}$$

The magnetic diffusion coefficient is

$$D_\mathrm{m} = \frac{c^2}{4\pi}\eta, \tag{8}$$

where η is the plasma resistivity. Using $L_T \sim 0.3\ R$, the dispersion relation [Eq. (3)] can be rewritten as

$$\gamma^2 \sim \frac{2P}{\rho L_T^2} - \frac{m^2 B^2}{\rho(2\pi R)^2\left(1 + D_\mathrm{m} k_\perp^2 \gamma^{-1}\right)}$$

$$\sim \frac{2B^2\beta}{\rho\pi R^2} - \frac{m^2 B^2}{4\rho\pi^2 R^2\left(1 + D_\mathrm{m} k_\perp^2 \gamma^{-1}\right)}. \tag{9}$$

When $\gamma^2 \le 0$, the (minimum) condition for perturbation stabilization caused by the effects of field-line bending becomes

$$\beta - \frac{m^2}{8\pi\left(1 + D_\mathrm{m} k_\perp^2 \gamma_\mathrm{max}^{-1}\right)} \le 0 \tag{10}$$

or

$$m > \sim \sqrt{8\pi\beta\left(1 + D_\mathrm{m} k_\perp^2 \gamma_\mathrm{max}^{-1}\right)}, \tag{11}$$

where

$$\gamma_\mathrm{max} = \gamma\,\big|_{m=0} \tag{12}$$

is the maximum growth rate that occurs when $m = 0$, i.e., sausage instability. As indicated by Eq. (3), the effect of field-line bending on stabilizing perturbations will be significantly reduced when $D_\mathrm{m} k_\perp^2 \gamma^{-1} \ge 1$ (Ref. 4).

When compared to typical tenuous plasmas with low-plasma β's ($\ll$1), typical laser-produced HED plasmas have, as discussed in the previous section, relatively large plasma β's, allowing a much higher mode-number cutoff for stabilizing perturbations. For physical quantities of experiments relevant to the laser–foil interactions[6–8,15] on OMEGA[16] [taking typical values in the region around the plasma edge after the laser turns off (Fig. 118.18)], $n_i \sim 1 \times 10^{18}$ cm^{-3}, $n_\mathrm{e} \approx Zn_i \sim 3.5 \times 10^{18}$ cm^{-3}, $T_\mathrm{e} \sim 0.4$ keV, $B \sim 0.3$ MG, and $\beta \sim 1$, with an estimated mode-number cutoff of $m \sim 6$. Inserting these numbers in Eq. (9), the growth rate as a function of the mode numbers is plotted in Fig 118.19.

After evolving through a linear regime, the growth of instabilities enters a nonlinear phase. In this phase, the unstable perturbations in the outward motion move into a region with reduced ambient pressure, resulting in reduced plasma density

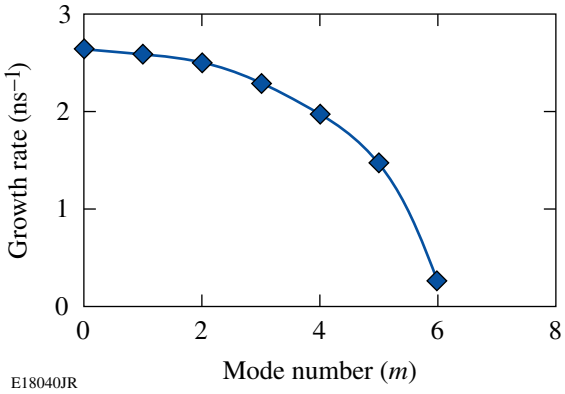

Figure 118.19
Growth rate determined using Eq. (3) is plotted as a function of the mode number for the plasma conditions discussed in this article, showing that the effects of stabilization will be cut off at $m \sim 6$.

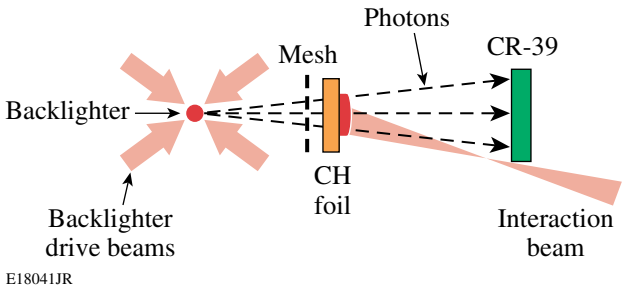

Figure 118.20
Schematic illustration of the experiment setup for face-on proton radiography. Distances from the backlighter are 1.3 cm for the mesh, 1.5 cm for the CH foil (5 μm thick), and 30 cm for the CR-39 detector.[6]

around the apex[4] and a reduced B field (causing a reduction of the field-line bending). These self-focusing effects tend to drive instabilities nonlinearly, leading to explosive growth.[17] Conversely, the nonlinear effects of inward motion of unstable perturbations tend to be stabilized, resulting from the field compression and plasma flow into the valleys.[17] The combined effects result in a finger-like structure: an explosive growth of outward instabilities and stabilized inward perturbations.[4]

Experiments

Pressure-driven, resistive instabilities were studied with monoenergetic proton radiography,[6–9,15,18] as shown schematically in Fig. 118.20, using a backlighter that produced pulsed protons at the discrete energy of 15 MeV (fusion products of the nuclear reaction D + ^{3}He $\longrightarrow$ α + p, generated from D^{3}He-filled, thin-glass-shell implosions driven by 20 OMEGA laser beams[16]). Plasmas and B fields were generated through laser–plasma interactions on a plastic (CH) foil by a single laser beam (hereafter called the *interaction beam*) with a wavelength of 0.351 μm, linearly polarized, and incident at 23° from the normal direction. The 1-ns-long square laser pulse had an energy of ~400 J and a spot diameter of ~800 μm determined by phase plate SG4 (defined as 95% energy deposition),[19,20] resulting in a peak laser intensity of the order of 10^{14} W/cm. The nickel mesh used was 60 μm thick with 150-μm period and 75-μm holes.[6–9,15,18] Radiographs were recorded using CR-39 detectors.[21] The duration of each "exposure," determined by the emission time of the backlighter-produced protons, was ~130 ps. Since the backlighter-to-foil flight time for the protons was ~0.28 ns, an image representing the state of the field (at the foil at time t_a after the onset of the interaction beam) was made by starting this beam at time t_a + 0.28 ns after the mean backlighter-production time.

Data and Discussion

Face-on proton-radiograph images are shown in Fig. 118.21 (see Ref. 6). Each image is labeled with a time that represents the interval between the start of the interaction beam and the arrival of the backlighter protons and shows how the proton

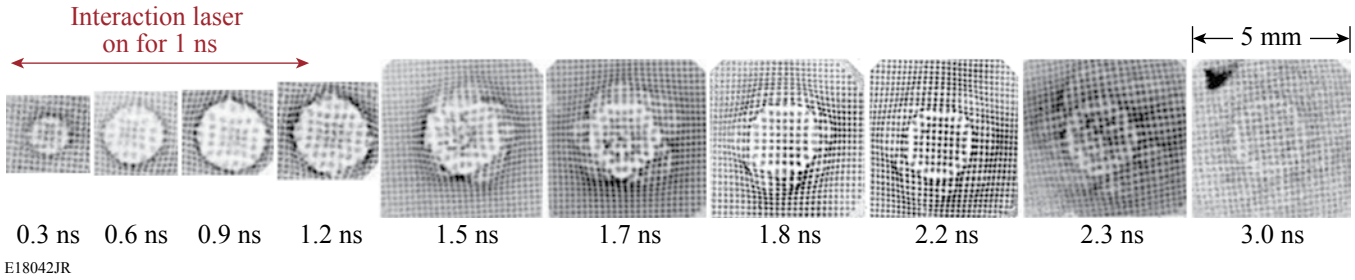

Figure 118.21
Measured face-on D^{3}He proton images showing the spatial structure and temporal evolution of B fields generated by laser–plasma interactions. Each image is labeled at the time between the arrival at the foil of the interaction beam and the arrival of the imaging protons. The images illustrate the transition from the 1-ns illumination period (with 2-D symmetric expansion of B fields), to a post-laser decay phase with 3-D structures emerging around the bubble edge and in the interior, as the expanding bubble cools and becomes increasingly resistive.

beamlets are deflected while passing through the B field that forms around the bubble.[22–24] The images show that while the laser beam is on ($t < 1.2$ ns), the field structure expands approximately in tandem with a hemispherical plasma bubble, maintaining 2-D cylindrical symmetry. Each image has a sharp circular ring where beamlets pile up after passing through the edges of the bubble, where the B fields are largest. This circle is a magnified image of the bubble edge because the angular deflection of each beamlet is proportional to $\int \mathbf{B} \times d\vec{\ell}$ (where $d\vec{\ell}$ is the differential pathlength along the proton trajectory) and $\mathbf{B} \times d\vec{\ell}$ points away from the bubble center.

When the laser turns off ($t > 1.2$ ns), the bubble continues to expand as the field decays and becomes distinctly asymmetric, indicating instability growth. This is contrary to the 2-D LASNEX simulations that cannot model 3-D asymmetries. It might be argued that the observation of a 3-D structure renders a comparison with the 2-D simulations irrelevant, but 3-D codes are not yet available and it is important to consider only the data at hand. (Work is currently underway on combining the 3-D hydrocode *HYDRA* with a field-generating package.[25]) Experimental measurements, such as those shown here, are important because they directly reveal previously unpredicted physical phenomena, indicate the fundamental importance of 3-D processes in certain regimes (such as in the decay phase), and provide invaluable information for benchmarking a true 3-D code. A rough estimate suggests that high-mode-number modes ($m \sim 3$ to 6) occur and are superimposed on the expanding plasma bubble. The time evolution of the imaging spatial structures clearly indicates that these modes are unstable and that their amplitudes grow continuously (Fig. 118.21). As described in the previous sections, the experimental conditions and plasma-bubble configuration satisfy the requirements for the appearance of pressure-driven resistive interchange instabilities: first, the bubble has unfavorable field curvature relative to the pressure gradient ($\boldsymbol{\kappa} \bullet \nabla P > 0$), in which field lines are concave toward the plasma and plasma pressure tends to expand outward; second, at these post-driven times, the fluid behavior near the bubble edge is dominated by field and resistive effects. Plasma resistivity significantly reduces the stabilization associated with field-line bending, making it possible for high-mode-number perturbations ($m > 1$) to destabilize and grow. As a consequence, these conditions result in the interchange of fields between the inside and outside of the bubble. Pure fluid instabilities such as the Widnall type[26] might be visible while the laser is on (when B fields have little impact on the plasma flow but are frozen in); there is no evidence that this is occurring.

The quantitative comparison of measured time evolution of rms deviations, defined as deviation of the outer-bubble boundary from the average radii, is given by:

$$\Delta r^2 = \frac{1}{N}\sum_{i}^{N}\left(r_i - \bar{r}\right)^2 , \tag{13}$$

where N is the total number of the deviations, with calculated growth in the linear growth regime [Eq. (3)] given in Fig. 118.22. Experimental data are reasonably well reproduced using theoretical predictions and provide compelling evidence to support that they are caused by interchange instabilities. This agreement also suggests that the instability has dominant mode numbers $m \sim 3$ to 5. The measurement uncertainties are large, reflecting the uncertainties involved in determining the amplitudes of various perturbation modes. Finger-like structures associated with nonlinear growth do not appear. This suggests that the fields have dissipated sufficiently before the onset of nonlinear growth. This will be a topic for future study.

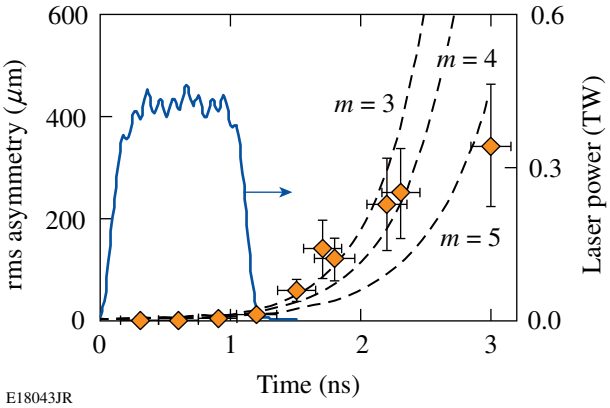

Figure 118.22
Measured time evolution of rms deviations of the outer-bubble boundary from the average radii (averaged azimuthally over angles from individual images) are shown to be reasonably consistent with the predicted growth of interchange instabilities. The solid curve is the time history of the laser intensity.

Summary

Pressure-driven, resistive magnetohydrodynamic interchange instabilities in laser-produced, high-energy-density plasmas have been studied with proton radiography. Unstable, high-mode-number perturbations ($m > 1$) occur around the expanding plasma bubble edge after the laser has turned off. The quantitative consistency between experimental data and theoretical prediction provides strong evidence for the occurrence and growth of interchange instabilities. A cutoff relation

for stabilization, $m > \sim\left[8\pi\beta\left(1 + D_{\mathrm{m}}k_{\perp}^{2}\,\gamma_{\max}^{-1}\right)\right]^{1/2}$, has been found in the linear growth regime and found to match the data. Experimental measurements are important for directly revealing, in a different context, previously unpredicted physical phenomena. They indicate the fundamental importance of 3-D processes in certain regimes and provide invaluable information for benchmarking 3-D code development.

ACKNOWLEDGMENT

The work was performed at the LLE National Laser User's Facility (NLUF), and was supported in part by US DOE (DE-FG52-07NA28059 and DE-FG52-06N826203), LLNL (B543881 and LDRD-ER 898988), LLE (414090-G), and the Fusion Science Center at the University of Rochester (412761-G).

REFERENCES

1. H. P. Furth, J. Killeen, and M. N. Rosenbluth, Phys. Fluids **6**, 459 (1963).
2. B. Coppi, Phys. Rev. Lett. **12**, 6 (1964).
3. J. P. Freidberg, *Ideal Magnetohydrodynamics* (Plenum Press, New York, 1987).
4. D. Biskamp, *Magnetic Reconnection in Plasmas*, Cambridge Monographs on Plasma Physics (Cambridge University Press, Cambridge, England, 2000).
5. R. P. Drake, *High-Energy-Density Physics: Fundamentals, Inertial Fusion, and Experimental Astrophysics, Shock Wave and High Pressure Phenomena* (Springer, Berlin, 2006).
6. C. K. Li, F. H. Séguin, J. A. Frenje, J. R. Rygg, R. D. Petrasso, R. P. J. Town, P. A. Amendt, S. P. Hatchett, O. L. Landen, A. J. Mackinnon, P. K. Patel, M. Tabak, J. P. Knauer, T. C. Sangster, and V. A. Smalyuk, Phys. Rev. Lett. **99**, 015001 (2007).
7. C. K. Li, F. H. Séguin, J. A. Frenje, J. R. Rygg, R. D. Petrasso, R. P. J. Town, P. A. Amendt, S. P. Hatchett, O. L. Landen, A. J. Mackinnon, P. K. Patel, V. A. Smalyuk, T. C. Sangster, and J. P. Knauer, Phys. Rev. Lett. **97**, 135003 (2006).
8. C. K. Li, F. H. Séguin, J. A. Frenje, J. R. Rygg, R. D. Petrasso, R. P. J. Town, O. L. Landen, J. P. Knauer, and V. A. Smalyuk, Phys. Rev. Lett. **99**, 055001 (2007).
9. C. K. Li, F. H. Séguin, J. R. Rygg, J. A. Frenje, M. Manuel, R. D. Petrasso, R. Betti, J. Delettrez, J. P. Knauer, F. Marshall, D. D. Meyerhofer, D. Shvarts, V. A. Smalyuk, C. Stoeckl, O. L. Landen, R. P. J. Town, C. A. Back, and J. D. Kilkenny, Phys. Rev. Lett. **100**, 225001 (2008).
10. L. Spitzer, *Physics of Fully Ionized Gases*, 2nd rev. ed., Interscience Tracts on Physics and Astronomy (Interscience, New York, 1962).
11. S. I. Braginskii, in *Reviews of Plasma Physics*, edited by Acad. M. A. Leontovich (Consultants Bureau, New York, 1965).
12. M. G. Haines, Phys. Rev. Lett. **78**, 254 (1997).
13. G. B. Zimmerman and W. L. Kruer, Comments Plasma Phys. Control. Fusion **2**, 51 (1975).
14. P. D. Nielsen and G. B. Zimmerman, Lawrence Livermore National Laboratory, Livermore, CA, Report UCRL-53123 (1981).
15. R. D. Petrasso, C. K. Li, F. H. Séguin, J. R. Rygg, J. A. Frenje, R. Betti, J. P. Knauer, D. D. Meyerhofer, P. A. Amendt, D. H. Froula, O. L. Landen, P. K. Patel, J. S. Ross, and R. P. J. Town, "Lorentz Mapping of Magnetic Fields in Hot, Dense Plasmas," to be published in Physical Review Letters.
16. J. M. Soures, R. L. McCrory, C. P. Verdon, A. Babushkin, R. E. Bahr, T. R. Boehly, R. Boni, D. K. Bradley, D. L. Brown, R. S. Craxton, J. A. Delettrez, W. R. Donaldson, R. Epstein, P. A. Jaanimagi, S. D. Jacobs, K. Kearney, R. L. Keck, J. H. Kelly, T. J. Kessler, R. L. Kremens, J. P. Knauer, S. A. Kumpan, S. A. Letzring, D. J. Lonobile, S. J. Loucks, L. D. Lund, F. J. Marshall, P. W. McKenty, D. D. Meyerhofer, S. F. B. Morse, A. Okishev, S. Papernov, G. Pien, W. Seka, R. Short, M. J. Shoup III, M. Skeldon, S. Skupsky, A. W. Schmid, D. J. Smith, S. Swales, M. Wittman, and B. Yaakobi, Phys. Plasmas **3**, 2108 (1996).
17. S. C. Cowley and M. Artun, Phys. Rep. **283**, 185 (1997).
18. C. K. Li, F. H. Séguin, J. A. Frenje, R. D. Petrasso, P. A. Amendt, R. P. J. Town, O. L. Landen, J. R. Rygg, R. Betti, J. P. Knauer, D. D. Meyerhofer, J. M. Soures, C. A. Back, J. D. Kilkenny, and A. Nikroo, Phys. Rev. Lett. **102**, 205001 (2009).
19. T. J. Kessler, Y. Lin, J. J. Armstrong, and B. Velazquez, in *Laser Coherence Control: Technology and Applications*, edited by H. T. Powell and T. J. Kessler (SPIE, Bellingham, WA, 1993), Vol. 1870, pp. 95–104.
20. D. D. Meyerhofer, J. A. Delettrez, R. Epstein, V. Yu. Glebov, V. N. Goncharov, R. L. Keck, R. L. McCrory, P. W. McKenty, F. J. Marshall, P. B. Radha, S. P. Regan, S. Roberts, W. Seka, S. Skupsky, V. A. Smalyuk, C. Sorce, C. Stoeckl, J. M. Soures, R. P. J. Town, B. Yaakobi, J. D. Zuegel, J. Frenje, C. K. Li, R. D. Petrasso, D. G. Hicks, F. H. Séguin, K. Fletcher, S. Padalino, C. Freeman, N. Izumi, R. Lerche, T. W. Phillips, and T. C. Sangster, Phys. Plasmas **8**, 2251 (2001).
21. F. H. Séguin, J. L. DeCiantis, J. A. Frenje, C. K. Li, J. R. Rygg, C. D. Chen, R. D. Petrasso, J. A. Delettrez, S. P. Regan, V. A. Smalyuk, V. Yu. Glebov, J. P. Knauer, F. J. Marshall, D. D. Meyerhofer, S. Roberts, T. C. Sangster, C. Stoeckl, K. Mikaelian, H. S. Park, H. F. Robey, and R. E. Tipton, Phys. Plasmas **13**, 082704 (2006).
22. The effects of scattering on proton deflection are minimum because of the negligible energy loss as the 15-MeV backlighting protons pass through the plasmas ($\rho L \sim 0.5$ mg/cm^2) (Refs. 23 and 24).
23. C. K. Li and R. D. Petrasso, Phys. Rev. Lett. **70**, 3059 (1993).
24. V. L. Highland, Nucl. Instrum. Methods **129**, 497 (1975).
25. M. M. Marinak *et al*., Phys. Plasmas **8**, 2275 (2001).
26. S. E. Widnall, D. B. Bliss, and C.-Y. Tsai, J. Fluid Mech. **66**, 35 (1974).

Extended Model for Polymer Cholesteric Liquid Crystal Flake Reorientation and Relaxation

Introduction

The suspension of polymer cholesteric liquid crystal (PCLC) flakes in a fluid creates the possibilities for a particle-based, electrically driven technology with a wide variety of applications ranging from displays and electronic paper to electro-optic polarizers and filters. The technology produces devices with a bright, saturated, and circularly polarized reflective "OFF" state. When an electric field, as low as tens of millivolts per micrometer, is applied, the flakes reorient at ~90° to the electrodes, creating a dark, nonreflective "ON" state.[1] The PCLC flakes can be microencapsulated, and the technology is compatible with flexible substrates and roll-to-roll processing.[2] Originally produced by freeze-fracturing thin PCLC films,[3] PCLC flakes can now be manufactured with specific sizes and shapes,[4] altered electro-optic properties,[5] and enhanced reflectivity.[6]

The main mechanism for flake reorientation, Maxwell–Wagner polarization, is strengthened by extrinsic charges that accumulate at the surface of the flake when an electric field is applied. As these charges continue to migrate toward the edges of the flake, a dipole moment is induced. The charges responsible for the flake polarization come from ionic contaminants on and within the flakes themselves, the host fluid, and the device substrates.[1]

An early theoretical model for PCLC flake motion included both a hydrodynamic and an electrostatic term.[1] Flake rotation is taken to occur about its center of mass, so the force of gravity was not considered. This early model predicts flake reorientation well, but it has no mechanism for modeling flake *relaxation* (defined as the flake's return to its initial position once the electric field is removed). Upon re-evaluation of the mechanics of flake rotation, it became clear that many flakes tend to rotate about a pivot point near or at their edge. This article discusses a new extended theoretical model that includes a gravity term and presents experimental data that support this extended model. Both reorientation (torques caused by electric-field, viscous flow, and gravity present) and relaxation (viscous and gravity torques only) are discussed.

Theory

Previously, we described the derivation of a theoretical model that assumes a PCLC flake subjected to an external electric field will reorient about its center of mass and along its longest axis a_1 with a negligible moment of inertia.[1] This configuration leads to the inclusion of only the electrostatic Γ_E and hydrodynamic Γ_H torques because gravity, which acts on the center of mass, would not affect motion. A series of experiments showed that flakes often reorient about the edge of their longest side (Fig. 118.23).

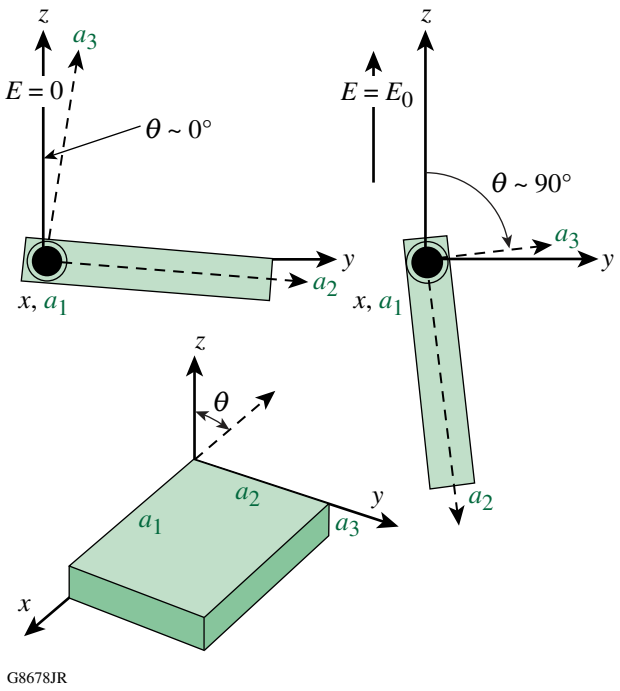

Figure 118.23
A two-dimensional cross-sectional depiction of a PCLC flake with its semi-axes defined as $a_1 > a_2 > a_3$. The electric field is applied along the z axis. Modeling presumes a particle position is (a) at $\theta \sim 0°$ for $E = 0$ and (b) at $\theta \sim 90°$ for $E = E_0$.

Rotation about a flake's edge makes the torque caused by gravity, Γ_G, relevant to the equation of motion governing flake behavior and extends the theoretical model to describe reorientation as

$$\Gamma_E - \Gamma_H - \Gamma_G = 0. \quad (1)$$

The electrostatic torque about the a_i axis, which drives flake reorientation, is given as

$$\Gamma_{Ei} = \frac{4}{3}\pi a_i a_j a_k \varepsilon_h K_j^* K_k^* \left(A_k - A_j\right) E_{0j} E_{0k} = C_{Ei} \sin\theta \cos\theta, \quad (2)$$

where E_0 is the electric-field magnitude, $E_{0j} = E_0 \sin\theta$ and $E_{0k} = E_0 \cos\theta$ are projections of an electric field applied in the z direction.[7] The lengths of the particle semi-axes are designated as a_i, a_j, and a_k, and a depolarization factor A_i is defined along each axis. The indices i, j, and k are ordered according to the right-hand coordinate system. To find A_j, assign $i \longrightarrow j$, $j \longrightarrow k$, and $k \longrightarrow i$; s is a symbolic variable in the elliptical integral.

$$A_i = \frac{a_i a_j a_k}{2} \int_0^\infty \frac{ds}{\left(s + a_i^2\right)\sqrt{\left(s + a_i^2\right)\left(s + a_j^2\right)\left(s + a_k^2\right)}}. \quad (2a)$$

The complex Clausius–Mossotti function K_i^* is defined as

$$K_i^* = \frac{\left(\varepsilon_p - i\frac{\sigma_p}{\omega}\right) - \left(\varepsilon_h - i\frac{\sigma_h}{\omega}\right)}{\left(\varepsilon_h - i\frac{\sigma_h}{\omega}\right) + A_i\left[\left(\varepsilon_p - i\frac{\sigma_p}{\omega}\right) - \left(\varepsilon_h - i\frac{\sigma_h}{\omega}\right)\right]}. \quad (2b)$$

The dielectric permittivity and conductivity of the host fluid, ε_h and σ_h; the particles, ε_p and σ_p; and the electric-field frequency ω are the main parameters in the Clausius–Mossotti term. The constant C_{Ei} contains all parameters in the electrostatic torque term. The electrostatic term is complex because of the inclusion of the material conductivities. The hydrodynamic torque counteracts the electrical torque,

$$\Gamma_{Hi} = \frac{16}{3}\pi a_i a_j a_k \eta_0 \frac{\left(a_j^2 + a_k^2\right)}{\left(a_j^2 A_j + a_k^2 A_k\right)} \Omega_i = C_{Hi} \Omega_i, \quad (3)$$

where η_0 is the fluid viscosity, Ω_i is the angular velocity about axis i, and C_{Hi} is a constant including all other parameters. The gravitational torque is found to be

$$\Gamma_{Gi} = \frac{4}{3}\pi a_i a_j a_k \left(\rho_p - \rho_h\right) g a_j \cos\theta = C_{Gi} \cos\theta, \quad (4)$$

where ρ_p and ρ_h are the density of the particle and the host fluid, respectively, g is the acceleration of gravity, and C_{Gi} is a constant including related gravity-term parameters. For very small applied electric fields, the electrical torque term Γ_E would no longer be able to overcome the gravity term Γ_G and flake reorientation would not occur. Because the condition under which flakes do not reorient was not relevant to this work, the minimum effective electric field was not investigated.

1. Reorientation Time

The time required for a flake to reorient from an initial position at the angle θ_0° to its final position at θ_f is found by rearranging the equation of motion to define the angular velocity along the axis a_i:

$$\Omega_i = \frac{d\theta}{dt} = \frac{\cos\theta\left(C_{Ei}\sin\theta - C_{Gi}\right)}{C_{Hi}}. \quad (5)$$

Equation (5) is then integrated to find the reorientation time t required to attain the angle θ_f from the flake's initial position at angle θ_0:

$$t = \frac{C_{Hi}}{C_{Ei}^2 - C_{Gi}^2} \left\{ \begin{array}{l} \left(C_{Gi} - C_{Ei}\right)\ln\left[\cos\left(\frac{\theta}{2}\right) + \sin\left(\frac{\theta}{2}\right)\right] \\ -\left(C_{Ei} + C_{Gi}\right)\ln\left[\cos\left(\frac{\theta}{2}\right) - \sin\left(\frac{\theta}{2}\right)\right] \\ + C_{Ei}\ln\left[C_{Gi} - C_{Ei}\sin(\theta)\right] \end{array} \right\}_{\theta_0}^{\theta_f}. \quad (6)$$

The inclusion of the gravity term makes the resulting equation for reorientation time more complicated. The linear dependence of the host fluid's viscosity is retained, but the electric field's dependence is no longer inversely quadratic and it varies depending on system parameters. Although it is common to use the real component of the equation when the modeled motion is much slower than the electric-field oscillation, we have shown previously that, using the real component poorly predicts the reorientation time as a function of electric-field frequency.[1] A remarkably closer agreement with experimental data is achieved by using the imaginary component, although no clear physical interpretation for this term has been proposed.

The extended model is used to calculate the reorientation time as a function of frequency (Fig. 118.24) for the newly introduced variable (the host fluid's density), ranging in value

from 900 to 1300 kg/m^3. For the calculation, the PCLC particle density is fixed at 1101 kg/m^3, and all other host fluid properties are based on those for propylene carbonate. When the particle and fluid densities are matched, the gravity term vanishes, resulting in the same predictions as the initial theory (dotted line in Fig. 118.24). The electrostatic torque diminishes and reorientation times steadily increase toward infinity as the electric-field frequency shifts up or down from its optimal value for flake reorientation time.

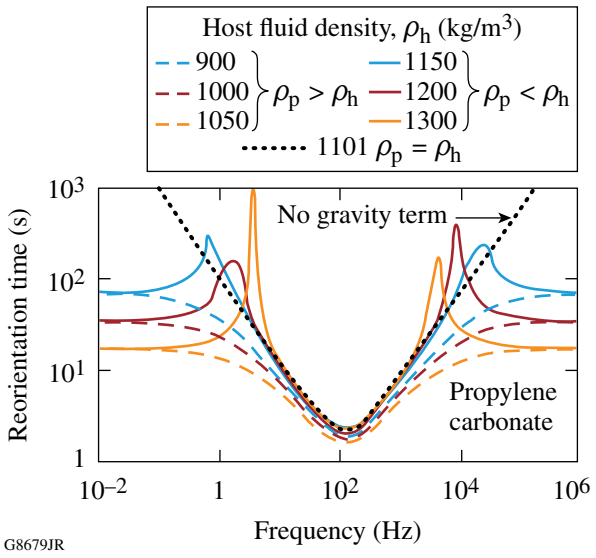

Figure 118.24
The reorientation time of a typical flake (ρ_p = 1099 kg/m^3, ε_p = 2.98, and $\sigma_p = 10^{-10}$ S/m) suspended in a fluid with the base properties of propylene carbonate (ε_h = 69, $\sigma_h = 10^{-7}$ S/m, and $\eta_0 = 2.8 \times 10^{-3}$ N × s/m^2) is examined as a function of the density of the host fluid, ρ_h. Particle semi-axes are a_1 = 30 μm, a_2 = 20 μm, and a_3 = 2 μm. The orientation angles $\theta_0 = 0.5°$ and θ_f = 89.5° are used to avoid singularities in applying Eq. (6).

The effect of the gravity term grows as the difference between the flake and the fluid density increases. When the particle density is *greater* than that of the host fluid ($\rho_p > \rho_h$), the extended theory predicts faster reorientation times (dashed lines in Fig. 118.24) than those predicted by the original theory. This result suggests that the gravity term is additive to the electrostatic torque driving flake reorientation. The reorientation times based on the extended model no longer increase toward infinity, as originally predicted. Instead, reorientation times at both extremes of the frequency range asymptote to a value equal to the ratio of the hydrodynamic term to the gravity term. The asymptotic value decreases as the host fluid density decreases and the difference between particle density and host fluid density grows.

The extended theory predicts a more-complicated frequency response when the density of the particle is *less* than that of the host fluid ($\rho_p < \rho_h$). Reorientation times near the curve minimum are predicted by the extended theory to be slightly lower. Outside this range, however, the gravity term *counteracts* the electrostatic term. Flake reorientation times start to *increase*, forming a peak when the contributions of the electrostatic and gravity terms lead toward canceling each other in the denominator of Eq. (6). When the electrostatic torque becomes negligible compared to the magnitude of the gravity term, the ratio of the hydrodynamic term to the gravity term once again defines the value of the reorientation times. At very low and very high frequencies, the reorientation time asymptotes to the same value for systems with the same absolute difference between particle and host fluid densities.

Depending on both the frequency of the applied electric field and the density of the host fluid, the gravity term either enhances or counteracts the electrostatic torque that is driving flake motion. Using propylene carbonate ($\rho_p < \rho_h$), it is possible to study how the relative strength of the electrostatic torque influences the shape of the predicted frequency response. The model is exercised with the same material parameters noted above, and the driving voltage is varied from 12.5 to 31.1 $mV_{rms}/\mu m$. The results show that higher driving voltages result in faster reorientation times over a broadening range of frequencies (see Fig. 118.25). Again, reorientation times at the frequency extremes asymptote to a value dictated by the ratio of the hydrodynamic and gravity terms. As the magnitude of the electrostatic torque diminishes with lower applied voltages,

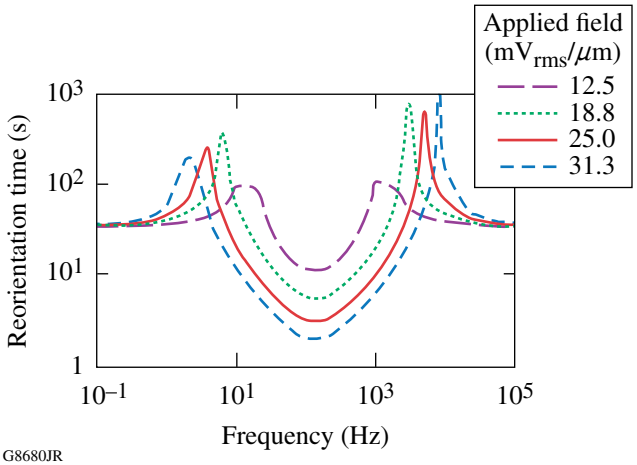

Figure 118.25
The reorientation time of a PCLC flake suspended in propylene carbonate ($\rho_p < \rho_h$ = 1200 kg/m^3) is examined as a function of driving voltage.

the extended model shows how the gravity term increasingly influences flake motion. As the electrostatic torque diminishes, it eventually cannot overcome gravity. For the condition where $\Gamma_E \sim \Gamma_G$, the reorientation time will approach infinity.

2. Relaxation Time

The inclusion of the gravity term in Eq. (1) provides a driving mechanism for motion of a reoriented flake when the electric field is removed, and it becomes possible to calculate the relaxation time t_{relax}. The relaxation time is defined as the time required for a flake to return from its "reoriented" position (typically $\theta_0 \sim 90°$) to its original position ($\theta_f \sim 0°$) once the electric field has been removed (Fig. 118.23 depicts a view of flake position). The hydrodynamic and the gravity terms are equated and, following the same procedure described previously, the relaxation time is determined:

$$t_{relax,i} = \frac{4\eta_0 \dfrac{\left(a_j^2 + a_k^2\right)}{\left(a_j^2 A_j + a_k^2 A_k\right)}}{\left|\rho_p - \rho_h\right| g a_j} \ln\left(\frac{1+\sin\theta}{\cos\theta}\right)_{\theta_0}^{\theta_f}. \qquad (7)$$

The relaxation time has a linear dependence on the host fluid's viscosity and an inverse dependence on the absolute difference between material densities. The flake's shape and orientation (with respect to the direction of gravity) also influence relaxation. When the density of the host fluid and the flake are matched, the relaxation time increases to infinity. Otherwise, the change in relaxation time is symmetric, decreasing as the absolute difference in densities between the two media increases. A comparison of the predicted relaxation times is given with experimental results in **Relaxation Time** (p. 84).

Experimental

The validity of the extended model is examined with experimental data for both reorientation and relaxation times of various PCLC flakes. Particle reorientation is observed in the standard particle/host fluid system of PCLC flakes suspended in propylene carbonate. Relaxation times are acquired for flakes suspended in various host fluids, so that the effect of the host fluid's density and viscosity can be studied.

1. Reorientation Time

The behavior of commercially produced, randomly shaped and sized polysiloxane PCLC flakes[8] in propylene carbonate is reproducible and well-documented.[1] Reorientation-time data presented by Kosc *et al.* were analyzed again and are shown in Fig. 118.26. PCLC flake reorientation was observed in a 44-μm cell gap at four driving voltages over a nearly three decade frequency range. The original gravity-free model (dashed lines) predicts reorientation times well. The extended theory continues to produce a good fit for some of the experimental data. This new model predicts vertical asymptotes at two specific frequencies, a feature that appears to coincide with the frequency band for which flake reorientation is experimentally observed at high driving fields. However, as the driving fields become lower, the extended model predicts longer reorientation times than those observed experimentally. Furthermore, the data no longer fit neatly within the frequency band between the vertical asymptotes or follow the asymptotes. This result suggests that, as the magnitude of the electrical torque diminishes, there is still some factor or effect that counteracts the gravity term and does not allow it to dominate as strongly as the extended theory predicts. Such a term may be related to the way in which the hydrodynamic torque term is utilized. The implicit assumption of steady rotation is not necessarily valid in the context of the obvious time-dependent rotation of the flake in the confine of space between the two electrodes. A similar observation can be made about the dependence of the hydrodynamic torque on the flake angle: one would expect that a flake parallel to the electrode would experience a different torque from the flake perpendicular to the electrodes when the electrode gap is comparable to the flake dimension; however, neither flake acceleration nor flake proximity to electrodes is considered in the theory.

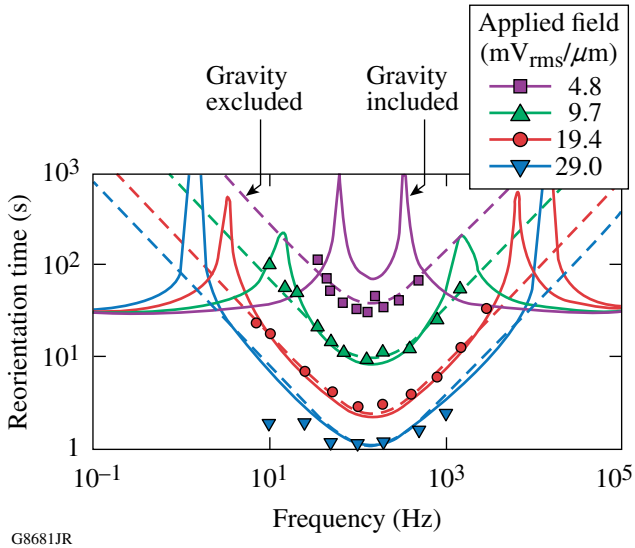

Figure 118.26
The reorientation times of a representative PCLC flake (semi-axes are a_1 = 17.5 μm, a_2 = 7.6 μm, and a_3 = 2.5 μm) suspended in propylene carbonate ($\rho_p < \rho_h$) are compared with the theoretical fit predicted by the original model (dashed lines) and the extended model (solid lines).

2. Relaxation Time

The relaxation time t_{relax} of flakes is investigated by suspending uniformly shaped and sized polysiloxane PCLC flakes manufactured in-house[4] in nine host fluids, including blends of propylene carbonate (PC) and the silicone oil E09, gamma-butyralactone (GBL), and ethylene glycol (EG) (Table 118.I). The densities and viscosities of neat (pure) fluids are tabulated from vendor literature. The density and viscosity values for the PC/E09 blends are based on use of the additivity law of mixtures (volume ratio is used) and literature values for the neat fluids.

Table 118.I: Properties of experimental neat and blended host fluids used for modeling are listed in order of decreasing density of the host fluid. The polysiloxane PCLC material is placed in the table for reference. Pure fluids are given in shadowed rows.

PC/E09	ρ_h (kg/m^3) at 20°C	η_0 (mPa • s) at 20°C	Relaxation time (min)
PC (Ref. 9)	1200	2.8	50 s
71/29	1141	5.2	2
GBL (Ref. 10)	1128	1.9	2
EG (Ref. 11)	1112	18	37
57/43	1112	6.3	12
54.5/45.5	1107	6.5	3
PCLC	1101	/	/
50/50	1098	6.9	15
33/67	1063	8.3	3
E09 (Ref. 12)	995*	11.0*	3

*Vendor data acquired at 25°C.

For all systems, the flakes are reoriented with an applied electric field of 40 $mV_{rms}/\mu m$, and the relaxation time is determined by measuring the time required for the flake to return to its original position once the driving field has been removed. Because the relaxation time is linearly dependent on the viscosity η_0 and the difference between the particle and host fluid density (ρ_p–ρ_h), the effect of both parameters can be considered independently. Both the densities and viscosities of these materials are temperature dependent. This temperature dependence introduces some uncertainty into the results because experiments are conducted at temperatures between 20°C and 23°C. Furthermore, the given relaxation times are a best estimate from observations of several flakes. Flake properties such as thickness and density are prone to variation because of their laboratory-based manufacturing process. Slight variations in these flake properties were most significant for systems where the host fluid's density was nearly matched with that of the PCLC flake or where the fluid viscosity was high, which for both cases results in long relaxation times.

To examine the effect of fluid density independent of fluid viscosity, the experimental and theoretical relaxation time data are divided by the fluid viscosity [Fig. 118.27(a)]. The predicted relaxation times show the easily recognizable inverse dependence on the (ρ_p–ρ_h) term in the denominator of Eq. (7). The experimental data agree well with the model, and flakes relax most quickly when the absolute magnitude of the difference between particle and fluid densities is the greatest. As the host fluid density of the PC/E09 mixtures approaches that of the PCLC flake, the relaxation times increase considerably. A similar analysis is performed to study the effect of the host fluid's viscosity. As shown in Fig. 118.27(b), the experimental data agree well with the predicted linear dependence of flake relaxation on fluid viscosity.

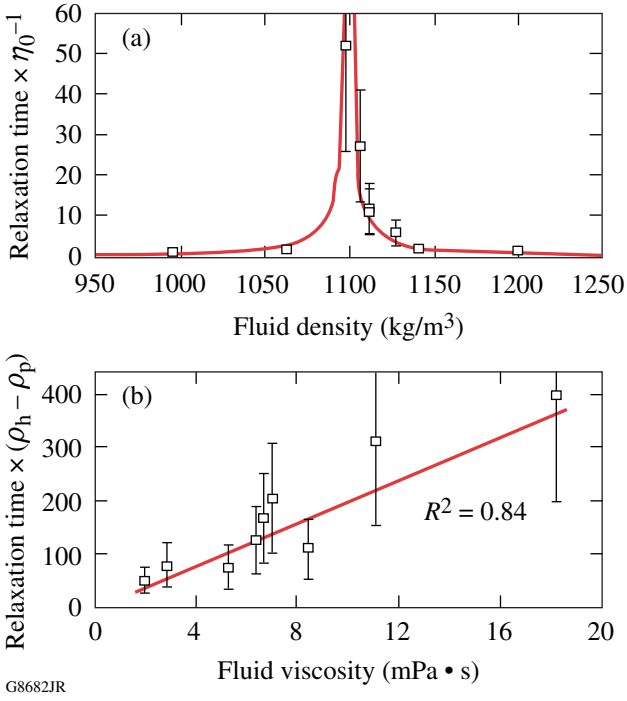

Figure 118.27
Relaxation times of a PCLC flake (semi-axes are $a_1 = 30\ \mu m$, $a_2 = 10\ \mu m$, and $a_3 = 2\ \mu m$) suspended in various host fluids are compared with the theoretical fit as a function of host fluid's (a) density and (b) viscosity. Error bars of 50% have been ascribed to the data.

Summary and Conclusions

The modeling of PCLC flake motion has been extended to include the effect of gravity in addition to the electrostatic

and hydrodynamic terms. The gravity term introduces vertical asymptotes, which, for high driving fields, appear to provide a boundary for the general frequency range in which flake motion is observed. For lower electric-field values, however, the model fit to the experimental data degrades, suggesting that additional terms might be needed to complete the model. The inclusion of the gravity term in the extended model provides, for the first time, a driving mechanism for modeling flake relaxation. Theory and experiment agree well in the demonstration of the relaxation time's linear dependence on the fluid viscosity and inverse dependence on the density difference between materials.

ACKNOWLEDGMENT

The authors would like to acknowledge the Laboratory for Laser Energetics at the University of Rochester for continuing support. This work was also supported by the U.S. Department of Energy Office of Inertial Confinement Fusion under Cooperative Agreement No. DE-FC52-08NA28302, the University of Rochester, and the New York State Energy Research and Development Authority. The support of DOE does not constitute an endorsement by DOE of the views expressed in this article.

REFERENCES

1. T. Z. Kosc, K. L. Marshall, S. D. Jacobs, and J. C. Lambropoulos, J. Appl. Phys. **98**, 013509 (2005).

2. G. P. Cox, K. L. Marshall, M. Leitch, C. Fromen, T. Knab, D. Berman, and S. D. Jacobs "Modeling Microencapsulation Effects on the Electro-Optic Behavior of Polymer Cholesteric Liquid Crystal Flakes," submitted to Advanced Functional Materials.

3. E. M. Korenic, S. D. Jacobs, S. M. Faris, and L. Li, Mol. Cryst. Liq. Cryst. **317**, 197 (1998).

4. A. Trajkovska-Petkoska, R. Varshneya, T. Z. Kosc, K. L. Marshall, and S. D. Jacobs, Adv. Funct. Mater. **15**, 217 (2004).

5. A. Trajkovska Petkoska and S. D. Jacobs, Mol. Cryst. Liq. Cryst. **495**, 334 (2008).

6. K. L. Marshall, K. Hasman, M. Leitch, G. Cox, T. Z. Kosc, A. Trajkovska-Petkoska, and S. D. Jacobs, in *2007 SID International Symposium*, edited by J. Morreale (Society for Information Display, San Jose, CA, 2007), Vol. XXXVIII, Book II, pp. 1741–1744.

7. T. B. Jones, *Electromechanics of Particles* (Cambridge University Press, New York, 1995).

8. Wacker-Chemie, Consortium für Electrochemische Industrie GmbH, Zielstattstrasse 20, D-81379 München, Germany.

9. C. M. Hansen, *Hansen Solubility Parameters: A User's Handbook*, 2nd ed. (CRC Press, Boca Raton, FL, 2007), p. 129.

10. Technical Leaflet, BASF Aktiegesellschaft, 67056 Ludwigshafen, Germany (2006).

11. Engineers Edge, Monroe, GA 30656. See http://www.engineersedge.com/fluid_flow_data.htm (2009).

12. Gelest, Inc., Morrisville, PA 19067.

Modeling the Effects of Microencapsulation on the Electro-Optic Behavior of Polymer Cholesteric Liquid Crystal Flakes

Introduction

Polymer cholesteric liquid crystal (PCLC) flakes are micrometer-scale platelets of PCLC material either generated by freeze fracturing of well-aligned, environmentally robust macroscopic PCLC films or formed in controlled shapes and sizes by means of a number of photolithographic, molding, or stamping techniques (Fig. 118.28).[1–3] Both processes rely on shear stress applied to the PCLC material surface during film or particle formation to align the helical molecular structure normal to the film surface. The unique temperature stability and optical properties of the parent films are preserved.

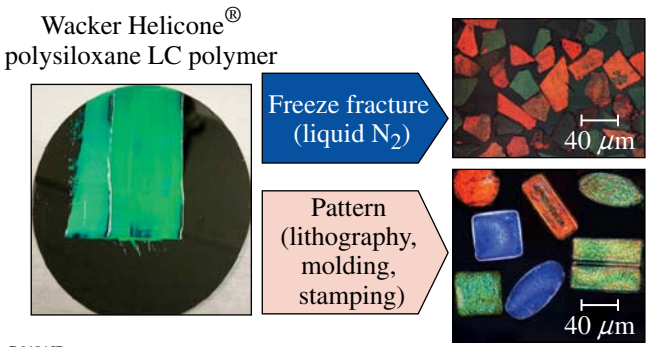

Figure 118.28
Methods for forming PCLC flakes from well-aligned parent films [blade-coated film on a 4-in.-diam polished silicon wafer (left), freeze fractured into flakes (top right)] or from shaped flakes made by soft lithography (bottom right).

First developed in the 1990s for passive optical applications, PCLC flakes display a Bragg-like (selective) reflection effect, where incident light of a specific wavelength and (circular) polarization component is strongly reflected from the flake to produce highly saturated, circularly polarized colors.[1] "Selective reflection" occurs when the incident light satisfies the condition $\lambda = \overline{n}\, p$, where $\overline{n}$ and p are the average refractive index and the helical pitch length, respectively, of the PCLC material. This selective reflection is caused by the helical structure inherent to the PCLC material and can be designed to reflect either left- or right-handed circularly polarized light, depending on the molecular structure of the PCLC polymers from which they are comprised. The individual color states depend on the flake's helical pitch length, which may be tuned from the deep UV (nanometer-scale) to the IR (micrometer-scale) region, including the entire visible spectrum. The polymeric structure effectively "locks in" the helical pitch, making the selective reflection colors insensitive to temperature over a very broad temperature range.

1. Application of PCLC Flakes to Switchable Particle Devices

Switchable particle-based technologies are of increasing interest for a number of applications as industry looks to develop products with unique optical properties and capabilities. An obvious application for reflective particles is information displays that require low power consumption and high brightness. As a result of their intrinsic selective reflection, PCLC flakes can provide bright, saturated colors without the need for additional color filters and polarizers.[4] Composite PCLC flake systems composed of either stacked left- and right-handed PCLC materials, or a half-wave-plate material sandwiched between two materials of the same handedness, can potentially lead to particle displays with reflectivities exceeding 80% (Ref. 5). A PCLC particle display does not require backlighting in daytime light conditions and would be uniquely suited for point-of-sale devices, portable devices, and flexible media on either flat or curved surfaces (e.g., large-area signs, automobile dashboards, heads-up displays, and electronic paper). Other potential applications include switchable and tunable devices for color manipulation (i.e., switchable or tunable color filters); switchable and tunable optical retarders or modulators for polarized light at desired wavelengths or bandwidths; switchable micropolarizers; switchable "smart windows" for either energy or privacy control; switchable coatings for use in decorative applications; and switchable coatings for applications in military security, camouflage, substrate reflectance control, document security, anticounterfeiting, and object tagging or identification.[6]

2. Electro-Optical Behavior of PCLC Flakes

Kosc *et al*. were the first to investigate the switchable behavior of irregularly shaped PCLC flakes in an applied electric field.[7–10] When flakes in an appropriate host fluid are subjected

to an ac electric field, flake reorientation occurs as a result of Maxwell–Wagner (MW) interfacial polarization. Charges accumulate at the interface of the flake and the fluid, inducing a dipole on the flake. The applied electric field then acts on that dipole to reorient the flake parallel to the electric field. Interfacial polarization is driven by the difference between the flake and fluid dielectric constants and conductivities. Devices containing these "polarizing pigments" suspended in a commodity dielectric host fluid (e.g., silicone oil) at concentrations ranging from 3 wt% to 5 wt% switch rapidly (<1 s) at very low voltages $\left(10 \text{ to } 100 \text{ mV}_{\text{rms}}/\mu\text{m}\right)$ (Refs. 4 and 11). Figure 118.29 shows the electric field–induced behavior of a PCLC flake/host fluid suspension in a typical, sandwich-cell geometry.[9,12] Figure 118.29(a) indicates the dimensions of the rectangular-shaped, 3:1-aspect-ratio polysiloxane PCLC flakes used for the work reported here.[2] With no field applied, the flakes lie nearly parallel to the substrates and selectively reflect one circularly polarized component of the incident light. An electric field applied to patterned electrodes produces flake reorientation by MW polarization and extinguishes the selective reflection color exposing the black back plane of the device [Fig. 118.29(c)]. The angle of rotation can range from ~10° to 90°, depending on the dielectric constant and conductivity of both the flakes and the host fluid; 15° of rotation is often sufficient to extinguish the reflectivity.

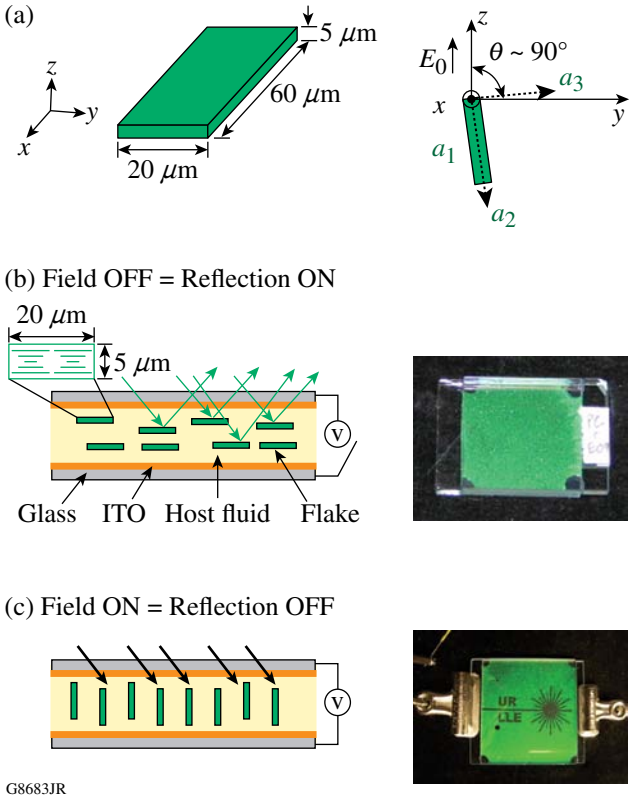

Figure 118.29
(a) Dimensions and coordinate system of a shaped PCLC flake. (b) Flakes lie approximately parallel to the cell substrates when no electric field is applied and appear colored as a result of selective reflection caused by the helical molecular structure of cholesteric liquid crystals, as depicted by the enlarged cross-sectional view of a flake. The longest axis is drawn into the page. (c) Flakes reorient with one long axis parallel to the applied field. As viewed from the incident light direction, rotated flakes appear dark since light is absorbed by the black back plane.

Trajkovska-Petkoska *et al.* extended this work to shaped flakes, layered flakes, and doped flakes.[3,13,14] Uniformly shaped flakes lead to more-uniform reorientation times in an applied electric field. When the difference between host and flake conductivities is increased by doping, faster reorientation times attributable to both rotational and translational motion in a dc regime are observed. A combination of translational and rotational motion is observed when the dopant is not uniformly distributed throughout the particle. In moderately conductive hosts, 90° flake orientation is observed in the dc regime. Trajkovska-Petkoska *et al.* also expanded upon the original reorientation time model developed by Kosc *et al.* by including a gravity term for modeling flake relaxation times upon removal of the electric field.[13,15] This expanded analytical model was used for the calculations presented here.

3. Microencapsulation of PCLC Flake/Fluid Host Suspensions

For PCLC flakes to achieve their potential in many switchable particle device applications, high-volume and low-cost manufacturing techniques such as roll-to-roll processing can be developed by microencapsulation.[16–23] Microencapsulation as applied to PCLC flakes involves suspending the PCLC flakes in a host fluid and then encapsulating this flake/host fluid suspension by either (1) forming discrete, optically transparent shells (capsules) from a dilute polymer encapsulation medium that can in turn be dispersed into the body of a film-forming transparent polymer or (2) emulsifying the suspension directly into the body of the film-forming polymer to form discrete capsules. Microencapsulation is necessary to prevent flake migration or agglomeration and to allow one to apply the flake/host fluid system to any surface (rigid, flexible, or curved). Application may take place by a number of means, including knife coating, die coating, roll coating, and printing via ink-jet techniques.

In this work, we report on a method to model and predict the electro-optic (EO) behavior of microencapsulated, shaped PCLC flakes. Experimental results are presented to confirm the validity of the modeling as a tool for developing systems for switchable-device applications.

Modeling and Devices

1. Materials Systems

The materials used in this work were chosen for a number of compelling reasons. All the materials selected are available commercially in large quantities and at low cost and are essentially nontoxic. The host fluids were chosen to span a wide range of dielectric constants and conductivities to include a range of small to large electric-field interactions. Both the aqueous and nonaqueous polymer binder solutions employed in this work are easily emulsified and cast with standard laboratory equipment. The photoresist and UV-curable epoxy were selected because of their resistance to the chosen host fluids and their ability to be processed with standard laboratory equipment. The materials used in this work and their properties are listed in Table 118.II.

2. Modeling Methodology

The electric field that acts directly on the PCLC flake influences its EO behavior. In an ac electric field, the strength of the rotational torque applied to the flake depends on

1. the effective electric-field strength acting on the flake
2. the strength of the MW polarization induced on the flake surface, which is controlled by
   a. the difference between the dielectric constants of the flake and host fluid
   b. the difference between the conductivities of the flake and host fluid

When a dc field is applied, the EO behavior results from either MW polarization or electrophoresis. The dominating effect will depend on

1. the intrinsic charge on the flake in the host fluid
2. the strength of MW polarization induced on the flake surface by the difference between the dielectric constants of the flake and host fluid
3. the effective strength of the electric field acting on the flake

The rotational reorientation of a PCLC flake is the result of a balance of torques applied to the flake.[13,15] The electrostatic torque Γ_E from the applied electric field acts to reorient the flake as shown when moving from the "field OFF" state [Fig. 118.29(b)] to the "field ON" state [Fig. 118.29(c)]. The resistance to rotation is the sum of the torques caused by the hydrodynamic force (Γ_H) and gravity (Γ_G):

$$\Gamma_E = \Gamma_H + \Gamma_G. \tag{1}$$

The Clausius–Mosotti factor $\left(K_i^*\right)$ is a measure of the strength of the effective polarization of the flake. This factor incorporates the dielectric constant and conductivity of both the PCLC flake (ε_p, σ_p) and host fluid (ε_h, σ_h), the depolarization factor of the flake (A_i), and the frequency of the applied electric field (ω):

Table 118.II: Properties of materials used for modeling and/or experiments.

Material	ε	σ (S/m)	ρ (kg/m^3)	η_0 (mPa • s)	Function
PCLC flakes*	2.2	1×10^{-9}	1100	n/m	Particle
SIT7757	2.7	3×10^{-8}	1070	35	Host fluid
DMS-E09	7.0	9×10^{-8}	995	9	Host fluid
Propylene carbonate	60.0	1×10^{-4}	1200	2	Host fluid
SU-8 3050 photoresist	3.2	2.13×10^{-8}	n/m	n/a	Well/cube (walls)
SU-8 2015 photoresist	3.2	2.13×10^{-8}	n/m	n/a	Cube (top/bot)
OG142-13 UV epoxy	6.9	2.8×10^{-7}	n/m	n/a	Adhesive
PVA	2.0	1×10^{-9}	n/m	n/a	Binder
Porcine gelatin	5.4	1.79×10^{-6}	n/m	n/a	Capsule shell
Gum arabic	6.5	1.08×10^{-4}	n/m	n/a	Capsule shell
PDMS	2.6	1×10^{-9}	1030	n/a	Binder

n/m = not measured
n/a = not applicable
*flake: L × H × D = 20 × 5 × 60 μm

$$K_i^* = \frac{\left(\varepsilon_p - i\frac{\sigma_p}{\omega}\right) - \left(\varepsilon_h - i\frac{\sigma_h}{\omega}\right)}{\left(\varepsilon_h - i\frac{\sigma_h}{\omega}\right) + A_i\left[\left(\varepsilon_p - i\frac{\sigma_p}{\omega}\right) - \left(\varepsilon_h - i\frac{\sigma_h}{\omega}\right)\right]}. \quad (2)$$

The electrostatic torque that drives flake reorientation may be written as a function of the flake's semi-axes (a_i, a_j, and a_k), the dielectric constant of the host fluid (ε_h), the imaginary portion of the Clausius–Mosotti factor $\left(K_i^*\right)$, the depolarization factor of the flake (A_i), the strength of the electric field applied to the flake (E_0), and the angle of the flake (θ) relative to the electric field:

$$\Gamma_{Ei} = \frac{4}{3}\pi a_i a_j a_k \varepsilon_h K_j^* K_k^* \left(A_k - A_j\right) E_0^2 \sin\theta\cos\theta = C_{Ei}\sin\theta\cos\theta. \quad (3)$$

The hydrodynamic torque (Γ_{Hi}) counteracts the electrostatic torque and may be defined as

$$\Gamma_{Hi} = \frac{16}{3}\pi a_i a_j a_k \eta_0 \frac{\left(a_j^2 + a_k^2\right)}{\left(a_j^2 A_j + a_k^2 A_k\right)}\Omega_i = C_{Hi}\Omega_i, \quad (4)$$

where a_i is the length of the flake semi-axes, η_0 is the host fluid viscosity, A_i is the depolarization factor of the flake, and Ω_i is the angular velocity of the flake about its axis. The torque caused by gravity (Γ_{Gi}) is specific to the configuration in which the experiments are conducted. In this work the test devices lie flat and the force of gravity acts in the $-z$ direction [Fig. 118.29(a)]. The gravitational torque is a function of the PCLC flake volume (V_p), density of both the flake (ρ_p) and host fluid (ρ_h), gravity (g), flake dimension (a_j) and the angle of the flake (θ) relative to the electric field [Fig. 118.29(a)]:

$$\Gamma_{Gi} = V_p\left(\rho_p - \rho_h\right) g a_j \cos\theta = C_{Gi}\cos\theta. \quad (5)$$

Substituting Eqs. (3)–(5) into Eq. (1) we can solve for the angular velocity of the flake

$$\Omega_i = \frac{d\theta}{dt} = \frac{C_{Ei}\sin\theta\cos\theta - C_{Gi}\cos\theta}{C_{Hi}}. \quad (6)$$

Equation (6) may then be integrated for the time to reorient the PCLC flake from an initial angle $\theta_0 \sim 0°$ to its final position $\theta_f \sim 90°$ as

$$\int dt = C_H \int \frac{d\theta}{C_E \sin\theta\cos\theta - C_G\cos\theta} \quad (7)$$

$$t = \frac{C_{Hi}}{C_{Ei}^2 - C_{Gi}^2}\left\{\begin{array}{l}\left(C_{Gi} - C_{Ei}\right)\ln\left[\cos\left(\frac{\theta}{2}\right) + \sin\left(\frac{\theta}{2}\right)\right] \\ -\left(C_{Ei} + C_{Gi}\right)\ln\left[\cos\left(\frac{\theta}{2}\right) - \sin\left(\frac{\theta}{2}\right)\right] \\ + C_{Ei}\ln\left[C_{Gi} - C_{Ei}\sin(\theta)\right]\end{array}\right\}_{\theta_0}^{\theta_f}. \quad (8)$$

To develop the analytical model shown above, a basic test cell with only a flake/host fluid suspension in the cell gap between the electrodes was studied in previous work to characterize PCLC flake motion in ac and dc electric fields (Fig. 118.29).[7,12–15] This type of cell is used as a baseline for the work reported here.

As the complexity of the cell design increases, the boundary conditions required for an analytical solution make it much more challenging to calculate the electric field applied to the flake. To account for the added boundary conditions created by the microencapsulation of the PCLC flake/host fluid suspension, another method must be found to model the electric field within the test cell. Finite-element-analysis–based software, Comsol Multiphysics (Comsol), offers a straightforward method to account for these boundary conditions in the calculation of the electric field acting on the PCLC flake. The calculation of the electric field combined with the analytical model enables one to predict PCLC flake motion caused by MW polarization in an electric field for complex cell geometries.

Finite-element-analysis–based software was used to analyze the electric field for six types of test cell configurations with three types of host fluids for each configurational variant. The six configurations studied are illustrated in Fig. 118.30. The *basic* cell [Fig. 118.30(a)] with only a flake/host fluid suspension in the cell gap is used as a baseline for our work. The *microwell* cell [Fig. 118.30(b)] adds vertical walls (composed of photoresist) to the cell gap to constrain the flake/host fluid suspension. The fluid is still in contact with the electrodes as in the basic cell and the electric field experiences a *continuous* material path between the electrodes just as in the basic cell. The *microcube* cell [Fig. 118.30(c)] builds on the microwell configuration of Fig. 118.30(b) by adding a layer of photoresist above and below the host fluid that creates a *discontinuous* path for the electric field between the electrodes. For *direct encap-*

sulation cells, two possible methods of assembly are shown. *Direct encapsulation type I* [Fig. 118.30(d)] has the flake/host fluid constrained in a capsule. The path for the electric field is both discontinuous and nonuniform because the curved edges of the capsule are parts of the path between the electrodes. This configuration also includes a layer of epoxy adhesive used for assembly between the binder layer and the top electrode. *Direct encapsulation type II* [Fig. 118.30(e)] also has the flake/host fluid suspension constrained in a capsule similar to type I except there is no adhesive layer between the binder layer and top electrode. Finally, the *coacervation* cell [Fig. 118.30(f)] represents a device that, once assembled, is very similar to the direct encapsulation devices. Here there is an additional discontinuous material forming a separate capsule shell that further complicates the path of the electric field.

The different encapsulation types are intended to show an evolution of complexity in moving from a test cell with only a flake/host fluid suspension in an applied electric field to a flake/host fluid suspension microencapsulated within discrete gelatin capsules. Figure 118.31(a) illustrates a coacervation-type test cell (gelatin capsules) used for electro-optic characterization; the gelatin capsules have been dispersed into a separate film-forming polymer binder, coated onto an indium tin oxide (ITO)–coated substrate and then attached to a second substrate with a UV-cured epoxy. Figure 118.31(b) represents a 2-D cross section of the cell to be modeled. Figure 118.31(c) is

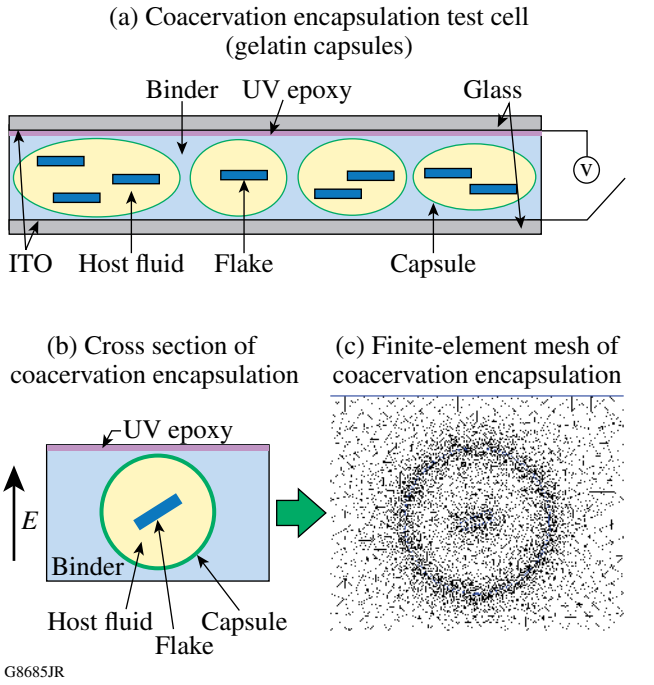

Figure 118.31
(a) Illustrated cross section of a gelatin-gum arabic microcapsule test cell, a more-complex version of the configuration shown in Fig. 118.29 that is based on Fig. 118.30(f); (b) the equivalent cross section for analysis with fluid, flake, gelatin-gum arabic capsule, UV epoxy and polymer binder boundaries in the cell gap; (c) finite-element mesh of the coacervation test cell cross section generated with Comsol Multiphysics.

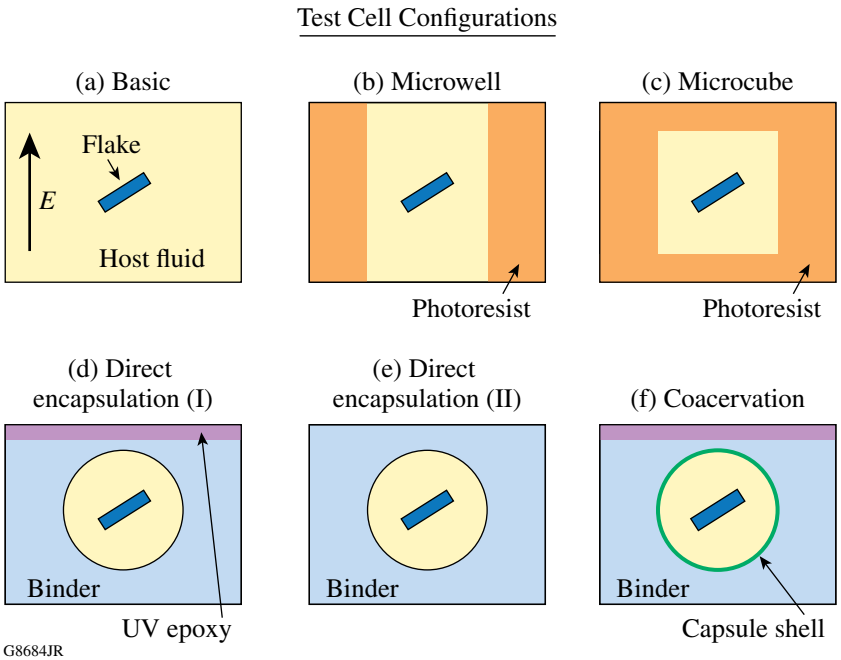

Figure 118.30
Six configurations of PCLC flake test cells studied. (a) Basic cell: Contains only a flake/host fluid suspension in the cell gap. (b) Microwell: Insulative vertical walls (photoresist) confine the flake/host fluid suspension within the well; fluid is in contact with electrodes. (c) Microcube: The cube (photoresist) fully encapsulates the flake/host fluid suspension; fluid is not in contact with electrodes. (d) Direct encapsulation (I): A polymer binder (capsule) fully encapsulates the flake/host fluid suspension. The fluid is not in contact with the electrodes, and there is an epoxy layer between the polymer binder and the top electrode. (e) Direct encapsulation (II): The polymer binder (capsule) fully encapsulates the flake/host fluid suspension. The fluid is not in contact with electrodes and there is no epoxy layer between polymer binder and top electrode. (f) Coacervation encapsulation: A polymer binder surrounds a capsule, a thin shell of material different than the binder layer, which fully encapsulates the flake/host fluid suspension. The fluid is not in contact with electrodes and there is an epoxy layer between the polymer binder and the top electrode.

the matching finite-element mesh generated within Comsol, using the "In-Plane Electric Currents" module to analyze the electric field. The gelatin-type capsule with a UV epoxy layer in this configuration is the most complex material set studied in this work.

To model each of the test configurations, a representative 2-D cross section is generated using the Comsol module. Each sub-domain (geometric section) is assigned a value for conductivity, dielectric constant, and thickness in the $-x$ direction (into the plane of the page, as shown in Fig. 118.29). The glass substrates and ITO layers are not included in the model. An ac voltage (7.5 V_{rms} unless noted) is applied to the lower boundary (electrode) of the model and the top boundary (electrode) is set to ground potential. The side boundaries are defined as electrically insulating. The ac frequency is set at 100 Hz and the overall cell gap is 150 μm unless noted other-wise. The flake angle, with respect to the electrode, is fixed at 20° to calculate the electric field for all configurations. The critical cell dimensions, materials, and their properties used in each configuration are listed in Tables 118.II and 1118.III. The flake dimensions are as shown in Fig. 118.29(a). For direct comparison of microencapsulation effects on the electric field, only the materials' properties of SU-8 3050 photoresist were used to model photoresist as well as binder layers, even though experiments were conducted with binders made from SU-8 3050, SU-8 2015, PVA (polyvinyl alcohol), and polydimethylsiloxane (PDMS). All four materials have low conductivity and dielectric constant; using only SU-8 3050 for modeling makes the comparison between microencapsulation types straightforward and does not significantly affect the results.

As shown in Fig. 118.31(c), the model is divided into a continuous mesh of finite elements. Each configuration includes a sub-domain of the host fluid in a 1-μm-thick area immediately surrounding the flake. The normal component of the electric field $\left\{\text{e.g., } E_0 = \text{sqrt}\left[(E_z)^2 + (E_y)^2\right]\right\}$ is integrated over this sub-domain to calculate the value of the electric field acting on the flake due to the boundary conditions for each configuration. The analytical model, however, assumes $E_0 \sim E_z$ because E_y is perpendicular to the electrodes from which the electric field is applied. For ease of calculation in this work, the normal component is used as a reasonable approximation for E_0 because $E_z \geq 10\ E_y$, as verified in Comsol over a variety of boundary conditions. For the basic cell, this integration is not necessary because the medium in the cell gap (and thus the electric field) surrounding the flake is homogenous, but this step becomes important when the flakes are encapsulated. Once the electric

Table 118.III: Test cell configuration dimensions and materials used for modeling.

Configuration	Cell gap (μm)	Wall height (μm)	Wall width (μm)	Top/ bottom thickness (μm)	Capsule diam (μm)	Capsule shell thickness (μm)	Epoxy layer thickness (μm)	Wall material	Top/ bottom layer material	Binder material	Capsule material
Basic^{+++}	150	n/a	n/a	n/a	n/a	n/a	n/a	n/a	n/a	n/a	n/a
Microwell^{+++}	150	150	50	n/a	n/a	n/a	n/a	SU-8	n/a	n/a	n/a
Microcube^{+++}	150	150	50	20	n/a	n/a	n/a	SU-8	SU-8	n/a	n/a
Direct Encapsulation (I)$^{++,\#}$	190	n/a	n/a	n/a	100	n/a	40	n/a	n/a	PVA/ SU-8	n/a
Direct Encapsulation (II)$^{+,\#}$	150	n/a	n/a	n/a	100	n/a	n/a	n/a	n/a	PDMS/ SU-8	n/a
Coacervation^{++}	190	n/a	n/a	n/a	100	1	40	n/a	n/a	PVA	Gelatin-gum arabic

n/a = not applicable

$^{+}$Propylene carbonate host fluid tested

$^{++}$SIT7757, DMS-E09 host fluids tested

$^{+++}$SIT7757, DMS-E09, propylene carbonate host fluids tested

$^{\#}$SU-8 3050 material properties used for modeling to allow one to directly compare microencapsulation types

field acting on the flake has been calculated, this value is input into the analytical model developed previously.[13,15] The analytical model results are then calculated using Mathematica software (Wolfram Research) to evaluate the PCLC flake reorientation times as a function of the electric field's amplitude and frequency and the physical properties of the flake/host fluid system.[13,15]

3. Device Preparation

A minimum of two prototype test cells for each of the six configurations shown in Fig. 118.30 were prepared and evaluated for EO flake behavior. Each prototype was similar to the devices shown in Fig. 118.29, but without patterned electrodes. All of the devices were made using rectangular, 3:1-aspect-ratio polysiloxane PCLC flakes [see Fig. 118.29(a)].[2] Sources for all materials and preparation methods for each configuration are identified below.

The PCLC material is a non-crosslinked cyclic polysiloxane (Wacker-Chemie GmbH, Munich, Germany) with a glass transition temperature T_g between 40°C and 50°C. The PCLC flakes were made by soft lithography using a patterned silicon wafer[24] to make a mold from a two-part PDMS molding formulation.[25] The PCLC material was blade coated into the mold at 195°C (Refs. 2,3).

Propylene carbonate (99.5%, Acros Organics) was used as a host fluid with high dielectric constant and conductivity. DMS-E09 (Geleste) was used as a host fluid with moderate dielectric constant and conductivity. SIT7757 (Geleste) was used as a host fluid with low dielectric constant and conductivity.

Electro-optical test cells were fabricated using 25-mm × 25-mm × 3-mm ITO-coated substrates (Thin Film Devices), cleaned by a detergent wash (Extran MA 02, EMD Chemicals). The basic test cells used 80-μm microspheres (Duke Scientific) mixed into EPO-TEK OG 154 UV curing epoxy (Epoxy Technology) to set the test cell's gap spacing. A drop of OG-154 epoxy/microspheres mixture was applied to the corners of the cell, with the substrates offset so that clips could be attached for electrical connection to the cells. The ac voltage was supplied from a Stanford Research function generator, model DS345, and an HP 6827A Bipolar Power Supply/Amplifier. The dc voltage was supplied by a Fluke High Voltage Power Supply model 412B. A Blak Ray Longwave UV lamp, model B 100AP, was used to cure the epoxy at 365 nm. The two outside edges of the cell were sealed with epoxy and cured. The cell was filled with flake/host fluid suspension (~1% flakes) by capillary action and the remaining two edges sealed with epoxy and cured.

Microwell cells were made by spin coating SU-8 3050 photoresist (MicroChem) at 1000 rpm onto ITO-coated substrates. The microwells were photo-patterned into the SU-8 3050 using a chrome mask (Semiconductor/Microsystems Fabrication Laboratory, RIT) and Blak Ray Longwave UV lamp, model B 100AP. The wells were developed and edge bead was removed using a MicroChem Developer Solution. Next, a drop of OG-154 epoxy without microspheres was applied to the corners of the cell. The microwells were filled with a flake/host fluid suspension by flood coating the microwells and using the top substrate to squeeze out the excess flake/host fluid suspension to an unpatterned area. The cell gap is set by the height of the microwells. The substrates were aligned such that the top and bottom substrates were offset so that clips could be attached for electric connection to the cells from the Stanford Research function generator and ac amplifier or dc power supply. The OG 154 epoxy at the corners of the cell was partially cured; then the cell was edge sealed with epoxy and fully cured.

The microcube cells were constructed following the same procedure as the microwell cells except that a 20-μm layer of SU-8 2015 photoresist (MicroChem) was spin coated onto the top and bottom substrates and exposed and developed before the microwells were photo-patterned onto the bottom substrate. The assembly procedure for the microcube devices is the same as that for the microwell devices described earlier.

Direct encapsulation cells were made by emulsifying the flake/host fluid suspension (~1% PCLC flakes) into a 20% aqueous solution of 80% hydrolyzed PVA (Aldrich Chemical). Emulsification was accomplished with low shear by adding a total of 1 g of the components into a 4-ml vial and rotating at ~45 rpm for 15 min. A portion of the emulsion, which depends on the size of the substrate to be coated, was then cast by hand onto an ITO-coated substrate and left to dry for 24 h. Once dry, OG142-13 UV epoxy (Epoxy Technology) was applied to the top of the PVA film; the second substrate was then applied and the cell cured with UV light (365 nm).

The complex coacervation cells were made in two steps: (a) the flake/host fluid suspension was microencapsulated by complex coacervation into gelatin-gum arabic capsules; (b) the capsules were dispersed into a polymeric binder and made into a test cell. Microencapsulation was accomplished by emulsifying 3 g of the flake/host fluid suspension into 6 g of a 1% aqueous solution of gum arabic (Aldrich Chemical) at 55°C using a high-shear mixer (IKA Ultra Turrax Tube Disperser, Cole-Parmer Instrument). Then 6 g of a 1% solution of porcine gelatin (Aldrich Chemical) were added and further emulsified,

and the temperature was reduced to 41°C. Next, the emulsion was diluted by the drop-wise addition of 50 g of water. The pH was then reduced to 4 by the drop-wise addition of 30 g of a 0.2% aqueous solution of acetic acid to induce coacervation. Coacervation continued for 30 min and then the batch was cooled to 5°C. Agitation was continued for 40 min and then the hardening agent, 10 g of a 5% aqueous solution of glutaraldehyde, was added drop-wise. Agitation continued for 1 h and then 100 g of a 4% aqueous solution of NaOH was added drop-wise to raise the pH to ~10 and complete the hardening reaction. The batch of finished capsules was then warmed to room temperature, being dispersed with low shear into 1 g of a 20% aqueous solution of PVA. A film of the dispersion was then cast by hand onto an ITO substrate, and the cell was prepared following the same procedure as a direct encapsulation cell.

4. Characterization

Each device was tested within 48 h after assembly to reduce the effect of aging on the test cell. Aging may increase the reorientation time of PCLC flakes if the ITO electrodes are not insulated from the host fluid.[13] The flake motion and response times were characterized by streaming video with time stamping using a Leitz Orthoplan polarizing optical microscope (POM) (Wetzlar, Germany) in reflection mode coupled with a MicroPix C1024 CCD camera and Streampix software (CCD Direct).

Optical images were taken using a Leica DMXR POM (Leica Microsystems) in reflection mode coupled with a Q-Imaging Retiga 4000R Fast camera and QCapture Pro software (Media Cybermetics).

The dielectric properties of each test cell and selected materials were measured using a Solartron 1260 Impedance Gain-Phase Analyzer (Solartron Analytical) and collected with Zplot and Zview (Scribner Associates) PC interface software.

Results and Discussion

1. Effect of Cell Geometry on the Electric Field

The environment (cell geometry) surrounding the flake has a large effect on flake motion because it can influence the strength of the applied electric field, which is directly proportional to the electrostatic torque applied to the flake. We calculated the effect of the cell geometry (device configuration) on the electric field while keeping the properties of both the fluid and the flake constant. Figure 118.32 shows the Comsol modeling results for four configurations where a PCLC flake is suspended in the high dielectric constant host fluid propylene carbonate (PC) in a 150-μm-thick test cell with an applied electric potential of 7.5 V_{rms}. The material properties of the photoresist SU-8 3050 were used to model the microwell/microcube walls and the direct encapsulation binder to enable one to directly compare the electric fields between the device geometries. The resulting plots of the electric fields are shown as the test cell geometry changes from a basic configuration [Fig. 118.32(a)] to a direct encapsulation type-II cell [Fig. 118.32(d)].

When the path of the electric field between the electrodes encounters constant material properties, as in both the basic and microwell configurations, a strong electric field is present in the cell gap [Figs. 118.32(a) and 118.32(b)]. This is characterized by the dark gray areas throughout most of the cell gap. A slight drop of the electric field in localized areas around the flake is denoted by a light gray. Additionally, if the dielectric constants and conductivities of the host fluid and PCLC flake are very different, the model predicts a high electrostatic torque on the flakes. When the path of the electric field between the electrodes does not encounter constant material properties, as in both the microcube and direct encapsulation type-II configurations [Figs. 118.32(c) and 118.32(d)], the model prediction depends on the material properties of the system. When the electric field passes from a low-dielectric-constant material such as SU-8 3050 (ε = 3.2) into a high-dielectric-constant material such as PC (ε = 60), the electric field drops off dramatically. This is seen as regions of very dark gray surrounding the flake in the microcube and direct encapsulation type-II examples [Figs. 118.32(c) and 118.32(d)]. In such cases, even when the dielectric constant and conductivity mismatch between PC and PCLC is large, the flake will experience low electric-field strength and therefore low electrostatic torque. This represents a nonfunctional device configuration.

In addition, a distortion in the electric field results as it encounters material composition changes that are non-normal to the direction of the electric-field orientation. This phenomenon is apparent in both the microcube example at the corners of the microcube and the direct encapsulation example near the edges of the capsule wall [Figs. 118.32(c) and 118.32(d)], where the arrows denoting the electric field are at an angle to, rather than perpendicular to, the top electrode.

2. Effect of Host Fluid on the Electric Field

If the cell geometry is held constant and several host fluids are considered, an equally dramatic effect is observed in the effective electric-field strength as it passes from a region of low to high dielectric constant. In Fig. 118.33, from left to right, a microcube cell is shown with the host fluid properties

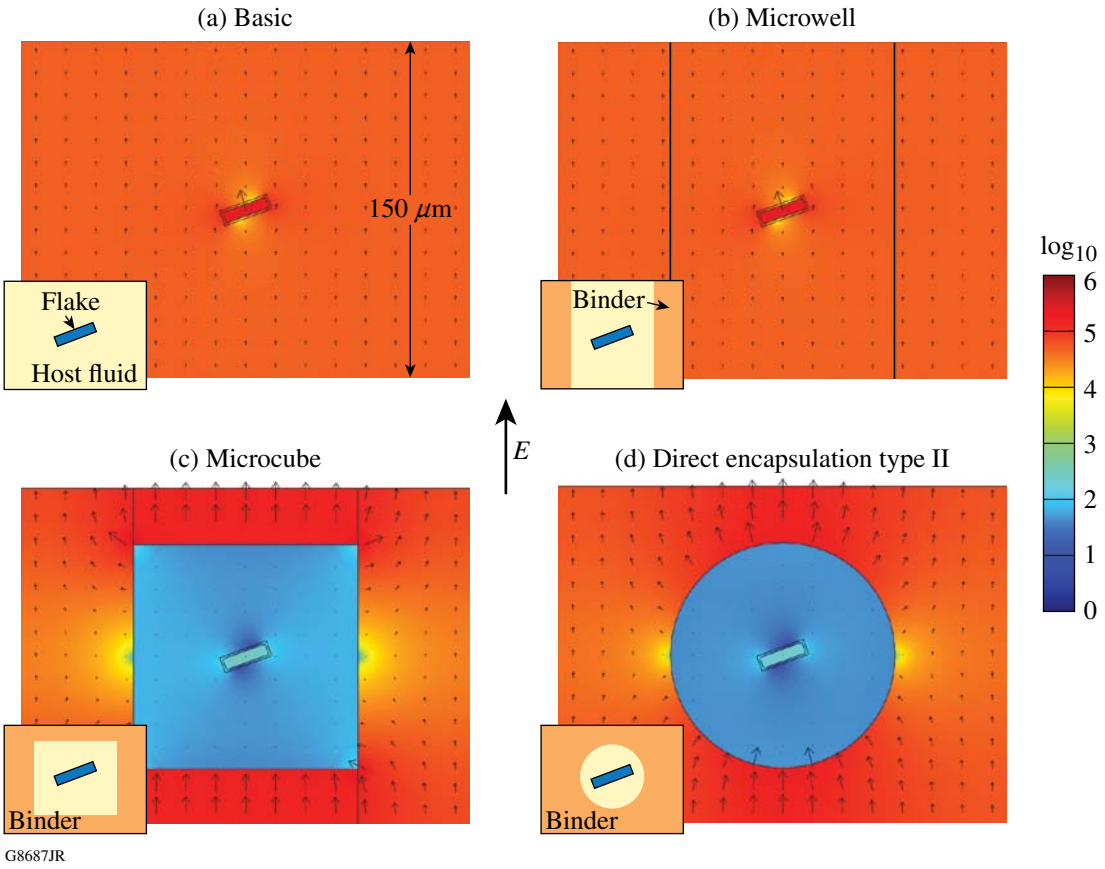

Figure 118.32
Comsol Multiphysics output of the electric field as a function of test cell geometry (insets highlight geometry). The fluid surrounding the flake has the properties of propylene carbonate ($\varepsilon = 60$), the flake is PCLC ($\varepsilon = 2.2$), the encapsulating material (binder) is SU-8 3050 ($\varepsilon = 3.2$), and the applied voltage to the 150-μm-thick cell is 7.5 V_{rms}. The direction and size of the arrows represent the direction and strength of the electric field, the surface plot density also represents the strength of the electric field, and the scale range is 0 (black) to 10^6 (white) V/m. (a) Basic and (b) microwell configurations have strong uniform electric fields because the materials in the path of the electric fields have uniform dielectric properties. (c) Microcube and (d) direct encapsulation configurations have non-uniform electric fields because materials in the path of the electric fields have dissimilar dielectric properties. Note the electric-field distortion (arrow directions at an angle) near the corners and edges of the microcube and capsule in direct encapsulation.

changing from low ε and σ [e.g., SIT7757: $\varepsilon = 2.7$, $\sigma = 10^{-8}$, Fig. 118.33(a)] to moderate ε and low σ [e.g., DMS-E09: $\varepsilon = 7$, $\sigma = 10^{-8}$, Fig. 118.33(b)] to high ε and σ [e.g., PC: $\varepsilon = 60$, $\sigma = 10^{-4}$, Fig. 118.33(c)]. For all three cells the applied electric potential was 7.5 V_{rms}, the cell thickness was 150 μm, and the flake angle θ was set to 20°. Field strength and, therefore, color within the microcube and adjacent to the flake change from high (light gray) to moderately high (gray) to low (dark gray).

The effect on the magnitude of the electric field combined with the dielectric constant mismatch can be seen in Fig. 118.33(d), where the predicted reorientation times are plotted corresponding to the microcube cells shown in Figs. 118.33(a) and 118.33(b). As seen in Fig. 118.33(d), SIT7757 has a higher electric field acting on the flake, but with a similar dielectric constant to the flake a longer reorientation time results. Although DMS-E09 has a lower effective electric field, it has a greater difference in dielectric constant with the flake and therefore a faster reorientation time. No curve was plotted for PC as the host fluid in Fig. 118.33(c) because the electric field acting on the flake was so small that no reorientation took place. This is a nonfunctional material combination.

The ac electric field had a range of frequencies over which the induced charge buildup at the flake/host fluid interface caused by MW polarization had the mobility needed to form an induced dipole on the flake. The electric field then acted on the induced dipole to reorient the flake. In Fig. 118.33(d), when the frequency of the electric field was matched to the charge mobility, a minimum reorientation time was achieved. The

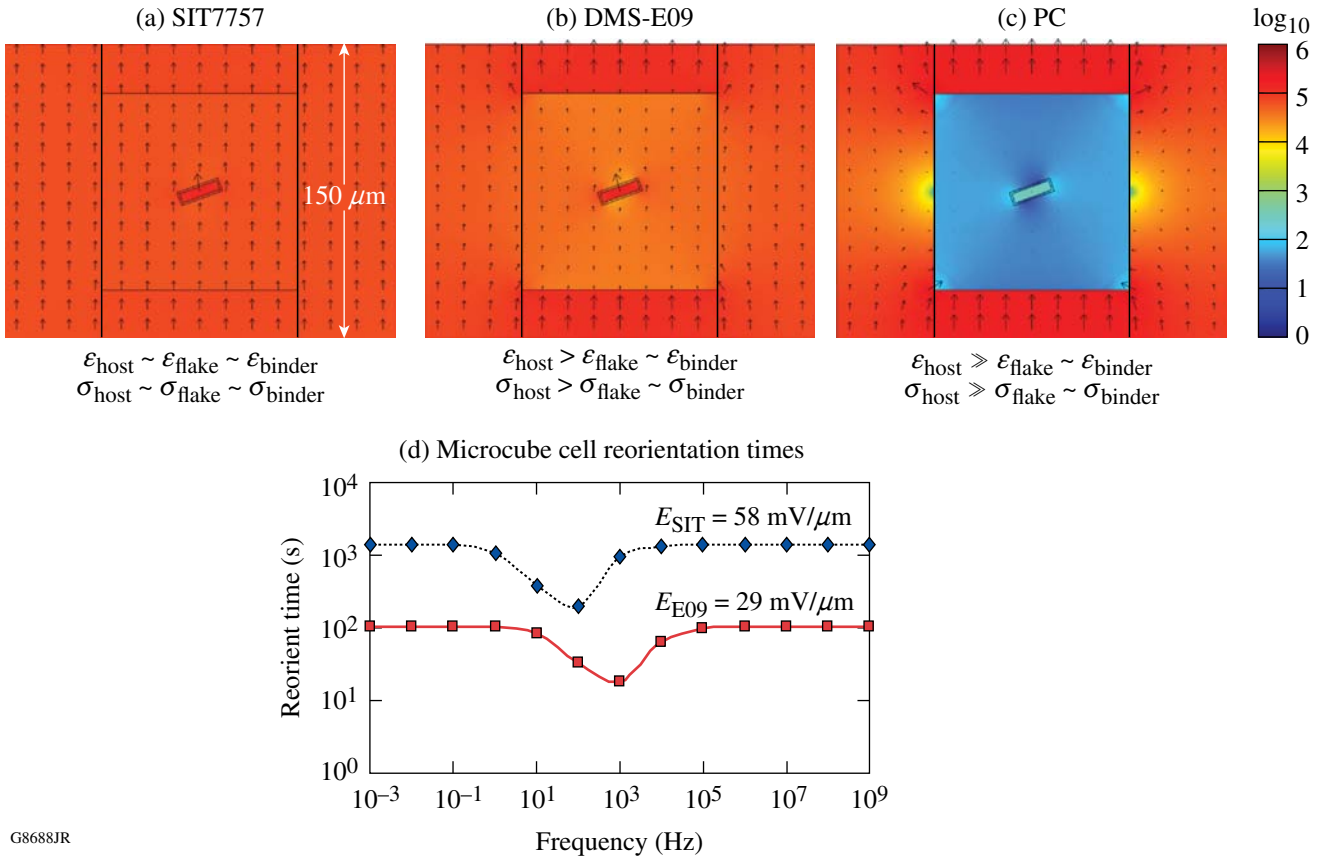

Figure 118.33
Electric field as a function of fluid properties in a microcube cell. The direction and size of the arrows represent the direction and strength of the electric field; the surface plot density also represents the strength of the electric field; and the scale range is 0 (black) to 10^6 (white) V/m. (a) Low ε, σ (SIT7757), (b) moderate ε, σ (DMS-E09), and (c) high ε, σ (PC). (d) A corresponding plot of predicted reorientation times for SIT7757 and DMS-E09 with an applied potential of 7.5 V_{rms} to a 150-μm-thick cell as a function of ac frequency and type of host fluid. The terms E_{SIT}, E_{E09} are the calculated electric fields acting on the PCLC flake for each host fluid. No curve for PC is shown because E_{PC} is insufficient to reorient the flake (see text).

particular range of frequencies at which reorientation occurs depends on the composition of the materials system, as seen in Fig. 118.33(d). The SIT 7757 oil has a minimum predicted reorientation frequency of ~200 Hz, while DMS-E09 has a minimum predicted frequency of ~1000 Hz.

Experimental evidence shows that, independent of the host fluid, as reorientation time increases, there is a point at which no physical reorientation will take place. The electrostatic torque on the flake is not enough to overcome counteracting forces such as electrostatic attraction to a surface. Therefore, reorientation will not physically be observed for a PCLC flake in SIT7757 oil, even though a minimum reorientation time of ~120 s is predicted in Fig. 118.33(d). Reorientation of PCLC flakes in DMS-E09 oil, however, is expected near 1000 Hz with response times <60 s.

For PC, the analytical portion of the model predicts an unrealistic *negative*-frequency–independent response for the reorientation time and therefore it is not plotted in Fig. 118.33(d). When the electric field becomes insufficient to reorient the flake, the analytical model will predict a reorientation time <0, indicating flake reorientation in a negative direction (to $\theta \sim 0°$) as a result of the gravitational torque.[13,15]

3. Material and Geometry Selection for Increased Electrostatic Torque

Additional modeling was conducted to determine how PCLC flake/host fluid suspensions would behave in microencapsulated geometries resembling electrophoretic (EP)-type devices.[18,19,26,27] Figure118.34(a) shows a direct encapsulation type-II cell configuration resembling a typical EP device that consists of a PCLC flake in a low-dielectric-constant

fluid that has been encapsulated into a low-dielectric-constant film-forming binder. The resulting high electric field is nearly uniform because the dielectric constants and conductivities of all components are similar. For an EP device, a system with low dielectric constants and conductivities is ideal. For a PCLC flake device, however, both high electric-field penetration and dielectric mismatch of the fluid and particle are needed for MW reorientation to occur. Therefore, the device pictured in Fig. 118.34(a) is nonfunctional.

One obvious way to achieve high electrostatic torque in a direct encapsulation type-II configuration is to microencapsulate a low-dielectric-constant PCLC flake and a moderate-dielectric-constant host fluid within a film-forming binder with a moderate dielectric constant, as shown in Fig. 118.34(b). The slightly darker gray region within the capsule and adjacent to the flake denotes a high electric-field strength. The strong electric field combined with the mismatch in dielectric constant between the flake and the host fluid leads to a functional,

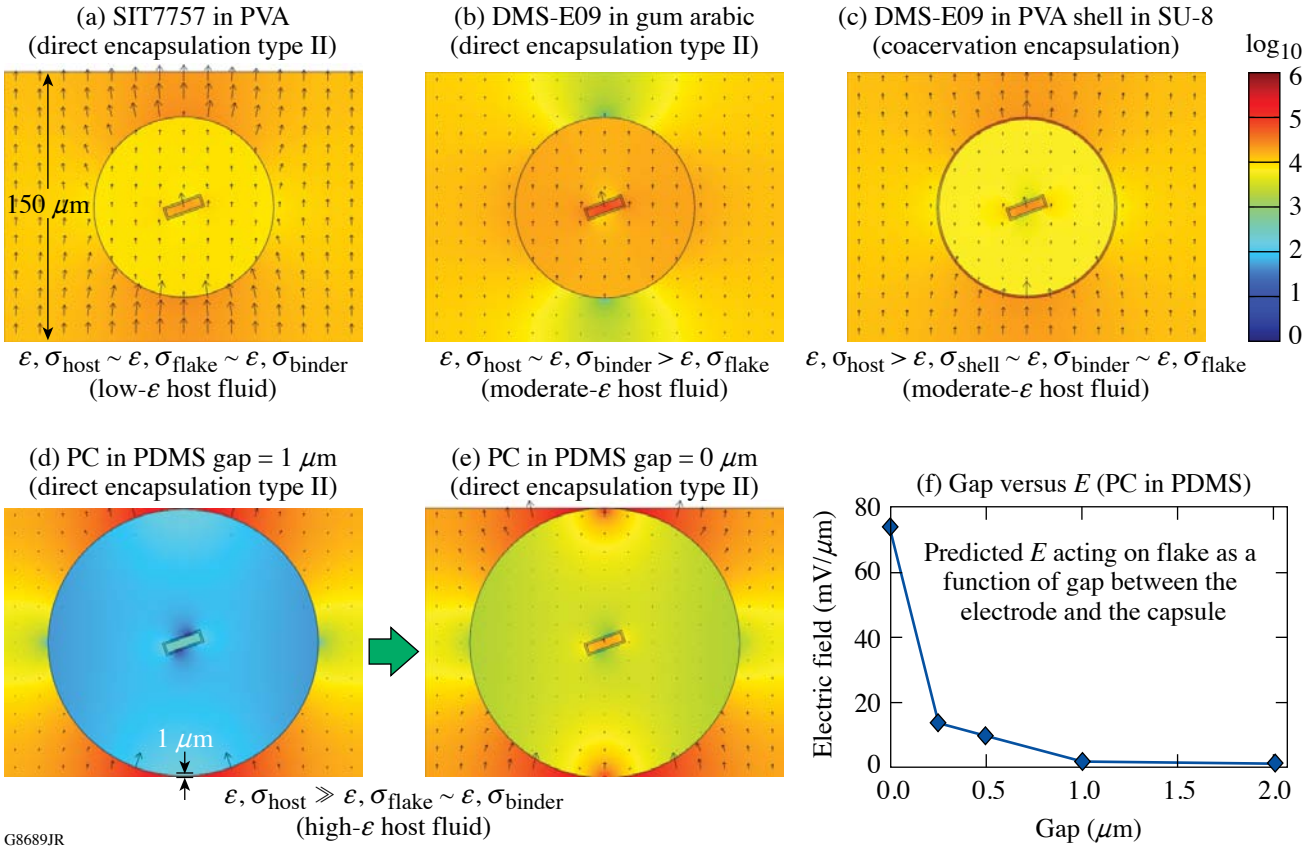

Figure 118.34
Material and geometry effects of microencapsulation on the electric field at an applied potential of 7.5 V_{rms} for a 150-μm cell gap. The bar scale for the electric field's magnitude on all plots has a range of 0 (black) to 10^6 (white) V/m. (a) PCLC flake suspended in a low-dielectric-constant host fluid encapsulated in a low-dielectric-constant binder (e.g., SIT7757 in PVA) shows high electric-field magnitude in the host fluid. (b) PCLC flake suspended in a moderate-dielectric-constant host fluid encapsulated in a moderate-dielectric-constant binder (e.g., DMS-E09 in Gum Arabic) shows high electric-field magnitude in the host fluid. (c) PCLC flake suspended in a moderate-dielectric-constant host fluid encapsulated in a low-dielectric-constant capsule, with a 1-μm-thick wall, dispersed in a moderate-dielectric-constant binder (e.g., DMS-E09 encapsulated in a PVA capsule dispersed in a SU-8 3050 binder) shows high electric-field magnitude in the host fluid. (d) PCLC flake suspended in a high-dielectric-constant host fluid directly encapsulated in a low-dielectric-constant binder (e.g., PC emulsified into a PDMS binder) with a 1-μm gap between the electrodes and capsule wall shows low electric-field strength in the host fluid. (e) PC emulsified into a PDMS binder, as in (d), but now the capsule bridges the gap between the electrodes, resulting in a moderate electric-field magnitude in the host fluid. (f) Plot showing the increase in electric-field magnitude as the gap between the capsule wall and electrode decreases. The difference in the plots of electric-field strength for (a), (b), and (c) is caused by material changes only.

MW-driven PCLC flake device. The distortion of the electric field near the poles [i.e., darker areas above and below the capsules shown in Fig. 118.34(b)] is caused by abrupt changes in dielectric properties along the path of the electric field between electrodes. At the capsule's closest point to the electrodes, the electric-field lines are perpendicular to the capsule and the change in the electric field is the greatest.

An added level of sophistication that would improve process flexibility is to encapsulate the flake/host fluid suspension in a capsule shell of a different material than that of the binder prior to dispersing into a film-forming binder. Such a system would create a greater choice in polymer binders. Concerns such as poor capsule formation caused by miscibility of the host fluid in the binder or a wide distribution of capsule sizes present because of nonuniform mixing, are no longer an issue because the capsules are created in a prior process. Figure 118.34(c) shows this type of configuration (coacervation encapsulation) with the flake/host fluid suspension encapsulated in a capsule shell composed of PVA. For the material set indicated, the polymer binder (SU-8 3050) and host fluid (DMS-E09) are miscible with each other and require the flake/host fluid suspension to be encapsulated before being dispersed in the polymer binder. In Fig. 118.34(c), this material combination is shown to give a moderately high electric field acting on the flake. As in previous examples, care must be taken when selecting materials. If a capsule shell with too high a dielectric constant is used, it will shield the host fluid and flake from the electric field and result in a nonfunctional device. A further level of sophistication can also be added to customize the capsule shells; additives may be incorporated to promote flake bistability or charge control.

Another less-obvious way to make a functional device is to use an approach that is similar to the nonfunctional direct encapsulation type-II configuration in Fig. 118.32(d). A host fluid with higher dielectric constant (PC) can be directly encapsulated into an immiscible low-dielectric-constant binder (PDMS) and still result in a functional device if the gap between the electrode and capsule wall is very small (<1 μm). As seen in the transition from Figs. 118.34(d) to 118.34(e), the electric field can be greatly enhanced within the host fluid if the capsule is in contact with the cell electrode. As shown by the plot in Fig. 118.34(f), the greater the portion of the cell gap that is filled by the capsule, the higher the magnitude of the electric field acting on the PCLC flake. A gap of 2 μm between the capsule and electrodes gives an electric field of $E = 1$ mV/μm, while a gap of 0.5 μm gives $E = 15$ mV/μm, and a gap of 0 μm gives $E = 74$ mV/μm.

4. Maxwell–Wagner Behavior in an ac Electric Field

Each device configuration listed in Table 118.II was tested in both ac and dc fields. Our modeling reported here focuses on flake reorientation caused by MW behavior in an ac electric field. As predicted by the modeling work shown in Fig. 118.32 with PC as the host fluid, MW reorientation behavior was observed in basic [Fig. 118.32(a)] and microwell [Fig. 118.32(b)] configurations, but not in microcube [Fig. 118.32(c)] and direct encapsulation type-II [Fig. 118.32(d)] configurations. No MW reorientation is either predicted theoretically or observed experimentally for any configuration when SIT7757 is used as the host fluid for PCLC flakes. Maxwell–Wagner reorientation behavior is both predicted and observed with all six types of encapsulation geometries shown in Fig. 118.30 when DMS-E09 is used as the host fluid. The moderate dielectric constant of the host fluid permits a significant electric field within the host fluid for all configurations while still providing a reasonable difference in dielectric constants when compared to the PCLC flake. This balance of dielectric constants in the cell gap makes it possible for MW polarization-induced effects to occur for all geometries.

To illustrate the effectiveness of our modeling method, the predicted and observed reorientation times as a function of frequency and geometry for DMS-E09 are compared in Fig. 118.35. Cell types with the host fluid in contact with the ITO layer [e.g., basic, microwells, Figs. 118.35(a) and 118.35(b)] show a wide frequency range for the minimum MW reorientation time in ac electric fields, even extending into the mHz (millihertz) regime. Cell types where DMS-E09 is insulated from the ITO layer [e.g., microcubes and direct encapsulation type II, Figs. 118.35(c) and 118.35(d)] show MW reorientation in the ac regime and have a minimum reorientation time at a higher frequency than predicted. When the flake/host fluid suspension is in contact with the ITO layer, ions have been shown to diffuse out of the ITO and increase the conductivity of the test cell.[13] In a basic cell type, with a host fluid having a high dielectric constant (e.g., PC), the increased ion concentration from the ITO lowers the frequency for the minimum reorientation time. As shown in Fig. 118.35, the observed frequency for minimum reorientation times in DMS-E09 are slightly higher than predicted. The difference in frequency ranges over which the two host fluids show MW reorientation behavior is likely caused by the difference in ion mobility between the two fluids (PC: $\sigma = 10^{-4}$ S/m; DMS-E09: $\sigma = 10^{-8}$ S/m).

5. Electrophoretic Behavior in a dc Electric Field

Further modifying the analytical portion of the model makes it possible to predict MW flake reorientation in a dc electric field.[14] Additionally, EP translation of low-dielectric-

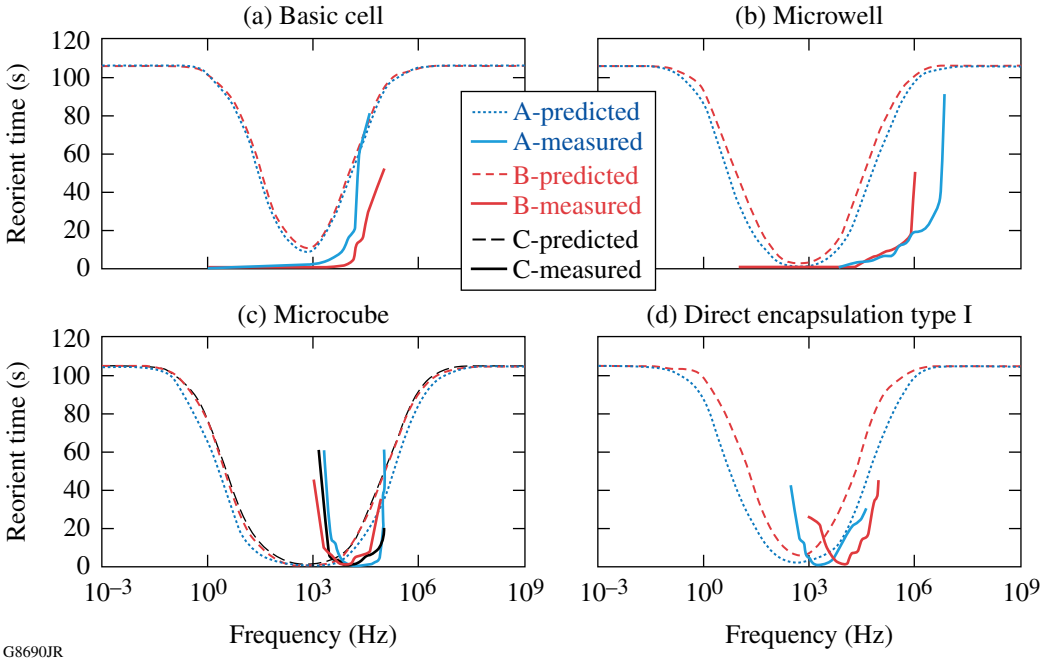

Figure 118.35
Plots of predicted versus observed flake reorientation times in DMS-E09 in an ac electric field: (a) basic, (b) microwell, (c) microcube, and (d) direct-encapsulation, type-I cell types. A, B, and C are individual test cell labels. The differences between predicted and observed values are likely caused by low ion mobility in the DMS-E09 host.

constant PCLC flakes in a dc electric field is also possible. Unfortunately, the analytical portion of the model used here is not applicable to EP motion so no predictive modeling was done. In a dc electric field with SIT7757 as the host fluid, EP motion has been observed for all geometry types. This observation indicates that the flakes have an intrinsic charge in SIT7757. The direction of translation is toward the positive electrode, which implies a negatively charged particle. Figure 118.36 shows the observed translation times as a function of applied voltage for different geometries. All configurations follow the same relationship, with the translation time decreasing with increasing electric-field strength. This behavior is to be expected because the EP force is directly proportional to the effective electric field.[28] Also, all materials in the cell gap (e.g., SIT7757, PVA, SU 8 3050) have low dielectric constants and conductivities. Therefore all configurations have very similar electric-field values acting on the PCLC flakes, and only the minimum voltage for initial translation is different for each configuration. Electrophoretic motion of PCLC flakes in a dc electric field has also been observed in both DMS-E09 and PC as host fluids; however, it is combined with MW reorientation at low electric-field strengths and chaotic electrorotation at higher field strengths.

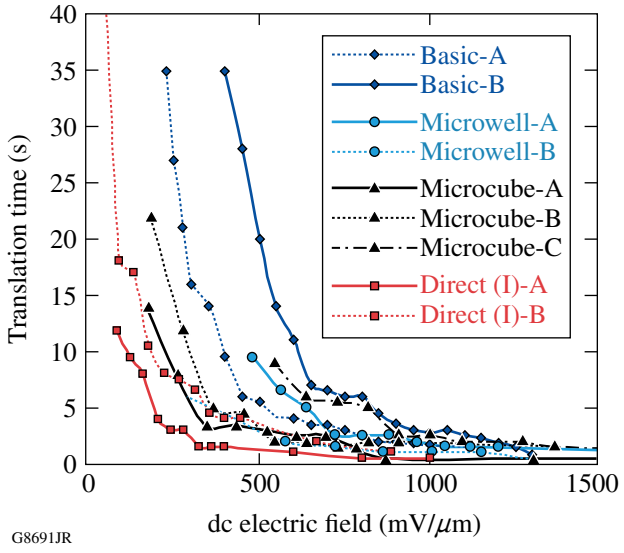

Figure 118.36
Observed PCLC flake electrophoretic translation times in SIT7757 as a function of applied dc electric-field magnitude and test cell geometry. All configurations follow the same relationship, with the translation time decreasing with increasing electric-field strength. A, B, and C are individual test cell labels.

Conclusions

By using a combination of Comsol Multiphysics and an analytical model developed by our group, we have shown that we can predict both the resultant electric field for any given device geometry and its effect on PCLC flake motion caused by MW interfacial polarization. The effect of the surrounding environment on the PCLC flake's electro-optical behavior depends greatly on both the materials used and the type of microencapsulation geometry. The MW reorientation behavior of PCLC flakes is directly proportional to both the effective electric field acting on the flake and the difference in dielectric constants and conductivities between the host fluid and flake. The optimal cell geometry for MW reorientation will have a balance of uniform dielectric constants and conductivities along the path of the electric field and a mismatch in dielectric constants between the host fluid and flake. With proper matching of device geometry and material properties, we have shown that it is possible to encapsulate a range of host fluids and PCLC flakes while maintaining MW reorientation capability for the flake/host fluid suspension. In addition we have also demonstrated good control over EP-type motion of microencapsulated PCLC flakes in a host fluid with low dielectric constant and conductivity.

The bright reflective colors and inherent circular polarization of PCLC flakes make them promising candidates for switchable reflective particle–based applications, including switchable conformal coatings for micropolarizers, large planar areas, and flexible media for information display applications (e.g., electronic paper). The ability demonstrated in this work to predict the effect of materials' properties and device geometry on the electro-optical behavior of PCLC flake/host fluid suspensions is a critical and significant step forward in the advancment of this unique materials technology toward viable commercial applications.

ACKNOWLEDGMENT

The authors would like to thank T. Kosc for her assistance and advice with the PCLC flake analytical modeling and interpretation and acknowledge the Laboratory for Laser Energetics at the University of Rochester for continuing support. This research was also supported by the U.S. Department of Energy Office (DOE) of Internal Confinement Fusion under cooperative agreement DE-FC52-08NA28302, the University of Rochester, and the New York State Energy Research and Development Authority. The support of the DOE does not constitute an endorsement by the DOE of views expressed in this article.

REFERENCES

1. E. M. Korenic, S. D. Jacobs, S. M. Faris, and L. Li, Mol. Cryst. Liq. Cryst. **317**, 197 (1998).
2. A. Trajkovska-Petkoska, R. Varshneya, T. Z. Kosc, K. L. Marshall, and S. D. Jacobs, Adv. Funct. Mater. **15**, 217 (2004).
3. A. Trajkovska-Petkoska, S. D. Jacobs, T. Z. Kosc, and K. L. Marshall, U.S. Patent No. 7,238,316 (3 July 2007).
4. K. L. Marshall, T. Z. Kosc, A. Trajkovska-Petkoska, E. Kimball, and S. D. Jacobs, presented at the 4th Annual Flexible Microelectronics and Displays Conference, Phoenix, AZ, 1–3 February 2005.
5. K. L. Marshall, K. Hasman, M. Leitch, G. Cox, T. Z. Kosc, A. Trajkovska-Petkoska, and S. D. Jacobs, in *2007 SID International Symposium*, edited by J. Morreale (Society for Information Display, San Jose, CA, 2007), Vol. XXXVIII, Book II, pp. 1741–1744.
6. K. L. Marshall, T. Z. Kosc, S. D. Jacobs, S. M. Faris, and L. Li, U.S. Patent No. 6,665,042 B1 (16 December 2003).
7. T. Z. Kosc, "Motion of Polymer Cholesteric Liquid Crystal Flakes in an Electric Field," Ph.D. thesis, University of Rochester, 2003.
8. T. Z. Kosc, K. L. Marshall, S. D. Jacobs, J. C. Lambropoulos, and S. M. Faris, Appl. Opt. **41**, 5362 (2002).
9. T. Z. Kosc, K. L. Marshall, and S. D. Jacobs, U.S. Patent No. 6,829,075 B1 (20 May 2003).
10. T. Z. Kosc, K. L. Marshall, and S. D. Jacobs, U.S. Patent No. 7,042,617 (9 May 2006).
11. K. L. Marshall, E. Kimball, S. McNamara, T. Z. Kosc, A. Trajkovska-Petkoska, and S. D. Jacobs, in *Liquid Crystals VIII*, edited by I.-C. Khoo (SPIE, Bellingham, WA, 2004), Vol. 5518, pp. 170–181.
12. T. Z. Kosc, K. L. Marshall, S. D. Jacobs, and J. C. Lambropoulos, J. Appl. Phys. **98**, 013509 (2005).
13. A. Trajkovska-Petkoska, "Enhanced Electro-Optic Reorientation of Polymeric Cholesteric Liquid Crystal Flakes in Host Fluids," Ph.D. thesis, University of Rochester, 2007.
14. A. Trajkovska Petkoska, T. Z. Kosc, K. L. Marshall, K. Hasman, and S. D. Jacobs, J. Appl. Phys. **103**, 094907 (2008).
15. T. Z. Kosc, A. Trajkovska Petkoska, J. C. Lambropoulos, K. L. Marshall, and S. D. Jacobs, "Extended Model for Polymer Cholesteric Liquid Crystal Flake Reorientation and Relaxation," submitted to the Journal of Applied Physics.
16. E Ink Corp. Product Page, Electronic Paper Displays, E Ink Corporation, Cambridge, MA 02138.
17. Y. Chen *et al*., Nature **423**, 136 (2003).
18. B. Comiskey *et al*., Nature **394**, 253 (1998).
19. H. L. Guo and X. P. Zhao, Opt. Mater. **26**, 297 (2004).
20. I. Shiyanovskaya *et al*., in *2005 SID International Symposium*, edited by J. Morreale, Digest of Technical Papers, 1st ed. (Society for Information Display, San Jose, CA, 2005), Vol. XXXVI, Book II, pp. 1556–1559.
21. S. W. Stephenson *et al*., in *2004 SID International Symposium*, edited by J. Morreale, Digest of Technical Papers, 1st ed. (Society for Information Display, San Jose, CA, 2004), Vol. XXVIII, Book II, pp. 774–777.

22. J. Szep, Computerworld – Mobile & Wireless (5 April 2007).

23. T. Z. Kosc, Opt. Photonics News **16**, 18 (2005).

24. Semiconductor & Microsystems Fabrication Laboratory, Kate Gleason College of Engineering, Rochester Institute of Technology, Rochester, NY 14623-5603.

25. Sylgard 184, Dow Corning Corporation, Midland, MI 48686-0994.

26. J. K. Song, H. J. Choi, and I. Chin, J. Microencapsul. **24**, 11 (2007).

27. J. K. Song *et al*., Mol. Cryst. Liq. Cryst. **464**, 263 (2007).

28. I. D. Morrison and S. Ross, *Colloidal Dispersions: Suspensions, Emulsions, and Foams* (Wiley-Interscience, New York, 2002).

Capillarity and Dielectrophoresis of Liquid Deuterium

Introduction

The current target used for laser-driven inertial confinement fusion experiments is a shell (0.9 mm in diameter) with a 100-μm-thick wall of solid cryogenic deuterium and tritium (DT) ice.[1] The interior of this shell contains more DT, but in liquid form. Future more-powerful laser drivers, such as the National Ignition Facility constructed at Lawrence Livermore National Laboratory, will use larger targets—up to ~4.7 mm in diameter with ~350-μm wall thickness and yielding energies up to ~18 MJ each.[2] The present approach to making these targets is to create shells of a low-density polymer foam and then to use these as mandrels to form the final DT-ice structures. Using current techniques, these targets, which are very complex with stringent mechanical specifications, are batch produced in a process that takes as long as two weeks.[3] Given the sizeable tritium content for the larger targets (>15 Ci) and the fact that a fusion-powered electric power plant of reasonable size (~1000 MW) will consume >500,000 of these targets per day,[4] such a long production cycle would necessitate an exceptionally large inventory of highly radioactive tritium. To reduce these inventories to tractable levels, a fully automated, just-in-time approach to target production is needed. It is our proposition that a system based on microfluidics may be able to meet this requirement.[5]

One critical step in target preparation is the fueling process, where liquid DT is loaded into the shells, which themselves are fragile. The current technique involves permeating the gas through an outer membrane, a process requiring a slow pressure ramp-up to an ultimate value of 1000 bars.[6] For a commercial-scale fusion power plant, this process is far too slow and cumbersome. Furthermore, it necessitates a level of human intervention that is undesirable in any commercial process involving a highly mobile radioactive isotope such as tritium. Therefore, an important goal of the present program is to develop an alternate technique for fueling of laser targets. In this article, we report on experiments that use the dielectrophoretic (DEP) force to manipulate liquid deuterium remotely and reliably at temperatures below ~30 K. In the early years of the space program, liquid DEP was seriously considered as a means to manage cryo-propellants in zero gravity,[7,8] so it is only natural to reopen its consideration for the present application.

Background

Liquid DEP enlists the so-called ponderomotive force, which selectively attracts dielectric liquids with relatively higher dielectric constant into regions where the imposed electric field is stronger. Fluids with relatively lower dielectric constant, including vapor and gas, are simultaneously repelled from the strong electric field. The critical requirement for DEP liquid management is the nonuniformity of the electric field imposed by the particular design of the electrodes. The dielectrophoretic effect is influenced by the electrical conductivity (σ) of the liquid. In general, joule heating presents a serious obstacle to the use of liquid DEP management when $\sigma > \sim 10^{-4}$ S/m [which is the conductivity of deionized (DI) water]; but most liquid cryogens, including H_2 and D_2, are very highly insulating dielectrics. As a result, DEP manipulation of such liquids is relatively easy to exploit using properly designed electrodes and easy to control via voltage modulation.[a]

Despite obvious difficulties in handling them, the critical properties of the isotopes of cryogenic hydrogen—H_2, D_2, and T_2—have been intensively studied. Many published measurements as well as some crucial extrapolations intended to fill gaps in the data have been obtained.[9] We can anticipate that the microfluidic behavior of cryogenic liquid hydrogen will be unique based on its physical properties. For example, liquid deuterium has very low density (~0.18 gm/cm^3), dielectric constant ($\kappa \sim 1.25$), and surface tension (0.0038 N/m), at least compared to room-temperature liquids. Furthermore, the liquid maintains zero contact angle against almost all solid materials.[10] Also, the useable range of temperatures and (saturated vapor) pressures spans conditions from the triple point (T = 18.7 K, p = 17 kPa) almost to the critical point (T = 38 K, p = 1.7 MPa), the consequence being rather strong temperature

[a]Due to its radioactivity and abundant β particles, tritium may very well behave like a conductive liquid. Some speculation on the effect of such bulk charge transport on electric field–mediated microfluidics is considered in the **Discussion** section of this article.

dependencies for some of the important fluid properties. Low viscosity creates still another distinction of likely importance in the dynamics of target fueling, although this issue is not addressed in this article. For ~10 to ~100-μl-D_2 droplets (the size range appropriate for laser targets), the capillary force is significant, but the liquid DEP force can be made comparable or dominant if care is taken to avoid electric breakdown.

This article presents experiments with a simple, parallel plate geometry intended to investigate the basic capillary and DEP force-coupled hydrostatics of liquid D_2 in the temperature range from ~19 to ~27 K. We find that a simple model adequately describes the effectively additive natures of the capillary and DEP forces upon the net height of rise against gravity. We further demonstrate a hydrostatic bifurcation effect that might ultimately be exploited in dispensing and metering liquid D_2 for application in the fueling of laser targets.

Basic Theory

The capillary rise of a liquid covered by a gas or vapor of negligible density between two parallel and vertical plates is h_{cap} (Ref. 11):

$$h_{cap} \approx 2\gamma \cos\theta_c \big/ \left(\rho_1 - \rho_v\right) g d, \tag{1}$$

where γ = surface tension, ρ_1 and ρ_v = liquid and vapor mass densities, θ_c = contact angle, d = plate spacing, and g = 9.81 m/s^2 is the terrestrial acceleration caused by gravity. Usually, $\rho_1 \gg \rho_v$. The geometry is illustrated in Fig. 118.37(a). Equation (1) assumes that $h_{cap} \gg d$ and also that the plates are wide compared to their spacing, that is, $w \gg d$. The Bond number (Bo), a useful dimensionless modulus that may be identified from Eq. (1),

$$\mathrm{Bo} \equiv h_{cap} \big/ d = 2\gamma \cos\theta_c \big/ \left(\rho_1 - \rho_v\right) g d^2 \tag{2}$$

measures the relative importance of surface tension and gravity. For Bo $\gg$ 1, the transverse profile of the liquid meniscus between the plates assumes the shape of a circular arc. In the classic case of a sessile droplet resting on a flat surface, one replaces the plate spacing d in Eq. (1) by the droplet radius. Then, the magnitude of Bo tells us whether the droplet takes the shape of a spherical cap (Bo $\gg$ 1) or a flattened disk (Bo $\ll$ 1).

If the liquid is a dielectric, the plates are conductive electrodes, and voltage V is applied between them, the ponderomotive (DEP) effect exerts an additional upward force on the liquid column [refer again to Fig. 118.37(a)]. Pellat studied this behavior in 1895.[12] Assuming, as before, that the plates are very wide compared to the spacing, the dielectric height of rise is[13]

$$h_{DEP} \approx \left(\kappa_1 - \kappa_v\right)\varepsilon_0 V^2 \big/ 2\left(\rho_1 - \rho_v\right) g d^2, \tag{3}$$

where κ_1 and κ_v are the liquid and vapor dielectric constants, respectively, $\varepsilon_0 = 8.854 \times 10^{-12}$ F/m, and V is the rms voltage applied to the electrodes. Note that typically $\kappa_v \approx 1.00$. It is convenient here to define a new dimensionless modulus called the electric Bond number (Be):

$$\mathrm{Be} \equiv h_{DEP} \big/ d = \left(\kappa_1 - \kappa_v\right)\varepsilon_0 V^2 \big/ 2\left(\rho_1 - \rho_v\right) g d^3. \tag{4}$$

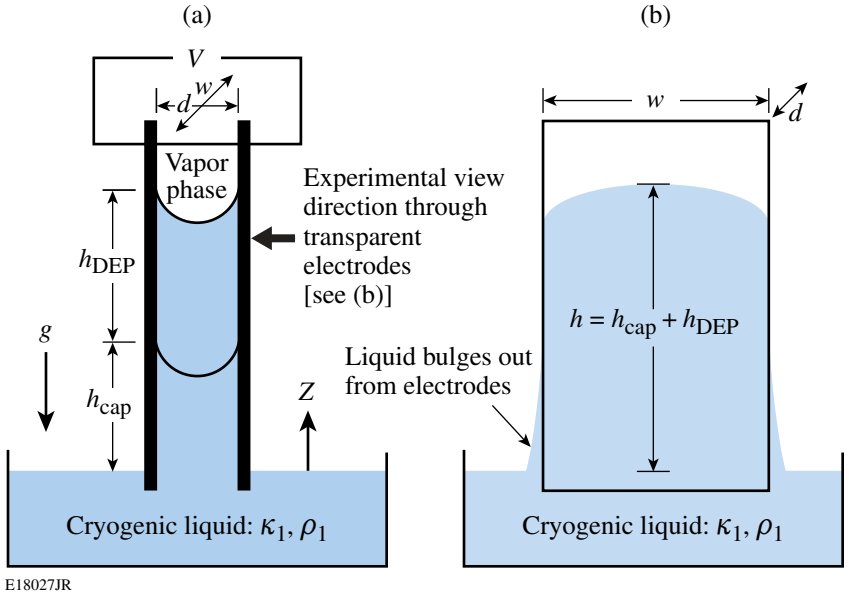

Figure 118.37
The parallel plate geometry. In the absence of voltage, the capillary rise is h_{cap}. (a) The side view depicts the expected circular profile of the meniscus and the contact angle $\theta_c = 0°$, which characterizes deuterium with almost all solids. When voltage is applied, the liquid rises an additional amount h_{DEP}. Unlike electro-wetting, the DEP force has virtually no influence on the contact angle. (b) Cross sections show the liquid bulging outward toward the bottom.

This modulus measures the strength of the DEP force compared to gravity.

Note that Eqs. (1) and (3) are additive contributions to the *hydrostatic* equilibrium; neither capillarity nor DEP can develop the dynamic pressure head required to pump liquid continuously from point to point. If a temperature gradient is properly imposed along the length of an electrode structure, as in the case of the dielectrophoretic heat pipe,[14] liquid motion can be induced, but it is the temperature gradient that drives the motion, not the electric field. No time-average electric power is supplied to the system, just as the wick in a capillary heat pipe supplies no pumping power. It is also possible to siphon dielectric liquid between an upper and a lower reservoir using the DEP effect.[15] The electric field imposed by the electrodes maintains fluid communication between the reservoirs but, just as in a regular tube siphon, gravity establishes the pressure head that moves the liquid.

Elementary considerations reveal that the capillary and DEP contributions to the height of rise are simply additive, so that the net measurable effect is $h = h_{\mathrm{cap}} + h_{\mathrm{DEP}}$. The ratio Be/Bo measures the relative importance of the DEP and capillary contributions:

$$\frac{\mathrm{Be}}{\mathrm{Bo}} = \left(\kappa_1 - \kappa_{\mathrm{v}}\right)\varepsilon_0 E^2 d \Big/ 4\gamma \cos\theta_{\mathrm{c}}\,, \tag{5}$$

where the rms (root-mean-square) electric field strength $E = V/d$ appears in Eq. (5). Electrical breakdown in the covering gas or vapor usually imposes a limit on the maximum electric field, that is, $E < E_{\mathrm{b}}$. For saturated D_2 vapor at $T = 20$ K, the breakdown field strength is $E_{\mathrm{b}} \approx 2 \times 10^7\ \mathrm{V_{rms}/m}$ (Ref. 16). Equation (5) shows that, if the electric field E is limited by breakdown, the way to increase the relative importance of the DEP force is to increase κ, d, or θ_{c}. Assuming an electrode spacing of $d = 1$ mm, a safety margin for the applied electric field of $E = 0.25\ E_{\mathrm{b}}$, and using the properties of liquid D_2 at $T = 20$ K, Eq. (5) gives Be/Bo ≈ 3.5. As a result, the DEP force can be made to dominate over capillary rise.

The hydrostatic profile of the liquid along the vertical sides is difficult to model because it depends on hard-to-determine details of the shape of the sides of the plates. The vertical profile is further influenced by the strongly nonuniform electric field. In general, the liquid always bulges outward near the bottom and recedes inward near the top, as depicted with some exaggeration in Fig. 118.37(b). For cryogenic deuterium, with its low surface tension $\gamma \approx 0.0038$ Nt/m and zero contact angle $\theta_{\mathrm{c}} \approx 0°$, this bulging is actually minimal. The highest reach of the liquid occurs midway between the edges of the electrodes. On either side of the high point, the meniscus curves steadily down to where it becomes vertical along both edges. The 3-D shape of the liquid surface at the top of the column is best predicted by numerical means.

Experiments Using Parallel Electrodes

The experimental plates are made of glass treated with indium tin oxide (ITO), 1.1 mm thick, ~15 mm high, and 7.6 mm wide. The ITO layer is conductive but transparent, making it possible to observe and record the shape of the liquid meniscus along the width of the electrodes. The electrode assembly is placed in a chamber connected to a cryostat so that it can be cooled as low as the triple point of D_2. By carefully managing the inventory of gaseous deuterium introduced into the cryostat and controlling the temperature, we condense liquid D_2 in a pool at the bottom of the chamber. This pool serves as the reservoir depicted in Figs. 118.37(a) and 118.37(b). The viewing ports in the present experimental chamber are on the top and bottom, requiring placement of a mirror inside to view the liquid rise.

Figure 118.38 shows the liquid rise viewed through the ITO-treated glass electrodes for a range of applied voltages. It is important to note that the profile of the meniscus along the width of the electrodes does not change appreciably as the voltage is increased, indicating that the electric field has negligible influence on the curvature of the liquid/vapor surface. Height-of-rise data from individual digital images like those in Fig. 118.38 are gathered by measuring the vertical distance from the equilibrium level of the liquid in the pool to the highest point of the meniscus. Despite small systematic errors, due primarily to uncertainty about the exact location of the equilibrium liquid level outside the plates, these data compare quite favorably to the 1-D model prediction. Figure 118.39(a) plots the net height-of-rise data for experiments performed at several temperatures. The solid lines in this figure are predictions for $h = h_{\mathrm{cap}} + h_{\mathrm{DEP}}$ based on the 1-D hydrostatic models used to obtain Eqs. (1) and (3). For these curves, we employed the set of approximate, fitted temperature-dependent expressions for dielectric constant $\kappa_{\mathrm{l}}(T)$, liquid and vapor densities $\rho_{\mathrm{l}}(T)$ and $\rho_{\mathrm{v}}(T)$, and surface tension $\gamma(T)$ found in the **Appendix**. Some of the data are obtained at temperatures lying outside the advertised range for the dielectric constant expression, but any resulting error is not expected to be significant because $\kappa_{\mathrm{l}}(T)$ is a rather weak function of temperature.

Figure 118.39(b) plots measured height-of-rise data and predictive curves directly as a function of temperature T for several fixed voltage values. While voltage—actually the electric

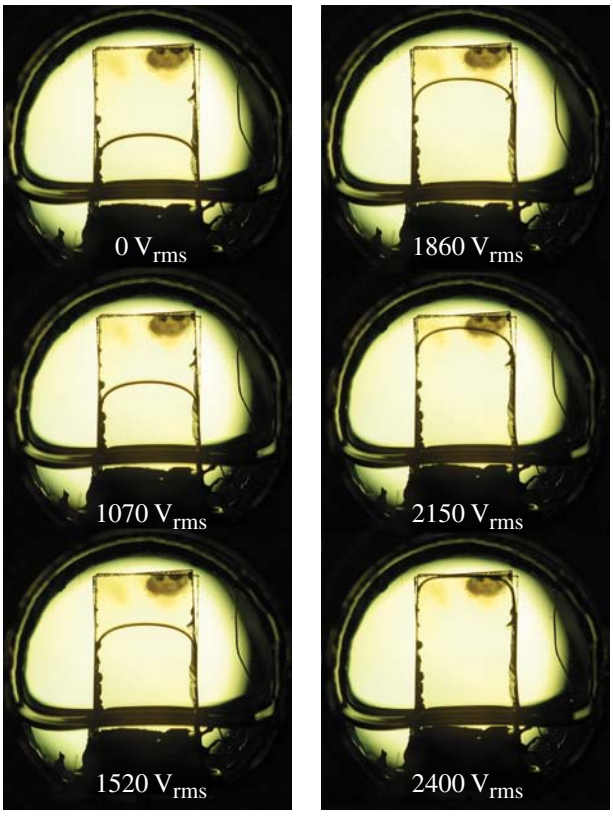

Figure 118.38
Meniscus of cryogenic D_2 at $T = 18.7$ K viewed through parallel, transparent ITO glass electrodes; $w = 7.6$ mm, $d = 0.86$ μm for 1-kHz ac voltages ranging from 0 to 2400 V_{rms}. Frequency must be high enough to avoid surface wave instabilities but is otherwise not important.

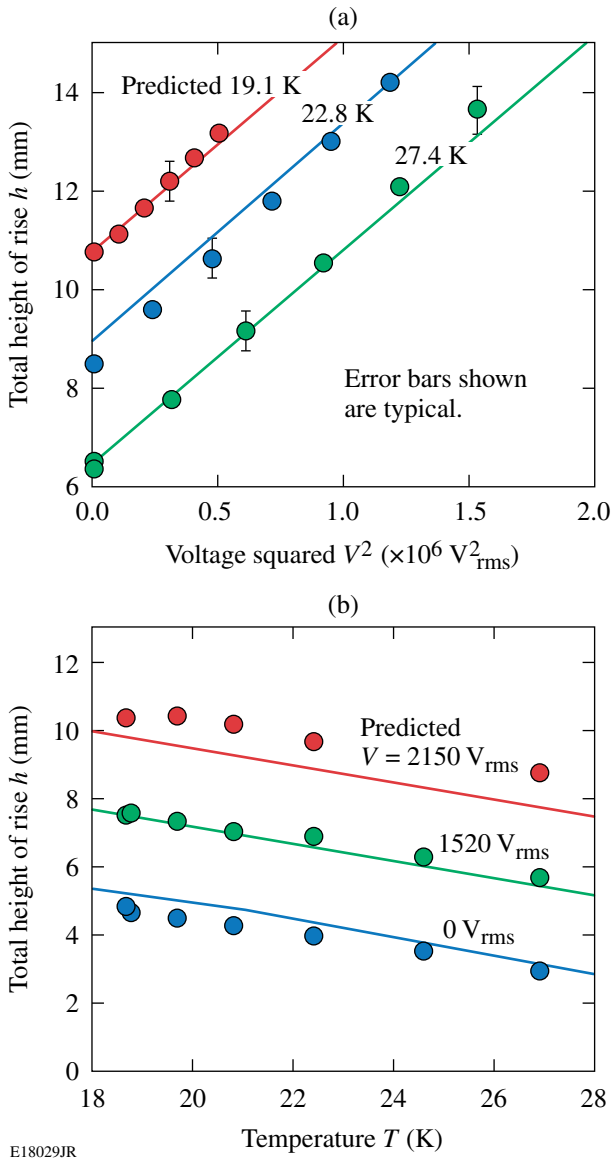

Figure 118.39
Height-of-rise data and predictions using $h(V) = h_{cap} + h_{DEP}(V)$ for liquid deuterium using parallel electrodes: $w = 7.6$ mm, $d = 0.43$ (± 0.02) mm. (a) h versus voltage V at various temperatures; (b) h versus temperature at several fixed voltages.

field magnitude $E = V/d$—does not influence the shape of the meniscus, the images in Fig. 118.40 do reveal that the temperature does have some effect. The measured radius of curvature in the plane of the electrodes at the midpoint increases from ~7 mm at $T = 18.8$ K to ~11 mm at $T = 26.9$ K, reflecting an ~45% drop in the surface tension at the higher temperature. Over this same temperature range, the density changes by only ~10%. Temperature is not believed to appreciably influence the contact angle θ_c.

One factor very critical to the success of Eqs. (1) and (3) in predicting the net height of rise is the condition $w \gg d$, where w and d are, respectively, the plate width and spacing. In this limit, the influence of the vertical sidewalls becomes less and less significant, and the uniform electric field approximation inherent in Eq. (3) becomes more valid. A 1-D model, of course, cannot predict the curved profile evident in the images of Fig. 118.38. To overcome this modeling deficiency, a finite-element computation was used to solve for the 3-D surface between the plates. This analysis, based on a numerical energy minimization, is summarized in the next section.

Simulations

The significant curvature of the liquid surface parallel to the electrode plates evident in Fig. 118.38 reveals that surface wetting can influence the maximum, measurable height of rise, h, if the plates are not sufficiently wide. For this reason, we used the Surface Evolver software of K. Brakke[17] to solve for the

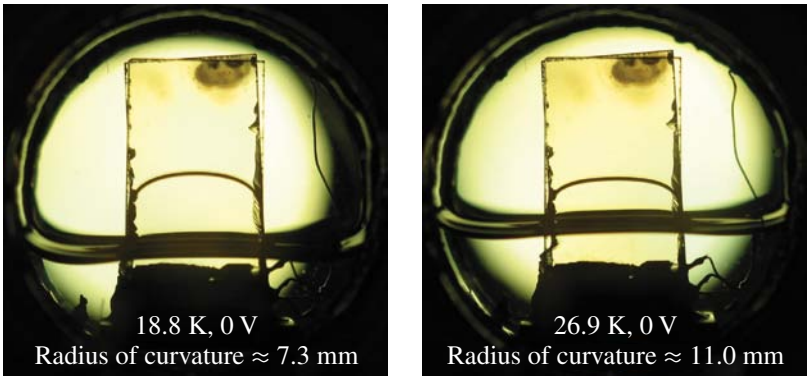

Figure 118.40
Effect of temperature on meniscus shape. The temperature, but not the electric field E, influences the profile of the meniscus along the width of the electrodes through its influence on surface tension and density.

shape of the liquid meniscus. This finite-element tool is based on a computational algorithm that seeks the minimum energy configuration of a static liquid volume subject to wall constraints, contact angle, gravity, and certain other body forces.[b]

Figure 118.41 shows various views of the numerical solution for the meniscus of D_2 using geometric parameters representative of the actual experiment, at temperature $T = 18.7$ K and with no voltage applied. Figure 118.41(a) provides an oblique view of the elevated liquid between the plates, and Fig. 118.41(b) shows an end-on view of the meniscus. One thing to note about the numerical solution is that the contact angle made by the liquid at the walls does not quite go to zero, presumably because of the level of mesh refinement. An enlarged view of the meniscus, shown in Fig. 118.41(c), reveals details of the actual 3-D liquid surface near the top. Note that the two radii of curvature are of opposite signs. It is for this reason that the liquid height at the midpoint is always less than the value predicted by the 1-D model. The view normal to the parallel plates [Fig. 118.41(d)] is the same afforded by viewing the experiment through the transparent ITO glass plates. A curve fitted to an experimental image of the actual meniscus is superimposed for comparison. Correspondence is reasonable, except for very close to the vertical edges of the plates, where the actual location and configuration of the contact line cannot, in fact, be modeled with any confidence. The height of rise h_{cap} calculated from the 1-D model [Eq. (1)] is also provided in Fig. 118.41(d).

To investigate in greater detail the influence of plate width w on the profile of the liquid deuterium meniscus and the height of rise h_{cap}, additional simulations were performed using Surface Evolver. Again, the DEP effect was not incorporated into the model. These results, shown in side view only, are provided in Fig. 118.42. Note that as the width is increased, the maximum height of the meniscus at the midpoint approaches h_{cap}, which

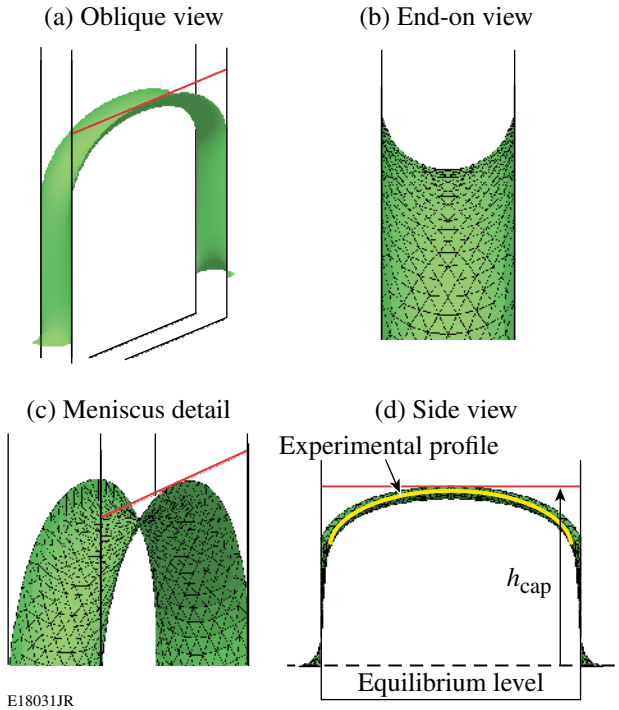

Figure 118.41
Numerical solution obtained using Surface Evolver software for the shape of the liquid meniscus between parallel plates for $w = 7.6$ mm, $d = 0.86$ mm, and $T = 18.7$ K. (a) Oblique view; (b) end-on view showing the contact angle $\theta_c \approx 0°$; (c) close-up of the meniscus; (d) view perpendicular to parallel plates with superimposed image from the experiment.

[b]The Surface Evolver software accommodates any body force that can be transformed into a surface or line force using the divergence theorem. In principle, electrical forces can be handled in this fashion; however, solution for the electric field on each facet of the mesh becomes necessary. Convergence then involves solving a tightly coupled problem where the mesh and the highly nonuniform electric field influence one another, i.e., both electric field and surface shape must be solved simultaneously. Surface Evolver is not designed to do this.

is predicted by the 1-D model [i.e., Eq. (1)]. For the value of the plate spacing used in the calculation, $d = 0.86$ mm, this point is reached at $w \approx 7$ mm. For larger values of w, the meniscus exhibits a virtually flat section in the middle. It is evident, both from experiment and from the simulations supporting them, that the vertical sidewalls' influence on the profile can be significant.

Experiments Using Converging Electrodes

The electrohydrostatic behavior of dielectric liquids becomes more interesting if the electrodes, still planar, are made to converge toward the top, as shown in Fig. 118.43(a). If the ratio of the spacing at the bottom and the top, b/a, is large enough, the liquid column exhibits a bifurcation, which was first observed with conventional room-temperature dielectric liquids. If the electrodes are planar, the relationship of the height of rise h to the applied voltage V takes the form of a cubic equation whenever $a \neq b$. This equation is obtained using the Maxwell stress tensor and hydrostatic pressure balance to account for the upward DEP force, under the assumption $a < b \ll w < H$:

$$\underline{h}^3 - 2\underline{h}^2 + (1 + \mathrm{Bo})\underline{h} - (\mathrm{Bo} + \mathrm{Be}) = 0, \tag{6}$$

where $\underline{h} = \alpha h/b$ is the normalized height of rise, a and b are the plate spacings at the top and bottom, respectively, H is the electrode height, and $\alpha = (b–a)/H$. A derivation of Eq. (6) is presented elsewhere.[18] If $a < b \ll H$, then α is approximately the angle between the plates in radians. For convenience, Eq. (6) employs modified definitions for the Bond numbers given below:

$$\mathrm{Bo} = 2\alpha\gamma\cos\theta \Big/ \left(\rho_1 - \rho_v\right) g b^2$$

and (7)

$$\mathrm{Be} = \alpha\left(\kappa_1 - \kappa_v\right)\varepsilon_0 V^2 \Big/ \left(\rho_1 - \rho_v\right) g b^3 .$$

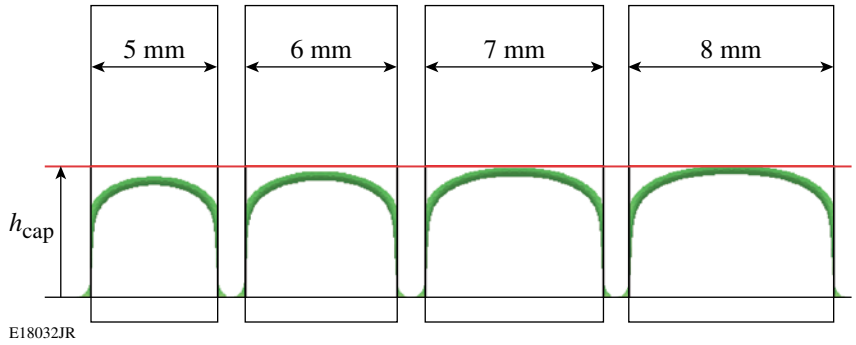

Figure 118.42
Side view of liquid D_2 meniscus profile between plates of spacing $d = 0.86$ mm at $T = 18.7$ K calculated using Surface Evolver for different values of the plate width: $w = 5$, 6, 7, and 8 mm. The top of the liquid column does not reach h_{cap}, the value predicted by the 1-D model, unless $w \geq 7$ mm. This result certainly scales directly with plate spacing d.

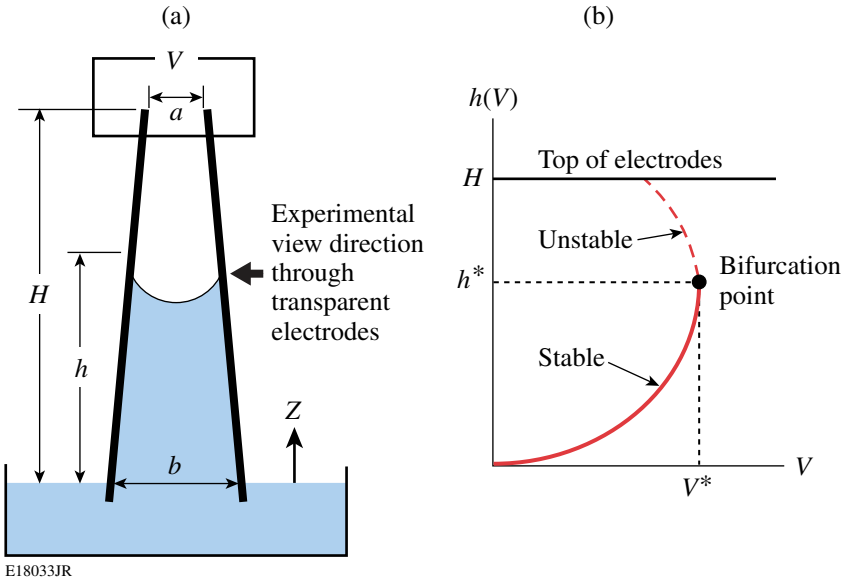

Figure 118.43
The converging plate experiment. (a) Electrode geometry and definitions of parameters. (b) Representative $h(V)$ curve with bifurcation point at (V^*, h^*). A bifurcation of the hydrostatic equilibrium is expected only if the electrode height H exceeds the critical value, i.e., $H > h^*$.

Given the cubic nature of Eq. (6), the easiest way to explore the hydrostatics of the converging plate geometry is to plot V as a function of $\underline{h}$. Referring to Fig. 118.43(b), the point on the curve where $dh/dV \longrightarrow \infty$, identified as ($V^*$, h^*), becomes an observable bifurcation of the hydrostatic equilibrium if the condition $0 < h^* < H$ is met. For this case, as voltage is increased, the liquid column rises steadily upward until, at voltage V^*, it jumps from $h = h^*$ all the way to the top of the electrodes, i.e., $h \longrightarrow H$. If the liquid column is already at the top and the voltage is turned back down, then, according to the model, static equilibrium is lost on both vertical sides at the same point, $z = h^*$, where the liquid jump occurred, and at the same voltage $V = V^*$. It is easily shown from pressure balance arguments that, as the voltage is being reduced, $z = h^*$ will always be the first point on the entire free surface where hydrostatic pressure equilibrium can no longer be maintained. The surface thus collapses inward on both sides at $z = h^*$, usually trapping liquid at the top. This trapped inventory remains near the top even when the voltage is reduced to zero, possibly because of contact angle hysteresis. While this behavior occurs just as predicted in the case of room-temperature dielectrics,[18] experiments using cryogenic D_2 yield some differences.

Figures 118.44 and 118.45, respectively, show images from an experiment performed using liquid deuterium with the voltage first monotonically increased and then decreased. For increasing voltage (Fig. 118.44), the column rises steadily until, at some voltage between 1590 and 1599 V_{rms}, it jumps the rest of the way to the top, just as predicted by the 1-D model. On the other hand, when the voltage is then reduced (Fig. 118.45), the surface does not fully collapse at $V = V^*$ but instead forms a neck that becomes narrower and narrower as V is further reduced. Eventually, the neck does rupture, but our observation is that the volume of liquid trapped near the top is neither well controlled nor very reproducible. Data obtained from this experiment are plotted in Fig. 118.46, along with the prediction from Eq. (6). For rising voltage, the model predicts a column height h with reasonable accuracy; the discrepancies are almost certainly due to (1) uncertainties in the values for a and b, which must be measured before the fixture is cooled

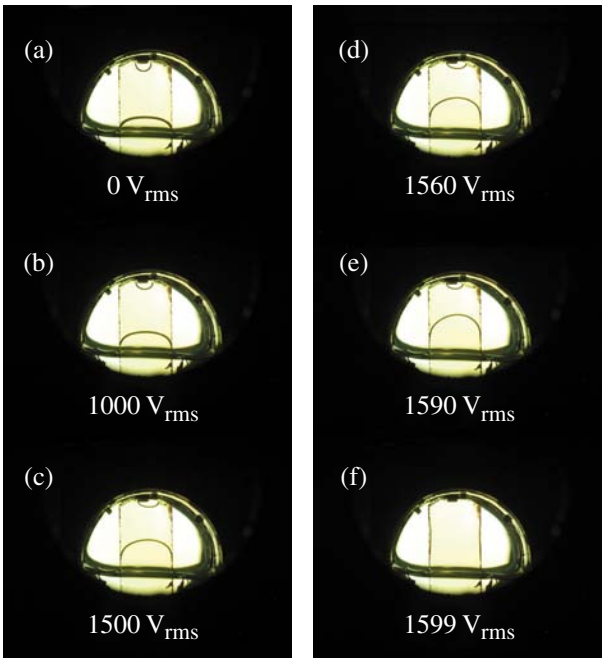

E18034JR

Figure 118.44
Meniscus of cryogenic D_2 at 23.9 K viewed through transparent, slightly convergent ITO-glass electrodes; w = 7.6 mm, H = 12 mm, a = 0.42 mm, b = 1.41 mm, for increasing ac voltages at 1 kHz. The small droplet visible at the top was trapped in a previous experiment. (a) $V = 0$ V_{rms}; (b) $V = 1000$ V_{rms}; (c) $V = 1500$ V_{rms}; (d) $V = 1560$ V_{rms}; (e) $V = 1590$ V_{rms}, meniscus approaching h^*; (f) $V = 1599$ V_{rms}, liquid has jumped to the top.

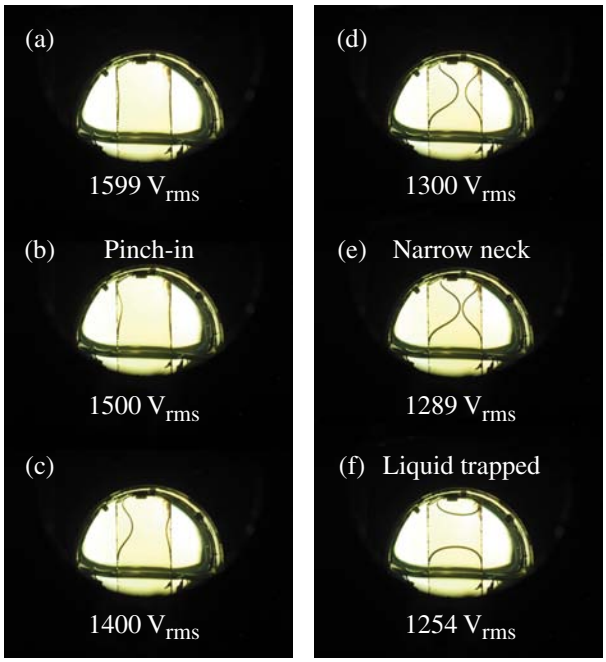

E18035JR

Figure 118.45
Meniscus of cryogenic D_2 at 23.9 K viewed through transparent, slightly convergent ITO-glass electrodes; w = 7.6 mm, H = 12.0 mm, a = 0.42 μm, b = 1.41 μm, for decreasing ac voltages at 1 kHz. (a) $V = 1599$ V_{rms}; (b) $V = 1500$ V_{rms}, surface starting to recede inward; (c) $V = 1400$ V_{rms}, further receded; (d) $V = 1300$ V_{rms}, further receded; (e) $V = 1289$ V_{rms}, only a narrow neck remains; (f) $V = 1254$ V_{rms}, neck has ruptured and liquid is trapped at the top.

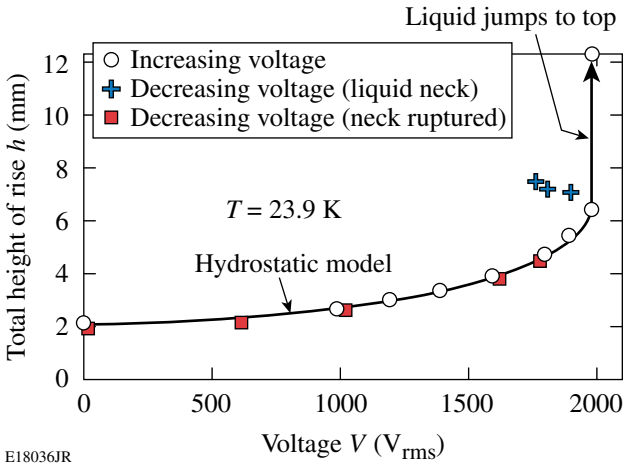

Figure 118.46
Experimental data and predicted $h(V)$ curve from Eq. (6) for converging plates, $w = 7.6$ mm, $H = 12$ mm, $a = 0.42$ μm, $b = 1.41$ μm. The data obtained for increasing voltage match the prediction very well. For decreasing voltage, data indicated by crosses (+) indicate the location along the vertical side where the interface is pinched in the most. The squares (■) denote the height of the column after the neck has ruptured.

down, and (2) a slight misalignment of the plates. A clear manifestation of this misalignment is the evident asymmetry of the meniscus profile that increases as voltage is raised. The data in Fig. 118.46 for reducing voltage are plotted in two groups: The crosses (+), indicating the locations of the narrowest point of the liquid neck shown in Figs. 118.45(b)–118.45(e), seem to correlate reasonably well with the calculated value of h^*. The squares (■), indicating measured column height values after the neck has ruptured, closely follow the cubic relation [Eq. (6)].

In the experiment shown in Figs. 118.44 and 118.45, the plates were maintained in position by a spacer positioned at the top–middle. This spacer has the effect of retaining some of the liquid at the top, even when the voltage is reduced to zero. Without this spacer, the trapped liquid always seems to fall. Such behavior is unlike the highly repeatable trapping phenomenon observed with room-temperature dielectrics,[18] where wetting hysteresis may help to hold the trapped liquid near the top when the voltage is removed.

Discussion

The bifurcation behavior of liquid D_2 differs from the prediction based on the 1-D model and also from experiments with room-temperature dielectric liquids, but only when the voltage is reduced toward V^* from values above it. The cause of this discrepancy seems to be the very low contact angle that cryogenic deuterium exhibits against the ITO glass–coated electrodes. In contrast, the contact angles for the dielectric liquids used in earlier experiments conducted at room temperature were in the range of ~70° to ~90° (Ref. 18). When $\theta_c \approx 0°$, a thin, remarkably stable filament of liquid between two plates persists, probably because its concave inter-electrode profile makes it energetically favorable. Equation (6) fails to predict the observed behavior for lowering voltage because the existence (and stability) of such filaments is not accounted for in the 1-D hydrostatic model. The data in Fig. 118.46 do suggest that surface equilibrium starts to fail near $z = h^*$ as we would expect, irrespective of the formation of the filament.

One major question about the use of DEP in laser target fueling is not addressed here: namely, that the liquid fuel for laser targets will necessarily contain liquid tritium, which is highly radioactive. The energetic electrons (β particles) emitted by tritium add space charge to the liquid bulk, rendering the liquid effectively conductive, although probably not ohmic in nature. One hypothesis is that the small current detected to flow in liquid D_2 when an electric field is applied is actually due to very small but unavoidable levels of tritium contamination.[19,20] If there is sufficient tritium present, the mobile charges may make the liquid behave as an electrical conductor. In that case, the DEP mechanism will become inoperative; however, it could still be possible to actuate the liquid electrically by exploiting the electrowetting mechanism. To do so, it is necessary to coat the electrodes with a thin dielectric layer. Electrowetting has been intensively studied and demonstrated to be very effective in the transport and manipulation of many room-temperature liquids ranging from DI water to liquid mercury.[21] An investigation of the electrowetting behavior in liquid DT would be an interesting, if challenging, experimental undertaking.

Conclusion

A simple, 1-D hydrostatic model for the behavior of liquid deuterium between parallel plates under combined capillarity and liquid dielectrophoresis successfully predicts the height of rise as long as the plates are sufficiently wide compared to their spacing, i.e., $w/d \gtrsim 8$. The capillary and DEP effects are additive: $h = h_{cap} + h_{DEP}$. The actual 3-D meniscus shape is predicted with reasonable accuracy using the Surface Evolver tool, which seeks a numerical solution using finite elements and surface energy minimization. If the plates are made to converge toward the top, the hydrostatic equilibria include a bifurcation effect if the ratio of the electrode separation at the bottom and the top (b/a) is large enough. This bifurcation might be used to trap liquid; however, at present, the reproducibility of the trapped volume for liquid D_2 is not good because of the formation of a highly stable liquid filament, which forms because cryogenic deuterium perfectly wets the plates. Precise

metering of cryogenic liquids using the bifurcation effect may not be possible unless this phenomenon can be avoided.

Beyond its potential use in the fueling of small targets for laser fusion, other interesting applications for electric field–mediated cryo-microfluidics may be envisioned. One possibility is in the emerging field of cryo-preservation, i.e., the long-term storage of biological cells at low temperature to be later thawed and used in therapeutic treatments. The barrier to a practical technology of cryo-preservation is the shear number of samples that have to be preserved and the difficulties associated with proper freezing and thawing of cells without incurring damage.[22] The capability offered by liquid DEP to dispense, move, and manipulate small volumes of liquid nitrogen might prove very useful in this field. The properties of N_2 relevant to cryo-DEP—namely, dielectric constant $\kappa \approx 1.4$, surface tension $\gamma \approx 0.009$ Nt/m, and density $\rho \approx 0.8$ kg/m^3 at temperature $T = 77$ K—suggest that this liquid can be manipulated readily by combining dielectrophoretic microfluidics and temperature control.

Appendix: Temperature-Dependent Properties of Liquid D_2

For convenience, empirical relations for the temperature dependencies of the relevant liquid deuterium properties are provided below. SI units are used and the temperature T is in degrees Kelvin:

liquid mass density in kg/m^3 [curve fit based on Ref. 9, p. 62]:

$$\rho_1(T) = -0.005231\,T^3 + 0.3119\,T^2 - 8.225\,T + 252.9, \quad 18.7\ \text{K} \le T \le 35\ \text{K} \tag{A1}$$

saturated vapor mass density in kg/m^3 [curve fit based on Ref. 9, p. 57]:

$$\rho_v(T) = 2.03 \times 10^{-7} \times 10^{\left[0.5671\,T + 0.01508\,T^2 + 0.000156\,T^3\right]}, \quad 18.7\ \text{K} < T < 35\ \text{K} \tag{A2}$$

liquid-vapor surface tension in Nt/m [curve fit based on Ref. 9, p. 64]:

$$\gamma(T) = 1.759 \times 10^{-7}\,T^3 - 1.356 \times 10^{-5}\,T^2 + 1.296 \times 10^{-4}\,T + 4.986 \times 10^{-3}, \quad 18.7\ \text{K} \le T \le 37\ \text{K} \tag{A3}$$

liquid dielectric constant [curve fit based on data in Ref. 19]:

$$\kappa_1(T) = 1.361 - 0.00403\,T, \quad 20\ \text{K} \le T \le 23\ \text{K} \tag{A4}$$

Cryogenic deuterium perfectly wets most solids, in other words, $\theta_c = 0°$ (Ref. 10). Known exceptions exist for liquid D_2 in contact with pure Cs and Rb.[23]

ACKNOWLEDGMENT

The hydrostatic simulations were performed using the Surface Evolver software, which is freely available from K. Brakke of Susquehanna University, Selinsgrove, PA (USA) at www.susqu.edu/brakke/evolver/evolver.html. This research is supported by the Office of Inertial Confinement Fusion of the Department of Energy (Cooperative Agreement No. DE-FC52-08NA28302), the Laboratory for Laser Energetics at the University of Rochester, and the New York State Energy Research and Development Authority. Additional support for K. Kentch from Eastman Kodak Company is gratefully acknowledged.

REFERENCES

1. P. W. McKenty, V. N. Goncharov, R. P. J. Town, S. Skupsky, R. Betti, and R. L. McCrory, Phys. Plasmas **8**, 2315 (2001).
2. T. J. B. Collins, J. A. Marozas, R. Betti, D. R. Harding, P. W. McKenty, P. B. Radha, S. Skupsky, V. N. Goncharov, J. P. Knauer, and R. L. McCrory, Phys. Plasmas **14**, 056308 (2007).
3. M. S. Tillack *et al*., in *Proceedings of the 20th IEEE/NPSS Symposium on Fusion Energy* (IEEE, Piscataway, NJ, 2003), pp. 624–627.
4. J. D. Sethian *et al*., Nucl. Fusion **43**, 1693 (2003).
5. D. R. Harding, T. B. Jones, Z. Bei, D. H. Edgell, and S. H. Chen, presented at the 18th Target Fabrication Meeting, Lake, Tahoe, CA, 11–15 May 2008.
6. D. R. Harding, T. C. Sangster, D. D. Meyerhofer, P. W. McKenty, L. D. Lund, L. Elasky, M. D. Wittman, W. Seka, S. J. Loucks, R. Janezic, T. H. Hinterman, D. H. Edgell, D. Jacobs-Perkins, and R. Q. Gram, Fusion Sci. Technol. **48**, 1299 (2005).
7. R. G. Fax, M. Hurwitz, and J. R. Melcher, J. Spacecr. Rockets **6**, 961 (1969).
8. Y. Suda *et al*., Cryogenics **36**, 567 (1996).
9. P. C. Souers, *Hydrogen Properties for Fusion Energy* (University of California Press, Berkeley, 1986), Chap. 5.
10. R. J. Good and G. V. Ferry, in *Advances in Cryogenic Engineering*, edited by K. D. Timmerhaus (Plenum Press, New York, 1963), Vol. 8, pp. 306–310.
11. M. Dreyer, A. Delgado, and H. J. Rath, J. Colloid Interface Sci. **163**, 158 (1994).
12. H. Pellat, C.R. Hebd. Seances Acad. Sci. **123**, 691 (1896).

13. T. B. Jones Jr. and J. R. Melcher, Phys. Fluids **16**, 393 (1973).

14. T. B. Jones, Mech. Eng. **96**, 27 (1974).

15. T. B. Jones, M. P. Perry, and J. R. Melcher, Science **174**, 1232 (1971).

16. K. N. Mathes, Electro-Technol. **72**, 72 (1963).

17. K. Brakke, *The Surface Evolver*, ver. 2.30, Susquehanna University, Selinsgrove, PA, software available from http://www.susqu.edu/brakke/evolver/evolver.html, 1 January 2008.

18. T. B. Jones, J. Appl. Phys. **45**, 1487 (1974).

19. W. L. Willis, Cryogenics **6**, 279 (1966).

20. P. C. Souers *et al*., Cryogenics **20**, 247 (1980).

21. J. Lee and C.-J. Kim, J. Microelectromech. Syst. **9**, 171 (2000).

22. H. Zimmermann *et al*., IEE Proc., Nanobiotechnol. **151**, 134 (2004).

23. D. Ross, P. Taborek, and J. E. Rutledge, Phys. Rev. B **58**, R4274 (1998).

A Stable Mid-IR, GaSb-Based Diode Laser Source for Cryogenic Target Layering at the Omega Laser Facility

Introduction

Mid-IR, 3- to 3.5-μm laser sources are important for various applications including gas sensing, spectral analysis, infrared illumination, countermeasures, medical diagnostics, and others. One particular application is the layering of cryogenic targets for inertial confinement fusion (ICF) implosions at the Omega Laser Facility.[1] Cryogenic targets are used to maximize the fuel density in ICF implosions. These targets consist of ~900-μm-diam microcapsules that are permeation filled with over 1000 atm of D_2 (deuterium–deuterium) or DT (deuterium–tritium) gas and then cooled to ~18.7 K so that the gas is frozen and the capsules are no longer permeable. The frozen deuterium is then "layered" so that it is uniformly distributed around the inner surface of the capsule.[2]

The layering process relies on the target being in an isothermal environment—a layering sphere that is uniformly illuminated by 3- to 3.5-μm, mid-IR light. The wavelength is tuned to the absorption peak in the fuel material (3160 nm with 22-nm FWHM for D_2 targets). Since thicker regions of ice will have a longer path length, they absorb more radiation, so they will be relatively hot spots; likewise thinner ice will absorb less radiation and be relatively cold spots. Fuel material will then sublime from the hotter regions and condense and refreeze on the thinner, colder regions, leading to a uniform distribution of fuel material (see Fig. 118.47). For this process to produce layers with the required uniformity, the temperature must be held very close to the material's melting point. As a result, the mid-IR source's output power and spectrum must be temporally stable to avoid overheating and melting the ice layer.

Currently a mid-IR optical parametric oscillator (OPO) is used to layer the targets.[3] Until recently, this was the only choice to achieve the required power of >100 mW in this wavelength range. The development of a mid-IR, GaSb-based quantum well diode that produces >100 mW of output power at room temperature[4–6] presents a new choice for the layering laser source.

This article presents, for the first time, the spectral and output-power stability studies of a GaSb-based diode laser operated at room temperature.

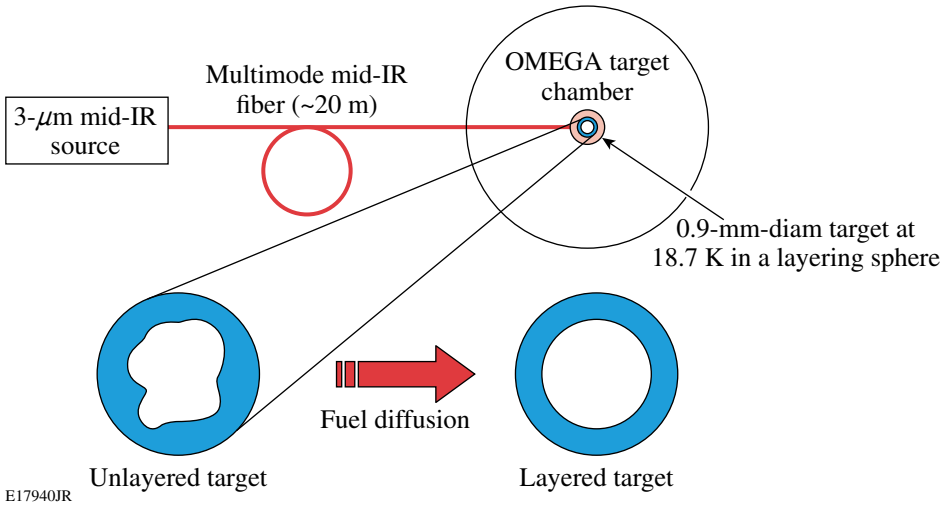

Figure 118.47
Cryogenic target layering at the Omega Laser Facility requires a stable mid-IR light source.

Diode Laser Growth and Assembly

Laser heterostructures were grown using the Veeco GEN-930 solid-source, molecular-beam-epitaxy system on Te-doped GaSb substrates. The band structure of a 3-μm emitter is shown in Fig. 118.48. The cladding layers were 2.5-μm and 1.5-μm-wide $Al_{0.6}Ga_{0.4}As_{0.05}Sb_{0.95}$ doped with Te (n side) and Be (p side), respectively. Graded-bandgap, heavily doped transition layers were introduced between the substrate and n-cladding and between the p-cladding and p-cap to assist carrier injection. The nominally undoped $Al_{0.2}In_{0.2}Ga_{0.6}As_{0.02}Sb_{0.98}$ waveguide layer with a total thickness of about 800 nm contained two 12-nm-wide $In_{0.54}Ga_{0.46}As_{0.23}Sb_{0.77}$ quantum wells (QW's) centered in the waveguide and spaced 40 nm apart. Thick waveguide and cladding layers were lattice matched to GaSb. The compressive strain in the QW's was about 1.8%. The wafer was processed into 100-μm-wide, oxide-confined, gain-guided lasers. Two-mm-long neutral-reflection (NR ~30%) and high-reflection (HR ~95%) coated lasers were In soldered epi-side down onto Au-coated polished copper blocks (D-mount).

The 3000-nm laser diode assembled on a D-mount was placed on a thermo-electric cooler (TEC) mounted on a heat sink. A laser diode driver provided up to 3000-mA low-noise current with 1-mA resolution. The same driver provided TEC temperature control. The temperature of TEC cold plate was varied from 14°C to 20°C. Because this diode has not been tested for lifetime and temperature/current damage, the output power as measured by a FieldMaster GS power meter (Coherent) was limited to 50 mW, although a maximum output power of 130 mW at 17°C has been demonstrated.[4] Currently diode lasers with output power >200 mW can be safely operated. Figure 118.49 shows output-power versus driver-current dependencies at various temperatures. The output power slightly decreases as the temperature increases, as expected.

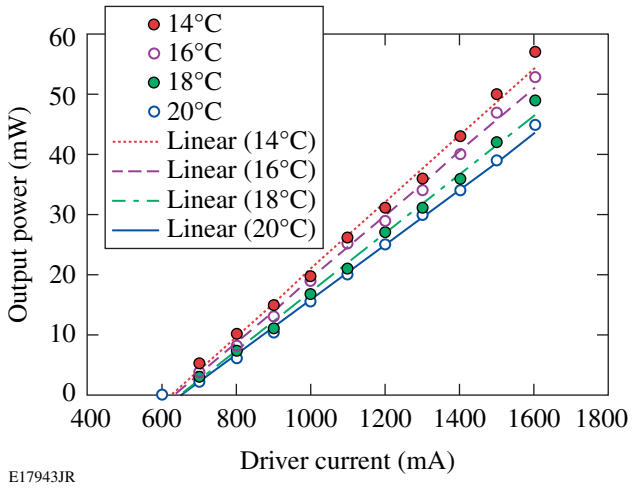

Figure 118.49
The diode laser's output-power versus driver-current dependencies at different temperatures.

Spectral and Output-Power Stability of a Diode Laser

The laser output-power's stability is excellent—less than 1% rms variations at 14°C over 1 h (see Fig. 118.50). The output power decreases as the temperature increases, and at the same time output-power variations are slightly higher at higher temperatures. The change in power variation increase is small but is well pronounced as shown in Fig. 118.51.

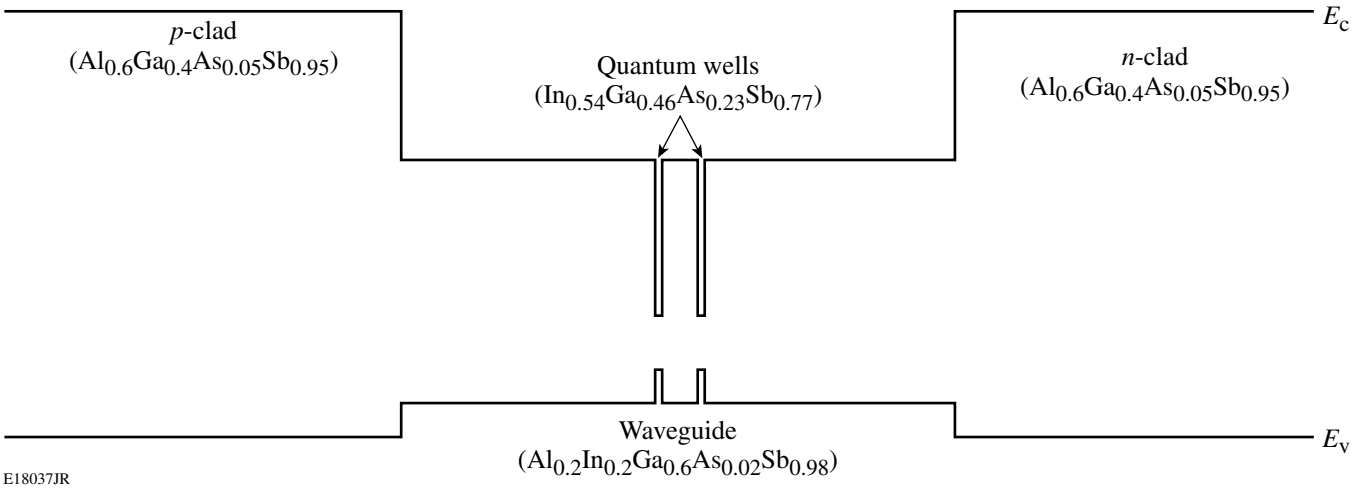

Figure 118.48
Band structure of a 3-μm emitter: E_c—the bottom of the conductive band; E_v—the top of the valence band.

A Nicolet 6700 Fourier transform infrared (FTIR) spectrometer (Thermo Scientific) with a 0.5-nm spectral resolution around a 3000-nm wavelength was used for spectral measurements. The spectrometer was calibrated using 1152.3-nm and 3391.3-nm He–Ne laser spectral lines. The diode-laser output-spectrum's peak position and shape change dramatically (over 20 nm) with current at constant TEC temperature [see Fig. 118.52(a)]. Once the current is set, the spectral shape is stable. To provide the required spectral and output-power stability

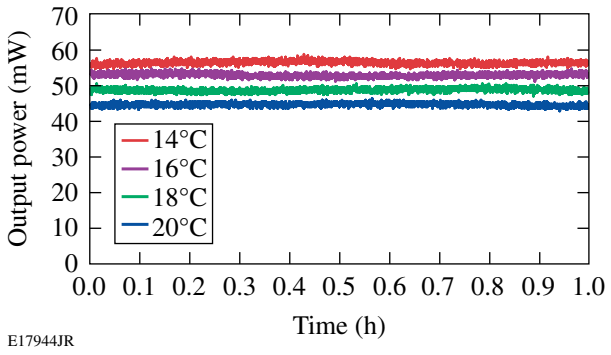

Figure 118.50
The diode laser's output-power stability is excellent (<1% rms variations at 14°C).

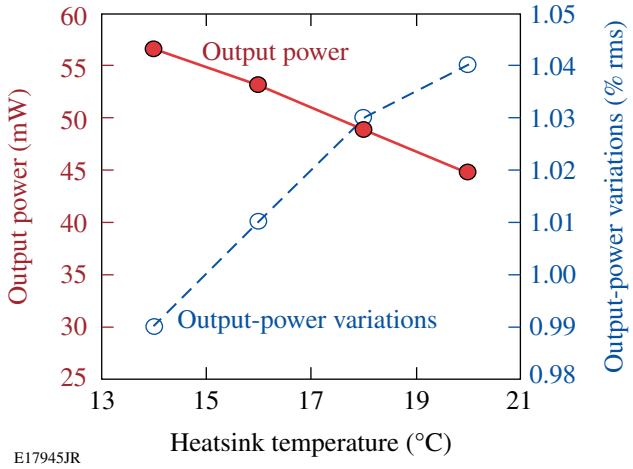

Figure 118.51
The diode laser's output power decreases and output-power variations increase with increasing temperature.

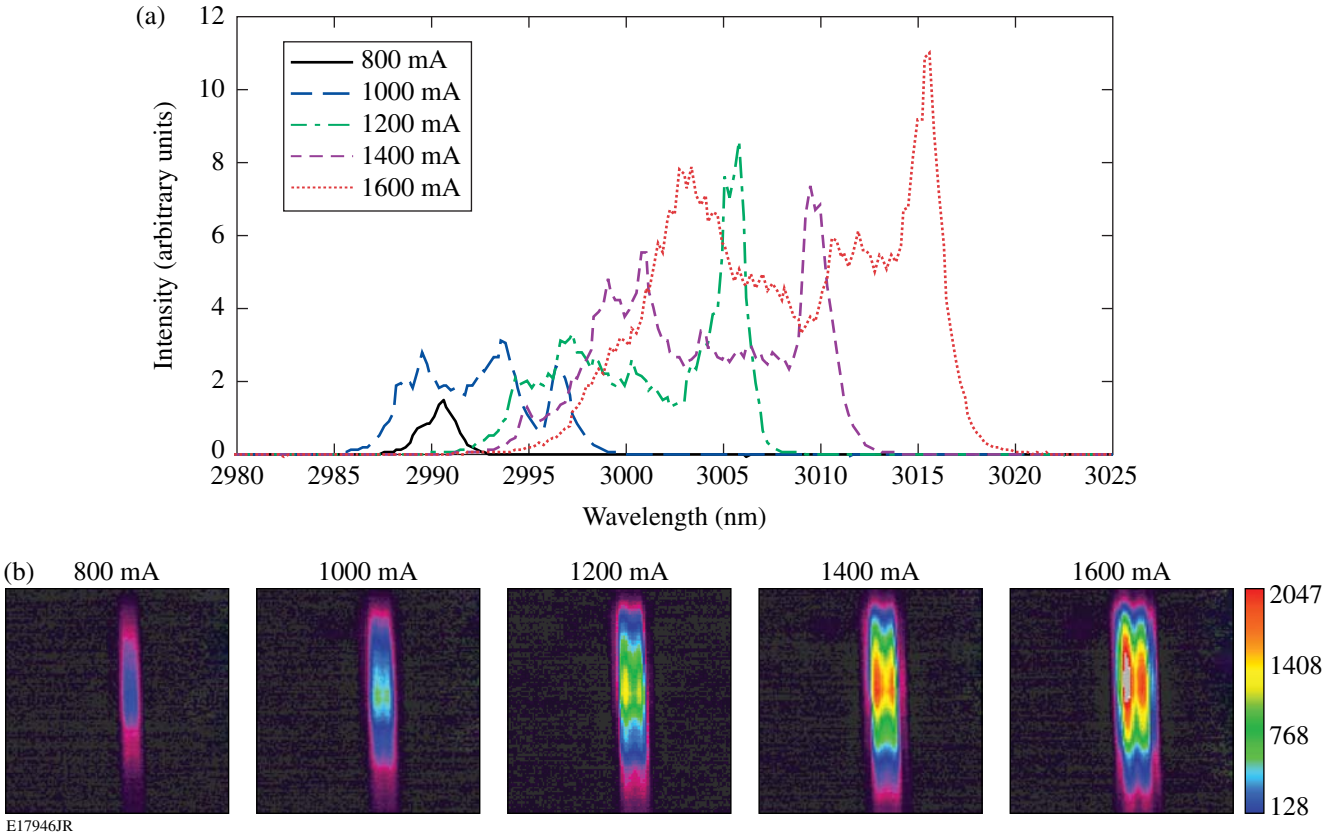

Figure 118.52
The diode laser's spectral shape and position change with (a) driver current as well as (b) beam profile. Data were taken at 14°C.

the diode laser's output power should be set for maximum and then the laser should be temperature tuned to a D_2-ice absorption peak for this application. An external attenuator should be used to achieve the required level of target illumination.

The output beam's profile taken with a Pirocam III mid-IR camera (Spiricon) is not uniform along the diode output stripe and changes slightly with current [Fig. 118.52(b)]. The output divergence is typical for diode lasers and is ~65° along the fast axis and ~20° along the slow axis. Two ways of delivering radiation to a layering sphere are considered: using multimode mid-IR delivery fiber or mounting the diode laser directly on a layering sphere. In both cases the diode laser-beam profile quality will not affect the layering process.

The spectral stability of the diode laser over time was measured at various temperatures. Figure 118.53 shows four groups of spectra taken at 1600-mA current and various temperatures. Each group contains five spectra taken at 15-min intervals, i.e., over a 1-h period. At 14°C, the spectrum consists of two peaks with approximately equal intensities. The left peak intensity decreases and its stability becomes lower as the temperature increases. The stability of the left peak at 20°C is low due to the fact that it lases close to the threshold. This explains the lower output-power stability for this particular diode at higher temperatures. At the same time, the important criterion can be drawn for diode-laser selection for cryogenic target layering: a diode laser that is temperature tuned to the required wavelength must have a smooth and compact spectrum without low-intensity parts. The spectral nonuniformities of the laser diode output can be associated with lateral fluctuation of the quantum-well parameters across the wafer, owing to a nonoptimized growth regime of the quinary InAlGaAsSb barrier alloy used in the laser heterostructure to improve hole localization in the active region. It was shown that other diode-fabrication batches with an optimized growth regime result in lasers that have smooth and compact spectra. This criterion can be met by the careful selection of diode lasers from different batches.

Conclusion and Future Research

We have studied the spectral and output-power stability of a 3-μm-wavelength mid-IR diode laser and demonstrated the highly stable operation of a diode laser at up to >50 mW of output power with <1% rms variations at 1600-mA current and 14°C TEC temperature. It has been shown that spectral shape can affect the output-power stability. Future research will consist of building diode lasers that can be tuned to the target's ice absorption band (3160 nm) with a smooth and compact spectrum at the required wavelength. Highly efficient multimode, mid-IR fiber launching will be considered for delivering the radiation to a layering sphere, or the diode laser may be directly mounted on it.

ACKNOWLEDGMENT

This work was supported by the U.S. Department of Energy Office of Inertial Confinement Fusion under Cooperative Agreement No. DE-FC52-08NA28302, the University of Rochester, and the New York State Energy Research and Development Authority. The support of DOE does not constitute an endorsement by DOE of the views expressed in this article. SUNY work was supported by US Air Force Office of Scientific Research under grant FA95500410372, and by US Army Research Office grant W911NF0610399.

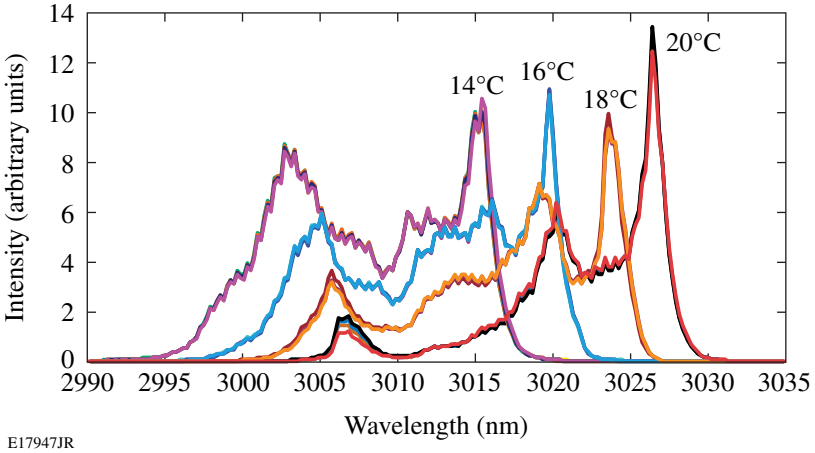

Figure 118.53
The diode laser's spectral stability decreases with an increase of temperature.

REFERENCES

1. T. R. Boehly, D. L. Brown, R. S. Craxton, R. L. Keck, J. P. Knauer, J. H. Kelly, T. J. Kessler, S. A. Kumpan, S. J. Loucks, S. A. Letzring, F. J. Marshall, R. L. McCrory, S. F. B. Morse, W. Seka, J. M. Soures, and C. P. Verdon, Opt. Commun. **133**, 495 (1997).

2. T. C. Sangster, R. Betti, R. S. Craxton, J. A. Delettrez, D. H. Edgell, L. M. Elasky, V. Yu. Glebov, V. N. Goncharov, D. R. Harding, D. Jacobs-Perkins, R. Janezic, R. L. Keck, J. P. Knauer, S. J. Loucks, L. D. Lund, F. J. Marshall, R. L. McCrory, P. W. McKenty, D. D. Meyerhofer, P. B. Radha, S. P. Regan, W. Seka, W. T. Shmayda, S. Skupsky, V. A. Smalyuk, J. M. Soures, C. Stoeckl, B. Yaakobi, J. A. Frenje, C. K. Li, R. D. Petrasso, F. H. Séguin, J. D. Moody, J. A. Atherton, B. D. MacGowan, J. D. Kilkenny, T. P. Bernat, and D. S. Montgomery, Phys. Plasmas **14**, 058101 (2007).

3. L. M. Elasky, D. J. Lonobile, W. A. Bittle, D. R. Harding, A. V. Okishev, and J. D. Zuegel, presented at the 15th Target Fabrication Specialists' Meeting, Gleneden Beach, OR, 1–5 June 2003.

4. T. Hosoda *et al*., Appl. Phys. Lett. **92**, 091106 (2008).

5. L. Shterengas *et al*., Appl. Phys. Lett. **92**, 171111 (2008).

6. L. Shterengas *et al*., Appl. Phys. Lett. **93**, 011103 (2008).

Shock-Ignition Experiments on OMEGA at NIF-Relevant Intensities

Shock ignition is a two-step inertial confinement fusion (ICF) concept in which a strong shock wave is launched at the end of the laser pulse to ignite the compressed core of a low-velocity implosion.[1] Two-step processes separate fuel assembly and ignition, relaxing driver requirements and promising high gains.[1,2] The gain of an ICF implosion can be significantly enhanced by launching a strong spherically convergent shock at the end of the compression (or assembly) pulse.[1,3–5] Another advanced-ignition concept is fast ignition,[6] which relies on a high-intensity, short-pulse laser generating an energetic beam of particles to trigger ignition. Shock ignition relies on highly shaped laser pulses, which might be produced by the pulse-shaping capabilities of the already operating National Ignition Facility (NIF).[7] Recent two-dimensional (2-D) simulations[4] have described shock-ignition designs with as low as 250 kJ of total laser energy. Proof-of-principle experiments[1,8] could be carried out at the NIF. The spherically convergent shock wave (ignitor shock) propagates through the shell during the coasting phase of the implosion and enhances the hot-spot compression, significantly improving the ignition conditions. The ignitor shock is launched at the end of the laser pulse by a spike with intensity in the range of 3×10^{15} to 10^{16} W/cm^2. This shock collides with the return shock near the inner shell surface. The return shock is the shock wave driven by the hot-spot pressure and propagating outward through the shell. After the ignitor and return shock collide, a third shock wave, resulting from the collision, propagates inward, leading to further compression of the hot spot. The final fuel assembly develops a centrally peaked pressure profile. Such non-isobaric assemblies exhibit a lower ignition threshold than standard isobaric assemblies. This mechanism is effective only in thick-shell implosions, where the ignitor shock wave significantly increases in strength as it propagates through the converging shell.[1]

Previous shock-ignition experiments[9] on OMEGA[10] studied fuel assembly with 60-beam symmetric implosions with 18 kJ of UV laser energy using 40-μm-thick, 0.9-mm-diam, warm surrogate plastic shells filled with deuterium gas of various pressures. The shock wave was launched by a spike in the laser power at the end of the pulse. The maximum intensity on target during the late power spike was $\sim 8 \times 10^{14}$ W/cm^2, and the resulting shock wave was relatively weak (the shock pressure was only 20 Mbar higher than the unshocked plasma pressure). These experiments showed a significant improvement in the performance of low-adiabat, low-velocity implosions compared to conventional implosions without a late spike in the laser pulse shape and showed that shock-wave timing is crucial to optimizing implosion performance. This shock-ignition campaign achieved the highest areal density ever measured on OMEGA (a neutron-rate–averaged areal density of 0.22 g/cm^2 and a peak areal density exceeding 0.3 g/cm^2) and neutron yields 4× larger than in conventional implosions.[9]

Parametric plasma instabilities[11] such as stimulated Brillouin scattering (SBS), stimulated Raman scattering (SRS), and two-plasmon-decay (TPD) instability are of concern in an ignition target design with spike-pulse intensities in the range of 10^{15} to 10^{16} W/cm^2 and full width at half maximum (FWHM) pulse durations of several hundred picoseconds. The instabilities increase the back-reflection of the laser light from the target, degrading the laser energy coupling to the capsule. They increase the fraction of the laser energy transferred to suprathermal electrons, a potential source of preheat that reduces the final core compression. In contrast to conventional hot-spot ignition, low-energy hot electrons generated during the power spike may have a positive effect on the implosions for shock ignition. The areal density increases rapidly during the final stages of the implosion. If the range of the hot electrons generated during the intensity spike is less than the shell thickness, they are stopped in the shell and augment the hydrodynamically driven shock wave. The effect of hot electrons on a shock-ignition target[12] was modeled in 1-D for a marginal igniting target using a multigroup diffusion model[13] for the hot electrons. The ignition window for a shock-launching time is considerably wider when the effects of moderate-energy hot electrons (a NIF-scale target can efficiently stop up to 150-keV electrons) are included, showing that hot electrons can indeed be beneficial for the shock-ignition scheme as long as their range is shorter than the shell's thickness.

This work provides the first measurements of parametric instability and preheat for conditions relevant for shock ignition (spherical target, long density scale length, and intensities above 2×10^{15} W/cm^2). Important physics issues including the hot-electron energy content, the hot-electron temperature, and laser backscattering for various intensities and time delays between fuel assembly and shock generation are studied. Switching from a 60-beam to a 40- plus 20-beam configuration with dual pulse shapes makes it possible to use tightly focused beams that generate a stronger shock compared to previous experiments. The data will help validate the shock-ignition target concepts at ignition-relevant intensities of ~5×10^{15} W/cm^2.

Figure 119.1 shows a schematic of the experiments described here. The compression pulse consisted of a shaped, low-adiabat laser pulse using 40 beams of OMEGA.[10] A late shock was driven by the remaining 20 beams that were delayed and focused on the compressed core to achieve intensities at the critical surface ranging from ~2×10^{15} to ~8×10^{15} W/cm^2. Plasma instabilities in density regions of up to quarter-critical density led to the generation of energetic electrons. Some of the fast electrons streamed into the hot core, heating it.

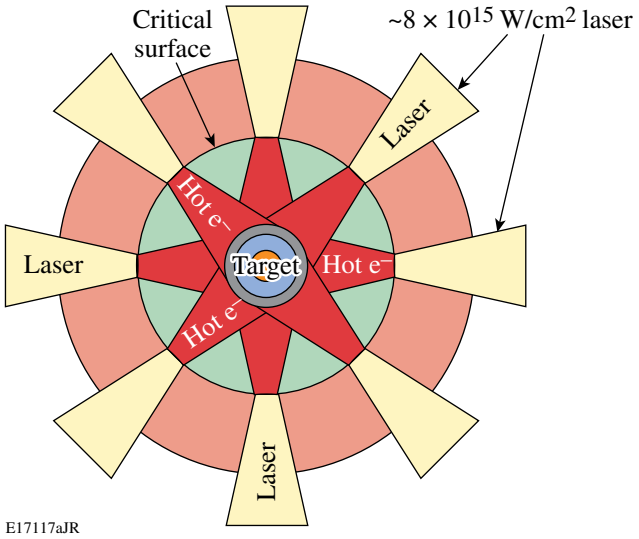

Figure 119.1
Schematic of the setup for studying laser–plasma interactions and preheating at high laser intensities relevant to shock ignition. Forty of the OMEGA laser beams implode the capsule at low intensities. Twenty delayed beams are tightly focused onto the critical density surface, where plasma instabilities lead to the generation of energetic electrons. Some of them will stream into the dense core.

The targets were 36-μm-thick, 430-μm-outer-radius, deuterated plastic (CD) shells coated outside with a 0.1-μm layer of aluminum and filled with D_2 gas with a pressure of ~30 atm. The capsules were imploded by 40 beams using a low-adiabat ($\alpha \sim 1.5$) pulse shape[14] at ~13.6 kJ of UV laser energy. The adiabat α is defined as the ratio of the plasma pressure to the Fermi pressure of a degenerate electron gas.[15] The solid curve in Fig. 119.2(a) shows the drive pulse shape comprising an ~100-ps (FWHM) Gaussian picket pulse preceding a shaped main-drive portion that consisted of a low-power foot and a moderate-power plateau with a total duration of 2.6 ns. The 351-nm-wavelength laser light of the 40 beams was smoothed with polarization smoothing[16] and distributed phase plates.[17] The delayed 20 beams (~4.6 kJ) that used an ~600-ps FWHM square pulse shape (dotted curve) were tightly focused on the shell without polarization smoothing or phase plates.

The experimental observables were the neutron yield,[18] the backscattered laser energy,[19] the hard x-ray signal,[20] and the neutron-rate–averaged areal density.[21] The laser light reflected back from the imploded capsule was measured from two beam ports [a shock-beam port (#25) and a drive-beam port (#30)], which were equipped with a full-aperture backscatter station (FABS).[19] The FABS measured the light backscattered into the final focusing lens aperture by down-collimating the reflection off the front surface of a full-aperture, uncoated glass wedge in the beamline onto a diagnostics table. Time-resolved spectra were recorded by two streaked spectrometers covering the wavelength ranges of 351±3 nm for SBS and 450 to 700 nm for SRS. The total backscattered energy in either of these spectral ranges was measured by calorimeters with an uncertainty of ±10%. The hard x-ray (HXR) signals (with photon energies >20 keV) were measured by the HXR detector with four channels measuring x rays >20, >40, >60, and >80 keV, respectively.[20] Areal densities (ρR) were inferred from secondary proton spectra.[21]

The delay time defined by the onset of the high-intensity beams with respect to the start of the drive pulse was varied from 2.3 to 2.9 ns. The effect on neutron and HXR yield is shown in Figs. 119.2(b) and 119.2(c) and on ρR in Fig. 119.2(d). The different symbols represent various focus conditions, where the number refers to the focus position in vacuum with respect to the shell's center. A negative number means that the focus is in front of the target toward the laser. The neutron yield increases by a factor of ~7 from 5×10^8 to ~3.5×10^9 for the shortest time delay. Two reference implosions with only the 40 drive beams produced neutron yields of 1.4×10^8 and 3.7×10^8; the solid line in Fig. 119.2(b) represents the average of both yields. The HXR yield's dependence on delay time is

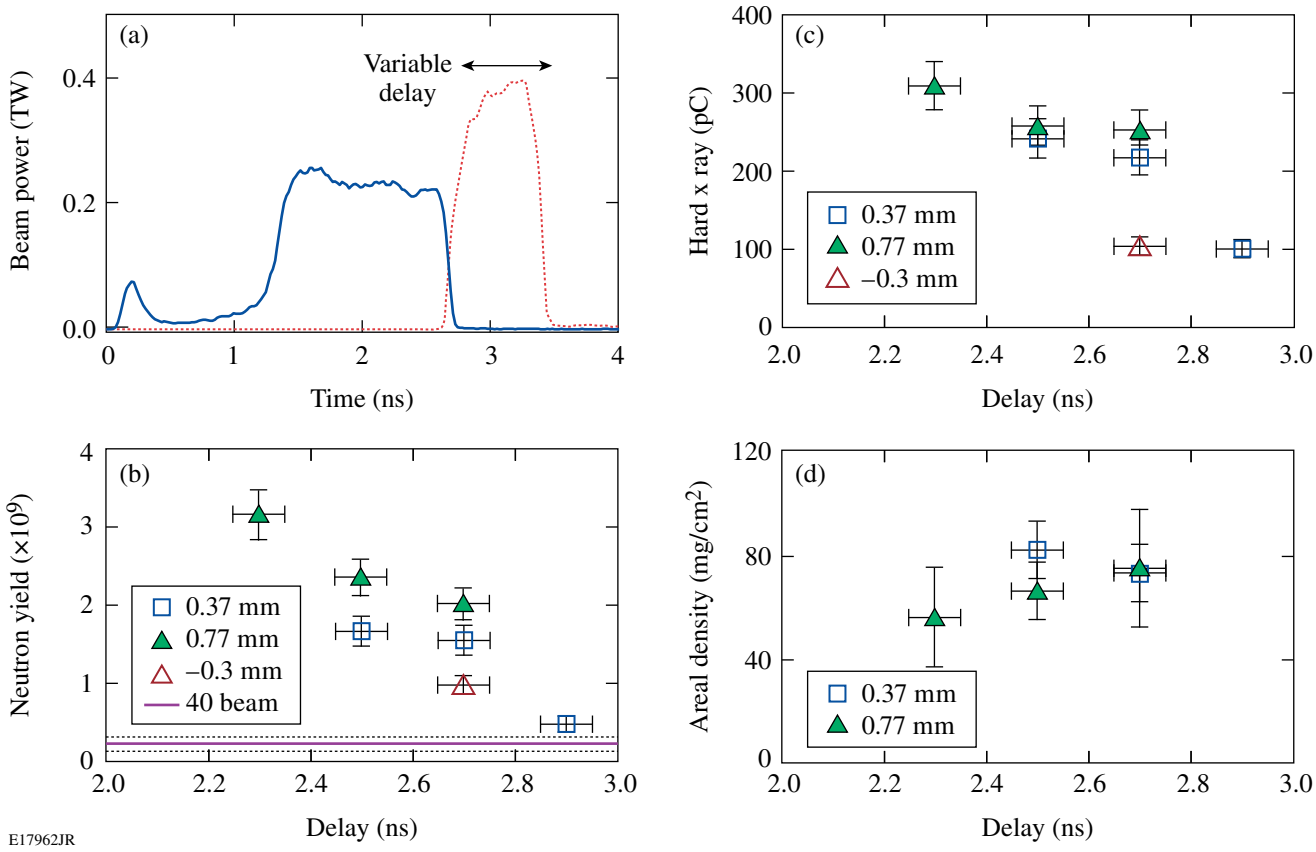

Figure 119.2
(a) Drive-pulse shape (solid) and high-intensity pulse (dotted), [(b)–(d)] measured neutron yield, hard x-ray yield, and neutron-rate–averaged areal density, respectively. The different symbols represent various focus positions with respect to the critical-density surface. The solid line in (b) is the average yield for 40-beam implosions and the dotted lines represent the error range. The 40-beam implosions produced no measurable HXR signal, and neutron yields were too low to obtain a ρR measurement.

similar. Figure 119.2(c) shows that signals measured by the >40-keV channel increase with shorter delay.

The HXR signal provided information on the hot-electron energy and temperature. Based on a calibration[22] of the hard x-ray detector, ~16±6% (~310-pC HXR signal) to ~5±2% of the shock-beam energy was converted into hot electrons. The conversion efficiency was highest for short delays when there was a partial overlap between the drive and shock pulses [Fig. 119.2(c)]. The hot-electron temperature was determined by fitting estimated values from the convolution of an exponentially decaying hard x-ray spectrum with the sensitivity of the different channels of the HXR detector to the measured four channels.[23] The inferred temperature was ~40 to 45 keV for all the shots, independent of laser intensity.

The implosions were nonuniform with a dominant $\ell = 2$ mode, which was caused by an unbalanced target illumination. The power imbalance was ~10.6%, given as the root-mean-square variation of the laser power on target. A typical value for a 60-beam symmetrical illumination on a spherical target is ~2% power imbalance.[24] The nonuniformity of the implosion is clearly seen in the x-ray pinhole camera image [Fig. 119.3(a)], which shows a strongly perturbed core with a 40-beam implosion. The core distortion was reduced when the 20 delayed, tightly focused beams were coupled into the target [Fig. 119.3(b)]. Figure 119.3(c) shows pinhole images from a symmetric implosion with a low-adiabat pulse shape and a similar target at a higher laser energy. Figures 119.2(b) and 119.2(c) show that despite large target illumination nonuniformity, a significant amount of the high-intensity pulse energy was coupled into the capsule, producing up to ~20× more neutrons and a strong HXR signal. The correlation of increasing neutron yield with a higher HXR signal suggests that the increased yield was partially due to hot electrons coupled into the outer regions of the compressing target. The late shock

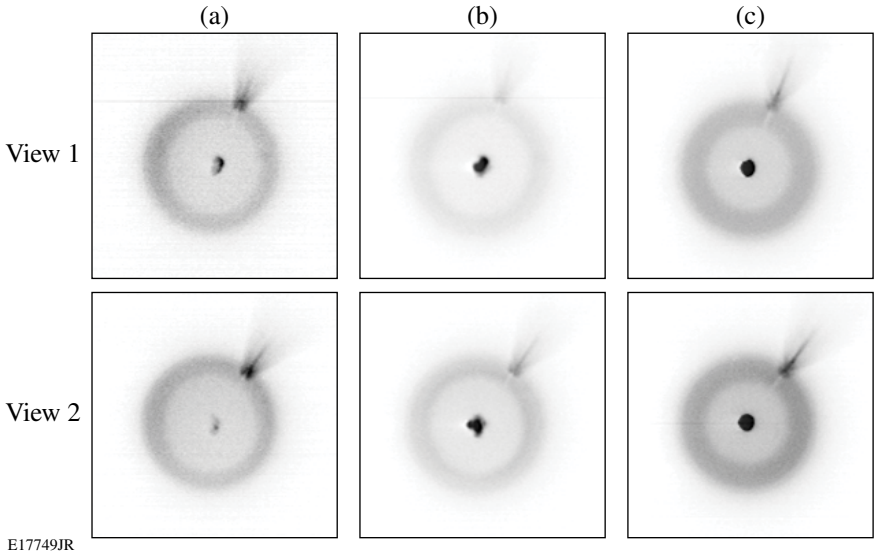

Figure 119.3
X-ray pinhole camera images from three different implosions. (a) Reference implosion with 40 drive beams, (b) 40- plus 20-beam implosion for a 0.77-mm focus position and a 2.3-ns time delay, (c) 60-beam uniform illumination. The feature at the upper right edge is due to the target stalk.

appears to be driven by a combination of the standard ablative and hot-electron drives.

The areal density does not change significantly with delay. The measured maximum ρR is 82±11 mg/cm^2, which is the average of four lines of sight, and the error bar is the standard deviation. This is ~30% lower than the expected ~115 mg/cm^2, which is scaled down from the measured 130±17 mg/cm^2 (Ref. 14) that was obtained with a more-uniform 60-beam implosion with the same fill pressure, the same adiabat, and an energy of 20 kJ and using the scaling of ρR with the laser energy to the power 1/3 (Ref. 14). For these shots, the standard deviation of the measured ρR varies from 15% to 35% of the mean ρR value, showing a large fluctuation of the areal density. The ρR degradation is most likely due to the strongly nonuniform implosion. Neutron yields from the 40-beam implosions were too low to obtain a ρR measurement.

The plasma reflectivity and HXR production from hot electrons were measured for various laser intensities. This was achieved through an intensity scan by shifting the focus of the 20 shock-driving beams relative to the shell's center. The nominal (in vacuum) laser intensity is quoted for the location of the critical-density plasma surface calculated by a 1-D hydrodynamic simulation.[13] The distance from the critical density to the capsule center was ~0.3 mm at 2.7 ns. For the lens position at –0.3 mm, the 20 beams were tightly focused on the critical-density location. The focus diameter of the 20 shock beams is estimated with ~80 μm, which gives a best-focus intensity up to ~8×10^{15} W/cm^2 for the shock beams in vacuum. The foci of the 20 shock beams did not overlap at the critical density for all lens positions used. No overlapped-beam effects[20] were expected and the HXR signal was dominated by single-beam interaction with the target.

Figure 119.4(a) shows the measured hard x-ray signal normalized to the estimated laser focus area versus lens position. The x-ray signal and consequently the hot-electron production increase with laser intensity presumably because of a larger growth in laser–plasma instabilities such as SRS and TPD, the primary sources of hot electrons.[20] Figure 119.4(b) shows the measured amount of laser backscatter energy of one shock beam (25) versus laser intensity. It increases from ~10% at ~2×10^{15} W/cm^2 to ~36% at ~8×10^{15} W/cm^2. The contribution from the SBS signal increases moderately from ~7% to 12%, while the SRS signal grows by almost a factor of ~5 from 5% to 24% and dominates the backscattering energy at the highest intensity. The simultaneously measured back-reflection through a neighboring drive-beam port (30) remained constant at the level of the implosions without the 20 shock beams for all beam delays and lens positions. This shows that the light from the shock beams was scattered back in a narrow cone and did not spill over into adjacent ports. No measurable signal of the 3/2 harmonic of the laser wavelength was measured for all inten-

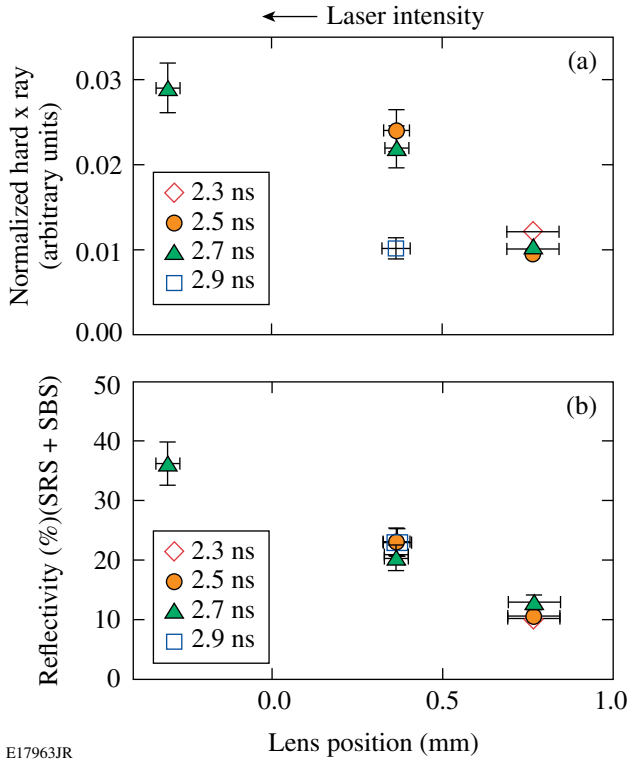

Figure 119.4
Measured (a) hard x-ray signal normalized to nominal beam focus area and (b) backscattered light versus lens focus position with respect to the shell's center. The laser intensity at the critical density is highest for the negative lens position corresponding to an intensity of $\sim 8 \times 10^{15}$ W/cm^2. The various symbols represent different time delays.

sities. The half-harmonic signal decreased by more than two orders of magnitude with higher intensities. At the maximum intensity, the half-harmonic signal was below the detection threshold, indicating no significant contribution of TPD to the hot-electron production. These experiments measured higher backscattering levels than other experiments at comparable laser intensities but different plasma conditions.[25] Measurements of parametric instabilities for indirect-drive–relevant ignition-plasma conditions with millimeter-density scale length and 15% critical-density targets report backscatter at 5×10^{15} W/cm^2 of up to 10%.[25] The absorbed energy rather than the backscattered light is the key issue. If 36% of the laser light is backscattered and 64% is absorbed, it represents a higher absorption fraction than the prediction of collisional absorption at these intensities (~40% to 50%). Because of the highly nonuniform plasma conditions and nonuniform illumination during the shock spike, the measurement of the scattered light through a few lines of sight cannot be used to infer the total absorbed fraction. In the pessimistic case where the predicted absorbed energy is reduced by the backscattered fraction, this can be remedied by an increase in spike power.

In conclusion, shock-ignition laser–plasma experiments in spherical geometry have been performed with nominal laser intensities of up to $\sim 8 \times 10^{15}$ W/cm^2. This was achieved by low-adiabat compression of warm plastic shells filled with D_2 gas by 40 beams and tightly focusing 20 beams on the compressed core. The additional 20 high-intensity beams enhanced the neutron yields by up to a factor of ~20, indicating a good coupling of the shock-beam energy to the core. A significant amount of backscattered laser energy from the high-intensity beams of up to 36% was measured at the highest laser intensity and about 20% at $\sim 5 \times 10^{15}$ W/cm^2. At high intensities, the back-reflection was dominated by SRS with some contribution from SBS but no significant contribution from TPD. About 10% of the high-intensity beam energy was converted into hot electrons. A hot-electron-energy distribution was generated with temperatures between ~40 and 45 keV, independent of laser intensity. This is beneficial for shock ignition since these electrons are stopped in a thin outer layer of the imploding target, augmenting the strong hydrodynamic shock. The reduction in driver energy caused by backscattering losses might be compensated by increasing the incident laser energy without the danger of preheating the target.

ACKNOWLEDGMENT

This work was supported by the U.S. Department of Energy Office of Inertial Confinement Fusion under Cooperative Agreement No. DE-FC52-08NA28302, the OFES Fusion Science Center grant No. DE-FC02-04ER54789, the OFES ACE FI grant No. DE-FG02-05ER54839, the University of Rochester, and the New York State Energy Research and Development Authority. The support of DOE does not constitute an endorsement by DOE of the views expressed in this article.

REFERENCES

1. R. Betti, C. D. Zhou, K. S. Anderson, L. J. Perkins, W. Theobald, and A. A. Solodov, Phys. Rev. Lett. **98**, 155001 (2007).

2. R. L. McCrory, D. D. Meyerhofer, R. Betti, R. S. Craxton, J. A. Delettrez, D. H. Edgell, V. Yu Glebov, V. N. Goncharov, D. R. Harding, D. W. Jacobs-Perkins, J. P. Knauer, F. J. Marshall, P. W. McKenty, P. B. Radha, S. P. Regan, T. C. Sangster, W. Seka, R. W. Short, S. Skupsky, V. A. Smalyuk, J. M. Soures, C. Stoeckl, B. Yaakobi, D. Shvarts, J. A. Frenje, C. K. Li, R. D. Petrasso, and F. H. Séguin, Phys. Plasmas **15**, 055503 (2008).

3. R. Betti and C. Zhou, Phys. Plasmas **12**, 110702 (2005).

4. X. Ribeyre *et al.*, Plasma Phys. Control. Fusion **50**, 025007 (2008).

5. A. J. Schmitt, J. W. Bates, S. P. Obenschain, S. T. Zalesak, D. E. Fyfe, and R. Betti, Fusion Sci. Technol. **56**, 377 (2009).

6. M. Tabak *et al*., Phys. Plasmas **1**, 1626 (1994).

7. E. I. Moses, J. Phys., Conf. Ser. **112**, 012003 (2008).

8. L. J. Perkins, R. Betti, K. N. LaFortune, and W. H. Williams, Phys. Rev. Lett. **103**, 045004 (2009).

9. W. Theobald, R. Betti, C. Stoeckl, K. S. Anderson, J. A. Delettrez, V. Yu. Glebov, V. N. Goncharov, F. J. Marshall, D. N. Maywar, R. L. McCrory, D. D. Meyerhofer, P. B. Radha, T. C. Sangster, W. Seka, D. Shvarts, V. A. Smalyuk, A. A. Solodov, B. Yaakobi, C. D. Zhou, J. A. Frenje, C. K. Li, F. H. Séguin, R. D. Petrasso, and L. J. Perkins, Phys. Plasmas **15**, 056306 (2008).

10. T. R. Boehly, D. L. Brown, R. S. Craxton, R. L. Keck, J. P. Knauer, J. H. Kelly, T. J. Kessler, S. A. Kumpan, S. J. Loucks, S. A. Letzring, F. J. Marshall, R. L. McCrory, S. F. B. Morse, W. Seka, J. M. Soures, and C. P. Verdon, Opt. Commun. **133**, 495 (1997).

11. W. L. Kruer, *The Physics of Laser–Plasma Interactions*, Frontiers in Physics, Vol. 73, edited by D. Pines (Addison-Wesley, Redwood City, CA, 1988).

12. R. Betti, W. Theobald, C. D. Zhou, K. S. Anderson, P. W. McKenty, S. Skupsky, D. Shvarts, V. N. Goncharov, J. A. Delettrez, P. B. Radha, T. C. Sangster, C. Stoeckl, and D. D. Meyerhofer, J. Phys., Conf. Ser. **112**, 022024 (2008).

13. J. Delettrez, R. Epstein, M. C. Richardson, P. A. Jaanimagi, and B. L. Henke, Phys. Rev. A **36**, 3926 (1987); M. C. Richardson, P. W. McKenty, F. J. Marshall, C. P. Verdon, J. M. Soures, R. L. McCrory, O. Barnouin, R. S. Craxton, J. Delettrez, R. L. Hutchison, P. A. Jaanimagi, R. Keck, T. Kessler, H. Kim, S. A. Letzring, D. M. Roback, W. Seka, S. Skupsky, B. Yaakobi, S. M. Lane, and S. Prussin, in *Laser Interaction and Related Plasma Phenomena*, edited by H. Hora and G. H. Miley (Plenum Publishing, New York, 1986), Vol. 7, pp. 421–448.

14. C. D. Zhou, W. Theobald, R. Betti, P. B. Radha, V. A. Smalyuk, D. Shvarts, V. Yu. Glebov, C. Stoeckl, K. S. Anderson, D. D. Meyerhofer, T. C. Sangster, C. K. Li, R. D. Petrasso, J. A. Frenje, and F. H. Séguin, Phys. Rev. Lett. **98**, 025004 (2007).

15. C. D. Zhou and R. Betti, Phys. Plasmas **14**, 072703 (2007).

16. T. R. Boehly, V. A. Smalyuk, D. D. Meyerhofer, J. P. Knauer, D. K. Bradley, R. S. Craxton, M. J. Guardalben, S. Skupsky, and T. J. Kessler, J. Appl. Phys. **85**, 3444 (1999).

17. Y. Lin, T. J. Kessler, and G. N. Lawrence, Opt. Lett. **21**, 1703 (1996).

18. V. Yu. Glebov, D. D. Meyerhofer, C. Stoeckl, and J. D. Zuegel, Rev. Sci. Instrum. **72**, 824 (2001).

19. W. Seka, D. H. Edgell, J. P. Knauer, J. F. Myatt, A. V. Maximov, R. W. Short, T. C. Sangster, C. Stoeckl, R. E. Bahr, R. S. Craxton, J. A. Delettrez, V. N. Goncharov, I. V. Igumenshchev, and D. Shvarts, Phys. Plasmas **15**, 056312 (2008).

20. C. Stoeckl, R. E. Bahr, B. Yaakobi, W. Seka, S. P. Regan, R. S. Craxton, J. A. Delettrez, R. W. Short, J. Myatt, A. V. Maximov, and H. Baldis, Phys. Rev. Lett. **90**, 235002 (2003).

21. F. H. Séguin, J. A. Frenje, C. K. Li, D. G. Hicks, S. Kurebayashi, J. R. Rygg, B.-E. Schwartz, R. D. Petrasso, S. Roberts, J. M. Soures, D. D. Meyerhofer, T. C. Sangster, J. P. Knauer, C. Sorce, V. Yu. Glebov, C. Stoeckl, T. W. Phillips, R. J. Leeper, K. Fletcher, and S. Padalino, Rev. Sci. Instrum. **74**, 975 (2003).

22. V. A. Smalyuk, D. Shvarts, R. Betti, J. A. Delettrez, D. H. Edgell, V. Yu. Glebov, V. N. Goncharov, R. L. McCrory, D. D. Meyerhofer, P. B. Radha, S. P. Regan, T. C. Sangster, W. Seka, S. Skupsky, C. Stoeckl, B. Yaakobi, J. A. Frenje, C. K. Li, R. D. Petrasso, and F. H. Séguin, Phys. Rev. Lett. **100**, 185005 (2008).

23. C. Stoeckl, V. Yu. Glebov, D. D. Meyerhofer, W. Seka, B. Yaakobi, R. P. J. Town, and J. D. Zuegel, Rev. Sci. Instrum. **72**, 1197 (2001).

24. F. J. Marshall, J. A. Delettrez, R. Epstein, R. Forties, R. L. Keck, J. H. Kelly, P. W. McKenty, S. P. Regan, and L. J. Waxer, Phys. Plasmas **11**, 251 (2004).

25. J. D. Moody *et al*., Phys. Rev. Lett. **86**, 2810 (2001).

Laser-Driven Magnetic-Flux Compression in High-Energy-Density Plasmas

In the magnetic-fusion-energy (MFE) concept, a strong magnetic field confines the plasma and reduces the electron thermal conduction to the vessel wall.[1] The magnetic pressure of typical ~0.1-MG fields in MFE is higher than the total energy density of the plasma (with $\beta = 2\mu_0 p/B^2 < 1$). MFE plasmas are fully magnetized and characterized by a Hall parameter $\omega_{ce}\tau \gg 1$ since the modest gyrofrequency ω_{ce} is matched by long collision times τ. In contrast, typical inertial confinement fusion (ICF) plasmas have collision frequencies higher by 10 to 12 orders of magnitude because of their extreme density. In such systems, thermal conduction losses are a major factor in the energy balance of an implosion. While it may be more difficult, magnetizing the hot spot in ICF implosions can lead to improved gain in implosions of massive targets with relatively low implosion velocity[2] or to a reduction of the energy required for ignition. However, tens of MG are needed to achieve $\omega_{ce}\tau \sim 1$ in the hot spot of a typical direct-drive DT ignition target[3] with a hot-spot density of ~30 g/cc and a temperature of ~7 keV. Such a field is higher than both the self-generated magnetic fields (see Ref. 4) and the external fields that can be generated by coils. Magnetic-flux compression[5] is a viable path to generating tens-of-MG magnetic fields with adequate size.[6] Magnetic-flux compression has been successfully achieved using the radial compression of a metallic liner driven by high explosives[7,8] or by pulsed power. The latter approach has been pursued by the Z-pinch[9] (including wire-array targets) and magnetized-target-fusion[10] communities. The results from the first experiments on a new approach that provides very effective flux compression are reported here. The field is compressed by the ablative pressure exerted on an imploding ICF capsule by the driving laser.[11] This approach was proposed in the 1980s (Ref. 12) as a way to achieve record compressed fields with possible applications for fusion,[13] but no laser experiments were performed. There are numerous advantages to this approach because the implosion velocity is high (a few 10^7 cm/s) and the hot plasma is an effective conductor that traps the embedded (seeded) initial magnetic field with minimal resistive diffusion. This approach can be used to magnetize high-energy-density plasmas for a number of applications ranging from controlled fusion to laboratory astrophysics.

Figure 119.5 describes a cylindrical implosion on OMEGA that used axial seed fields embedded in the target prior to compression.[14] The target was a 20-μm-thick, 0.86-mm-diam CH cylindrical shell filled with D_2 gas. Some of the physical details of this concept are described in Refs. 11 and 15. The shock-heated and ionized D_2 fuel traps the seed magnetic field, which would otherwise diffuse much faster through the relatively cold (resistive) imploding shell. The seed field was provided by a Helmholtz-like double coil [Fig. 119.6(a); coil diameter and separation are both 4 mm], coaxial with the cylindrical target.[16] The more-complicated min-B magnetic geometries used in magnetic-confinement-fusion (MCF) magnetic mirror experiments were not used here because the magnetohydrodynamic (MHD) instability must be considered more carefully. A portable capacitive discharge system[16] delivers up to 80-kA current to the coils. The on-axis seed field was 50 to 90 kG at the target and 120 to 160 kG in the coil planes because of the coil separation chosen to avoid obscuring laser beams.

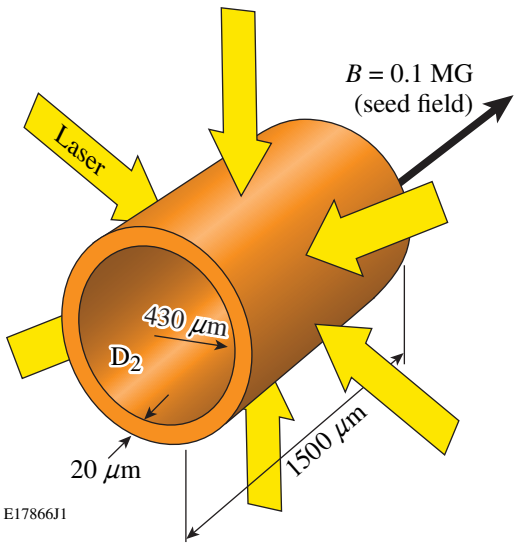

Figure 119.5
Laser-driven flux compression in a cylindrical target. A D_2-gas fill inside the plastic shell traps the seed field after shock ionization.

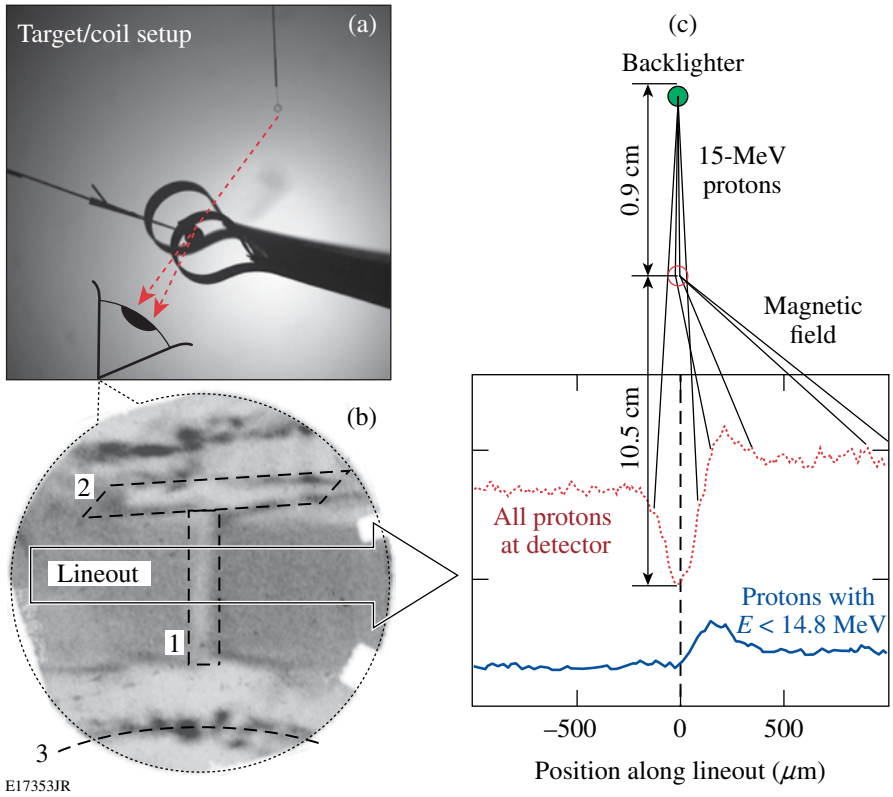

Figure 119.6
(a) Photo of the target/coil setup. (b) Proton density map for shot 51069. Darker areas represent higher fluence: (1) compressed core, (2) target plug, and (3) coil shadow. (c) Lineouts in two energy bands expose the deflected protons (E_k < 14.8 MeV, solid line; all protons, dotted line).

The compressed fields within the dense, optically thick ICF plasmas are difficult to measure. Proton deflectometry based on the method described in Refs. 17–19 is a viable diagnostic that has been implemented on OMEGA. A monoenergetic ($\Delta E/E \sim 0.03$), point-like (size/object distance ~0.01), time-gated (an ~150-ps burst) proton source is provided by a glass sphere, filled with D^3He gas and driven in an exploding pusher scheme by several tightly focused OMEGA beams. The 14.7-MeV protons produced by the D-^{3}He fusion reactions are accelerated to ~15.2 MeV by charging the backlighter target and recorded on a CR-39 nuclear track detector that provides both spatial and energy resolution (via the track diameter) of the particles incident on the surface.[20] The data [Fig. 119.6(b)] were generated as a convolution in space (source size, scattering at the object and detector) and time (finite duration) of the proton burst interacting with the field and target structure. None of the radial striations reported in Ref. 18 for spherical implosions was seen around the compressed core in these experiments, possibly because the target was imaged more than a nanosecond after the laser was turned off. Turbulent field structure was present around the target plugs and stalk, but, while interesting, its morphology is beyond the scope of this article and will not be discussed.

A discrimination of tracks by energy (track diameter) was implemented to separate the core- (strong-field) traversing protons from the background, "free-space" particles that land in the same area of the detector. This is shown in Fig. 119.6(c), where the proton density map for shot 51069 [Fig. 119.6(b)] was used to construct two lineouts by taking a band of data and averaging over its width. The lower curve in Fig. 119.6(c) is from tracks with only energy E_k < 14.8 MeV caused by an additional slowdown through the magnetized target. It shows an asymmetric peak in the proton density caused by deflection in the target field. In contrast, the data from multiple "null" experiments performed to establish the particle-density pattern for implosions with no seed field retain central symmetry in the cross-core lineouts (Fig. 119.7); i.e., the low-energy peak lines up with the trough of the high-energy proton lineout.

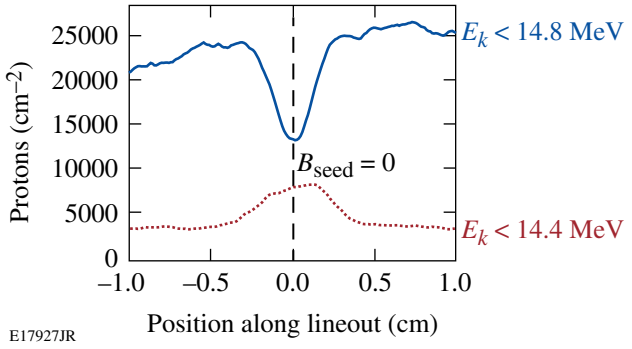

Figure 119.7
Cross-core lineouts from proton radiograph of shot 49693—an implosion with no external magnetic field—show that the core-traversing protons remained undeflected.

To predict and interpret the experimental data, a simulation package based on the Monte Carlo (MC) particle-transport framework Geant4 (Ref. 21) was developed. After including the field topology and material parameters predicted by the *LILAC*-MHD code[22] for the time of proton probing, the particle-transport code computes the deflection pattern under the combined action of the field and scattering/energy-loss processes. A comparison (Fig. 119.8) of the MC simulation predictions (solid) and experimental data (dotted) for shot 49704, in which a compressed field of 13 MG was predicted by the hydrocode, shows very good agreement in both the total fluence and low-energy-band lineouts. In Fig. 119.8(b), only the protons that had an incident energy lower than 14.8 MeV were included. The target in shot 49704 had a seed field of 10 kG and was probed relatively early in the implosion. In later experiments, where the proton burst occurred at or near peak compression, the experimental lineouts at intermediate energies exhibited a double-deflection pattern with a second deflection peak farther from the center [Fig. 119.9(a), shot 51069]. This was first seen in Monte Carlo simulations [Fig. 119.9(b)] and was caused by an abrupt jump of the field in the small volume of the hot spot from much lower values in the shell (responsible for the first deflection). Early in time, at a low compressed field, these two peaks were essentially merged, as is the case with shot 49704. A comparison of the data for shot 51069, which had a 56-kG seed field, and the simulation shows good qualitative agreement, capturing the double-peak-deflection pattern. The protons that were slowed down the most (dashed–dotted curve) were those that crossed through the shell but not the hot spot, missing the peak field. From the 1.9-cm deflection of the secondary peak, one can estimate an average product $\langle R_B B_{\max} \rangle \approx 2\theta e/m_p v_p$ of 0.052 Tm, corresponding to an ~30-MG hot-spot field for a predicted hot-spot size of 17 μm.

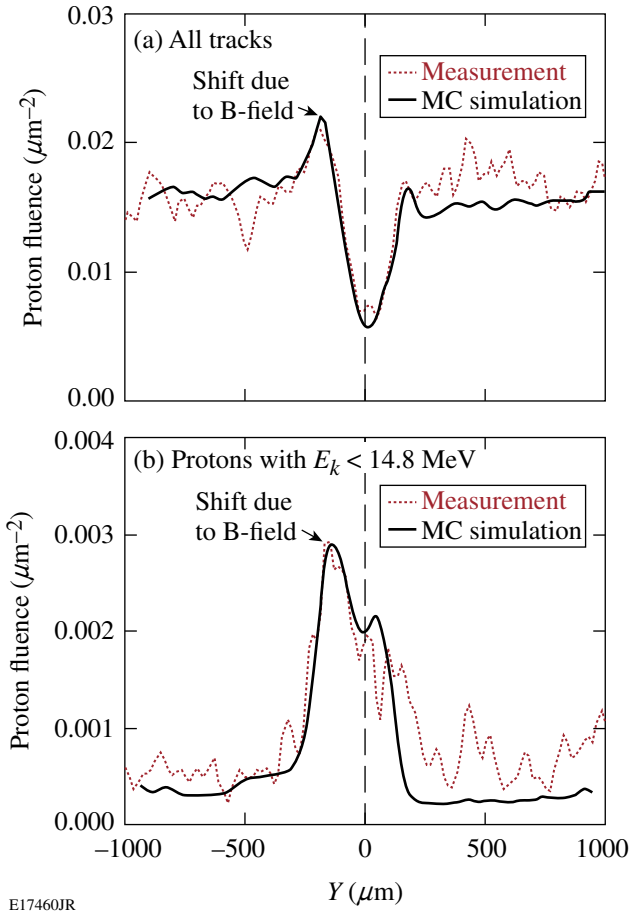

Figure 119.8
Direct comparisons of measured (dotted) and MC simulated (solid) proton-density lineouts across the core in shot 49704: (a) all protons; (b) protons intercepting the target (E_k < 14.8 MeV) (isolated by track diameter).

When the seed-field direction was reversed (by reversing the current in the coils), the deflection pattern (Fig. 119.10, shot 52532) reversed direction, with the deflection now away from the target stalk (a spatial reference fixed for all shots). This confirms the magnetic nature of the deflection and supports the "relocation" of the high-field deflection to the other side of the core. This is also evident in lineouts at several energies shown in Fig. 119.10(b), where, in addition to the offset peak near the center (at ~2.5 cm), there is again a concentration of tracks away from it (at 0.4 cm), caused by the peak of the compressed field in the hot spot. Analysis of the second peak deflection in shot 52532 revealed that the higher seed field (–62 kG), as compared to shot 51069, was amplified to at least –36 MG. The larger second peak area for Fig. 119.10(b) suggests higher hot-spot uniformity as more protons fall into these energy bands after being slowed down. The fields determined from Figs. 119.9 and 119.10 are the most conservative values, given

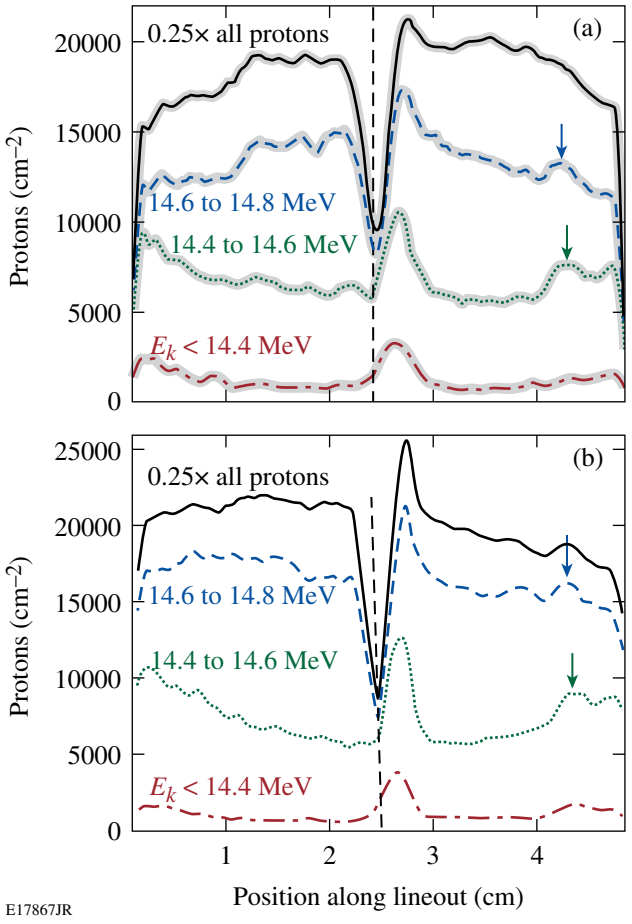

Figure 119.9
(a) Partitioning of the data in energy bands for shot 51069 exposed the protons that traverse the high field in the target center. (b) Partitioning in energy bands in the Monte Carlo simulation. The arrows in these plots indicate a second deflection peak at 1.9 cm from the target center.

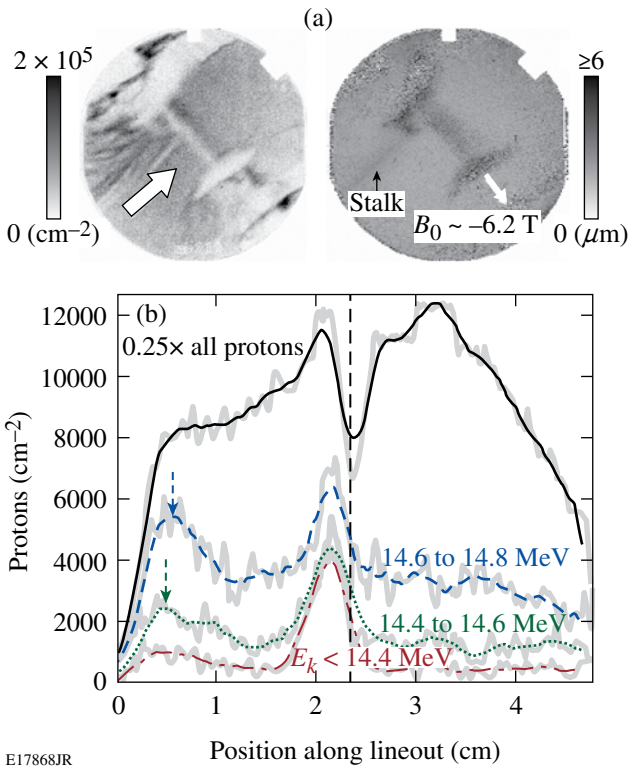

Figure 119.10
(a) Proton track density and diameter maps for shot 52532. The stalk is on the left, and deflection is to the right (seed field reversed). (b) Smoothed total (solid) and reduced-energy-band lineouts show large deflection matching a compressed field >36 MG. The arrows in (b) indicate the second deflection peak.

by the lowest field B_{max}, spread over the largest radius R_B, that can result in the observed deflection $\theta \sim \langle R_B B_{max} \rangle$ without violating the flux conservation condition $\Phi \sim \langle R_B^2 B_{max} \rangle \leq \Phi_0$. If the more realistic case is considered, where up to 40% of the initial magnetic flux ($\Phi_0 \approx 360$ G cm^2) is lost as predicted by the hydro simulation, the estimated magnetic fields must be revised upward to match the observed deflections.

The effect of the amplified magnetic field on the hot-spot conditions was expected to be rather small for this experimental configuration. The 1-D hydrocode predicts a 2× to 3× increase in the yield caused by the temperature increase from thermal insulation in the hot spot. Note that higher temperatures are accompanied by lower hot-spot densities (Fig. 119.11, solid line) and lower plasma pressures since the total pressure (plasma + magnetic) is approximately independent of the magnetic field (the minimum volume-averaged hot-spot beta is ~300, but is of the order of unity in the center). The highest neutron yield of 5.8×10^8 was measured in shot 49704 with a 10-kG seed field. With the present setup, however, and due to target parameter variations (gas pressure, orientation, positioning, and build quality), the $B_0 = 0$ yields already have variations of more than a factor of 3 (between 7.7×10^7 and 4.5×10^8). Such large shot-to-shot variations prevent an accurate assessment of the fusion yield enhancement caused by magnetic insulation. In addition, the scale of the experiment is such that the hot-spot ions most likely to undergo fusion reactions (at the Gamow peak) are essentially in the kinetic regime. This can be seen from Table 119.I, where $n_{e,hs} = 8 \times 10^{22}$ cm^{-3}, $T_{hs} = 1.5$ keV, the Gamow peak is at 8.2 keV, and the Coulomb logarithms for the collisions of the 8-keV ions with thermal electrons and ions are $\Lambda_{ie} \approx 5$ and $\Lambda_{ii} \approx 8.6$, respectively. It is clear that the ions, having an ~6-μm mean free path, will undergo only a few collisions before leaving the hot spot. The electrons are fully magnetized but are thermally decoupled from the ions since the thermal equilibration time is of the order of 100 ps.

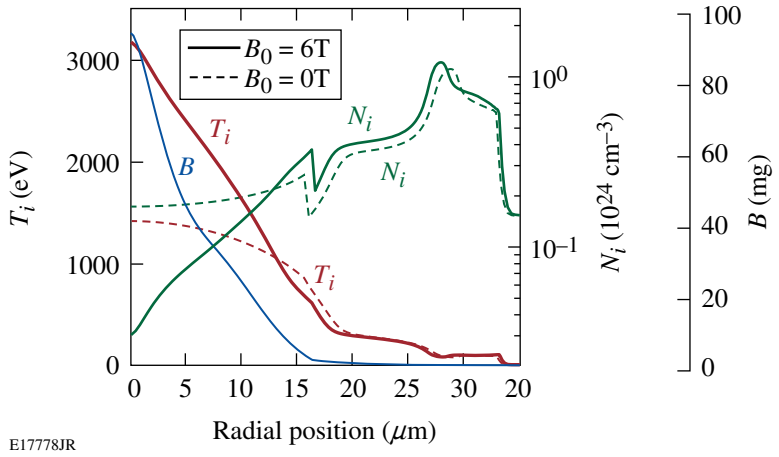

Figure 119.11
Ion temperature (T_i) and density (N_i) from *LILAC*-MHD simulations with (solid line) and without (dashed line) the magnetic field show that, along with a temperature increase caused by the magnetic field, a drop in the hot-spot density is predicted.

Table 119.I: Collision frequency (ν_{ie}, ν_{ii}), Hall parameter of ions $\left(\omega_{ci}/\nu_{ii}\right)$, mean free paths, and Larmor radii for a simulated cylindrical magnetized hot spot (R = 18 mm) with an averaged field of 30 MG.

ν_{ie} ns^{-1}	ν_{ii} ns^{-1}	ω_{ci}/ν_{ii}	mfp$_{ie}$ μm	mfp$_{ii}$ μm	r_L, μm
5.4	147	0.97	151	5.6	5.7

The situation should improve significantly in planned spherical magnetized implosions where the hot-spot density and collisionality are significantly higher.

In summary, very high magnetic-flux compression has been achieved using the ablative pressure of the OMEGA laser to drive a cylindrical shell at high implosion velocity, trapping and compressing the embedded external field to tens of MG, high enough to magnetize the hot-spot plasma. Finding the parameter space where target performance will be most affected by the compressed magnetic field is the next step in these studies.

ACKNOWLEDGMENT

The authors thank Dr. F. Y. Thio and Dr. A. Velikovich for many illuminating discussions and for their encouragement in pursuing these novel experiments. This work was supported by the U.S. Department of Energy Office of Fusion Energy Sciences under Grants DE-FG02-04ER54768 and DE-FC02-ER54789 and by the Office of Inertial Confinement Fusion under Cooperative Agreement No. DE-FC52-08NA28302, the University of Rochester, and the New York State Energy Research and Development Authority. The support of DOE does not constitute an endorsement by DOE of the views expressed in this article.

REFERENCES

1. J. A. Wesson, *Tokamaks*, 3rd ed. (Clarendon Press, Oxford, 2004); A. H. Boozer, Rev. Mod. Phys. **76**, 1071 (2004).

2. R. Betti, K. Anderson, T. R. Boehly, T. J. B. Collins, R. S. Craxton, J. A. Delettrez, D. H. Edgell, R. Epstein, V. Yu. Glebov, V. N. Goncharov, D. R. Harding, R. L. Keck, J. H. Kelly, J. P. Knauer, S. J. Loucks, J. A. Marozas, F. J. Marshall, A. V. Maximov, D. N. Maywar, R. L. McCrory, P. W. McKenty, D. D. Meyerhofer, J. Myatt, P. B. Radha, S. P. Regan, C. Ren, T. C. Sangster, W. Seka, S. Skupsky, A. A. Solodov, V. A. Smalyuk, J. M. Soures, C. Stoeckl, W. Theobald, B. Yaakobi, C. Zhou, J. D. Zuegel, J. A. Frenje, C. K. Li, R. D. Petrasso, and F. H. Séguin, Plasma Phys. Control. Fusion **48**, B153 (2006).

3. P. W. McKenty, V. N. Goncharov, R. P. J. Town, S. Skupsky, R. Betti, and R. L. McCrory, Phys. Plasmas **8**, 2315 (2001).

4. J. A. Stamper, Laser Part. Beams **9**, 841 (1991).

5. Fields of 10^8 G have been associated with the high-current electron beams created in short-pulse laser–plasma interactions, but the small scale of these azimuthal fields precludes their use for hot-spot thermal insulation in ICF.

6. F. Herlach, Rep. Prog. Phys. **31**, 341 (1968); F. Herlach, Rep. Prog. Phys. **62**, 859 (1999).

7. C. M. Fowler, W. B. Garn, and R. S. Caird, J. Appl. Phys. **31**, 588 (1960).

8. A. D. Sakharov, Sov. Phys. Usp. **9**, 294 (1966).

9. F. S. Felber, M. A. Liberman, and A. L. Velikovich, Phys. Fluids **31**, 3675 (1988); F. S. Felber *et al.*, J. Appl. Phys. **64**, 3831 (1988).

10. R. C. Kirkpatrick, I. R. Lindemuth, and M. S. Ward, Fusion Technol. **27**, 201 (1995).

11. O. V. Gotchev, N. W. Jang, J. P. Knauer, M. D. Barbero, R. Betti, C. K. Li, and R. D. Petrasso, J. Fusion Energy **27**, 25 (2008).

12. M. A. Liberman and A. L. Velikovich, J. Plasma Phys. **31**, 381 (1984).

13. A. Hasegawa *et al*., Phys. Rev. Lett. **56**, 139 (1986).

14. T. R. Boehly, D. L. Brown, R. S. Craxton, R. L. Keck, J. P. Knauer, J. H. Kelly, T. J. Kessler, S. A. Kumpan, S. J. Loucks, S. A. Letzring, F. J. Marshall, R. L. McCrory, S. F. B. Morse, W. Seka, J. M. Soures, and C. P. Verdon, Opt. Commun. **133**, 495 (1997).

15. J. P. Knauer, O. V. Gotchev, P. Chang, D. D. Meyerhofer, R. Betti, F. H. Séguin, C. K. Li, J. A. Frenje, and R. D. Petrasso, presented at the Innovative Confinement Concepts Workshop and US-Japan Workshop on Improvement in the Confinement of Compact Torus Plasmas, Reno, NV, 24–27 June 2008.

16. O. V. Gotchev, J. P. Knauer, P. Y. Chang, N. W. Jang, M. J. Shoup III, D. D. Meyerhofer, and R. Betti, Rev. Sci. Instrum. **80**, 043504 (2009).

17. C. K. Li, F. H. Séguin, J. A. Frenje, J. R. Rygg, R. D. Petrasso, R. P. J. Town, P. A. Amendt, S. P. Hatchett, O. L. Landen, A. J. Mackinnon, P. K. Patel, V. Smalyuk, J. P. Knauer, T. C. Sangster, and C. Stoeckl, Rev. Sci. Instrum. **77**, 10E725 (2006).

18. J. R. Rygg, F. H. Séguin, C. K. Li, J. A. Frenje, M. J.-E. Manuel, R. D. Petrasso, R. Betti, J. A. Delettrez, O. V. Gotchev, J. P. Knauer, D. D. Meyerhofer, F. J. Marshall, C. Stoeckl, and W. Theobald, Science **319**, 1223 (2008).

19. C. K. Li, F. H. Séguin, J. R. Rygg, J. A. Frenje, M. Manuel, R. D. Petrasso, R. Betti, J. Delettrez, J. P. Knauer, F. Marshall, D. D. Meyerhofer, D. Shvarts, V. A. Smalyuk, C. Stoeckl, O. L. Landen, R. P. J. Town, C. A. Back, and J. D. Kilkenny, Phys. Rev. Lett. **100**, 225001 (2008).

20. F. H. Séguin, J. A. Frenje, C. K. Li, D. G. Hicks, S. Kurebayashi, J. R. Rygg, B.-E. Schwartz, R. D. Petrasso, S. Roberts, J. M. Soures, D. D. Meyerhofer, T. C. Sangster, J. P. Knauer, C. Sorce, V. Yu. Glebov, C. Stoeckl, T. W. Phillips, R. J. Leeper, K. Fletcher, and S. Padalino, Rev. Sci. Instrum. **74**, 975 (2003).

21. S. Agostinelli *et al*., Nucl. Instrum. Methods Phys. Res. A **506**, 250 (2003).

22. N. W. Jang, R. Betti, J. P. Knauer, O. Gotchev, and D. D. Meyerhofer, Bull. Am. Phys. Soc. **51**, 144 (2006).

Lorentz Mapping of Magnetic Fields in Hot, Dense Plasmas

Spontaneous generation of magnetic ($\boldsymbol{B}$) fields occurs pervasively in galactic[1,2] and stellar[3] settings and in numerous laboratory plasma experiments.[2,4] For the case of the hot, dense plasmas of laser–plasma experiments[4,5] or for scaled astrophysics experiments in the laboratory,[2,4] self-generated magnetic and electric fields are often intertwined and inextricably coupled to the dynamics of the plasma evolution. This coupling makes the field-generation process complicated and also means that the effects of the fields can directly or indirectly act back on the plasma itself. Measuring local, self-generated fields, and distinguishing between electric ($\boldsymbol{E}$) and magnetic fields, is a formidable task.[6]

This article describes a monoenergetic proton radiography method that, when used in combination with Lorentz force mapping, allows one to precisely measure plasma field strengths as well as unequivocally discriminate between electric and magnetic fields. Electromagnetic fields in a high-energy-density plasma can be measured by passing monoenergetic protons through the plasma and observing how their trajectories are deflected by the fields. Any trajectory bending is due to the Lorentz force

$$\boldsymbol{F} = q\left(\boldsymbol{E} + \frac{\boldsymbol{v} \times \boldsymbol{B}}{c}\right), \tag{1}$$

where q is the proton charge and $\boldsymbol{v}$ is the proton velocity, acting over a path length ℓ characteristic of the fields' spatial extent. For true quantitative analysis of data it is critical that $\boldsymbol{v}$ be known accurately. If it is known in advance whether a field is $\boldsymbol{B}$ or $\boldsymbol{E}$, Eq. (1) can be used directly to relate any observed trajectory bending to field strength. If bending is observed but there is no absolute knowledge of which field is present, the individual contributions of $\boldsymbol{E}$ and $\boldsymbol{B}$ can be determined by making two independent measurements. This discrimination can be accomplished by three methods, although practical implementation is often challenging: The first method measures the same plasma in the same way but with the direction of $\boldsymbol{v}$ reversed; the second measures the same plasma but with protons of two discrete values of $|\boldsymbol{v}|$; and the third measures two plasmas that are identical except for the reversal of any $\boldsymbol{B}$ field.

The experiment reported here utilized the third method to resolve ambiguities of field identity and field strength. The experimental setup used monoenergetic proton radiography, as illustrated in Fig. 119.12(a). A pulse of 14.9-MeV protons was generated from fusion reactions of deuterium (D) and helium-3 (^{3}He) in a D_2-^{3}He–filled, glass-shell capsule driven by 17 OMEGA[7] laser beams. This proton source was completely characterized using spectral,[8] spatial,[9] and temporal[10] diagnostics; it had a mean energy of 14.9±0.1 MeV, a spectral half-width <1.5% (or half-width in the proton velocity distribution <0.75%), an emission region FWHM of 45 μm, and a duration of 130 ps. The protons were used to image two identical, expanding plasma bubbles, formed on opposite sides of a 5-μm-thick plastic (CH) foil by two 1-ns-long laser interaction beams. Both beams had spot diameters of 850 μm and intensities of 8×10^{13} W/cm^2; they were fired simultaneously and incident at 23.5° from the normal to the foil. To break the nearly isotropic proton fluence into "beamlets" (~1000 protons each) whose deflections could easily be observed and quantified, 150-μm-period nickel meshes were placed on opposite sides of the foil. Figure 119.12(b) is the resulting radiograph, recorded on a CR-39 nuclear track detector,[8] with laser timing adjusted so that the bubbles were recorded 1.36 ns after the onset of the interaction beams.

The top bubble image in Fig. 119.12(b) is a type that we have recently begun studying[11,12] and contrasting to predictions of the 2-D radiation–hydrodynamic code LASNEX.[13] The simulations indicated that proton deflections are purely a result of a toroidal $\boldsymbol{B}$, parallel to the foil, arising from the $\nabla n_e \times \nabla T_e$ magnetic-field source term (where n_e and T_e are the electron number density and temperature).[14,15] While the data and simulations were qualitatively similar, there was a consistent, quantitative mismatch between them throughout the bubble evolution (predicted apparent bubble sizes were ~25% smaller than observed;[16,17] predicted field strengths were larger overall than observed; and field morphology details differed). This discrepancy effectively precluded use of the simulations to justify any *a priori* assumption that observed proton deflections were caused exclusively by a $\boldsymbol{B}$ field and not by any component $\boldsymbol{E}_{\|}$ (parallel to the foil) of an $\boldsymbol{E}$ field.

To provide direct experimental identification of the field type as well as strength, the current experiment was designed so the second bubble reversed the sign of any $\boldsymbol{B}$ relative to the first bubble (as seen from the detector) while leaving any $\boldsymbol{E}_{\|}$ unchanged. If the $\boldsymbol{B}$ reversal had no effect on deflections of the monoenergetic protons used to image the plasma, any deflections would necessarily have been dominated by $\boldsymbol{E}_{\|}$. If the reversal resulted in equal but oppositely directed deflections of the monoenergetic protons, it would demonstrate the clear dominance of $\boldsymbol{B}$. Qualitatively, the latter is what is seen in the image: the bubble on the front side of the foil (top of image) appears expanded, while the bubble on the back side appears contracted.

Figure 119.12(c) shows the absolute values of the beamlet deflection angles θ as a function of position at the foil; θ is calculated from the apparent displacement of a beamlet in an image relative to where it would be without deflection. The peak θ values occur at the foil on two circles of the same radius, and the amplitudes are the same for both circles. This is seen quantitatively in Fig. 119.13(a), which shows θ as a function of radius measured from each bubble's center. Because of Eq. (1) and the fact that $\boldsymbol{B}$ is reversed between the bubbles while $\boldsymbol{E}$ is not, it follows that we can decompose the total deflections $\theta_{\text{top}}(r)$ and $\theta_{\text{bottom}}(r)$ for the top and bottom bubbles into parts due only to $\boldsymbol{B}$ and $\boldsymbol{E}$ by assuming the two bubbles are otherwise equivalent. Then

$$\theta_{\text{top}}(r) = \theta_{\boldsymbol{E}}(r) + \theta_{\boldsymbol{B},\text{top}}(r)\,, \tag{2}$$

$$\theta_{\text{bottom}}(r) = \theta_{\boldsymbol{E}}(r) - \theta_{\boldsymbol{B},\text{top}}(r)\,, \tag{3}$$

from which it follows that

$$\theta_{\boldsymbol{E}}(r) = \left[\theta_{\text{top}}(r) + \theta_{\text{bottom}}(r)\right]/2\,, \tag{4}$$

$$\theta_{\boldsymbol{B}}(r) = \left[\theta_{\text{top}}(r) - \theta_{\text{bottom}}(r)\right]/2\,. \tag{5}$$

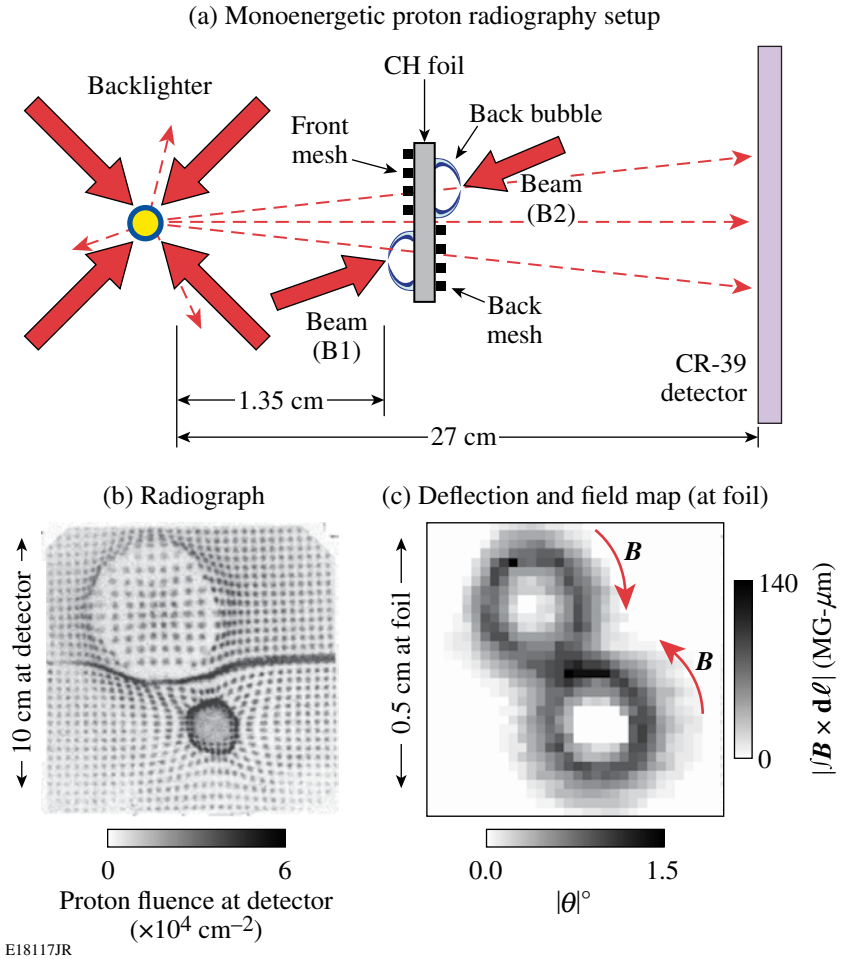

Figure 119.12
(a) Proton radiography setup, (b) proton radiograph of two laser-generated plasma bubbles, and (c) spatial map of proton beamlet deflection angle (or equivalently the magnetic field strength) as a function of position on the foil. Note in Fig. 119.13(b) that the deflections are associated almost exclusively with a $\boldsymbol{B}$ field near the foil, meaning that (c) can also be viewed as a magnetic field map. Part (c) shows that the two bubbles were actually the same size, even though the apparent sizes are different in the radiograph. Orientation of the images is as seen from behind the detector, looking toward the backlighter. The radiograph was acquired during OMEGA shot 46535.

The results are shown in Fig. 119.13(b) after converting $\theta_{\boldsymbol{B}}(r)$ and $\theta_{\boldsymbol{E}}(r)$ to $\int \boldsymbol{B} \times \mathbf{d}\boldsymbol{\ell}$ and $\int \boldsymbol{E}_{\parallel} \times \mathbf{d}\boldsymbol{\ell}$ using Eq. (1). The vertical display scales for $\boldsymbol{E}$ and $\boldsymbol{B}$ were selected so the relative amplitudes of the curves indicate the relative amounts of proton deflection. The effect of $\boldsymbol{B}$ greatly dominates the effect of $\boldsymbol{E}_{\parallel}$, whose measured amplitude is smaller than measurement uncertainties.[18]

Figure 119.12(c) reveals a toroidal topology for the $\boldsymbol{B}$ field, with a shell thickness of about 400 μm. An estimate of the maximum local $|\boldsymbol{B}|$ is then 100 MG-μm/400 μm ~ 0.3 MG. For this field, the Hall parameter $\omega_{ce}\tau$ (where ω_{ce} is the electron gyrofrequency and τ is the electron–ion collision time[14,15]) is of order 1. Since thermal conductivity is proportional to $1/\left[1+(\omega_{ce}\tau)^2\right]$ (Refs. 14 and 19), it follows that field-induced inhibition of thermal transport across the plasma bubble boundary will occur.

Interestingly, this may provide insight as to why the simulations, while correctly predicting that a toroidal $\boldsymbol{B}$ field was the primary cause of the deflections, could overestimate the field and underestimate the bubble size. Thomson-scattering[20] measurements indicated that the actual electron temperature T_e was ~40% lower than the value predicted by LASNEX (450 μm away from the foil and 600 μm from the central axis of a bubble, the measured T_e was 470 eV while the predicted value was 780 eV). With the predicted plasma temperature too high, the predicted magnetic diffusivity would be too low [since it is proportional to $T^{-3/2}$ (Ref. 14)] and the predicted $\boldsymbol{B}$ field would dissipate too slowly, leading to higher field strengths, higher $\omega_{ce}\tau$, and an even more slowly decaying electron temperature. Such considerations and more detailed data/simulation comparisons will be important for advancing our basic understanding and our predictive capabilities with various codes.

The absolute experimental determination here that the fields responsible for the structure of Fig. 119.12(b) are magnetic allows us to revisit the images of Refs. 11 and 12 (showing radiographs of similar plasma bubbles on one side of the foil only) with confidence that they also reflect magnetic fields. Reference 11 shows images that represent the complete time evolution of bubble structure throughout the 1-ns laser pulse and for an additional 2 ns afterward. Those images were recorded with the same integration time (~130 ps) as used here and show the temporal evolution of the plasma bubble radius and field magnitude. In addition, a breakdown in azimuthal symmetry was observed at times slightly later than that of Fig. 119.12(b) here.

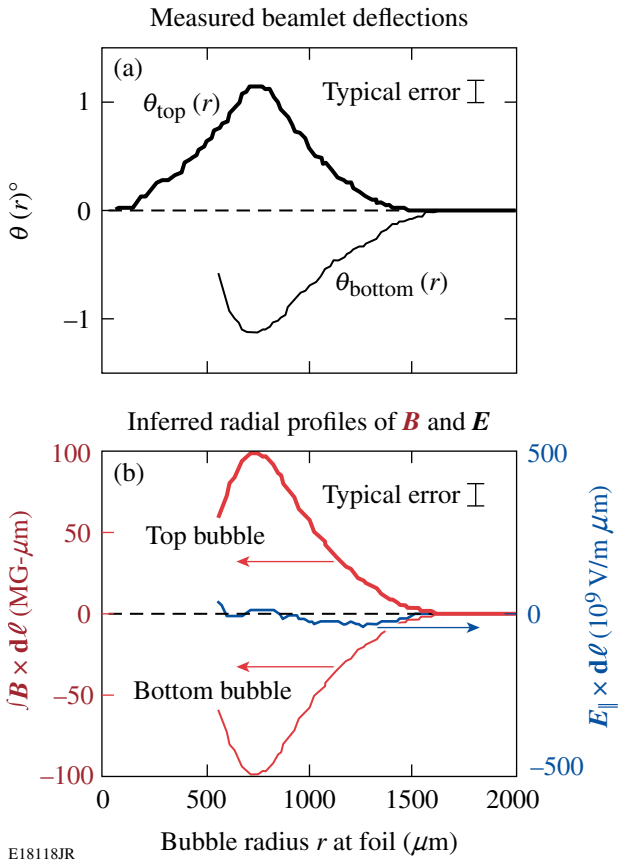

Figure 119.13
Measured beamlet deflection angles θ as a function of radius r in the top and bottom bubbles of Fig. 119.12(b) (positive is away from the bubble center), and inferred radial profiles of $\int \boldsymbol{B} \times \mathbf{d}\boldsymbol{\ell}$ and $\int \boldsymbol{E}_{\parallel} \times \mathbf{d}\boldsymbol{\ell}$ in the two bubbles. In (b), the vector $\int \boldsymbol{B} \times \mathbf{d}\boldsymbol{\ell}$ is plotted as a positive number for a toroidal $\boldsymbol{B}$ field in the clockwise direction of Fig. 119.12(c), while $\int \boldsymbol{E}_{\parallel} \times \mathbf{d}\boldsymbol{\ell}$ is plotted as positive for an $\boldsymbol{E}$ field pointing away from the bubble center. $\boldsymbol{B}$ has opposite directions in the two bubbles, while $\boldsymbol{E}$ has the same direction. Note that the absence of information about θ_{bottom} for $r <$ ~500 μm reflects the overlap of beamlets in the center of the bottom bubble image in Fig. 119.12(b), which prevented beamlet deflection measurements in that region.

Essential to the successful implementation of the technique of field discrimination and quantification are the isotropic and monoenergetic characteristics of the protons (the velocity uncertainty was <1% over the imaged plasma). Other recent important methods of ion generation from intense laser–plasma interactions,[21–23] while useful in different radiographic settings, would be compromised in the present context because of the energy spread and anisotropy of the ion fluences. In addition, other techniques of single-point field measurement at extremely high laser intensities (~10^{20} W/cm^2, Ref. 24) do not generate global field maps that show the entire laser–plasma morphology, a prerequisite to understanding plasma dynamics.

Variations of this monoenergetic proton radiography are now being applied to other important plasma/field problems in high-energy-density physics. For example, recent work in inertial confinement fusion[25,26] showed, through single-sided monoenergetic proton radiography, the presence of strong striated fields around an imploding capsule.[6] Unresolved in this work was the issue of whether the fields were magnetic or electric; yet the identification of field type is of paramount importance because different fields would involve different generation mechanisms and would have a significantly different impact on plasma evolution (through such processes as thermal transport modification). By simultaneously irradiating a subject implosion from two different directions, the methodology described above can unambiguously discern whether these fields are magnetic or electric. If magnetic, it is quite possible that the striations are a result of an electrothermal instability,[27] potentially leading to the seeding of Rayleigh–Taylor instabilities[27] that could deleteriously impact implosion dynamics.[28]

In another experiment involving accelerating, rippled plasma foils,[29] $\boldsymbol{B}$ fields are suspected—as a consequence of the Rayleigh–Taylor instability[28]—to cause the monoenergetic proton deflections seen when the foil was irradiated from a single side.[30] However, unique field and instability identification could be established by proton backlighting, from one direction, of a foil with ripples on both sides [in a fashion similar to that depicted for the two plasma bubbles in Fig. 119.12(a)]. (In such an experiment, the mesh would be removed.) In general, applying these field-mapping radiographs to a large class of high-energy-density plasmas will lead to quantifying the nature, the physical extent, and the evolution of embedded, spontaneous fields. By inference, this should also lead to new insights into the origin and dynamics of the pervasive fields of stellar jets[31] and nebulae,[32] a major goal of laboratory astrophysics.[2,33]

ACKNOWLEDGMENT

This work was supported by the Fusion Science Center (FSC) at the University of Rochester (grant no. DE-FG03-03NA00058), the National Laser Users' Facility (DE-FG52-07NA28059), the Office of Defense Programs (DE-FG52-06NA26203), Lawrence Livermore National Laboratory (subcontract Grant No. B5504974), and the Laboratory for Laser Energetics at the University of Rochester (subcontract Grant No. 412160-001G)—all through the U.S. Department of Energy. J.R.R. also acknowledges the FSC for his postdoctoral appointment. In addition, the authors express their gratitude to General Atomics and the Laboratory for Laser Energetics (LLE) for target fabrication and to LLE's laser operations team.

REFERENCES

1. W. Baumjohann and R. A. Treumann, *Basic Space Plasma Physics* (Imperial College Press, London, 1996).
2. B. A. Remington *et al*., Science **284**, 1488 (1999).
3. E. N. Parker, Astrophys. J. **128**, 664 (1958).
4. R. P. Drake, *High-Energy-Density Physics: Fundamentals, Inertial Fusion, and Experimental Astrophysics*, Shock Wave and High Pressure Phenomena (Springer, Berlin, 2006).
5. W. L. Kruer, *The Physics of Laser Plasma Interactions*, Frontiers in Physics (Westview Press, Boulder, CO, 2003).
6. J. R. Rygg, F. H. Séguin, C. K. Li, J. A. Frenje, M. J.-E. Manuel, R. D. Petrasso, R. Betti, J. A. Delettrez, O. V. Gotchev, J. P. Knauer, D. D. Meyerhofer, F. J. Marshall, C. Stoeckl, and W. Theobald, Science **319**, 1223 (2008).
7. J. M. Soures, R. L. McCrory, C. P. Verdon, A. Babushkin, R. E. Bahr, T. R. Boehly, R. Boni, D. K. Bradley, D. L. Brown, R. S. Craxton, J. A. Delettrez, W. R. Donaldson, R. Epstein, P. A. Jaanimagi, S. D. Jacobs, K. Kearney, R. L. Keck, J. H. Kelly, T. J. Kessler, R. L. Kremens, J. P. Knauer, S. A. Kumpan, S. A. Letzring, D. J. Lonobile, S. J. Loucks, L. D. Lund, F. J. Marshall, P. W. McKenty, D. D. Meyerhofer, S. F. B. Morse, A. Okishev, S. Papernov, G. Pien, W. Seka, R. Short, M. J. Shoup III, M. Skeldon, S. Skupsky, A. W. Schmid, D. J. Smith, S. Swales, M. Wittman, and B. Yaakobi, Phys. Plasmas **3**, 2108 (1996).
8. F. H. Séguin, J. A. Frenje, C. K. Li, D. G. Hicks, S. Kurebayashi, J. R. Rygg, B.-E. Schwartz, R. D. Petrasso, S. Roberts, J. M. Soures, D. D. Meyerhofer, T. C. Sangster, J. P. Knauer, C. Sorce, V. Yu. Glebov, C. Stoeckl, T. W. Phillips, R. J. Leeper, K. Fletcher, and S. Padalino, Rev. Sci. Instrum. **74**, 975 (2003).
9. F. H. Séguin, J. L. DeCiantis, J. A. Frenje, C. K. Li, J. R. Rygg, C. D. Chen, R. D. Petrasso, J. A. Delettrez, S. P. Regan, V. A. Smalyuk, V. Yu. Glebov, J. P. Knauer, F. J. Marshall, D. D. Meyerhofer, S. Roberts, T. C. Sangster, C. Stoeckl, K. Mikaelian, H. S. Park, H. F. Robey, and R. E. Tipton, Phys. Plasmas **13**, 082704 (2006).
10. J. A. Frenje, C. K. Li, F. H. Séguin, J. Deciantis, S. Kurebayashi, J. R. Rygg, R. D. Petrasso, J. Delettrez, V. Yu. Glebov, C. Stoeckl, F. J. Marshall, D. D. Meyerhofer, T. C. Sangster, V. A. Smalyuk, and J. M. Soures, Phys. Plasmas **11**, 2798 (2004).
11. C. K. Li, F. H. Séguin, J. A. Frenje, J. R. Rygg, R. D. Petrasso, R. P. J. Town, P. A. Amendt, S. P. Hatchett, O. L. Landen, A. J. Mackinnon, P. K. Patel, M. Tabak, J. P. Knauer, T. C. Sangster, and V. A. Smalyuk, Phys. Rev. Lett. **99**, 015001 (2007).
12. C. K. Li, F. H. Séguin, J. A. Frenje, J. R. Rygg, R. D. Petrasso, R. P. J. Town, O. L. Landen, J. P. Knauer, and V. A. Smalyuk, Phys. Rev. Lett. **99**, 055001 (2007).

13. G. B. Zimmerman and W. L. Kruer, Comments Plasma Phys. Control. Fusion **2**, 51 (1975).

14. S. I. Braginskii, in *Reviews of Plasma Physics*, edited by Acad. M. A. Leontovich (Consultants Bureau, New York, 1965), Vol. 1.

15. M. G. Haines, Phys. Rev. Lett. **47**, 917 (1981).

16. The disagreement between experiment and LASNEX simulation appeared to be less pronounced than this in an earlier publication,[17] but that was because the simulation utilized slightly incorrect imaging system dimensions.

17. C. K. Li, F. H. Séguin, J. A. Frenje, J. R. Rygg, R. D. Petrasso, R. P. J. Town, P. A. Amendt, S. P. Hatchett, O. L. Landen, A. J. Mackinnon, P. K. Patel, V. A. Smalyuk, T. C. Sangster, and J. P. Knauer, Phys. Rev. Lett. **97**, 135003 (2006).

18. Measurement of electric fields perpendicular to the foil in a single-bubble experiment was presented in C. K. Li, F. H. Séguin, J. A. Frenje, J. R. Rygg, R. D. Petrasso, R. P. J. Town, P. A. Amendt, S. P. Hatchett, O. L. Landen, A. J. Mackinnon, P. K. Patel, V. Smalyuk, J. P. Knauer, T. C. Sangster, and C. Stoeckl, Rev. Sci. Instrum. **77**, 10E725 (2006).

19. D. S. Montgomery *et al*., Phys. Rev. Lett. **73**, 2055 (1994).

20. D. H. Froula *et al*., Rev. Sci. Instrum. **77**, 10E522 (2006).

21. B. M. Hegelich *et al*., Nature **439**, 441 (2006).

22. M. Borghesi *et al*., Phys. Rev. Lett. **81**, 112 (1998).

23. A. J. Mackinnon *et al*., Phys. Rev. Lett. **97**, 045001 (2006).

24. M. Tatarakis *et al*., Nature **415**, 280 (2002).

25. J. Nuckolls *et al*., Nature **239**, 139 (1972).

26. S. Atzeni and J. Meyer-ter-Vehn, *The Physics of Inertial Fusion: Beam Plasma Interaction, Hydrodynamics, Hot Dense Matter*, International Series of Monographs on Physics (Clarendon Press, Oxford, 2004).

27. M. G. Haines, Can. J. Phys. **64**, 912 (1986).

28. A. Nishiguchi, Jpn. J. Appl. Phys. **41**, 326 (2002).

29. V. A. Smalyuk, S. X. Hu, V. N. Goncharov, D. D. Meyerhofer, T. C. Sangster, D. Shvarts, C. Stoeckl, B. Yaakobi, J. A. Frenje, and R. D. Petrasso, Phys. Rev. Lett. **101**, 025002 (2008).

30. R. Petrasso, Bull. Am. Phys. Soc. **52**, 97 (2007).

31. P. Hartigan *et al*., Astrophys. J. **661**, 910 (2007).

32. J. J. Hester *et al*., Astrophys. J. **456**, 225 (1996).

33. D. D. Ryutov *et al*., Phys. Plasmas **8**, 1804 (2001).

Characterization and Optimization of Yb-Doped Photonic-Crystal Fiber Rod Amplifiers Using Spatially Resolved Spectral Interferometry

Introduction

New Yb-doped photonic-crystal fibers (PCF's) have enabled fiber-based chirped-pulse–amplification (CPA) systems to produce millijoule-level pulses, compressible to femtosecond pulse widths.[1,2] Rigid double-clad fiber rods are commercially available with large effective areas (>2300 μm^2) and high pump absorption (~30 dB/m at 976 nm) for efficient amplification in less than a meter of fiber. The combination of large effective areas and short amplifier lengths limits the suppression of higher-order modes (HOM's), however, and these fibers may support several modes in addition to the fundamental. The rigid rod construction reduces the coupling between the weakly guided fundamental and other modes in the fiber. HOM's may be excited when the signal is injected, which is typically done by focusing a free-space beam into the core. Relatively small amounts of HOM that are co-polarized with the fundamental mode can significantly degrade the beam quality and pointing stability because they interfere coherently.[3,4]

This article reports the first application of a recently proposed technique, S^2 imaging,[5,6] to measure the modes of a Yb-doped PCF amplifier at full power. The technique, based on spatially resolved spectral interferometry, can detect small amounts of HOM that beat with the fundamental mode. S^2 imaging measures HOM fields relative to the fundamental mode without requiring *a priori* knowledge of the design of the fiber or its mode content. S^2 imaging provides feedback when optimizing signal injection and is more sensitive than measuring the amplifier gain.

S^2 Imaging

S^2 imaging detects HOM content from fringes in the spatially resolved spectra that are sampled across the beam profile. Nicholson *et al*. showed that an HOM's profile and its intensity and phase relative to the fundamental mode can be directly calculated from the spatially dependent fringe visibility.[5] Consider two modes defined by the spectral fields $E_1(x,y,\omega)$ and $E_2(x,y,\omega)$, where E_1 is assumed to be the fundamental mode (such as the LP_{01}) and E_2 is an HOM that is coherent and co-polarized with E_1. As $|E_1|$ is nonzero across the beam, E_2 can be expressed as

$$E_2(x,y,\omega) = \alpha(x,y,\omega)E_1(x,y,\omega), \tag{1}$$

where $\alpha(x,y,\omega)$ is the relative field amplitude of the HOM at a given position in the beam. It is a complex function: $|\alpha|\exp(i\phi_\alpha)$. After propagation with relative group delay, $\Delta\tau_G$, the mode fields are related by

$$E_2(x,y,\omega) = \alpha(x,y,\omega)E_1(x,y,\omega)\exp(-i\omega\Delta\tau_G). \tag{2}$$

Spectral interference between the two fields produces a combined spectral intensity of the form

$$\begin{aligned} I(x,y,\omega) &= \left|E_1(x,y,\omega) + E_2(x,y,\omega)\right|^2 \\ &= I_1(x,y,\omega)\left[1 + |\alpha|^2 + 2|\alpha|\cos(\omega\,\Delta\tau_G - \phi_\alpha)\right]. \end{aligned} \tag{3}$$

The spectrum contains fringes because of the relative group delay between the modes. Assuming that α and $\Delta\tau_G$ are slowly varying functions of frequency and there are several fringes across the spectrum, standard Fourier analysis is used to extract the relative powers of the two modes. The ac sidebands produced by the modal interference have an amplitude relative to the dc peak that is given by

$$f(x,y) = \frac{2|\overline{\alpha}|\exp(-i\phi_\alpha)}{1+|\alpha|^2}, \tag{4}$$

where $\overline{\alpha}(x,y)$ is the spectral average of $\alpha(x,y,\omega)$ that can be calculated directly from $f(x,y)$:

$$\overline{\alpha}(x,y) = \frac{1-\sqrt{1-4|f(x,y)|^2}}{2f(x,y)}. \tag{5}$$

The relative power of the HOM to the fundamental is obtained from $\overline{\alpha}(x,y)$ and the total intensity integrated over the entire spectrum, $I_T(x,y)$:

$$P_2/P_1 = \iint I_2(x,y)\mathrm{d}x\mathrm{d}y \Big/ \iint I_1(x,y)\mathrm{d}x\mathrm{d}y$$

$$= \frac{\iint I_T|\overline{\alpha}|^2\Big/\left(1+|\overline{\alpha}|^2\right)\mathrm{d}x\mathrm{d}y}{\iint I_T\Big/\left(1+|\overline{\alpha}|^2\right)\mathrm{d}x\mathrm{d}y}. \quad (6)$$

Since the S^2 technique is fundamentally interferometric in nature, the relative phase between the modes at a given position in the beam is encoded on the phase of the spectral oscillations at that position. Equation (4) shows that the phase between the modes across the beam, $\phi_\alpha(x,y)$, is given by the phase of $f(x,y)$. The phase of the fundamental mode does not vary across the beam, so $\phi_\alpha(x,y)$ represents the phase variation across the HOM. An LP_{11} mode, for example, has two lobes with a π-phase shift between them, which can be measured using S^2 imaging.[5] Although only one HOM was considered here, multiple HOM's can be imaged simultaneously providing the relative group delays between each HOM and the fundamental mode are sufficiently different that the sidebands are clearly resolved. Reference 6 extends this analysis to cases where (1) the excitation of the HOM's is distributed along the fiber device and (2) the coupling between the modes and their relative group delays is frequency dependent. While this alternate method of analysis is more general, it requires that each HOM is weak compared to the fundamental mode (relative power less than –15 dB) to ensure S^2 imaging does not underestimate the HOM power.

Experimental Setup

The experimental setup is shown in Fig. 119.14. The Yb-doped PCF fiber (DC-200/70-PM-Yb-ROD from Crystal Fibre A/S) was a rigid rod (0.8-m × 1.7-mm diameter) with angle-cleaved end faces (4°). The signal core, formed by a hexagonal matrix of air holes, has an effective area of 2300 μm^2, corresponding to a mode-field diameter (MFD) = 55 μm and a numerical aperture (N.A.) ≈ 0.015. Boron-doped stress-applying parts (SAP's) limit propagation to a single linear polarization in the signal wavelength range.[2] The amplifier was pumped at 976 nm using multimode pigtailed diodes. An output power of 16 W at 1055 nm with 16.6 dB of gain was obtained for ~50 W of absorbed pump power.

The amplifier output was sampled using a single-mode fiber probe (MFD = 6 μm, N.A. = 0.14) and a fiber-coupled spectrometer (Ocean Optics HR2000+). The beam was attenuated using three uncoated reflections and neutral-density (ND) filters. The PCF end face was imaged onto the fiber probe with 6× magnification so that the MFD of the probe fiber was less than 1/50 of the beam's diameter ($1/e^2$). High-speed actuators (Newport LTA) were used to translate the fiber probe across the beam and the spectrum was measured at each point. The total acquisition time for a scan (32 × 32) was approximately 6 min. The half-wave plate was set to either align the amplifier output with the polarizer or rotate the polarization by 45°. In the first

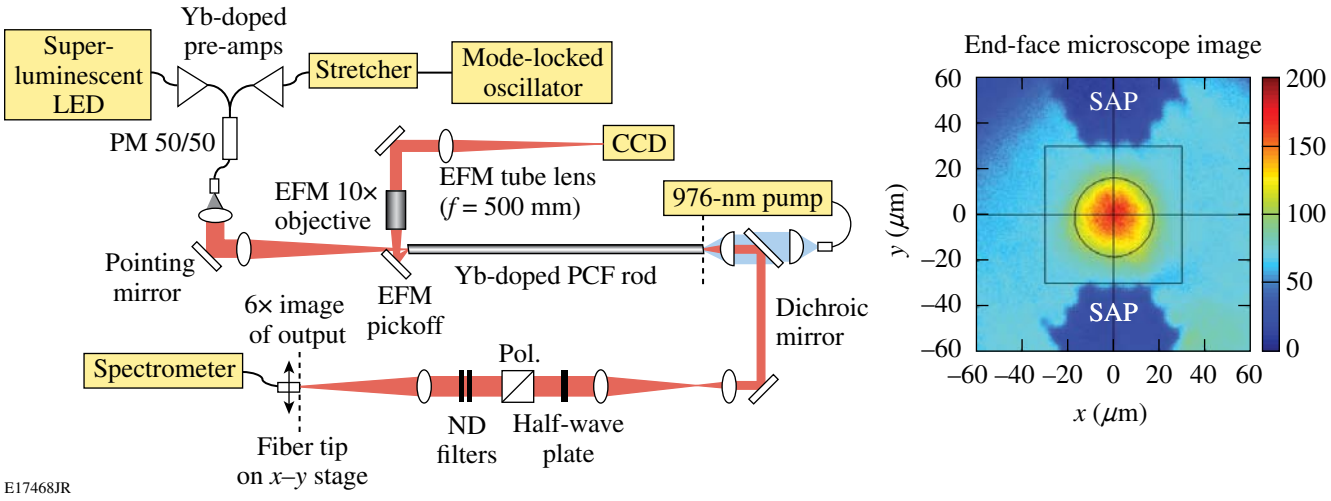

Figure 119.14
Experimental setup. The EFM image shows signal beam at injection, aligned between the two SAP regions that are backlit by the pump.

case, fringes were produced by HOM's that were co-polarized with the fundamental mode. In the second, fringes could potentially be produced by HOM's that were orthogonally polarized to the fundamental. Thus, the relative polarization state of the HOM to the fundamental was determined by comparing the fringe visibility for both wave-plate settings.

One challenge in applying S^2 imaging to short amplifiers is that the relative group delay between modes is short, resulting in spectral fringes with a long period. A combination of stretched Yb oscillator pulses at 1055 nm and output from a superluminescent light-emitting diode (SLED) at 1035 nm was injected to provide at least four fringes across the spectrum. Each spatially resolved spectrum was first normalized by the spectrum integrated over the beam before Fourier analysis so that the entire wavelength range (1020 to 1060 nm) could be used.

Independent measurements of the signal beam offset at injection were provided using an end-face microscope (EFM) to image the input end of the PCF amplifier. The EFM used a pickoff mirror located a few millimeters from the fiber end and a microscope objective to capture the signal reflection from the angle-cleaved fiber face. In addition, the EFM collected part of the residual pump light exiting the fiber at large angles. Figure 119.14 shows a typical EFM image with signal and pump light present. The pickoff angle exceeded the numerical aperture of pump light guided in the two trapezoidal SAP's; therefore, they appear as dark regions that indicate the location of the signal core. Using standard image-processing techniques, this simple setup can measure signal-to-core overlap at the end face with micron-level precision.

Experimental Results of S^2 Imaging Measurements

Figure 119.15(a) shows the amplified spectrum integrated over the entire beam for the SLED and mode-locked oscillator (ML OSC). Figure 119.15(b) shows two examples of spatially resolved spectra, measured at positions of low- and high-fringe visibility, after normalization by the integrated spectrum. The corresponding Fourier magnitudes are plotted versus group delay in Fig. 119.15(c) and show an interference peak at a group delay of 420 fs/m.

Mode images were extracted using the spatial dependence of 420-fs/m peak. The images are shown in Fig. 119.16 along with a direct charge-coupled-device (CCD) measurement of the beam. The dimensions for all images correspond to the amplifier output before the 6× magnification in front of the fiber probe. The modes are the fundamental LP_{01} mode and the LP_{11} mode, which is aligned with the SAP axis. The LP_{11} mode was determined to be co-polarized with the LP_{01} mode by rotating the half-wave plate before the polarizer and noting that the fringe visibility remained constant. In principle, S^2 imaging can detect many HOM's from a single scan. In this case only one clear mode was observed, corresponding to the generation of the LP_{11} mode at injection into the amplifier. Other modes could be present, such as HOM's generated from scattering from inhomogeneities distributed along the amplifier length. The relative group delay depends on the scattering position, and, therefore, fringes are produced with a range of periods from a minimum value set by the total length of the amplifier to larger values. Detecting HOM's from such distributed coupling is possible[4] but was not feasible given the signal-to-noise ratio of the data.

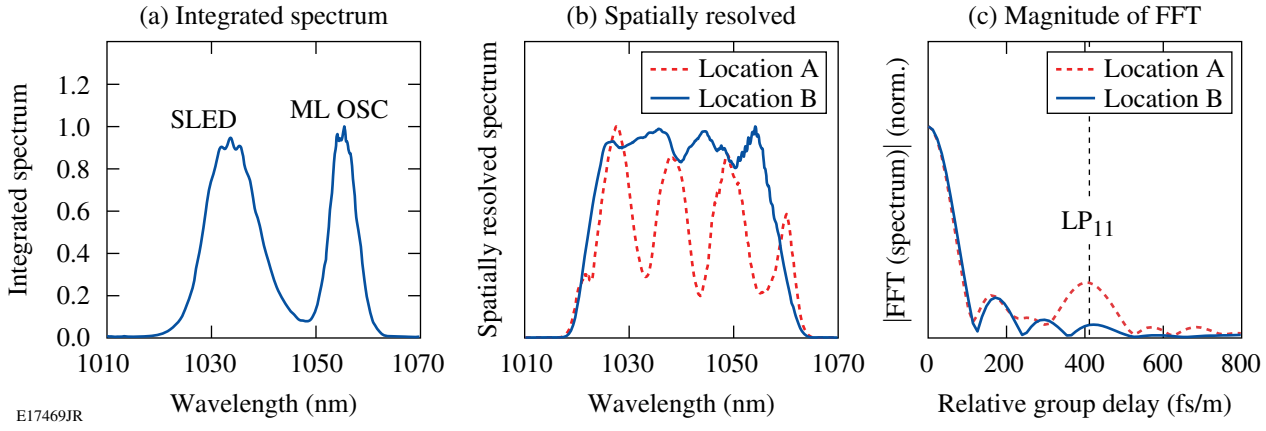

Figure 119.15
(a) Integrated amplified spectrum. (b) Spatially resolved spectra, after normalization with the integrated spectrum, at locations of low- and high-fringe visibility (solid and dashed, respectively). (c) Corresponding Fourier transform magnitudes, with dashed line showing the location of LP_{11} signal.

S^2 imaging provides a direct measurement of the beam profile at a given wavelength. This method of viewing the data is presented as a sequence of images in Fig. 119.17. The relative LP_{11} power in this case was –13 dB. As the wavelength changes, the beam centroid moves vertically in the y direction, along the LP_{11} axis (see Fig. 119.18). This beam motion is a direct

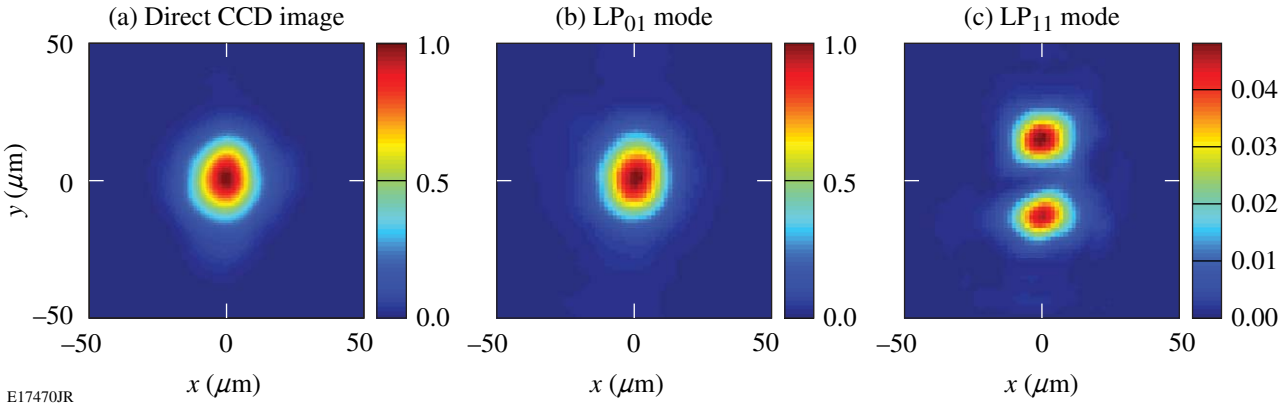

Figure 119.16
(a) Output beam as measured using a 12-bit CCD. [(b), (c)] Modes reconstructed using the S^2 technique.

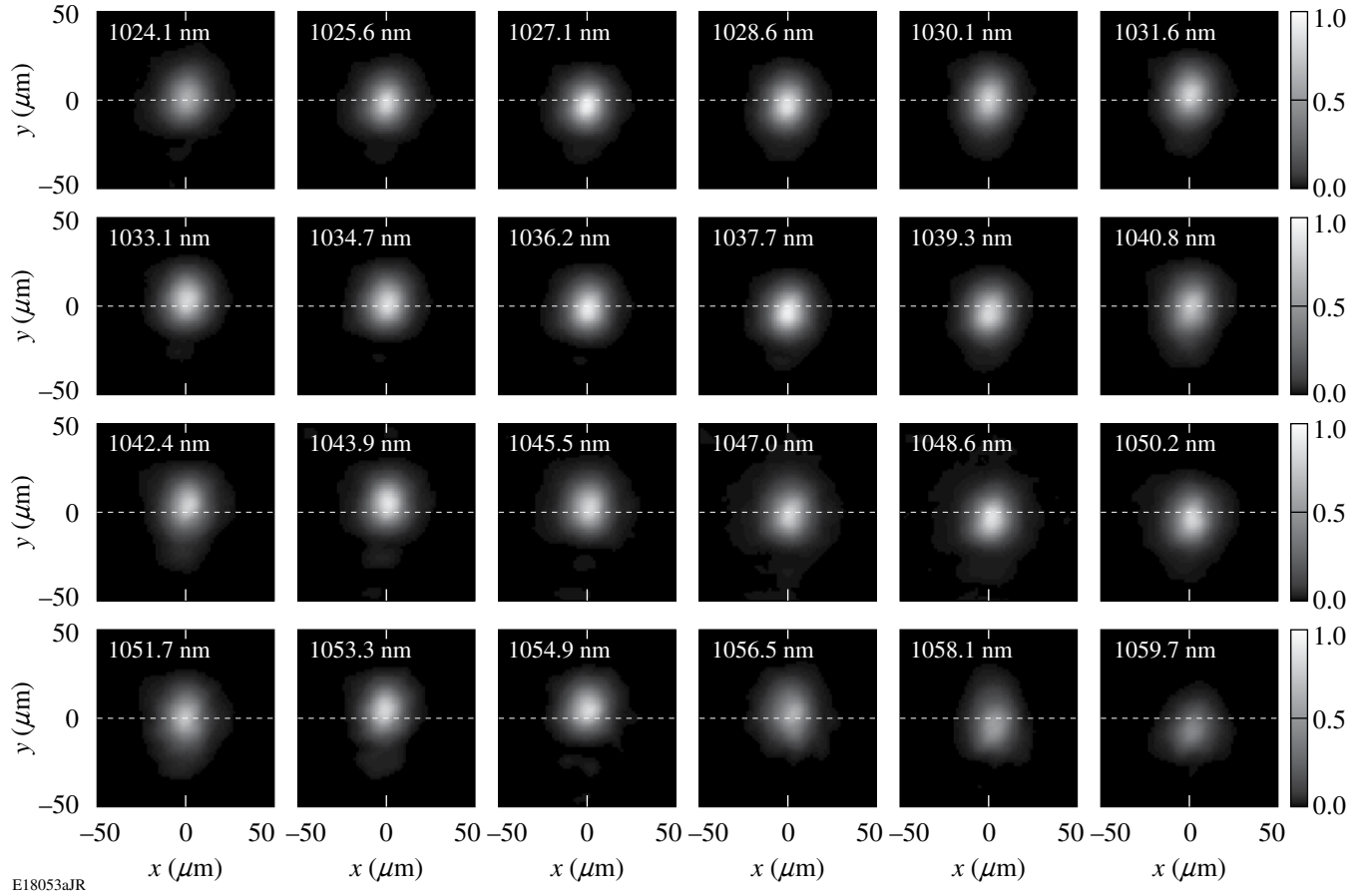

Figure 119.17
Spectrally resolved images that are measured by the S^2 technique. The oscillation of the beam with wavelength in the y direction is due to the wavelength dependence of the phase between the LP_{01} and LP_{11} modes.

consequence of the coherence and co-polarization of the two modes. At wavelengths corresponding to a positive y centroid, the upper lobe of the LP_{11} mode interferes constructively with the LP_{01} mode, and the lower lobe interferes destructively. This oscillation would not be seen if the modes were incoherent or orthogonally polarized.

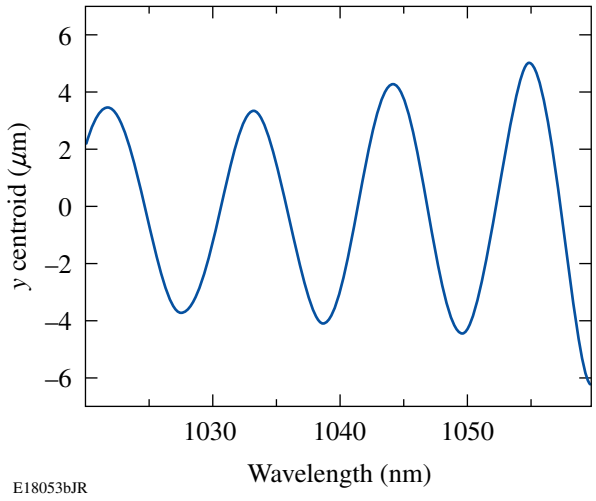

Figure 119.18
The beam centroid in the y direction as a function of wavelength.

These observations raise important questions about the impact of HOM's in broadband amplifiers. When the signal bandwidth is much larger than the fringe period, deflection of the beam centroid at each wavelength will average to zero over the full spectrum. Although the integrated beam profile is broadened along the HOM axis, it is relatively insensitive to phase fluctuations between the modes. If the signal bandwidth is less than the fringe period, phase fluctuations significantly alter the integrated beam profile since there is insufficient bandwidth to average out the beam variations at each spectral component. For this amplifier, a Gaussian signal bandwidth equal to single fringe period (FWHM = 11 nm) corresponds to a 150-fs transform-limited pulse. The relative phase of the modes was stable during the S^2 scan (several minutes), in part because the fundamental mode and the HOM propagate along the same length of fiber. Long-term stability will depend on the details of the amplifier's thermal environment and stability of signal injection, so no general conclusions can be drawn from these data.

Impact of Misalignment at Signal Injection on HOM Content

The impact of misalignment at injection was evaluated by offsetting the beam with the pointing mirror (see Fig. 119.14), using the EFM to quantify the amount of offset at signal injection, and the S^2 measurements to measure the resulting HOM content. The results are shown in Fig. 119.19. Significant amounts of LP_{11} were excited when injection was misaligned along the axis of the LP_{11} mode (the y axis). This offset direction increases the mode overlap between the input signal beam and one of the lobes of the LP_{11} mode, producing a larger fraction of the LP_{11} mode at injection. The power in LP_{11} was only –13 dB below that for LP_{01} for a 15-μm offset (~30% of the MFD). The large misalignment reduced the amplifier gain by only ~0.5 dB.

Simulations using a simple step-index model predict that these levels of LP_{11} can have a small but measurable impact on the amplifier beam's quality. The fiber parameters were chosen to match the MFD and N.A. of the amplifier (core radius a =

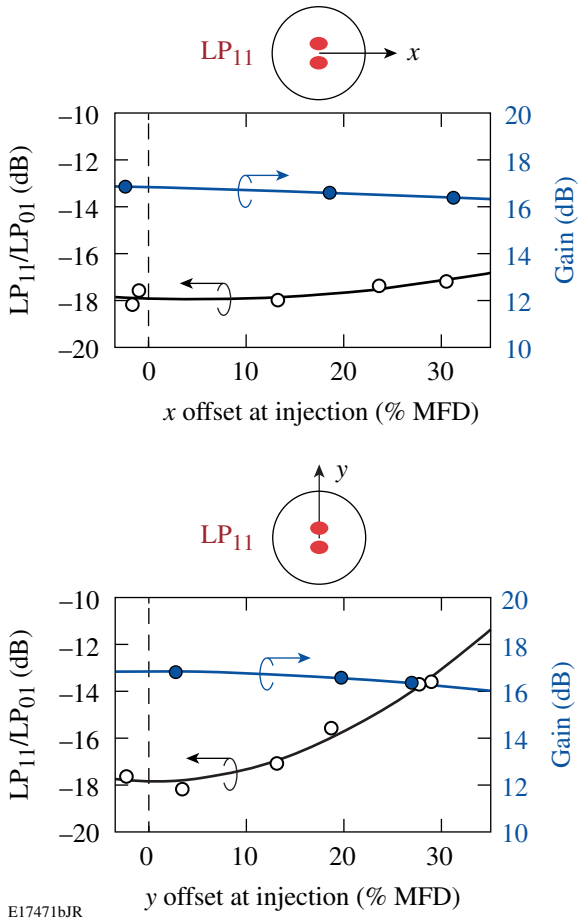

Figure 119.19
Relative power in LP_{11} mode versus injection offset. Offset along the (a) x direction (across SAP axis) and (b) the y direction (along SAP axis). Also shown is the gain in dB as a function of offset.

28 μm; index difference $\Delta = 5.3 \times 10^{-5}$) and to set the LP_{11} mode close to cutoff ($V = 2.50$). While these calculations did not include the full model for the PCF design or birefringence, some qualitative conclusions can be reached. Figure 119.20 shows the simulated values of beam quality (M^2) in the x and y directions plotted as a function of the ratio of LP_{11} to LP_{01} powers, where the LP_{11} mode is aligned with the y axis as in Fig. 119.16(c). This orientation of LP_{11} produces degradation of M^2 that is more severe in the y direction. The value of M_y^2 depends on the relative phase between the modes.[3]

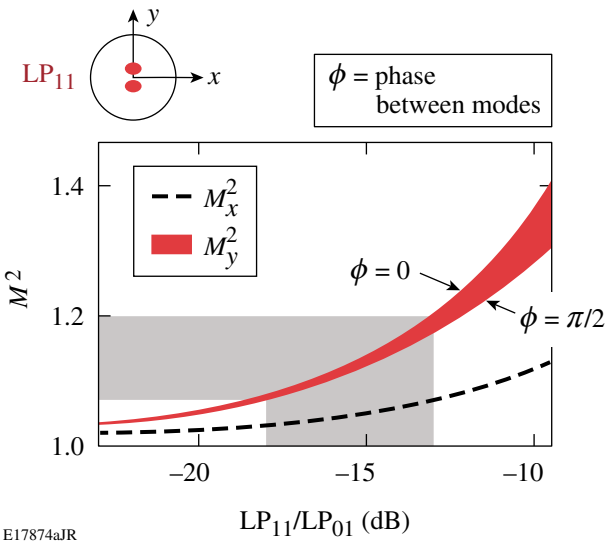

Figure 119.20
Simulations using a simple step-index model showing the impact LP_{11} content can have on the beam quality M^2. Results are shown along both x and y directions as a function of relative power of LP_{11} and LP_{01} modes. The M^2 degradation is more severe along the y direction (the axis of the LP_{11} mode) and depends on the relative phase ϕ between the modes. The grey region shows the range of LP_{11} content measured in the PCF amplifier and the corresponding range of M^2 values predicted by this simple model.

Measurements of M^2 show degradation when the amount of LP_{11} is increased by misaligning the signal at injection (see Fig. 119.21). The largest increase occurs in M_y^2 (as predicted by the simulations) and when the injection offset is along the y axis (as predicted by the S^2 measurements). This is consistent with the fact that this offset direction produces the largest amount of LP_{11}. M^2 degradation from x-axis offsets cannot be explained by the level of LP_{11} alone. It is likely that other higher-order leaky modes or spatially incoherent scattering within the amplifier that is not resolved in the S^2 measurements but can degrade M^2 are responsible.

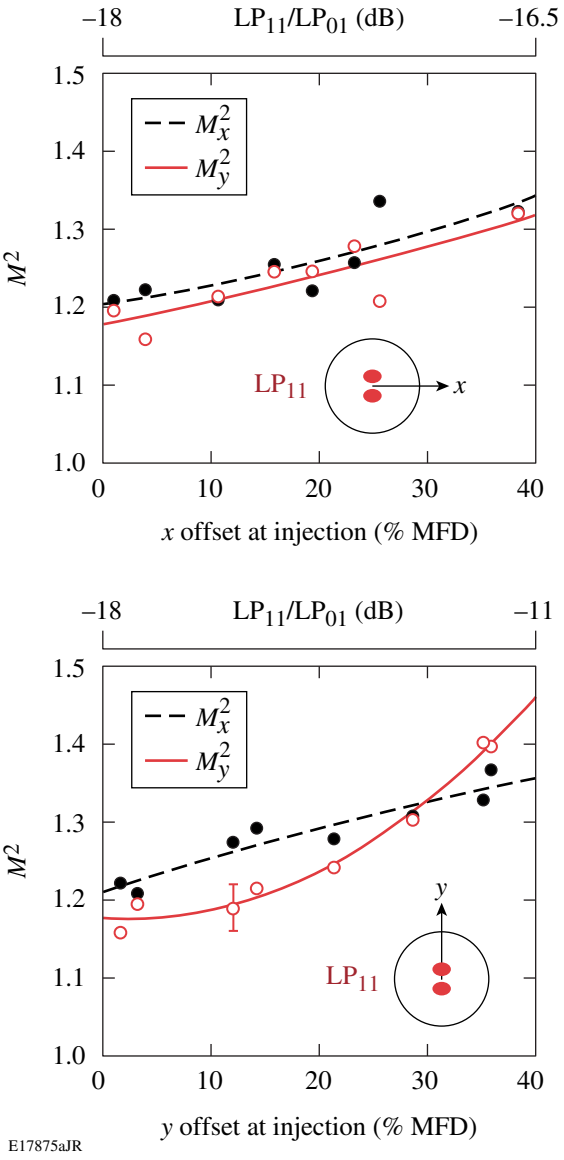

Figure 119.21
Measured M^2 for injection offsets. Offset in the (a) x direction and (b) y direction. Inset shows the offset direction relative to the orientation of the LP_{11} mode.

In conclusion, S^2 imaging has been used for the first time to measure higher-order mode content of a large-mode-area amplifier at full power. Minor modifications to the technique were necessary to accommodate the short amplifier length and small relative group delay. An HOM corresponding to the co-polarized LP_{11} mode was clearly observed with an axis aligned to the birefringent axis of the polarizing amplifier. The power in the LP_{11} mode relative to the fundamental LP_{01} mode depended on the alignment of the signal at injection. A relative power of

–18 dB was measured when optimally aligned. LP_{11} content increased when the injected beam was offset, particularly when the offset direction was toward one of the LP_{11} lobes. An offset of ~30% of the 55-μm MFD increased the LP_{11} content to –13 dB while only decreasing the amplifier gain by ~0.5 dB.

ACKNOWLEDGMENT

The authors thank Jeff Nicholson, Ingmar Hartl, and Martin Fermann for helpful discussions. This work was supported by the U.S. Department of Energy Office of Inertial Confinement Fusion under Cooperative Agreement No. DE-FC52-08NA28302, the University of Rochester, and the New York State Energy Research and Development Authority. The support of DOE does not constitute an endorsement by DOE of the views expressed in this article.

REFERENCES

1. F. Röser *et al*., Opt. Lett. **32**, 3495 (2007).
2. O. Schmidt *et al*., Opt. Express **16**, 3918 (2008).
3. H. Yoda, P. Polynkin, and M. Mansuripur, J. Lightwave Technol. **24**, 1350 (2006).
4. S. Wielandy, Opt. Express **15**, 15,402 (2007).
5. J. W. Nicholson *et al*., Opt. Express **16**, 7233 (2008).
6. J. W. Nicholson *et al*., IEEE J. Sel. Top. Quantum Electron. **15**, 61 (2009).

Optical Differentiation and Multimillijoule ~150-ps Pulse Generation in a Regenerative Amplifier with a Temperature-Tuned Intracavity Volume Bragg Grating

Introduction

Optical differentiators have recently received considerable attention based on their potential application in all-optical signal-processing circuits[1] and optical pulse shaping.[2–4] In Ref. 4 an ultrafast optical differentiator based on long-period fiber grating with subpicosecond temporal resolution was demonstrated. An ultrafast optical differentiator based on an asymmetric Mach–Zehnder interferometer was proposed in Ref. 5. An optical-differentiator operation using a GaAs/AlAs short-period super lattice near an optical absorption band edge was demonstrated in Ref. 6.

Holographic volume Bragg gratings (VBG's) represent a new class of robust, highly efficient, and spectrally selective optical elements that are recorded in photo-thermo-refractive glass.[7] VBG's have spectral and angular dispersions that are higher than any dispersive elements previously used. VBG's are stable at elevated temperatures, have an optical damage threshold similar to that of bulk glass materials, and have high diffraction efficiency and low losses that enable one to use them in laser resonators.

An optical differentiation in a regenerative amplifier (RA) with a temperature-tuned VBG as an intracavity spectral filter is reported for the first time. Using an RA with a VBG as a spectral filter greatly improves optical differentiator performance because of multiple passes through the filter and significant RA gain that increases differentiator efficiency and makes its practical application possible.

One of the appealing applications of an RA in differentiation mode is producing multimillijoule ~150-ps pulses—important for laser–matter interaction studies and laser micromachining. Producing these pulses usually requires a mode-locked oscillator in combination with a regenerative amplifier[8] or a Q-switched microchip laser[9] that requires an additional amplifier because of low, <1-μJ output-pulse energy. In this article a simple and reliable multimillijoule ~150-ps laser system based on an RA operating in differentiation mode with a temperature-tuned VBG as a resonator spectrally selective mirror is demonstrated for the first time.

Experimental Setup

The Nd:YLF diode-pumped RA shown in Fig. 119.22(a) is almost identical to the one described in Ref. 10 except that it has a longer cavity length. The RA has a folded linear cavity with a round-trip time of 21 ns, which makes it possible to amplify pulses as long as 13-ns FWHM in duration. The Nd:YLF active element was oriented for a 1053-nm operational wavelength. It was pumped by a 150-W, fiber-coupled laser diode array (Apollo Instruments, Irvine, CA), which was operated in a pulsed mode, producing 1-ms pump pulses at 805 nm with a 5-Hz repetition rate. The RA intracavity Pockels cell driven by fast electrical circuitry makes it possible to inject and cav-

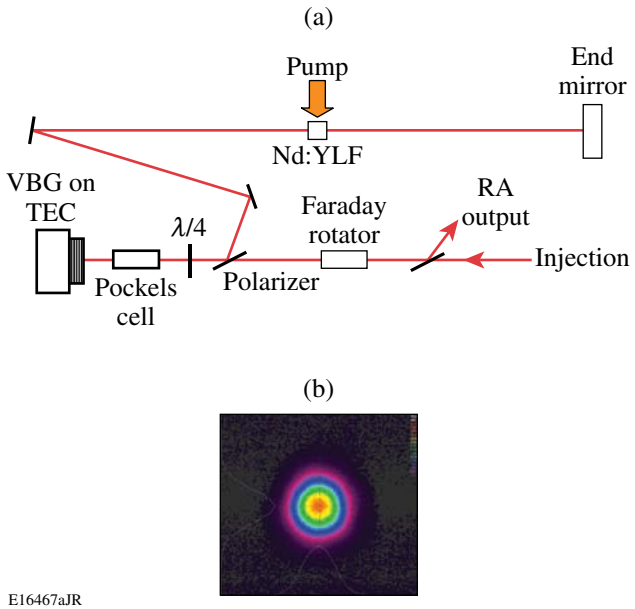

Figure 119.22
(a) A Nd:YLF diode-pumped regenerative amplifier (RA) with a temperature-tuned VBG as a resonator end mirror has been demonstrated. (b) The RA output beam profile corresponds to the TEM_{00} resonator mode. TEC: thermoelectric cooler

ity dump the amplified pulse. The injected pulse was mode matched to the RA resonator and, after a certain number of round-trips, reached its maximum energy and was dumped from the RA cavity. An AR-coated, temperature-tuned VBG (OptiGrate, Orlando, FL) at a 0° angle of incidence was used [Fig. 119.23(a)]. Introducing a VBG as an RA spectrally selective mirror did not alter RA performance, owing to the VBG's high-diffraction efficiency (up to 99.7%). The VBG's high optical quality ensured RA performance in the TEM_{00} resonator mode [Fig. 119.22(b)]. The VBG bandwidth was 240-pm FWHM. The wavelength dependence of the VBG reflectivity is shown in Fig. 119.23(b). The VBG reflectivity maximum can be temperature tuned at an ~10-pm/°C rate. The VBG temperature was maintained with 0.1°C accuracy.

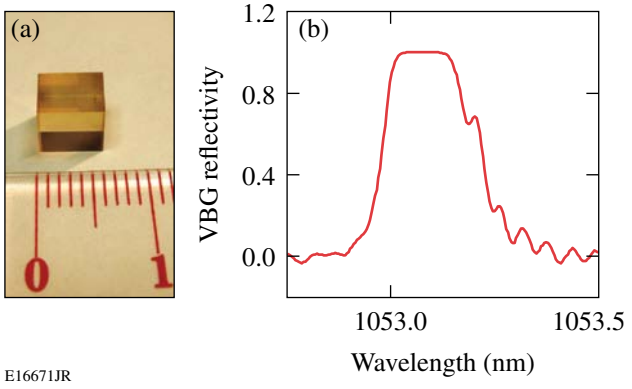

Figure 119.23
(a) VBG's are robust, spectrally selective optical elements that are recorded in photo-thermo-refractive glass. (b) Reflectivity of the VBG used in this experiment was 99.7% with a 240-pm FWHM bandwidth centered at 1053.08 nm.

Optical Differentiation in the RA

The 2.4-ns FWHM precompensated square pulse described in Ref. 11, which is obtained using a system that contains a stabilized single-frequency fiber laser, integrated-optic modulators, and fiber amplifier,[12] is injected into the cavity. If the VBG in the RA is tuned to the maximum of the injected pulse spectrum (shortest RA buildup time), the injected pulse is amplified, maintaining its shape with a slight distortion caused by gain saturation in the RA [see Fig. 119.24(a)]. When the VBG reflectivity is detuned by ~20 pm, positive feedback in the RA resonator is formed for injected pulse broadband components, and the RA performs as an optical differentiator, amplifying only rising and falling edges [Fig. 119.24(b)]. VBG peak-reflectivity detuning by 20 pm provides ~0.3% loss dif-

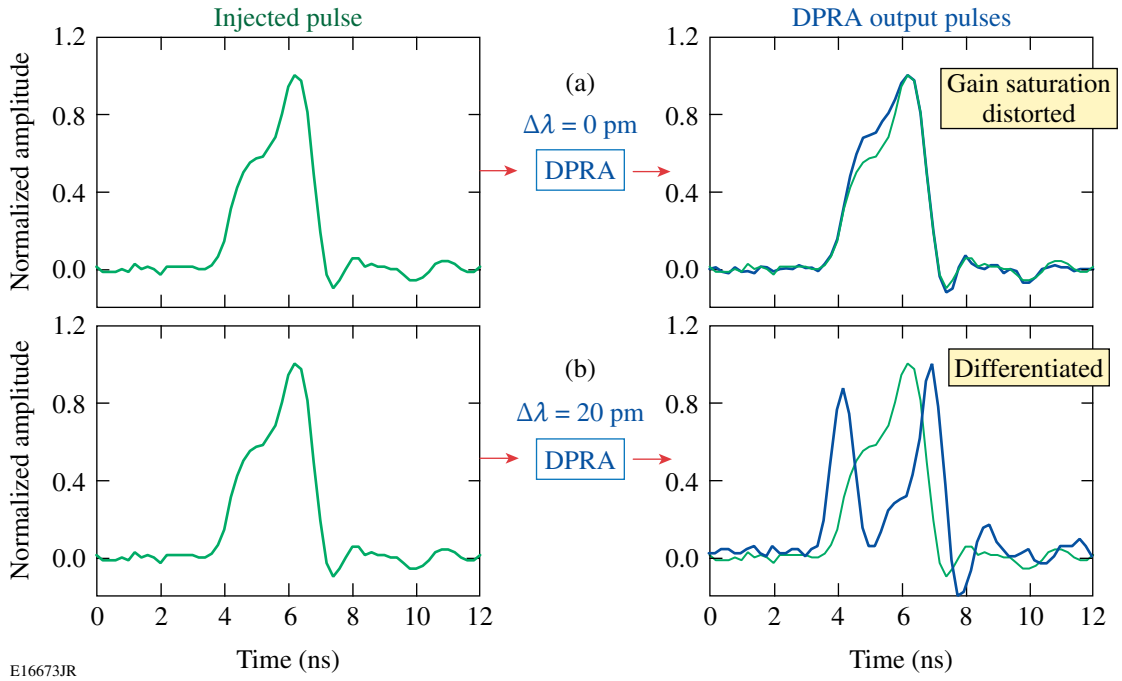

Figure 119.24
(a) The RA shows no peculiarities when VBG is tuned to the injected-pulse central wavelength. (b) The RA works as an optical differentiator when the VBG temperature is detuned from the injected pulse's center wavelength. Note that the gray lines in the right side output pulse are the original normalized injected pulse shape.

ference per round-trip for the injected pulse central wavelength (Fig. 119.25). The total number of round-trips in the RA is 50, which, combined with very high ~10^8 RA gross gain, causes enough discrimination that the center wavelength is not amplified, making the RA an optical differentiator.

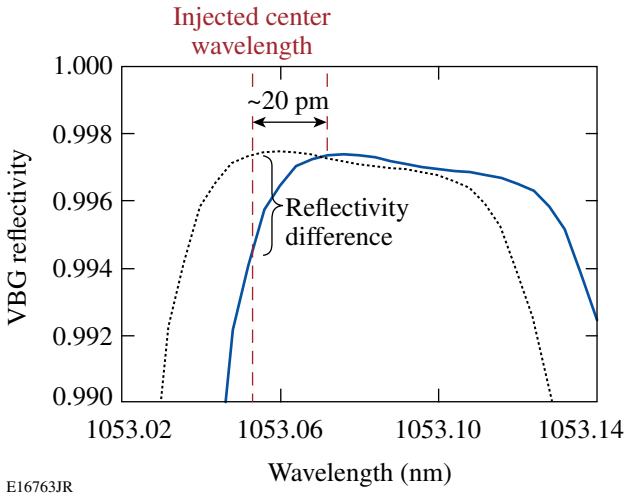

Figure 119.25
Wavelength detuning by 20 pm, which leads to a VBG reflectivity difference of ~0.3% per round-trip, is enough to provide differentiation in the DPRA.

Generation of a Multimillijoule Picosecond Pulse in an RA in Differentiation Mode

One application of an RA as an optical differentiator is generating energetic short pulses without mode-locking. In Ref. 2 it is shown that the generation of an optical pulse with an arbitrary shape may be reduced to the problem of producing an arbitrary spectral filter. An optical differentiator is required as a spectral filter to produce a δ-function pulse. This type of filter with a quarter-wave antireflection coating in reflection mode was proposed in Ref. 2. The efficiency of this device is very low. Using an RA as an optical differentiator provides high efficiency in generating short pulses, owing to significant RA gain and multiple round-trips.

Injecting a step-like pulse is required for producing short pulses out of an RA. The output pulse width is defined by the sharp-edge duration of the injected pulse. A step-like pulse can be produced by using an air breakdown,[2] a fast pulse-shaping system,[12] or a stimulated Brillouin scattering (SBS) mirror.[13] In this article, a system that consisted of a single-frequency Q-switched laser, an SBS mirror, and an RA with a VBG was used. The Q-switched laser produced 4.9-ns-FWHM, 3-mJ TEM_{00} pulses at 1053 nm with a 5-Hz repetition rate. Output pulses were focused into an SBS cell filled with liquid carbon tetrachloride using a 60-mm-focal-length achromat (Fig. 119.26). The 3-ns-FWHM SBS-cell output pulses shown in Fig. 119.26 had a steep 300-ps leading edge, which can be made even shorter (<100 ps) by optimizing SBS cell performance.[13] The SBS cell reflectivity was ~50% when the incoming pulse energy was 2.8 mJ, which was set using a half-wave plate and polarizer combination. After attenuation, an SBS-steepened pulse was launched into a single-mode, polarization-maintaining fiber and injected into the RA with a VBG. The injected pulse energy was 250 nJ.

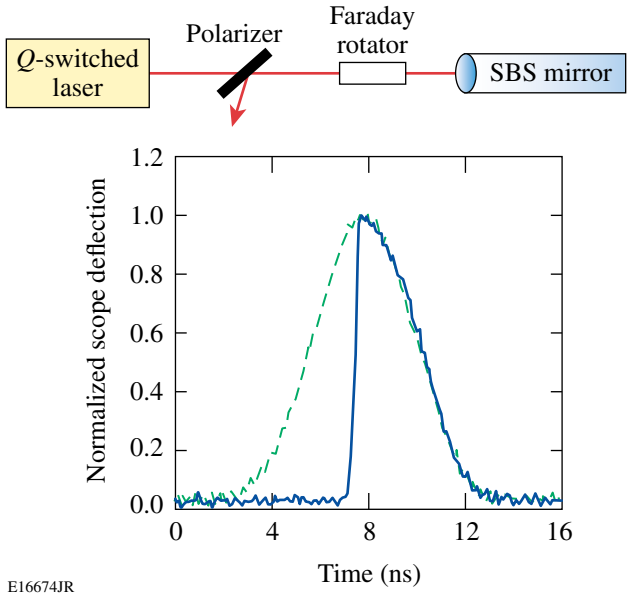

Figure 119.26
A step-like pulse shape with a sharp 300-ps leading edge was produced with an SBS mirror. The dashed line is the input pulse and the solid line is the output pulse from the SBS cell.

When the maximum of the VBG reflectivity curve is tuned to the maximum of the injected pulse spectrum, the RA works in regular regime, producing the amplified up-to-12-mJ pulses shown in Fig. 119.27(a). Pulse shortening from 3-ns to 1.25-ns FWHM occurs as a result of gain saturation in the RA and the sharp leading edge of the injected pulse. When the VBG is detuned from the central wavelength by 25 pm, the RA operates as an optical differentiator and amplifies the leading-edge portion of the injected pulse, producing a 150-ps-FWHM, 12-mJ TEM_{00} pulse at 1053 nm with a 5-Hz repetition rate [Fig. 119.27(b)].

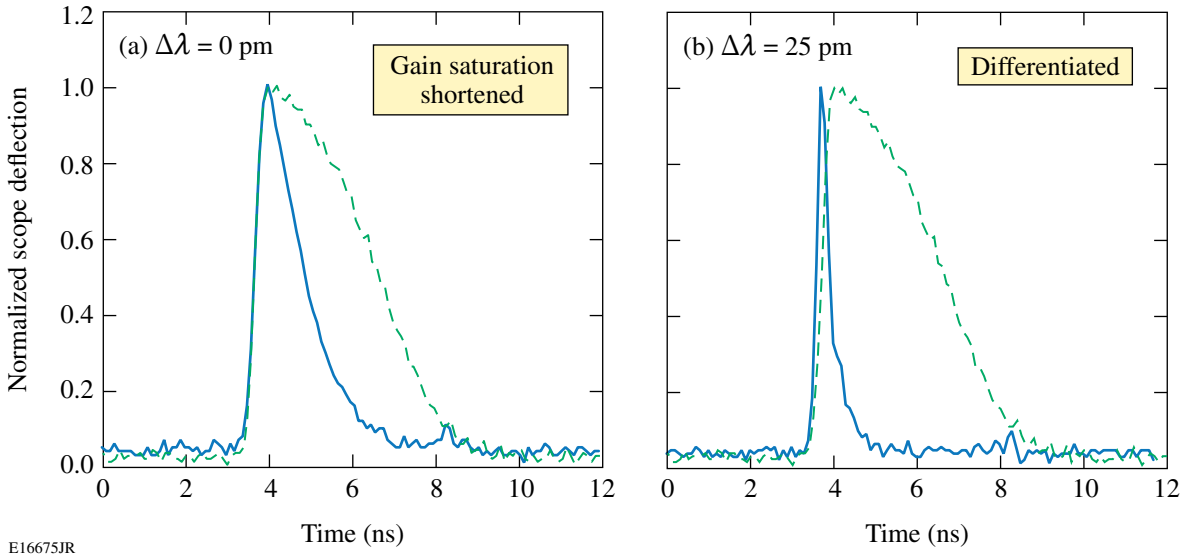

Figure 119.27
(a) The RA with a VBG tuned to the injection central wavelength produced shortened nanosecond pulses as a result of gain saturation of the step-like pulse. (b) When a VBG is temperature detuned, the RA produces 150-ps FWHM multimillijoule pulses after differentiation of a step-like pulse. The dashed line is the input pulse to the RA and the solid line is the RA output pulse shape.

Conclusion

It has been demonstrated for the first time that a regenerative amplifier with a temperature-tuned volume Bragg grating as a spectrally selective resonator mirror works as an optical differentiator when the VBG reflection peak is detuned from the central laser wavelength. A simple, reliable laser system that produces multimillijoule ~150-ps pulses without mode-locking using an RA with a VBG as an optical differentiator has been realized.

ACKNOWLEDGMENT

This work was supported by the U.S. Department of Energy Office of Inertial Confinement Fusion under Cooperative Agreement No. DE-FC52-08NA28302 and the University of Rochester. The support of DOE does not constitute an endorsement by DOE of the views expressed in this article.

REFERENCES

1. N. Q. Ngo *et al*., Opt. Commun. **230**, 115 (2004).
2. E. Yablonovitch, IEEE J. Quantum Electron. **11**, 789 (1975).
3. M. Kulishov and J. Azaña, Opt. Lett. **30**, 2700 (2005).
4. R. Slavík *et al*., Opt. Express **14**, 10,699 (2006).
5. Z. Li *et al*., in *Proceedings Symposium IEEE/LEOS Benelux Chapter*, edited by A. M. J. Koonen *et al*. (IEEE, Eidenhoven, The Netherlands, 2006), pp. 173–176.
6. M. Hosoda *et al*., Appl. Phys. Lett. **65**, 2913 (1994).
7. L. B. Glebov *et al*., in *Laser Weapons Technology III*, edited by W. E. Thompson and P. H. Merritt (SPIE, Bellingham, WA, 2002), Vol. 4724, pp. 101–109.
8. W. Koechner, *Solid-State Laser Engineering*, 4th rev. ed., Springer Series in Optical Sciences, Vol. 1 (Springer, Berlin, 1996).
9. G. J. Spühler *et al*., J. Opt. Soc. Am. B **16**, 376 (1999).
10. A. V. Okishev and J. D. Zuegel, Appl. Opt. **43**, 6180 (2004).
11. A. V. Okishev, C. Dorrer, V. I. Smirnov, L. B. Glebov, and J. D. Zuegel, Opt. Express **15**, 8197 (2007).
12. J. R. Marciante and J. D. Zuegel, Appl. Opt. **45**, 6798 (2006).
13. M. D. Skeldon, A. Okishev, A. Babushkin, and W. Seka, in *First Annual International Conference on Solid State Lasers for Application to Inertial Confinement Fusion*, edited by M. André and H. T. Powell (SPIE, Bellingham, WA, 1995), Vol. 2633, pp. 422–429.

Slow Crack Growth During Radiative Cooling of LHG8 and BK7 Plates

Introduction

Because of their low resistance to fracture and low thermal conductivity, many ceramics and glasses are susceptible to thermal shock. A common thermal shock configuration consists of a component at an initially uniform high temperature suddenly exposed to a cooling medium at a lower temperature. The more-rapid temperature decrease at the surface induces a tensile stress, while the component's interior is in a state of compression. Kingery[1,2] has discussed in detail the effects of material and cooling medium properties on thermal shock. The relevant figures of merit governing thermal shock have been reviewed by Hasselman[3] and Wang and Singh.[4]

Depending on the thermal conductivity of the component, its dimensions, and the heat transfer coefficient induced by the cooling medium, there may exist a state of "severe" thermal shock (where the tensile thermal stresses at the component surface depend only on the material's thermomechanical properties) or "mild" thermal shock (where the surface tensile stresses depend on the material's thermomechanical properties and the Biot number, involving the cooling heat transfer coefficient, specimen size, and component thermal conductivity). The heat transfer coefficient itself depends on the flow between the component and the cooling medium (forced or natural), the dimensions of the component, and the cooling medium's thermophysical properties (viscosity, density, and thermal diffusivity). The conditions for severe or mild thermal shock along with an extensive discussion of the contributions of the thermomechanical properties can be found in Refs. 5–7.

Since the Biot number is an important factor in determining the severity of thermal shock, ceramics and glasses behave differently under thermal shock conditions. Ceramics have higher thermal conductivity and, therefore, lower Biot numbers, leading to conditions prone to mild thermal shock. Glasses, on the other hand, have a low thermal conductivity and are thus liable to severe thermal shock. A large amount of work exists in the literature on thermal shock of ceramics[3–9] but less on thermal shock of glasses.[10]

This article discusses the radiative cooling of two optical glasses: the borosilicate crown BK7 and the phosphate LHG8. Under radiative cooling conditions, the usual thermal shock analysis does not apply because the surrounding temperature continuously changes with time as does the heat transfer coefficient (and thus the Biot number). We determine the relevant thermal and stress fields numerically using finite elements and then use these results to study crack growth at the heaviest stressed locations. We discuss fracture in terms of strength, fracture toughness, and slow crack growth under transient temperature and stress fields.

Material Properties

The two materials investigated here are the borosilicate crown glass BK7, a commonly used optical glass, and the phosphate glass LHG8 often used in laser applications. The glass properties are listed in Table 119.II.

We observe that LHG8 is about twice as brittle in terms of fracture toughness K_c as BK7, while it is also twice as soft. In Table 119.II, we have also calculated the fracture strength for these glasses, assuming different sizes of initial flaw size into the surface. Table 119.II gives a range for the fracture toughness of LHG8. The higher value $\left(0.51\ \text{MPa}\sqrt{\text{m}}\right)$ is cited in Campbell *et al.*,[11] while the lower value $\left(0.43\ \text{MPa}\sqrt{\text{m}}\right)$ is cited in DeGroote *et al.*[12] Notice, however, that a typical uncertainty in K_c is ±10%. In this sense, these measurements agree.

Suratwala *et al.*[13] have measured the slow crack growth in LHG8 using the double-cleavage-drilled-compression method. They showed that the rate of crack growth v depends on the amount of OH concentration in the glass. They reported data in the temperature range of 25°C to 300°C and water vapor pressure in the range of 2 to 92 mmHg. These data can be fitted by

$$v = \frac{v_I v_{II}}{v_I + v_{II}} \tag{1}$$

Table 119.II: Material properties of the two glasses studied.

Property and Units	BK7	LHG8
Density ρ, kg/m^3	2510	2830
Heat capacity cp, J/kg.K	858	750
Thermal conductivity k, W/m.K	1.114	0.58
Thermal diffusivity D, m^2/s	5.2×10^{-7}	2.7×10^{-7}
Young's modulus E, GPa	82	50
Poisson ratio ν	0.21	0.26
CTE α, K^{-1}	8.3×10^{-6}	12.7×10^{-6}
Fracture toughness K_c, MPa$\sqrt{\text{m}}$	0.82	0.43 to 0.51
Fracture strength, MPa (assumes scratch a is 50 μm deep)	59	31 to 36
Fracture strength, MPa (assumes scratch a is 500 μm deep)	19	10 to 12
Fracture strength, MPa (assumes scratch a is 1000 μm deep)	13	7 to 8
Hardness, GPa	6.8±0.3	3.4

with

$$v_I = v_0 \left(\frac{p_{H_2O}}{p_0} \right)^m \exp\left(\frac{K_{app} b - Q_I}{RT} \right),$$
$$v_{II} = C \frac{p_{H_2O}}{p_0} \exp\left(\frac{-Q_{II}}{RT} \right), \quad (2)$$

where p_0 is the atmospheric pressure 760 mmHg. The parameters are listed in Table 119.III. The subscripts I and II correspond to region I (stress controlled) and region II (diffusion controlled) crack growth.[13,14] The harmonic mean in Eq. (1) essentially selects the lower of v_I, v_{II}. Notice that the applied stress intensity factor K_{app} affects the crack growth rate v_I (but not v_{II}).

For the case of a quarter circular crack at the edge of a plate under tension, the applied stress intensity factor is

$$K_{app} = \Omega \, \sigma_{app} \sqrt{\pi a}, \quad (3)$$

where Ω is a geometrical factor (~0.80), σ_{app} is the applied tension, and a is the crack depth (see Lambropoulos *et al.*[15] for the geometrical factor Ω describing a quarter circular crack along an edge).

For the case of BK7, we used the data of Wiederhorn and Roberts,[14] who measured slow crack growth in BK7 and other glasses with a double cantilever beam technique. They reported data for BK7 at temperatures of 23°C, 104°C, 154°C, and 226°C under vacuum (10^{-5} Torr), as well as for BK7 in air and RT under 100% RH.

Table 119.III: Data for slow crack growth in LHG8 from Suratwala *et al.*[13]

Parameter	Units	LHG8-L (128-ppmw OH)	LHG8-H (773-ppmw OH)
v_0	10^6 m/s	7.3	7.3
m	dimensionless	1.20	1.20
Q_I	kJ/mol	253	239
b	m$^{5/2}$/mol	0.48	0.48
C	m/s	180	180
Q_{II}	kJ/mol	26	26

For numerical computation, we have fitted the data at the crack growth rates of 10^{-5} m/s, 10^{-6} m/s, and 10^{-7} m/s for these four temperatures. We fitted these data to the form

$$v_I = v_0 \exp\left(\frac{K_{app} b - Q}{RT}\right) \tag{4}$$

by a numerical procedure that minimized the error, defined as

$$\%\text{error}(v_0, b, Q) = 100 \times \frac{\sum_1^{12} \left[\ln v(v_0, b, Q) - \ln v_i\right]^2}{\sum_1^{12} (\ln v_i)^2}. \tag{5}$$

The best fit gave a minimum error of 0.62% and corresponded to the parameters

$$\begin{aligned} \ln v_0 &= 10.10, \\ b &= 0.21 \text{ m}^{5/2}/\text{mol}, \\ Q &= 227.5 \text{ kJ/mol}, \end{aligned} \tag{6}$$

describing the slow crack growth of BK7 at "vacuum" conditions. These data will be used to predict crack growth in BK7 under vacuum conditions.

Finite Element Analysis: Temperature and Stress

Both materials modeled are in the form of rectangular plates with an areal extent of 800 × 400 mm^2. The BK7 plates are 80 mm thick; the LHG8 plates are 40 mm thick. These dimensions will be consistent throughout the remainder of our work. The BK7 and LHG8 thicknesses are different because thermal stress is known to scale with thickness, while LHG8 is less strong than BK7. In a sense, therefore, the stronger BK7 plates are more severely stressed than the thinner LHG8.

The plate was initially placed in an oven at a uniform high temperature. The oven temperature slowly diminished with time, so that all six sides of the plate underwent radiative cooling into an ambient whose temperature changed with time. In both cases of LHG8 and BK7, it was assumed that the initial temperature was uniform and equal to a high value of 200°C. The surroundings' (ambient) temperature decayed exponentially with a time constant τ that may vary from minutes to hours to days. The eventual temperature was room temperature, again taken as uniform (see Fig. 119.28).

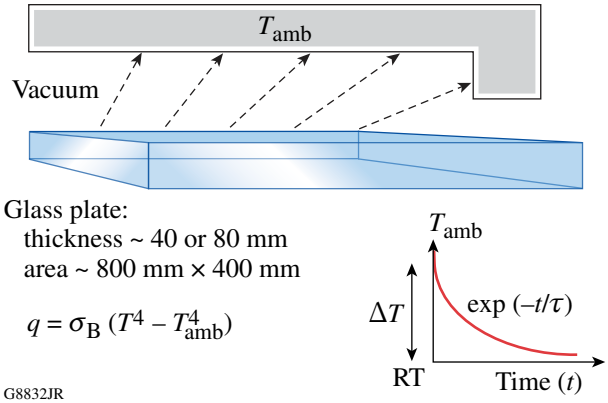

Figure 119.28
The geometry of a thin plate cooled by radiation. The ambient temperature decayed exponentially from the initial temperature of 200°C to the final temperature (RT) with a time constant τ.

The coordinate system was centered at the plate's center, with –400 mm < y < 400 mm, –200 mm < x < 200 mm, and the coordinate z varying –20 mm < z < 20 mm for LHG8 or –40 mm < z < 40 mm for BK7.

The boundary condition on all six edges of the glass plate was taken as radiating into a medium of ambient temperature $T_{amb}(t)$, i.e.,

$$q\left[\text{W/m}^2\right] = \sigma_B \left(T^4 - T_{amb}^4\right), \tag{7}$$

where σ_B is the Boltzmann constant 5.67 × 10^{-8} W/(m^2.K^4), T is the absolute temperature at the glass surface, and T_{amb} is the (time-dependent) temperature of the surroundings (ambient), taken to vary as

$$T_{amb}(t) = 293 + 180 \exp\left(-t/\tau\right), \tag{8}$$

where the time constant τ models the rate at which the surroundings temperature decays with time. The ambient temperature drops from 200°C to 86°C in time τ and to 29°C in time 3τ. The initial condition is

$$T(x, y, z, t = 0) = 473 \text{ K}. \tag{9}$$

The temperature $T(x,y,z,t)$ is governed by the time-dependent, 3-D heat conduction equation. A typical temperature evolution is shown in Fig. 119.29.

Once the temperature was determined, the stresses were calculated by using COMSOL® (version 3.4).[16] We note some

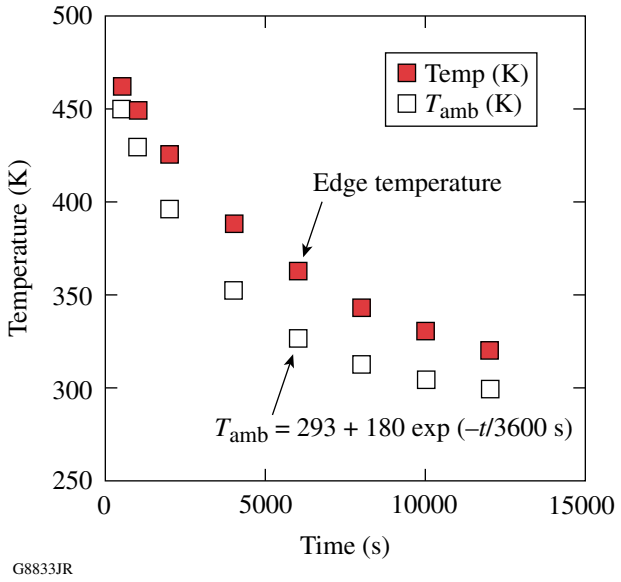

Figure 119.29
Temperature evolution along the edge center of the long edge in a 40-mm-thick LHG8 plate. The temperature relaxation constant τ = 1 h. The ambient temperature is also shown.

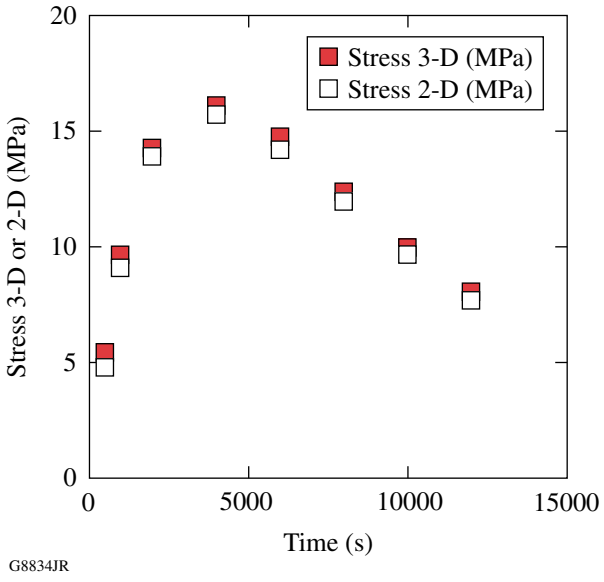

Figure 119.30
Thermal stress evolution along the edge center of the long edge in a 40-mm-thick LHG8 plate. The temperature relaxation constant τ = 1 h. For short times, the temperature was high and uniform, so the thermal stress was low. These results show the thermal stress calculated via 3-D or 2-D (plane-strain) approaches. Both approaches give similar stress levels.

features of the resulting stress distribution: At early times, the temperature was high but mostly uniform; therefore the thermal stress was very small. At long times, the temperature was low and again mostly uniform; therefore the thermal stress was also low. As a result, the thermal stress became largest at some intermediate time. An example of stress evolution along the center of the long edge is shown in Fig. 119.30.

We also observed that the Biot number was neither small nor very large. To extract an applicable heat transfer coefficient h_{eff}, we linearized the surface-cooling constitutive law to read

$$q\left[\text{W}/\text{m}^2\right] = 4\sigma_B T_{\text{amb}}^3 \left(T - T_{\text{amb}}\right) = h_{\text{eff}}\left(T - T_{\text{amb}}\right). \quad (10)$$

Evaluating h_{eff} at T_{amb} = 473 K or at 300 K, we found that h_{eff} was in the range of 24 to 26 W/m^2.K, so that the Biot number

$$\text{Bi} = h_{\text{eff}} L/k \quad (11)$$

(with 2L as the plate thickness) was in the range of 0.2 to 0.8 for LHG8 and 0.2 to 0.9 for BK7. We concluded that the temperature gradients in the plate cannot be neglected and indeed must explicitly be accounted for.

Notice that if h_{eff} were very large (i.e., if Bi $\gg$ 1, corresponding to very rapid quenching by ΔT), the surface thermal stress would be

$$\sigma_{\max} = \frac{\alpha E \Delta T}{1 - \upsilon} \quad (12)$$

with ΔT representing the temperature drop (here 180°C), α the coefficient of thermal expansion, and E the Young's modulus. This estimate would give a stress of about 150 MPa for either BK7 or LHG8, i.e., a stress significantly higher than the strength of the glass (see Table 119.II). The fact, however, that the applicable Biot number Bi is of the order of 1 means that such estimates of stress as in Eq. (12) are not applicable and stresses must be explicitly computed.

Figure 119.31 shows the stress distribution in LHG8 cooled at the rate τ = 4 h. The long and intermediate edges of the plate were the most highly stressed. Figure 119.32 compares directly the evolution of temperature and stress at the center of the long edge for a plate of LHG8 and a plate of BK7. Strong size effects (i.e., increasing stresses with increasing plate thickness) and rate effects (i.e., stresses increasing with more-rapid cooling), from extensive stress calculations by finite element methods, are shown for LHG8 in Fig. 119.33.

We will next determine how a surface flaw in the most heavily stressed area (the center of the long edges) will grow as the temperature and stress evolve at that point. To examine

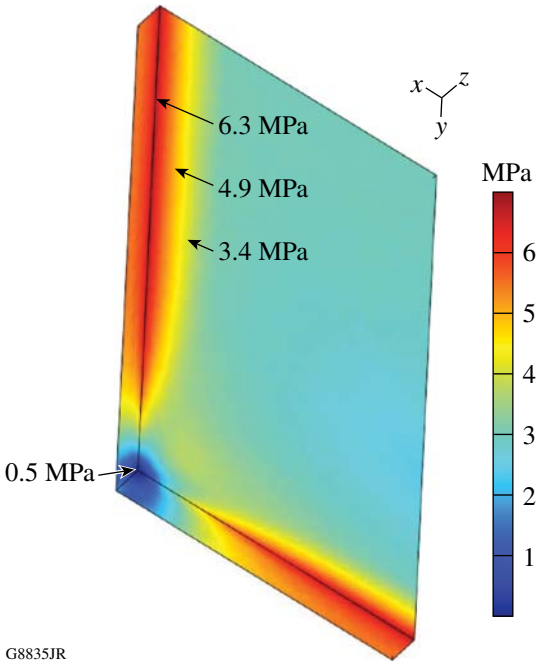

Figure 119.31
Thermal stress distribution at time $t = 8000$ s (about 2.2 h) in a 40-mm-thick LHG8 plate. Only 1/8 of the plate is shown. The plot shows the maximum principal stress, at a time when the thermal stress at the edge was close to maximum. The temperature relaxation constant $\tau = 4$ h. The long edges at $x = \pm 200$ mm, $y,z = \pm 20$ mm and intermediate edges at $x,y = \pm 400$ mm, $z = \pm 20$ mm were in a state of tension of magnitude 6.9 MPa. The plate's long edges and intermediate edges were similarly stressed and the stresses at these locations were the highest.

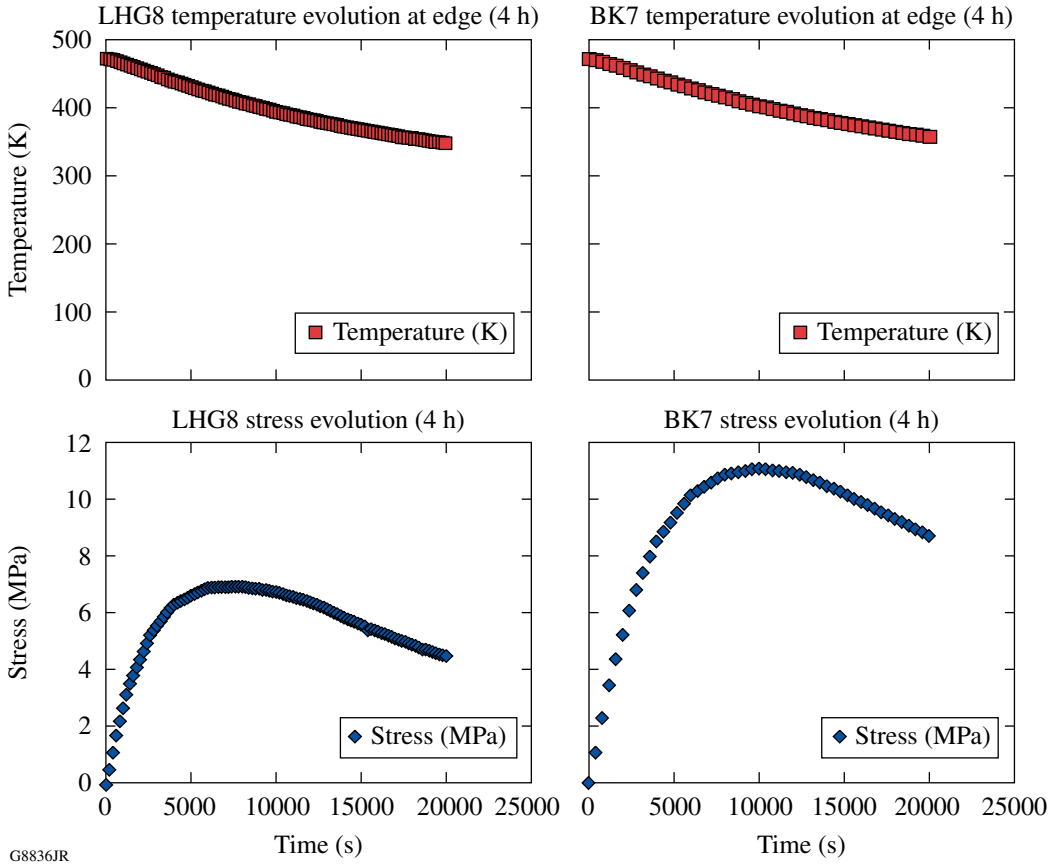

Figure 119.32
The evolution of temperature at the center of the long edge and the stress at the same point for plates of LHG8 (40 mm thick) and BK7 (80 mm thick). In both cases, the time constant for the oven temperature decay was $\tau = 4$ h.

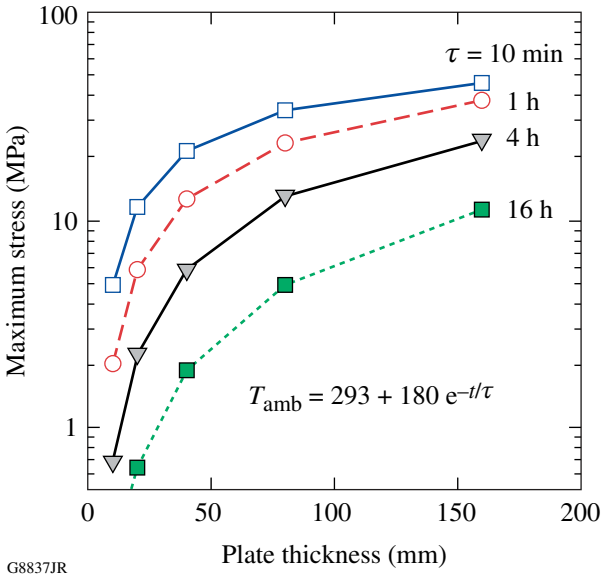

Figure 119.33
The maximum thermal stress (occurring at the center of the long plate edges) depends on the plate thickness and the rate at which the ambient temperature decays. These results are for the case of LHG8 glass plates. Thicker plates lead to larger stresses, as do more-rapid temperature cooling rates.

crack growth we need two auxiliary results: first, the depth of the initial flaw in the glass long edge (a figure to be estimated from the abrasive size used to finish that edge); second, a way of describing crack growth, from that initial crack depth value, as temperature and stress evolve with time.

It is important here to keep distinct the terminology of the various types of cracks resulting from finishing the plate surfaces. By subsurface damage (SSD) we mean the average flaw depth, a quantity that can be estimated from the abrasive used to finish that edge or from the peak-to-valley roughness at that point. This is different from the deepest flaw size $\langle c \rangle_{\max}$, which will control the strength at that point.

We have shown in previous work on glasses and crystals[17] that the subsurface damage can be estimated from the abrasive used to finish a surface by

$$\text{SSD} \sim 2 \times (\text{abrasive size}). \tag{13}$$

On the other hand, Suratwala *et al.*[18] have shown that the maximum flaw depth in fused silica is about 8× the average flaw depth:

$$\langle c \rangle_{\max} \sim 8 \langle c \rangle_{\text{av}}. \tag{14}$$

By identifying the average crack depth $\langle c \rangle_{\text{av}}$ with the subsurface damage SSD, we arrive at

$$\langle c \rangle_{\max} \sim 16\times (\text{abrasive size}). \tag{15}$$

For example, when finishing with 15-μm abrasives, one would expect a 240-μm flaw depth into the glass surface.

Notice here that the relation between average and deepest flaw size in Eq. (14) was measured[18] for the case of fused silica and its applicability to LHG8 and BK7 is not known. On the other hand, these estimates are for finishing flat surfaces. Given the fact that the area most heavily stressed is the edge of the plate (i.e., the intersection of two flat surfaces), it is again not entirely clear how to extend Eqs. (13)–(15) to our case. In any case, we must keep these caveats in mind while estimating the deepest flaw at the edge by Eq. (15).

Cracking in LHG8 Versus BK7

For fracture in radiatively cooled BK7 and LHG8 plates, we adopted several different approaches. In the strength approach, fracture was taken to occur when the applied stress σ_{app} reached the fracture strength of the glass σ_{F}. Therefore, for safe operation, we required

$$\sigma_{\text{app}} < \sigma_{\text{F}} \Rightarrow \text{safe}. \tag{16}$$

For a typical glass, the figure of merit for strength is about 50 MPa. As shown in Table 119.II, the strength of LHG8 is 10 MPa, while the strength of BK7 is 20 MPa. The applied stresses are shown in Fig. 119.32. For LHG8 the maximum stress is 7 MPa, while for BK7 it is 11 MPa. The conclusion is that, based on the strength approach, both LHG8 and BK7 are safe under these cooling conditions.

The main drawback of this approach is that the strength of a glass surface is not a well-described quantity. This drawback is addressed by using the fracture toughness approach.

In the fracture toughness approach, cracking will occur when the applied stress intensity factor K_{app} reaches the material's fracture toughness for a given flaw size. The applied stress intensity is given by Eq. (3). Therefore, for safe operation, we require

$$K_{\text{app}} = \Omega\, \sigma_{\text{app}} \sqrt{(\pi a)} < K_{\text{c}}, \quad \text{or } a < \frac{1}{\pi}\left(\frac{K_{\text{c}}}{\Omega\, \sigma_{\text{app}}}\right)^2. \tag{17}$$

For a quarter circular crack along an edge, $\Omega = 0.80$ (Ref. 15). Using $K_c = 0.43$ to 0.51 MPa$\sqrt{\text{m}}$ for LHG8 and $\sigma_{app} = 7$ MPa (from Fig. 119.32), we conclude that any flaw size more shallow than 1.9 to 2.7 mm is safe. Repeating for BK7 with $\sigma_{app} = 11$ MPa from Fig. 119.32, we find that any flaw size $a < 2.8$ mm is safe.

The drawback of the fracture toughness approach is that it assumes that the fracture toughness is a property that is independent of temperature.

For the slow crack growth approach, crack growth evolves according to

$$\frac{da}{dt} = F\left\{K_{app}\left[a(t)\right], T(t)\right\}, \tag{18}$$

$$K_{app}(t) = \Omega\, \sigma_{app}(t)\sqrt{\pi a(t)}, \tag{19}$$

where the function F is given by Eq. (1) or (4), and the stress $\sigma_{app}(t)$ and temperature $T(t)$ are shown in Fig. 119.32.

The data for LHG8 were modeled with the following parameters (see **Material Properties**, p. 145):

$$\begin{aligned} v_0 &= 7.3 \times 10^6 \text{ m/s}, \\ b &= 0.48 \text{ m}^{5/2}/\text{mol}, \\ Q_I &= 239 \text{ kJ/mol} \end{aligned} \tag{20}$$

(corresponding to LHG8 with higher OH concentration and, therefore, greater propensity for cracking). It is also important here to note that although the fit in Eq. (2) is for any pressure and the pressure in the oven is "vacuum," we have used the slowest experimental data reported,[14] i.e., we have taken $p_{H_2O} = 2$ mmHg.

For the case of BK7, we repeat the procedure for F given by Eq. (4) with

$$\begin{aligned} v_0 &= 2.4 \times 10^4 \text{ m/s}, \\ b &= 0.21 \text{ m}^{5/2}/\text{mol}, \\ Q_I &= 227.5 \text{ kJ/mol}. \end{aligned} \tag{21}$$

In both cases, the crack growth rate depends on the depth of the initial flaw size. If the initial crack depth is too deep, the crack will grow catastrophically at some time, leading to a complete fracture of the plate. We have numerically determined an initial flaw size that is just below this critical condition.

Figure 119.34 shows the critical growth condition for LHG8. The initial crack size was about 970 μm. Any crack size deeper than this will lead to catastrophic failure of the plate. It is seen that crack growth has three regions: For early times, there is little growth because the thermal stress is low. For very long times, crack growth is also low because the temperature is low. For intermediate times, however, crack growth is appreciable because both stress and temperature are sufficiently high. For the case of LHG8, the final crack size will be about 1200 μm, but the plate will not fail catastrophically.

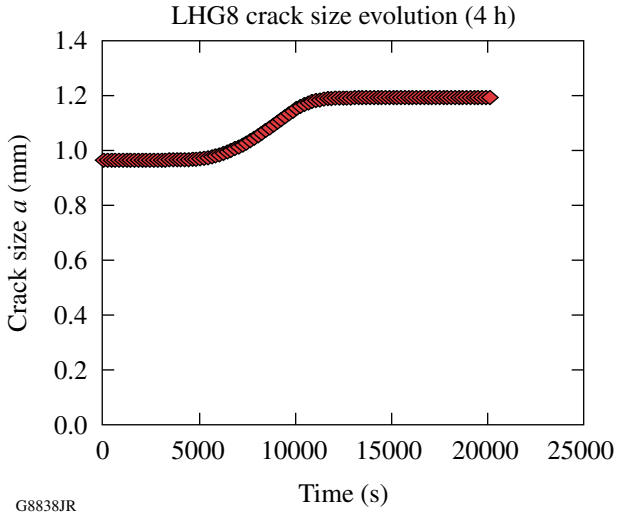

Figure 119.34
Crack growth in the center of the long edge of a 40-mm-thick LHG8 plate. The initial flaw size was 970 μm. Any flaw size deeper than this will lead to catastrophic failure.

A similar analysis for the BK7 plate leads to the conclusion that for BK7 the critical initial flaw depth was 1650 μm.

The predicted crack growth rate for LHG8 is shown in Fig. 119.35. Notice that there is an initial incubation period (temperature was high but stresses were low) and a final period at which crack growth stopped (the temperature was too low). The crack growth rate was largest, about 50 to 60 nm/s, for intermediate times where both temperature and stresses were significant; indeed, this was slow crack growth.

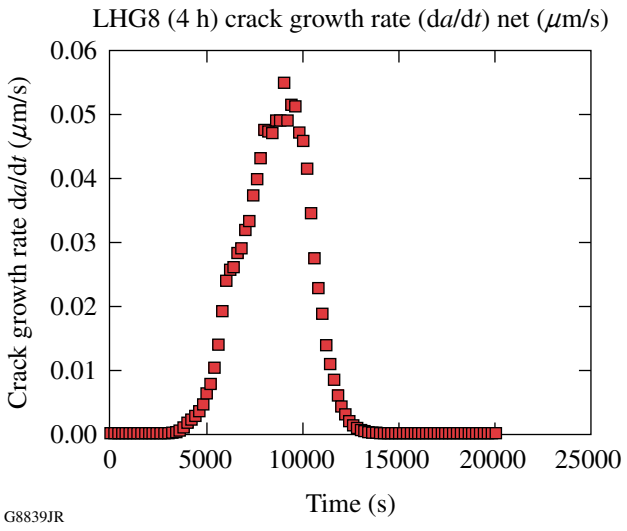

Figure 119.35
Predicted crack growth rate at the midpoint of the long edge of a 40-mm-thick LHG8 plate. The initial flaw size was 970 μm. Any flaw size deeper than this will lead to catastrophic failure.

We observe that although BK7, being twice as thick as LHG8, has higher thermal stresses, it has slower crack growth behavior and can tolerate cracks up to 1650 μm along the center of its long edge. LHG8 can tolerate cracks only up to 970 μm.

The slow crack growth approach incorporates crack growth as a function of temperature and applied stress; in other words, the material properties' dependence on temperature.

Conclusions

Several conclusions may be drawn from our work. First, 40-mm-thick LHG8 plates are inherently weaker than 80-mm-thick BK7 plates. This is a non-obvious conclusion because, in general, thicker plates are subjected to higher stresses.

Second, for both LHG8 and BK7, the most adversely stressed areas are the midpoints of the long edges, and there are strong size and rate effects in the buildup of thermal stress during radiative cooling. If all edges have similar crack distributions following finishing, the midpoints of these long edges would then be critical areas of crack growth because they are the most highly stressed.

The third conclusion concerns the choice of the fracture approach. The strength approach is inadequate because strength of a glass surface, let alone of a glass edge, is a parameter that depends on many finishing parameters so that it can hardly be seen as a material property. Even if one could identify a strength value, the case study in the previous section shows that the strength approach would predict that both the LHG8 and BK7 plates would be safe. If anything, the fracture toughness and slow crack growth approaches show that this is not the case.

The fracture toughness approach is a "liberal" criterion, predicting that the worst allowable flaw size in LHG8 would be in the range of 1.9 to 2.7 mm and for BK7 about 2.8 mm.

The slow crack growth criterion is more conservative. It predicts that for LHG8 the worst allowable initial flaw is 0.97 mm deep, while for BK7 it is 1.65 mm.

ACKNOWLEDGMENT

This work was supported by the U.S. Department of Energy Office of Inertial Confinement Fusion under Cooperative Agreement No. DE-FC52-08NA28302, the University of Rochester, and the New York State Energy Research and Development Authority. The support of DOE does not constitute an endorsement by DOE of the views expressed in this article.

REFERENCES

1. W. D. Kingery, J. Am. Ceram. Soc. **38**, 3 (1955).
2. W. D. Kingery, H. K. Bowen, and D. R. Uhlmann, *Introduction to Ceramics*, 2nd ed., Wiley Series on the Science and Technology of Materials (Wiley, New York, 1976), Secs. 16.1–16.3.
3. D. P. H. Hasselman, Ceram. Bull. **49**, 1033 (1970).
4. H. Wang and R. N. Singh, Int. Mater. Rev. **39**, 228 (1994).
5. D. P. H. Hasselman, J. Am. Ceram. Soc. **52**, 600 (2006).
6. J. P. Singh, J. R. Thomas, and D. P. H. Hasselman, J. Am. Ceram. Soc. **63**, 140 (2006).
7. H. Hencke, J. R. Thomas Jr., and D. P. H. Hasselman, J. Am. Ceram. Soc. **67**, 393 (2006).
8. A. G. Tomba-Martinez and A. L. Cavalieri, J. Am. Ceram. Soc. **85**, 921 (2002).
9. A. G. Tomba-Martinez and A. L. Cavalieri, J. Eur. Ceram. Soc. **21**, 1205 (2001).
10. O. Peitel and E. D. Zanotto, J. Non-Cryst. Solids **247**, 39 (1999).
11. J. H. Campbell and T. I. Suratwala, J. Non-Cryst. Solids **263 & 264**, 318 (2000).
12. J. E. DeGroote, A. E. Marino, J. P. Wilson, A. L. Bishop, J. C. Lambropoulos, and S. D. Jacobs, Appl. Opt. **46**, 7927 (2007).
13. T. I. Suratwala *et al.*, J. Non-Cryst. Solids **263 & 264**, 213 (2000).

14. S. M. Wiederhorn and D. E. Roberts, Institute for Materials Research, National Bureau of Standards, Washington, DC, NBS Report 10892, NASA PR 1-168-022, T-5330A (1972).

15. J. C. Lambropoulos, H. Liu, and Y. Wu, "Thermal Shock and Post-Quench Strength of Lapped Borosilicate Optical Glass," to be published in the Journal of Non-Crystalline Solids. See also: Y. Zhang, Y. Wu, H. Liu, and J. C. Lambropoulos, in *Optical Manufacturing and Testing VII*, edited by J. H. Burge, O. W. Faehnle, and R. Williamson (SPIE, Bellingham, WA, 2007), Vol. 6671, p. 66710H.

16. COMSOL® and COMSOL Multiphysics® are registered trademarks of COMSOL AB, Tegnérgatan 23, SE-111 40 Stockholm, Sweden.

17. J. A. Randi, J. C. Lambropoulos, and S. D. Jacobs, Appl. Opt. **44**, 2241 (2005).

18. T. Suratwala *et al*., J. Non-Cryst. Solids **352**, 5601 (2006), see p. 5615, Fig. 15.

Finite Element Simulation of Metal–Semiconductor–Metal Photodetector

Introduction

Low-temperature–grown GaAs (LT-GaAs), deposited by molecular beam epitaxy, has been known for its ultrashort, subpicosecond photocarrier lifetime and relatively high carrier mobility. Therefore, in recent years LT-GaAs has been the material of choice for the fabrication of photonic devices such as photoconductive switches,[1,2] both of the metal–semiconductor–metal (MSM)[3] and freestanding types,[4] for the generation of subpicosecond electrical pulses for ultrafast device characterization,[5] THz time-domain spectroscopy,[6] antennas for the generation and detection of THz radiation,[7] as well as for optical photomixers.[8,9]

Much effort has gone into achieving high efficiency for LT-GaAs material and the design of optimal geometries for the device structures; however, further performance improvement of LT-GaAs–based photonic devices is expected by optimizing the device contacts. Historically, LT-GaAs MSM's have been constructed with electrodes consisting of surface-contact metallization such as, e.g., Ni-Au, Ti-Au, or Ti-Pd-Au.[10] For decades the properties of metal contacts to III–V semiconductors have been intensively studied.[11,12] From these studies it is well known that a contact metallization that creates Schottky contacts on conventional *n*-doped GaAs shows ohmic behavior on LT-GaAs, even without annealing.[10] The annealing of contacts to LT-GaAs is restricted to temperatures below 600°C since higher temperatures lead to a drastic change in the properties of the LT-GaAs material itself. The speed of response for the ohmic-type MSM photodetector is generally limited by the carrier lifetime, which in the case of LT-GaAs is so short (~150 fs) that the device capacitance sets the practical limit. Unfortunately, the ultrashort carrier lifetime translates into relatively low mobility of the LT-GaAs material, resulting in low-efficiency LT-GaAs devices, as compared to other photodetectors, such as *p-i-n* diodes.[13] Recently, however, MSM devices with alloyed[12,14] and recessed[9,15] electrodes have been found to exhibit improved performance through optimization of the device contacts. Reference 14 reported a twofold improvement in efficiency using alloyed contacts based on Au-Ge eutectic, and Ref. 15 reported a 25% increase in sensitivity using recessed surface contacts.

This article presents a finite element model to analyze the photoresponse of two types of LT-GaAs MSM's, both of the same device geometry, but one with non-alloyed surface contacts and the other with alloyed contacts. Based on experimental work,[14] the simulated photodetectors consist of interdigitated conductors, patterned on a 1.5-μm-thick LT-GaAs layer, grown by molecular beam epitaxy at 250°C, followed by *in-situ* isothermal annealing at 600°C. We can, therefore, directly correlate our simulations with the experimental results and understand the physical reasons for the improved photoresponse efficiency of the alloyed-contact LT-GaAs MSM's without sacrificing the response times. We demonstrate that indeed the latter devices have better-than-twice the sensitivity of the surface-contact structures and better-than-50% improvement in response time. We further use our model to propose the configuration of optimized devices.

Finite Element Model

The finite element simulations presented here were created with the COMSOL Multiphysics® Finite Element Analysis (FEA) software package[16] using the generalized electrostatics mode. In this mode, the equation of continuity is combined with Gauss's law, and the partial differential equation to be solved is

$$-\nabla \cdot \left[\left(\sigma + \varepsilon_0 \varepsilon_r / T\right) \nabla V - \mathbf{J}^{\mathrm{e}}\right] = \rho_0 / T, \qquad (1)$$

where σ and $\varepsilon_r \varepsilon_0$ are the material's conductivity and permittivity, respectively, V is the electric potential, $\mathbf{J}^{\mathrm{e}}$ is an externally sourced current density, ρ_0 is the given space-charge density at $t = 0$, and T is a time constant chosen to be large relative to the maximum charge relaxation time of the system. For the simulations presented here, $\mathbf{J}^{\mathrm{e}}$ and ρ_0 are set to zero and T was chosen to be 10^{-2} s. Increasing T above 10^{-2} s had no effect on the results; making it too large, however, could result in an ill-conditioned FEA formulation.

The model geometry is a two-dimensional cross section of one of the photoconductive LT-GaAs channels plus the electrodes. The results of the simulation are given per meter, and the result is multiplied by the overall length of the channel, which

is 147 μm. Figure 119.36 shows a schematic of the MSM top view and cross section used for simulation. The model boundary condition is electrical insulation everywhere, except for the small spans, where the electrode intersects the boundary and the condition is a fixed electrical potential. The actual fabricated device[14] had an area of 400 μm^2 and an electrode finger width and spacing of 1 μm and 1.5 μm, respectively. The alloyed-electrode MSM consisted of a Ni-Au/Ge-Ni-Au layer stack with 5-, 90-, 25-, and 50-nm thickness, respectively, alloyed at 420°C for 90 s. The surface-contact device had a Ni-Au layer with a thickness of 10 to 160 nm.

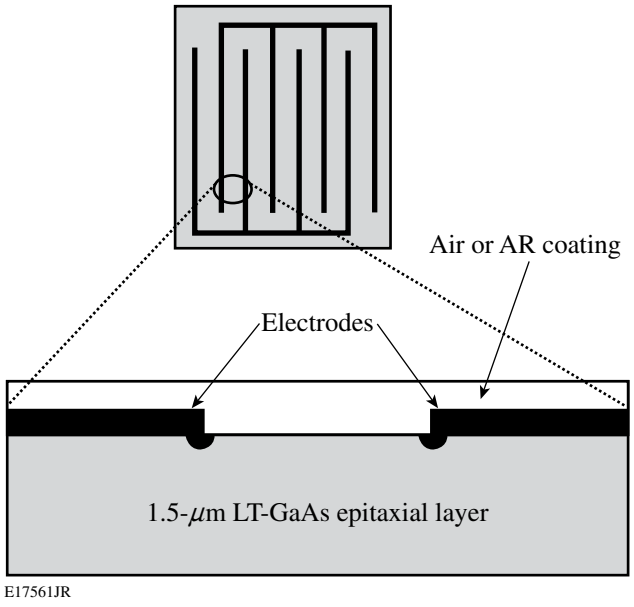

Figure 119.36
Schematic top view of an MSM device and side view of one photoconductive channel, with electrodes on each side.

Figures 119.37 and 119.38 show arrow plots of the electric field and current density, created with COMSOL Multiphysics®. The simulation results in Fig. 119.37 are for the alloyed-electrode device, illuminated by 850-nm-wavelength light, with a nominal alloy depth of L = 200 nm. The simulation results in Fig. 119.38 are for the surface-contact device, with identical illumination conditions. The length of the arrows is scaled according to the magnitude of the quantity they represent. We note in Fig. 119.37 that for the alloyed device, the electric field is uniformly distributed in the photoconductive region, and the current density in this region decays as does the intensity of the incident light. On the other hand, the surface contact device in Fig. 119.38 shows a very different electric field distribution, and the current is channeled entirely through the corner insets of the electrodes.

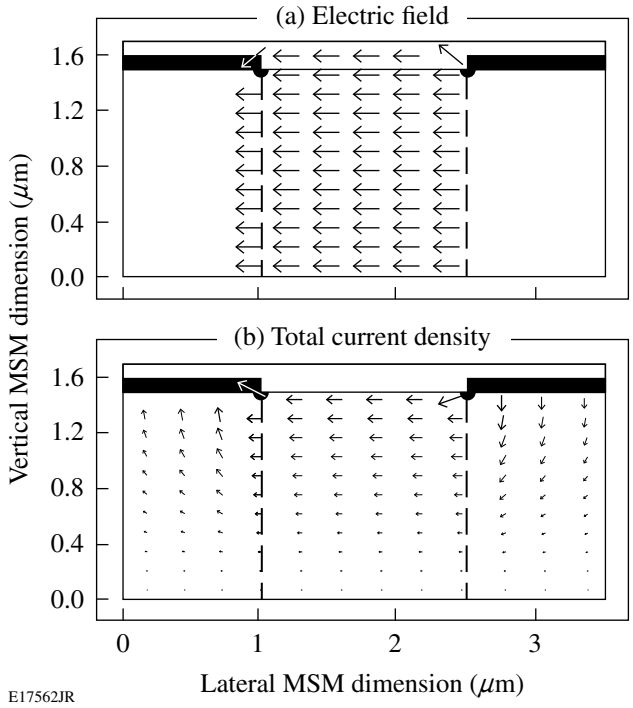

Figure 119.37
Arrow plots of the (a) electric field and (b) current density for the alloyed-contact device with L = 200 nm. These plots were created using COMSOL Multiphysics®.[16]

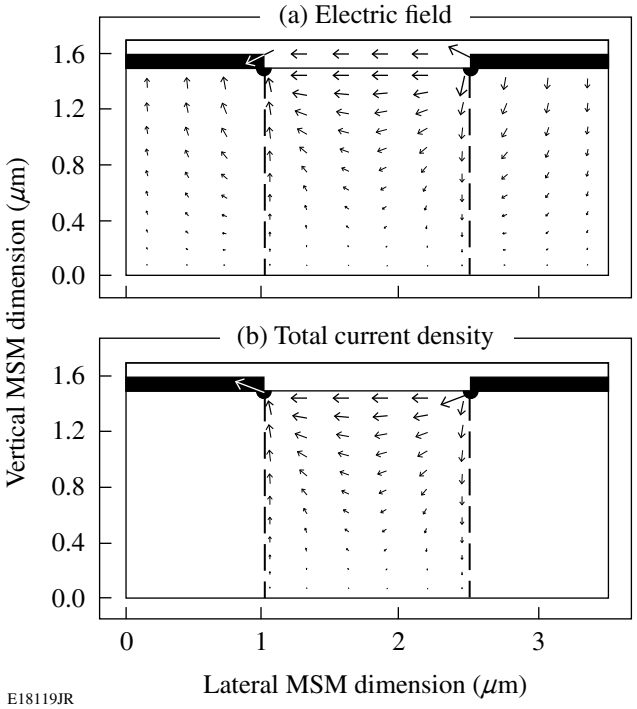

Figure 119.38
Arrow plots of the (a) electric field and (b) current density for the surface-contact device. These plots were created using COMSOL Multiphysics®.[16]

For the FEA model, each device was divided into five subdomains, consisting of the two electrodes, the photoconductive region, and the two LT-GaAs regions under the electrodes. For simplicity, the two electrodes were assigned a conductivity $\sigma = 45.6 \times 10^6$ S/m, typical for Au. The conductivity profile of the photoconductive region was calculated based on illumination with 160 μW of continuous-wave light, consistent with the experimental setup in Ref. 14. The transmission coefficient was calculated as 43%, based on the LT-GaAs refractive index of 3.64 at 850 nm (Ref. 17), and the internal quantum efficiency (QE) was taken as 1. These factors, in addition to 40% loss of input power as a result of the reflectivity of the metal electrodes, give $G = 1.77 \times 10^{14}$ s^{-1}, the overall (volume) carrier-generation rate. By assuming that the carrier generation decays in the same manner as incident 850-nm light with a penetration depth l = 1 μm, and integrating over the photoconductive volume, the carrier generation at the surface was calculated to be $G_S = 9.47 \times 10^{23}$ (s • cm^3)$^{-1}$.

To relate G_S to σ, it is necessary to compute the resulting steady-state carrier density. This was done by setting the generation equal to the Shockley–Read–Hall recombination rate, simplified by assuming that the recombination centers are located at the bandgap. The electron and hole concentrations at the surface, n_s and p_s, respectively, can then be calculated as

$$n_s = p_s = n_i + 2 \cdot G_S \cdot \tau, \tag{2}$$

where n_i is the intrinsic GaAs carrier concentration and τ is the carrier lifetime. Taking for LT-GaAs at 300 K, $n_i = 1.8 \times 10^6$ cm^{-3}, τ = 150 fs (Ref. 5), and the mobility for photogenerated carriers to be $\mu \approx 200$ cm^2/(V • s) (Ref. 1), we may then compute the surface conductivity $\sigma_s = 2n_s\mu = 1.8$ mS/m, and, subsequently, the conductivity profile

$$\sigma = \sigma_s \cdot \exp\left(\frac{-z}{l}\right), \tag{3}$$

where z is the distance from the LT-GaAs surface.

So far everything said about our MSM FEA model applies to both the alloyed and non-alloyed devices. The difference between the two is the conductivity profile under the contacts. In the case of the non-alloyed device, the conductivity of the region under the contact is simply that of LT-GaAs, which is essentially an insulator. In the case of the alloyed device, a Ni-AuGe-Ni-Au layer stack forms the electrode. Subsequent alloying at 420°C for 90 s causes Ge atoms to migrate into the LT-GaAs, with an expected penetration depth of L = 200 nm (Ref. 18). As a result, the conductivity at the interface between the contact metallization and the alloyed LT-GaAs is that of Ge and decays exponentially to the conductivity of LT-GaAs under the contact. The σ profile under the alloyed contact is therefore

$$\sigma_{ac} = (\sigma_{Ge} - \sigma_{LT}) \cdot \exp\left(\frac{-z}{L}\right) + \sigma_{LT}, \tag{4}$$

where σ_{Ge} = 2.2 S/m and $\sigma_{LT} = 1.15 \times 10^{-8}$ S/m are the conductivities of Ge and LT-GaAs, respectively.

One additional feature that requires some explanation is the semicircular inset at the inside corner of each electrode shown in Fig. 119.36. In the case of the alloyed-contact MSM, this feature has no effect on results; it is, however, essential for modeling the surface-electrode device since without it there would be no lateral path for current. Figure 119.36 is not to scale and the corner insets are exaggerated for clarity. The actual radius used in our modeling was only 50 nm, based on the simple estimation that the carriers generated near the edge of the surface electrode may drift/diffuse into the insulating region toward the electrode on the scale of the carrier mean free path, equal in our case to ~66 nm, for a Fermi velocity of 4.4×10^5 m/s (Ref. 12) and τ = 150 fs. A change of ±50% in this radius did not impact results of the model.

Results

1. Responsivity

For the alloyed-contact device, the responsivity predicted by the model was 8.6×10^{-4} A/W, while the actual measured value in Ref. 14 was 13.7×10^{-4} A/W. For the surface-electrode MSM, the corresponding simulation and experimental values were 3.7×10^{-4} A/W and 6.2×10^{-4} A/W, respectively. Considering the approximations involved, the results of the FEA model can be considered reasonably close to measured. The responsivity is dependent on μ, quantum efficiency, transmission coefficient of LT-GaAs, alloy depth, and the contact resistance. If we, for example, used a carrier mobility of only $\mu \approx 320$ cm^2/(V • s), instead of 200 cm^2/(V • s), we would get full agreement between our model and the experiment. We note here that although the relatively low values of μ for LT-GaAs have been well documented,[8] some sources have reported μ's as high as 2000 cm^2/(V • s) (Refs. 19 and 20), depending on the sample processing. For QE the range of numbers in the literature spans from 1 (Ref. 21) to 0.07 (Ref. 5). We assumed the ideal case of QE = 1. Our transmission coefficient was calculated to be 43%, based on the refractive index of GaAs at

850 nm, and, finally, the depth of alloying under the contacts was taken to be 200 nm based on the expected (but not measured) depth stated in Ref. 14.

In view of the above, the responsivity ratio of MSM's with alloyed to non-alloyed contacts is of particular interest. The FEA model yielded a ratio of 2.3, while the experimental value in Ref. 14 was 2.2. Therefore, we may conclude that our model does a good job of predicting the improvement in responsivity obtained using photodetectors with alloyed contacts.

2. Capacitance and Transient Response

Typically, photoconductive devices turn on much faster than they turn off since the rising part of the photoresponse limits how fast optical energy is delivered to the photocarriers and simply corresponds to the integral of the optical-pulse intensity. The turn-off time, on the other hand, depends on the mechanism of carrier sweep (Schottky type) or on the carrier lifetime in the photoconductive region. In the case of LT-GaAs devices exhibiting ohmic contacts, the latter is true; however, since τ is in the femtosecond range, the actual device turn-off time is limited by stored charge and the equivalent lumped-element resistive-capacitive (RC) time constant.

Table 119.IV shows the capacitance of the alloyed- and surface-electrode devices in both the light-ON and light-OFF states, as predicted by the FEA model. The higher capacitance of the alloyed-contact MSM is expected from the device configuration and suggests that its photoresponse signal should be slower. However, the photoresponse measurements performed in Ref. 14 actually indicate that alloyed devices exhibit somewhat faster turn-offs, while in both cases, the turn-on time is about the same. The photoresponse transients in Ref. 14 show a turn-off time constant of the alloyed device to be 1.8 ps and 2.8 ps for the non-alloyed structure. In terms of our model, an improvement of the turn-off time in the alloyed-electrode MSM's can be understood if one considers the accumulated charge at the boundary between the LT-GaAs photoconductive region and either the alloyed or non-alloyed region under the electrode surface. In the ON state, both devices have a significant charge, accumulated at this boundary. In the case of the surface-contact MSM, however, this boundary effectively goes away when the device turns off, leaving the charge to dissipate through the volume of the very highly resistive LT-GaAs. On the other hand, in the alloyed-contact MSM case, the relatively high conductance of the alloyed-contact volume makes possible a much more efficient discharge of the equivalent capacitor. Based on the ratio of sensitivities of the two devices, the effective ON-state resistance of the alloyed device is 2.2× lower than that of the non-alloyed device. Thus, including the capacitances listed in Table 119.IV, the ratio of the corresponding RC time constants is 1.47 and should be the same as the ratio of the fall times of the respective photoresponse transients. Note that the experimentally measured ratio in Ref. 14 is 1.56, in excellent agreement with the prediction of our model. As a result, despite the larger geometrical capacitance, the alloyed-contact MSM is actually faster than the surface-electrode structure, as indeed was experimentally observed.

Table 1119.IV: MSM device capacitance in the OFF and ON states, with or without an AR coating.

	Surface contact	Alloyed contact
OFF, no AR	10.2 (fF)	17.0 (fF)
OFF, with AR	10.7 (fF)	17.5 (fF)
ON, no AR	10.4 (fF)	15.6 (fF)
ON, with AR	10.5 (fF)	16.0 (fF)

3. Device Optimization

The results of the FEA model are well correlated to experimental values; therefore, the model may be used to predict the effect of various parameters on MSM photoresponse performance. In this section, we look at how such technological parameters as the depth of the alloyed contacts, electrode spacing, or additional antireflection (AR) coating, influence the device's performance.

Figure 119.39 shows the responsivity as a function of alloy penetration depth L, which is the exponential spatial decay constant of σ under the alloyed contact [see Eq. (4)]. As the L

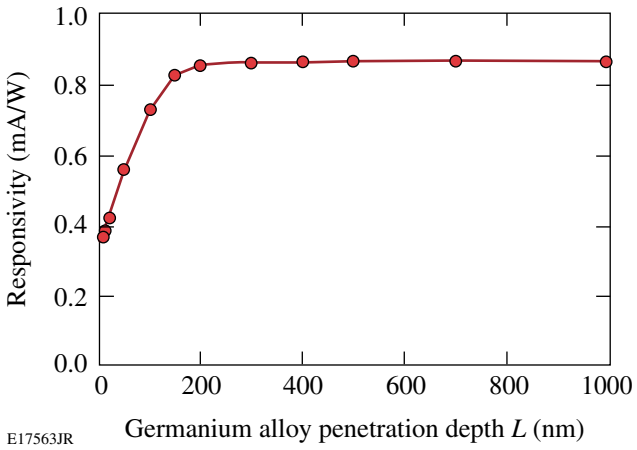

Figure 119.39
Responsivity versus the alloy penetration depth for an alloyed-contact MSM.

value decreases to zero, approximating the surface-type contact, the point where the responsivity curve intersects the y axis approaches the responsivity of the surface-electrode MSM. We observe in Fig. 119.39 that for $L > 200$ nm the curve flattens, so increasing L beyond 200 nm results in very little improvement. The latter is fully understandable looking at Fig. 119.37(a) and noting that at $L = 200$ nm the electric field is already fairly uniform down through the photoconductive region. The electric potential between the boundaries of the photoconductive region is also uniform and equal to the applied electrode potential, so current is strictly limited by the photoconductance.

Figure 119.40 shows the responsivity as a function of electrode spacing, for both an alloyed- and a surface-contact MSM. For the alloyed device, the relationship can be easily and precisely explained because the resistance of the photoconductive channel is proportional to its length. Therefore, the responsivity is proportional to current and, consequently, inversely proportional to the channel length. For the surface-electrode MSM, the relationship is not as simple due to the concentration of current at the corner insets of the electrodes, as seen in Fig. 119.38. The corner insert will come into play only when the spacing approximately equals the radius. As the spacing decreases for the surface-electrode device, the electric field gets pulled toward the surface. Therefore, carriers generated far below the surface do not contribute to the sensitivity.

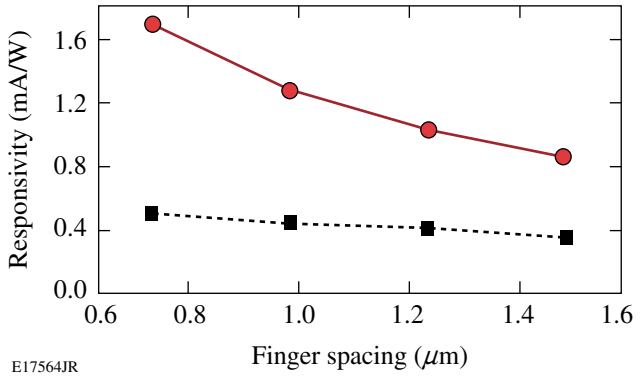

Figure 119.40
Responsivity versus the electrode finger spacing for an alloyed-contact (solid line) and surface-contact (dashed) MSM.

Finally, our FEA model predicts that an AR coating should obviously improve the device responsivity by decreasing the amount of reflected light, but, at the same time, the additional dielectric material deposited on top of the photodetector increases its capacitance. We observe a typical trade-off between the responsivity and speed. However, in the case of the alloyed-contact structures our simulations show (see Table 119.IV) that the actual increase in the capacitance is less than 5%. As a result, a well-designed AR coating in such structures clearly leads to an overall improvement in the photodetector's performance by increasing the responsivity without significant degradation in speed.

Conclusion

A simple FEA model, using the COMSOL Multiphysics® software package,[16] has been developed to simulate the photoresponse of the MSM photodetector. The two experimentally most-viable cases, namely devices with either alloyed- or non-alloyed-surface contacts, have been studied and have demonstrated that in both cases, both the photodetector responsivity and the time-domain response can be very accurately simulated. This approach also allows one to optimize the MSM design, indicating that deposition on the photodetector surface of an AR coating, while substantially increasing its responsivity, only marginally affects the photoresponse time constant.

ACKNOWLEDGMENT

This work is supported by the NSF NIRT Grant No. ECS-0609140. Additional support was provided by the U.S. Department of Energy Office of Inertial Confinement Fusion under Cooperative Agreement No. DE-FC52-08NA28302, the University of Rochester, and the New York State Energy Research and Development Authority. The support of DOE does not constitute an endorsement by DOE of the views expressed in this article.

REFERENCES

1. F. W. Smith, in *Low Temperature (LT) GaAs and Related Materials*, edited by G. L. Witt *et al.*, Mat. Res. Soc. Symp. Proc. Vol. 241 (Materials Research Society, Pittsburgh, PA, 1992), pp. 3–12.
2. S. Gupta, J. F. Whitaker, and G. A. Mourou, IEEE J. Quantum Electron. **28**, 2464 (1992).
3. S. Y. Chou, Y. Liu, and W. Khalil, Appl. Phys. Lett. **61**, 819 (1992).
4. M. Marso, M. Mikulics, R. Adam, S. Wu, X. Zheng, I. Camara, F. Siebe, A. Forster, R. Gusten, P. Kordoš, and R. Sobolewski, Acta Phys. Pol. A **107**, 109 (2005).
5. X. Zheng, Y. Xu, R. Sobolewski, R. Adam, M. Mikulics, M. Siegel, and P. Kordoš, Appl. Opt. **42**, 1726 (2003).
6. S. Kono *et al.*, Appl. Phys. Lett. **77**, 4104 (2000).
7. X.-C. Zhang, J. Lumin. **66 & 67**, 488 (1996).
8. S. Verghese, K. A. McIntosh, and E. R. Brown, Appl. Phys. Lett. **71**, 2743 (1997).
9. M. Mikulics *et al.*, Appl. Phys. Lett. **88**, 041118 (2006).

10. H. Yamamoto, Z-Q. Fang, and D. C. Look, Appl. Phys. Lett. **57**, 1537 (1990).

11. N. Braslau, J. B. Gunn, and J. L. Staples, Solid State Commun. **10**, 381 (1967).

12. N. Vieweg *et al*., Opt. Express **16**, 19,695 (2008).

13. S. Collin, F. Pardo, and J.-L. Pelouard, Appl. Phys. Lett. **83**, 1521 (2003).

14. M. Mikulics, M. Marso, S. Wu, A. Fox, M. Lepsa, D. Grützmacher, R. Sobolewski, and P. Kordoš, IEEE Photon. Technol. Lett. **20**, 1054 (2008).

15. M. Mikulics, S. Wu, M. Marso, R. Adam, A. Förster, A. van der Hart, P. Kordoš, H. Lüth, and R. Sobolewski, IEEE Photonics Technol. Lett. **18**, 820 (2006).

16. COMSOL® and COMSOL Multiphysics® are registered trademarks of COMSOL AB, Tegnérgatan 23, SE-111 40 Stockholm, Sweden.

17. J. S. Blakemore, J. Appl. Phys. **53**, R123 (1982).

18. M. Ogawa, J. Appl. Phys. **51**, 406 (1980).

19. K. Xie and C. R. Wie, in *Low Temperature (LT) GaAs and Related Materials Symposium*, edited by G. L. Witt *et al*., Mat. Res. Soc. Symp. Proc. Vol. 241 (Materials Research Society, Pittsburgh, PA, 1992), pp. 33–38.

20. A. C. Warren *et al*., in *Low Temperature (LT) GaAs and Related Materials Symposium*, edited by G. L. Witt *et al*., Mat. Res. Soc. Symp. Proc. Vol. 241 (Materials Research Society, Pittsburgh, PA, 1992), pp. 15–25.

21. Electrical Properties of Gallium Arsenide, IOFFE-Physico Technical Institute, St. Petersburg 194021, Russia, http://www.ioffe.ru/SVA/NSM/Semicond/GaAs/electrical.html.

The Omega Laser Facility Users Group Workshop 29 April – 1 May 2009

Introduction

More than 100 researchers from 29 universities and laboratories and 4 countries gathered at the Laboratory for Laser Energetics (LLE) for the first Omega Laser Facility Users Group (OLUG) Workshop (see Fig. 120.1). The purpose of the three-day workshop was to facilitate communication and exchanges among individual Omega users and between users and LLE; to present ongoing and proposed research; to encourage research opportunities and collaborations that could be undertaken at the Omega Facility and in a complementary fashion at other facilities (such as LULI or the NIF); to provide an opportunity for students and postdoctoral fellows to present their research on OMEGA in an interactive, yet congenial, atmosphere; and to provide feedback to LLE from the users about ways to improve the facility and future experimental campaigns. Interactions at the workshop were spirited and lively, as can be seen in the photographs shown in this article. The names and affiliations of the 156 members of OLUG can be found at **www.lle.rochester.edu/pub/OLUG/OLUGMEMBERS.pdf**.

Invited talks on the facility and science were given during the first two mornings of the workshop. The facility talks were especially useful for those not intimately familiar with the complexities of performing experiments on OMEGA and OMEGA EP. The six overview science talks, given by leading world authorities, described the breadth and excitement of high-energy-density (HED) science undertaken on OMEGA, both present and future. The final overview talk concerned

U963JR

Figure 120.1

More than 100 researchers from around the world, from 29 universities and laboratories, attended this workshop. Workshop reports and nearly all 62 presentations can be found at **http://ouw.lle.rochester.edu**. Plans for the next OLUG Workshop to be held 28 April–1 May 2010 are well underway, with significant financial support from the National Nuclear Security Administration (NNSA) already allocated for student/postdoctoral travel expenses.

the role and importance of science to the National Nuclear Security Administration (NNSA) mission. The next section of this article contains a summary of the range of presentations; nearly all presentations can be found in their entirety at **http://ouw.lle.rochester.edu**.

Thirty-two students and postdoctoral fellows (Fig. 120.2), 27 of whom were supported by travel grants from NNSA, attended the workshop and presented 31 of the 48 contributed poster and oral presentations. The presentations ranged from target fabrication to simulating important aspects of supernovae. The presentations generated lively discussions, probing questions, and friendly suggestions. Seventeen excellent contributed presentations were made by professional scientists and academics.

U964JR

Figure 120.2
Students and postdoctoral fellows. Thirty-two students and postdoctoral fellows attended and presented 31 of the 48 contributed poster and oral presentations. Equally important, the student/postdoctoral panel wrote an outstanding report (p. 176) on how to improve the Omega Facility and on the opportunities and challenges young researchers face in implementing experiments at OMEGA and other HED facilities.

An important function of the workshop was to develop a set of recommendations and findings to guide future priorities for OMEGA. These findings were grouped into five areas: 60-beam OMEGA, OMEGA EP, General User Issues, Information Flow, and Broader Issues. These categories comprise a report provided to the Omega Laser Facility management. The original report and the management response are described in **Findings and Recommendations of the Executive Committee** (p. 168) and can be found at http://ouw.lle.rochester.edu. LLE management will use these recommendations as a guide for making decisions about OMEGA operations, priorities, and future capabilities. To cement this process, OLUG Executive Committee members and Omega management have been meeting on a bimonthly basis to assess progress toward achieving these objectives.

One highlight of the workshop was the student/postdoctoral panel that discussed their experiences at the Omega Facility and their thoughts and recommendations on facility improvements. Wide-ranging and engaging discussions resulted in the student/postdoctoral report contained in **Findings and Recommendations of the Student/Postdoctoral Panel** (p. 176) and at http://ouw.lle.rochester.edu.

The next OLUG Workshop will be held at LLE on 28 April–1 May 2010. Meetings of the Users Group and interested members of the HED community are formulating plans for this workshop and reviewing progress on implementing the **Findings and Recommendations** (p. 168) of the first workshop. These meetings were held at the IFSA Conference (8 September 2009) and are planned for the APS conference in Atlanta (3 November 2009).

The Presentations

Sixty-two talks and posters presented during the 2009 workshop focused on ongoing fast- and shock-ignition experiments; materials under extreme conditions on OMEGA and, in the near future, at the NIF; the critical role that simulations play in designing and interpreting experiments; the physics connections between the Omega Facility and the European ICF program; and present and future laboratory astrophysics experiments on OMEGA and the NIF.

The facility talks presented important details and developments on the status and performance of the Omega Facility from pulse shaping and duration to beam smoothing; the qualification process for interfacing new experiments; the existing, and soon-to-be-operating, diagnostics; and the critical role of targets, from design and procurement to full characterization, fielding, and finally shooting.

Forty-eight contributed posters and talks covered a wide spectrum of work on the Omega Facility, from target fabrication to fast-ignition experiments to basic and novel nuclear physics experiments (see http://ouw.lle.rochester.edu). Work on the opportunities for taking physics platforms developed on OMEGA to other facilities that are both larger (the NIF) and smaller (Jupiter, Trident, and LULI) was presented. The presentations, invited and contributed, formed much of the basis for discussions regarding the Findings and Recommendations and future capabilities, found in the next section (p. 168).

The following photographs (Figs. 120.3–120.21) provide a representative sampling of the workshop's talks, interactions, and spirited ambiance. A much larger collection of photographs can be found at http://ouw.lle.rochester.edu.

U965JR

Figure 120.3
Postdoctoral fellow Dr. Angelo Schiavi (Roma University) discussed, on behalf of his European colleagues, the latest theoretical developments in fast ignition. Dr. Schiavi delighted workshop attendees, not only with the clarity and depth of his presentation, but with his humorous and entertaining remarks!

U966JR

Figure 120.4
Dr. Ryan Rygg, an LLNL postdoctoral fellow, was chair of the student/postdoctoral panel (see their report herein and on http://ouw.lle.rochester.edu). Dr. Rygg is a frequent experimenter at the Omega and Jupiter facilities and is collaborating with MIT researchers on nuclear diagnostics currently being implemented at the National Ignition Facility. He is a member of Dr. Rip Collins's Shock/Materials Group (see Fig. 120.5) at LLNL.

U967JR

Figure 120.5
Probing the interiors of the planets through materials experiments on OMEGA, and soon at the NIF, was the focus of LLNL's Dr. Rip Collins's presentation. Here he describes how the inaccessible (planet interiors) becomes accessible through such laboratory experiments. Dr. Collins's gave an animated description of the challenges of compressing a tofu-like material to densities of ~100 g/cm^3 (five times the density of gold).

U968JR

Figure 120.6
Professor Peter Norreys of Rutherford-Appleton Laboratory discussed the reasons that the testing and development of fast-ignition concepts on OMEGA are so critical in preparing for and guiding the European consortium's fast-ignition experiments. Dr. Norreys is a member of the OLUG Executive Committee.


U969JR

Figure 120.7
Postdoctoral fellow Dr. Carolyn Kurantz (University of Michigan) makes decisive and unequivocal points about the subtleties and challenges of laboratory astrophysics experiments that she and colleagues have been implementing on OMEGA as part of their NLUF program, an effort led by Prof. Paul Drake. Dr. Kurantz is a member of the student/postdoctoral panel, and Prof. Drake is a member of the Executive Committee.


U970JR

Figure 120.8
During a coffee break, LLE Ph.D. student Maria Barrios (right) discusses her work and presentation on shock-compressed materials with her former professor Dr. Sharon Stephenson (Gettysburg College).


U971JR

Figure 120.9
Postdoctoral fellow Dr. Louise Willingale (University of Michigan) contemplates her response to a workshop attendee's query about aspects of her OMEGA EP experiment involving proton emissions from OMEGA EP's short-pulse beam interacting with a flat target. Dr. Willingale is a member of the student/postdoctoral panel.


U972JR

Figure 120.10
Keith Thorp, the Omega Facility Manager, presented an overview of the planning, processes, and coordination needed to conduct a successful experiment on OMEGA. Such talks gave attendees the opportunity to meet with, and hear from, some of the key individuals responsible for operating and improving the facility. Mr. Thorp is one of the many dedicated staff members involved in, and orchestrating, the day-to-day facility operations.

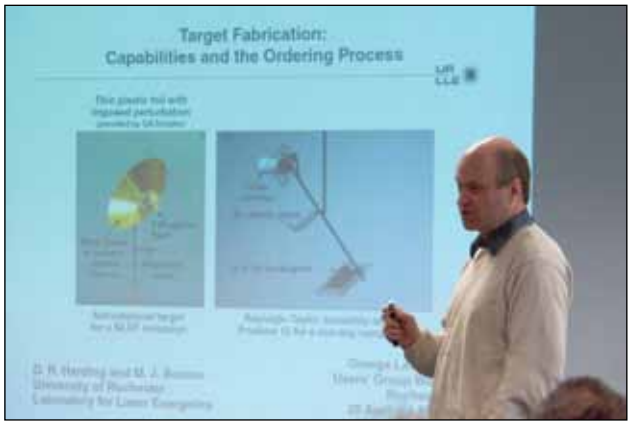

U973JR

Figure 120.11
Targets are a critical part of any experiment. Here, LLE's Dr. David Harding describes the range and complexity of targets that are designed and then meticulously assembled and characterized prior to their fielding. Each step in the process requires demanding attention to detail and design, often requiring many interactions between the experimenter and the target-manufacturing team. Most targets are manufactured at General Atomics (GA); the scope of GA's work was presented by Brian Vermillion. As the saying goes, "the targets are just as important as the laser"—a perspective that we are sure is shared by Dr. Harding.

U974JR

Figure 120.12
The crucial role that basic science, and OMEGA in particular, plays in NNSA's program was described by Dr. Chris Deeney, who heads the ICF branch of NNSA. NNSA was responsible for providing vital financial aid to 27 students and postdocs who attended the workshop.

U975JR

Figure 120.13
Spirited and lively discussions often ensued in poster and workshop breakout sessions, with the results of these discussions contained in the Reports of **Findings and Recommendations** [herein (p. 168) and at http://ouw.lle.rochester.edu]. Many of these "findings" are currently being implemented by OMEGA management, and discussions between management and the OLUG Executive Committee continue on a bimonthly basis.

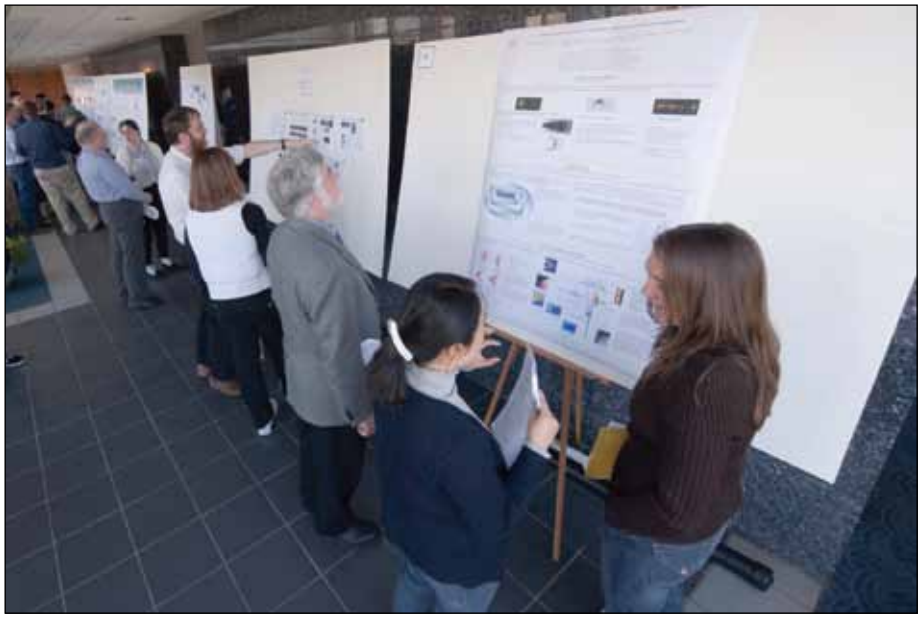
U976JR

Figure 120.14
The 62 workshop presentations, some of which are shown here during the poster session, covered a wide spectrum of cutting-edge, high-energy-density science relevant to OMEGA, the NIF, and other HED facilities.


U977JR

Figure 120.15
Here, Ph.D. student Teresa Bartel of the University of California–San Diego discusses her OMEGA EP experiments with Dr. Steve Craxton, one of LLE's theoretical physicists. Ms. Bartel's poster focused on proton beams relevant to fast ignition, one aspect of which was the exploration of proton-conversion efficiency achievable on OMEGA EP. A too-low proton-conversion efficiency would preclude this impulsive heating scheme for fast ignition. Ms. Bartel is a member of Prof. Farhat Beg's group.

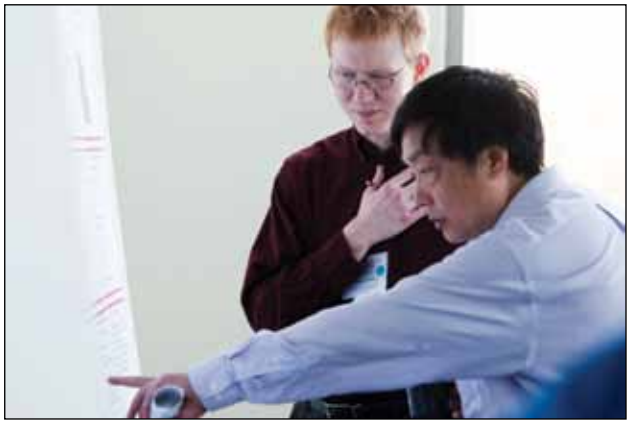
U978JR

Figure 120.16
Theoretical Ph.D. student Matt Terry of the University of Wisconsin–Madison listens intently to the query of experimentalist Dr. Chikang Li of MIT, regarding Matt's work on the stopping power of energetic particles in dense, hot plasmas. Such problems, while of basic interest to HED physics, are of special relevance to ICF where, for example, the stopping and energy deposition of alphas are crucial to the ignition instability. Matt discussed several theoretical stopping models and the differences between them. Could such differences, sometimes small, have subtle but nontrivial consequences on ignition criteria, making it either easier or more difficult to achieve ignition at the National Ignition Facility?


U979JR

Figure 120.17
At his poster about the measurements of fields associated with Rayleigh–Taylor (RT) instabilities, MIT Ph.D. student Mario Manuel talks with theoretical physicist Dr. Serge Bouget of CEA, France. Mr. Manuel's experimental investigation, conducted as part of MIT's NLUF program, utilizes monoenergetic 15- and 3-MeV protons to probe, via the Lorentz force, magnetic fields in RT experiments. Such posters, informal working groups, and frequent coffee breaks led to many opportunities for young researchers to interact and discuss their research with workers from a broad range of fields and experience within the world-wide high-energy-density physics community.


U980JR

Figure 120.18
The Omega Users Executive and Student/Postdoctoral Committees discuss details and assignments for writing the findings and recommendations of the workshop. The two committee reports and the initial management response can be found at http://ouw.lle.rochester.edu and in this document. The process of improving the Omega Laser Facility is an ongoing activity involving bimonthly meetings between the Executive Committee members and Omega management. Progress on the recommendations will be given in a satellite session at the Atlanta APS meeting (3 November 2009) and at the next OLUG Workshop (28 April–1 May 2010). An important finding of both committees was the excellence with which the Omega Laser Facility is run, offering exciting opportunities to users to perform world-class experiments.


U981JR

Figure 120.19
The French came in full force to the workshop, bringing a dashing but friendly contingent with exciting ideas and zest! Vive La France!


U982JR

Figure 120.20
A workshop banquet at the University of Rochester's Faculty Club offered an enjoyable evening for all workshop attendees.


U983JR

Figure 120.21
Our European colleagues share a light moment at the workshop banquet.

Findings and Recommendations of the Executive Committee

Executive Committee:

Richard Petrasso, Committee Chair, Massachusetts Institute of Technology
Hector Baldis, University of California–Davis
James Cobble, Los Alamos National Laboratory
Paul Drake, University of Michigan
James Knauer, LLE, University of Rochester (designated)
Roberto Mancini, University of Nevada–Reno
Peter Norreys, Rutherford Appleton Laboratory
Marilyn Schneider, Lawrence Livermore National Laboratory

1. Introduction

Extensive formal and informal discussions occurred during the workshop regarding (1) ways in which the Omega Facility could be more effective in using existing resources and (2) new capabilities or technologies that would be highly desirable. It is important to stress that there was a resounding response by the workshop attendees that the Omega Laser Facility is extremely well run and that the team operating it is both highly dedicated and very skilled.

Two workshop reports were written. The first, by the OLUG Executive Committee, was a summary of the views of the workshop attendees (108 professional scientists and engineers, academics, students, and postdocs from four countries). Its findings were grouped into five areas: 60-beam OMEGA, OMEGA EP, general user issues, information flow, and broader issues. The second report was written by the student/postdoctoral panel.

These two reports have many common issues, especially those relating to information flow and to the process of preparing for and executing campaigns in the OMEGA environment. This commonality is, in part, due to the challenging complexity, especially for new users, of the facility and its operations, even though there are myriad tools at the Omega Facility to navigate through this process. As will be obvious in the different sections of the Executive Committee report, these themes were often repeated. The management response was written to address the issues that were raised on the last day of the workshop (1 May 2009), and because sections of the Executive Report, as well as the management response, were written several days after the workshop, there is a slight mismatch between the issues of the formal Executive Report (contained herein in Secs. 2–6, pp. 168–172) and the Management Response. Because of the complexity of the issues involved and the need to iterate from recommendations to what is actually achievable from the management point of view, this report must be considered a work in progress. To that end, OLUG meets bimonthly with Omega management to discuss (1) what can be realistically achieved and (2) progress toward implementing the workshop findings and recommendations. Progress on the recommendations will be presented at the Atlanta APS meeting (3 November 2009) and at the next Omega Laser Facility Users Group Workshop (28 April–1 May 2010).

2. OMEGA (60 Beams)

The users developed a list of desired improvements to enhance the use of the 60-beam OMEGA Laser. The following information reflects both the degree of resonance across the users and the degree of importance to specific subgroups of users.

a. Delay and conflict information: A web page could be designed to provide the top 15 or so typical delays generated by decisions about how an experimental day is constructed. Examples would include the delays associated with repointing beams or moving a framing camera. This is of value to help users better develop their initial plans for shot days.

b. More options for driving the laser legs: The minimum functionality sought here is less than the ultimate one. The ultimate functionality would be the ability to drive any leg from any driver. We recognize that this is a tall order. The minimum functionality is the ability to use the smoothing by spectral dispersion (SSD) driver on one leg while using another driver on the other two legs. (This may include enabling the backlighter to drive on any two legs.) Having the capability to operate SSD and main drivers simultaneously could be quite important to x-ray Thomson-scattering experiments, an emerging area where much greater activity can be anticipated.

c. More static x-ray pinhole cameras: These diagnostics are rarely, if ever, critically important but are of value in assessing whether an experiment performed as intended. Their number has decreased in recent years and it would be helpful to see a few cameras re-activated.

d. More SG8 or similar phase plates: This would be particularly useful when users share shot days. Whether SG8's are the right choice or how this integrates with phase plates for OMEGA EP was not addressed. Most users agree that having some phase plates for OMEGA EP is far more important than having additional ones for the 60-beam OMEGA.

e. Spherical crystal imaging: This would be a very useful diagnostic if implemented and engineered to the point of being routinely available. The users understand that this would be an expensive prospect and do not rank it above other ways to spend the necessary funds. The users strongly encourage support for any effort by a major laboratory to implement this diagnostic.

3. OMEGA EP

a. Beam smoothing: Distributed phase plates (DPP's) significantly improve the spatial uniformity of irradiation in the focus of high-power laser beams. They reduce the growth of parametric instabilities, which have a number of deleterious effects, such as the generation of hot electrons (this causes preheat of the irradiated targets) and reduced coupling of laser energy to the plasma.

OLUG recommends the installation of 1-mm-spot-size DPP's on the long-pulse beamlines. This provision would benefit a number of users of the facility.

Temporal smoothing can be achieved with the implementation of smoothing by spectral dispersion (SSD). OLUG is aware that a preamplifier module (PAM) is being installed on the OMEGA laser to study two-dimensional SSD for direct-drive ICF at the National Ignition Facility (NIF).

OLUG urges facility management to make the necessary modifications to the NIF PAM so that it can be used as an alternate front end for OMEGA EP and allow for 2-D SSD studies to be implemented for the user community.

b. Pulse shaping: The NIF will be using long-pulse durations for some studies. Staging experiments from OMEGA EP to the NIF may need similar pulse shapes in the future.

OLUG recommends that options for implementing pulse shapes similar to the NIF's (100 ps to 30 ns) be explored by management so that an assessment of priorities can be made at the next OLUG meeting.

c. Intensity-contrast-ratio enhancement: The coupling of energy from the intense laser pulse to the fast-electron beam may be significantly affected by magnetic fields formed near the ablation front by the plasma generated by the prepulse. These fields have the effect of reducing the number of fast electrons entering the target. It may be necessary to improve the intensity contrast ratio to get better coupling.

OLUG recommends that options for enhancing the intensity contrast ratio be explored by management so that an assessment of priorities can be made at the next OLUG meeting.

d. Implementation of low-energy probe beams: Optical probes provide a range of powerful diagnostic tools that can be used to extract information from underdense laser-produced plasmas. Density gradients, for example, can be obtained from both shadowgraphy and Schlieren imaging, while density information can be extracted by unfolding interferograms and magnetic fields can be obtained with the simultaneous use of polarimetry. The working group is aware of the funded project to implement a 10-ps fourth-harmonic probe line for OMEGA EP by the end of this fiscal year.

OLUG urges management to make the completion and realization of this project a very high priority. These diagnostics will be of great assistance to a large number of users of the facility.

e. Addition of streaked optical pyrometry (SOP) with the active shock breakout (ASBO) diagnostic: The active shock breakout (ASBO) diagnostic has proved to be a valuable tool to study high-pressure equation of state of materials, as well as shock timing for inertial confinement fusion. The instrument has been used extensively by investigators based at a number of universities and national laboratories since the upgraded instrument was commissioned in 2006. A laser probe beam is used to illuminate the rear surface of the target. When the shock wave reaches the back surface of the witness plate, it rapidly heats the surface, resulting in a dramatic reduction in reflectivity of the probe beam. This makes it possible to measure shock-breakout times with high temporal and spatial resolution.

The provision of two "velocity interferometer for any reflector (VISAR)" channels is a unique feature of the upgraded instrument. These channels have different velocity sensitivities that make it possible to resolve any 2-D ambiguity that arises at velocity discontinuities. The working group agreed that the addition of passive streaked optical pyrometry (SOP) channels would be a valuable addition. These channels would make it possible to measure the lower radiation temperatures and shock pressures.

OLUG recommends the simultaneous provision of SOP with the ASBO diagnostic suite.

f. Spherical crystal imaging: Monochromatic x-ray imaging of high-photon-energy K_α radiation has proved to be a valuable tool in diagnosing energy transport in intense laser–plasma interactions. This has provided information in cone wire plasmas: for example, the energy coupling and the resistive electric field required to draw the return current. Many experiments will benefit from the provision of Ti, Cu, and higher-Z K_α imaging spectrometers.

OLUG recommends the provision of a spherical crystal imaging diagnostic on OMEGA EP.

g. Record of electromagnetic pulse (EMP) and radiological noise: High-intensity laser environments are harsh. Active diagnostics suffer considerable damage because of EMP, x-ray bremsstrahlung radiation, and (p,n)-induced activation of diagnostics placed close to the targets.

OLUG recommends that a record of instruments and detectors that have suffered from EMP and radiological noise damage be made available to facility users so that mitigation strategies can be undertaken when planning experiments.

h. Penalty and conflict information: It would be very useful when preparing experiments to have an appreciation of the time delays that are likely to occur as a result of changes to diagnostics, target alignment, and laser specifications during experimental campaigns.

OLUG recommends that a record of known delays be made available to facility users so that users are more aware of the costs of decisions.

4. General User Issues

A number of issues common to users of both OMEGA and OMEGA EP were discussed. These issues are based on operational details relevant to preparing and executing experiments, as well as the flow of information and communication between facility personnel and users, as well as among users themselves. The following points summarize these issues and *recommendations*:

(a) A number of users have indicated that it would be important to have available a larger volume of information and knowledge about facility operational details and the way in which they can impact the setup and execution of experiments. The information could include relationships between changes in laser-pulse energy, shaping, and smoothing options during a shot day, and their impact in shot delays, including a possible loss of shots. In general, the issue is, What is the optimal way to plan for these changes during a shot day (e.g., what is best to do first, second, etc.)? The idea is that what actually happens during the day (or half day) of shots is likely to be a compromise determined by practical facility operational details and considerations of science goals. How can changes and modification of diagnostic configurations during the shot day, relative to what was discussed in the initial plan, impact shot execution, and what conflicts or incompatibilities may arise?

The idea was proposed of having the option of starting the discussion process with relevant personnel in the facility several months ahead of time to detail the experimental proposal for the shots.

This is currently being done as the result of submitting the detailed experimental proposal two months ahead of the planned time. OMEGA and OMEGA EP users would like to have the option of starting this discussion process earlier or have alternative avenues available to them to address these issues.

(b) Another point of common concern is that of calibrating and characterizing diagnostics available on OMEGA and OMEGA EP. Flat fielding of streak and framing cameras is a typical example relevant to many users but certainly not the only one. The performance of streak and framing cameras has a broad impact on experiments since they are used in a variety of experimental campaigns, in different ways, to record valuable time-resolved data. Currently, users have to plan for characterizing and flat fielding these cameras as part of their own shot campaigns. The information they produce in this regard is potentially useful to many users. It would be more efficient and effective if this information could be made available to users on a standard basis and if it could be generated in such a way that it would not tax the shots dedicated to a given science campaign; i.e., it would not require dedicated shots allocated to a user that could have otherwise been used to address a science point. Two possible ways to address this issue were discussed. Characterization and flat fielding of streak and framing cameras could be done as a ride-along task; this would require planning and organization so that opportunities are not missed and sufficient and reliable information is recorded to achieve this goal. The facility could dedicate shots to perform this task or could include it as part of their regular facility maintenance.

Regardless of the way in which it is done, it was clear from discussions that there is a strong consensus among users

that characterizing and calibrating diagnostics available on OMEGA and OMEGA EP is an important point that affects many users and a critical issue that must be addressed.

(c) Evaluating and assessing the facility performance and the experimental campaign was an important topic of discussion since it provides an opportunity for users to convey feedback and comments to the facility management. Current procedures on OMEGA include an Effectiveness Assessment form that must be returned by the principal investigator (PI) to the Shot Director after each shot and an Experimental Critique sheet that is submitted during the week subsequent to the week of the shots. The sense among users was that, while there is value in the feedback provided in the Effectiveness Assessment form, this is done under pressure and too hurried. The quality of the feedback and comments provided in the Experimental Critique sheet is better the week after the shots. A thorough assessment of the experimental campaign, including the quality and quantity of the data recorded and how well the science goals were achieved, is something that often requires considerably more time.

OLUG recommends having the option to provide feedback on the experimental campaign, including facility performance, target fabrication, and level of accomplishment of science goals a few months after the shots. This feedback is likely to be the most accurate and realistic. The idea was also suggested to provide a place on the OMEGA web site accessible by users (via log-in and password) indicating the current status of OMEGA and OMEGA EP diagnostics.

(d) Better and more-complete information about the instruments and diagnostics available on OMEGA and OMEGA EP is needed.

This could be accomplished by establishing links in suitable web pages on the OMEGA web site, including (but not limited to) Shot Request Forms (SRF's), to internal reports and journal papers that document the details of instruments and diagnostics.

(e) The role that C. Sorce plays in LLNL experimental campaigns as a technical link between scientists (PI's) and facility engineers and technicians has been noted and praised by many users not involved in LLNL campaigns.

It was suggested that it would be useful to have a similar resource person to perform that task for all experimental campaigns.

(f) *OLUG recommends the continued use of Be in OMEGA and OMEGA EP shots.*

(g) *OLUG recommends additional office space be allocated for (outside) users when they are visiting and preparing for their shots.*

(h) *OLUG recommends that space be provided on the OMEGA web site to post information of common interest to many users as well as to establish web pages for areas of interest for groups of users, e.g., Thomson scattering, x-ray spectroscopy, particle measurements, etc.*

5. Information Flow

This topic involves better communication with Omega Facility users. In general, there is very good communication between LLE and users; however, the amount of information required for a successful campaign on OMEGA is very large. The suggestions represent the distilled recommendations of the Users Group to improve communication, *which is especially important for new users or those who have no LLE collaborators*.

a. Diagnostics: Just as the laser-pulse-shape "Help" page describes choices for laser pulses, a "Help" page for diagnostics would be of great benefit. This might be accomplished with an upgrade to the ***Diagnostic Status*** link on the OMEGA operations page. To the list of "Diagnostic Name" and "Lead Scientist," etc., the *upgrade* would add a brief description (a couple of sentences) of available SRF choices and links to published papers employing the diagnostic. For x-ray imagers, the page could list the date of the last flat fielding.

- If possible, a search-engine capability for diagnostics is attractive because it could enable would-be users to find out *who has recently used or is planning to use* specific diagnostics. The search could cover all SRF's within a +2/–1-month window with the idea of returning the names of PI's (who composed the SRF's) so that potential users of that diagnostic could contact them regarding how well it functioned and exchange details of actual/intended use. This should not violate accessibility/restriction of SRF's to users who may not be authorized to view an SRF in totality but is intended only to better communicate reasonable knowledge from one user to another. A corollary to this is an LLE-sponsored blog or "wiki" for areas of user interest, e.g., x-ray Thomson scattering or x-ray framing cameras.

- A new LLE notification procedure concerning *diagnostic status* would benefit users. Just like Laboratory staff are notified when credit for various training courses necessary for employment is about to expire, PI's could be notified if a primary diagnostic for their upcoming campaign becomes "unavailable." The implementation for this might involve automated email to all PI's for shots for the next ~2 months (a time period to be determined) when a diagnostic goes "off line." This may result in an increase of email to PI's who are not interested but could result in a reduction of surprises to PI's who are counting on using a particular diagnostic for future shots for which SRF's have not yet been created.

- Not all diagnostics are LLE diagnostics. Occasionally, it is desirable to test or flat field a user's diagnostic prior to the user's shot day. One means through which this might be accomplished is to provide an "empty-TIM" web page. Similar to the *Diagnostic Status* page, this page would list all empty TIM's for shots occurring during the next quarter. It could list the shot PI, the campaign, the target characteristics, and the laser energy on target. The intent is to make possible the *ride-along* testing of a user's diagnostic. Such multiplexing of experiments may increase the overall productivity of the facility. For example: the "neutron days" often conducted by V. Yu. Glebov attract a host of users with various TIM diagnostics that benefit from testing; the pointing shots conducted for LLE cryo shots can also be used in a similar way. If a user's imaging diagnostic or spectrometer can be fielded as a ride-along, or an x-ray flat fielding can be accomplished without costing a shot, this would increase productivity.

b. OMEGA EP Information: A high level of enthusiasm for OMEGA EP exists. Although it is recognized that OMEGA EP is a work in progress, the users' community is eager for status reports on OMEGA EP. OLUG recommends that, as soon as is practical, members of the users' group receive updates on OMEGA EP pulse-shaping capabilities, including

- minimum pulse length
- energy limits in relation to pulse width
- OMEGA EP contrast
- blast-shield status
- energy/power/focusability limits with blast shields

c. Miscellaneous: Similar updates are desirable for other OMEGA systems:

- phase-plate availability and numbers for both the 60-beam OMEGA and OMEGA EP
- DT-fill capability, especially with regard to changes in procedure that may affect LLE's ability to fill and field targets

6. Broader Issues

The Executive Committee, while recognizing that this issue is outside the scope of this report, expressed concern about the absence of direct support for diagnostic development at universities in general. This has an exacerbating effect on hands-on training in an era of increasingly formal facility operations. This issue is especially important to students and postdocs.

There is a general need for more small facilities as staging grounds for hands-on training, diagnostics, and experiment development. Again, students and postdocs are significantly impacted by this circumstance.

With regard to related research at other facilities, OLUG recommends that we proceed with the HIPER/US workshop to promote joint and complementary research on HEDP physics. In a similar vein, efforts should be made to coordinate and promote complementary physics research among Omega and other important HED laser facilities such as the NIF, LULI, RAL, Trident, and Texas PW. Through such coordinated activities and research, there are substantial opportunities to significantly advance the science of high-energy-density physics.

Initial Response of Omega Management to Findings and Recommendations

1. Introduction

LLE Management responded to the OLUG recommendations. Their response below was written on 1 May 2009. Since then, ongoing progress and updates have occurred and will be reported at the Atlanta APS Meeting (3 November 2009) and at the next Users Workshop. In addition, Omega management is meeting bimonthly with members of the OLUG Executive Committee to assess progress toward achieving these objectives.

2. OMEGA (60 beams)

(a) Penalty and conflict information would be helpful: e.g., pointing, framing-camera moves, phase plates, etc.

LLE Response: The LLE web site will be modified to make it easier to find this type of information.

(b) It would be desirable to be able to drive any legs from any driver, which has become a major problem for x-ray Thomson scattering.

LLE Response: Will submit a project in FY10 for evaluation. Cost and schedule are currently unknown. Significant resources are likely to be required.

(c) More static x-ray pinhole cameras would be helpful.

LLE Response: OMEGA H8 camera is now operational. LLE will evaluate target chamber (TC) port allocation for possible addition of fixed PHC's. It may be possible to deploy two or three decommissioned units.

(d) Spherical crystal imaging (diagnostic) would be a very useful diagnostic.

LLE Response: A crystal-imager project has been proposed by LLE for OMEGA EP but deferred until FY10. LLE is reviewing the requirements and benefits, but there are concerns that with the high energy of the OMEGA EP beams, significant target heating could shift the K-shell lines out of the imager-wavelength acceptance band. Any suggestions for system requirements are welcome from OLUG. There are currently no plans to provide a crystal imager for OMEGA.

3. OMEGA EP

(a) Phase plates with 1-mm spot size are essential to a number of users.

LLE Response: Two phase plates will be available starting in FY10. Four more substrates are on order and will be made into phase plates by FY11.

(b) SSD will also matter for a number of possible experiments.

LLE Response: SSD is not planned for OMEGA EP except on the NIF PAM (in mid-FY10), which will be able to feed Beam 3. Implementing SSD on additional beamlines would require significant resources.

(c) OLUG strongly endorses adding a simultaneous SOP to ASBO.

LLE Response: SOP cabinet location and beam path are part of the OMEGA EP ASBO design package. LLE believes that it has identified a streak camera for the SOP and, if available, will install it on OMEGA EP later in FY09 or early in FY10.

(d) Pulse-shaping equivalent to NIF capability will help a number of users (100 ps to 30 ns).

LLE Response: Current architecture does not support >10-ns operation. LLE is evaluating possible strategies to provide this capability as well as shorter pulses. Operating with individual beam-pulse durations greater than 10 ns will, however, require a significant redesign of the front end in addition to significant resources.

(e) Spherical crystal imaging would be very helpful.

LLE Response: A crystal-imager project has been proposed by LLE for OMEGA EP but has been deferred until FY10. LLE is reviewing the requirements and benefits, but there are concerns that with the high energy of the OMEGA EP beams, significant target heating could shift the K-shell lines out of the imager-wavelength acceptance band. Any suggestions for system requirements are welcome from OLUG. There are currently no plans to provide a crystal imager for OMEGA

(f) Low-energy probe beams would be helpful:

- 1ω chirped pulse via an air compressor to allow for adjustment;
- 2ω or 3ω would be better;
- up to 1 J would provide an x-ray option.

LLE Response: A fourth-harmonic probe is in development. It will provide a 10-ps (nonchirped) pulse of 20 mJ to 100 mJ at 263 nm. LLE's goal is to have the system installed in FY10, including light-collection optics that would allow for Schlieren imaging and grid refractometry. It will be on a fixed path in the plane, perpendicular to the backlighter direction, 60° from vertical.

(g) A record of experience with EMP versus the type of experiment, laser intensity, and diagnostics should be made available to users.

LLE Response: EMP signatures are currently collected on each short-pulse shot on OMEGA and OMEGA EP. Diagnostic EMI-related diagnostic failures are logged by the shot crew when encountered. We will organize and make this information available to users in the near future.

(h) Organized penalty and conflict information would be useful, e.g., blast shield.

LLE Response: LLE will organize and distribute this package shortly. It will also become available on the web site.

4. General User Issues

(a) Earlier assessment of conflicts or problems in the setup; e.g., it would be beneficial to have access to Scheduling Committee outputs six months in advance. Users also want to know what operational delays may be introduced by the initial plan.

LLE Response: Omega management staff are available for advance planning at the request of any user. Campaign proposals can be submitted at any time in advance of the two-month required date. Users can request an early evaluation of their proposal, although this will not include potential conflicts with other experiments the same week. Users should make this request to J. M. Soures.

(b) The need to establish a link to scientists/engineers/technicians as mentors (as C. Sorce does for LLNL).

LLE Response: LLE agrees with the need for this enhanced liaison function and will support to the limit of our resources. Specific requests are generally supported. Requests for links to LLE staff should be directed to J. M. Soures.

(c) Zero interframe timing for x-ray framing cameras would

- be a standard operating procedure each day
- be readily available on the web
- arrange calibration and testing as a dedicated instrument maintenance block of time

LLE Response: These operations currently occur as part of routine operations. We will make this information more readily available to the users in the near future through the web site. Calibration and testing where required for data analysis should be included in experiment planning.

(d) LLE should host wikis for areas of user interest, e.g., x-ray Thomson scattering, x-ray framing cameras, etc.

LLE Response: LLE could host a blog forum for users to discuss the status of operational diagnostics. Diagnostic status information is currently available on the web site. LLE will explore options that allow user dialogue.

(e) It is important to continue to use Be.

LLE Response: LLE expects to continue to support the use of Be at the Omega Facility. We are evaluating current regulations.

(f) Improved links to more information in SRF's and other material, especially for each diagnostic, including brief description, contact people, RSI or other reference, procedures, etc.

LLE Response: Improved documentation including an Equipment Qualification Package will be linked shortly via SRF web pages.

(g) Provide dedicated laboratory space for visiting groups:

- enable a user to make preparations without conflicts
- computer linkages in this laboratory or wherever preparations occur

LLE Response: Dedicated "side-lab" space is currently available in LLE rooms 175, 177, 182, and 6000 (OMEGA EP diagnostic workshop). Additional transient space is available upon request. Ethernet is available but must be pre-arranged. Note that space is limited.

(h) Comments on after-shot feedback process:

Quality is not entirely satisfying. The overall sense is that 20%, give or take, of the feedback is too hurried or pressured to be accurate. Issues like data quality are often not immediately clear.

- add "Shot Cycle Assessment" line to feedback form.

LLE Response:

- *The Experiment Effectiveness Assessment Form (EEAF) is used for tactical evaluation during shots by the shot crew. Best-effort feedback is the objective. Longer-term issues that take time to sort out should be included in the Experimental Critique one to two weeks after the campaign. If the information changes after the initial experimental critique is submitted, the user is encouraged to submit a revised critique.*

- *Users can review shot-cycle information, including cause and length of delays in real time on "OMEGA Availability" on the Operations web site. LLE is considering adding a "Comment" area for shot-cycle assessment to the EEAF.*

5. Information Flow

(a) Detailed information flow is a challenge, especially when strong internal connections are lacking, despite the fantastic job OMEGA is doing.

LLE Response: LLE is working on a presentation and table showing users how to use the database system to find specific shot-planning and analysis information.

(b) Put an "X-ray Framing Camera Status" and a "Streak Camera Status" page on the web for user access. Coordination and information flow for framing-camera flat fields and signal levels would also be very useful—to improve user planning (see wikis).

LLE Response: LLE could host a blog forum for users to discuss status of operational diagnostics. Diagnostic status information is currently available on the web site. LLE will explore options that allow user dialogue.

(c) Implement a search capability to enable all users to find out who has used or is planning to use specific diagnostics or other capabilities (including SRF's and PI's).

LLE Response: LLE will implement a "Recent Use" history database of each diagnostic that will be available to users.

(d) Implement automatic notification of diagnostic status during run up toward shots using this particular diagnostic.

LLE Response: Automated link to blog could be implemented. The best way to get this information, however, is for the users to read the Diagnostic Status page.

(e) There is a need for more information relating to changes in policy about DT fill, although, in general, users report good communication about policy changes.

LLE Response: Formal announcements of policy changes will be distributed via the Scheduling Committee. The committee meets biweekly (could the OLUG mailing list be used to distribute regular notices of changes in facility policy to users?).

(f) OMEGA EP information

- need focus, energy, and regular timing of update
- need to know, ASAP, focus ability versus energy through blast shields in OMEGA EP
- need to know, ASAP, contrast on OMEGA EP
- need to know status of TIM updates

LLE Response: LLE is actively developing the diagnostics to address these items. We want to make them available ASAP, subject to finite development time and resources. The LLE System Science staff believes that providing accurate information is extremely important and will release information only when they are confident that it is correct. They are actively working on these issues.

- Focus and energy operating envelope will be further explored in the coming months.
- Blast-shield use impact is being analyzed and will be disseminated when available.
- A high-contrast diagnostic is being deployed as a high priority.
- Initial capability is expected in FY09.
- TIM-10 and TIM-11 will be completed in Q4 FY09; TIM-15 is expected in Q1 FY10. Information will be posted on the Omega Laser Facility web page.

(g) Regular updates on phase-plate inventories and availability (both OMEGA and OMEGA EP) would be beneficial.

LLE Response: They will be selectable with far-field information on the SRF interface as soon as they are available. Much of this information already exists online in the DPP database.

6. Broader Issues

OLUG recommends consideration of the following issues:

(a) The absence of explicit support for diagnostic development in universities has an increasingly adverse effect on hands-on training in an area of increasingly formal facility operations.

(b) The availability of small facilities as staging grounds for hands-on training, diagnostics, and experiment development is a concern.

(c) OLUG encourages a HIPER/US workshop to promote joint and complementary research on HEDP physics.

LLE Response: These issues are beyond LLE's control, but LLE will work with NNSA to address them.

Findings and Recommendations of the Student/Postdoctoral Panel

OLUG Student/Postdoctoral Panel:

Ryan Rygg, Chair, Lawrence Livermore National Laboratory
Dan Casey, Massachusetts Institute of Technology
Carolyn Kuranz, University of Michigan
Hiroshi Sawada, University of California–San Diego
Louise Willingale, University of Michigan

A variety of topics were raised during the student/postdoctoral/new-user panel session at the OLUG meeting. Although the chance to perform experiments on OMEGA is a wonderful opportunity for students and postdocs, a number of issues are of particular concern for new users, especially those who are not members of groups with strong ties to LLE. In an effort to increase the effectiveness of experiments performed by students, postdocs, and other new users, the major areas of discussion are summarized below.

1. Information for New Users

Copious information about many aspects of OMEGA is available on the LLE web site. Navigating the web site to find relevant documents can be overwhelming for external users, however, partly because the information for external OMEGA users is intermingled with the much greater volume of information provided specifically for facility staff.

New users would benefit from a concise and easy-to-find overview of the location and purpose of relevant documents and resources. For example, the NLUF Users' Guide is a particularly useful resource, yet it is not well known by all external users and, in particular, would be hard to identify as a useful document for those new users not funded by NLUF.

Many also expressed a desire for readily accessible descriptions of available diagnostics. The current "Help" links from the SRF diagnostic pages are too cryptic to be very useful for inexperienced users, and the NLUF Users' Guide's diagnostics section is sometimes too far removed from the terse SRF labels to make it possible to evaluate which diagnostics are appropriate for a given experiment. It was proposed that a Diagnostic Summary page be provided (perhaps in parallel or perhaps merged with the Diagnostic Status page) that includes the diagnostic acronym, a two- to three-sentence description of its use and limitations, operational procedures, a link to relevant RSI papers, and examples of calibration or experimental data, if available. Links to this Diagnostic Description Summary page directly from the SRF form or SRF diagnostic Help page would also be useful.

In addition to a resource diagnostic summary, other information suggested as valuable on a *new users' summary page* includes concise (as compared to the 227-page NLUF Users' Guide) descriptions of the laser system's capabilities; tools to aid in experimental planning, such as delays incurred by laser or diagnostic-configuration changes; and a list of whom to contact with questions regarding various topics.

2. Engineering Liaison for External Users

One recommendation that was echoed in later sessions was to designate an engineering liaison for external users. OMEGA users are widely spread both nationally and internationally, and it is impractical for each group to have a representative at LLE for the weeks and months prior to a shot day to prepare and interface the experiment with the facility. These external users could share a designated representative who is familiar with the facility, knows of whom to ask which question, can perform some of the legwork in the weeks prior to shot day, and is up to date on the latest news/issues that may affect the experiment. The suggested archetype for this liaison is the role that C. Sorce currently performs for the national labs. In summary, students and postdocs would greatly benefit from contact with a designated junior technical staff member or liaison who could answer numerous questions.

3. Availability of Smaller Facilities

Finally, many expressed concerns regarding the continued availability of smaller-scale experimental facilities. Smaller-scale facilities provide a practical means of testing new diag-

nostics and experimental ideas prior to their implementation on OMEGA. In addition, they offer an opportunity for hands-on experience to students and postdocs in a relatively low stakes environment, where the cost of mistakes—an essential element of experience gain—is lessened.

Given OMEGA's limited experimental time and to help ascertain whether OMEGA is the proper facility, a list could be supplied of alternative smaller-scale experimental facilities for potential use for diagnostic and experimental development. Suggestions were also made to include the proposal process and deadlines, if any, for each facility in addition to the name, location, and description.

Conclusions and Future Workshops

This first OLUG workshop, with over 100 attendees, was the beginning of a process that will keep members of the inertial confinement fusion and high-energy-density physics communities involved in conversations and collaborations with each other and with the facility. OLUG Executive Committee members and facility management have been meeting on a bimonthly basis to assess progress, compatible with facility resources and impact, toward the implementation of the *Findings and Recommendations*. Progress will be reported on at a satellite meeting at the Atlanta APS Meeting (3 November 2009) and at the next OLUG Workshop.

The next Omega Lasers Users Group Workshop will be held at LLE on 28 April–1 May 2010. Significant financial support from NNSA has already been procured to help defray the cost of student and postdoc travel.

ACKNOWLEDGMENT

For capturing the ambiance and spirit of the workshop through his lens, we thank Eugene Kowaluk. We thank Irina Cashen, Sarah Frasier, Kathie Freson, Jenny Hamson, Karen Kiselycznyk, Katie Leyer, Jody Mayer, Lisa Stanzel, Jean Steve, and Jennifer Taylor for their gracious help and assistance. To NNSA, we gratefully acknowledge the financial assistance for student/postdoc travel expenses. We thank the University of Rochester's Fusion Science Center, which co-sponsors the OMEGA Users Group Workshops.

This updated review was compiled and edited by R. D. Petrasso (petrasso@psfc.mit.edu) of MIT's Plasma Science and Fusion Center with critical input and contributions by Workshop attendees, the Executive and Student/Postdoctoral Workshop Committees, and LLE management.

The Effect of Condensates and Inner Coatings on the Performance of Vacuum Hohlraum Targets

Introduction

Inertial confinement fusion (ICF) targets for the National Ignition Facility (NIF)[1] consist of a cryogenic capsule containing frozen deuterium–tritium (DT) fuel inside a gold or uranium hohlraum.[2] High-power laser beams enter the cylindrical hohlraum through a hole in each end cap, heating the interior to a temperature of ~300 eV (Ref. 3). This thermal radiation drives ablation of the capsule, causing it to implode and ignite the DT fuel. We report the results of experiments on the OMEGA laser[4] that support the national campaign to achieve ignition. These experiments used cryogenic hohlraums containing a sample of the ignition capsule ablator material and were driven to ~180 eV.

Although the primary purpose of these OMEGA experiments was to study the shock-timing technique for NIF ignition targets, we observed and identified the cause of an interesting discrepancy between the x-ray drive in cryogenic and identical room-temperature hohlraums. Namely, peak drive temperatures were 15% lower in cryogenic hohlraums than in identical warm hohlraums, and the temporal history of the drive was also changed. Furthermore, laser–plasma interaction processes produce hard x rays ($h\nu > 20$ keV) 100× more abundantly in cryogenic targets. Spatial nonuniformities in the x-ray emission were also observed within cryogenic hohlraums.

The reduced performance of the cryogenic targets resulted from the condensation of background gases on the inner walls of the cryogenic hohlraums. This was confirmed when hohlraum targets coated with thin (~2-μm) layers of CH reproduced the behavior of the cryogenic targets. The primary effect of low-Z coatings (CH and condensates) is the reduction of x-ray conversion efficiency within the hohlraum. They also produce longer plasma scale lengths that cause laser–plasma instabilities, which reduce the absorption of the drive laser and produce hot electrons and x rays. These finding are important to some non-ignition hohlraums that use low-Z liners[5–8] (or layers) on the inside hohlraum walls to tamp or resist the expansion of the laser-ablated wall material. In contrast, ignition hohlraums will be filled with a low-Z gas to keep the laser entrance hole open.[9,10] Windows are placed on the laser entrance holes to retain the gas; these windows also serve to protect the inside of the hohlraum from the deposition of condensates. Moreover, the NIF cryogenic targets are housed inside shrouds to minimize condensation until they open a few seconds before the shot. These OMEGA experiments confirm that eliminating condensation on cryogenic targets is crucial for optimal hohlraum performance.

Experimental Configuration

A series of experiments were performed on the OMEGA Laser System to demonstrate a technique to time the multiple shock waves in the ignition targets planned for the NIF.[11] This study used gold hohlraum targets with re-entrant cones to diagnose the shock-wave trajectories. The hohlraums were empty (also termed vacuum hohlraums): they contained no gas nor did they have windows on the laser entrance holes. Both warm and cryogenic targets were used in these experiments. (In the cryogenic targets, the liquid deuterium was confined to the re-entrant cones and did not enter the hohlraum.)

The hohlraums were made of 25-μm-thick Au, were 2.55 mm long and 1.6 mm in diameter, and contained 1.2-mm-diam laser entrance holes (LEH's). They were oriented along the P6–P7 axis of the OMEGA target chamber and driven with 38 OMEGA beams that had no beam smoothing (phase plates nor spectral dispersion) and were focused in three cones of beams (with different angles of incidence) in a standard configuration for hohlraums on OMEGA. The three cones of beams were five beams at 21°, five beams at 42°, and nine beams at 59° entering each end of the hohlraum (angles are relative to the hohlraum axis). These cones were each pointed along the hohlraum axis but outside the LEH by 0.725, 0.2, and 0 mm, respectively. They focused at 0.8, 0.5, and 0.0 mm (respectively) before these pointing positions. The drive pulse was a 2-ns temporally square pulse that produced spot intensities greater than 10^{14} W/cm^2 on the inner surface of the hohlraum. Figure 120.22 shows the hohlraum and drive-beam configuration with the x-ray and optical diagnostics used in the experiments.

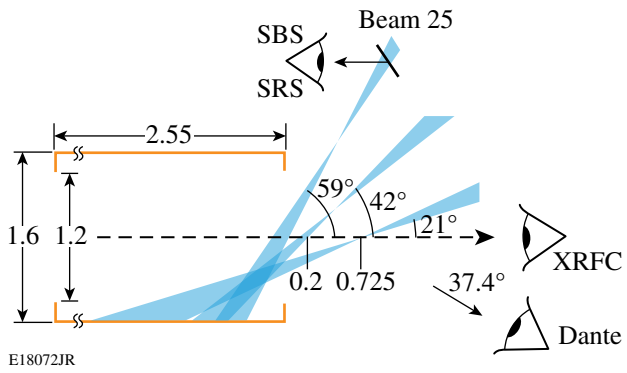

Figure 120.22
The experimental configuration where hohlraum targets are irradiated at each end by three cones of beams at 21°, 42°, and 59°. X-ray diagnostics viewed the hohlraum through the laser entrance hole and optical diagnostics detected light scattered back through Beam 25, a 59° beam.

These experiments employed a suite of diagnostics to monitor the performance of the hohlraums. The radiation temperature within the hohlraum was measured using the Dante diagnostic:[12–14] an array of 12 x-ray diode detectors filtered to provide the x-ray emission in various bands of x-ray energies. The responses of the detectors were absolutely calibrated (temporally and in x-ray energy) so the diode current could be converted into a temporal history of the x-ray flux in the energy band determined by the filtration. By fitting these multi-energy measurements to a blackbody distribution, one can determine the equivalent radiation temperature within the hohlraum as a function of time.[13,15] Another array of four x-ray photomultiplier tubes measured the integrated energy of hard x rays, i.e., those above cut-off energies of 20, 40, 60, and 80 keV (Ref. 16).

A framing x-ray pinhole camera[17] (XRFC) viewed the hohlraum along the hohlraum axis through the LEH. This device uses pinholes backed by both soft x-ray mirrors and x-ray filters to provide images of the hohlraum at x-ray energies of $h\nu$ = 0.5, 0.9, and 1.5 keV.

One of the drive-laser beams (Beam 25) has a diagnostic that records the temporal and spectral profiles of light reflected from the hohlraums back through the focus lens. This is done for two spectral regions: one near 351 nm (the drive-laser wavelength) and the other in the range 400 nm to 700 nm. These wavelength regions are used to diagnose the presence of stimulated Brillioun scattering (SBS) and stimulated Raman scattering (SRS), respectively. The total energy reflected back through the focus lens was measured with a calorimeter. These diagnostics were used to monitor the effects of nonlinear laser–plasma interaction processes that scatter the drive-laser light.

Radiation Temperature

In these experiments a distinct difference was observed in the behavior of warm (ambient temperature) and cryogenic ($T <$ 20 K) hohlraums. Figure 120.23 shows the radiation temperature (measured by Dante) in hohlraum targets as a function of laser drive energy. The upper red points are the measured peak radiation temperatures for warm hohlraums. The red curve is a $T_{rad} \alpha E^{0.25}$ power law fit to those data. All of these hohlraums had re-entrant diagnostic cones for the shock-timing experiments. In all but three, the tips of those cones were fitted with Be–Cu–Be sandwiches[11] that replicate the x-ray opacity of the ablator in an ignition capsule.[18] In Fig. 120.23, at ~12-kJ drive energy, three yellow squares show the radiation temperatures for identical hohlraum targets that had gold cone tips instead of

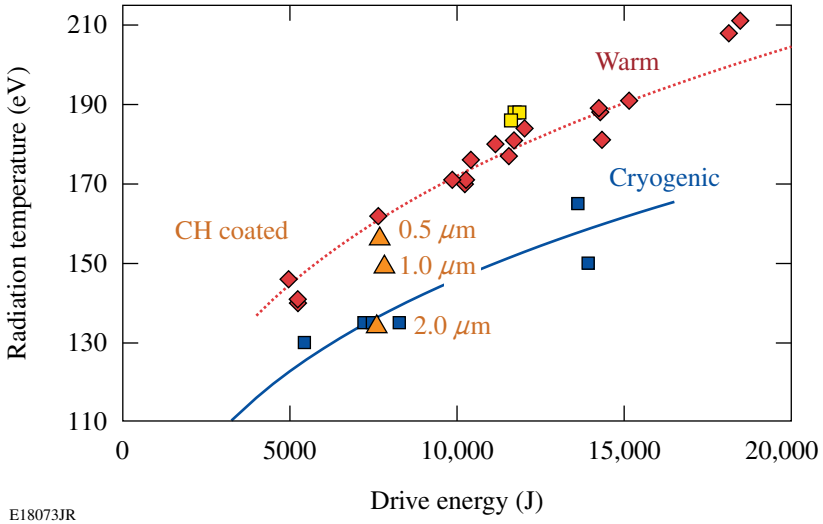

Figure 120.23
Hohlraum radiation temperature (as measured by Dante) as a function of drive-laser energy for warm hohlraums (red diamonds) and cryogenic hohlraums (blue squares). The red and blue curves are $T_{rad} \alpha E^{0.25}$ fit to the warm and cold data. The three yellow squares at 12 kJ are targets with cone tips made of gold instead of Be–Cu. The orange triangles are warm hohlraums coated with CH in the thicknesses shown.

the Be–Cu sandwiches. These gold-tipped targets show slightly higher radiation temperatures than the other warm targets, demonstrating the sensitivity of the radiation temperature to materials within the hohlraum. The Be–Cu sandwiches had a surface area that was ~10% of that of the hohlraum. The lower albedo of the Be surface reduces the x rays returned to the radiation field by that surface; therefore, when the Be sandwiches are replaced with gold, the radiation temperature rises.

The lower blue points and blue curve (again a $T_{rad} \alpha E^{0.25}$ fit) are the radiation temperatures for the cryogenic hohlraums. The hohlraums used for these data were identical to the ones discussed above: they were nominally empty and were fitted with the diagnostic cone. Liquid (cryogenic) deuterium filled the diagnostic cones but did not enter the hohlraum. The cryogenic targets show a 15% reduction in peak radiation temperature compared to identical warm ones.

Figure 120.24 shows the radiation temperature as a function of time for four experiments: two warm and two cryogenic. (The radiation temperatures plotted in Fig. 120.23 are the peak values of this type of data.) The upper bold and thin dotted lines are results for warm experiments performed at 14 kJ (shot 47240) and 7.5 kJ (shot 47241), respectively. These data exhibit the standard profile for radiation temperature produced by a 2-ns square pulse: an initial fast rise as hot, low-density plasma is created and the laser deposits energy into this plasma. This is followed by a slow rise as a thermal x-ray–driven Marshak wave[19] moves into the gold wall, producing a rise in the wall albedo. When the drive-laser pulse ends, the radiation temperature has peaked and the hohlraum begins to cool at a rate determined by its geometry and the total heated mass contained in the hohlraum. The warm experiments exhibit identical behavior, differing only in their magnitudes.

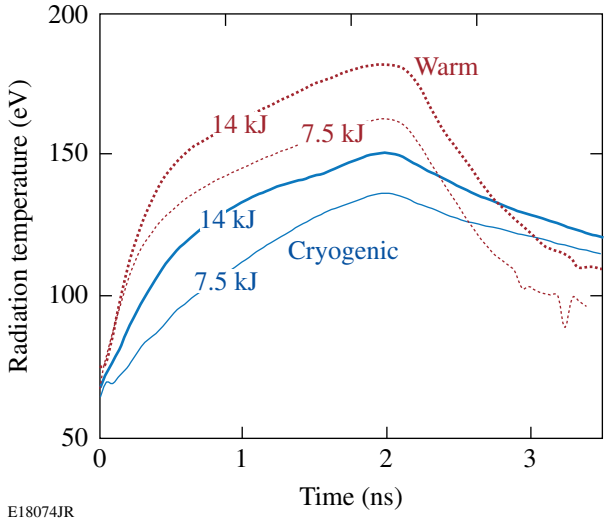

Figure 120.24
The temporal profile of the radiation temperature for four experiments: two warm targets (upper curves) at 14-kJ (bold dotted) and 7.5-kJ (thin dotted) drive energy and two cryogenic targets (lower curves) at 14-kJ (bold solid) and 7.5-kJ (thin solid) drive energy. The cryogenic targets show distinctly different behavior: lower rise times, lower peak temperatures, and decreased cooling rates.

The lower bold and thin solid curves are the radiation-temperature profiles for identical targets cooled to cryogenic temperatures and driven by similar energies [14 kJ (shot 48884) and 7.5 kJ (shot 48881)]. These shapes are distinctly different than the warm targets but are similar to each other. Their rate of rise is much slower, their peak temperatures are lower, and they cool at a significantly slower rate than the warm targets. The performance of the cryogenic hohlraums is reduced compared to warm ones: the peak temperatures are lower and the response time is slower.

Effect of CH Coatings

The differences between the warm and cryogenic targets appear to be the result of condensation layers that form on the inner walls of the cryogenic hohlraums. The cryogenic targets were mounted on the cold finger of a sizable cryogenic system[20] that connects to the OMEGA target chamber and has its own vacuum system. Targets were installed in the cryogenic system, which was evacuated (separately from the target chamber), and then the targets were cooled. As a result, the cryogenic hohlraum targets spent 20 to 50 min at temperatures below 70 K, where the pressure was $\geq 10^{-5}$ Torr. At these temperatures, background gases will condense on the cold surfaces. Residual gas analysis on the vacuum systems show that the background gases in these systems were comprised predominantly of water vapor, nitrogen, and oxygen.

In low-mass cryogenic targets, a protective shroud is frequently used to shield the target from thermal radiation. The cold surfaces of the shroud act as cryogenic pumps that produce lower pressure in the vicinity of the target. This reduces the level of background gas that can condense onto the cold target. The thermal mass of the cold finger for these hohlraums targets was sufficient to prevent heating by background radiation. For expediency the cryogenic hohlraum targets were fielded *without* a protective shroud. The targets easily maintained temperatures to produce liquid deuterium but were likely exposed to increased condensates. Simple estimates for condensation rates at the applicable pressures indicate that these targets could have had several microns of condensed material on them.

To test whether the behavior of the cryogenic targets resulted from condensation, hohlraums (identical to those described above) were lined with thin layers of parylene (CH) and irradiated in the same manner as the warm hohlraum targets. The results of three experiments with CH-lined targets are shown in Fig. 120.23 as orange triangles at ~7.8 kJ. Note that as the CH-coating thickness increases (0.5, 1.0, and 2.0 μm), the radiation temperature decreases, ultimately matching the cryogenic target results quite closely. This progression and the replication of the behavior of cryogenic targets are shown in Fig. 120.25 as another plot of radiation temperature as a function of time. The upper and lower curves are the thin curves from Fig. 120.24 for warm (red) and cryogenic (blue) targets. The data (orange) for the CH-lined target show that as the CH-coating thickness increases, the temporal profile better replicates the cryogenic target's behavior: The rate of rise decreases, the peak radiation temperature decreases, and the cooling time increases. The data for the 2-μm CH coating closely replicate the behavior of the cryogenic hohlraums, suggesting that the cryogenic targets have a condensation layer that is equivalent to ~2 μm of CH. [These CH-coated data are also consistent with previous results for hohlraums lined with 0.44 μm of CH (Ref. 21).]

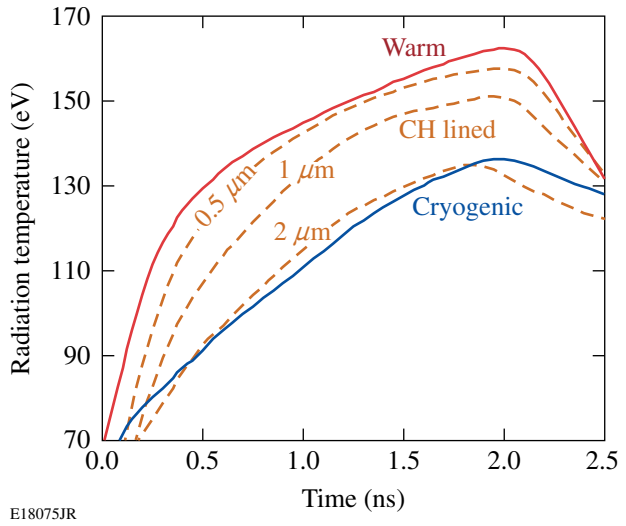

Figure 120.25
The effect of CH coatings on the temporal profiles of radiation temperatures. Profiles for warm and cryogenic hohlraums targets driven at 7.5 kJ are the red and blue curves (from Fig. 120.24). The orange curves depict the profiles for hohlraums with CH coatings of 0.5-, 1.0-, and 2.0-μm thicknesses.

X-Ray Emission

Figure 120.26 shows time-gated x-ray pinhole camera images of the targets, viewed through the LEH, for two shots: (a) a warm hohlraum driven by 14.2 kJ (shot 48879) and (b) a cryogenic hohlraum driven by 13.9 kJ (shot 48884). In both figures the left and right images were formed with 500-eV and 900-eV radiation, respectively. The center images were formed with radiation greater than 1.5 keV. For those lower-energy images, spectral discrimination was obtained with grazing-incidence mirrors; for the >1.5-keV image, a simple transmission filter was used. As a result, the left and right images are inverted (left for right) with respect to the center image. Note that the <1-keV x-ray images in both warm and cryogenic experiments are fairly uniform, as is the >1.5-keV x-ray image for the warm hohlraum. In contrast, the >1.5-keV x-ray image of the cryogenic hohlraum has significant structure.

The enlarged images are those at $h\nu > 1.5$ keV for (a) the warm and (b) the cryogenic experiments. The warm image has a fairly uniform emission profile within the hohlraum, and one can discern the outline of the lower-albedo Be cone tip. [For reference, Fig. 120.26(c) is an image of a hohlraum target through the LEH along the same direction as the framing camera that produced the images in Figs. 120.26(a) and 120.26(b).] The image of the cryogenic experiment exhibits strongly structured emission in radial spokes that are triangular in shape. This structure has a configuration similar to the pointing arrangement of a subset of the incident laser beams.

Three cones of laser beams enter the hohlraum through the LEH at angles of 21°, 42°, and 59° with respect to the hohlraum axis. The outer nine beams (at 59°) were pentagonally arranged with two beams on each edge (minus one beam not used in these experiments). Because of their steep angle of incidence, these beams are closest to the LEH and the x-ray emission from their spots is most visible from outside the hohlraum. Figure 120.26(d) is a simple drawing of the target and LEH showing the outer beams from their focal point (on the hohlraum axis) to the hohlraum wall. They are pointed at the center of the LEH but come to focus 0.8 mm before that point. The beams are diverging so the blowoff plasma flows into higher laser intensity as it expands off the hohlraum wall. Lastly, the low-Z material expanded more rapidly than the gold, therefore extending farther into the beam path.

The enlarged image in Fig. 120.26(b) shows the similarity to that beam configuration, with the dark areas representing the beam profiles where the x rays were created. Only eight beams appear in the image because one beam interacted obliquely with the diagnostic cone and had reduced x-ray brightness. X-ray images of the CH-lined targets exhibit spoke-like features similar to those in the cryogenic targets, as shown in Fig. 120.26(b).

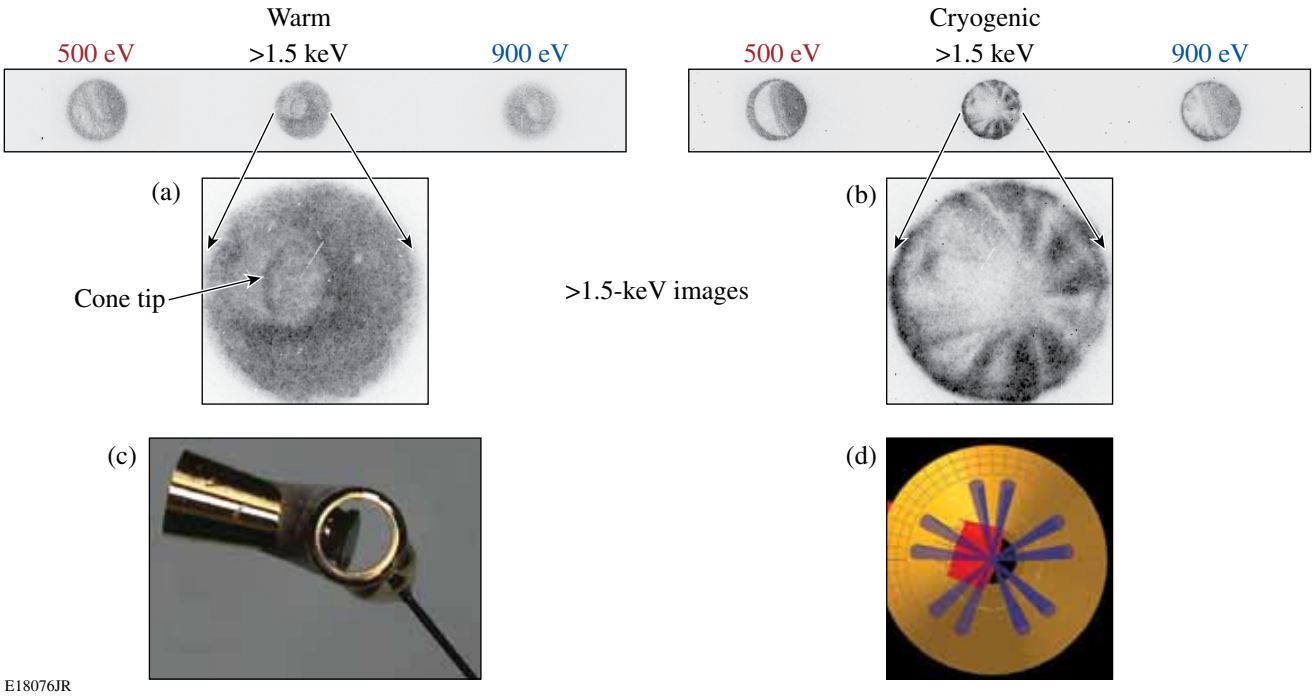

Figure 120.26
Framing x-ray pinhole camera images the hohlraum targets through the LEH and along the hohlraum axis for (a) a warm hohlraum target and (b) a cryogenic hohlraum target. The data for each comprise three images, each taken at 1.8 ns. The image on the left is 500-eV radiation and the right is 900-eV radiation. The center was radiated with $h\nu > 1.5$ keV. (The 1.5-keV images are expanded for clarity.) (c) Image of the hohlraum target through the LEH [at same view as that of Figs. 120.26(a) and 120.26(b)] showing the configuration of the hohlraum and VISAR cone. (d) Drawing of the LEH with the outlines of the outer cone of beams superposed. The x-ray emission in (b) has a similar structure.

Reflected Light and Hard X-Ray Measurements

The full-aperture backscatter diagnostics on Beam 25 (FABS25) resolve light scattered into the *f*/6 focusing optics temporally and spectrally in two wavelength bands, corresponding to stimulated Brillouin scattering (SBS, 351±2 nm) and stimulated Raman scattering (SRS, 400 nm to 700 nm). The temporal and spectral resolutions in these bands are typically ~40 ps and ~0.04 nm for the SBS channel and ~100 ps and ~15 nm for the SRS channel. All time-resolved spectra are shown in false-color images on logarithmic scales. The laser pulse shapes and the normalized, spectrally integrated scattered powers (Fig. 120.27) are superposed on the spectra in black and white, respectively. The SBS spectra also show a weak, narrow unshifted spectral component at 351 nm, caused by stray drive-laser light that misses the target.

Figure 120.27 shows SBS spectra for three hohlraum experiments: (a) a room-temperature hohlraum and (b) a cryogenic hohlraum, both driven at 14 kJ, and (c) a room-temperature hohlraum driven at 7.9 kJ. All hohlraum targets were gold and the hohlraum in Fig. 120.27(c) had a 2-μm layer of CH.

The corresponding SRS spectra are shown in Fig. 120.28. The intensity of Beam 25 at the LEH is estimated to be between 2 and 4×10^{15} W/cm^2. While a simple, uncoated gold hohlraum is not expected to have very much plasma near the LEH during most of the laser pulse, a hohlraum with low-Z layers (CH or condensates) may well have significant plasma near the LEH at early times. (This results from high-velocity blowoff from the hohlraum interior and from the edge of the LEH.) The highly blue shifted SBS signal early in Fig. 120.27(b) could result from a plasma that is rapidly expanding (highly supersonic) toward the laser. Alternatively, the incident light could be rapidly blue shifted as the result of a lateral influx of plasma into the beam.[22]

The broad bandwidth could be caused by strong coupling effects (high intensity near the LEH) but may also be associated with varying plasma conditions within the beam. The backscatter energies for both SBS and SRS for the three shots shown in Fig. 120.27 are given in Table 120.I, along with typical intensities at the LEH and at the hohlraum wall for Beam 25.

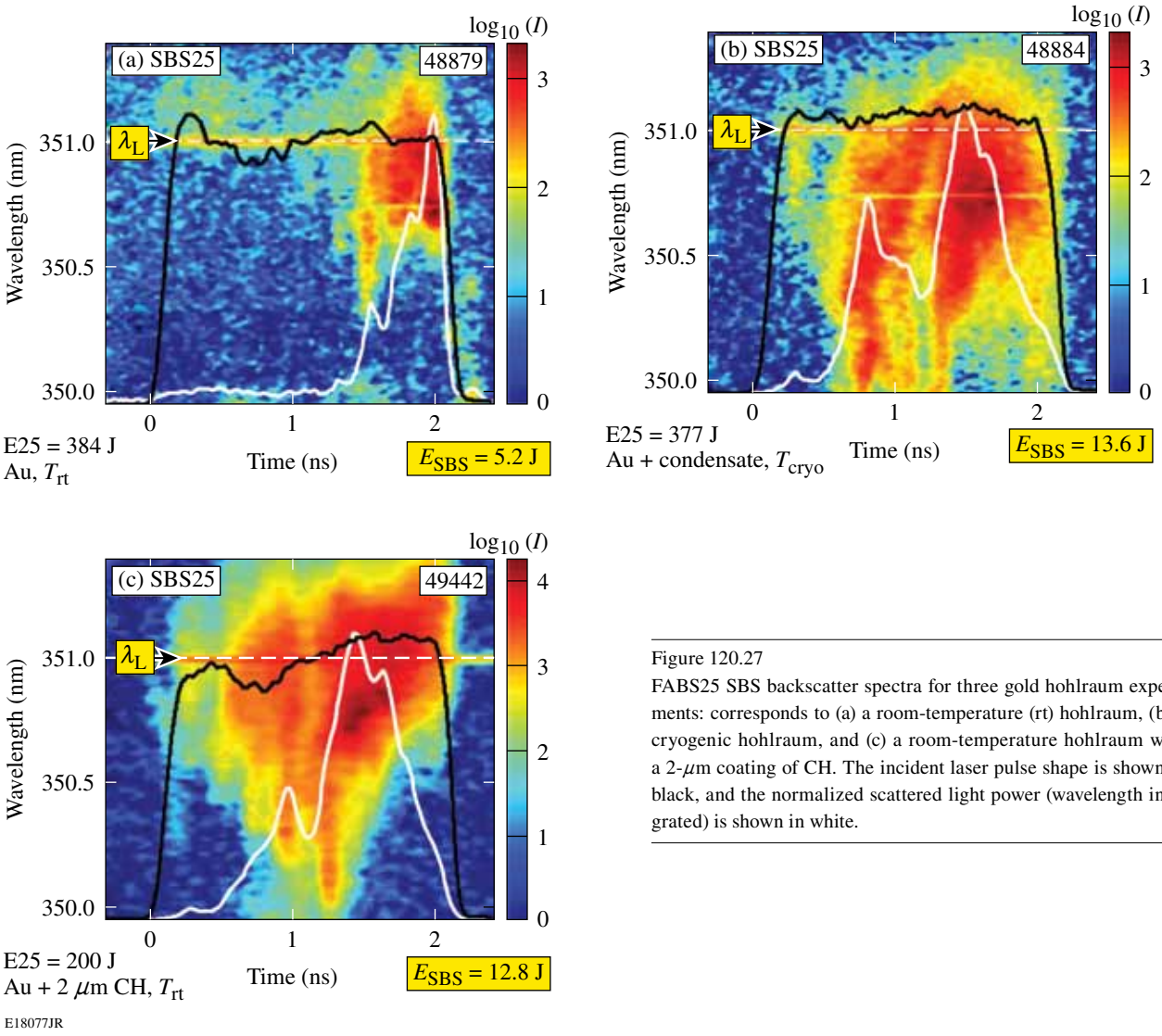

Figure 120.27
FABS25 SBS backscatter spectra for three gold hohlraum experiments: corresponds to (a) a room-temperature (rt) hohlraum, (b) a cryogenic hohlraum, and (c) a room-temperature hohlraum with a 2-μm coating of CH. The incident laser pulse shape is shown in black, and the normalized scattered light power (wavelength integrated) is shown in white.

Table 120.I: SBS and SRS backscatter energies and reflectivities.

Shot Number	I_{LEH}	I_{wall}	E_{SBS} (J)	E_{SRS} (J)
48879 (warm)	2 to 4 × 10^{15} W/cm^2	5 to 10 × 10^{14} W/cm^2	5 J (1.3%)	1.5 J (0.4%)
48884 (cryo)	2 to 4 × 10^{15} W/cm^2	5 to 10 × 10^{14} W/cm^2	13.6 J (3.6%)	19 J (5%)
49442 (CH-lined)	1 to 2 × 10^{15} W/cm^2	2 to 5 × 10^{14} W/cm^2	12.8 J (6.4%)	13 J (6.6%)

The SRS spectra indicate that the main part of this backscatter radiation emanates from density regions that are 12%–14% of n_c, where n_c is the critical density ($n_c = 10^{22}$ cm^{-3} for λ_L = 351 nm). [The wavelength scale shown in Fig. 120.28(a) was converted to a density scale in Fig. 120.28(c) based on the plasma-wave dispersion relation for $T_e = 2$ keV. The temperature correction is essentially negligible.] We conjecture that these relatively high densities are likely located close to the hohlraum wall inside the hohlraum and not at the LEH. There is extremely little SRS radiation for the room-temperature gold hohlraum, while significant SRS is observed for both the cryogenic gold hohlraum and the CH-coated room-temperature hohlraum.

Figure 120.29 shows the energy reflected back into Beam 25 as a function of incident beam energy. The warm, unlined hohlraums reflect 0.3%–1% of the beam energy, whereas the cryogenic and CH-lined hohlraums reflect 3%–7%. It is noteworthy that each of the CH thicknesses has the same high reflectivity as the cryogenic targets; no intermediate behavior for the thinner coatings is observed.

Figure 120.30 shows the total hard x-ray signal (in the $h\nu >$ 20-keV channel) as a function of total incident laser energy for the various targets. The hard x-ray signal increases dramatically (αE^7) above a threshold that depends on the type of target: For warm, unlined hohlraums, the hard x-ray signal does not reach 1 pC until the drive energy is ~7.6 kJ, whereas the cryogenic hohlraums reach that level at half that energy (3.8 kJ). For a given drive energy, the cryogenic hohlraums produce ~100× the hard x-ray flux of the warm, unlined hohlraums. The CH-lined targets show an increase in hard x-ray production as compared to the unlined hohlraums, with the thinnest CH

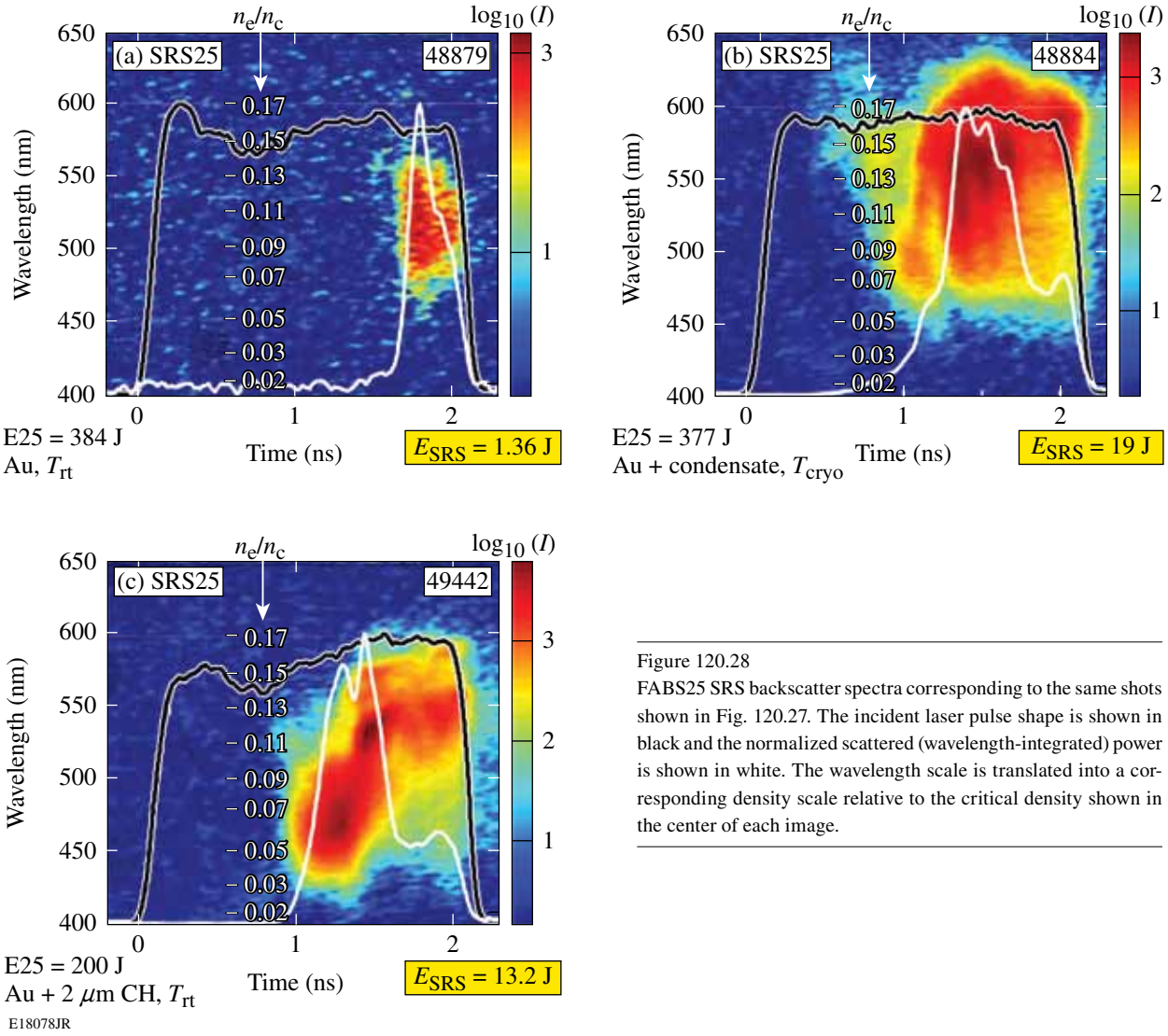

Figure 120.28
FABS25 SRS backscatter spectra corresponding to the same shots shown in Fig. 120.27. The incident laser pulse shape is shown in black and the normalized scattered (wavelength-integrated) power is shown in white. The wavelength scale is translated into a corresponding density scale relative to the critical density shown in the center of each image.

coating producing 10× that of the unlined targets. Increased CH thickness increases the hard x-ray production: the 2-μm case being 280× that of the uncoated warm target.

The radiation temperature results (Figs. 120.23 and 120.25) show that the CH-lined hohlraum replicates the behavior of the cryogenic hohlraums quite well. This effect is the result of the relatively low x-ray conversion efficiency of the low-Z materials (condensates and CH). Figures 120.29 and 120.30 show that there are some differences in the mechanisms by which condensates and CH coatings interact with the laser-scattered light and produce hard x rays. This is likely due to different materials (Z) of the two coatings affecting the plasma conditions and scale lengths. These laser–plasma coupling effects are small compared to that of the x-ray conversion but, nevertheless, can be important for the performance of hohlraum-driven targets because fast electrons and hard x rays are produced.

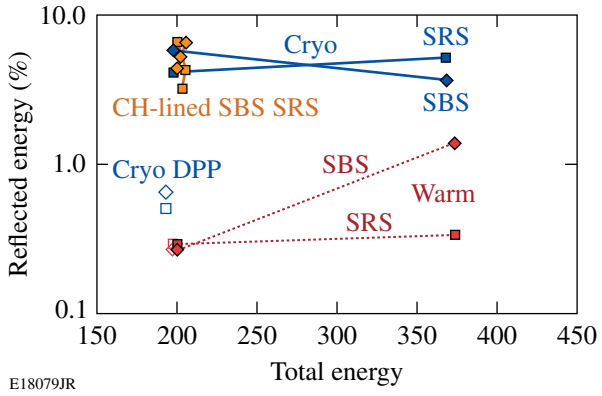

Figure 120.29
The reflected energy (% of incident) in Beam 25 as a function of energy and for various target types. The warm, unlined hohlraums reflect 0.3%–1% of the beam energy; the cryogenic and CH-lined hohlraums reflect 3%–7%.

Effect of Background Pressure

In one cryogenic experiment the target-cooling procedure was changed. Instead of cooling the target within the ancillary vacuum in the cryogenic system, the target was not cooled until it reached the center of the OMEGA target chamber, where the pressure was considerably lower. Figure 120.31 compares the radiation-temperature temporal profiles of a warm target (black), a cryogenic target cooled in the cart (blue), and a cryogenic target (shot 49453) cooled at the center of the target

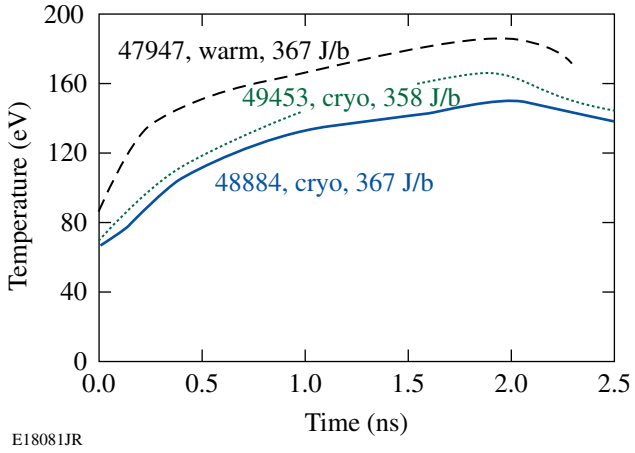

Figure 120.31
Radiation temperature temporal profiles for a warm target (black), a cryogenic target cooled in the cart (blue), and a cryogenic target cooled at the center of the target chamber (green). The cart has a higher background pressure than the target chamber and therefore a greater deposition rate for condensates.

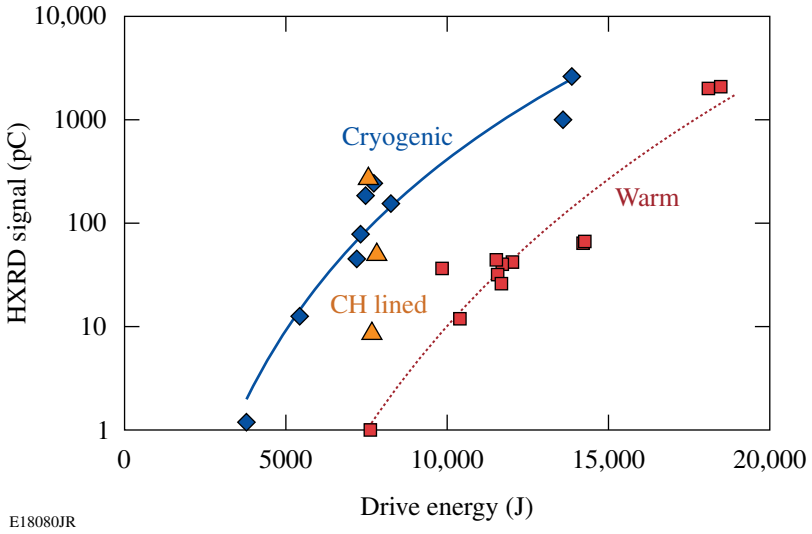

Figure 120.30
Hard x-ray signal (in the $h\nu > 20$-keV channel) as a function of total incident laser energy for the various targets. The cryogenic, CH-coated targets produce more hard x rays than the warm, uncoated targets. This is a result of the long-scale-length plasmas that are created when the low-Z coating is present.

chamber (green). The target cooled in the target chamber shows a higher peak radiation temperature, and its rate of rise and cooling rates are incrementally closer to the behavior of the warm target. The peak radiation temperatures for these two shots are the cryogenic target data at 14 kJ in Fig. 120.23. These data and the CH-coated–target data confirm that the reduced performance in the cryogenic targets results from the condensation of background gases inside the cryogenic hohlraums. In the case of shot 49453, the reduced background pressure reduced the deposition rate of condensate, producing a thinner layer within the hohlraum. This manifested itself as higher radiation temperature and a temporal profile that is closer to that of a warm hohlraum.

Effect of Focus Conditions

Laser-beam smoothing is used to enhance laser-target coupling and reduce laser–plasma instabilities. The results discussed above show that the reduced performance of cryogenic and coated hohlraum is due primarily to the presence of low-Z material and that laser–plasma coupling is less important. This is demonstrated by hohlraum experiments performed with different focal positions and with beams having distributed phase plates (DPP's)[23,24] in the drive-laser beams. In the former ("tight-focus case"), all of the targets were warm and all of the drive beams were pointed and focused at the center of the LEH. In the latter, the focus was the same as described above, but the beams were fitted with "elliptical" DPP's that produced circular spots at the LEH.[24] The results for these experiments are shown in Fig. 120.32, a repeat of Fig. 120.23 with green triangles depicting the tight-focus case and the open red (warm) and blue (cryogenic) points depicting data from experiments using the DPP's. Note that the tight-focus case exhibits a lower radiation temperature in the warm targets. This is likely due to increased scattered-light fractions associated with the high intensities produced at the LEH by this beam configuration. This conclusion is supported by the apparent scaling suggested by the points at higher drive energies, which have even lower radiation temperatures with respect to the standard-focus case. As the intensity (energy) increases, so do the effects of laser–plasma instabilities. For the DPP case, note that the open data points replicate the respective behaviors of warm and cryogenic targets. The radiation temperature is still lower for cryogenic targets. Refer back to Fig. 120.30 and note the open data points; they represent experiments with DPP's. Those data show that smoother beams (with DPP's) reduce the scattered-light fractions in cryogenic targets but do not alter the hard x-ray production. These data indicate that the scattered-light fraction plays a small role in the reduction in radiation temperature for cryogenic and CH-coated targets.

X-Ray Conversion Efficiency

The Dante diagnostic provides a direct measure of time-resolved x-ray power emitted from the hohlraum target. One of the most striking results of these experiments is that the x-ray energy radiated from the hohlraum lined with 2 μm of CH is a factor of 2 lower than that from an unlined hohlraum. This is observed in both the peak and the instantaneous fluxes (as in Figs. 120.23 and 120.25, respectively).

The data show that cryogenic targets reflect about 5%–7%, but this is insufficient to explain the 15% reduction in radiation temperature. The blackbody radiation temperature scales roughly as the one-fourth power of the energy absorbed by the hohlraum. To produce a 15% reduction in the radiation tem-

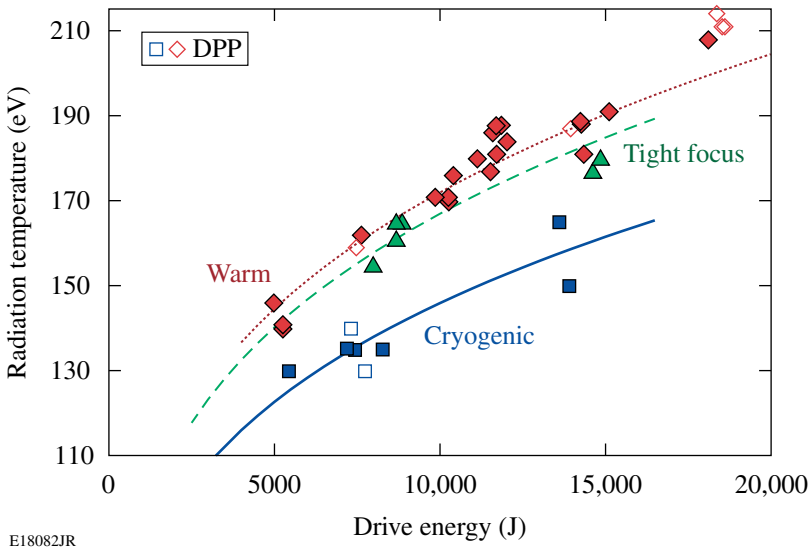

Figure 120.32
Radiation temperature versus drive energy (repeat of Fig. 120.23) with data for "tight-focus case" (green triangles) and for experiments using the DPP's with warm targets (red) and cryogenic targets (blue).

perature, the absorbed energy must be reduced to 50%. Instead, the reduction of radiation temperature is caused mainly by the addition of materials with low x-ray conversion efficiency. These materials interact with the laser and are heated but do not re-radiate x-ray energy as effectively as gold, so the radiation temperature is reduced.

Hohlraum targets have increased x-ray conversion efficiency[2,25] as compared to open (non-confined) targets, where the blowoff plasma is free to expand. In hohlraums, the plasma energy and mass accumulate within the hohlraum volume. Increased x-ray conversion efficiency results initially from the conversion of kinetic energy[26] but later is predominantly a result of emission from the accumulated material that is heated by the drive lasers. Experiments[27] show that the intensity of the x rays emitted from laser-irradiated plasmas in hohlraums is similar to that of open-geometry laser plasmas. The increase in hohlraum x-ray conversion efficiency, therefore, results from the confinement and heating of the gold blowoff plasma that creates larger regions of x-ray emission. When low-Z layers are added to hohlraums, they fill the hohlraum with a plasma that (a) does not emit x rays as efficiently as gold and (b) reduces the energy that ultimately reaches the gold wall. These significantly reduce the radiation temperature.

For the hohlraum radiation temperatures of interest in these experiments, the CH plasma (resulting from the 0.5- to 2.0-μm CH liners) provides little opacity to thermal x rays from the gold walls. The x-ray power invested in the heating of the gold hohlraum wall can be approximated by $(1-\alpha)\, A_w T^4$, where T is the hohlraum temperature, A_w is the wall area, and $(1-\alpha)$ is the absorbed x-ray fraction from the thermal-diffusion process [Eq. (2) of Ref. 28], based on the physics model for hohlraum energetics.[29] By implication, energy that is not radiated from the target, absorbed by the wall via penetration of the thermal wave, or directly backscattered from the target is therefore "lost" to the direct laser heating of the hot (>keV), low-density blowoff plasma. Figure 120.33 shows a plot comparing this lost energy for comparably driven hohlraums with bare Au walls and CH liner thicknesses of 0.5, 1.0, and 2.0 μm. In a hohlraum target, energy that directly heats the low-density, low-Z plasma constitutes inefficiency. A highly radiating plasma (e.g., gold) is advantageous, whereas a low-Z plasma tends to absorb the laser energy without significant re-radiation in the x-ray region. In Fig. 120.34, the measured radiation fluxes are recast into plots of x-ray conversion efficiency. It can be seen that the inferred x-ray conversion efficiencies reach levels as high as 85% in the unlined Au hohlraum but are reduced to as low as 50% in the hohlraum with the 2-μm CH liner.

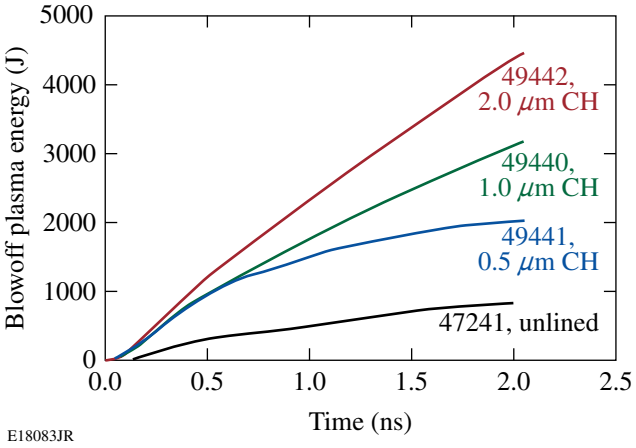

Figure 120.33
The plasma blow-off energy (or energy "lost") as a function of time for bare (black) and CH-coated (blue, green, and red) hohlraums.

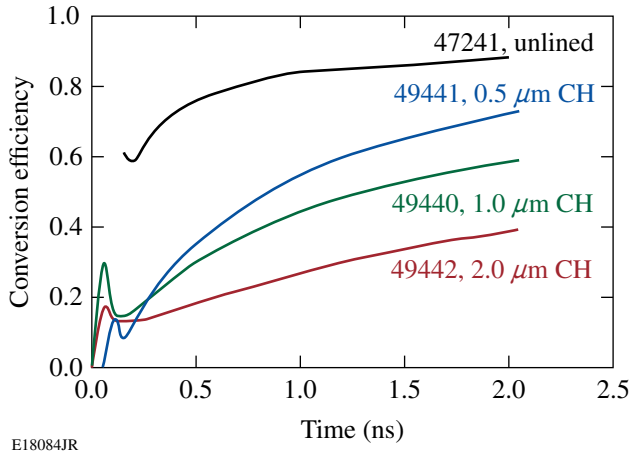

Figure 120.34
X-ray conversion efficiency as a function of time for bare (black) and CH-coated (blue, green, and red) hohlraums. Conversion efficiency is calculated from the x-ray flux (Dante) data.

Simulations

These experiments were simulated using the radiation–hydrodynamics code LASNEX.[30] Figure 120.35 shows the simulated radiation temperature as a function of time for four hohlraum experiments: (a) uncoated and [(b)–(d)] coated with 0.5, 1.0, and 2.0 μm of CH. The continuous curves are the simulations and the points (with error bars) are the Dante data. (These data are the warm and CH-lined data shown in Fig. 120.25 above.) The simulations model the radiation temperatures quite well. The magnitude and temporal behavior of each target are modeled as is the effect of CH coatings, where

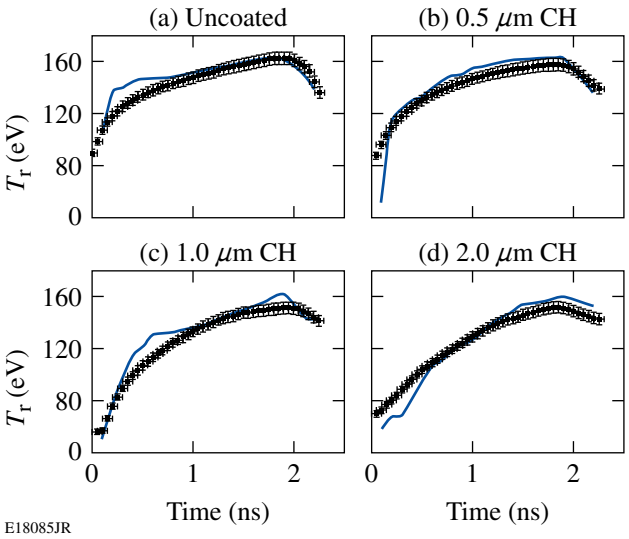

Figure 120.35
Simulation results for four warm hohlraum targets: (a) uncoated and coated with (b) 0.5, (c) 1.0, and (d) 2.0 μm of CH. Note that the behavior of these radiation temperature profiles is quite similar to the experiments depicted in Fig. 120.25.

the reduced rise time, lower peak radiation temperature, and slower temperature decrease are all replicated. The experimental scattered-light signals were input into the simulations, so the primary effect modeled here is the reduced x-ray conversion efficiency and the hydrodynamics of the liner material.

Summary

Experiments show that cryogenic vacuum hohlraums exhibit a significantly different behavior than identical warm hohlraums. The temporal profile of the radiation temperature for the cryogenic targets is changed with respect to the warm targets: early in the pulse the temperature rate of rise is lower, the peak temperature achieved is lower, and the cooling rate after the drive ceases is decreased. These observations are accompanied by significant changes in the x-ray emission structure within the hohlraum and by dramatic changes to the amount and character of the laser light that is reflected from the hohlraum.

For these experiments, the condensation of background gases onto the cold hohlraum surfaces is responsible for the degraded performance of the cryogenic hohlraums. This deposited material has lower x-ray conversion efficiency, which reduces the x-ray flux within the hohlraum. This affects the temporal rate of rise in the radiation temperature—its peak value. Experiments with identical warm hohlraum targets lined with 2 μm of CH replicated the behavior of the cryogenic hohlraum targets, confirming the effect of low-Z materials on the performance of hohlraum radiation temperature. The temporal profile of the radiation temperature in the lined targets was nearly identical to that of the cryogenic targets. This indicates that the cryogenic targets had a condensation layer equivalent to about 2 μm of CH, which is consistent with estimates for the background gas that were present in the cryogenic system.

In addition to these radiation effects, the absorption of the drive-laser energy is reduced as a result of increased scattering caused by SBS and SRS. These instabilities produce hot electrons and hard x rays that can be detrimental to the performance of ICF targets. The temporal and spectral features of reflected light in the CH-lined targets were similar to that of the cryogenic targets, again confirming that the cryogenic targets contained layers of low-Z condensation.

These results are useful because they demonstrate the effect that low-Z layers have on the performance of laser-driven hohlraums. These effects are important for vacuum hohlraums, i.e., those without LEH windows or fill gases within the hohlraum. Ignition hohlraums at the National Ignition Facility will have both and are expected to be immune to these effects because background gases will be unable to condense on the hohlraum's inner surfaces and the fill gas will be of low-enough density to have little effect on x-ray conversion.

ACKNOWLEDGMENT

This work was supported by the U.S. Department of Energy Office of Inertial Confinement Fusion under Cooperative Agreement No. DE-FC52-08NA28302, the University of Rochester, and the New York State Energy Research and Development Authority. The support of DOE does not constitute an endorsement by DOE of the views expressed in this article.

REFERENCES

1. J. A. Paisner, E. M. Campbell, and W. J. Hogan, Lawrence Livermore National Laboratory, Livermore, CA, Report UCRL-JC-117397, NTIS Order No. DE95010923 (1994). Copies may be obtained from the National Technical Information Service, Springfield, VA 22161.

2. J. D. Lindl *et al.*, Phys. Plasmas **11**, 339 (2004).

3. S. W. Haan *et al.*, Nucl. Fusion **44**, S171 (2004).

4. T. R. Boehly, D. L. Brown, R. S. Craxton, R. L. Keck, J. P. Knauer, J. H. Kelly, T. J. Kessler, S. A. Kumpan, S. J. Loucks, S. A. Letzring, F. J. Marshall, R. L. McCrory, S. F. B. Morse, W. Seka, J. M. Soures, and C. P. Verdon, Opt. Commun. **133**, 495 (1997).

5. J. D. Lindl, *Laser Program Annual Report 1978*, Lawrence Livermore National Laboratory, Livermore, CA, Report UCRL-50055-78, 2-77 (1978).

6. S. Pollaine, *Laser Program Annual Report 1988*, Lawrence Livermore National Laboratory, Livermore, CA, Report XDIV-90-0054, 246 (1988).

7. A. R. Thiessen, *Laser Program Annual Report 1988*, Lawrence Livermore National Laboratory, Livermore, CA, Report XDIV-90-0054 (1988).

8. S. Pollaine, *Laser Program Annual Report 1990/1991*, Lawrence Livermore National Laboratory, Livermore, CA, Report UCRL-LR-116901-90/91, 214 (1991).

9. S. W. Haan *et al.*, Phys. Plasmas **2**, 2480 (1995).

10. W. J. Krauser *et al.*, Phys. Plasmas **3**, 2084 (1996).

11. T. R. Boehly, D. H. Munro, P. M. Celliers, R. E. Olson, D. G. Hicks, V. N. Goncharov, G. W. Collins, H. F. Robey, S. X. Hu, J. A. Marozas, T. C. Sangster, O. L. Landen, and D. D. Meyerhofer, Phys. Plasmas **16**, 056302 (2009).

12. H. N. Kornblum, R. L. Kauffman, and J. A. Smith, Rev. Sci. Instrum. **57**, 2179 (1986).

13. C. Decker, R. E. Turner, O. L. Landen, L. J. Suter, H. N. Kornblum, B. A. Hammel, T. J. Murphy, J. Wallace, N. D. Delamater, P. Gobby, A. A. Hauer, G. R. Magelssen, J. A. Oertel, J. Knauer, F. J. Marshall, D. Bradley, W. Seka, and J. M. Soures, Phys. Rev. Lett. **79**, 1491 (1997).

14. C. Sorce *et al.*, Rev. Sci. Instrum. **77**, 10E518 (2006).

15. R. L. Kauffman *et al.*, Rev. Sci. Instrum. **66**, 678 (1995).

16. C. Stoeckl, V. Yu. Glebov, D. D. Meyerhofer, W. Seka, B. Yaakobi, R. P. J. Town, and J. D. Zuegel, Rev. Sci. Instrum. **72**, 1197 (2001).

17. D. K. Bradley *et al.*, Rev. Sci. Instrum. **66**, 716 (1995).

18. S. W. Haan *et al.*, Phys. Plasmas **12**, 056316 (2005).

19. R. E. Marshak, Phys. Fluids **1**, 24 (1958).

20. *LLE Review Quarterly Report* **103**, 128, Laboratory for Laser Energetics, University of Rochester, Rochester, NY, LLE Document No. DOE/SF/19460-626, NTIS Order No. PB2006-106675 (2005). Copies may be obtained from the National Technical Information Service, Springfield, VA 22161.

21. S. H. Batha and J. R. Fincke, Rev. Sci. Instrum. **75**, 3934 (2004).

22. T. Dewandre, J. R. Albritton, and E. A. Williams, Phys. Fluids **24**, 528 (1981).

23. Y. Lin, T. J. Kessler, and G. N. Lawrence, Opt. Lett. **20**, 764 (1995).

24. S. P. Regan, D. D. Meyerhofer, T. C. Sangster, R. Epstein, L. J. Suter, O. S. Jones, N. B. Meezan, M. D. Rosen, S. Dixit, C. Sorce, O. L. Landen, J. Schein, and E. L. Dewald, Bull. Am. Phys. Soc. **51**, 68 (2006).

25. L. J. Suter *et al.*, Phys. Plasmas **3**, 2057 (1996).

26. J. Massen, G. D. Tsakiris, and R. Sigel, Phys. Rev. E **48**, 2073 (1993).

27. F. Ze *et al.*, presented at the 1993 Topical Conference on Physics of Radiatively Driven ICF Targets, Monterey, CA (1993).

28. R. E. Olson *et al.*, Rev. Sci. Instrum. **74**, 2186 (2003).

29. M. D. Rosen, Phys. Plasmas **3**, 1803 (1996).

30. G. B. Zimmerman and W. L. Kruer, Comments Plasma Phys. Control. Fusion **2**, 51 (1975); J. A. Harte *et al.*, *ICF Quarterly Report: Special Issue: Computational Advances in ICF*, 150, Lawrence Livermore National Laboratory, Livermore, CA, Report UCRL-LR-105821-96-4 (1996).

Zirconia-Coated-Carbonyl-Iron-Particle–Based Magnetorheological Fluid for Polishing Optical Glasses and Ceramics

Introduction

Zirconia (ZrO_2) is a hard polishing abrasive used in conventional polishing of hard and soft glasses.[1] Monoclinic zirconia is the preferred crystalline form for glass polishing, although cubic zirconia is also used. Excellent removal rates and surface roughness values have been reported[2] for polymer [poly(arylene) ether] using 50 nm of zirconia in comparison to ceria (CeO_2), silicon oxide (SiO_2), and tin oxide (SnO_2). Fused silica (FS) polished with zirconia has been shown to leave surfaces that, upon laser damage testing in the UV and at 355 nm, exhibit superior damage resistance compared to surfaces polished with other abrasives.[3,4] Applications for such surfaces exist in UV/DUV/EUV lithography for the semiconductor wafer industry and in research laboratories that explore inertial confinement fusion. A polishing slurry consisting of a blend of zirconia and fumed silica was recently found to be optimal for chemical mechanical polishing (CMP) of a tetraethyl orthosilicate (TEOS) layer on a silicon wafer.[4,5] The advantages of using loose zirconia abrasives in conventional polishing are summarized by Menapace *et al.*[6]

Magnetorheological finishing (MRF) is a novel polishing technology that uses a magnetorheological (MR) fluid consisting of micron-sized magnetic carbonyl iron (CI) particles in an aqueous medium containing a nonmagnetic polishing abrasive like CeO_2 or nanodiamonds. MRF was commercialized in 1997 by QED Technologies[7,8] and is considered to be an excellent, deterministic process for finishing optics to high precision. A variety of computer numerically controlled (CNC) machines and MR fluids are used throughout the world on a regular basis.

In this article we report on a new development in MRF—a zirconia-coated magnetic CI powder. The coated CI particles are produced via a sol-gel synthesis process that has been scaled to kilogram (kg) quantities. The uniqueness of the MR fluid composition manufactured from this coated powder is twofold: first, free zirconia nanocrystalline abrasives are produced during the CI coating process, resulting (with the simple addition of water) in a self-polishing, abrasive-charged MR fluid for polishing; and second, the zirconia layer protects the CI particles from aqueous corrosion.

A zirconia-coated-CI–based MR fluid was designed, prepared, and circulated in an experimental MRF platform for a period of nearly three weeks with no signs of degradation or corrosion. A variety of optical glasses spanning a range of hardness values were tested, as well as several polycrystalline optical ceramics. In the following sections we briefly review MRF, MR fluids, and the issues of stability and corrosion. We then describe our zirconia-coated magnetic CI particle work and polishing experiments that validate the performance of this novel MR fluid.

Background

1. Magnetorheological (MR) Fluid

MR fluids are the key element of MRF technology.[9,10] In general, MR fluids consist of uniformly dispersed noncolloidal magnetic particles, e.g., CI, in a carrier fluid. Properties like plasticity, elasticity, and apparent viscosity change with the application of a magnetic field. A typical MR fluid for MRF applications[11] is compatible with most optical substrates, providing relatively high removal rates and acceptable smoothing for precision optics applications, without the risk of scratching the workpiece surface with oversized abrasive particles, as may happen with a solid lap. Material removal is accomplished primarily by nonmagnetic abrasive particles incorporated in the MR fluid. Two current commercial options are either cerium oxide (CeO_2) or nanodiamonds. "The choice of nonmagnetic abrasive material is dictated by the physical properties (e.g., hardness) and chemical properties (e.g., chemical durability) of the workpiece to be finished."[11]

2. MRF Technology

MRF is a subaperture polishing process. For a conventional MRF setup, the MR fluid is pumped through a delivery system and ejected through a nozzle in the form of a ribbon onto a rotating vertical wheel. The ribbon stiffens upon passing into a region with a high magnetic field in the vicinity of the

workpiece. The MRF removal function is characterized by a D-shaped polishing spot in the zone of contact between the ribbon and the workpiece,[12] and the material removal rate is determined by the time of contact (e.g., dwell time) as well as other process and workpiece parameters.[9,13] The temperature of the MR fluid is controlled by a chiller normally set to ~20°C.

Shorey *et al.*,[13] DeGroote *et al.*,[12] and, most recently, Miao *et al.*[14] have reported on experiments performed on an MRF platform designated as a spot-taking machine (STM) with characteristics similar to those of a conventional MRF machine. The STM is limited to partial motion up and down into the MR fluid ribbon, under computer control, but without workpiece rotation capabilities. This permits one to take only MRF spots on a part. The STM fluid delivery system uses peristaltic pumps to limit exposure of the MR fluid to mechanical parts. The pump flow rate is thus slower in comparison to the centrifugal pumps used in many commercial MRF machines, but this configuration allows one to test different types of fluid compositions without the risk of damaging the fluid delivery system. The STM was used for all of the work reported here.

3. Stability of MR Fluids

The MRF removal function is very sensitive to the stability of the MR fluid. Changes in MR fluid properties can reduce the determinism of MRF over time (the nominal life time of a standard MR fluid is ~2 weeks compared to 3 to 4 months with a polyurethane polishing pad[15]). Stabilizers such as glycerol may be added[11] to improve fluid stability (i.e., control viscosity and keep both magnetic and nonmagnetic particles in suspension). For glass polishing, however, an excess amount of glycerol inhibits the water hydration at the workpiece surface that is needed to soften the glass surface.[16]

Even though the MR fluid has only limited exposure to the atmosphere, it can still absorb carbon dioxide, which lowers the pH of the fluid and contributes to the oxidation of CI.[11] Corrosion may cause the MR fluid to change its compositional properties, which subsequently result in an unpredictable MRF removal function. Using deionized (DI) water as the carrier fluid provides only a limited solution to the problem. The use of buffers such as sodium carbonate (Na_2CO_3) increases the fluid pH to ~10, resulting in a more-stable fluid. Na_2CO_3 reduced the corrosion problem sufficiently to make possible the development of a commercial MR fluid for MRF.[11]

Schinhaerl *et al.*[17] studied the stability of a commercial CeO_2-based MR fluid over a period of 6 weeks in terms of the fluid density and pH. They found that the fluid density (~3.6 kg/liter) was essentially unchanged over the course of 6 weeks and therefore was not a good indication of fluid stability/viability. The fluid pH decreased from ~11 after preparing the fluid (i.e., mixing the solids and the liquids) to ~9.6 after 3 days of circulating in the MRF machine. The reduction in pH was attributed to exposure to air (i.e., on the wheel, where the MR fluid ribbon was formed). The fluid was continuously collected off the wheel and pumped back into the fluid reservoir with very little additional change in pH over 6 weeks of use (without replenishing the fluid during the experiment). Removal rates for an N-BK7 flat disk dropped by ~50% from ~4.9 μm/min to ~2.4 μm/min after 6 weeks, but the resulting surface roughness was unchanged.

In a more recent study, Schinhaerl *et al.*[18] compared five different commercial diamond- and CeO_2-based MR fluids. The removal rate was studied for soft, medium, and hard optical substrates (SF57, N-BK7, and quartz, respectively). As expected, the removal rate scaled inversely with material hardness. Per Ref. 18, "The harder the material, the lower the removal rate. Diamond fluids cause a higher material removal (than) cerium oxide–based fluids." Each fluid exhibited a different flow rate, which was associated with different CI particle dispersion characteristics and/or different concentrations of CI. This may have had an effect on the resulting material removal characteristics (e.g., smoothness and amount of material removed).

4. Purposefully Modified MR Fluids for Unique Materials

A water-based MR fluid is used for most optical finishing applications. The commercial MR fluids contain nonmagnetic abrasives such as CeO_2 (C10) and diamonds (D20, D10, and D11) to enhance material removal and to control final surface roughness for a wide range of optical materials.[7] The development of modified fluid compositions that are compatible with a wider range of optical materials is summarized in this section.

Water-soluble crystals have important applications in optics. One example is potassium dihydrogen phosphate (KDP/KH_2PO_4), whose solubility is ~21.7 g/100 g of water at room temperature.[19] KDP is the only nonlinear, single-crystal electro-optical material that can be grown in sizes large enough for use as a switch or as a frequency converter in solid-state lasers that investigate inertial fusion, such as the OMEGA and OMEGA EP lasers at the University of Rochester's Laboratory for Laser Energetics (LLE) and the National Ignition Facility (NIF) at Lawrence Livermore National Laboratory

(LLNL). Arrasmith *et al.*[20] showed that a nonaqueous MR fluid, composed of 40-vol % CI, 0.05-vol % nanodiamonds, and ~60-vol % dicarboxylic ester (DAE), when used as the carrier fluids could successfully polish a previously diamond turned KDP part to an rms surface roughness of ~2 nm, removing all diamond-turning marks.

Substituting the conventional nonmagnetic abrasives in an MR fluid (i.e., CeO_2 or nanodiamonds) with other commercial polishing abrasives may result in improved surface smoothing of relatively soft materials. DeGroote *et al.*[21] reported on the use of 200-nm–sized monoclinic zirconia powder for smoothing surfaces of the polymer PMMA.

Kozhinova *et al.*[22] showed that an MR fluid containing mechanically soft CI (~4-μm diameter)[13] and alumina abrasives could yield improved surface roughness for chemical vapor deposition (CVD) polycrystalline zinc sulfide (ZnS). This chemically altered MR fluid composition also showed no significant dependence on the initial surface preparation (single-point diamond turning, pitch polishing, or deterministic microgrinding).

Zirconia Coating of CI Powders

Many coating and surface treatments applied to CI particles for use as MR fluids in industrial applications (e.g., vibration dampers,[23] clutches,[23] and actuating modules[24]) have achieved the following benefits: improved sedimentation stability, improved dispersability, improved oxidation and corrosion resistance, and stability at higher solids concentrations. Coating media that have been explored include nonmagnetic metals, ceramics, high-performance thermoplastics, thermosetting polymers, polyvinyl butyral,[25] polystyrene nanospheres,[26] silicon,[27] phosphates,[28] metal oxides like silica and zirconia, and combinations of some of the above.[29] Enhancement of the particle surface with nitrogen has also been reported.[30] Of the many coating application methods employed, the sol-gel method has often been used because it is suited to a variety of materials and offers excellent process control.[31–33]

Here we report on zirconia coating of CI [$d_{50} \sim 1.1$ μm (Ref. 34)] for MRF via a sol-gel technique. The synthesis process was successfully demonstrated to produce a thin layer of zirconia on the CI particle surface. The zirconia sol (pH ~ 1) was prepared at room temperature using a zirconia butoxide precursor and nitric acid as discussed in detail by Shen *et al.*[35] for batches of CI up to 50 g. In this work a modified synthesis protocol made it possible to coat kilogram quantities of CI by minimizing the total volume of solvent used, i.e., coating the maximum amount of CI in as little water as possible. This approach allowed us to increase the amount of solids in a batch (~200 g per batch) and minimize the number of batches needed to produce >3 kg of coated particles in less than 10 days. The synthesis procedure is further detailed in Appendix A.

1. Characterization

Characterization of CI in terms of coated particle surface morphology, density, particle-size distribution, and corrosion resistance under accelerated acidic conditions is discussed in this section. A brief description of the instrumentation used for particle characterization is also provided.

a. Morphology, size, and surface properties. Scanning electron microscopy (SEM) was used to obtain morphological data for uncoated and coated CI particles. Measurements were made with a thermal field-emission–type SEM (resolution 1.3 to 2.1 nm at 15- to 1-kV acceleration voltage, respectively).[36] Two types of samples were observed: free particles (uncoated and coated) and cross-sectioned particles (uncoated and coated). The technique for preparing particle cross sections using MRF is described in Appendix B.

Figure 120.36(a) shows uncoated CI particles ranging in size from ~0.5 to 2 μm. This distribution of particle sizes was consistent with the manufacturer's CI powder particle size distribution data [$d_{10} = 0.5$, $d_{50} = 1.1$, and $d_{90} = 2.2$ μm (Ref. 34)]. The particles are spherical and their surfaces are relatively smooth. Figure 120.36(b) shows a cross-sectional SEM image of uncoated particles, identifying three particles with particle size ranging from ~1 to 1.3 μm. No surface layers are apparent.

A coated CI particle (size ~1.4 μm) is shown in Fig. 120.36(c). There is a thin, rough zirconia layer over the particle surface. The top of this layer consists of overlapping nanocrystallites of faceted zirconia, ~50 to 100 nm in size. The cross-sectional SEM image of a coated particle reveals the coating to be continuous, with a thickness of 5% to 15% of the uncoated particle diameter [see Fig. 120.36(d), where the particle size is ~1.1 μm and the coating thickness is ~100 nm]. We hypothesize from this preliminary observation that the coating process does not increase the overall particle size of the powder by more than 5% to 15%.

Figure 120.36(e) shows nanocrystalline zirconia crystals adjacent to a coated CI particle. These free zirconia crystals are co-generated out of the precursor used during the synthesis process (see Appendix A). The crystals are relatively uniform in size (nominal size 10 to 50 nm). The crystals appear to exist

as agglomerates in this image. We hypothesize that within the environment of the STM delivery system (i.e., under mixing and shear) these agglomerates rapidly break up, producing a nanocrystalline, free zirconia-charged MR fluid for polishing. Attempts were made to separate the dried zirconia-coated CI powder into magnetic and nonmagnetic fractions, but these attempts failed. Zirconia coating and free zirconia crystals were identified by Shen *et al.*[35] using energy-dispersive x-ray spectroscopy (EDX) techniques, which agree with other work[37] on zirconia synthesis at low temperatures. From this point onward the term "zirconia-coated CI" refers to both the coated CI particles and the co-generated free nanocrystalline zirconia abrasives as one unit.

The faceted coating texture of the coated CI particles may also explain why the initially grey, uncoated CI powder appears black after processing. Zirconia powders are known to be white to off-white in color.[38] Roughening via light trapping to enhance absorption of visible light has been reported for single-crystal silicon in solar energy applications.[39] The silicon wafer's surface turns from metallic grey to black in appearance. We believe that this absorption phenomenon is manifest for our coated CI particles.

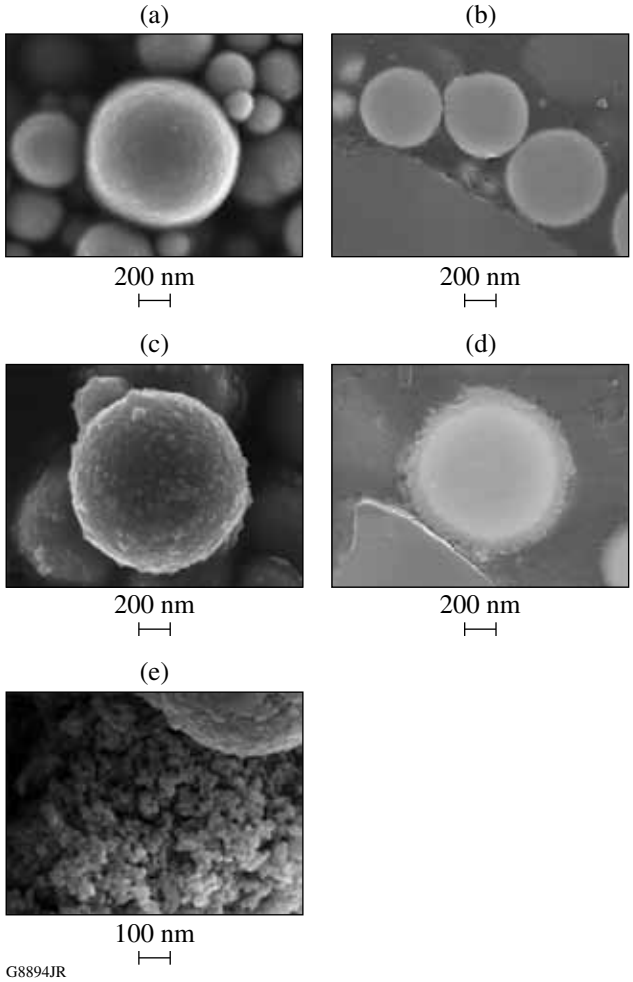

Figure 120.36
SEM images of uncoated CI (a) and zirconia-coated CI (c) and their cross sections [(b) and (d), respectively]; (e) free zirconia nanocrystals.

Contact angle testing was performed with a video microscope system[40] to investigate the affinity of the CI powder for water. Uncoated and coated CI powder samples were prepared as ~100-μm-thick dry films on glass microscope slides by a simple hand pressing/compacting process. A single drop of DI water (~4 μL) was placed on each film surface and viewed in the microscope. For both powder samples, the first drop was absorbed. However, when a second drop was deposited on the surface of the uncoated powder film at the same location, it resulted in a preserved drop whose contact angle was ~90°. Only with the deposition of four drops was it possible to measure a contact angle for the coated powder film, and the resulting contact angle was found to be ~12°. This test was repeated at several randomly chosen locations for each powder film with the same results. We conclude that the initially uncoated CI powder is hydrophobic and becomes hydrophilic after the sol-gel zirconia treatment process is applied.

b. Density. Density measurements were performed using a gas (helium) pycnometer at room temperature.[41] A sample of uncoated or coated CI powder was placed in a 1-cm^3 sample cup (stainless steel, provided by the manufacturer) and baked in vacuum (~432 mm Hg) at ~100°C for ~30 min. The sample was transferred to a desiccator and cooled down to room temperature before being measured. This minimized exposure to the atmosphere (~33% relative humidity). The density of uncoated CI was 7.68±0.04 g/cm^3 (average of 4 samples measured), a value consistent with that reported by the manufacturer (>7.5 g/cm^3 from Ref. 34). The density of the zirconia-coated CI was 6.72±0.07 cm^3 (average of 26 samples from eight 200-g batches). [The density of monoclinic zirconium oxide (ZrO_2) is ~5.7 g/cm^3].[42]

2. Accelerated Corrosion Resistance Test

Aqueous corrosion tests were conducted for uncoated and coated CI powders to provide a qualitative indication of coating coverage over the particle surface and to detect variations from batch to batch. Corrosion tests were conducted by preparing small batches of MR fluid, where each batch contained a mixture of 5 mL of an acetic acid–based aqueous solution (pH 4.4) and 1 g of CI particles (uncoated or coated). Each batch was stirred using a magnetic stirrer on a magnetic hot plate set

to 200 rpm and 30°C. While stirring, a 0.2-ml sample of the batch was extracted with a digital EDP rapid charger pipette (Rainin Instrument Co.) at intervals of 2, 5, 10, 20, 30 min, up to 1 h and then every several hours for up to 22 days. Extracted samples were deposited on a paper towel. The coloration of the towel provided a qualitative indication of the onset of corrosion.

Results are shown in Fig. 120.37(a) for the uncoated CI powder. A yellow/brownish-orange color was observed for the sample extracted from the acidic environment after 5 min. This coloration is consistent with that of goethite (FeOOH), a known product of corrosion.[43] Figure 120.37(b) shows the results obtained for samples taken from one batch of zirconia-coated CI. No corrosion products were observed, even after 530 h (22 days), at which time the test was terminated. Similar results were obtained for seven additional batches under the same testing conditions, suggesting that the coating completely covered the CI particles. Thermal gravimetric analysis in air at temperatures above 300°C (Ref. 35) showed improved resistance against oxidation for the zirconia-coated CI particles, supporting the qualitative results of this corrosion test.

(a)

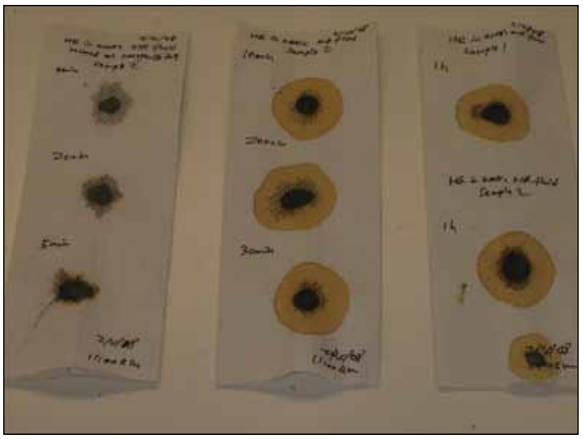

(b)

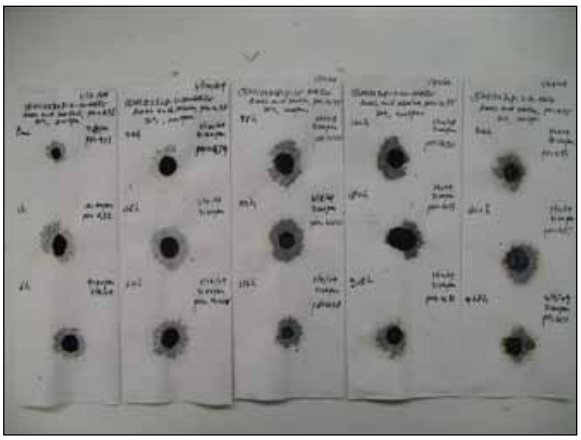

G8895JR

Figure 120.37
Images from a corrosion towel test: (a) uncoated CI up to ~1 h; (b) zirconia-coated CI up to ~530 h.

3. Design and Preparation of a Zirconia-Coated-CI-Particle–Based MR Fluid

Maximum removal rates are achieved for MR fluids whose magnetic CI particle concentrations are high. However, increasing the magnetic particle solids concentration also causes a rise in the out-of-field viscosity of the MR fluid. Off-line composition studies are required to determine how much CI can be incorporated into a carrier liquid without causing pump failure of the fluid delivery system. This section describes the development of high-solids-concentration, coated-CI-composition MR fluid using viscosity measurements and the techniques used to prepare a larger batch for experiments in the STM.

a. Viscosity. Off-line viscosity measurements were performed using a cone and plate–style viscometer, temperature stabilized at 25±0.5°C (Ref. 44). Several 15-ml batches of coated CI powder in DI water were prepared with solids concentrations of 35 vol % and 40 vol %. The coated powder was added to DI water in a series of small portions without any other dispersing agents. Hand shaking was performed for a portion, followed by high shear mixing at approximately 25,000 rpm for 5 min. This procedure was repeated in increments to elevate the solids concentration. Uniformly dispersed slurries were ultimately produced. Shortly after mixing, a 0.5-ml sample was extracted from a batch and injected into the viscometer for measurement. Viscosity as a function of shear rate from 50 s^{-1} to 1000 s^{-1} was recorded.

With this instrument it was not possible to measure the viscosity of a 40-vol %-coated-CI-particle MR fluid. Successful measurements were obtained at a 35-vol % solids concentration, where the fluid exhibited shear thinning behavior. Because the shear rate of the MR fluid leaving the nozzle of the STM was ~800 s^{-1}, attention was focused on the MR fluid viscosity at this shear rate. The 35-vol %–coated CI particle's viscosity at 800 s^{-1} was found to be 110±11 cP (average of three separate measurements). For comparison, 50-ml samples of commercial ceria–based and nanodiamond-based MR fluids were prepared and evaluated under identical conditions. Their viscosities at a shear rate of 800 s^{-1} were found to be 89±2 cP and 111±13 cP, respectively. It was concluded that a water–based, 35-vol %-solids-concentration, coated-CI-particle MR fluid could be successfully pumped and circulated in the STM.

b. MR fluid preparation. Using our synthesis process, we successfully produced >4 kg of zirconia-coated CI powder. However, only ~2.3 kg of powder was needed to prepare a sufficient volume of MR fluid (i.e., 1 liter) to begin tests on the STM. The composition that was prepared is given in Table 120.II.

Table 120.II: Composition of MR fluid based on zirconia-coated CI.

Component	Density (g/cm^3)	Mass (g)	Vol. (mL)	Vol %	Mass %
ZrO_2-coated CI	6.7	2345	350	35	78
DI water	1	650	650	65	22
Total		2995	1000	100	100

Incorporation of these hydrophilic particles into an aqueous suspension without the aid of a dispersing agent was difficult. To overcome this difficulty, the coated CI powder was slowly added to the water while mixing at ~1000 rpm (comparable to the mixing speeds used in the STM fluid reservoir) until a uniform slurry (as inspected by eye) was achieved. Then the fluid was transferred into the STM reservoir for continuous mixing while circulating in the STM delivery system in bypass mode for ~30 min before directing the fluid over the STM wheel to form a ribbon. Machine settings while in bypass mode were ~70 rpm for the pump and ~1000 rpm for the mixer, whereas after the fluid was directed over the wheel, the pump speed was increased to ~115 rpm, the mixer speed was unchanged, the wheel was set to rotate at ~200 rpm, and the electric current to the magnet was set at ~15 A (resulting in an ~2-kG fringing field strength). The resulting ribbon height was ~1.5 mm, which was kept constant by adjusting the pump speed as needed. Throughout the spotting experiment described on p. 199, constant part immersion at a depth of ~0.3 mm was used for all tested materials. Unless specified, all machine operating conditions were kept constant throughout the experiment.

Spotting Experiment

In this section we introduce the materials used for spotting experiments and the metrology used to characterize these samples [the MRF platform was discussed in **MRF Technology** (p. 190)]. Most samples were prepared from commercial materials.

1. Substrate Materials

A wide range of optical glasses and hard ceramics were chosen for this study. Table 120.III lists these materials in order of increasing hardness, separated by type (i.e., glasses and ceramics). The optical glasses represent a wide range of glasses spread over the entire glass table. The polycrystalline ceramics are of interest in military[48] applications such as windows and domes as well as in other commercial applications.

Samples were prepared by LLE's Optical Fabrication Shop. Glass substrates were first ground with 40, 20, and 9 μm of Al_2O_3 (Ref. 49) on a cast iron backing plate and then polished with CeO_2 (Ref. 50) on a pitch[51] lap. Ceramic substrates were ground with diamonds (6 μm)[52] on a glass backing plate. The glass plate had grooves to promote diamond distribution and to reduce scratches. The ceramic substrates were polished with diamonds (0.5 μm)[53] on pitch.[51] ZnS was ground with 40, 20, and 9 μm of Al_2O_3 (Ref. 49) on a glass tool. The ZnS was polished on a tool made of 10% beeswax and 90% #73 Gugolz with a mixture of 50% Praxair A (0.3 μm) Al_2O_3 and 50% Syton HT-50 colloidal silica (from Ref. 22). Initial surface roughness data for all polished parts are tabulated in Table 120.III.

2. Metrology

The sample surface figure and spot shape after MRF processing were examined using a laser interferometer.[54] Valid data for spots required spot depths less than ~0.2 μm; otherwise, dropout occurred and no data could be collected. Alternatively, we used a white-light interferometer[55] equipped with 1× objective for spots deeper than 0.2 μm. The field of view for this instrument and objective was 14.7 mm by 10.7 mm.

A white-light interferometer[46] equipped with a 50× Mirau objective, which provided a 350 × 350-μm measurement area, was used to measure surface roughness. The areal rms surface roughness values reported in Tables 120.IV–120.VI represent an average over five measurement sites on the surface of the initially polished samples or within the depth of deepest penetration (ddp) for each spot. The lineout rms surface roughness values reported in these tables represent an average of 500 profiles (100 per areal measurement automatically distributed by the software) within the area of measurement. Within spots, lineouts are taken parallel to the direction of ribbon motion over the part surface to better evaluate smoothing by MRF on a nonrotating part (see Ref. 47 for further discussion).

Results and Discussion

Three silicate glasses—S-BSL-7, BK-7, and FS—were used as baseline materials for the experiment. Removal rates and roughness values were recorded for these glasses over time as out-of-field MR fluid viscosity was purposefully altered. All results are presented in a table and selected data are plotted. Spot-polishing results at a fixed viscosity for all glasses and the ceramics are then tabulated and examined as a function of material hardness. Finally, we comment on the evolution of

Table 120.III: Substrate materials used for the experiment, in order of increasing hardness and separated by type (i.e., glasses and ceramics)[a].

Material ID	Source	Dimensions ∅ × h (mm)	ρ (g/cm^3)	Tg (°C)	E (GPa)	Poisson's ratio v	Vickers hardness at 200 gf (GPa)[b]	Fracture toughness K_c (MPa m$^{1/2}$)[b]	Initial areal rms (nm)[c]	Initial line rms (nm)[d]
Glasses										
S-FPL 53	OHARA (FCD 100 HOYA Equiv.)	47.3 × 7.7	3.63	436	69.4	0.302	3.75	0.52	1.13±0.03	0.28±0.02
KzFS N4	SCHOTT	48.9 × 7.8	3.2	492	60	0.29	3.8	--	1.26±0.04	0.29±0.02
LHG 8	HOYA	38.8 × 11.1	2.83	485	62	0.26	4.01	0.5	0.89±0.08	0.22±0.02
S-PHM 52	OHARA (PCD 4 HOYA Equiv.)	50.3 × 9.3	3.67	587	71.5	0.292	4.4	0.49	0.80±0.05	0.20±0.01
PBM 2Y	OHARA	50.2 × 7.7	3.61	436	57.1	0.223	4.6	0.66	2.12±0.44	0.48±0.07
S-NPH 2	OHARA	50.3 × 7.8	3.58	650	99.1	0.249	5.1	0.58	2.19±0.15	0.37±0.10
S-FSL 5	OHARA (FK 5 SCHOTT Equiv./ FC 5 HOYA Equiv.)	50.3 × 9.5	2.46	500	62.3	0.227	5	0.63	4.11±1.50	0.74±0.90
S-LAL 10	OHARA (LaK 10 SCHOTT Equiv./LaC 10 HOYA Equiv.)	50.2 × 7.8	3.98	674	103.9	0.288	5.5	0.8	0.74±0.04	0.18±0.01
S-NBM 51	OHARA	50.3 × 7.9	2.93	554	81.7	0.243	6.25	0.84	1.13±0.07	0.25±0.02
S-TIH 6	OHARA (SF L6 SCHOTT Equiv./ FD 60 HOYA Equiv.)	50.2 × 7.8	3.37	604	93.1	0.261	6.3	0.63	1.53±0.22	0.31±0.40
S-BAL 35	OHARA (SK 5 SCHOTT Equiv./ BaCD 5 HOYA Equiv.)	49.9 × 7.9	3.31	669	83.2	0.25	6.7	0.86	1.14±0.06	0.25±0.03
S-BSL 7	OHARA (BK 7 SCHOTT Equiv./ BSC 7 HOYA Equiv.)	60.1 × 11.8 (50.2 × 7.9)	2.52	576	80	0.205	6.9	0.86	0.79±0.01	0.21±0.01
S-LAH 64	OHARA (LaF N 21 SCHOTT Equiv./TaF 4 HOYA Equiv.)	50.3 × 9.6	4.3	685	122.4	0.294	8.5	1.08	0.68±0.06	0.44±0.02
BK 7	SCHOTT	39.9 × 19.6	2.51	559	81	0.208	8.58	0.8	1.05±0.04	0.25±0.01
FS	CORNING	50.0 × 9.6	2.201	1090	72.7	0.16	9.45	0.7	0.74±0.02	0.21±0.00
TAFD 5	HOYA	52.2 × 11.1	4.92	670	125.9	0.3	11.27	1.54	0.62±0.08	0.15±0.00
Polycrystalline Ceramics										
Material ID	Source	Dimensions ∅ × h (mm)	ρ (g/cm^3)	Grain size (μm)	E (GPa)	Poisson's ratio v	Vickers hardness at 500 gf (GPa)	Fracture toughness K_c (MPa m$^{1/2}$)	Areal rms (nm)	Line rms (nm)
CVD ZnS[f]	NA	40.4 × 6.5	4.09	~3–8	96.5	0.41	3.47	0.8	1.22±0.12	0.26±0.03
Spinel	TA&T Optical Ceramics Div.	35.1 × 2.1	3.58	100–200	273	0.26	13.63	2.07	1.78±0.67	0.22±0.03
ALON	SURMET	46.1 × 10	3.681[e]	150–250[e]	334	0.24	15.77[e]	2.837[e]	2.83±0.48	0.39±0.06
PCA[g]	CERANOVA	38.0 × 2.1	3.99[e]	~0.3[e]	400	--	21.84[e]	3.3[e]	2.90±0.10	0.65±0.05
CVC SiC[h]	Trex	39.7 × 40.8 × 12.7	~3.2	5–15	456	0.21	27.9585	3.39	2.88±0.13	0.49±0.04

[a]Literature values (unless otherwise specified).
[b]Data from Lambropoulos *et al.*[45]
[c]Areal roughness was measured using a white-light interferometer[46] equipped with a 50× Mirau objective, which provided a 350- × 350-μm measurement area. The areal rms surface roughness represents an average of five measurement sites on the surface of the prepolished samples or within the depth of deepest penetration (ddp) for each spot.
[d]Lineout rms surface roughness represents an average of 500 profiles (100 per areal measurement automatically distributed by the software) within areal measurements.
[e]Data from Shafrir *et al.*[47] (unless otherwise specified).
[f]Zinc sulfide (ZnS) standard grade (see Table 5.3 in Ref. 48).
[g]CeraLumina™ polycrystalline alumina (PCA) disks were provided by CeraNova Corporation. Development of this material by CeraNova is funded by NAVAIR through the U.S. Government SBIR program; SBIR data rights apply.
[h]Rectangular part.

Table 120.IV: Results for spotting experiment on baseline glasses S-BSL-7, BK-7, and FS obtained over 18 days with a zirconia-coated-CI-particle–based MR fluid (for measurement conditions, see **Metrology**, p. 195).

	Material ID	Fluid pH	Viscosity (cP)	MRR (μm/min)	Areal rms (nm)	Line rms (nm)	Number of spots
Day 1	S-BSL 7	7.3	97	1.95	1.06±0.10	0.25±0.02	1
	S-BSL 7	7.3	87	1.845	1.17±0.12	0.25±0.01	1
	S-BSL 7	7.2	72	1.59±0.04	1.15±0.09	0.26±0.03	4
	FS	7.2	72	0.73±0.03	0.97±0.08	0.25±0.01	2
Day 2	S-BSL 7	7.2	53	1.62±0.05	1.40±0.37	0.26±0.02	4
	FS	7.2	53	0.765	0.90±0.06	0.23±0.01	1
Day 3	BSL7	8.3	51	2.06±0.04	2.21±1.38	0.37±0.29	2
Day 4	BSL7	8.4	51	2.06±0.11	1.71±0.86	0.28±0.03	2
Day 9	S-BSL7	8.3	51	1.965	1.35±0.22	0.25±0.02	1
	BK 7		51	2.22	1.95±0.52	0.27±0.03	1
	BK 7		70	2.835	2.54±0.58	0.77±0.50	1
	FS		70	1.365	1.47±0.17	0.35±0.02	1
Day 10[(a)]	S-BSL7	8.4	51	2.1	1.67±0.94	0.37±0.23	1
	BK 7		51	2.445	1.11±0.09	0.25±0.02	1
	S-BSL7		70	2.61	1.23±0.31	0.23±0.01	1
	BK 7		70	2.88±0.17	MISSING	MISSING	2
	FS		70	1.275	1.04±0.14	0.30±0.06	1
Day 11	S-BSL7		70	2.89±0.16	1.11±0.06	0.42±0.35	2
	S-BK7		70	2.96	1.40±0.24	0.24±0.01	1
	FS		70	1.47	1.06±0.11	0.25±0.03	1
Day 16	S-BSL7	8.3	70	3.20	1.30±0.21	0.25±0.01	1
	S-BSL7		90	3.96	1.11±0.04	0.26±0.02	1
Day 17[(b)]	S-BSL7	8.3	90	4.10±0.10	1.21±0.22	0.26±0.03	5
	FS		90	1.92±0.06	1.07±0.21	0.24±0.02	5
Day 18	S-BSL7	8.2	90	3.75	1.04±0.07	0.24±0.01	1
	FS		90	1.95	0.88±0.04	0.24±0.02	1
	S-BSL7		70	3.36	1.09±0.13	0.24±0.01	1
	FS		70	1.68	0.86±0.04	0.23±0.03	1
	S-BSL7		50	2.72	1.08±0.26	0.22±0.00	1
	FS		50	1.28	0.88±0.04	0.24±0.01	1

[(a)]At the end of day 9, 250 mL of zirconia-coated-CI-particle–based MR fluid (40-vol % solid content with DI water) were added to the fluid vessel.

[(b)]A total of 3.3 g of nanodiamonds were added to the fluid (increments of 0.8 g).

Table 120.V: Results for spotting experiment on optical glasses obtained over 2 days with a zirconia-coated-CI-particle–based MR fluid (for measurement conditions, see **Metrology**, p. 195).

	Day 1: Viscosity ∼ 72 cP, pH ∼ 7.3				Day 2: Viscosity ∼ 53 cP, pH ∼ 7.4			
Material ID	MRR (μm/min)	Areal rms (nm)	Line rms (nm)	Number of spots	MRR (μm/min)	Areal rms (nm)	Line rms (nm)	Number of spots
S-FPL 53	12.84	1.87±0.53	0.26±0.01	1	13.44±1.19	1.70±0.48	0.27±0.00	2
KzFS N4	6.24	1.86±0.08	0.36±0.07	1	5.73	1.73±0.24	0.29±0.02	1
LHG8	3.012	1.69±0.34	0.21±0.05	1	3.9	1.21±0.40	0.21±0.02	1
S-PHM 52	7.68	1.14±0.06	0.20±0.01	1	6.48	1.06±0.21	0.20±0.01	1
PBM 2Y	2.976	1.94±0.22	0.33±0.04	1	2.85	2.43±1.23	0.32±0.03	1
S-FSL 5	2.112	1.18±0.07	0.26±0.02	1	1.92	1.36±0.40	0.27±0.02	1
S-NPH 2	7.68	1.71±0.06	0.25±0.01	1	6.87	2.95±1.00	0.33±0.04	1
S-LAL10	4.272	1.98±0.14	0.37±0.06	1	3.795	1.33±0.08	0.33±0.08	1
S-NBM 51	2.82	1.63±0.12	0.29±0.02	1	2.715	1.33±0.08	0.26±0.02	1
S-TiH 6	3.276	1.77±0.12	0.32±0.03	1	3.27	1.60±0.06	0.32±0.05	1
BAL 35	3.072	1.45±0.13	0.31±0.04	1	3.015	1.26±0.23	0.26±0.04	1
S-LAH 64	3.024	1.36±0.18	0.26±0.04	1	2.715	0.99±0.04	0.20±0.03	1
TAFD5	2.832	1.58±0.07	0.29±0.06	1	2.52	0.92±0.10	0.19±0.01	1

Table 120.VI: Results for spotting experiment on polycrystalline ceramics obtained on days 11, 17, and 18 of the experiment with a zirconia-coated-CI-particle–based MR fluid (for measurement conditions, see **Metrology**, p. 195).

	Material ID	Fluid pH	Viscosity (cP)	MRR (μm/min)	Areal rms (nm)	Line rms (nm)	Number of spots
Day 11	ZnS	8.4	70	0.10±0.01	4.50±0.38	3.55±1.09	2
	Spinel			0.02±0.00	56.74±20.89	5.18±2.97	2
	ALON			0.03±0.00	19.05±4.29	2.56±0.52	2
Day 17[(a)]	Spinel	8.3	90	0.65±0.21	105.27±19.08	5.36±3.14	4
	ALON			0.62±0.09	488.3±189.8	20.34±13.14	2
Day 18	Spinel	8.2	90	0.62	18.68±4.19	1.11±0.41	1
	ALON			0.71±0.03	16.09±3.11	1.31±0.39	2
	PCA			0.25	3.87±0.08	0.95±0.07	1
	CVC SiC			0.12	12.94±1.55	2.22±0.34	1
	Spinel	8.2	70	0.68	26.44±9.44	1.84±0.86	1
	ALON			0.56	28.96±9.28	2.29±0.58	1
	PCA			0.21	5.08±0.11	1.18±0.19	1
	CVC SiC			0.09	13.70±0.53	2.19±0.46	1
	Spinel	8.2	50	0.39	20.32±4.58	1.50±0.86	1
	ALON			0.45	22.80±2.96	1.84±0.63	1
	PCA			0.14	5.04±0.18	0.98±0.09	1
	CVC SiC			0.06	11.96±0.70	1.93±0.47	1

[(a)]After a total addition of ∼3.3 g of nanodiamonds to the MR fluid reservoir.

the texture of the zirconia-coated CI particle surface over the life of the experiment.

1. MRF Spotting Results for Baseline Optical Glasses

Peak material removal rates and in-spot rms roughness (areal and lineout) are given in Table 120.IV for spots taken on S-BSL-7, BK-7, and FS over 18 days. Included in this table are the time evolution of MR fluid pH (measured periodically by inserting a probe[56] into the STM fluid reservoir) and out-of field viscosity (reported from flow and pressure sensors present in the STM fluid delivery system) at a shear rate of ~800 s^{-1}.

For ease of discussion, the removal rate data for S-BSL-7 and BK-7 are extracted from Table 120.IV and plotted in Fig. 120.38. The horizontal axis is arranged to track the number of the spot taken, annotated by the elapsed time in terms of the day of the experiment. Measurements of fluid pH and viscosity recorded at the time of spotting are also plotted.

The initial fluid pH after being loaded into the STM was ~7. It rose to pH ~ 8 after 3 days, remaining stable in time until day 18. Within hours on day 1 the initial fluid viscosity dropped from 100 cP to 72 cP, presumably caused by additional mixing. Thereafter, viscosity was easily controlled by the automated dripper on the STM. Viscosity was purposefully adjusted during the course of the experiment to 50 cP on day 2, back to 70 cP on day 10 (by turning off the automated STM dripper), and up to 90 cP at the end of day 16.

Peak material removal rates for S-BSL7 were stable at ~2 μm/min for the first 9 days. A typical 4-s–duration MRF polishing spot taken on day 1 is shown interferometrically in Fig. 120.39. The spot is symmetric in all aspects, with good edge definition along the leading and trailing edges. The lineout through the center of the spot shows a smoothly varying profile. Because MR fluid was lost from going into bypass operation each night, an additional charge of 250 mL (at 40 vol %) was added at the end of day 9. The removal rate followed the increase in viscosity caused by this addition of fluid. The peak removal rate climbed to nearly 3 μm/min at 70 cP from day 10 to day 16, with a further increase on day 16 to 4 μm/min at 90 cP. No additional increase in removal rate for this borosilicate glass was observed with the addition of 3.3 g of loose nanodiamond abrasives on day 17. We hypothesize that since the nanozirconia abrasives are hard compared to this borosilicate glass, the addition of even-harder nanodiamonds has no additional effect on removal. Saturation of the MRF peak removal rate for FS as a function of increasing nanodia-

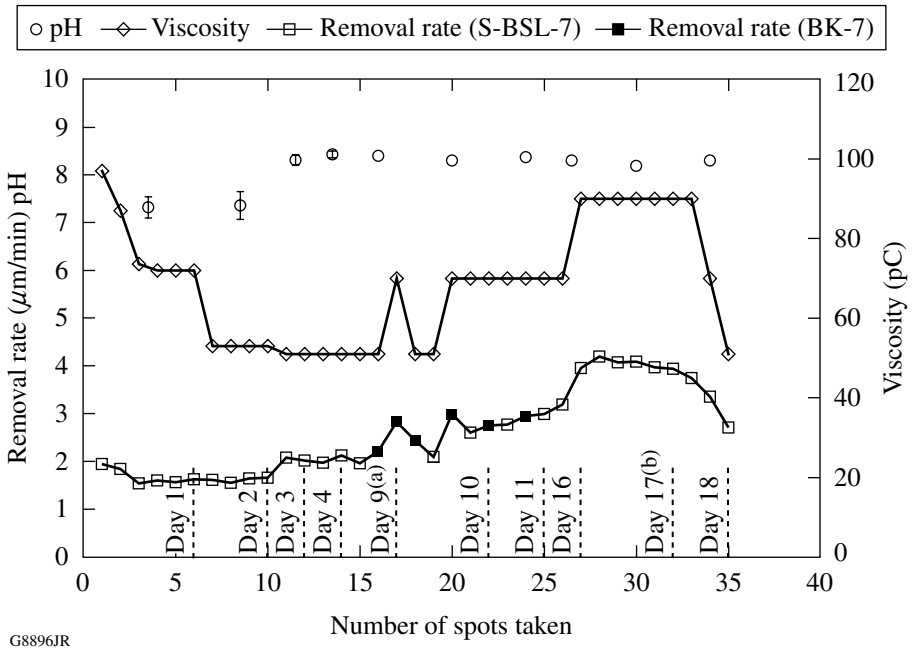

Figure 120.38
Evaluation of coated-CI MR fluid properties (pH and viscosity) and peak removal rates for glasses S-BSL-7 and BK-7 during the spotting experiment. Results are plotted against spot number and elapsed time (days of fluid circulation in the STM). (a) End of day 9: replenishing the fluid with an additional 250 mL (at 40 vol % CI). (b) Day 17: 3.3-g addition of nanodiamonds.

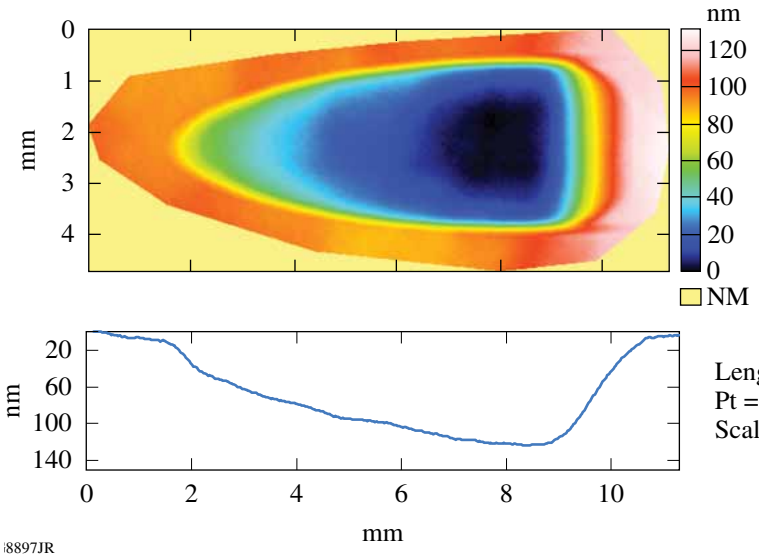

Figure 120.39
A 4-s–duration polishing spot taken on an S-BSL-7 part on day 1, using the coated-CI-particle MR fluid. The 3-D pseudo color image was measured on a white-light interferometer[55] with a 1× objective, giving a field of view of 14.7 mm by 10.7 mm. The lineout taken through the center of the part shows the spot depth to be ~124 nm.

mond abrasive concentration up to ~0.1 vol % was previously reported by Shorey *et al.*[13]

We hypothesize that the free nanozirconia abrasives in the MR fluid play the major role in promoting polishing the part. We are working on devising a method for separating out the nanozirconia particles from the zirconia-coated-CI powder. Such a separation procedure is required to evaluate the polishing behavior of the coated CI particles themselves.

Roughness values measured inside of MRF spots in the region of deepest penetration are given in Table 120.IV. The areal rms roughness data for all three glasses varied between 1.0 and ~1.5 nm throughout the experiment. The lineout rms data varied from 0.2 nm to 0.4 nm. These results are similar to the roughness value given in Table 120.III for the initially pitch polished surfaces, demonstrating the excellent smoothing capability for this zirconia-coated-CI MR fluid.

2. Optical Glass Survey

Additional spots were taken during days 1 and 2 on a variety of glasses with a range of mechanical, thermal, and optical properties. Results are summarized in Table 120.V at fluid viscosities of 53 cP and 72 cP. Areal roughness values were between 1-nm and 2-nm rms, not unlike the initial surface values given in Table 120.III. Again, lineout rms data inside spots were between 0.2 and 0.4 nm, demonstrating good smoothing.

Peak material removal rates are plotted as a function of glass hardness at three viscosities in Fig. 120.40. Soft glasses (H_V < 4 GPa) exhibited removal rates from ~4 μm/min to ~13 μm/min. Glasses increasingly harder than 5 GPa are polished with removal rates from 3 μm/min down to 2 μm/min, even for the hardest glass at 11.5 GPa (TaFD5). The range of glass removal rates given in Table 120.V are commensurate with values reported in the literature for commercial MR fluids used on commercial MRF machines,[57] and for experimental fluids used on the STM (see Refs. 12–13). We observe that our zirconia-coated-CI-particle MR fluid polished glasses over a broad range of hardness values with equal efficiency. In classical polyurethane pad-polishing experiments, Cumbo *et al.*[1] observed that, in comparison to ceria and alumina slurries, monoclinic zirconia was least sensitive to glass type (BK7, SF6, and FS) or slurry fluid chemistry. Our results are consistent with his observations.

3. Spotting Results for Polycrystalline Ceramics

Polycrystalline ceramics were spotted before and after the addition of nanodiamond abrasives. Table 120.VI summarizes the experimental conditions (pH and viscosity), peak material removal rate, surface roughness, and number of spots taken. For soft ZnS, material removal rates were relatively low in comparison to that observed for the glasses at a viscosity of ~70 cP. Inspection of the spots taken on the surface of ZnS indicated that the spot topography was irregular and textured. We conclude that, at pH 8, this zirconia-coated-CI-particle–based slurry is not suitable for polishing CVD polycrystalline ZnS.

Removal rates for hard ceramics ALON and Spinel were negligible at a viscosity of ~70 cP, and therefore other hard polycrystalline materials were not tested at this viscosity. On day 17 we increased the fluid viscosity to ~90 and added 3.3 g

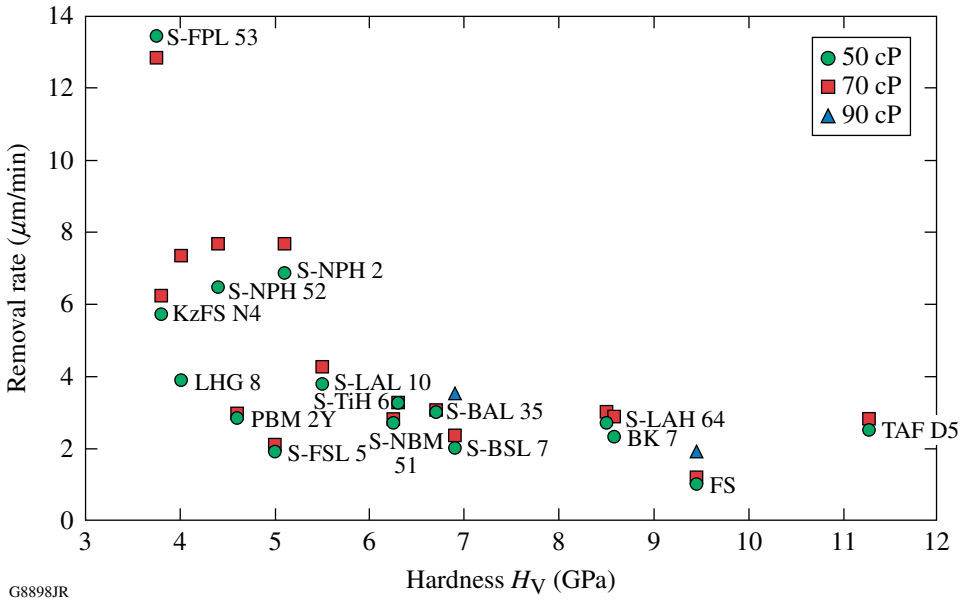

Figure 120.40
Peak removal rates for optical glasses as a function of Vickers hardness for three coated-CI-particle–based MR fluid viscosities. The MR fluid consisted of coated particles and water only.

of nanodiamonds. Material removal rates increased by a factor of ~30 for both materials. A further increase of ~15% in the removal rate for ALON was observed at the beginning of day 18 at 90 cP. Thereafter, fluid viscosity was purposefully reduced from 90 to 70 and finally to 50 cP. Spots were taken on samples of PCA and SiC. Figure 120.41 shows the relationship between removal rate and Vickers hardness at the three viscosities. The intermediate hardness ceramics (i.e., Spinel and ALON) appear to be more sensitive to changes in fluid viscosity than harder ceramics. We have no explanation for this, other than to note the differences in grain size [and possibly grain-size distribution for these materials (see Table 120.III)].

Roughness values measured inside the MRF spots in the region of deepest penetration are given in Table 120.VI. Significant roughening of Spinel and ALON immediately after the addition of 3.3 g of nanodiamonds shown on day 17 improved considerably after the nanodiamonds circulated in the STM delivery system over night (i.e., day 18). On day 18, areal rms surface roughness varied from ~5 nm for PCA to ~22 nm for the intermediate hardness ceramics (i.e., Spinel and ALON). The lineout rms data varied from ~0.9 nm (PCA) to ~2.3 nm (ALON).

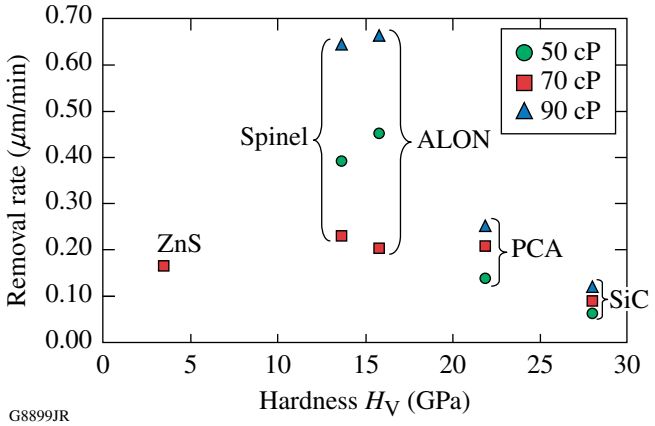

Figure 120.41
Peak removal rates for polycrystalline ceramics as a function of Vickers hardness for three coated-CI-particle–based MR fluid viscosities. The MR fluid consisted of coated particles, loose nanodiamond abrasives, and water.

4. Evolution of Coated-CI Topography Throughout the Experiment

The evolution of coated-CI surface topography throughout the experiment was studied via SEM. Figure 120.42 shows SEM images of zirconia-coated CI particles after different durations of use in the STM delivery system, from 3 to 22 days.

The images indicate that the spherical particles maintain their coated, faceted nanocrystalline zirconia texture even after 22 days of circulation and use. The low magnification images of the particles after 3 days of circulation show that the distribution of particle sizes is between ~0.5 to ~2 μm, a range that is comparable to the published data of uncoated CI used in the synthesis process. This provides additional support to our statement (see **Morphology, Size, and Surface Properties**, p. 192) that the zirconia layer is thin relative to the size of the CI particle and therefore does not change the initial powder-size distribution in a significant way. High-magnification images of the coated particles after use in the STM for 10 and 22 days confirm that the zirconia-coating layer is unabraded and well adhered to the particles.

The persistence of a thin layer of zirconia is further established in Fig. 120.43, which shows several coated-particle cross sections after 22 days of circulation in the STM system. Visual examination of fluid samples extracted from the fluid reservoir were deposited on a paper towel. The coloration of the towel provided a qualitative indication of the onset of corrosion (not shown here). This test showed no evidence of corrosion, suggesting that our sol-gel process effectively coated the CI particles with zirconia and that the coating did not wear under the experiment conditions.

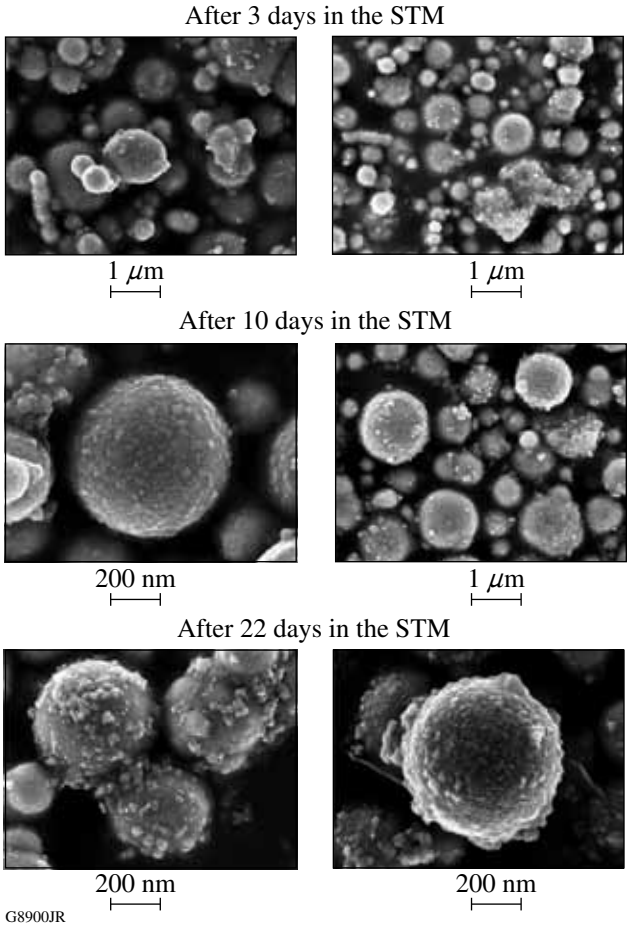

Figure 120.42
SEM images of zirconia-coated CI after being circulated in the STM delivery system for 3, 10, and 22 days, respectively.

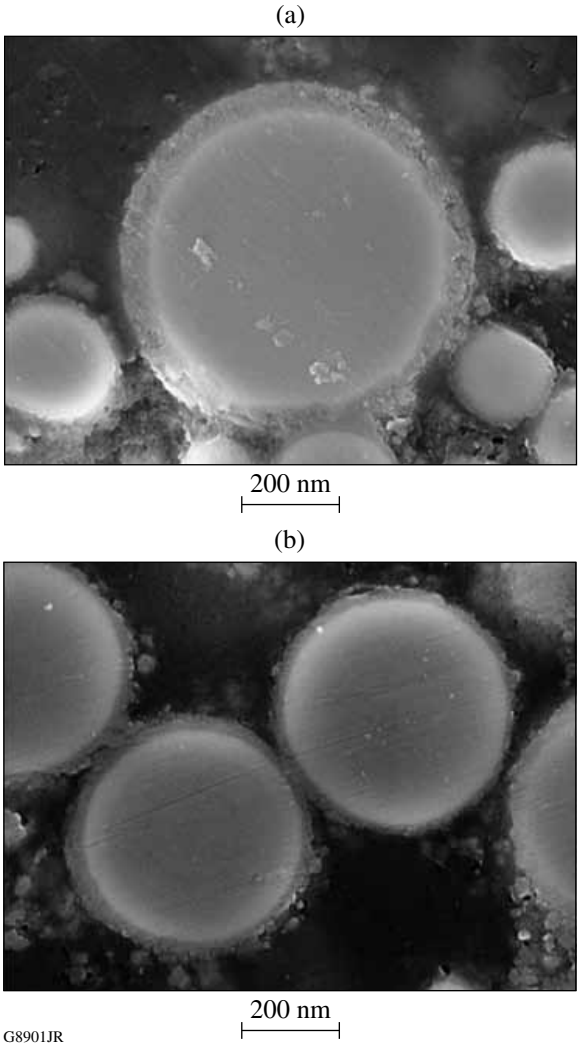

Figure 120.43
SEM cross-sectional images of zirconia-coated CI after being circulated in the STM delivery system for 22 days.

Summary

Here we have reported on a new development in MR fluids for MRF applications. A zirconia-coated-CI-particle–based MR fluid was designed, prepared in kilogram quantities, and circulated using an experimental MRF setup for three weeks with no signs of MR fluid degradation or corrosion. The fluid

composition contained free nanozirconia polishing abrasives generated in the coating process. When mixed with only water, the resulting MR fluid was stable at pH 8 for 18 days. This zirconia-coated-CI-particle–based fluid exhibited stable material removal rates and smooth surfaces inside spots for a variety of optical glasses and polycrystalline ceramics.

ACKNOWLEDGMENT

The authors thank Alex Maltsev and Mike Kaplun from the Laboratory for Laser Energetics (LLE) at the University of Rochester for sample preparation and acknowledge LLE for continuing support. Two of the coauthors (C. Miao and R. Shen) are LLE Horton Fellows. Research was sponsored by the U.S. Army Armament, Research, Development, and Engineering Center (ARDEC) and was accomplished under Cooperative Agreement Number W15QKN-06-2-0104 and the U.S. Department of Energy Office of Inertial Confinement Fusion under Cooperative Agreement No. DE-FC52-08NA28302, the University of Rochester, and the New York State Energy Research and Development Authority. The views and conclusions contained in this document are those of the authors and should not be interpreted as representing the official policies, either expressed or implied, of U.S. Army ARDEC or the U.S. Government. The support of DOE does not constitute an endorsement by DOE of the views expressed in this article. The U.S. Government is authorized to reproduce and distribute reprints for Government purposes notwithstanding any copyright notation hereon.

Appendix A: Synthesis Procedure of Zirconia-Coated CI Using the Sol-Gel Technique

This appendix describes the sol-gel synthesis procedure for coating CI powder. The first step was the preparation of zirconia sol-gel. Zirconia sol was prepared by mixing 1000 mL of DI water [H_2O], 73 mL of zirconium (IV) butoxide [$Zr(OC_4H_9)_4$], and 30 mL of nitric acid [HNO_3] at room temperature to produce ~1100 mL of sol. The mixing process is completed when the solution is clear (pH ~ 1).

Second, the following procedure was followed to prepare a 200-g batch of zirconia-coated CI at 10-vol % zirconia sol:

- CI powder (200 g) was dispersed in DI water (600 mL) in a 2-liter flask.
- The mixture/flask was placed in an ultrasonic bath for 30 min at room temperature.
- The flask was then placed in a water bath on top of a hot plate, and the mixture was agitated using a mechanical stirrer (~60 rpm).
- Zirconia sol (400 mL) was added to the flask containing the CI and water. The amount of sol determined the thickness of the zirconia coating and the amount of free zirconia nanocrystals formed.
- The water bath temperature was set to 70°C and was left to stir for 4 h after which the hot plate was turned off and the mixture continued to stir overnight.
- Finally, the zirconia-coated CI particles were separated out from the liquid mixture (~10 pH) using a magnet and washed three times with ~2 liters of DI water and ethanol. The particles were dried in an aluminum foil pan in a fume hood for 2 to 3 days to a moisture level of less than 2 wt%.[58]
- The dried particles were then milled by hand with a mortar and pestle to form a uniform powder.

Appendix B: Sample Preparation Procedure for SEM

This appendix describes the preparation of samples for SEM imaging. Two types of samples were prepared: loose particles and imbedded particles for cross sectioning. Loose particles of both uncoated and zirconia-coated CI powder (<1 g) were spread over an SEM-designated stub covered with a double-sided carbon tape. No conductive layer was required for uncoated CI, but a conductive layer of gold/palladium alloy was used for the zirconia-coated CI particles to minimize the effect of electric charge accumulation on the specimen during electron irradiation to yield good image quality. In general, for both sample types, a low electron beam voltage was used (~3 to 5 kV) with a relatively short SEM working distance (~2 to 5 mm).

The following procedure was taken to prepare samples of imbedded particles for cross sectioning:

- 3 g of CI particles (uncoated or coated) were milled by hand with a mortar and pestle, subsequently mixed with 3 g of conductive molding compound.[59]
- A sample press[60] was preheated to ~200°C, filled with 10 g of pure conductive molding compound, and then covered with the mixture of CI and molding compound on top.
- A pressure of 4500 psi was applied for ~10 min and the sample was allowed to cool down at room temperature for ~20 min.
- The final puck dimension was ~30 mm in diameter by ~15 mm high.

- Samples were spotted on our spot-taking machine (STM, discussed in **MRF Technology**, p. 190) using a standard MR fluid with nanodiamonds. A spotting time of ~30 min produced a visible spot. This "spotting" procedure provides a new deterministic polishing technique for cross sectioning encapsulated particles for SEM.

REFERENCES

1. M. J. Cumbo, D. Fairhurst, S. D. Jacobs, and B. E. Puchebner, Appl. Opt. **34**, 3743 (1995).
2. D. Towery and M. A. Fury, J. Electron. Mater. **27**, 1088 (1998).
3. D. W. Camp *et al.*, in *Laser-Induced Damage in Optical Materials: 1997*, edited by G. J. Exarhos *et al.* (SPIE, Bellingham, WA, 1998), Vol. 3244, pp. 356–364.
4. M. A. Nichols *et al.*, U.S. Patent No. 6,099,389 (8 August 2000).
5. S.-W. Park, Y.-J. Seo, and W.-S. Lee, Microelectron. Eng. **85**, 682 (2008).
6. J. A. Menapace *et al.*, U.S. Patent No. 6,920,765 (26 July 2005).
7. QED Technologies, LLC, Rochester, NY 14607.
8. J. D. T. Kruschwitz, Opt. Photonics News **17**, 10 (2006).
9. V. W. Kordonski and D. Golini, in *Proceedings of the Sixth International Conference on Electro-Rheological Fluids, Magneto-Rheological Suspensions and Their Applications*, edited by M. Nakano and K. Koyama (World Scientific, Singapore, 1998), pp. 837–844.
10. V. W. Kordonski, D. Golini, P. Dumas, S. J. Hogan, and S. D. Jacobs, in *Smart Structures and Materials 1998: Industrial and Commercial Applications of Smart Structures Technologies*, edited by J. M. Sater (SPIE, Bellingham, WA, 1998), Vol. 3326, pp. 527–535.
11. S. D. Jacobs, W. Kordonski, I. V. Prokhorov, D. Golini, G. R. Gorodkin, and T. D. Strafford, U.S. Patent No. 5,804,095 (8 September 1998).
12. J. E. DeGroote, A. E. Marino, J. P. Wilson, A. L. Bishop, J. C. Lambropoulos, and S. D. Jacobs, Appl. Opt. **46**, 7927 (2007).
13. A. B. Shorey, S. D. Jacobs, W. I. Kordonski, and R. F. Gans, Appl. Opt. **40**, 20 (2001).
14. C. Miao, S. N. Shafrir, J. C. Lambropoulos, J. Mici, and S. D. Jacobs, Appl. Opt. **48**, 2585 (2009).
15. For a medium-hardness polyurethane polishing pad (SUBA X pads) on a double-sided polishing machine, the useful lifetime is within the range of 100 to 110 h. Pads on a single-sided polishing machine last considerably longer, approximately three to four months. From personal communication with Mr. Mike Naselaris, Sydor Optics, Rochester, NY (2009).
16. T. S. Izumitani, *Optical Glass*, American Institute of Physics Translation Series (American Institute of Physics, New York, 1986), p. 197.
17. M. Schinhaerl *et al.*, in *Current Developments in Lens Design and Optical Engineering V*, edited by P. Z. Mouroulis, W. J. Smith, and R. B. Johnson (SPIE, Bellingham, WA, 2004), Vol. 5523, pp. 273–280.
18. P. Schinhaerl *et al.*, in *Detectors and Associated Signal Processing II*, edited by J.-P. Chatard and N. J. Peter (SPIE, Bellingham, WA, 2005), Vol. 5965, pp. 659–670.
19. P. A. Barata and M. L. Serrano, Fluid Phase Equilib. **141**, 247 (1997).
20. S. R. Arrasmith, S. D. Jacobs, I. A. Kozhinova, L. L. Gregg, A. B. Shorey, H. J. Romanofsky, D. Golini, W. I. Kordonski, S. Hogan, and P. Dumas, in *Finishing of Advanced Ceramics and Glasses*, edited by R. Sabia, V. A. Greenhut, and C. G. Pantano, Ceramic Transactions, Vol. 102 (The American Ceramic Society, Westerville, OH, 1999), pp. 201–210.
21. J. E. DeGroote, H. J. Romanofsky, I. A. Kozhinova, J. M. Schoen, and S. D. Jacobs, in *Manufacturing and Testing V*, edited by H. P. Stahl (SPIE, Bellingham, WA, 2004), Vol. 5180, pp. 123–134.
22. I. A. Kozhinova, H. J. Romanofsky, A. Maltsev, S. D. Jacobs, W. I. Kordonski, and S. R. Gorodkin, Appl. Opt. **44**, 4671 (2005).
23. B. M. Kavlicoglu *et al.*, in *Smart Structures and Materials 2002: Damping and Isolation*, edited by S. A. Gregory (SPIE, Bellingham, WA, 2002), Vol. 4697, pp. 393–400.
24. W. Zhou, C.-M. Chew, and G.-S. Hong, in *Proceedings of the 2005 IEEE/ASME International Conference on Advanced Intelligent Mechatronics* (IEEE, New York, 2005), pp. 473–478.
25. I. B. Jang *et al.*, J. Appl. Phys. **97**, 10Q912 (2005).
26. F. F. Fang and H. J. Choi, Phys. Status Solidi A **204**, 4190 (2007).
27. T. J. Swihart, U.S. Patent No. 4,731,191 (15 March 1988).
28. H. Rutz and F. G. Hanejko, U.S. Patent No. 5,063,011 (5 November 1991).
29. T. Atarashi and K. Nakatsuka, U.S. Patent No. 6,280,658 (28 August 2001).
30. J. C. Ulicny and Y. T. Chang, U.S. Patent No. 6,929,757 (16 August 2003).
31. K. D. Weiss, D. J. Carlson, and D. A. Nixon, U.S. Patent No. 5,578,238 (26 November 1996).
32. H. Pu, F. Jiang, and Z. Yang, Mater. Lett. **60**, 94 (2006).
33. J. C. Ulicny *et al.*, U.S. Patent Appl. No. 11/971,298; Pub. No. US 2008/0185554 A1 (7 August 2008).
34. Carbonyl Iron (CI) HQ, BASF Aktiengesellschaft Inorganic Specialties, Ludwigshafen, Germany.
35. R. Shen, S. N. Shafrir, C. Miao, M. Wang, J. C. Lambropoulos, S. D. Jacobs, and H. Yang, "Synthesis and Corrosion Study of Zirconia Coated Carbonyl Iron Particles," to be published in the Journal of Colloid and Interface Science.
36. SUPRA 40VP Scanning Electron Microscope (SEM), Zeiss-Leica, Germany.
37. L. Kumari, W. Li, and D. Wang, Nanotechnology **19**, 195602 (2008).

38. Zirconium Oxide Material Safety Data Sheet, Zircar Zirconia, Inc., Florida, NY 10921-0287.

39. S. Koynov, M. S. Brandt, and M. Stutzmann, Appl. Phys. Lett. **88**, 203107 (2006).

40. VCA 2500xe Video Contact Angle System, AST Products, Inc., Billerica, MA 01821.

41. AccuPyc II 1340 Gas Pycnometer, Micromeritics Instrument Corporation, Norcross, GA 30093-2901.

42. D. R. Lide, *CRC Handbook of Chemistry and Physics: A Ready-Reference Book of Chemical and Physical Data: 2008–2009*, 89th ed. (CRC Press, Boca Raton, FL, 2008), p. 4-101.

43. R. M. Cornell and U. Schwertmann, *The Iron Oxides: Structures, Properties, Reactions, Occurrences, and Uses*, 2nd ed. (Wiley-VCH, Weinheim, 2003), p. XVIII.

44. Brookfield Cone and Plate Viscometer Model DV-III CP, Brookfield Engineering Laboratories, Inc., Middleboro, MA 02346.

45. J. C. Lambropoulos and R. Varshneya, in *Frontiers in Optics 2004*, OSA Technical Digest (Optical Society of America, Rochester, NY, 2004), Paper OTuA1.

46. Talysurf CCI 3000 Noncontact 3-D Surface Profiler (Taylor Hobson, Inc., Rolling Meadows, IL 60008-4231). The 50× objective (0.37 × 0.37 mm^2) and four phase averages were used for each measurement, unfiltered. The Talysurf CCI has a maximum resolution of 0.1 Å in the z-axis and 0.47 mm in the x–y axis (maximum optical resolution).

47. S. N. Shafrir, J. C. Lambropoulos, and S. D. Jacobs, Appl. Opt. **46**, 5500 (2007).

48. D. C. Harris, in *Materials for Infrared Windows and Domes: Properties and Performance*, Tutorial Texts in Optical Engineering (SPIE Optical Engineering Press, Bellingham, WA, 1999), Vol. PM70, p. 145.

49. Microgrit Micro Abrasives Corporation, Westfield, MA 01086-0669.

50. Hastilite Precision Polishes for Advanced Optics (PO), J. H. Rhodes, a Division of Universal Photonics, Inc., Franklin Springs, NY

51. 915 Pitch, Universal Photonics, Inc., Hicksville, NY 11801-1014.

52. Buehler METADI Diamond Suspension (water based), Buehler Ltd., Lake Bluff, IL 60044-1699.

53. Kay Diamond Products, LLC, Boca Raton, FL 33487.

54. Zygo Mark IVxp Interferometer (Zygo Mark IVxp™, Zygo Corporation, Middlefield, CT 06455). This instrument is a 4-in. HeNe Fizeau interferometer with a wavelength of 632.8 nm. Peak-to-valley (p–v) for surface flatness and depth of deepest penetration (ddp) of the spot was measured in microns.

55. NewView 5000 Noncontact Profilometer (Zygo Corporation, Middlefield, CT 06455).

56. Beckman 210 pH Meter, Beckman Instruments Inc., Fullerton, CA 92643.

57. D. Golini and S. D. Jacobs, in *Advanced Optical Manufacturing and Testing*, edited by L. R. Baker, R. B. Reid, and G. M. Sanger (SPIE, Bellingham, WA, 1990), Vol. 1333, pp. 80–91.

58. The moisture content is measured using an Arizona Instrument Computrac Max-1000 moisture analyzer, Arizona Instrument, LLC, Tempe, AZ 85281.

59. Probemet Conductive Molding Compound, Buehler Ltd., Lake Bluff, IL 60044-1699.

60. Specimen Mounting Press, Buehler Ltd., Lake Bluff, IL 60044-1699.

All-Fiber Optical Magnetic Field Sensor Based on Faraday Rotation in Highly Terbium Doped Fiber

Magnetic field sensors have been widely used for navigation, vehicle detection, current sensing, and spatial and geophysical research. Many techniques developed for magnetic field sensors are based on electronics, including superconducting quantum interference devices (SQUID's), search coils, fluxgates, Hall-effect sensors, anisotropic magnetoresistive devices, and giant magnetoresistive devices.[1] All-fiber optical magnetic field sensors are desirable because of their immunity to electromagnetic interference, low weight, small size, and long-distance signal transmission for remote operation.

Many all-fiber magnetic field sensors use material coatings. For example, if a magnetostrictive or metal jacket is deposited on the fiber, the optical phase can be changed by strain or Lorentzian force, respectively, when immersed in a magnetic field.[2,3] In another method, a fiber end is coated with a composite material and butt coupled to another fiber. The optical coupling between the fibers changes with the transverse displacement of the coated fiber in the magnetic field.[4] In yet another method, iron film is deposited on a side-polished fiber Bragg grating. The reflective wavelength of the fiber grating shifts with the strain induced by a magnetic field.[5]

Faraday rotation can also be used for magnet sensors. Because the Verdet constant of silica fiber is small [~1.1 rad/(Tm) at 1064 nm], the fiber is usually coiled multiturn to increase the polarization rotation angle. This kind of magnet sensor is often used for current sensing.[6,7] However, bend-induced linear birefringence affects the state of polarization and quenches the desired Faraday effect. In this article, an all-fiber optical magnet sensor based on Faraday rotation is demonstrated. The device is made of a fiber Faraday rotator spliced to a fiber polarizer. The fiber Faraday rotator is a 2-cm-long terbium-doped (Tb) fiber, which is sufficiently short to avoid bending. The fiber polarizer is Corning SP1060 single-polarization fiber (PZ).

The magnetic sensing principle is shown in Fig. 120.44. Linear-polarized input light from the laser source is transmitted to the Tb fiber via polarization-maintaining (PM) fiber. The polarization of the light rotates when the Tb fiber experiences a magnetic field along the axis of light propagation. The light then goes through the fiber polarizer, which extinguishes light whose polarization is not aligned to its principle axis. PM fiber transmits the remaining light to a detector. Because of the polarizer, the power received at the detector is a function of the polarization rotation angle given by Malus' Law.[8] Since the polarization rotation angle in the Tb fiber is related to the magnetic field strength by the Faraday effect, the magnetic field can be measured by monitoring the output power of the sensor.

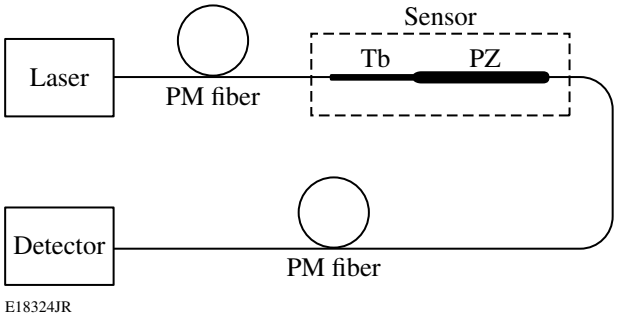

Figure 120.44
Sensing principle of an all-fiber Faraday magnet sensor. PZ: single-polarization fiber; PM: polarization-maintaining fiber.

Terbium doping is an effective way to increase the Verdet constant in the fiber to reduce the fiber length and avoid coiling. Highly terbium doped silicate glasses were designed and fabricated. Boron oxide and aluminum oxide were added into the glass composition to improve the solubility of terbium oxide. Fifty-six-wt% terbium-oxide–doped glass is used as the core glass. The rod-in-tube technique was used for single-mode fiber fabrication. The fiber pulling temperature is around 1000°C. The N.A. and diameter of the core are 0.14 and 4 μm, and cladding diameter of the fiber is 130 μm. The propagation loss of the fiber is measured to be 0.11 dB/cm at 1310 nm using the cutback technique. The effective Verdet constant was measured to be -24.5 ± 1.0 rad/(Tm), using the measurement technique described in Refs. 9 and 10.

Single-polarization fiber is a type of fiber in which only one polarization mode can propagate. This kind of fiber has large birefringence to separate the two orthogonal polarization modes so that each has a different cutoff wavelength. Therefore, within a certain wavelength region, one polarization mode propagates while the other is eliminated because of high loss. In this way, the fiber functions as a polarizer. Such large birefringence can be introduced via stress from boron-doped rods, elliptical core/cladding, or air holes.

In this experiment, Corning SP1060 fiber was used as the polarizing element.[11] With two air holes on either side of an elliptical core, large birefringence and therefore spectrally separated fundamental-mode cutoff were achieved. The core diameter along the major axis was 8 μm, and the clad diameter was 125 μm, with a core N.A. of 0.14. The propagation loss of the surviving mode was 0.1 dB/m at 1060 nm. The center wavelength was 1065 nm and the bandwidth was 25 nm. The polarization extinction ratio was dependent on the length of the fiber. A 1-m PZ fiber was used in the experiment and was coiled with a 15-cm diameter to shift the PZ bandwidth toward the shorter wavelength, resulting in an extinction ratio >16 dB at a 1053-nm working wavelength.

The experimental configuration used to test the sensor is shown in Fig. 120.45. A 2-cm section of Tb-doped fiber, spliced between the PM fiber and 1-m section of PZ fiber, went through a magnet tube. Linearly polarized 1053-nm light was launched into the PM fiber. The polarization directions of the PM and PZ fibers were aligned with a rotational difference of θ_0, which should have been set between 20° to 70° to obtain a nearly linear response curve of magnetic field strength as a function of measured power. The N48 NdFeB magnet tube was 4 cm long with inner and outer diameters of 5 mm and 6 cm, respectively. As the magnet was translated along the fiber, the magnetic field imposed on the Tb fiber changed.

Magnetic fields can be readily calculated by using the geometrical shape of the magnet.[12] The axial component of the magnetic field distribution along the central axis of the magnet tube was derived to be

$$B_z(z) = \frac{B_r}{2}\left\{\frac{z + l/2}{\left[a_1^2 + (z + l/2)^2\right]^{1/2}} - \frac{z + l/2}{\left[a_2^2 + (z + l/2)^2\right]^{1/2}} - \frac{z - l/2}{\left[a_1^2 + (z - l/2)^2\right]^{1/2}} + \frac{z - l/2}{\left[a_2^2 + (z - l/2)^2\right]^{1/2}}\right\}, \quad (1)$$

where a_1 and a_2 are the inner and outer radii, respectively, l is the length of the magnet, and B_r is the residual magnetic flux density. Figure 120.46 shows the calculated $B_z(z)$ for the N48 magnet used in the experiment (B_r = 1.35 T) along with the measured magnetic field outside the magnet. The physical ends of the magnet are also shown for reference. The magnetic field, measured only outside the magnet because the probe size is larger than a_1, agreed very well with the theoretical curve calculated from Eq. (1). The averaged magnetic density flux B_{av} experienced by the 2-cm length of Tb fiber (calculated in the center of Tb fiber) is also shown in the figure. This curve is nearly linear from −3 to −1 cm along the z axis. This region will be used in the measurement.

After considering the extinction ratio of the polarizing fiber, Ex, the relative transmission through the PZ fiber is derived as[13]

$$I/I_0 = \cos^2(\theta_0 + \theta) + \sin^2(\theta_0 + \theta)\,10^{(-\mathrm{Ex}/10)}, \quad (2)$$

where I/I_0 is the measured output power normalized to its maximum I_0, $\theta = VB_{av}L$ is the Faraday rotation angle in the Tb fiber, and V and L are the effective Verdet constant and the length of the Tb fiber, respectively. In the experiment, Ex = 18 dB and $\theta_0 = 50°$. The experimental and theoretical curves of the relative transmission are shown in Fig. 120.47. The error is determined to be 0.01 by a polarization-stability measurement. The experimental data agree well with the theoretical curve, both of which show a nearly linear response. The nominal

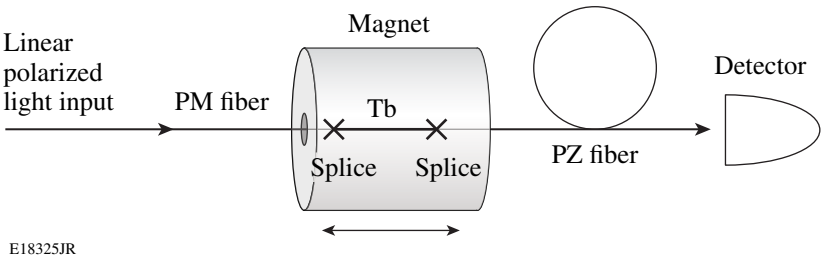

Figure 120.45
Experimental configuration of an all-fiber magnet sensor.

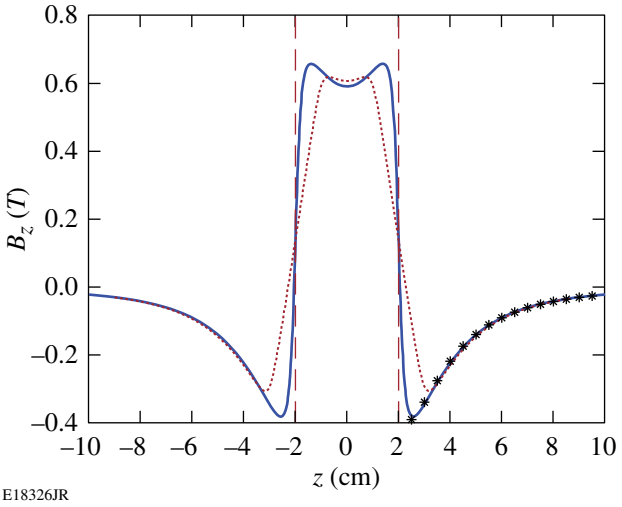

Figure 120.46
Theoretical (solid) and measured (star) magnetic density flux distribution B_z along the center axis z. The dashed lines represent the magnet ends and the dotted line represents B_{av}, the magnetic density flux averaged over a 2-cm length along the axis z.

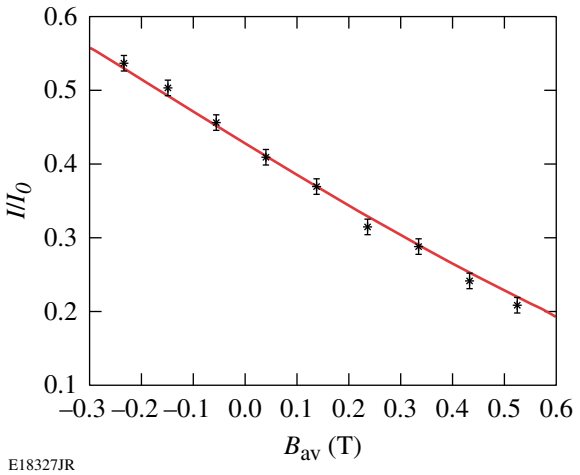

Figure 120.47
Measured (star) and calculated (solid) relative transmission of an all-fiber magnet sensor.

transmission loss through the device is 10 dB, mainly induced by the mode mismatch between the PZ and Tb fibers and the splicing loss between the Tb and silica fibers.

The sensitivity of the all-fiber sensor is given by $d\theta/dB_{av} = VL = 0.49$ rad/T. This can be increased by increasing the effective Verdet constant and/or length of the Tb fiber. Since the polarization rotation may go beyond 90°, a maximum detected magnetic field $B_{max} = (\pi/2)/VL$ of 3.2 T can be measured in this configuration without ambiguity. A larger magnetic field could be measured by decreasing the effective Verdet constant or the length of the Tb fiber.

The resolution of the magnetic sensor is obtained by taking the derivative and absolute value of both sides of Eq. (2):

$$\Delta B = \frac{\Delta I}{I_0 VL \sin\left[2\left(\theta_0 + \theta\right)\right]} = \frac{\Delta I}{I_0} \frac{2B_{max}}{\pi \sin\left[2\left(\theta_0 + \theta\right)\right]}. \quad (3)$$

In this equation, the effect of the extinction ratio was neglected, which is appropriate for Ex > 20. Increasing the effective Verdet constant and the length of the Tb fiber could also help to increase the resolution, at the expense of reducing B_{max}. The most effective way is to decrease the ratio $\Delta I/I_0$. For example, if the detector resolution is at the nW level, increasing I_0 to the mW level yields a sensor resolution of 2.0×10^{-6} T, with B_{max} still at 3.2 T. In the experiment, $\Delta I/I_0$ is around 10^{-2}, making the minimum measurable magnetic field 0.02 T. If higher resolution and higher B_{max} are both required, two all-fiber magnetic field sensors could be co-located. In this scenario, one sensor has a large VL product to obtain the desired resolution; the other one has a small VL product to obtain the desired maximum detected magnetic field by removing the ambiguity of the other sensor.

The Verdet constant of the Tb fiber is dependent on the temperature; for example, $1/V\, dV/dT$ is around 10^{-4}/K for silica.[14] To mitigate the impact of temperature on the measurement results, a fiber-grating temperature sensor could be cascaded or co-located with the magnetic field sensor to monitor the temperature near the magnetic field sensor. In this way, the sensor can give accurate results, providing the device has been calibrated as a function of temperature.

Since the all-fiber magnetic field sensor can measure only magnetic fields parallel to its axis, three orthogonally oriented sensors can be combined to provide a complete three-dimensional magnetic field sensor.

In conclusion, an all-fiber optical magnetic field sensor has been demonstrated. It consists of a fiber Faraday rotator and a fiber polarizer. The fiber Faraday rotator uses a 2-cm-long section of 56-wt%-terbium–doped silicate fiber, and the fiber polarizer is Corning SP1060 single-polarization fiber. The all-fiber optical magnetic field sensor has a sensitivity of 0.49 rad/T and can measure magnetic fields from 0.02 T to 3.2 T.

ACKNOWLEDGMENT

This work was supported by the U.S. Department of Energy Office of Inertial Confinement Fusion under Cooperative Agreement No. DE-FC52-08NA28302, the University of Rochester, and the New York State Energy Research and Development Authority. The support of DOE does not constitute an endorsement by DOE of the views expressed in this article. This work is also supported in part by Wright-Patterson Air Force Research Laboratory under contract FA8650-09-C-5433. The authors would like to acknowledge the technical support of Dr. R. L. Nelson and W. D. Mitchell from AFRL.

REFERENCES

1. J. E. Lenz, Proc. IEEE **78**, 973 (1990).
2. A. Yariv and H. V. Winsor, Opt. Lett. **5**, 87 (1980).
3. H. Okamura, J. Lightwave Technol. **8**, 1558 (1990).
4. V. Radojevic *et al.*, J. Magn. Magn. Mater. **272–276**, e1755 (2004).
5. C.-L. Tien *et al.*, IEEE Trans. Magn. **42**, 3285 (2006).
6. G. W. Day *et al.*, Opt. Lett. **7**, 238 (1982).
7. V. Annovazzi-Lodi, S. Merlo, and A. Leona, J. Lightwave Technol. **13**, 2349 (1995).
8. W. E. Gettys, F. J. Keller, and M. J. Skove, *Physics, Classical and Modern* (McGraw-Hill, New York, 1989).
9. L. Sun, S. Jiang, J. D. Zuegel, and J. R. Marciante, Opt. Lett. **34**, 1699 (2009).
10. L. Sun, S. Jiang, and J. R. Marciante, "All-Fiber Optical Isolator Based on Faraday Rotation in Highly Terbium-Doped Fiber," submitted to Optics Letters.
11. D. A. Nolan *et al.*, Opt. Lett. **29**, 1855 (2004).
12. M. McCaig and A. G. Clegg, *Permanent Magnets in Theory and Practice*, 2nd ed. (Wiley, New York, 1987).
13. J. R. Marciante, N. O. Farmiga, J. P. Kondis, and J. R. Frederick, Opt. Express **11**, 1096 (2003).
14. P. A. Williams *et al.*, Appl. Opt. **30**, 1176 (1991).

Femtosecond Optical Pump–Probe Characterization of High-Pressure–Grown $Al_{0.86}Ga_{0.14}N$ Single Crystals

The group-three–nitride (III-N) semiconducting system, in general, and (Al,Ga)N compounds, in particular, have attracted a very strong interest in recent years for the development of optoelectronic devices from the green to deep-ultraviolet wavelength range.[1] Moreover, III-N materials have also well-documented advantages in high-temperature and high-power electronics, as well as in acoustic-wave applications.[2–4] A considerable amount of research has been devoted to the epitaxial growth of (Al,Ga)N films, using MOCVD and/or MBE methods.[5,6] The growth of bulk, dislocation-free (Al,Ga)N crystals is also critical not only for getting much-needed single-crystal substrates for homoepitaxy, but also for applications where the devices operate based on the volume-absorption principle, e.g., x-ray and other radiation detectors. Unfortunately, the growth of even small, high-quality (Al,Ga)N single crystals, especially those with the high Al content, is very challenging, and only very recently, the synthesis of $Al_xGa_{1-x}N$ crystals with the Al content x between 0.5 and 1 has been reported by Belousov *et al.*[7]

In this article, we report our femtosecond, time-resolved pump–probe spectroscopy studies in $Al_{0.86}Ga_{0.14}N$ (AlGaN) single crystals and demonstrate that the observed transient transmissivity signal is a superposition of the femtosecond correlation signal caused by a coherent process of simultaneous absorption of both the pump and probe photons and a conventional, picosecond-in-duration hot-electron cooling. The pump–probe correlation studies, typically called a two-photon absorption (TPA) process, are important in nonlinear optics and have been investigated in many semiconducting materials, such as GaAs, GaN, and (In,Ga)N;[8] the large magnitude of the TPA coefficients β are reported in Ref. 9. Moreover, the TPA measurement is a useful tool for characterizing optical pulse widths and determining the optical energy gap in wide-bandgap semiconductor materials. At the same time, the photoresponse relaxation transient, which in our case follows the initial correlation spike, provides information about the electron–phonon decay time and the across-bandgap carrier recombination.

Our single AlGaN crystals used in this study were synthesized from solution at high temperatures using a high-pressure gas system, which consists of a compressor, pressure intensifier, and a high-pressure chamber of 40-mm internal diameter with an internal, three-zone furnace. First, a polycrystalline (Al,Ga)N precursor pellet was synthesized by a solid-phase reaction in a cubic anvil at 30 kbar and 1800°C from a mixture of high-purity GaN and AlN powders (Alfa Ceasar). The prereacted pellet acted as an Al source and was placed in the Ga melt in the upper part of a graphite crucible. The graphite crucible had an internal diameter of 14 mm and a length of 70 mm. For the AlGaN crystal growth, we applied a nitrogen pressure of up to 7.5 kbar and a temperature of up to 1760°C, following our earlier, experimentally derived pressure-versus-temperature diagram.[7] The synthesis process was conducted under the constant thermal gradient of about 20 K/cm for 6 to 7 days. The crystals grown in the colder part of the graphite crucible were colorless, up to $0.8 \times 0.8 \times 0.8$ mm^3 in size, and exhibited the hexagonal form and wurtzite structure. After processing, the samples were etched from the remaining unreacted Ga/Al melt using hydrochloric acid and *aqua regia*. The structural composition was determined by a laser-ablation, inductively coupled plasma mass spectrometry technique.

Our time-resolved photoresponse studies were performed in a transmission configuration, using a two-color, femtosecond pump–probe technique. We used a passively mode-locked Ti:sapphire laser as a source of 100-fs-wide, 76-MHz-repetition-rate optical pulses, tunable in the 720- to 860-nm range. The Ti:sapphire output was split into two beams by a 60/40 beam splitter. The pump beam, frequency doubled by using a BaB_2O_4 crystal, was focused onto the surface of the AlGaN crystal with a spot diameter of ~100 μm at an incident angle of ~20°. The probe pulses, directly generated by the Ti:sapphire laser, were delayed with respect to the pump by passing through a computer-controlled delay stage and were near normally aimed at the sample on the same area as the pump beam with a spot diameter of ~10 μm. The small spot size of the probe

beam ensured that it probed a region with uniform pump photoexcitation and somewhat relaxed the stringent requirement for the delay-stage alignment. The probe light transmitted through the sample was filtered from any scattered pump photons by a near-infrared filter and collected by a photodetector. The photodetector signal was measured by a lock-in amplifier, synchronized with an acousto-optical modulator operating at frequency of 99.8 KHz. We stress that in our experiments both the pump and probe beams had an average power incident on a sample of a same order (with a typically used ratio $P_{\text{pump}}/P_{\text{probe}}$ of 1:2) and their photon energies were much smaller than the expected ~6-eV bandgap of our AlGaN sample. All experiments were performed at room temperature.

Figure 120.48 presents a typical time-resolved normalized differential transmissivity ($\Delta T/T$) transient, obtained by exciting our AlGaN crystal with a 380-nm pump and probed with a 760-nm probe. Figure 120.48(a) depicts the full transient in a long-time window, and the dashed line is a numerical fit, which will be described later. We observe an initial (near-zero delay), subpicosecond-in-duration negative spike, followed by a much-slower exponential decay. In Fig. 120.48(b), we show the same waveform (solid squares), but on a much-shorter (<3 ps) time scale, and note that the experimental $\Delta T/T$ transient can be very accurately decomposed into a Gaussian-shaped pulse (open triangles) of a full width at half maximum (FWHM) of 310 fs and a second transient (open circles) with an approximately 1-ps-wide rise time, modeled as the error function, and a slow [on the scale of Fig. 120.48(b)] exponential decay. The superposition of the above two transients (open squares) fits our experimental data extremely well [see also dashed line in Fig. 120.48(a)].

Based on our decomposition procedure, we can interpret the ultrafast Gaussian pulse as a TPA-type correlation signal since the 310-fs FWHM coincides well with the overlap of our ~150-fs-wide pump and probe pulses. The TPA signal can be observed only when both the pump and probe photons are simultaneously incident on the sample and their total energy is greater than the material's bandgap E_g. Therefore, we must conclude that in our case, the correlation effect actually involves three photons (one pump photon and two probe photons) since any other combination would give a total photon energy that would be either much too large or too low. The second, slow component of the experimental transient is a typical $\Delta T/T$ pump–probe photoresponse signal, associated in direct-bandgap semiconductors (i.e., in III-N materials) with across-the-bandgap electron-hole excitation, followed by a subsequent cooling of photo-induced electrons. On a long time scale, the relaxation component of the $\Delta T/T$ transient can be fitted [Fig. 120.48(a) (dashed line)] as a bi-exponential decay with an initial 12-ps time constant, followed by a slow, ~130-ps-

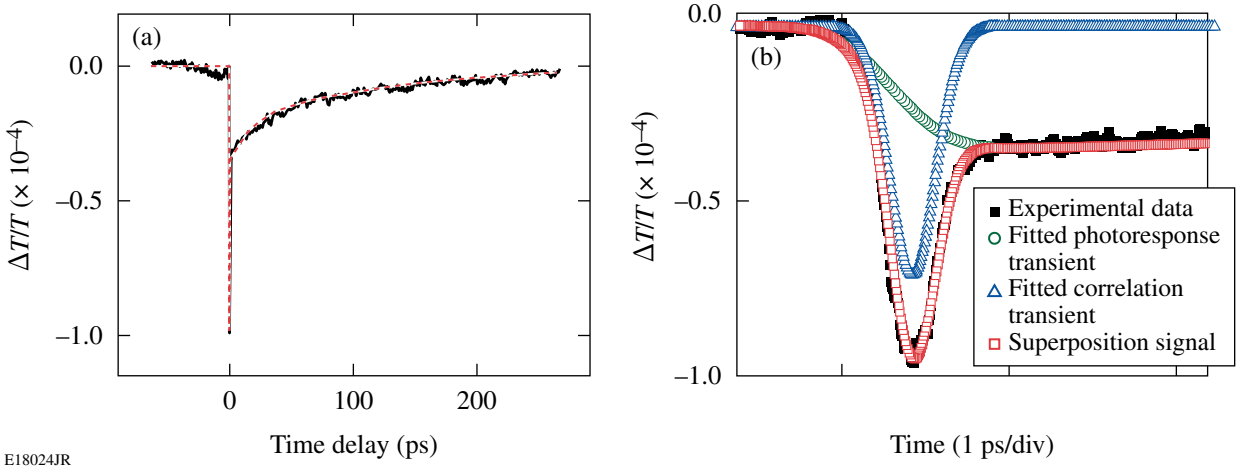

Figure 120.48
(a) Time-resolved $\Delta T/T$ transient measured for the pump λ = 380 nm and the probe λ = 760 nm. The red dashed line represents a theoretical fit. (b) The same $\Delta T/T$ transient (black squares), but on a much-shorter time scale. The blue triangles are the best fit corresponding to a Gaussian-shaped correlation signal of the pump and probe photons. The green circles fit the photoresponse component of the transient, with the rising part represented by the error function and the decay modeled as a double-exponent relaxation. The red squares correspond to the superposition of the correlation and photoresponse components and overlay the experimental data. The fit of the red squares in (b) is identical to the red dashed line in (a).

long relaxation. The fast decay time constant represents the electron–phonon relaxation process toward a quasi-equilibrium condition at the bottom of the conduction band, while the slow time constant is the carrier lifetime, which includes both the radiative (across the bandgap) and nonradiative (trapping) recombination.

We have also studied the amplitude dependence of the photon-correlation signal deconvoluted from the experimental $\Delta T/T$ transient on the pump power's density (see Fig. 120.49) and have found that, in the regime of low attenuation of the incident pump and probe beams, it followed a linear behavior, well-established for the TPA process:[10]

$$\Delta T/T = -\beta d P_{\text{eff}}, \tag{1}$$

where d is the sample thickness and P_{eff} is the effective, absorbed pump-beam power per pulse. The data presented in Fig. 120.49 were collected for the pump-beam wavelength λ = 380 nm and d = 1 mm. Using Eq. (2) and taking into account that in our experiment the pump spot diameter is 100 μm and its absorption coefficient is ~80%, the linear fit (solid line) in Fig. 120.49 allowed us to calculate β = 0.42±0.02 cm/GW. We note that our β value is significantly smaller than the ones observed in other III-N materials [e.g., for GaN, β = 12 cm/GW at 377 nm (Ref. 8)], apparently due to a much larger E_g value for (Al,Ga)N.

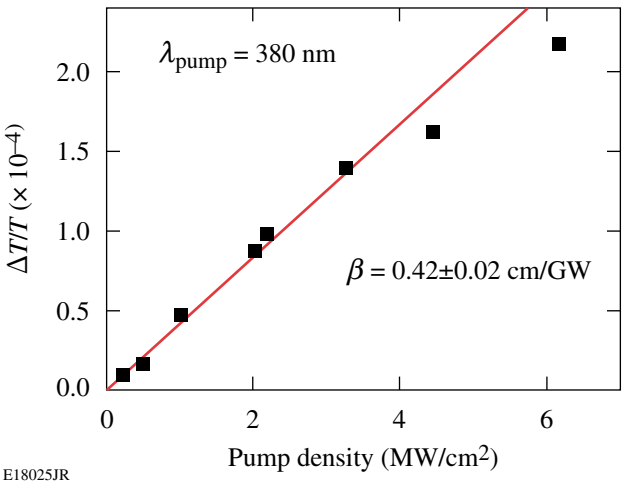

Figure 120.49
Dependence of the correlation signal amplitude (squares) on the pump power's intensity, measured for a 380-nm pump wavelength. The solid red line is the linear best fit and its slope corresponds to the β coefficient.

Following the procedure discussed in connection with Fig. 120.49, we obtained β coefficients for the pump λ's ranging from 360 nm to 430 nm. The results (solid circles) are summarized in Fig. 120.50 and compared directly with the theoretical model of Sheik–Bahae *et al.*,[11] derived for wide, direct-bandgap semiconductors:

$$\beta(\omega) = K\frac{\sqrt{E_p}}{n_0^2 E_g^3} F_2\left(\frac{\hbar\omega}{E_g}\right), \tag{2}$$

where K is a material-independent constant, E_p is the matrix element related to the interband momentum and is ~21 eV for most semiconductors, n_0 is the refractive index, and the $F_2\left(\hbar\omega/E_g\right)$ function is given as $F_2 = (2x-1)^{3/2}/(2x)^5$.

In our case, K = 3100, E_g = 5.81 eV (from our bandgap measurement presented below), and n_0 is a function of λ and for our AlGaN sample is given by $n_0(\lambda) = 2.02 + 4.7e^{-\lambda/93.86}$ (Ref. 5). We observe a very good agreement of our experimental β values with the Sheik–Bahae model, within the pump light λ's achievable by our experimental setup. The inset in Fig. 120.50 presents a subset of the same data (β values very close to zero) as the main panel, but plotted as a function of total energy of photons incident on our sample and participating in the pump–probe correlation process (one pump photon and two probe photons). In this way, we can observe the optical

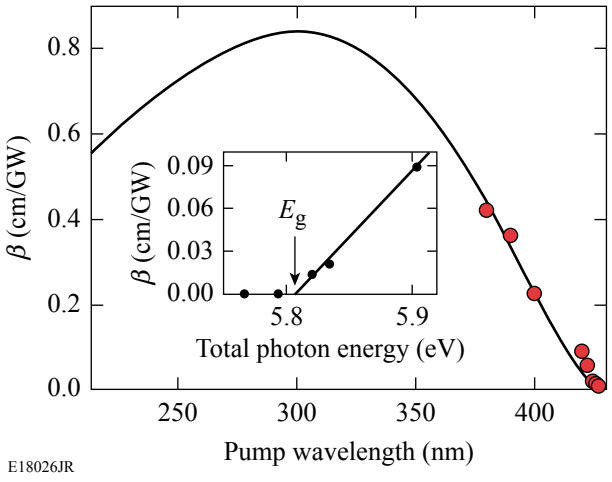

Figure 120.50
The correlation coefficient β as a function of the pump beam's wavelength. The red circles are our experimental data points, while the solid line corresponds to the Sheik–Bahae theory [Eq. (3)]. The inset shows β dependence on the total energy of absorbed photons with the optical bandgap absorption edge indicated.

transition edge in detail, and a simple linear fit allows us to very accurately determine the optical E_g of our AlGaN crystal to be equal to 5.81±0.01 eV.

We have performed time-resolved characterization of AlGaN single crystals using femtosecond pump–probe spectroscopy with both the pump and probe beams having wavelengths much longer than the wavelength corresponding to the AlGaN bandgap. Examination of our experimental data showed that two different processes contributed simultaneously to the $\Delta T/T$ transients observed on our experiments. The first was the ~300-fs-wide correlation signal, observed near the zero-delay point and corresponding to the photon correlation process involving a coherent (simultaneous) absorption of one pump and two probe photons. It was followed by a second, much slower (tens of picosecond in duration) relaxation transient representing photoresponse and cooling of photo-excited carriers. Analysis of the correlation signal amplitude on both the pump photon power and wavelength allowed us to obtain the correlation β coefficient for our AlGaN crystal and its spectral dependence. We demonstrated that, within our laser-tuning range, $\beta(\lambda)$ agreed very well with the Sheik–Bahae theory. We also determined that the optical E_g of AlGaN was 5.81±0.01 eV. The dynamics of the photoresponse decay component demonstrated that the carrier relaxation in AlGaN was dominated by trapping since the measured 130-ps time constant was relatively short.

ACKNOWLEDGMENT

The authors would like to thank Prof. D. Günther from the Laboratory for Inorganic Chemistry, ETH Zurich, for his assistance in (Al,Ga)N mass spectrometry characterization. J. Z. acknowledges support from the Frank Horton Graduate Fellowship Program at the University of Rochester Laboratory for Laser Energetics, funded by the U.S. Department of Energy Office of Inertial Confinement Fusion under Cooperative Agreement No. DE-FC52-08NA28302 and the New York State Energy Research and Development Authority. The support of DOE does not constitute an endorsement by DOE of the views expressed in this article.

REFERENCES

1. S. N. Mohammad, A. A. Salvador, and H. Morkoc, Proc. IEEE **83**, 1306 (1995).
2. Q. Chen *et al.*, Appl. Phys. Lett. **70**, 2277 (1997).
3. U. K. Mishra *et al.*, Proc. IEEE **96**, 287 (2008).
4. S. Wu, P. Geiser, J. Jun, J. Karpinski, J.-R. Park, and R. Sobolewski, Appl. Phys. Lett. **88**, 041917 (2006).
5. M. Stutzmann *et al.*, Mater. Sci. Eng. B **B50**, 212 (1997).
6. Y. Koide *et al.*, J. Appl. Phys. **61**, 4540 (1987).
7. A. Belousov, S. Katrych, J. Jun, J. Zhang, D. Günther, R. Sobolewski, and J. Karpinski, J. Cryst. Growth **311**, 3971 (2009).
8. C.-K. Sun *et al.*, Appl. Phys. Lett. **76**, 439 (2000).
9. S. Krishnamurthy, K. Nashold, and A. Sher, Appl. Phys. Lett. **77**, 355 (2000).
10. C. Rauscher and R. Laenen, J. Appl. Phys. **81**, 2818 (1997).
11. M. Sheik-Bahae *et al.*, IEEE J. Quantum Electron. **27**, 1296 (1991).

LLE's Summer High School Research Program

During the summer of 2009, 16 students from Rochester-area high schools participated in the Laboratory for Laser Energetics' Summer High School Research Program. The goal of this program is to excite a group of high school students about careers in the areas of science and technology by exposing them to research in a state-of-the-art environment. Too often, students are exposed to "research" only through classroom laboratories, which have prescribed procedures and predictable results. In LLE's summer program, the students experience many of the trials, tribulations, and rewards of scientific research. By participating in research in a real environment, the students often become more excited about careers in science and technology. In addition, LLE gains from the contributions of the many highly talented students who are attracted to the program.

The students spent most of their time working on their individual research projects with members of LLE's technical staff. The projects were related to current research activities at LLE and covered a broad range of areas of interest including experimental diagnostic development, computational modeling of implosion physics, laser physics, experimental and theoretical chemistry, materials science, cryogenic target characterization, target vibration analysis, and computer control systems (see Table 120.VII).

The students attended weekly seminars on technical topics associated with LLE's research. Topics this year included laser physics, fusion, holography, glass fracture, nonlinear optics, electrostatics, and electronic paper. The students also received safety training, learned how to give scientific presentations, and were introduced to LLE's resources, especially the computational facilities.

The program culminated on 26 August with the "High School Student Summer Research Symposium," at which the students presented the results of their research to an audience including parents, teachers, and LLE staff. The students' written reports will be made available on the LLE Web site and bound into a permanent record of their work that can be cited in scientific publications.

Two hundred and forty-nine high school students have now participated in the program since it began in 1989. This year's students were selected from a record 80 applicants.

At the symposium LLE presented its 13th annual William D. Ryan Inspirational Teacher Award to Mr. Jeffrey Klus, a mathematics teacher at Fairport High School. This award is presented to a teacher who motivated one of the participants in LLE's Summer High School Research Program to study science, mathematics, or technology and includes a $1000 cash prize. Teachers are nominated by alumni of the summer program. Mr. Klus was nominated by Nicholas Hensel and Angela Ryck, participants in the 2008 Summer Program. Nick describes Mr. Klus as "a great teacher" with an "obvious enjoyment of teaching and the material he teaches. Sarcastic quips and quirky comments were always close at hand in class, bringing humor to the otherwise droll, factual world of mathematics…I will always remember Mr. Klus's love for teaching, his continually enjoyable humor, and the way he treated all of his students as equals…He inspired in me a fresh love for math." Angela agreed about the humor Mr. Klus brought to class. She wrote, "Mr. Klus is a legend in my school…His entertaining stories kept us laughing at our seats, and the kids who rarely smiled in math class beamed in his presence…My favorite thing about Mr. Klus is that he encourages students to try new things… Mr. Klus has had an enormous effect on my education, and he is truly an inspiration to me." Ms. Pam Ciranni, Assistant Principal of Fairport High School, added, "Jeff is the driving force behind the AP computer classes. He is an advisor to the masterminds and chess clubs. He is a mentor to the other teachers. He is a consummate professional, understands the students' needs, and acts with the students as a peer."

Table 120.VII: High School Students and Projects—Summer 2009.

Name	High School	Supervisor	Project Title
Dustin Axman	Irondequoit	R. Rombaut, R. Russo	A Graphical Network Interface to Oscilloscopes
Leela Chocklingham	Brighton	K. L. Marshall	Abrasion-Resistant Anti-Reflective Silane Sol-Gel Coatings
Ted Conley	McQuaid	J. Bromage	Automated Injection for High-Power Fiber Amplifiers
Cheryl Liu	Pittsford Sutherland	J. P. Knauer	Neutron Detection with High Bandwidth and High Dynamic Range
Trevor Lu	Webster Thomas	D. H. Edgell	X-Ray Phase-Contrast Characterization of Cryogenic Targets
Evan Miller	Pittsford Mendon	J. A. Delettrez	Electron Reflection in Monte Carlo Simulations with the Code GEANT
Lindsay Mitchel	Spencerport	R. S. Craxton	Exploration of the Feasibility of Polar Drive on the LMJ
Justin Owen	Irondequoit	R. Kidder, C. Kingsley, M. Spilatro	Using Networked Data Services for System Analysis and Monitoring
Ben Petroski	Livonia	W. T. Shmayda	Water Desorption from Copper at Room Temperature
Aaron Van Dyne	Brighton	J. A. Marozas	Optimization of 1-D Multiple-FM SSD Designs for OMEGA EP and the NIF
Marisa Vargas	Webster Thomas	C. Dorrer, K. L. Marshall	Laser Beam Shaping with Optically Patterned Liquid Crystals
Kate Walden	Wayne	T. C. Sangster, M. Burke	The Effect of Alcohol Hydroxide Solutions on the Bulk Etch Rate of CR-39
Victor Wang	Webster Thomas	K. L. Marshall	Computational Modeling of Optically Switchable Azobenzenes
Paul Watrobski	Penfield	W. Theobald	UV Probe Beam for Plasma Characterization and Channeling Experiments
Mia Young	Penfield	R. Epstein	Analysis of Implosion Radiographs
Harvest Zhang	Brighton	L. Lund	Resonance and Damping Characterization in Cryogenic Fusion Targets

FY09 Laser Facility Report

During FY09 the Omega Laser Facility conducted 1153 target shots on OMEGA and 349 target shots on OMEGA EP for a total of 1502 combined target shots (see Table 120.VIII). OMEGA conducted 24 DT and 24 D_2 low-adiabat spherical cryogenic target implosions. Triple-picket pulse-shaping developments highlighted the ongoing development of direct-drive cryogenic implosion capability. A planar cryogenic platform to measure spherical shock timing was validated and used extensively to support spherical cryogenic experiments. A total of 31 planar cryo target shots were taken. The OMEGA Availability and Experimental Effectiveness averages for FY09 were 93% and 96%, respectively.

Table 120.VIII: OMEGA Facility target shot summary for FY09.

OMEGA Target Shot Summary					
Laboratory	Planned Number of Target Shots	Actual Number of Target Shots	NIC	Shots in Support of NIC	Non-NIC
LLE	476	488	68	420	0
LLNL	200	230	125	0	105
NLUF	145	165	0	0	165
LANL	85	93	3	0	90
LBS	70	73	0	0	73
CEA	45	51	0	0	51
AWE	30	35	0	0	35
U. Mich.	10	11	0	0	11
SNL	5	7	7	0	0
Total	1066	1153	203	420	530
OMEGA EP Target Shot Summary					
Laboratory	Planned Number of Target Shots	Actual Number of Target Shots	NIC	Shots in Support of NIC	Non-NIC
LLE	215	212	0	212	0
LLNL	40	42	16	0	26
NLUF	40	43	0	0	43
LBS	45	36	0	0	36
LANL	10	11	0	0	11
CEA/AWE	5	5	0	0	5
Total	355	349	16	212	121

OMEGA EP was operated extensively in FY09 for a variety of internal and external users. A total of 298 short-pulse IR target shots were conducted. Of these, 212 target shots were taken on the OMEGA EP target chamber and 86 joint target shots were taken on the OMEGA target chamber. Beams 1 and 2 were activated to target in the UV, and the first four-beam UV target shots were conducted. A total of 76 OMEGA EP target shots included UV beams. OMEGA EP averaged 4.7 target shots per day with Availability and Experimental Effectiveness averages for FY09 of 90% and 97%, respectively. Highlights of other achievements for FY09 are shown in Table 120.VIII.

OMEGA pulse-shaping capability continues to evolve to meet the demands of producing triple-picket–shaped pulses for cryogenic experiments (see Fig. 120.51). New environmental hardware and controls upgrades to the Driver Electronics Room have improved temperature and humidity stability. The thermal stability improvements resulted in better stability for the temporal pulse shape. As a result, triple-picket pulse shapes that meet increasingly demanding specifications are now routinely achieved. Pulse-shape measurement diagnostics and analysis software continue to become more sophisticated to accurately predict picket energies and UV pulse shapes.

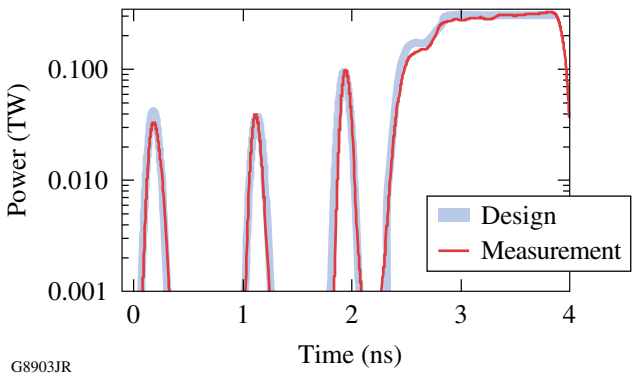

Figure 120.51
OMEGA average pulse shape from a cryogenic target implosion (shot 55723) using pulse shape HE330201T. This shot produced 300-mg/cm^2 ρR, the highest-recorded ρR to date.

The Omega Laser Facility added a planar Moving Cryogenic Transfer Cart (MCTC) to the existing inventory of five MCTC's, bringing the active total to two planar target MCTC's and four spherical target MCTC's. It is an important addition since the planar MCTC's can be interleaved to increase the number of planar experiments that can be carried out in a single shot day. Up to five planar target shots were taken in a single shot day in FY09, and with some minor adjustments to MCTC operations in FY10, the total will be increased further. Planar cryogenic target shots have been particularly instrumental in combination with shock-timing diagnostics to optimize the performance of cryogenic implosions.

A significant change was made in FY09 to the mounting system used for cryogenic implosions. The previous "C-mount" that used four spider-silk supports to suspend the target was replaced by a single-stalk-mount design that has proven to be an operationally robust component. The high-pressure fill, transfer to MCTC, and deployment attrition rates were reduced to negligible levels while maintaining and improving target performance metrics. Operationally, the key metrics are laser pulse shape, layer quality, and target offset (displacement from target chamber center at shot time). The fraction of targets with high-quality layers has increased to ~85%, and the target offset performance has improved to ~50%. Offset remains a difficult challenge and is being addressed through improved use of the tools built into the Target Viewing System and a re-engineered MCTC for spherical targets.

The Target Viewing System (TVS) upgrade in FY08 resulted in new tools becoming available for cryogenic target operations. The primary tool that has been used to make significant improvements in the cryogenic target offset is a pair of 2000-frame-per-second fast cameras. These cameras were used in FY09 to characterize the dynamic performance of the four spherical target MCTC's. There are sources of mechanical instability that occur as a result of the rapid removal of the cryogenic shroud system that occasionally perturb the target beyond acceptable levels; however, a significant fraction of targets are now within the desired 20 μm or less of displacement from target chamber center. This was achieved by three main improvements: use of the fast cameras for characterizing the target alignment carefully with shrouds in place and removed, optimizing the retraction trajectories, and cold-head-pump–induced vibration management.

A Grating Inspection System (GIS) was installed and activated on both OMEGA EP compressors. The GIS is an illumination and imaging scanning system that measures scattered light from the fourth grating of the compressor to detect optical damage. The system can identify grating damage site growth that is 500 μm or larger. The GIS is a key facility diagnostic that is routinely operated after each laser shot to ensure that maximum energy is available to short-pulse users, without risking damage to the gratings.

OMEGA EP was routinely operated at ≥1 kJ in a 10-ps pulse. An exploratory energy-ramp campaign was conducted with energies up to 2.1 kJ on target at ~10 ps to characterize short-pulse optic damage growth rates.

Determining the fraction of laser energy transferred into energetic electrons in intense laser–matter interactions is a vital parameter in high-fluence backlighter development and advanced ignition experiments, including fast ignition. Foil targets were irradiated in OMEGA EP experiments at laser intensities of $I > 10 \times 10^{18}$ W/cm^2 with up to 2.1 kJ of laser energy and pulse durations between 10 to 12 ps. These are the highest-energy, short-pulse laser–matter interaction experiments ever conducted. These experiments demonstrate that powerful electron sources can be generated with high-power, short-pulse lasers in the multikilojoule regime.

The temporal contrast of the two short-pulse OMEGA EP beamlines has been measured up to 0.5 ns before the main pulse. The diagnostic operated for more than 60 high-energy shots, demonstrating very good reliability and reproducibility. No evidence of short prepulse was found prior to main pulse, and an incoherent pedestal generated by the optical parametric chirped-pulse–amplifier's front-end was precisely characterized. The pedestal extends a few nanoseconds before the main pulse and has an intensity of less than 10^{-6} of the peak intensity for a 10-ps pulse. Approximately 10^{-4} of the laser energy is contained in this. Since the pedestal's energy contrast ratio is independent of the compressed pulse width, the intensity contrast would be an order of magnitude larger for a 1-ps pulse (i.e., $>10^7$). Contrast improvements based on LLE-demonstrated technologies are planned for the future to increase the intensity contrast.

There is considerable demand for high-pressure experiments on OMEGA EP. The velocity interferometry system for any reflector (VISAR) is the primary instrument for these experiments. A VISAR diagnostic based on the OMEGA system was installed in June 2009. This system worked as designed on the first shot and is now available for the high-pressure experiments scheduled on OMEGA EP in FY10.

National Laser Users' Facility and External Users' Programs

Under the governance plan implemented in FY08 to formalize the scheduling of the Omega Laser Facility as an NNSA facility, OMEGA shots are allocated by campaign. The majority of the FY09 target shots (56.6%) were allocated to the National Ignition Campaign (NIC), and integrated experimental teams from LLNL, LANL, SNL, and LLE conducted a variety of NIC-related experiments on both the OMEGA and OMEGA EP Laser Systems. Twenty percent (20%) of the FY09 shots were allocated to high-energy-density stewardship experiments (HEDSE) from LLNL and LANL. Under this governance plan, 25% of the facility shots were allocated to basic science experiments. Roughly half of these were dedicated to university basic science, i.e., the National Laser Users' Facility (NLUF) Program, and the remaining shots were allotted to the Laboratory Basic Science (LBS) Program, comprising peer-reviewed basic science experiments conducted by the national laboratories and LLE/FSC.

The Omega Facility is also being used for many experiments by teams from the Commissariat à l'Énergie Atomique (CEA) of France and the Atomic Weapons Establishment (AWE) of the United Kingdom. These programs are conducted on the basis of special agreements put in place by DOE/NNSA and the participating institutions.

The external users during this year included a record 11 collaborative teams that participated in the NLUF Program as shown in Table 120.IX. Ten teams from LLNL, LANL, and LLE were allotted shots under the LBS Program (Table 120.X). Integrated experimental teams from the national laboratories and LLE conducted 851 shots for the NIC, and investigators from LLNL, LANL, and LLE conducted over 232 shots for the HEDSE programs. A total of 56 shots were conducted by scientists from CEA and 35 shots were carried out by scientists from AWE.

Table 120.IX: FY09–FY10 NLUF Projects.

Principal Investigator	Affiliation	Proposal Title
F. Beg	University of California, San Diego	Systematic Study of Fast-Electron Transport and Magnetic Collimation in Hot Plasmas
R. P. Drake	University of Michigan	Experimental Astrophysics on the OMEGA Laser
R. Falcone	University of California, Berkeley	Detailed *In-Situ* Diagnostics of Multiple Shocks
U. Feldman	ARTEP, Inc.	OMEGA EP–Generated X-Ray Source for High-Resolution 100- to 200-keV Point-Projection Radiography
Y. Gupta	Washington State University	Ramp Compression Experiments for Measuring Structural Phase Transformation Kinetics on OMEGA
P. Hartigan	Rice University	Dynamics of Shock Waves in Clumpy Media
R. Jeanloz	University of California, Berkeley	Recreating Planetary Core Conditions on OMEGA, Techniques to Produce Dense States of Matter
K. Krushelnick	University of Michigan	Intense Laser Interactions with Low-Density Plasmas Using OMEGA EP
R. Mancini	University of Nevada, Reno	Three-Dimensional Studies of Low-Adiabat Direct-Drive Implosions on OMEGA
M. Meyers	University of California, San Diego	Response of BCC Metals to Ultrahigh Strain Rate Compression
R. D. Petrasso	Massachusetts Institute of Technology	Monoenergetic Proton and Alpha Radiography of Laser-Plasma-Generated Fields and of ICF Implosions

Table 120.X: Approved FY09 LBS Experiments.

Principal Investigator	Affiliation	Proposal Title	Facility Required
R. Betti	LLE/FSC	Ultra-Strong Shock and Shock-Ignition Experiments on OMEGA EP	OMEGA EP long pulse/short pulse
H. Chen	LLNL	Electron–Positron Jets	OMEGA EP short pulse/2 beams
J. H. Eggert	LLNL	Powder X-Ray Diffraction on OMEGA: Phase Transitions in Tin	OMEGA
M. B. Hegelich	LANL	Proton and Light Ion Production for Fast Ignition and Warm Dense Matter Applications	OMEGA EP short pulse
D. G. Hicks	LLNL	A New Technique for Efficient Shockless Compression to Several Mbar: Studies Using X-Ray Absorption Spectroscopy	OMEGA 40 beams
A. J. MacKinnon	LLNL	Fast Electron Transport in Hot Dense Matter	OMEGA EP long pulse
H.-S. Park	LLNL	Study of High-Z Material Properties Under Compression Using High Energy Backlighter Diffraction	OMEGA EP long pulse/short pulse
P. K. Patel	LLNL	Fundamental Benchmarking of Relativistic Laser–Matter Interaction Physics	OMEGA EP short pulse
S. P. Regan	LLE	Probing Hydrogen–Helium Warm Dense Matter (WDM) with Inelastic X-Ray Scattering: Toward the Equation of State of Jupiter's Core	OMEGA
W. Theobald	LLE	Integrated Core Heating for Fast Ignition	OMEGA and OMEGA EP

In this section, we briefly review all the basic science activity on OMEGA during FY09, including NLUF and LBS Programs, briefly summarize the FY09 NIC and high-energy-density experiments, and conclude with a summary of CEA and AWE activities.

FY09 NLUF Programs

FY09 was the first of a two-year period of performance for the NLUF projects approved for the FY09–FY10 funding and OMEGA shots. Eleven NLUF projects were allotted OMEGA and OMEGA EP shot time and received a total of 165 shots on OMEGA and 43 shots on OMEGA EP in FY09. Some of this work is summarized in this section. A new solicitation will be issued by the DOE in FY10 for NLUF grants for the period FY11–FY12.

Systematic Study of Fast-Electron Generation and Transport

Principal Investigators: T. Yabuuchi and F. N. Beg (University of California, San Diego)

Co-investigators: H. Sawada (University of California, San Diego); R. B. Stephens (General Atomics); M. H. Key and P. Patel (LLNL); D. Batani (University of Milano, Bicocca); and L. A. Gizzi (IPCF-CNR)

Understanding fast-electron generation and transport in the cone and hot, dense plasma is crucial to the success of the cone-guided fast-ignition scheme. The goal of the University of California at San Diego's NLUF project is to investigate the fast-electron transport in hot plasmas and to demonstrate collimation of fast electrons by an external magnetic field. The project consists of three steps: (1) characterization of fast-electron source and transport through the cone tip; (2) study of fast-electron transport in hot, dense plasmas; and (3) demonstration of fast-electron collimation with an external magnetic field. The first step of the project is described here: a copper wire is attached to the tip of a hollow gold cone to investigate the characteristics of the fast electrons through the tip of the cone after they are generated by the OMEGA EP 10-ps pulse.

Figure 120.52 shows the schematic of the experimental setup of cone/wire shots on the OMEGA EP laser. The one short pulse (interaction pulse) was focused into the cone/wire target. Here, the wire (40-μm diam, 1 mm long) was made of copper and attached to the tip of a gold cone with a 20-μm-thick sidewall capped with 6-μm-thick, 30-μm-inner-diam foil. The detailed target information is shown in the inset of Fig. 120.52. The Cu K_α x-ray emission from the wire was diagnosed with a highly oriented pyrolytic graphite (HOPG) spectrometer at

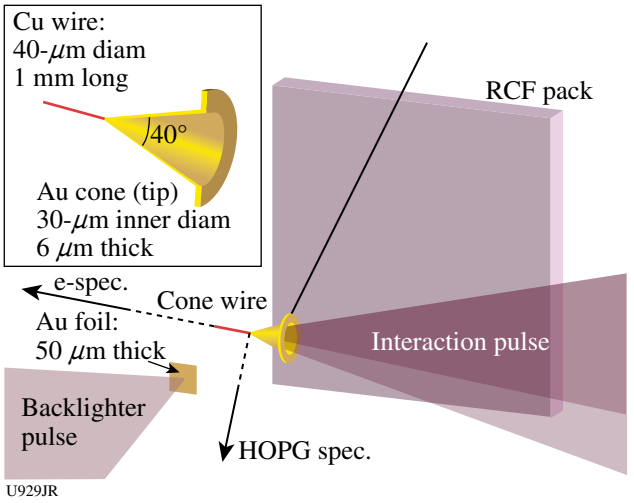

Figure 120.52
Experimental setup for cone/wire shots with proton deflectometry. The directions of the x-ray and electron spectrometers are indicated in the figure. The detailed cone/wire information is shown in the inset.

the normal direction to the wire axis. The energy spectra of the fast electrons were measured along the wire direction, i.e., on the interaction laser axis. In addition, the second short pulse (backlighter pulse) was used to generate a high-energy proton beam to measure the electrostatic field around the cone/wire target using a proton deflectometry technique. The backlighter pulse axis was perpendicular to the axis of the interaction pulse. A stack of radiochromic films (RCF's) was positioned on the axis of the backlighter pulse to detect protons at various energies, which can provide the electric field information at various timings, depending on the proton energies with a magnification of 9. The detectable proton energy range was 5 MeV to 60 MeV. The temporal resolution of the proton deflectometry was 10 ps to 50 ps. In the experiment, the interaction pulse energy was varied from 260 J to 820 J at a 10-ps pulse duration. At the best-focus position, 80% of the laser energy was contained within a 45-μm-diam spot. The beam-pointing stability was monitored with an x-ray pinhole camera that can also monitor the plasma inside the cone. A 0.7-ps pulse duration was used as the backlighter pulse to minimize the proton-generation time window. The energy of the backlighter pulse was up to 300 J.

The Cu K_α signal was observed on the HOPG spectrometer with a signal-to-background contrast of up to 1.4. The Cu K_α x-ray signal was observed to be linearly dependent on the interaction pulse energy as shown in Fig. 120.53(a). The results indicate that the coupling efficiency from the laser to the K_α photons is quasi-constant in the energy range of 260 J to 814 J; therefore, more electrons pass through the tip of the cone at the higher laser energy. The energy spectra of the vacuum electrons observed at 260-J and 814-J shots are shown in Fig. 120.53(b). Preliminary data analysis of the spectra shows that the slope temperature varies from 1.7 MeV to 2.5 MeV.

Figure 120.54 shows the proton radiographs observed on a shot with 260 J in the interaction pulse. Figure 120.54(a) shows a radiograph taken before the interaction pulse is incident on

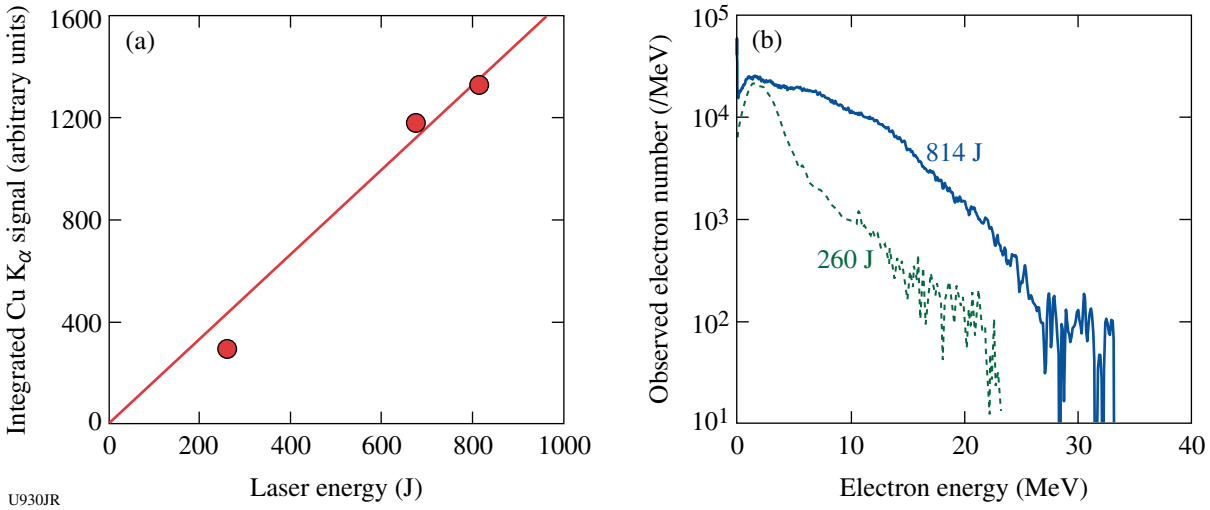

Figure 120.53
(a) Dependence of integrated Cu K_α signal on laser energy. The straight line is a linear fit to the data. (b) Energy spectra of vacuum fast electrons measured on the wire axis.

the cone/wire target by protons with an energy of ~18 MeV. The proton beam deflected by the electrostatic field around the target was observed with low-energy protons (5 MeV) as shown in Fig. 120.54(b). Protons were deflected by the electrostatic field only in the vertical direction in the figure because the magnetic field was in the azimuthal direction around the wire and canceled out any deflection. The electrostatic field strength observed in Fig. 120.54(b) was estimated at approximately tens of kV/μm using a simple calculation of proton ray tracing. Note that the maximum field strength could be higher than this estimate because the field strength can vary within a much shorter time scale than the temporal resolution of the diagnostic setup. Hybrid/PIC (particle-in-cell) modeling has been performed to investigate the fast electrons propagating through the cone tip. The transport study with such fast electrons in hot, dense plasmas and in an external magnetic field will be performed in the coming year.

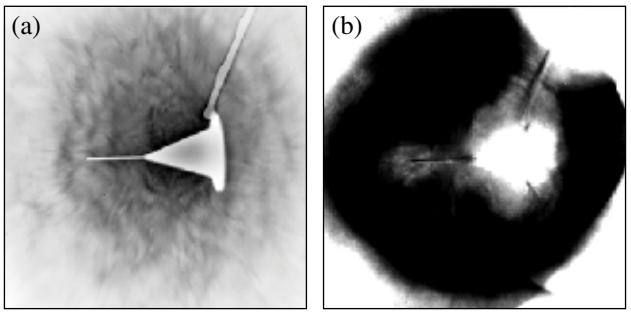

U931JR

Figure 120.54
Cone/wire target proton backlight images observed with (a) ~18-MeV and (b) 5-MeV protons at an interaction pulse energy of 260 J. The 5-MeV protons passed through the cone/wire target at about 200 ps after the interaction pulse hits the target.

Experimental Astrophysics on the OMEGA Laser

Principal Investigator: R. P. Drake (University of Michigan)
Co-investigators: D. Arnett (University of Arizona); T. Plewa (Florida State University); J. Glimm, D. Swesty, X. Li, and A. C. Calder (State University of New York–Stony Brook); I. Sokolov, J. Holloway, and K. Powell (University of Michigan); J. P. Knauer and T. R. Boehly (LLE); and B. A. Remington, H. F. Robey, J. F. Hansen, A. R. Miles, S. H. Glenzer, and D. H. Froula (LLNL)

The OMEGA laser can create conditions of very high energy density that are relevant to astrophysical phenomena. This is feasible because OMEGA can produce pressures greater than 10 Mbar on areas of square millimeters. This project explores the contribution of hydrodynamic instabilities to structure in supernovae and the dynamics of radiative shock waves. Radiative shock waves produce shocked matter so hot that it radiates away most of its thermal energy. This causes a complex, three-dimensional internal structure to develop, perhaps made even more complex by an instability. This three-dimensional structure is studied using x-ray radiography and other diagnostics. To better diagnose it, a stereoscopic imaging experiment was recently performed.

In the experiment, ten OMEGA laser beams irradiated a beryllium drive disk with UV light for 1 ns. The beams deposited a total energy of ~3.8 KJ, giving an average irradiance of $\sim 7 \times 10^{14}$ W/cm^2, generating an ablation pressure of ~46 Mbar in the beryllium drive disk. The ablation pressure first shocked and then accelerated the Be material, which then acted as a piston to drive a shock down a cylindrical shock tube filled with xenon gas. The shock moved through the xenon with an average velocity of the order of 150 km/s, which was fast enough to cause radiative effects to play a dramatic role in the shock dynamics. An additional ten OMEGA laser beams irradiated two vanadium foils on the stereoscopic backlighting target for 200 ps, creating the x rays used to image the shock tube through pinholes. To investigate the radiative shock at different velocities, we varied the drive-disk thicknesses and backlighting times. The two detectors were spaced at 37.4° and collected the x rays onto film backed by image plates. Figure 120.55 shows the images from a single target, taken 1 ns apart.

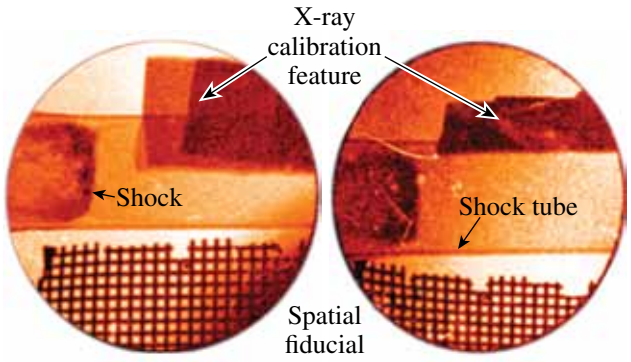

U932JR

Figure 120.55
Stereoscopic radiographs of a radiative shock in xenon gas. One can see the radiating shock, shock tube, the spatial fiducial, and the x-ray calibration feature used in the experiment. The shock, which moved from left to right within the shock tube, produced dense xenon that absorbed the diagnostic x rays, revealing its structure.

Detailed In-Situ *Diagnostics of Multiple Shocks*

Principal Investigators: R. W. Falcone (University of California, Berkeley); H. J. Lee (SLAC); and T. Döppner, O. L. Landen, and S. H. Glenzer (LLNL)

X-ray Thomson-scattering diagnostics were employed to measure the electron density and temperature of shock-compressed matter in the Fermi-degenerate state, which is of great interest to test dense-plasma modeling and to address fundamental physics questions such as the equation of state and the structure of dense matter. Powerful laser-produced x-ray sources of 6 keV have been used to probe the dense state, making possible a quantitative *in-situ* diagnostic.[1] A 250-μm-thick beryllium (Be) foil [Figs 120.56(a) and 120.56(b)] was driven by 12 beams smoothed with distributed phase plates (SG-4) in a counter-propagating geometry of heater beams. Laser intensities of 2×10^{14} W/cm^2 in 3-ns-long flat pulses were applied onto each side of the Be.

The Compton-scattering spectrum measured at a scattering angle of $\theta = 140°$ accessing the noncollective scattering regime with $\alpha = 0.4$ and $k = 5.88$ Å^{-1} shows a parabolic spectrum downshifted in energy from the incident radiation by the Compton effect;[2] the shift is determined by the Compton energy $E_C = h^2k^2/2m_e = 130$ eV. The theoretical fits to the measured spectra in Figs. 120.56(c) and 120.56(d) show that the electron density (n_e) changes with delay time. Radiation–hydrodynamic calculations using Hyades estimate the collision of two shocks around 4.3 ns. Calculated spectra using the theoretical form factor indicate compression by a factor of 5 with $n_e \sim 1.4 \times 10^{24}$ cm^{-3} by a collision of counter-propagating shocks. Further analysis will address the density and temperature evolution according to the shock propagation.

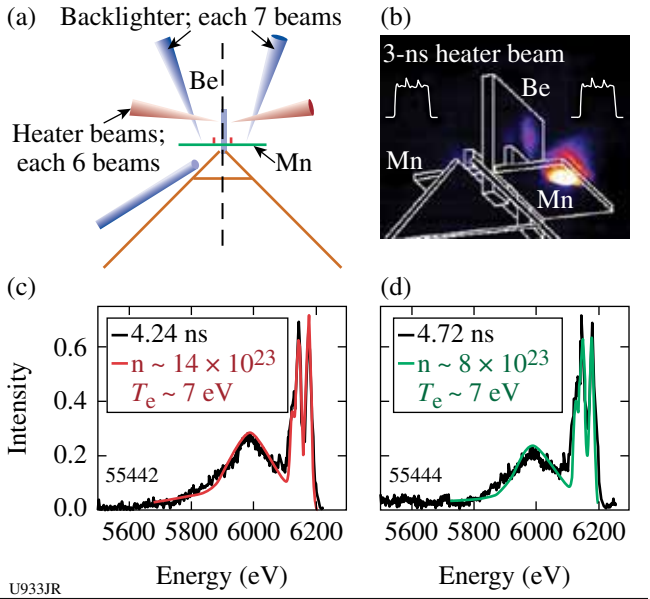

Figure 120.56

(a) Target configuration and (b) time-integrated image for $E > 2$ keV showing the emission produced by heater and probe beams. Scattering data and fit at (c) 4.24 ns and (d) at 4.72 ns.

OMEGA EP–Generated X-Ray Source for High-Resolution 100- to 200-keV Point-Projection Radiography

Principal Investigator: U. Feldman (Artep Inc.)

During the first three months of this NLUF project (which began 15 December 2008) the OMEGA EP transmission crystal spectrometer (ECS) was designed and underwent the required design reviews that assured compliance with the Omega EP Facility requirements. The small standoff distance (25.4 cm) between the target chamber center (TCC) and the ECS crystal made it necessary, on one hand, to place massive shielding fairly close to the TCC as protection from the harsh OMEGA EP hard x-ray radiation environment and, on the other hand, to ensure that the total instrument weight would not exceed the 100-lb limit and that the instrumental center of gravity would be within the TIM's (ten-inch manipulator's) allocated position. The competing requirements forced a totally new spectrometer design.

During May and June the spectrometer parts were machined and assembled and the crystal was cut and polished. In mid-July the crystal was installed and the spectrometer was aligned using the NIST 400-keV industrial tungsten x-ray source. Figure 120.57 shows the spectrometer at the NIST facility and the tungsten spectra recorded on the Rowland circle and at 20 in. and 40 in. from it. On 17 July 2009 the ECS was shipped to LLE for final checks.

On 26–27 August, the ECS was placed in TIM-13 and recorded data from 14 shots. The first shot of each day was at an energy of 35 J to 40 J and a duration of 9 ps to 10 ps; the remainder of the shots were at ~1000 J and 9 ps to 10 ps. Additional information on the shots is provided in Table 120.XI. The low-energy shots, which were focused on a thin foil of Gd, produced clean spectra; on the high-energy shots, however, the spectra were obscured by high background emission. The bright background emission was eventually identified as fairly soft x-ray radiation that was scattered from the general direction of the center of the target chamber. The scattered soft x-ray radiation was eventually removed from the spectra by a 1.2-mm-thick aluminum strip that was placed in front of the image plate and acted as a soft x-ray filter. Spectra from a Gd foil target are shown in Fig. 120.58.

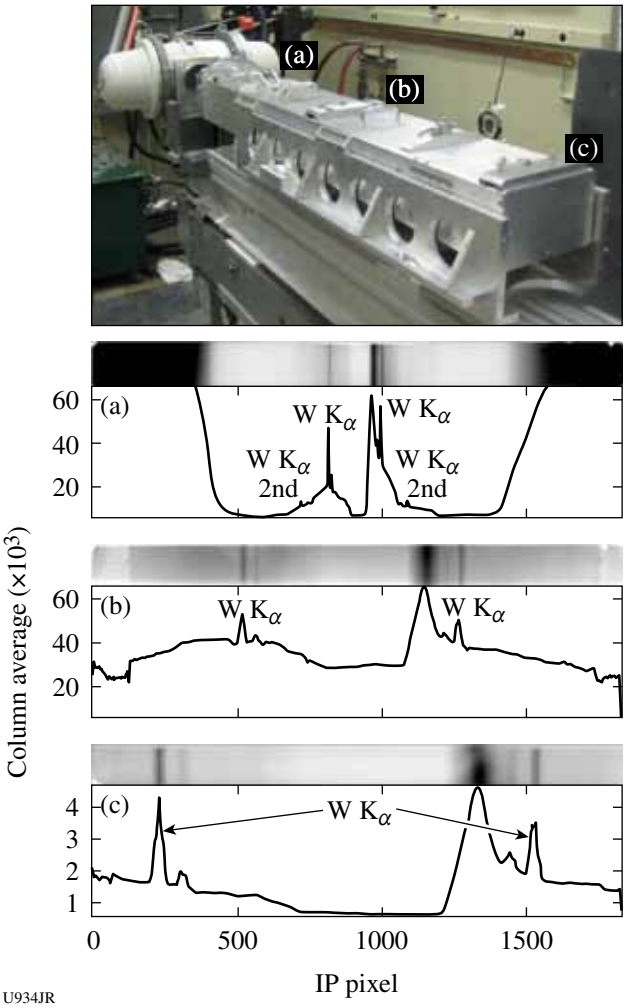

Figure 120.57
The ECS spectrometer at the NIST x-ray facility and sample x-ray spectra at IP positions (a), (b), and (c), on the Rowland circle and at 20 and 40 in. from it, respectively.

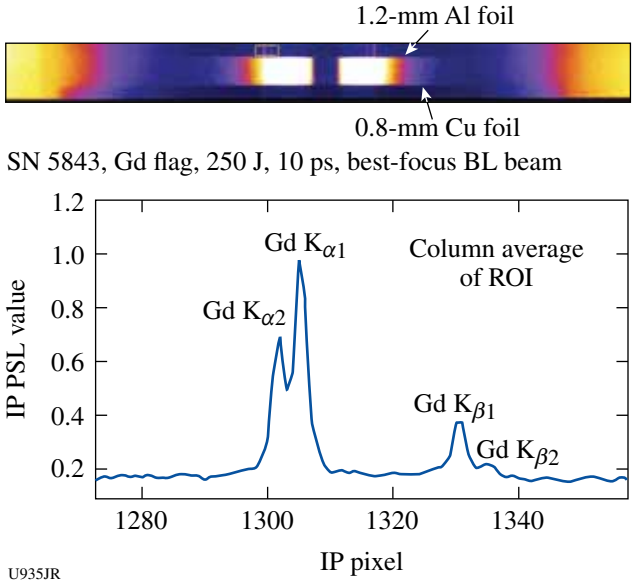

Figure 120.58
X-ray spectra on the ECS from a Gd foil target.

Table 120.XI: Shots on OMEGA EP within PPRad-EP-09, 26–27 August 2009.

Shot numbers	Beam energy (J)	Pulse	Target	Target description	RID	Results
5827	36	9 to 10 ps	FEP-8	Dy foil	29390	Data on ECS, TCS
5828	984	9 to 10 ps	Al-7	Hf foil	28653	No lines
5829	986	9 to 10 ps	Al-1	Ho Dy Tb	29384	No lines
5831	980	10 ps	FEP-2	Ho Dy Tb	29385	No lines
5833	987	10 ps	FEP-9	Dy foil	29386	Lines on TCS
5834	488	9 ps	Al-2	Ho Dy Tb	29388	No lines
5835	486	9 ps	FEP-1	Ho Dy Tb	29389	No lines
5839	35	10 ps	Gd flag	1 × 1 × 0.127 mm	29404	Lines
5840	982	10	Gd flag	1 × 1 × 0.127 mm	29405	Lines on all
5841	998	10	Au flag	2 × 2 × 0.05 mm	29410	No lines on ECS
5842	990	9	Gd flag	1 × 1 × 0.127 mm	29411	Lines maybe on ECS
5843	249	10	Gd flag	1 × 1 × 0.127 mm	29412	Nice lines on ECS
5844	975	9	Au flag	2 × 2 × 0.05 mm	29413	TCS in TIM 13
5845	1053	9	Au flag	2 × 2 × 0.05 mm	29414	Au lines on ECS

Preliminary results indicate that although the laser was focused to about 50 μm, the size of the emitting source was significantly larger (~400 μm).

During September the front end of the three image plate holders was modified by adding a layer of 0.5- to 1.0-mm aluminum. Additional shielding will be provided between the crystal and the TCC. It is expected that these additions will greatly reduce or completely eliminate the scattered radiation problem.

Second-Year Plans

The plan for the second year is to replace the image plate at the 60-in. location, which has pixel sizes of 100 μm or larger, with a pair of electronic detectors that will have a pixel size of the order of ~25 μm. The design of the electronic system is in progress. The design change will be implemented on the ECS before the next scheduled run on the OMEGA EP laser in July 2010.

Artep Inc., as part of an earlier project that was associated with measurements of hard x-ray sources on the sun, developed a Soller collimator that consisted of tens to hundreds of foils stacked together. The collimator's pitch (foil thickness and space) is as small as 50 μm. Attempts will be made to manufacture and install such a collimator in the optical pass. It is expected that the collimator will not only prevent scattered radiation from reaching the detector but more importantly will provide spectra with spatial resolution of the order of 30 μm at the source.

Ramp Compression Experiments for Measuring Structural Phase Transformation Kinetics on OMEGA

Principal Investigators: T. S. Duffy, J. Wang, and G. Finkelstein (Princeton University); R. F. Smith, J. H. Eggert, P. M. Celliers, D. Braun, and M. Bastea (LLNL); T. R. Boehly (LLE); and Y. M. Gupta (Washington State University)

This proposal was awarded 1.5 shot days on OMEGA in FY09 to explore phase transformations and their associated kinetics in new high-pressure regimes (200 to 500 GPa). These initial shots were focused on two materials that are very important in the study of planetary science: quartz and Fe. To keep these samples in the solid phase (i.e., avoid melt), it is important to minimize the temperature rise during compression. To achieve this, the target package was designed to launch a ramp compression wave into the sample of interest. Here, the compression is quasi-isentropic and the temperature is much smaller than for comparable pressures achieved through shock compression. As shown in Fig. 120.59(a), a composite pulse shape of ~10-ns duration (18 beams) from the OMEGA laser was used as input into a gas-filled halfraum. This generated a time-dependent x-ray drive, which, via a 20-μm diamond abla-

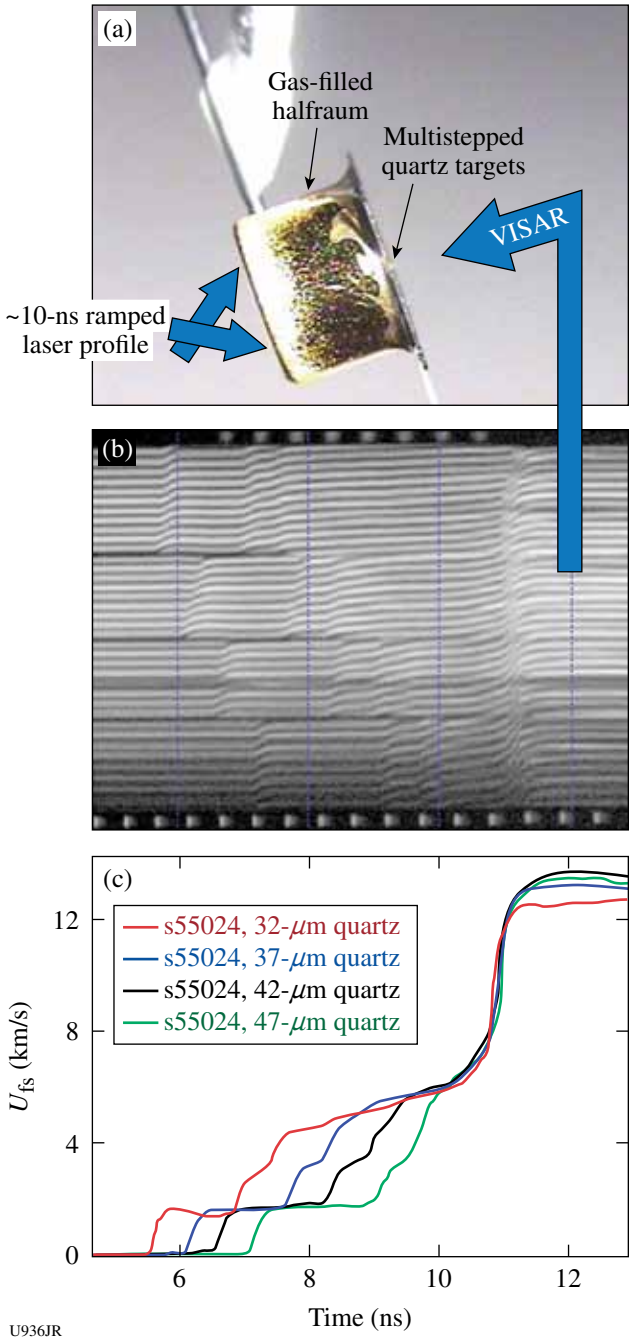

Figure 120.59
(a) A 10-ns ramped laser drive (18 beams) was used to compress a multistepped quartz target without shock. (b) The free-surface velocity was recorded using a velocity interferometer (VISAR). (c) The structured free-surface velocity profiles contain information with respect to phase transformations.

tor, launched a ramp compression wave into a multistepped quartz sample. The transmitted compression wave was recorded with a line-imaging velocity interferometer [i.e., velocity interferometer system for any reflector (VISAR), a.k.a. active shock breakout diagnostic] for each step [Fig. 120.59(b)]. These free-surface velocity profiles (U_{fs}) are shown in Fig. 120.59(c). Here the peak velocity of ~14 km/s was equivalent to a peak pressure of ~260 GPa. The structured nature of these profiles was consistent with the material undergoing one or more structural phase transformations as the pressure within the sample was steadily increased.

In addition to quartz, multistepped Fe samples (Fig. 120.60) were also shot. The target design is described in Fig. 120.59(a). The main difference between the quartz and Fe designs was that each had a unique composite laser-pulse profile, which was optimized from the material's equation of state. The composite pulse shape for Fe is shown in Fig. 120.60(a). This pulse shape resulted in the velocity profiles in a 40-/47-/54-/61-μm multistepped Fe sample shown in Fig. 120.60(b). Here, the peak velocity of 7.1 km/s corresponds to a peak pressure of ~250 GPa.

In FY09 a total of 16 shots were taken for this experiment. Analysis is ongoing for both the quartz and Fe data sets to extract equation-of-state (stress-density) and phase-transformation information. Future campaigns will focus on optimizing the design to ramp compress to peak pressures exceeding 5 Mbar (500 GPa). For reference the peak pressure at the center of the Earth is ~360 GPa.

Laboratory Experiments of Supersonic Astrophysical Flows Interacting with Clumpy Environments

Principal Investigator: P. Hartigan (Rice University)
Co-investigators: R. Carver and J. Palmer (Rice University); J. M. Foster, P. A. Rosen, and R. Williams (AWE); B. H. Wilde and M. Douglas (LANL); A. Frank (University of Rochester); and B. E. Blue (General Atomics)

Strong shock waves occur in many astrophysical systems, and the morphology of the emission lines that occur from the hot gas behind these shocks is often highly clumpy. The objective of this sequence of NLUF experiments is to develop scaled laboratory experiments to study the hydrodynamics of clumpy supersonic flows. The laboratory work complements new astrophysical images from the Hubble Space Telescope that were motivated by the results of a previous NLUF program.

In the past year, a new target concept was designed and tested in which several dozen 130-μm-diam sapphire spheres were embedded within a cylindrical foam target and a strong shock was propagated through this composite. We also compared how the shock propagation differs between a highly clumped target and a uniform one with the same overall density. The shots were successful, and we were able to observe the small clumps as they were entrained within the passing shock. This situation has a close astrophysical analog in many outflows from young stars (see Fig. 120.61).

In the last year the Astrophysical Journal accepted a paper by this collaboration that describes the results from the previous set of experiments examining the shock waves that occur when a collimated jet deflects from a single large obstacle.

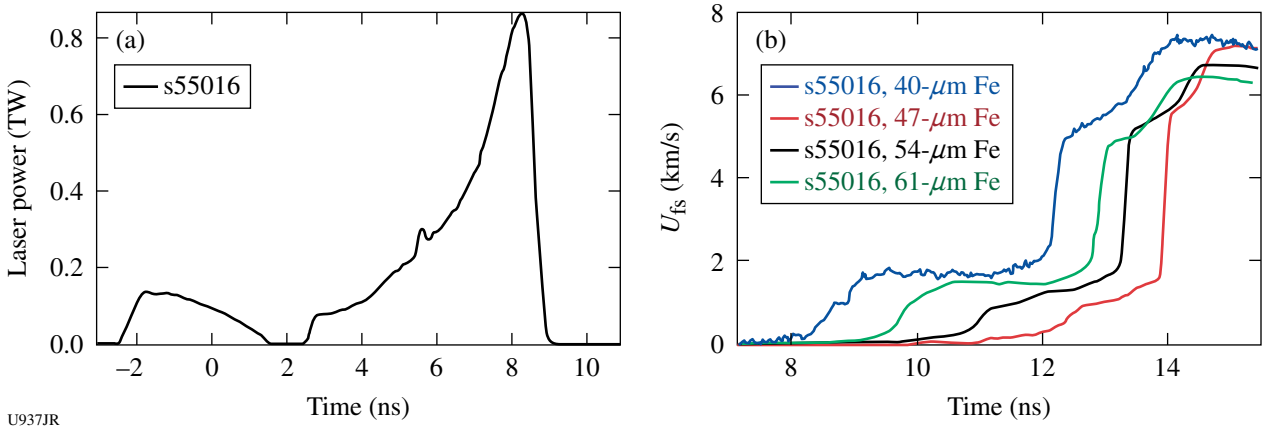

Figure 120.60
(a) Composite laser pulse shape (18 beams) was used to compress a multistepped Fe target without shock. (b) The free-surface velocity was recorded using a velocity interferometer (VISAR). Peak pressures of 3 Mbar were achieved in the Fe sample.

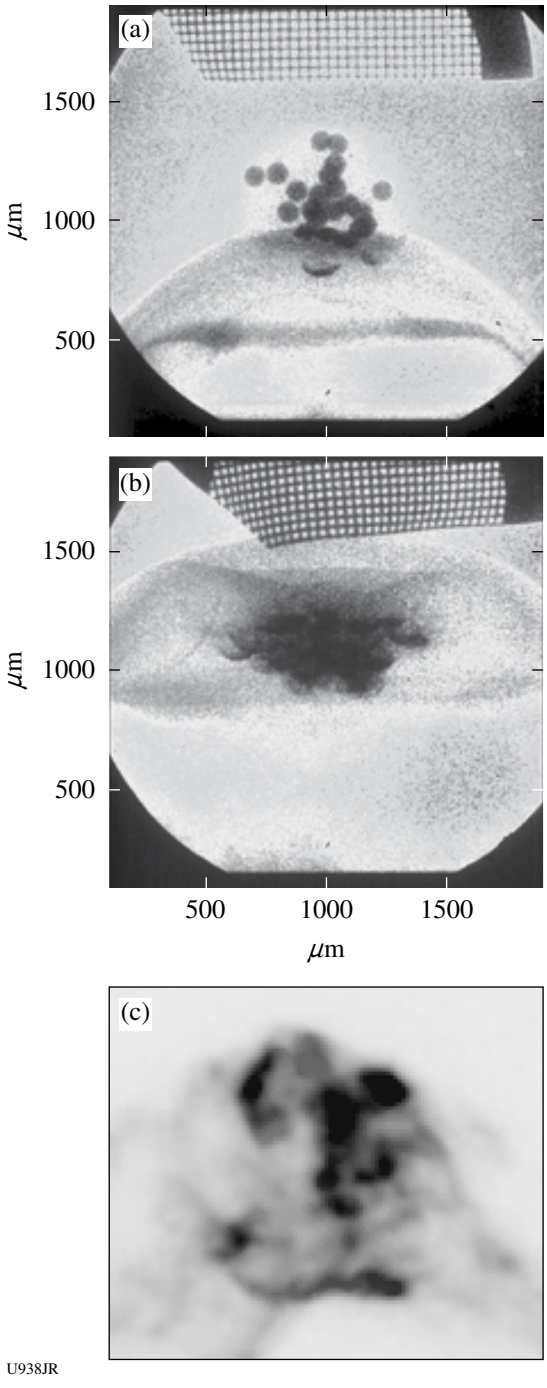

Figure 120.61
[(a),(b)] A strong bow shock propagates through a foam within which are embedded numerous sapphire spheres. Small bow shocks form around each of the spheres as they are overrun and entrained by the main shock wave. The scales are in microns, and the herringbone pattern at the top is a grid used to verify the scale of the images. (c) The astrophysical analog, HH 47, as observed with the Hubble Space Telescope. In all cases the clumps are embedded in a flow that moves from the bottom to the top in the figures.

FY09 Low-Density Plasma Interactions

Principal Investigators: L. Willingale, K. Krushelnick, and A. Maksimchuk (University of Michigan); P. M. Nilson, C. Stoeckl, and T. C. Sangster (LLE); and W. Nazarov (University of St. Andrews)

The propagation of relativistically intense laser pulses into near-critical-density plasma has been shown to be influential on the rear-side proton acceleration,[3] and it is of interest for fast-ignition scenarios to determine laser penetration.[4,5] Investigations of proton acceleration and laser propagation using the OMEGA EP laser (1000 J, 10 ps, 2×10^{19} W/cm^2) interacting with low-density targets have been performed. Very low density, submicron-pore-size CHO foam targets (3 to 100 mg/cm^3) produce plasmas of between 0.9 n_c and 30 n_c, where n_c is the nonrelativistic critical density. Proton beams are observed from the rear side to have maximum energies of up to 51 MeV.

Also, proton radiography, which can image quasi-static electromagnetic fields and density perturbations, is used to investigate the interaction of the 1000-J, 10-ps laser pulse interaction with a 1.5-n_c plasma. A schematic of this experiment is shown in Fig. 120.62. Using the second OMEGA EP short-pulse beam (700 fs, 250 J) to create the proton beam (proton energy of up to 60 MeV) and detecting the different proton energy images using a radiochromic film stack make it possible to obtain a picosecond resolution "movie" of the 10-ps laser interacting

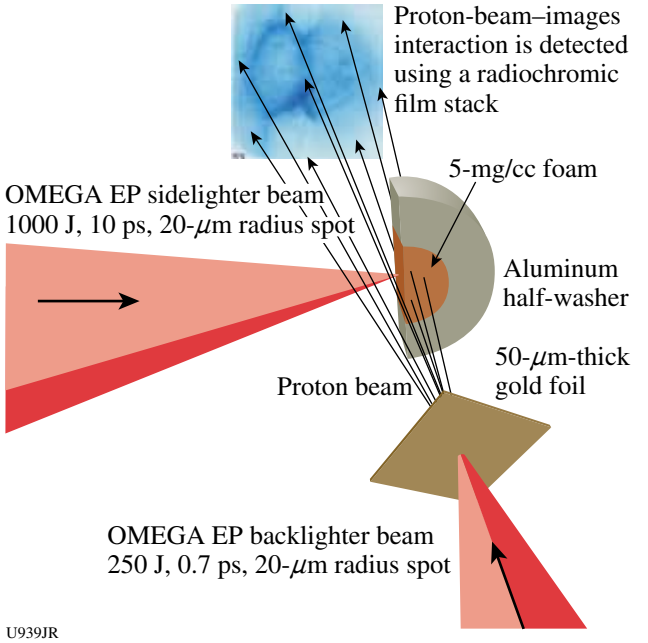

Figure 120.62
Experimental setup for the proton radiography.

with the foam target. The transit time from the proton source foil to the interaction means the different energy protons pass the main interaction at different times. The technique also requires that the interpulse timing be known accurately, which was verified using the ultrafast x-ray streak camera. Examples of the proton radiographs are shown in Fig. 120.63. The most-striking feature is the rapidly expanding front, back toward the laser from the target surface. It is traveling at a velocity of up to 1×10^8 ms^{-1}, which corresponds to proton energies of about 50 MeV. Filamentary structures are observed where the laser has passed through the pre-plasma.

Three-Dimensional Studies of Low-Adiabat Direct-Drive Implosions on OMEGA

Principal Investigator: R. Mancini (University of Nevada, Reno)

Determining the spatial structure of implosion core temperature conditions is of current interest in inertial confinement fusion experiments. Three methods have been developed and tested in OMEGA direct-drive implosions to extract temperature spatial profiles from the analysis of narrowband x-ray images recorded with a DDMMI instrument. The targets consisted of plastic shells filled with deuterium gas and a trace amount of argon for diagnostic purposes and driven with a low-adiabat $\alpha \sim 2$ pulse shape. The analysis methods treat space integration and radiation transport effects with different levels of approximation.

The emissivity ratio of $\mathrm{Ly}_\beta/\mathrm{He}_\beta$ argon lines is strongly dependent on electron temperature T_e but only weakly dependent on electron density N_e; therefore, it can be used as a temperature diagnostic. The first method considers the ratio of $\mathrm{Ly}_\beta/\mathrm{He}_\beta$ image intensities. If we neglect the radiation transport effect, each intensity point on the image plane can be interpreted as the line integral of the emissivity along a given chord in the plasma source. Therefore, the ratio of $\mathrm{Ly}_\beta/\mathrm{He}_\beta$ intensities on the image plane corresponds to the ratio of average emissivities along chords in the core, and this ratio can be converted into an average or effective electron temperature T_e integrated along the chord. The result of this analysis is displayed in Fig. 120.64. The x and y coordinates in the surface plot correspond to the coordinates on the image plane. The

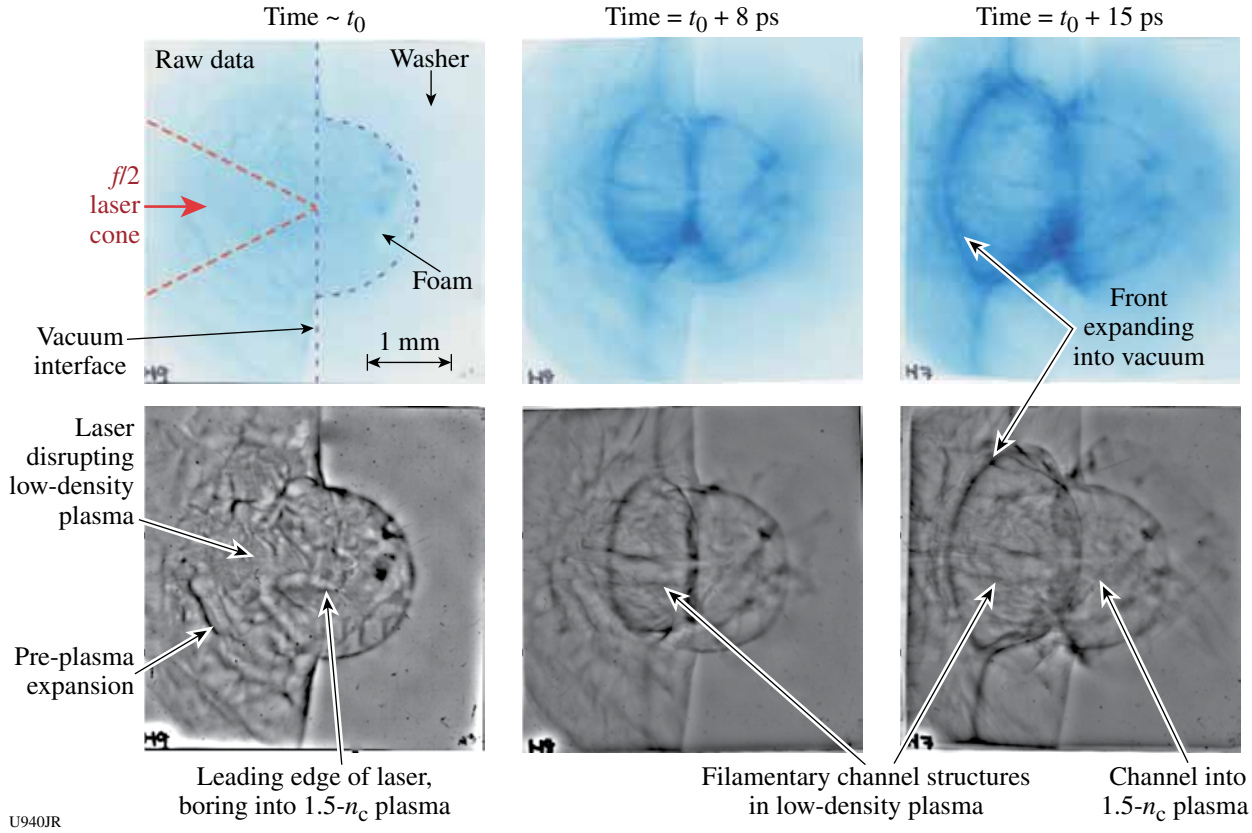

Figure 120.63

Proton images from a single shot of the 1000-J, 10-ps laser (coming in from the left) interacting with the 5-mg/cm^3 foam target. The top row shows the raw data; the bottom row shows the same images enhanced to bring out the features.

electron temperature T_e varies in the range from 900 eV near the core edge to 1400 eV in a region off core center. We note that no symmetry assumptions or geometry inversions are required to perform this analysis.

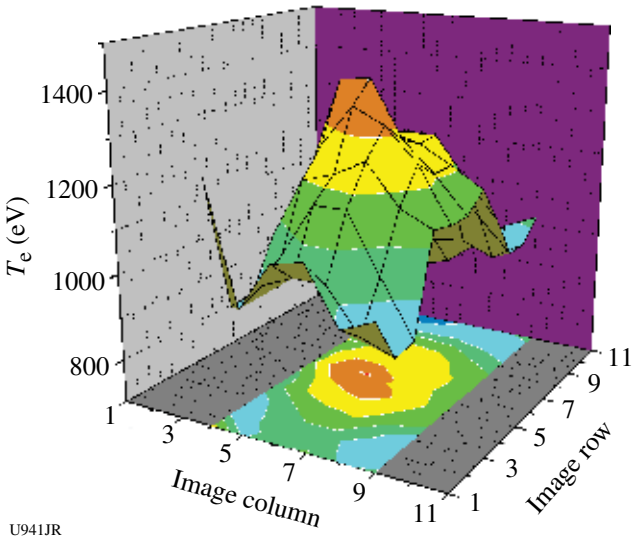

Figure 120.64
Electron-temperature T_e spatial distribution obtained from the ratio of Ly_β/He_β image intensities.

The second method splits the core into a collection of core slices and uses an Abel inversion procedure for each core slice to go from intensity distribution on the image plane to emissivity profile in the plasma source. The Abel inversion unfolds the line integration corresponding to chords in each core slice to yield local emissivity in the core slice, but it still assumes negligible radiation-transport effects. Also, the application of the Abel inversion procedure requires local axial symmetry in each core slice. To satisfy this condition, intensity profiles associated to a given core slice must be made symmetric about a suitable center point. This operation partially removes some of the asymmetries observed on the image, thereby yielding Abel-inverted emissivities as a function of radial coordinate r in the core slice. As a result, the ratio of Abel-inverted Ly_β/He_β emissivities can be converted into a spatial profile of T_e as a function of the radial coordinate in the core slice, i.e., $T_e(r)$. The collection of $T_e(r)$ profiles from all core slices represents a quasi-three-dimensional map of the electron-temperature spatial distribution. The result of this analysis is shown in Fig. 120.65. The x and y coordinates in the surface plot now correspond to core slice label and a projection of the radial coordinate in the core slice on the image plane. While this analysis still neglects the radiation-transport effect, the unfolding of the chord line integration via the Abel inversion results in an electron temperature that ranges from about 900 eV near core edge to 1900 eV inside the core but off the core center. This temperature distribution is axially symmetric in each core slice but it still has some of the asymmetry present in the image data.

Finally, the third method is an attempt to unfold both the chord line integration and the radiation-transport effect. As in the second method, the core is split into slices and each core slice is assumed to be axially symmetric. Then, a multi-objective Pareto genetic algorithm is used to drive a search in parameter space with the goal of finding the temperature and density profiles that yield the best simultaneous and self-consistent fits (i.e., approximations) to three objectives: the He_β image intensity distribution, the Ly_β image intensity distribution, and the space-integrated line spectrum. Alternatively, the Ly_β/He_β image intensity ratio can also be used as an objective instead of one of the image intensities. Optimal fits are obtained by following up the genetic algorithm search with a "fine-tuner" step driven by a nonlinear least-squares minimization algorithm. The image intensity distribution on the image plane is approximated by transporting the line radiation, one photon energy at a time, inside the core slice via an integration of the radiation transport equation. The result of this analysis is shown in Fig. 120.66. Accounting for both space integration and radiation transport effects yields a temperature spatial distribution in the core that spans the range from 900 eV near core edge to 2250 eV inside the core, resulting in a temperature spatial structure with the steepest gradients. Therefore, neglecting space integration and radiation transport effects leads to a

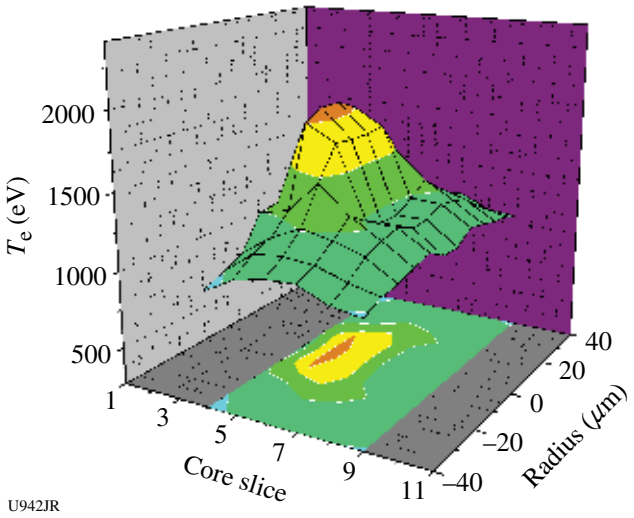

Figure 120.65
Electron-temperature T_e spatial distribution obtained from the ratio of Ly_β/He_β Abel-inverted emissivities.

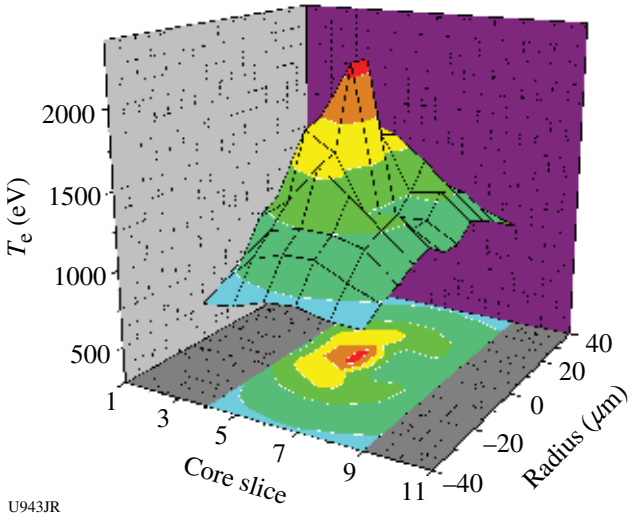

Figure 120.66
Electron-temperature T_e spatial distribution obtained from a search and reconstruction method driven by a Pareto genetic algorithm.

temperature spatial structure characteristic of the shallowest spatial gradients, while taking both effects into account yields a spatial structure with the steepest spatial gradients. Work is in progress to extend these methods to account for image data recorded simultaneously along three lines of sight with three DDMMI identical instruments.

Proton Radiography of Direct- and Indirect-Drive ICF Experiments and HEDP Plasmas

Principal Investigators: R. D. Petrasso and C. K. Li (Massachusetts Institute of Technology)
Co-investigators: F. H. Séguin and J. A. Frenje (MIT); J. P. Knauer and V. A. Smalyuk (LLE); J. R. Rygg and R. P. J. Town (LLNL).

MIT's NLUF Program has continued an ongoing series of experiments utilizing charged-particle radiography in the study of plasmas and transient electromagnetic fields generated by the interactions of OMEGA laser beams with plastic foils, direct-drive inertial confinement fusion (ICF) target capsules, hohlraums, indirectly driven ICF targets, and plastic or metal foils combined with foam cylinders (for laboratory-scaled astrophysical jets). This work, involving novel studies of field instabilities, magnetic reconnection, ICF implosion dynamics, and self-generated electromagnetic fields in ICF implosions and hohlraums, has already resulted in many publications, including six in Physical Review Letters[6–11] and one in Science,[12] as well as several invited talks[13–21] and many contributed talks at conferences. While most of the experiments have used exploding-pusher backlighters on OMEGA to produce monoenergetic protons and alpha particles,[22] work this year used protons from backlighter foils driven by OMEGA EP short-pulse beams. One experiment involved the simultaneous use of both types of backlighter.

Illustrating one of these important series of experiments, Fig. 120.67 shows the basic setup that was used for the first observations of self-generated fields associated with laser-irradiated hohlraums.[10] An exploding-pusher backlighter was driven by 21 OMEGA beams, while two hohlraums to be studied were driven by ten beams each (the isotropic emission of the backlighter makes it possible to image multiple objects simultaneously in different directions), as shown in Fig. 120.67(a). The backlighter produced short bursts (~130 ps) of monoenergetic protons at two different energies (3.3 MeV and 15 MeV), as shown in Fig. 120.67(b), and the special detector pack based on CR-39 nuclear track detectors made it possible for separate images to be recorded at each energy. As indicated in the left part of Fig. 120.67(a), a metal mesh was placed on the end of each holhraum nearest the backlighter; this divided the incident particles into beamlets whose deflec-

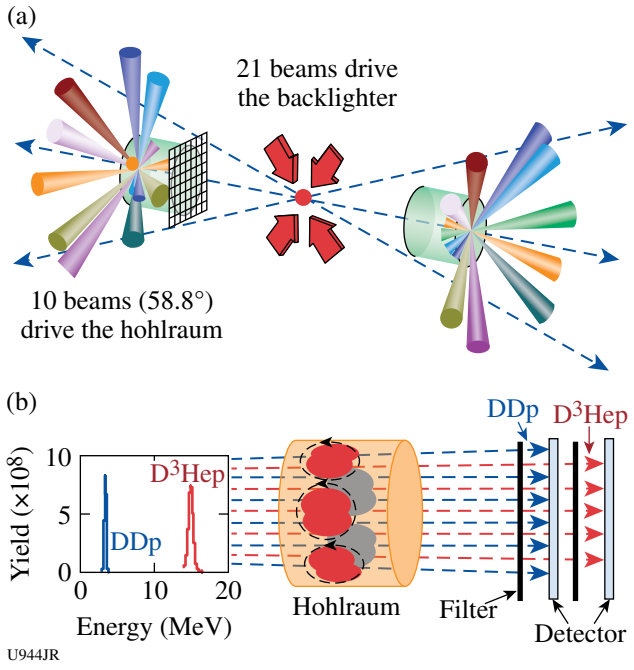

Figure 120.67
(a) Experimental setup, with proton backlighter, subject hohlraums, and laser beams. (b) Typical energy spectrum and CR-39 detector pack. The distance between the backlighter and the mesh (detector) was 0.7 (27) cm. Filters in the detector pack were carefully chosen so that 3.3-MeV and 15-MeV protons were recorded on the front and back detectors, respectively.

tions in the image plane could be measured for quantification of particle trajectory bending within the hohlraum caused by electric and/or magnetic fields.

Figure 120.68 shows sequences of proton images covering a time period from the beginning of the laser pulse (t = 0 ns) to 0.8 ns after it was turned off ($t \approx 1.8$ ns). At earlier times ($t \geq 0.9$ ns) the beamlet arrays in the 15-MeV images [Fig. 120.68(a)] show minimal displacement by fields or plasma, but beamlets have different sizes at different times, reflecting the presence of an E field of $\sim 2 \times 10^9$ V m^{-1} at ~0.37 ns that then decays away. At later times the 15-MeV beamlets show some chaotic spatial structure, indicating that their trajectories have been affected by large-field and plasma effects. In the 3.3-MeV images, beamlet arrays are coherently distorted by t = 0.52 ns and disappear altogether (due to stronger deflections) at later times. Quantitative analysis of the beamlet displacements indicates the presence of B fields with peak values of ~10^6 Gauss. The five-prong asterisk-like fluence pattern in the 3.3-MeV proton images at $t \geq 1.01$ ns was shown to be a consequence of the staggered distribution of laser beams on each hohlraum wall. The ten beams were grouped into five pairs that produced five plasma bubbles; the asterisk pattern was caused by scattering of the protons in Au-plasma jets between the bubbles shooting inward from the hohlraum wall at about ~Mach 4 (~1000 μm ns^{-1}). The Au density was inferred to be ~10 mg cm^{-3} (note that this should not occur in an ignition hohlraum, where a gas fill would impede the jets). These experimental results have important implications for understanding the precise conditions and plasma dynamics inside vacuum hohlraums and provide an impetus for the further development of 3-D multifluid codes with self-consistent field generation.

FY09 Laboratory Basic Science Programs

Ten proposals were approved and allocated 25 shot days on the Omega Facility in FY09 (Table 120.X). Unfortunately, because of the DOE funding shortfall in FY09, only 17 days (109 shots) of LBS experiments were actually funded and carried out during this fiscal year. The FY10 solicitation for the LBS Program resulted in 25 proposals with shot requests totaling 63.5 shot days. After peer review by an independent committee, 13 LBS proposals have been recommended for 29 shot days in FY10. Three additional shot days were recommended and approved for FY09 make-up shots. The approved FY10 LBS proposals are listed in Table 120.XII. This section includes brief summaries of LBS experiments carried out in FY09.

Electron–Positron Jets

Principal Investigators: H. Chen and S. C. Wilks (LLNL)
Co-investigators: J. F. Myatt and C. Stoeckl (LLE);
and E. Lang (Rice University)

On 16 April 2009, an LLNL/LLE team performed a Laboratory Basic Science experiment on the OMEGA EP Laser System to study positron production in high-intensity laser interactions with high-Z targets. The OMEGA EP backlighter produced ~1 kJ in a 10-ps laser pulse that interacted with a 1-mm-thick Au target. The positrons that were emitted from the rear side of the target were measured with a magnetic positron spectrometer. A quasi-monoenergetic positron beam was observed with a maximum energy of ~20 MeV as shown in Fig. 120.69. It is estimated that 10^{12} positrons were produced. This is a factor of ~10 more than were produced with a 260-J, 10-ps laser in LLNL experiments.[23] It was anticipated that the number of positrons produced would scale approximately with the laser energy.[24] The quasi-monoenergetic positron

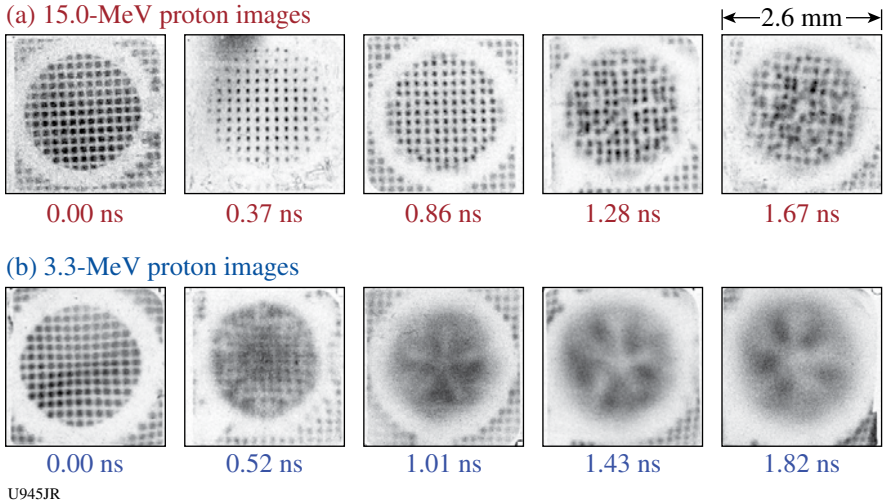

Figure 120.68
Radiographs of a laser-driven, vacuum Au hohlraum at different times, taken with (a) 15.0-MeV and (b) 3.3-MeV protons, illustrating spatial structure and time evolution of proton deflection and beamlet size. Pairs of images in (a) and (b) were taken in the same shot, but they represent different sample times because of different proton velocities. In each image, darker means higher fluence; the gray-scale mapping is different in each image to account for the different backlighter yields.

Table 120.XII: Approved FY10 LBS Experiments.

Principal Investigator	Affiliation	Proposal Title	Facility Required
R. Betti	LLE/FSC	Integrated Shock-Ignition Experiments on OMEGA	OMEGA
P. M. Celliers	LLNL	Measurement of the Viscosity of Shock-Compressed Fluids: Studies of Water and Silica	OMEGA
H. Chen	LLNL	Producing Pair Plasma and Gamma-Ray Burst Using OMEGA EP	OMEGA EP
D. E. Fratanduono	LLE	Optical Properties of Compressed LiF	OMEGA and OMEGA EP
D. H. Froula/J. S. Ross	LLNL	First Observations of Relativistic Plasma Effects on Collective Thomson Scattering	OMEGA
S. H. Glenzer	LLNL	Capsules Adiabat Measurements with X-Ray Thomson Scattering	OMEGA
D. G. Hicks	LLNL	Ramp and Multi-Shock Compression of Iron to Several Megabars: Studies Using Extended and Near Edge X-Ray Absorption Spectroscopy	OMEGA
H.-S. Park	LLNL	Study of High-Z Material Properties under Compression Using High-Energy Backlighter Diffraction	OMEGA EP
P. K. Patel	LLNL	Benchmarking Laser-Electron Coupling at Fast Ignition–Relevant Conditions	OMEGA EP
S. P. Regan	LLE	Validating Inelastic X-Ray Scattering from H and H/He Warm Dense Matter with Shock Velocity Measurements: Toward the Equation of State of Jupiter's Core	OMEGA
R. Smith/J. H. Eggert/ S. M. Pollaine	LLNL	Phase Transformation Kinetics	OMEGA
C. Stoeckl/ W. Theobald/W. Seka	LLE	Channeling in Long-Scale-Length Plasmas	OMEGA EP
W. Theobald	LLE	Integrated Core Heating for Fast Ignition	OMEGA and OMEGA EP

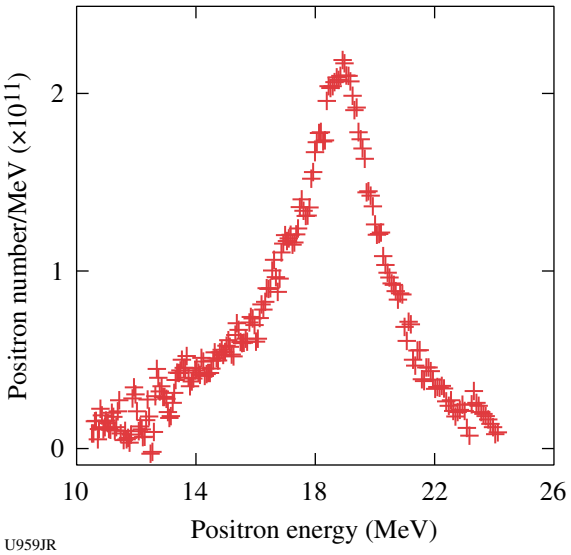

Figure 120.69
Positron spectrum measured on the OMEGA EP laser.

spectrum is likely a cause of positron acceleration from the sheath formed by escaping electrons on the rear surface of the target. The differences between the two experiments will be studied to understand the consequences of these results. The positron-production rate during the laser shot appears to be the highest ever observed in the laboratory.

Positron research has extended over diverse fields from particle physics and astrophysics to medical application. This often requires the production of large numbers of positrons on a short time scale, which has been difficult to supply. The new OMEGA EP results could profoundly alter the direction of the quest of establishing a laser-produced positron source for research in these fields.

X-Ray Absorption Fine Structure Measurements of Iron Compressed to a Few Megabars

Principal Investigators: Y. Ping and D. G. Hicks (LLNL)
Co-investigators: J. H. Eggert (LLNL); B. Yaakobi and T. R. Boehly (LLE); and R. Hemley (Carnegie)

X-ray absorption fine structure (XAFS) measurements were performed on iron that was ramp and multishock compressed to a pressure of a few megabars. By dynamically compressing a few-micron-thick iron sample sandwiched between thin diamond anvils, near-constant pressure conditions were produced inside the iron with the bulk of the pressure evolution taking place in the adjacent, x-ray-transparent diamond anvils. A spherical, imploding backlighter source was used to produce a smooth broadband source of x rays for the absorption measurement. Several different target configurations were studied in the single day of shots performed in FY09 to establish the optimum configuration of target versus backlighter drive and how best to achieve simultaneous measurements of the pressure using a velocity interferometer system for any reflector (VISAR). Success was achieved by maximizing the number of beams used on the backlighter and driving the target package with a stacked, multishock pulse. The resulting XAFS spectra (Fig. 120.70, compared to an undriven target) were analyzed using the FEFF code and found to give a compression of 1.55 and a temperature of 6000 K, with a pressure of 2.5 Mbar obtained from the VISAR. A modified analysis is being developed to determine the radial distribution function $g(r)$ from these data. Future work will scan through different regions of pressure, density, and temperature space to map out the iron phase diagram.

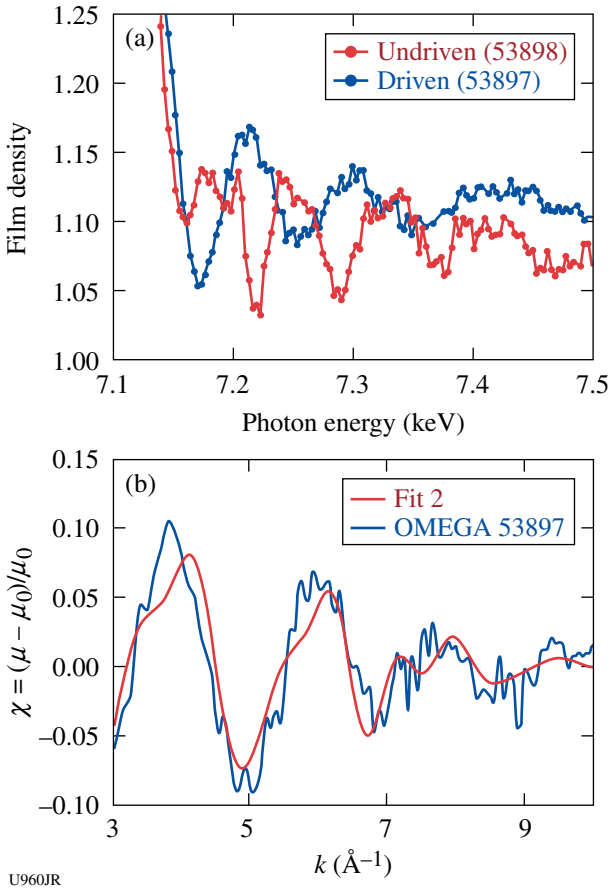

Figure 120.70
(a) Comparison of raw x-ray absorption spectra for undriven iron and multishocked iron compressed to ~2.5 Mbar. (b) A best fit to the x-ray absorption coefficient as a function of wave number gives a compression of 1.55 and a temperature of 6000 K.

Probing H/He Warm Dense Matter with Inelastic X-Ray Scattering: Toward the Equation of State of Jupiter's Core

Principal Investigator: S. P. Regan (LLE)
Co-investigator: G. Gregori (LLNL)

The objective of this research is to measure the equation of state (n_e, T_e, Z) of direct-drive, shock-heated, planar cryogenic H/He targets using spectrally resolved x-ray scattering (i.e., inelastic x-ray scattering) in the 1- to 100-Mbar range. The H/He warm dense matter is relevant to planetary interiors. The largest planet in our solar system, Jupiter, is composed primarily of H and He, having a predicted pressure in the tens-of-megabars range. The research has a synergistic relationship with the programmatic direct-drive inertial confinement fusion (ICF) research being conducted at the Omega Facility. It works in parallel with the ICF research, which uses inelastic x-ray scattering to study the equation of state (EOS) of direct-drive, shock-heated, planar cryogenic deuterium targets. In the truncated LBS shot schedule, one day on OMEGA was dedicated to demonstrating this experimental platform. A planar liquid deuterium target was chosen to maximize the likelihood of success. The polyimide ablator was irradiated with a 6-ns constant-intensity (~10^{14} W/cm^2) laser drive forming an ~100-μm-thick layer of shocked deuterium, which is uniform in the transverse dimension over a 0.5-mm diameter. The 1-D predictions for the laser-ablation–driven shock wave are P = 12 Mbar, T_e = 22 eV, $n_e = 2 \times 10^{23}$ cm^{-3}, ρ = 0.8 g/cm^2, and Z = 1. A collimated beam of Cl Ly$_\alpha$ emission (2.96 keV) was scattered from the shocked deuterium and detected with a gated x-ray spectrometer at a scattering angle of 90°. The measured spectrum of Cl Ly$_\alpha$ emission (2.96 keV) and He-like satellites transmitted through the shocked liquid deuterium is shown in Fig. 120.71(a). The measured spectrum of noncollective x-ray scattering for Cl Ly$_\alpha$ emission at 90° (diamonds) is compared

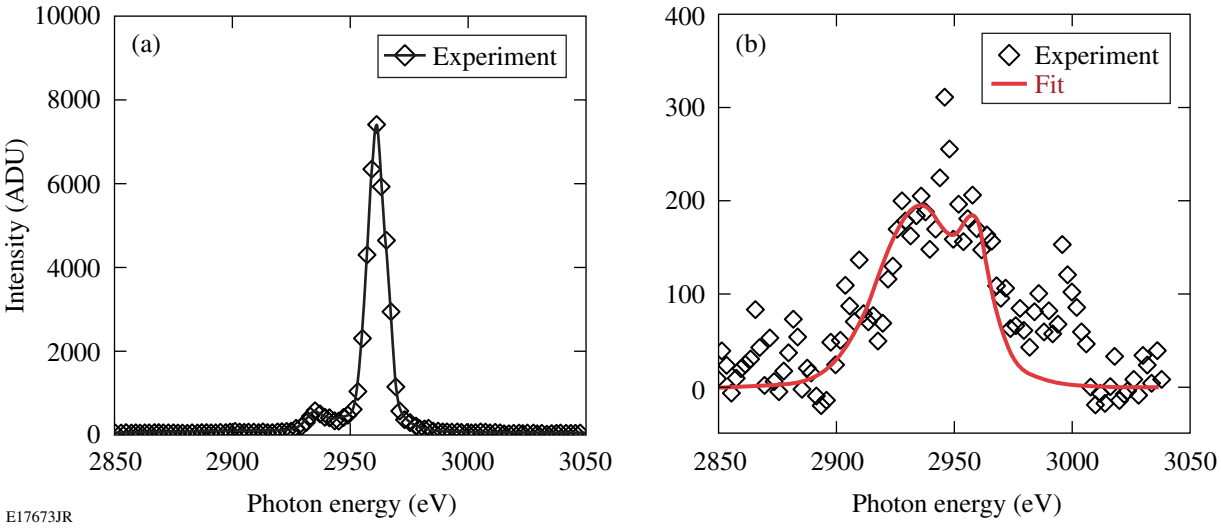

Figure 120.71
(a) Measured spectrum of Cl Ly$_\alpha$ emission (2.96 keV) and He-like satellites transmitted through the shocked liquid deuterium; (b) measured spectrum of noncollective x-ray scattering for Cl Ly$_\alpha$ emission at 90° (diamonds) compared with spectrum predicted for $T_e = 20$ eV, assuming $n_e = 1 \times 10^{23}$ cm^{-3} and $Z \sim 1$.

with spectrum predicted (red curve) for $T_e = 20$ eV, assuming $n_e = 1 \times 10^{23}$ cm^{-3} and $Z \sim 1$ in Fig. 120.71(b). The initial results are promising; however, further optimization in the experiment is needed to improve the noisy, scattered x-ray signal.

Integrated Shock-Ignition Experiments on OMEGA

Principal Investigators: W. Theobald and R. Betti (LLE)

Parametric plasma instabilities are of concern in an ignition target design with spike-pulse intensities in the range of 10^{15} to 10^{16} W/cm^2 and pulse durations of approximately several hundred picoseconds. The instabilities degrade the laser energy coupling to the capsule and increase the fraction of the laser energy transferred to hot electrons, which is a potential source of preheat that can reduce the final core compression in functional ICF implosions.

To test the effect of laser–plasma instabilities and hot electrons, shock-ignition laser–plasma experiments have been performed on the OMEGA laser with shock-generating laser intensities of up to ~8×10^{15} W/cm^2 (Ref. 25). Figure 120.72 shows a schematic of the experiments. The compression pulse

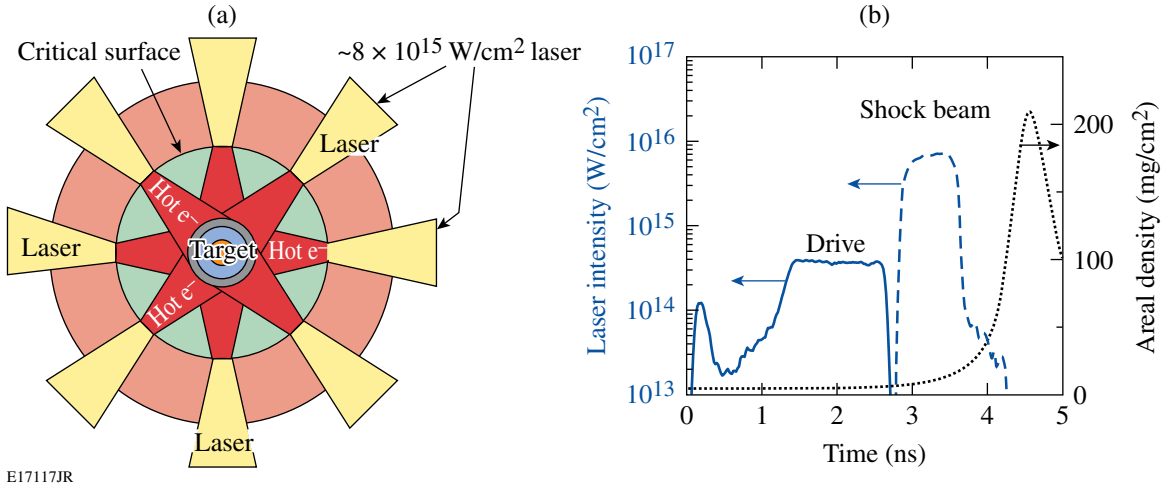

Figure 120.72
(a) Schematic of the setup for studying laser–plasma interactions and preheating at high laser intensities relevant to shock ignition. Forty of the OMEGA laser beams implode the capsule at low intensities. Twenty delayed beams are tightly focused onto the critical-density surface, where plasma instabilities lead to the generation of energetic electrons heating the dense core. (b) Pulse shapes of the 40 drive beams (solid), 20 shock beams (dashed), and areal-density evolution (dotted).

consists of a shaped low-adiabat pulse (solid) using 40 OMEGA beams with ~13.6 kJ of UV laser energy. The targets were 36-μm-thick, 430-μm-outer-radius, deuterated plastic shells coated outside with a 0.1-μm layer of aluminum and filled with D_2 gas with a pressure of ~30 atm. A late shock was driven by the remaining 20 UV beams that were delayed and tightly focused on the compressed core to achieve intensities at the critical-density surface ranging from $\sim 2 \times 10^{15}$ to $\sim 8 \times 10^{15}$ W/cm^2.

The effect of high-intensity shock beams on neutron and hard x-ray yields was studied as a function of the delay between the 40 and 20 beams [Figs. 120.73(a) and 120.73(b)]. The delay time defined by the onset of the high-intensity beam with respect to the start of the drive pulse was varied from 2.3 ns to 2.9 ns. The neutron yield increased by a factor of ~7 from 5×10^8 to $\sim 3.5 \times 10^9$ for the shortest time delay. Two reference implosions with only 40 drive beams produced neutron yields of 1.4×10^8 and 3.7×10^8; the solid line in Fig. 120.73(a) represents the average of these yields. Figure 120.73(b) shows the hard x-ray signal, which is indicative of hot-electron production. A similar trend is observed for the hard x-ray yield, showing a larger amount of hot electrons generated at shorter time delays. The measured neutron yields of the 40-beam implosion show that, despite large target-illumination nonuniformity, a significant amount of the high-intensity-pulse energy is coupled into the capsule, producing up to ~20× more neutrons and a strong hard x-ray signal.

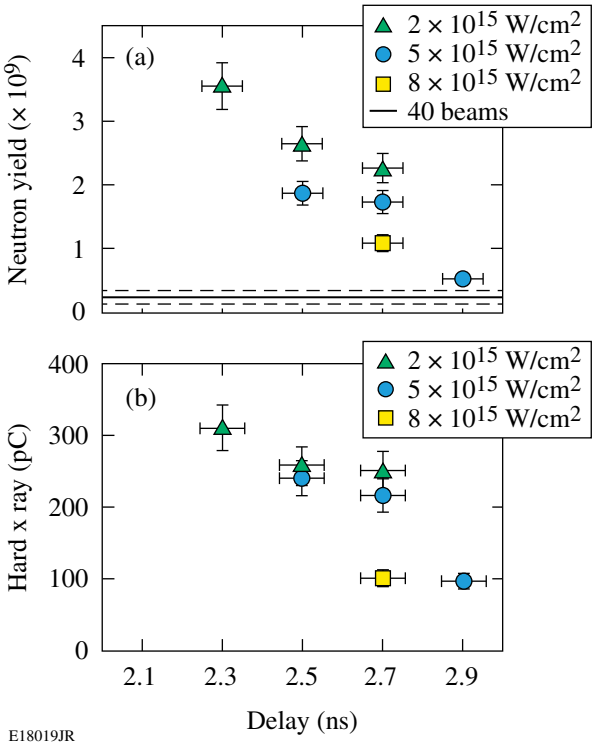

Figure 120.73
(a) Measured neutron yield and (b) hard x-ray yield versus the delay time of the high-intensity beam. The different symbols represent different focus positions with respect to the critical-density surface. The solid line in (a) is the average yield for 40-beam implosions; the dashed lines represent the error range. The 40-beam implosions produced no measurable hard x-ray signal.

Integrated Fast-Ignition Experiments

Principal Investigators: W. Theobald and C. Stoeckl (LLE)
Co-investigators: R. Betti and J. A. Delettrez (LLE); R. S. Stephen (General Atomics); and A. J. MacKinnon (LLNL)

Integrated fast-ignition (FI) experiments[26] began in FY09 at the Omega/Omega EP Laser Facility. The targets were 40-μm-thick empty CD shells of ~870-μm outer diameter, where a hollow gold cone with a full opening angle of 34° was inserted through a hole in the shell (see Fig. 120.74). The cone had a sidewall thickness of 10 μm with 10- and 15-μm-thick tips. A low-adiabat laser pulse comprised of a short picket pulse and a shaped ~2.7-ns drive pulse with 351-nm wavelength and ~18 kJ of energy imploded the capsule. The 1053-nm-wavelength short pulse was injected through the hollow cone, had an energy of 1 kJ and a duration of 10 ps, and was focused to a spot of ~40-μm diameter containing 80% of the laser energy. The corresponding peak laser intensity at the center of the tip of the cone was estimated to be $\sim 6 \times 10^{18}$ W/cm^2.

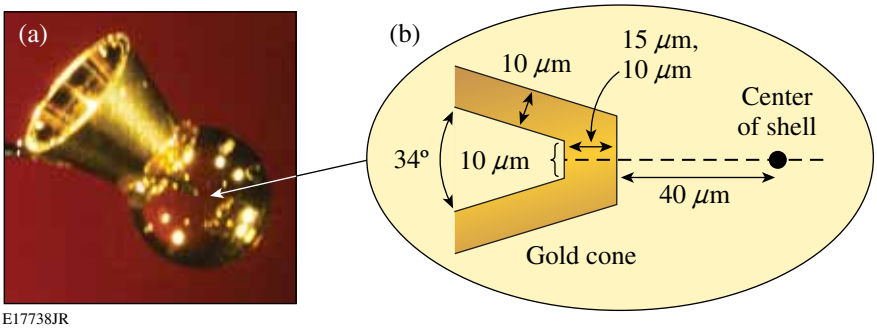

Figure 120.74
(a) Photograph of a gold re-entrant cone target; (b) schematic showing the cone-tip dimensions.

X-ray images show a threefold increase in x-ray emission with short-pulse energy of up to 1 kJ compared with similar implosions without a short-pulse beam. The pinhole images provide only qualitative information. Yield measurements of the 2.45-MeV neutrons from D–D fusion reactions are required to obtain quantitative information on the coupling efficiency. Neutron-yield measurements were challenging because of the emission of an intense γ-ray pulse. The strong background consisted of bremsstrahlung emission generated by MeV electrons streaming through the gold cone target. The γ-ray pulse induced a fluorescence background in the neutron detectors that persisted for several hundred nanoseconds and masked the much weaker neutron signal. A new neutron detector that was developed to overcome this problem now reliably measures neutron yields in integrated FI experiments. The detector uses an organic liquid scintillator that is saturated with molecular oxygen.

Figure 120.75 shows the measured neutron yield from integrated shots obtained at various arrival times of the short-pulse laser. The solid line represents the measured yield without the short-pulse laser. The neutron yield increased more than a factor of 2 with an appropriately timed OMEGA EP beam producing up to $1.5\pm0.6 \times 10^7$ additional neutrons. Initial *DRACO/LSP* simulations were performed to study core heating in the integrated fast-ignition (FI) experiments. The calculated neutron-yield increase caused by fast-electron heating is $\sim 2 \times 10^7$ if it is assumed that ~10% of the short-pulse energy is converted into fast electrons. The simulations did not take radiation transport and power balance into account, which leads to an over-prediction of density and temperature of the imploding shell. The calculated neutron-yield increase caused by the short-pulse laser is probably optimistic because the predicted higher density leads to a larger fraction of stopped fast electrons and because the gold cone material was not included in the electron-transport calculation. Fast-electron transport through the tip of the gold cone is significantly affected by the material properties and will affect the neutron yield.

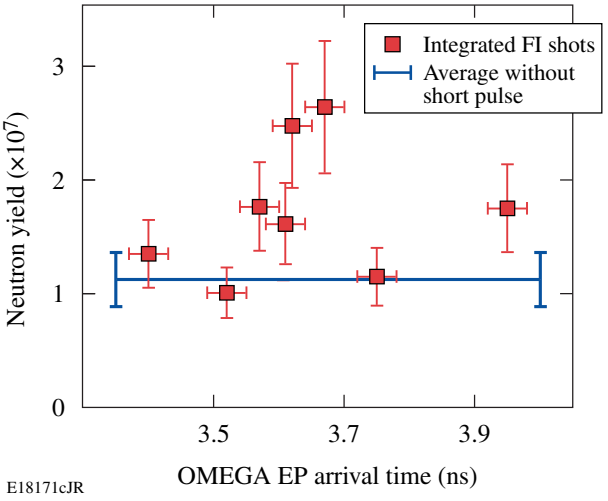

Figure 120.75
Measured D–D neutron yield from integrated fast-ignition shots (squares) versus timing of the short-pulse laser. The solid line represents the measured yield without the short-pulse laser.

FY09 LLNL OMEGA Experimental Programs

In FY09, LLNL led 238 target shots on the OMEGA Laser System. Approximately half of these shots supported the National Ignition Campaign (NIC). The remainder were dedicated to experiments for the high-energy-density stewardship experiments (HEDSE).

Objectives of the LLNL-led NIC campaigns on OMEGA included

- *Laser–plasma interaction studies in physical conditions relevant for the National Ignition Facility (NIF) ignition targets*
- *Demonstration of* T_r *= 100-eV foot-symmetry tuning using a re-emission sphere*
- *X-ray scattering in support of conductivity measurements of solid-density Be plasmas*
- *Experiments to study the physical properties (thermal conductivity) of shocked-fusion fuels*
- *High-resolution measurements of velocity nonuniformities created by microscopic perturbations in NIF ablator materials*
- *Development of a novel Compton radiography diagnostic platform for inertial confinement fusion (ICF) experiments*
- *Precision validation of the equation of state for quartz*

The LLNL HEDSE campaigns included the following:

- *Quasi-isentropic (ICE) drive used to study material properties such as strength, equation of state, phase, and phase-transition kinetics under high pressure*
- *Development of a high-energy backlighter for radiography in support of material strength experiments using OMEGA EP and the joint OMEGA/OMEGA EP configuration*
- *Debris characterization from long-duration, point-apertured, point-projection x-ray backlighters for NIF radiation transport experiments*

- *Demonstration of ultrafast temperature and density measurements with x-ray Thomson scattering from short-pulse-laser–heated matter.*
- *The development of an experimental platform to study nonlocal thermodynamic equilibrium (NLTE) physics using direct-drive implosions*
- *Opacity studies of high-temperature plasmas under LTE conditions*
- *Characterization of copper (Cu) foams for HEDSE experiments*

1. National Ignition Campaign

Laser–Plasma Interactions: The FY09 laser–plasma interaction experiments continued to emulate the plasma conditions expected along the laser-beam path in inertial confinement fusion designs. An interaction beam (Beam 30) aligned along the axis of a gas-filled hohlraum is used to study laser-beam propagation. This year, the effect of polarization smoothing was shown to increase laser-stimulated Brillouin scattering backscatter thresholds by about the 1.6× factor expected analytically and from simulations.[27] Second, the sensitivity of stimulated Raman scattering to density was checked in NIC-relevant plasmas.[28] The results will be presented as an invited talk at the APS DPP 2009 meeting.

Symmetry Diagnosis by Re-emission Sphere: The indirect-drive NIC proposes to set the first 2 ns of hohlraum radiation symmetry by observing the instantaneous soft x-ray re-emission pattern from a high-Z sphere in place of the ignition capsule. The soft x-ray measurements require low-Z windows over diagnostic holes and the laser beams that otherwise would interact with these windows have to be turned off. To assess this technique under NIC conditions, we used the Omega Laser Facility to image the re-emission of Bi-coated spheres placed inside a vacuum hohlraum with 200-ps temporal, 50- to 100-μm spatial, and 30% spectral resolution. The experiment is shown schematically in Fig. 120.76. Different from the previous experiments performed in scale-0.6 NIF hohlraums,[29] the new experiments were performed in larger scale-0.93 NIF hohlraums, making it possible to achieve a hohlraum laser-entrance-hole (LEH) size and inner laser-beam illumination, similar to upcoming NIF experiments, by azimuthally steering four inner beams away from the diagnostic window. Furthermore, compared to the experiments of Ref. 29, these experiments use a less-perturbing off-axis stalk rather than a thin CH tent to hold the capsule.

As shown in Fig. 120.77, by using 1-ns square laser pulses, we achieved hohlraum radiation temperatures measured with Dante that are similar to those calculated for future NIF experiments. The laser beams smoothed with SG4 phase plates generated intensities at the hohlraum wall that are similar to the foot of the NIF ignition design.

We acquired good re-emission images in the 0.4- to 1.3-ns time interval corresponding to 85- to 115-eV NIF foot hohlraum temperatures for both 900- and 1200-eV energy bands at several inner-to-outer beam power balances; the images are shown in Fig. 120.78. The x-ray background from the sphere stalk was negligible, validating the target design for upcoming NIF re-emit experiments. The data confirm the required measurement accuracies of <3% P_2/P_0 and P_4/P_0 Legendre mode flux asymmetry demonstrated in Ref. 29. Furthermore, the image signal-to-noise ratio is in agreement with a Planckian model for sphere re-emission, similar to Ref. 29.

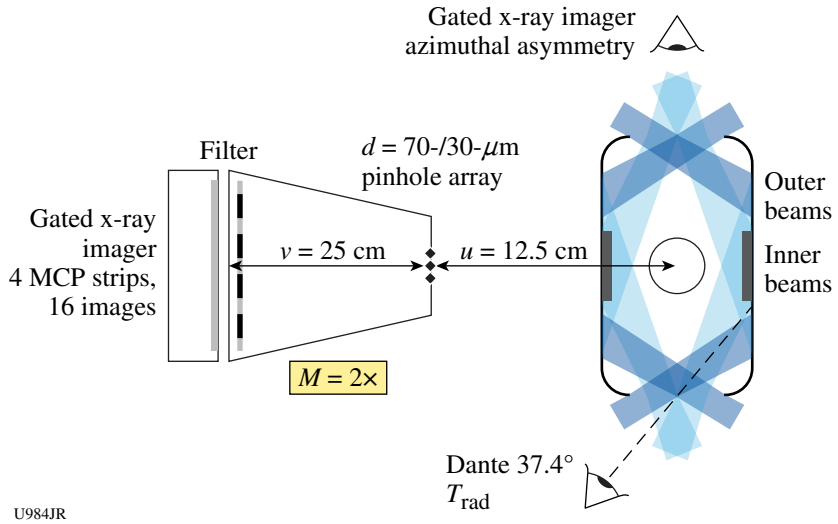

Figure 120.76
Re-emission experimental setup for the NIF and OMEGA.

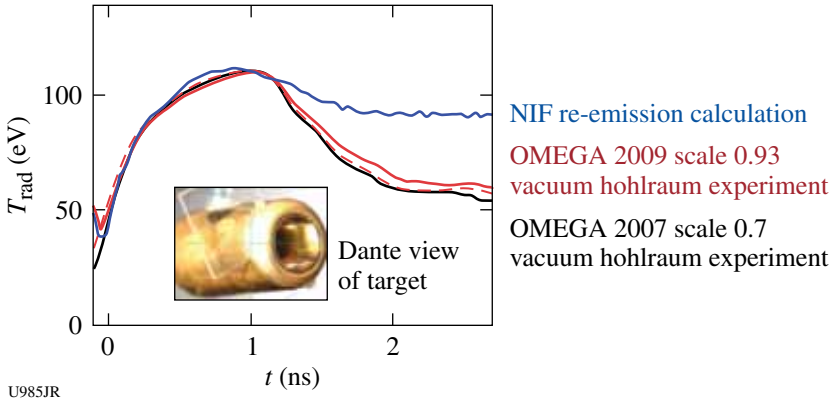

Figure 120.77
Hohlraum radiation temperatures measured with Dante in the OMEGA experiments and calculated for the NIF.

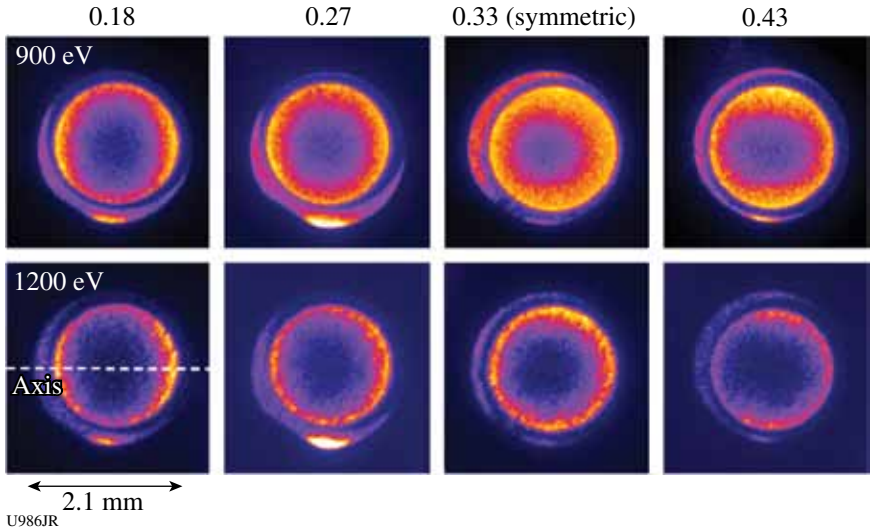

Figure 120.78
Re-emission images acquired at t = 0.8 ns at 900-eV and 1200-eV energy bands versus inner-to-outer beam power balance (in units of inner/total laser power).

As shown in Fig. 120.78, by changing the inner-to-outer beam power balance that will be used to tune early time P_2/P_0 in NIF ignition targets, we were able to change the radiation symmetry at the capsule from pole hot to equator hot. Figure 120.79 shows the measured average P_2/P_0 as a function of power balance.

The measured P_2/P_0 sensitivity to power balance per beam is consistent with Ref. 29, where smaller hohlraums, larger LEH (75% versus 60% of the hohlraum diameter), and fewer inner beams (4 versus 8) were used. In both experiments the measured 1200-eV to 900-eV P_2/P_0 relative sensitivity of 2 is larger than the $h\nu$ ratio (1.33), which is given by an ideal Planckian model for the sphere re-emission. This difference is under investigation.

X-Ray Thomson Scattering—Conductivity of Warm, Dense Matter: The goal of these FY09 experiments was to isochorically heat a 250-μm Be foil to sufficiently high temperatures in order to observe upshifted plasmon signals with collective x-ray Thomson scattering (XRTS). Quantitatively measuring the ratio of upshifted over downshifted plasmon strength enables one to infer the electron-plasma temperature based on first principles from the detailed balance relation, i.e., it is proportional to the Boltzmann factor $\exp\left(-h\nu_{res}/k_B T_e\right)$, with $h\nu_{res}$ the plasmon shift.

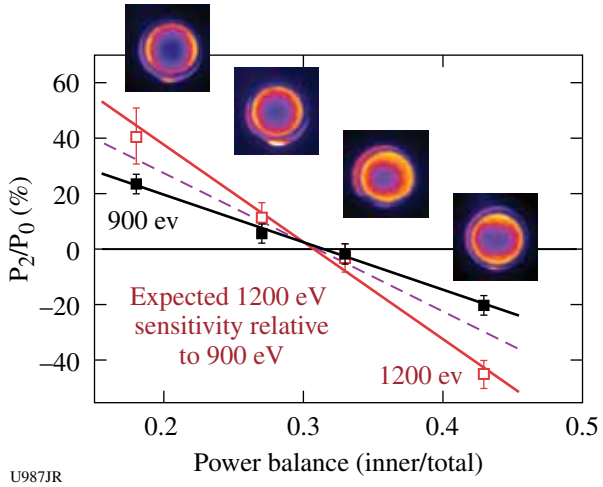

Figure 120.79
Re-emission images measured at 0.8 ns at 900 eV for constant and the corresponding P_2/P_0 versus inner-to-outer beam power balance

We utilized the XRTS target platform, which had been proven very successful in experiments on shock-compressed Be. For isochoric heating we employed L-shell x rays[30,31] that were created in thin Ag, Au, or Rh foils that were directly mounted to the Be, cf. Fig. 120.80(a) for a schematic experimental setup. Time delayed to the 10 heater beams, 16 probe beams created the Cl Ly$_\alpha$ x-ray probe at 2.96 keV. The source spectrum is plotted in Fig. 120.80(b). The x rays scattered off the rear Be surface under a 40° scattering angle were recorded by the gated Thomson spectrometer, which is based on high-opacity pyrolitic graphite as the Bragg crystal.

We obtained the best results with a silver x-ray converter foil. The scattering spectrum (black solid line), plotted in Fig. 120.80(b), shows inelastically scattered contributions that are up- and downshifted in energy compared to the Cl Ly$_\alpha$ source line. The plasmon features are rather broad since the collectivity parameter $\alpha = 1.22$, putting the experiment just into the collective scattering regime. The best fit (red line) to the data is achieved for T_e = 18 eV and $n_e = 1.8 \times 10^{23}$ cm^{-3}. The temperature is determined from detailed balance with an accuracy of 20%.

D_2 Thermal Conductivity: Reflectance and thermal conductivity of deuterium increase dramatically during compression above 1 Mbar. Simultaneous measurements of velocity, reflectance, and emissivity are being used to investigate the transport properties of cryogenic D_2 compressed by multiple shocks up to 6 Mbar at 7000 K (see Fig. 120.81). In FY10 reliability improvements to the experimental platform will enable one to measure D_2 transport properties across a wide region of phase space.

Capsule Instability Seeding by Shock Nonuniformity: Two consecutive shot days were devoted to CAPSEED campaigns in FY09. The primary focus of these campaigns was to study Be ablator samples of varying quality in order to compare them with results from detailed metrology such as grazing-angle x-ray scattering, electron microscopy, and surface profile measurements. The OMEGA high-resolution velocimeter (OHRV) diagnostic was configured with higher sensitivity than previ-

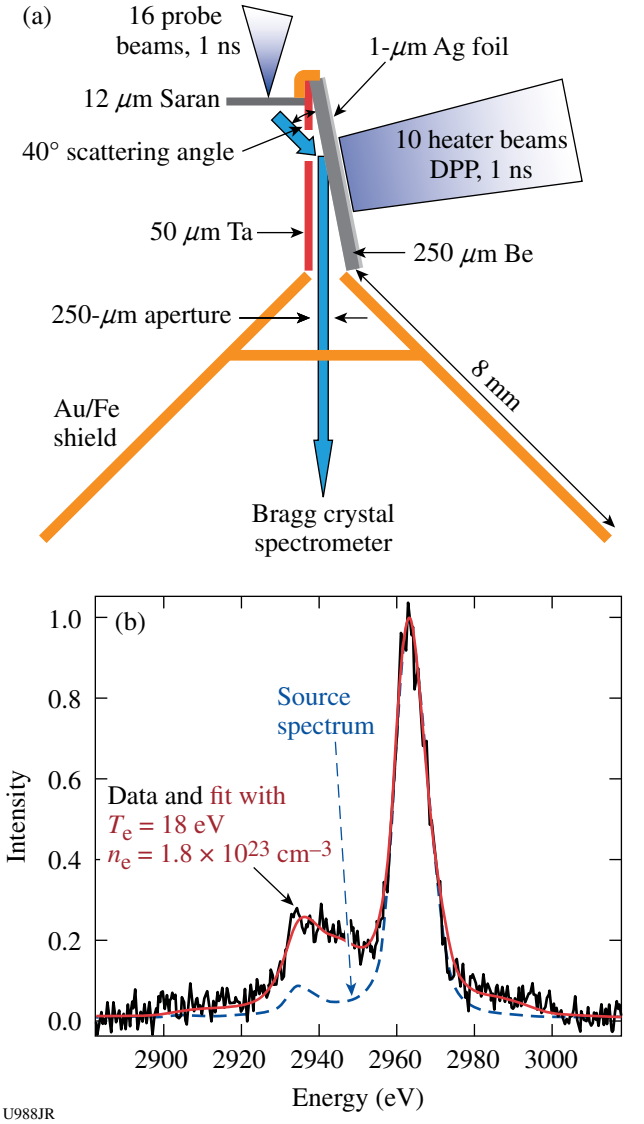

Figure 120.80
(a) Experimental setup to isochorically heat a 250-μm Be foil that is characterized with a Cl Ly$_\alpha$ x-ray probe at 2.96 keV. Shields block the direct line of sight to the spectrometer (toward the bottom). (b) X-ray Thomson scattering data show up- and downshifted plasmon signals that make it possible to infer temperature from a detailed balance relation.

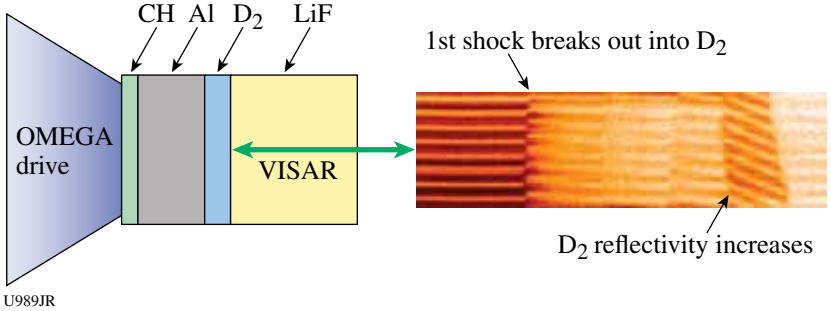

Figure 120.81
Experimental setup and VISAR record of multi-shock compressed D_2 to 6 Mbar. A dramatic increase in the D_2 reflectance can be seen in the streak record at the arrival of the final shock.

ous experiments to reduce the noise floor as low as possible. Analysis of the data led to several conclusions: (1) the velocity nonuniformities in high-quality Be samples are effectively at the noise floor of the OHRV, which meets the NIF requirement for ablator performance; and (2) poor-quality sample batches produced a higher level of nonuniformities than better-quality sample batches. The velocity nonuniformities observed in the poor-quality batches (Fig. 120.82) were attributed to the presence of a significant fraction of voids in the samples. The sample quality is batch dependent, so it is possible to identify high- and low-quality batches after fabrication. This will help to eliminate low-performing batches from the NIF experiments using electron microscopy and x-ray scattering. Future developments will focus on improving the noise floor of the instrument and continuing with high-sensitivity measurements on CH(Ge) and diamond samples.

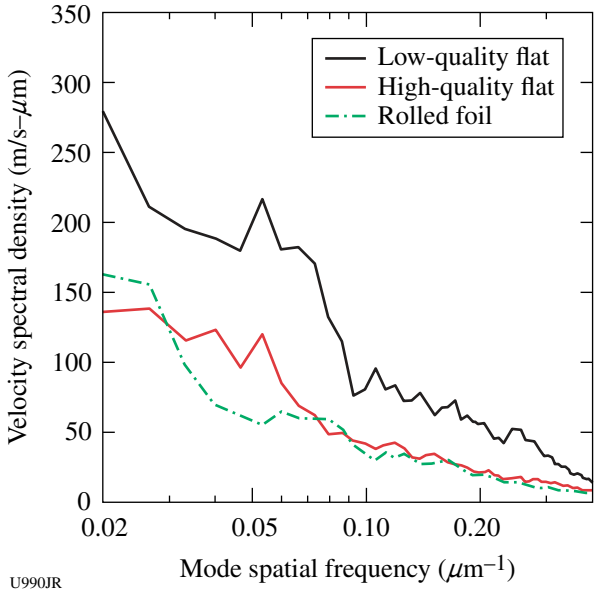

Figure 120.82
Velocity amplitude spectra recorded for three different Be sample types. The flats were Cu-doped sputtered Be foils, and the rolled foil was a polished sample of commercially available Be foil.

Compton Radiography: The goal of the Compton radiography campaign is to build a novel diagnostic platform for ICF. In FY09 we successfully obtained the first-ever radiographs of implosions, at photon energies around and above 60 keV, where Compton scattering largely dominated the opacity of the plastic shell. In our experiments we used 60 beams of the OMEGA laser for direct-drive implosions of 40-μm-thick, 870-μm-diam CH capsules filled with 3 atm of DD gas, located at OMEGA's target chamber center. As a backlighter we used a 10-μm-diam Au wire, 300 μm long, in a point-projection, end-on geometry 10 mm from the CH shell. The backlighter was driven by the OMEGA EP short-pulse beam, delivering ~1 kJ at 10 ps in a 100-μm-square spot size. The time delay between the OMEGA EP short pulse and the OMEGA laser pulses was chosen to match the time of peak compression predicted by *LILAC* 1-D simulations. To record the radiographs, we designed and built a dedicated Compton radiography snout (CRS) consisting of a three-stage collimator, a layered structure of Al–Pb to shield against neutrons and high-energy x and γ rays, and a permanent magnetic field to deflect electrons away from the radiography line of sight. CRS allows for the insertion of filters at different locations and hosts a Fujifilm BAS imaging plate detector at about 400 mm from target chamber center. By progressively increasing filtration in the CRS, we obtained good-quality radiographs (with a signal-to-noise ratio of a few at 2% contrast) at (average) photon energies of approximately 60 keV, 80 keV, and 100 keV. As an example, Fig. 120.83 shows a radiograph of the imploding CH shell, near peak compression, at t = 4 ns, obtained at a photon energy of ~60 keV. The

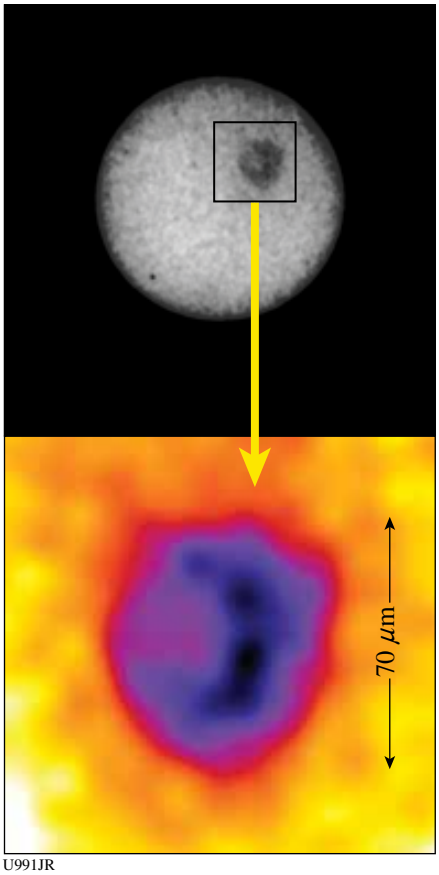

Figure 120.83
Compton radiograph of CH shell near peak compression: $\langle h\nu \rangle \sim 60$ keV. (a) CH shell radiograph inside the shadow of a CRS collimator; (b) blowup of radiograph.

diameter measured from the radiograph was 70 μm: very close to the value of 60 μm predicted by *LILAC* 1-D simulations. The CRS features a built-in step wedge filter that allows one to reconstruct the backlighting Bremsstrahlung spectrum and therefore measure the density from the radiograph.

Precision Validation of Quartz Equation of State (EOS): CH_n EOS measurements performed earlier in the year relied on quartz as the impedance-matching standard. The quartz (SiO_2) Hugoniot, measured several years ago on OMEGA, was found to be in good agreement with a linear shock velocity to particle velocity relation [see Fig. 120.84(a)]. This fit was also in agreement with earlier Russian measurements up to 6 Mbar and a single 20-Mbar point. However, given the sensitivity of impedance-matching measurements to uncertainties in the impedance-matching standard, it was necessary to further increase our confidence in the quartz Hugoniot. This was done by using a new "bootstrap" impedance-matching method, whereby quartz (ρ_0 = 2.65 g/cc) is impedance matched to another polymorph of SiO_2 fused silica (ρ_0 = 2.2 g/cc) [see Fig. 120.84(b)]. Since each Hugoniot probes a slightly different region of the SiO_2 high-pressure phase diagram, the results are highly sensitive to derivative quantities, in particular the slope of the U_s–U_p relation and the Gruneisen parameter.

2. High-Energy-Density Stewardship Experiments

Material Properties: In FY09 five experiment campaigns on OMEGA and OMEGA EP were performed in support of the material dynamics effort: thin-walled hohlraum drive development (1/2 day each, two campaigns); low-density foam reservoir tests (1/2 day); tantalum Rayleigh–Taylor experiment using OMEGA plus OMEGA EP in a joint experiment day; and high-energy backlighter characterization (one OMEGA EP day).

Quasi-Isentropic Compression Hohlraum Drive Development: The main goal of the first half-day of OMEGA shots was to test the thin-walled hohlraum's performance to decrease the late-time radiation temperature (Tr) to delay and reduce the strength of the late-time shock in the quasi-isentropic pressure drive platform. The thin-walled hohlraums had a 1-μm Au wall with 100-μm-thick epoxy backing. In this experiment the ablator was 75 μm of CH, to make a direct comparison with thick-walled hohlraum data from previous shots in March 2008. Our data suggest that the thin-walled hohlraums do delay the arrival of the late-time shock, so we will be able to utilize this platform for our strength experiment. The other goal for this campaign was to test low-density foams as the final layer in our reservoir. We tested 50-mg/cc SiO_2 aerogel (100 and 200 μm thick) and 100-mg/cc carbonized resorcinol formaldehyde (CRF) (50-μm-thick) foams. The ablator was 25 μm of Be. Comparison between the data and the simulations showed that these low-density foams worked well and showed no hydro-instabilities. The simulations of the velocity interferometry system for any reflector (VISAR) data show abrupt velocity steps for each reservoir layer, corresponding to the foam followed by the CH (12.5% Br) layer. The data also showed distinct velocity steps for each reservoir layer, but the transition between layers was smoother than the simulated results, likely because of hydrodynamic mixing at the interface. Both simulations and data showed a late-time stagnation shock.

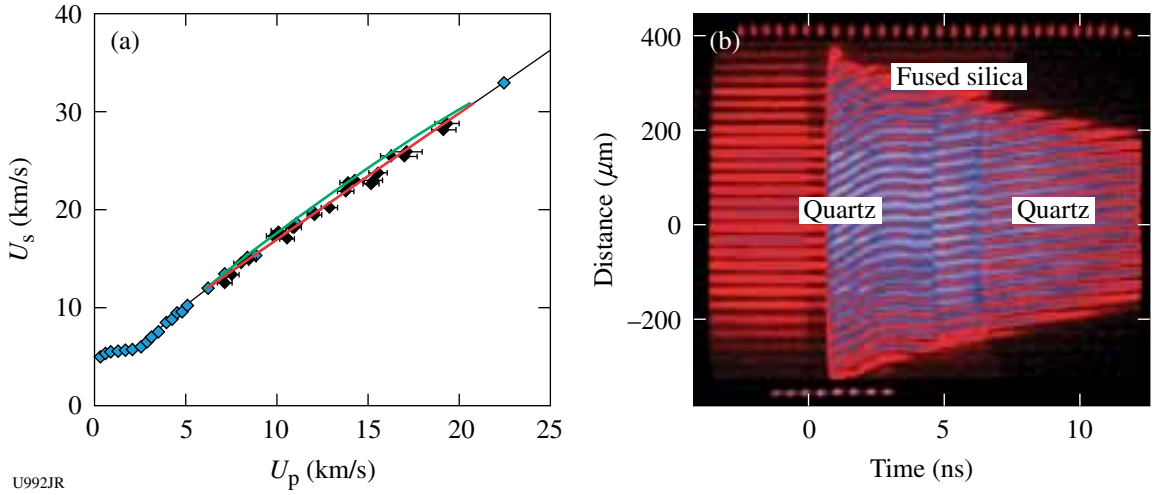

Figure 120.84
(a) Previously measured quartz Hugoniot. The red line provides the best linear fit to data; the green line provides a possible outlier fit to the data. New measurements were designed to determine possible deviations from the original linear fit. (b) Impedance matching of a quartz/fused silica/quartz target.

The goal of the second half-day of OMEGA shots was to test the thin-walled hohlraum drive using both Al and Ta witness samples to verify that they give consistent drive measurements. These two witness plate samples gave consistent results. The second goal of this half-day was to test the stacked CRF foam reservoir properties: 50 μm of 500-mg/cc CRF followed by 100 μm of 50-mg/cc CRF. We used 25-μm Be ablators for all shots during this half-day. This reservoir scales to a NIF design that reaches 5 Mb in a Ta-strength experiment. Post-shot simulations match well with the measured drive using the stacked foam reservoir. The simulated VISAR results predicted abrupt velocity steps, corresponding to each layer in the reservoir. The data, however, showed much smoother transitions between the different layers in the reservoir, likely because of hydrodynamic mixing between the layers. Provided this mixing is reproducible, this added smoothing improves the drive by minimizing shock heating.

ICE Gradient-Density Reservoir Development: The goal of this half-day of OMEGA shots was to test the foam reservoir performance for the material strength experiment. Therefore we used thick-walled hohlraums for this experiment (since the foam in the reservoir modifies only the early-time drive). We tested the low-density, 50-mg/cc SiO_2 foams by measuring the shock-breakout (SBO) times from 75/100/125 μm of SiO_2 foam thicknesses. The data matched the predictions. The second part of the experiment was to test stacked foam layers in the reservoir of 500-mg/cc CRF (50 μm thick) and 50-mg/cc SiO_2 (100 μm thick). The release profile and the SBO's on various material layers were compared to simulations, with poor agreement between the detailed interface arrival times and shape. This could be due to uncertainties in the EOS of the SiO_2 foam.

ICE Tantalum Rayleigh–Taylor Experiments: We have successfully performed the first OMEGA and OMEGA EP joint shots (60-beam long-pulse laser plus OMEGA EP short-pulse laser combined) to measure Ta Rayleigh–Taylor (RT) ripple growth to test models of Ta material strength at ~1-Mbar pressures and high strain rates of $\sim 10^7$ s^{-1}. The OMEGA EP laser was used to generate a high-energy backlighter (>20 keV) with high spatial resolution (<10 μm) to probe a 50-μm-thick Ta sample with 3-μm peak-to-valley sinusoidal ripples. We had four joint shots to measure the Ta RT growth, interleaved with six OMEGA-only (long-pulse) shots to measure the hohlraum drive. The joint-shot radiography technique worked well. For a few of the joints shots, the OMEGA EP beam slightly missed the 100-μm-diam micro-flat backlighter target, producing low-signal images. The growth-factor measurements require a good understanding of the backlight spectrum. Figure 120.85 shows the experimental configuration, Fig. 120.86 shows the target details, and Fig. 120.87 shows a resulting Ta RT radiography image using the high-energy Ag backlighter. Future

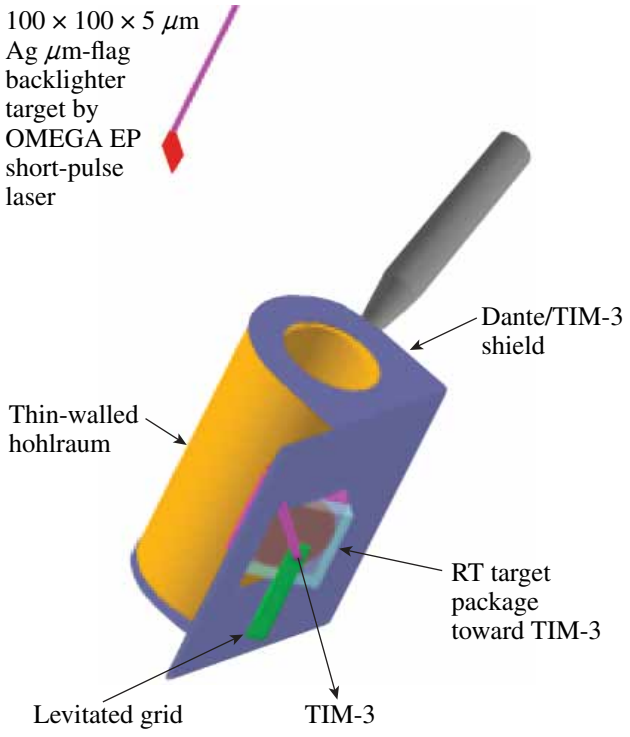

Figure 120.85
ICE tantalum Rayleigh–Taylor (ICE Ta RT)-09A experimental setup.

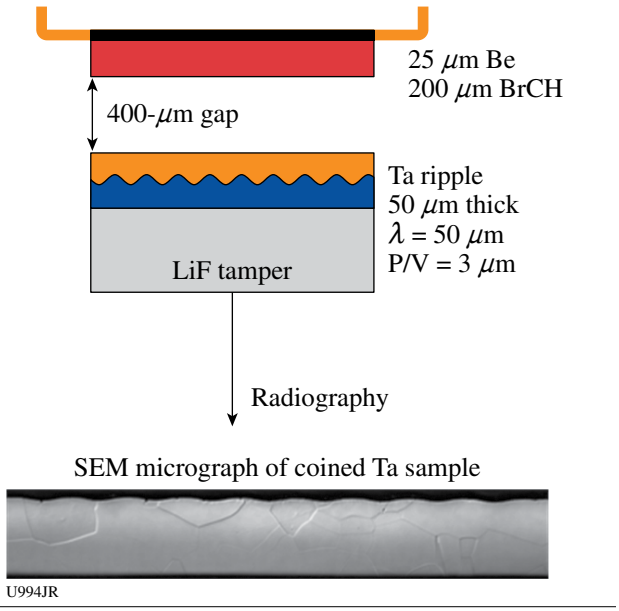

Figure 120.86
ICE tantalum Rayleigh–Taylor (ICE Ta RT) target details.

experiments will acquire data that will allow us to compare predictions of Ta strength using standard material models (PTW, Steinberg–Guinan) at ~Mbar pressure. In conclusion, we have demonstrated that Rayleigh–Taylor experiments for Ta (and other high-Z) samples are possible, and this type of experiment opens up a new capability for high-photon-energy radiography on OMEGA experiments. This experiment also led to three invited talks: IFSA 09 (The Sixth International Conference on Inertial Fusion Science and Applications, San Francisco, CA, September 2009); APS/DPP (American Physical Society, Atlanta, GA, November 2009); and JOWG-37 (Livermore, CA, October 2009).

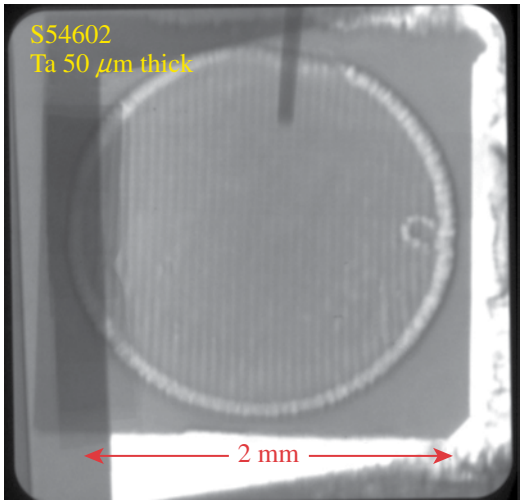

Figure 120.87
ICE Ta RT radiography using OMEGA + OMEGA EP joint shot.

High-Energy Backlighter (HEBL) Development: The goal of the HEBL OMEGA EP campaign was to measure the high-energy backlighter spectrum that would be utilized for the Ta Rayleigh–Taylor strength experiment on the NIF. The high-energy backlighter is created by the OMEGA EP short-pulse beam illuminating a micro-flag target. The absolute spectrum will be crucial to the quantitative analysis of results from the radio-graphy data. We utilized a transmission crystal spectrometer (TCS) that covers a 15- to 70-keV range; a Bremsstrahlung x-ray spectrometer that covers 70 keV to 1 MeV; and Ross-pair filters to get an absolute yield in the 20- to 70-keV range. We had six shots total and our settings were changed to test backlighter repeatability, laser spot-size dependency, and radiography object dependency. By combining detectors that span different energy ranges we were be able to produce a composite spectrum from 15 keV to 1 MeV, as shown in Fig. 120.88.

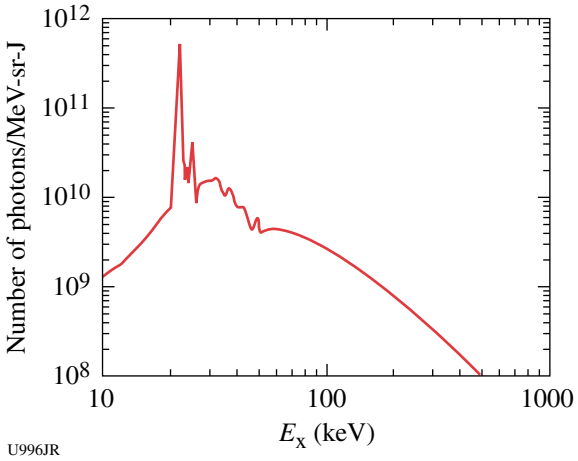

Figure 120.88
High-energy backlighter spectrum using the OMEGA EP short-pulse laser. Measurements were made using many different detectors.

Debris Characterization from Long-Duration Point-Source Backlighters: An 8-ns point-source backlighter developed on OMEGA was demonstrated on the NIF for streaked radiography. This configuration provided sufficient photons, high spatial resolution (~20 μm), and instrument protection from debris. To extend this to multiframe 2-D radiography, experiments were performed on OMEGA to characterize the debris and signal level. Pinhole-apertured point-projection backlighters generally produce either solid or liquid ballistic spall from the pinhole substrate, which generally is accelerated normal to the pinhole surface. On experiments where using a tilted pinhole substrate is undesirable, diagnostics must be protected from spall launched directly at the x-ray detector. This is traditionally done with thick pieces of beryllium that can offer protection without sacrificing x-ray transmission.

Alternate materials are being developed for debris mitigation for pinhole-apertured point-projection backlighters that are pointed directly at imaging diagnostics. We tested several thicknesses of aluminum and boron carbide (B_4C) for debris mitigation. Twenty OMEGA beams (10-kJ laser energy) drove a Ni pinhole-apertured point-projection backlighter (75-μm-thick Ta pinhole substrate) from P6 toward up to six 75-μm-thick or up to three 150-μm-thick filters. These filters were spaced at least 15 mm apart in the MSpec snout in TIM-6, with an image plate in the static pinhole camera array detector. We found (see Fig. 120.89) that three 150-μm-thick B_4C filters encapsulated in 8-μm Kapton let debris penetrate the rear-most filter once or twice, whereas three 75-μm-thick Al filters or two

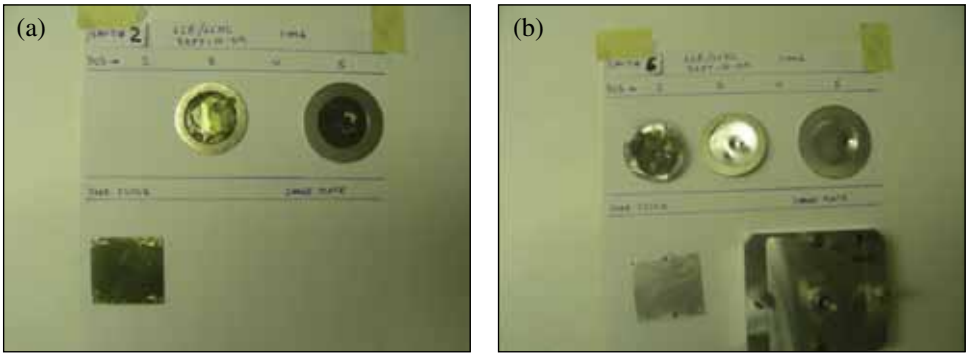

Figure 120.89
Damaged filters from debris testing. (a) Three 150-μm-thick B_4C-Kapton filters, showing one pinhole in the rear filter; (b) four 75-μm-thick Al filters, with the first three showing some ballistic damage, and a clean rear filter.

150-μm-thick Al filters stopped all the ballistic debris, leaving at least one clean rear filter. This suggests that the debris can be mitigated while allowing sufficient x-ray transmission.

X-Ray Thomson Scattering: The objective of this campaign was to demonstrate ultrafast temperature and density measurements with x-ray Thomson scattering from short-pulse-laser–heated matter. In March 2009, we used OMEGA EP to heat a 200-μm beryllium cube with a 1-kJ, 10-ps short-pulse laser beam and performed the first noncollective x-ray scattering measurements using a Zn K_α x-ray probe at 8.62 keV (see Fig. 120.90). The probing x rays were produced by the second OMEGA EP 10-ps short-pulse laser beam. On the first day of shots, we performed a total of four shots including the very first shots with two short-pulse beams fired simultaneously for target physics experiments. In addition, we successfully fielded the new Zink von Hamos high-efficiency x-ray spectrometer, a dedicated diagnostic developed for the K_α x-ray Thomson-scattering project. This instrument has shown elastic and inelastic scattering signals of beryllium with only 180 J in the probe beam.

Since these experiments were the first to use both OMEGA EP short-pulse laser beams simultaneously on target, we had to field

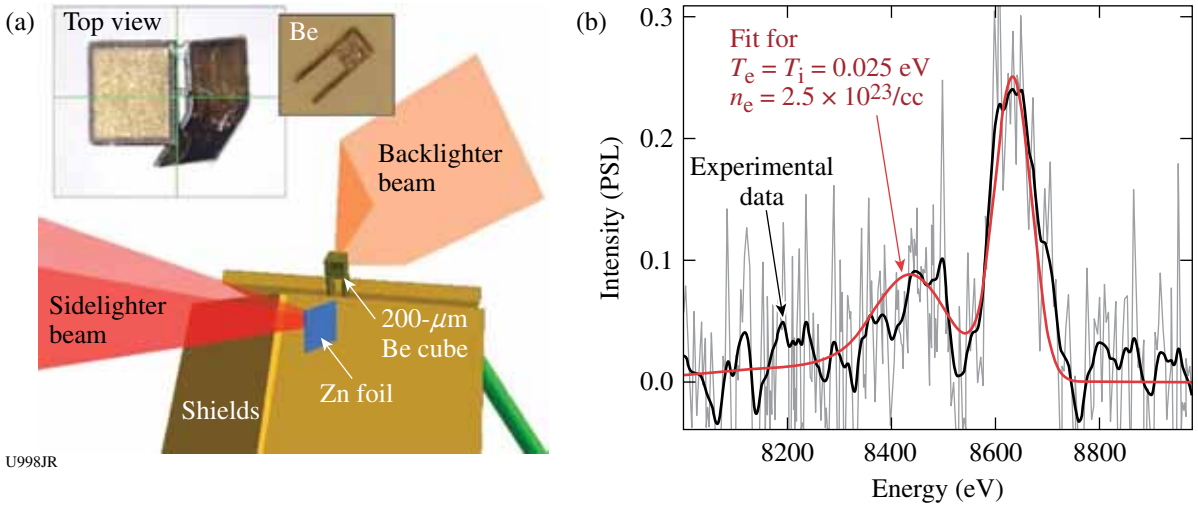

Figure 120.90
(a) Experimental setup showing the OMEGA EP backlighter beam heating a 200-μm Be cube. The OMEGA EP sidelighter beam creates a Zn K_α x-ray probe at 8.62 keV. Shields block the direct line of sight to the spectrometer (toward the bottom). (b) X-ray Thomson-scattering spectrum from cold beryllium, measured with only 180 J in OMEGA EP sidelighter beam. The downshifted inelastically scattered Compton feature is fitted with the parameters for cold, solid beryllium.

dedicated diagnostics to measure beam synchronization. We achieved synchronization to an accuracy of only 250±200 ps, which must be improved in the future to reach ~100 ps for this experiment. We also employed low-energy activation shots (50 J) to successfully record the x-ray source spectrum and to determine the spectrometer dispersion. The third shot of the day delivered ~1 kJ within a 10-ps pulse in the *backlighter* beam to heat the Be and ~1.3 kJ in the *sidelighter* beam to create the x-ray probe. Since the sidelighter shot was higher in energy than originally anticipated, we reduced the energy to 180 J on the last shot of the day. Nevertheless, we were able to record elastic- and inelastic-scattering signals of cold beryllium. This is a very promising result. We also assessed the bremsstrahlung level and background levels. These measurements will enable us to improve the experimental design to measure plasma temperatures of short-pulse-laser–heated beryllium with high temporal resolution using K_α x-ray Thomson scattering on future shots.

Non-LTE Implosions: The goal of the non-LTE campaign is to build a platform to study the energy balance in implosions by measuring ion, electron, and radiation temperatures as a function of high-Z dopant concentration. In our FY09 experiments, we used 60 beams of the OMEGA laser for direct-drive implosions of thin (4-μm) glass capsules filled with 10 atm of D^3He gas and Kr gas as a spectroscopic tracer. The relative concentration of DD and ^3He was varied during the shots, the Kr concentrations were 0.001 and 0.005 atm, and some capsules also contained as much as ~0.1 atm of Xe. As a time-resolved electron temperature (T_e) diagnostic, we fielded a mica conical crystal spectrometer that was coupled to a streak camera and viewed K-shell emission lines from the Kr dopant. Time-integrated spectra were also recorded with the HENEX spectrometer. We also fielded a high-resolution spectrometer to use the Doppler broadening of x-ray lines for measuring the ion temperature T_i.

We observed a decrease in the DD/DT yield ratio with increasing Xe concentration. This trend is well reproduced by LASNEX/DCA:T simulations. We observed an increase in the DD/DT yield ratio with increasing DD concentration as well as an increase in the ion temperature, inferred from proton and neutron emission time histories and spectra. Increasing Xe dopant concentration appears to reduce compression-phase T_i by coupling to radiative cooling.

We inferred the time-integrated electron temperature T_e from a Bremsstrahlung functional form fit to the continuum part of the spectra recorded by HENEX. As reported in Fig. 120.91, T_e shows a linear decrease with an increase in Xe dopant concentration: a behavior reproduced by simulations, although experimental measurements give values higher by a factor of about 30%.

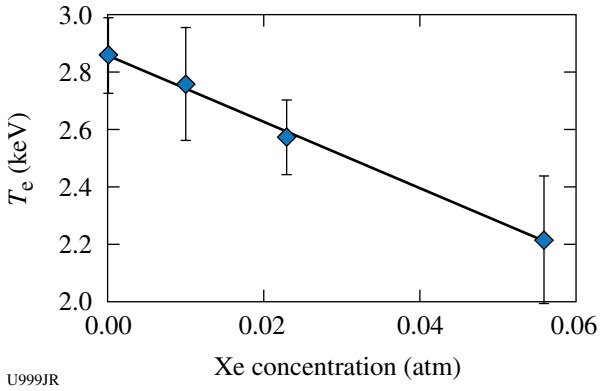

Figure 120.91
Time-integrated T_e, inferred from HENEX spectra, shows a linear decrease with an increase in Xe-dopant concentration.

We used the time-resolved spectra from the conical crystal spectrometer to study the temporal evolution of the Kr He$_\beta$ lines. The $He_{\beta 2}/He_{\beta 1}$ line ratio shows a peak in the central 50 ps of the Kr emission as well as a decrease with increasing Xe concentration, as shown in Fig. 120.92.

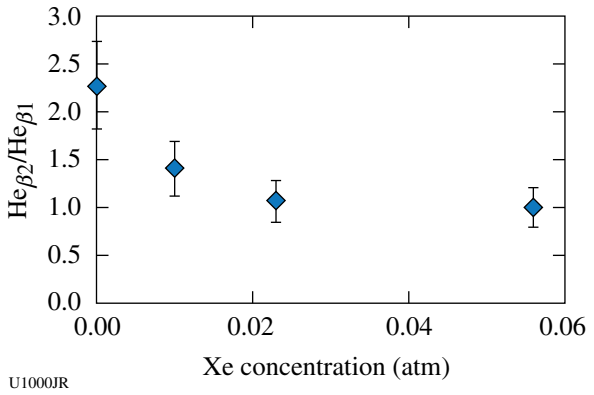

Figure 120.92
The $He_{\beta 2}/He_{\beta 1}$ line ratio, measured from conical crystal spectra, shows a decrease with increasing Xe concentration.

High-Temperature Plasma Opacity: In FY08 LLNL completed the development of a high-temperature laser opacity platform. In FY09, detailed x-ray transmission spectra from fully characterized, high-temperature plasmas were produced using the OMEGA laser to provide validation benchmarks for the x-ray opacity codes (and associated data tables) underlying

simulations of radiation transport experiments. Shots in FY09 produced detailed benchmark data on tantalum–titanium and sodium chloride–titanium plasmas. In these experiments, 24 beams heated a 1.6-mm-diam hohlraum, which in turn radiatively heated and expanded a tamped Ti foil. Additional beams drove two broadband backlighters: a rear-wall burnthrough halfraum (14 beams) and a Kr-filled "dynamic hohlraum" capsule implosion (10 beams). Looking through the sample to these backlighters, two broadband spectrometers characterized the sample transmission from 250 eV to 1600 eV and 3000 eV to 5500 eV, respectively; the lower energy band encompassed the bulk of the Rosseland mean opacity. The plasma density of 0.05±0.01 g/cc, measured by expansion radiography, agreed well with pre-shot calculations. The plasma temperature implied by the titanium ionization features in the 3000- to 5500-eV spectra was 110±5 eV (Fig. 120.93). Rosseland mean opacity data from 250 to 1600 eV is now being analyzed. Discrepancies with theory have been observed and are undergoing detailed investigation. For the future, an extension of these techniques to the NIF would enable us to investigate much hotter plasmas at conditions relevant to stellar core modeling, where recent observational data (helioseismology) contradict standard solar models. A small change in the technique will also enable us to perform a scaled experiment to study photoionized plasmas relevant to black hole accretion disk physics.

Characterization of Cu Foams: Two half-days of OMEGA shots (a total of eight) were used in support of characterization of Cu foams for HEDSE experiments. Material characteristics of interest included both the internal energy (EOS) and the opacity of the foams, at several Mbar of pressure. Pure metal foams are of use as backlighter sources, as low-density materials for radiation–hydrodynamic experiments and opacity experiments. The first set of shots used a hohlraum to drive a CH ablator paired with a Cu foam (density about 0.89 g/cm^3) and a SiO_2 payload (density 0.05 g/cc). The purpose of this experiment was to measure, on the same shot, shock breakout from the Cu into the (transparent) SiO_2, shock velocity in the SiO_2, and the position of the Cu/SiO_2 interface by point-projection radiography. The results are sensitive to the EOS of the Cu foam but not to the opacity. Post-shot simulations agreed with the experimental results. A typical radiograph from this series is shown in Fig. 120.94(a).

The second round of shots continued characterization of Cu foam by using the Cu as an ablator in a hohlraum-driven experiment. The Cu ablator for a typical target is shown during the machining process [Fig. 120.94(b)]; the Cu foam density was about 0.89 g/cm^3. The shock-breakout time and the foil burnthrough time are sensitive to the opacity as well as the internal energy of the foam. The post-shot simulations were again consistent with the experimental results. These results

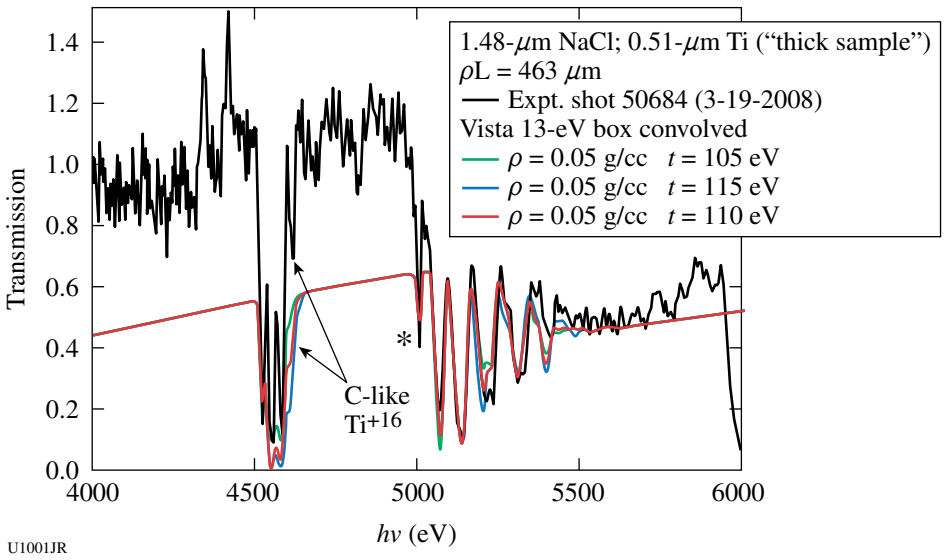

Figure 120.93
X-ray transmission opacity data from gated space-resolved titanium absorption spectra for photon energies from 4 keV to 5.9 keV. To the left are $n = 1$ to 2 absorption lines of F-like to C-like Ti, with the C-like feature being strongly temperature dependent. To the right are $n = 1$ to 3 lines of the same ions, plus a narrow feature from the Ne-like ion (*). Analysis using the VISTA opacity model indicates a temperature of 110±5 eV for densities in measured range, 0.050±0.010 g/cc.

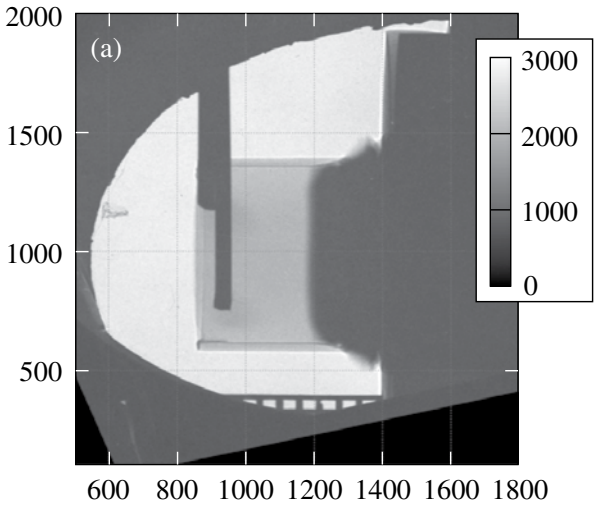

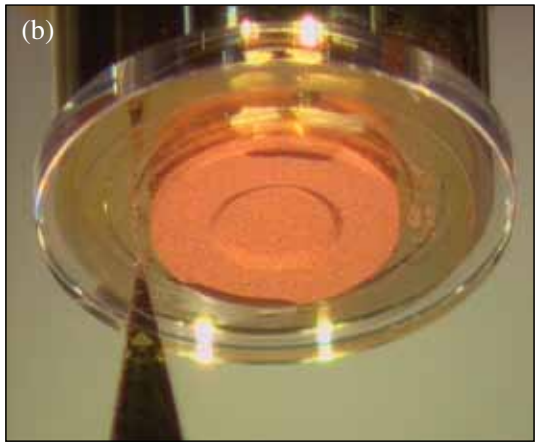

U1002JR

Figure 120.94
(a) A typical radiograph taken during a shock-breakout experiment; (b) a picture of one of the copper foam ablator targets.

will allow us to proceed in FY10 with designing experiments using this Cu foam.

This work performed under the auspices of the U.S. Department of Energy by Lawrence Livermore National Laboratory under Contract DE-AC52-07NA27344.

FY09 LANL OMEGA Experimental Programs

Los Alamos National Laboratory (LANL) successfully fielded a range of experiments on the OMEGA laser during FY09 in support of the national program. LANL conducted a total of 104 target shots: 93 on OMEGA and 11 on OMEGA EP. Collaborations with LLNL, LLE, LULI, NRL, MIT, NSTec, UCSD, and AWE remain an important component of LANL's program on OMEGA.

NIF-5: The NIF-5 campaign had many successes during the course of FY09. The NIF-5 spectrometer, a high-resolution x-ray spectrometer, was qualified for use on OMEGA. Preliminary analysis of the spectra indicates the spectrometer is performing as expected.

In June 2009, the NIF-5 campaign conducted experiments to study hydrodynamic features caused by a radiation drive. The target (Fig. 120.95) consisted of a gold hohlraum. Connected to the hohlraum was a gold tube and a Be tube. A plastic (CH) foam filled the Be tube and the Au tube and extended into the hohlraum. The hohlraum (1200-μm outer diameter) was heated on each end by 15 lasers beams using a 1-ns square pulse. The x rays created by this interaction then heated the CH foam. A Sc backlighter [Fig. 120.95(b)] was illuminated with laser beams to create x rays to diagnose the foam in the Be tube.

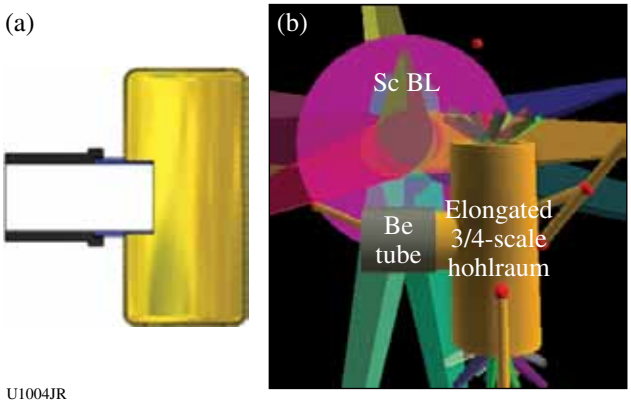

U1004JR

Figure 120.95
(a) A schematic of the target showing the placement of the foam in the Be tube, the Au tube, and the hohlraum; (b) a Visrad model showing the backlighter and the target.

Two of the radiographic images obtained are shown in Fig. 120.96. The top half of the figure shows a radiograph of a radiatively induced shock in a 120-mg/cm^3 foam, 5.9 ns after the hohlraum drive lasers were fired. The bottom half shows a radiograph of a radiatively induced shock in 104-mg/cm^3 foam, 4.7 ns after the hohlraum drive beams were fired. The results of these experiments are being analyzed and will be used to help improve our future simulations.

High-Z: The purpose of the high-Z project is to investigate the effect of high-Z dopants on D_2 fusion burn. This is an ongoing project in which we have obtained a large data set showing that dopant gases such as ^{3}He, Ar, Kr, and Xe degrade the yield in an inertial confinement fusion (ICF) implosion. This

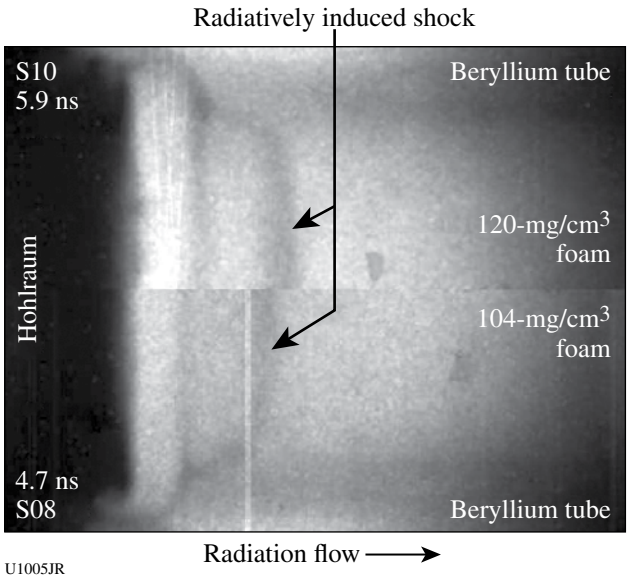

Figure 120.96
The top half of the figure shows a radiograph of a radiatively induced shock in a 120-mg/cm^3 foam, 5.9 ns after the hohlraum drive beams were fired. The bottom half shows a radiograph of a radiatively induced shock in 104-mg/cm^3 foam, 4.7 ns after the hohlraum drive beams.

degradation is more than calculated by our codes and occurs mostly during the latter compression stages of the implosion, after the initial shock reflects off the axis and hits the capsule shell. The reason for the degradation is unknown but understanding this degradation was the focus of FY09 activities.

The high-*Z* project successfully completed two full days of experiments on OMEGA in FY09. The first day of experiments focused on testing whether the OMEGA EP laser could be used as an x-ray backlighter for obtaining radiographs of imploded glass capsules. The capsule, a 4.3-mm-thick, 925-μm-diam SiO_2 capsule filled with 8.75 atm of deuterium and 0.1 atm of argon, was driven by a 0.6-ns-long pulse with a maximum energy of 239 J/beam and also by a distributed polarization rotator, an SG-4 phase plate, and full smoothing by spectral dispersion. The reason for radiographing the shell at late times is to determine if our simulation codes are correctly predicting the amount of ablation from the shell and the properties of the glass during the implosion. The backlighter was a 15-μm-thick iron foil illuminated by an OMEGA EP beam with a pulse length of about 10 ps and an irradiance of less than 5×10^{15} W/cm^2. We obtained nine shots on this shot day, five of which included the OMEGA EP laser. We were able to obtain good data on nearly every shot, although we determined that the x-ray intensity of the 6.7-keV Fe backlighter was not as bright as the implosion at the times of interest, as demonstrated in the results shown in Fig. 120.97. The spectral radiance of the backlighter, with a measured energy conversion efficiency of about 3×10^{-5}, was found to be weaker than the emission from the implosion by a factor of 8 (Fig. 120.98). The second day focused on testing a new experimental platform using Fe-doped glass shells. The doped shells were used to provide a source of Fe ions in the gas, which could then emit x rays that can be measured by an MMI (multiframe monochromatic imager) diagnostic. The MMI is useful in obtaining spatial profiles of temperature and density in the gas (something we do not presently measure) and would provide important information for understanding the yield degradation. On this day we were again quite successful in obtaining good data for a total of 12 shots. We used glass capsules that had 0%, 0.3%, or 0.9% Fe in the glass. We were able to measure the emission of the Fe lines but determined that the emission levels were too weak at these dopant levels to ensure successful application of the MMI diagnostic. We are pursuing plans to develop glass shells that have a higher concentration of Fe, but there are important target fabrication issues that remain to be addressed.

OMEGA EP Ions Campaign: LANL led a series of ion-generation experiments (26 March and 17 August) on OMEGA EP performed by experimental Principal Investigator (PI) K. Flippo with diagnostic PI's J. Cobble (TPIE) and D. Offermann (LANL PFPII-mod and THVL). These experiments were carried out in collaboration with UCSD, LLNL, and LLE/UR under the project leadership of LANL's M. Schmitt.

In the first series of shots (26 March), we had a total of seven shots on target that provided good data on the performance of OMEGA EP in terms of ion energies from dielectric targets [chemical vapor deposition (CVD) diamond] and conductors (Cu) using the PFPII loaded with Radiochromic film as the primary diagnostic. Figure 120.99 compares the beam quality and spectrum from (a) copper and (b) CVD diamond targets at 15-μm thicknesses. The beam profile from the 15-μm target had a well-defined outer edge of the proton beam and a higher temperature to the beam, 5.58 keV versus the beam from the copper target, which had a large defuse beam, and an inner darker beam, with a characteristic temperature of 3.79 keV. Overall the beam from the copper target contained more protons in the 4- to 36-MeV range, but fewer total ions in the higher end of the spectrum, 15 MeV to 36 MeV. Approximately 2.04% and 1.81% of the laser energy was converted into protons for CVD and copper, respectively.

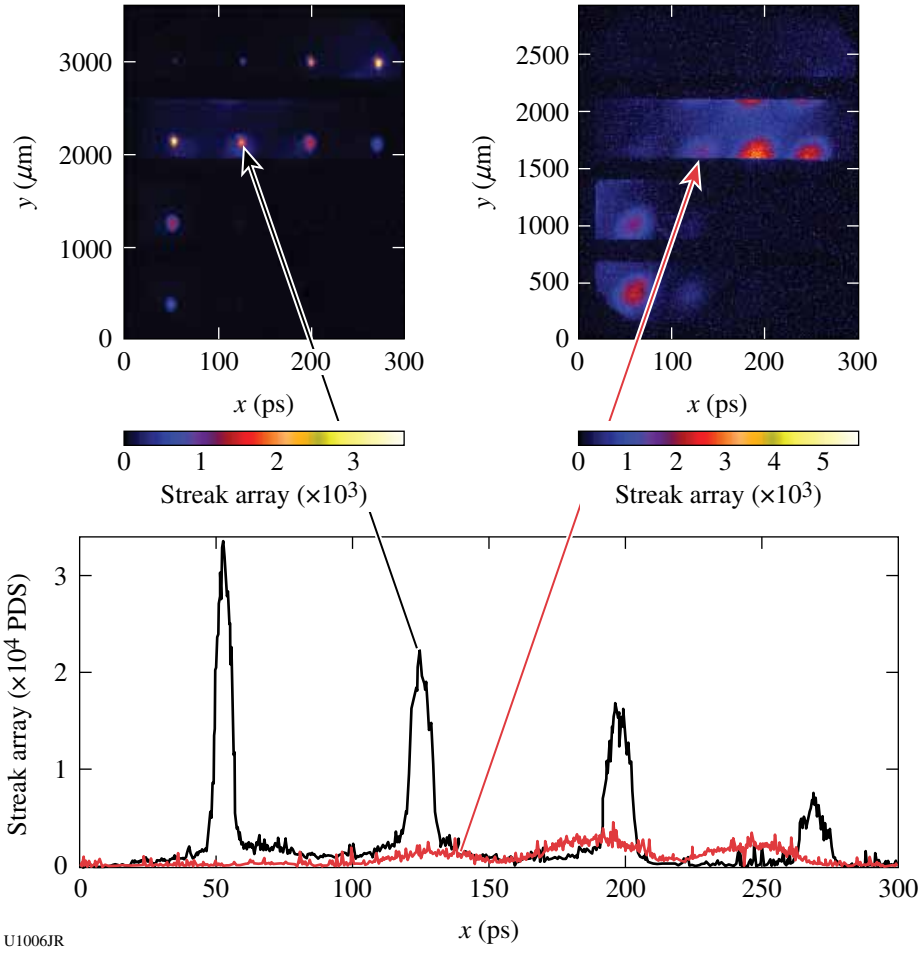

Figure 120.97
X-ray framing-camera images and lineouts from the OMEGA EP joint shots 53548 and 53549. Shot 53548 shows an image that includes the backlighter and the capsule, while shot 53549 shows the intensity of the backlighter only. The lineouts were taken from the second horizontal frame and show the relative intensity of the emission from the imploding capsule and the x-ray backlighter.

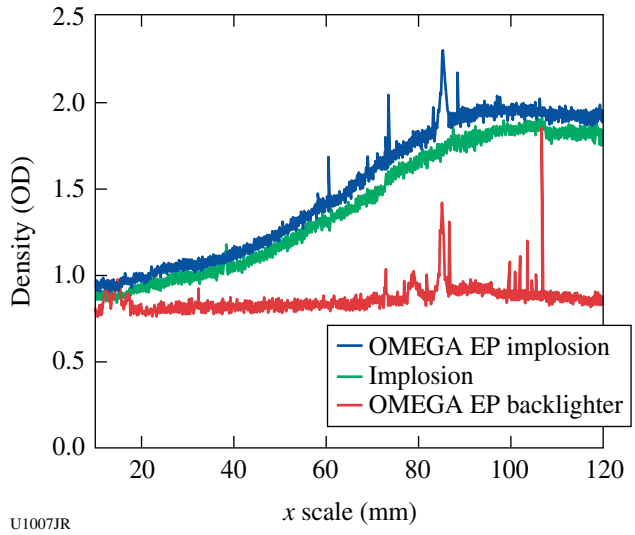

Figure 120.98
Spectral radiance measured by an XRS spectrometer showing the relative emissions of the implosion, backlighter, and the combined spectrum.

The second series of shots (18 August) yielded six shots, the first two on planar diamond foil targets, completing the data set begun in March. The completed data set (see Fig. 120.100) shows that proton beam energy from planar targets peaks around 45 MeV for a target thickness of about 24 μm for an OMEGA EP pulse length of 10 ps and a pulse energy of ~1000 J. These results are currently being prepared for a publication documenting the first ions generated at OMEGA EP; they were also presented at the IFSA 2009 conference in September.

The next four shots were used to perform focusing experiments on OMEGA EP using hemi-shell targets. The third shot of the day (the first hemi) was the first shot to give good data from LANL's new TPIE diagnostic (a ion energy and species analyzer). Preliminary analysis of the PFPII data indicates that the beam quality from the hemis is good and laminar.

The last shot explored the generation of ions over a large area of the hemi-shell (need for higher flux ion beam generation)

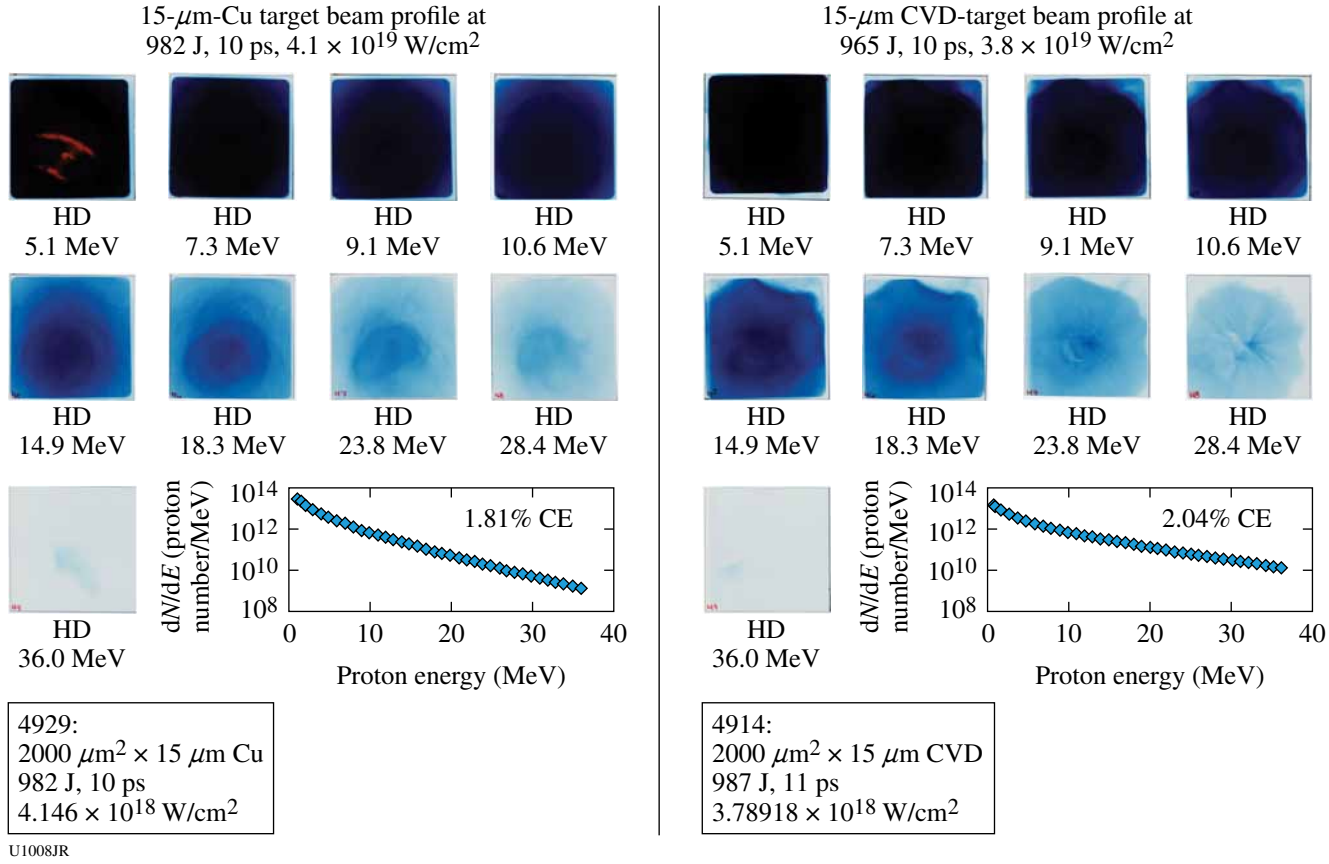

Figure 120.99
Comparison of 15-μm CVD diamond target (right panel) with 15-μm-copper target (left panel). The panels show PFPII data from the RCF film stack with energies associated for each layer, and a calculated proton spectrum fitting the data in the lower right of each panel.

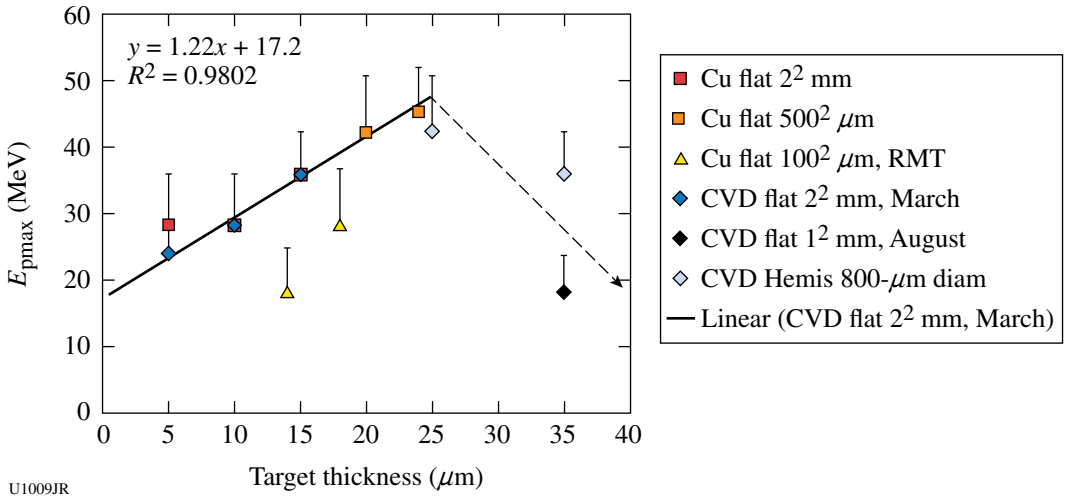

Figure 120.100
OMEGA EP proton scaling with target thickness and an area showing a linearly increasing trend toward 25-μm thickness for CVD (diamond) and Cu targets with areas greater than 100^2 μm^2, with a drop after 25 μm and lower performance in general for targets with areas smaller than 500^2 μm^2.

by using a large laser focus at the target. Data were generated using a copper grid behind the hemi that provided information on the focal quality of the ion beam. The TPIE diagnostic performed well in the completely retracted TIM position using a 250-μm pinhole aperture but with low flux. On a later shot, the TPIE was run in 30 in. and the CR39 moved to the 10-cm position to increase the flux and reduce noise. This provided us with information on the dynamic range of the TPIE instrument. Preliminary analysis of this data indicates that improved performance will be achieved if we add shielding to reduce the noise on the CR39.

Gamma Reaction History Diagnostics: A gamma reaction history (GRH) diagnostic has been developed for the National Ignition Campaign and thoroughly tested on OMEGA this year. The GRH is a follow-on design to the Gas Cherenkov Detector (GCD-1), which has been productive on OMEGA for the past ten years.[32] Figure 120.101 depicts the GRH currently installed on OMEGA. It is designed to detect the 16.7-MeV gamma rays that are emitted in approximately one of every 10,000 DT fusion reactions. These gammas are converted, primarily through Compton scattering, to relativistic electrons inside the domed port cover. The electrons traveling faster than the speed of light in a pressurized gas generate UV/visable Cherenkov radiation, which is collected with off-axis parabolic reflectors into an ultrafast photomultiplier tube (PMT).[33,34] Varying the pressure of the gas (typically CO_2 or SF_6) varies the index of refraction and hence the Cherenkov threshold (requires $v_e > c/n$, where v_e is the electron velocity, c is the speed of light, and n is the index of refraction of the gas). The electrical PMT signal is sent to a Mach–Zehnder modulator in the electronics enclosure for optical transmission to digitizers without loss of bandwidth.[35] A complete system impulse response has been measured to be ~95 ps—fast enough to measure the expected burn widths of 80 ps to 150 ps from the THD campaign planned for the spring of 2010 at the National Ignition Facility (NIF). Fiber-optic connectors make it possible for timing fiducials and calibration signals to be injected directly into the optical path and provide a dry-run capability for verifiable reliability.

The higher laser energies and neutron yields expected at the NIF dictate larger standoff distances for diagnostics. The advantage of gamma rays over neutrons is that they do not suffer velocity Doppler spreading with increasing distance, so gamma-ray detectors can be placed a significant distance from the imploding capsule without loss of signal bandwidth. Increasing standoff distance, however, also reduces the subtended solid angle and therefore measurement sensitivity, so the instrument must be designed to maximize sensitivity. The GCD-1 routinely operates at 20 cm from target chamber center (TCC) by insertion into a ten-inch manipulator (TIM). This necessitated a compact, coaxial design utilizing Cassegrain optics. By mounting the GRH outside the chamber, we were able to take advantage of off-axis light collection utilizing off-axis parabolic mirrors for increased Cherenkov light collection. The GRH-6m at the NIF will be only two orders of magnitude less sensitive than GCD-1 at 20 cm, even though it will be located 30× farther away from TCC. For the NIF, the GRH-6m will consist of four gas cell channels run in parallel for increased redundancy and reliability plus the ability to run at several gamma-ray threshold energies to diagnose various gamma rays of interest [e.g., $t(d,\gamma)$ at 16.7 MeV, $t(h,\gamma)$

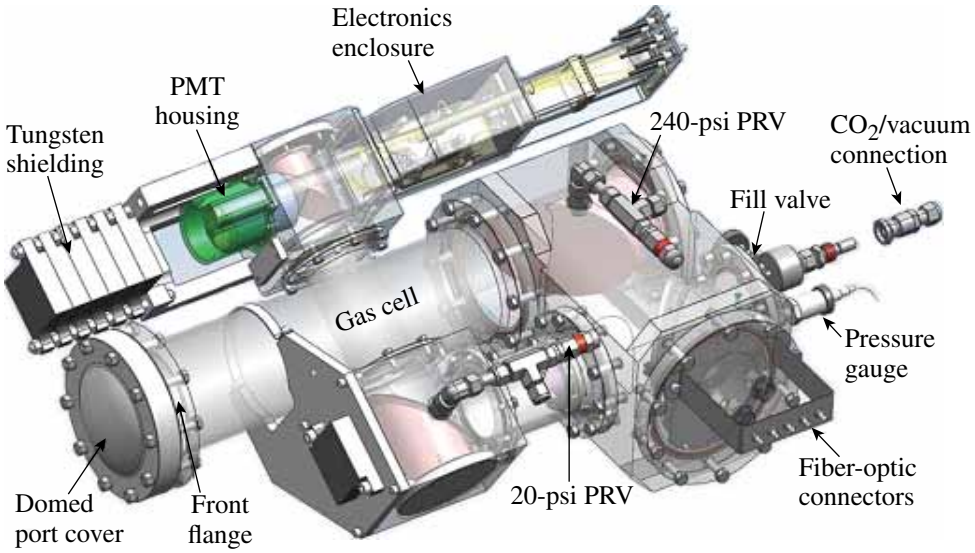

Figure 120.101
First GRH-6m channel, currently installed on OMEGA.

at 19.8 MeV, $^{12}C(n,n')\,\gamma$ at 4.4 MeV]. These detectors will be capable of measuring fusion bang times relative to the t_0 of the composite laser pulse to within 50 ps and burn widths to within 5 ps to 10 ps at yields $>1 \times 10^{13}$ at the NIF. These parameters will be key in diagnosing shell velocity and the various possible failure modes in attempts at ICF ignition on the NIF. The GRH may also prove useful as a means of providing a time-resolved measure of ablator ρR, indicative of ablator mass remaining and ablator/fuel mix.

Figure 120.102 shows a gamma-ray measurement from an imploded DT-filled plastic capsule with the GRH pressure with 100 psia of CO_2 (~6-MeV Cherenkov threshold). Also shown is a background measurement from a previous shot with the CO_2 removed, resulting in no Chernkov production, but still exhibiting direct gamma interaction with the PMT (this background is also present when the PMT input window is blocked with black tape). DT fusion gammas and n–γ from DT fusion neutrons passing through the imploding capsule [primarily $^{12}C(n,n')\,\gamma$ from CH capsules] interact directly with the PMT, causing the "precursor" peak approximately 4.1 ns before bang time. The speed-of-light transit time from TCC through the optical delay of the Cherenkov cell is calculated to be 4.26 ns longer than the direct line-of-sight (LOS) transit time from TCC to the microchannel plate (MCP) in the PMT (i.e., directly through the tungsten shielding). Other experiments have shown that 6 in. of tungsten shielding is adequate to eliminate direct LOS gammas (and x rays), so the precursor from these shots with 9 in. of shielding must be from gammas originating at TCC reaching the MCP on scattering paths delayed approximately 160 ps relative to a direct LOS path, or an extra 4.8 cm. Additional small peaks after the precursor are n–γ generated by interaction of DT neutrons with mass near TCC. Similar peaks have been correlated with various TIM-based diagnostics as they are moved near TCC. These masses must be closer than 22 cm from TCC to generate a signal before or at bang time because of the slower transit time of the neutrons. Although the current background levels are adequate for bang-time and burn-width measurements, the shielding being designed for the NIF will do a much better job of further reducing the background.

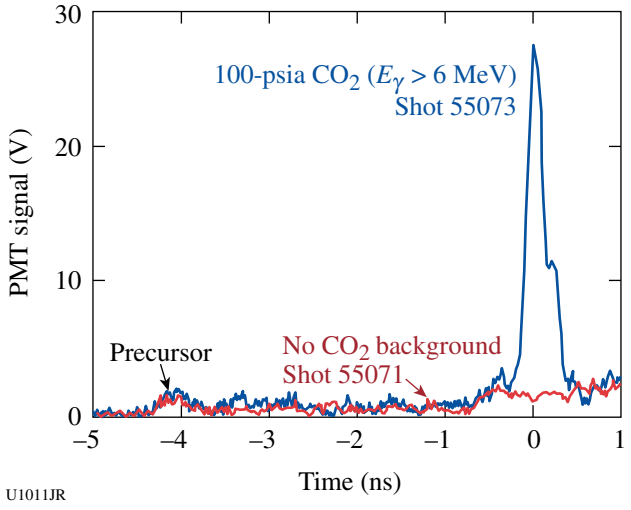

Figure 120.102
GRH data from high-yield shots with (blue) and without (red) pressurized CO_2.

In July the GRH was absolutely timed using x rays generated with 100-ps laser pulses directed onto gold ball targets. The γ-to-e^- converter in the GRH was replaced with a BC-422 x-ray sensitive scintillator for these shots. The x rays/scintillator photons have essentially the same transit time through the system as the γ rays/relativistic electrons/Cherenkov photons. As a result the x-ray pulse can be used to generate a t_0 time stamp on the scope from which the optical fiducial is calibrated. Figure 120.103 shows an x-ray shot and a high-yield shot overlaid by lining up the fiducials. The difference between the rising edge of the x-ray pulse and the peak of the fusion signal is representative of the absolute bang time.

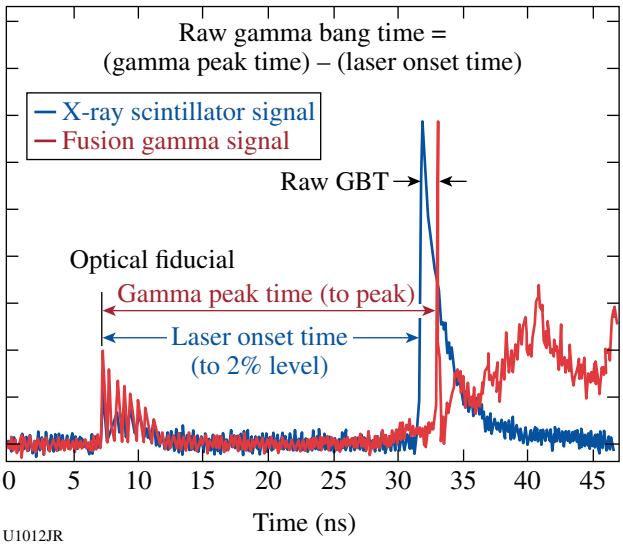

Figure 120.103
X-ray pulse from a gold ball target (blue) used to calibrate an optical timing fiducial overlaid with a Chernkov signal from a high-yield DT shot.

In addition to the GRH development, the Gas Cherenkov Detector also continued to provide valuable insight into gamma-ray physics. In particular, a secondary gamma experiment (a.k.a., "hockey puck" experiment) was carried out using GCD-1. The primary experimental objective was to simulate the neutron-induced secondary gamma (n–γ) production

from a NIF hohlraum, thermomechanical package (TMP), and implosion capsule. During four shot days within FY09 (November, April, May, and July), three group of pucks were placed between TCC and GCD: (1) Au and Cu pucks for the hohlraum, (2) Al and Si pucks for the TMP, and (3) SiO_2, Al_2O_3, and BeO pucks for an implosion glass capsule n–γ study. Three key experimental results were obtained in support of the NIF–GRH (gamma-ray reaction history) diagnostic development program:

1. Proximity n–γ sources were experimentally characterized. The GCD detected time-delayed and Doppler-broadened n–γ signals from all seven pucks. The high-bandwidth GCD can temporally distinguish DT–γ and n–γ signals as long as the proximity source is located at least 2 cm from TCC. The n–γ sensitivity's dependence on seven materials was found and used to validate the MCNP code. Silicon produced the strongest n–γ signal as expected by MCNP simulations.

2. It was experimentally confirmed that the GCD can cut off n–γ signals effectively by adjusting energy threshold, which will allow one to measure clean DT–γ without interference of n–γ at the NIF. At 9-MeV threshold, it is expected that DT–γ will be at least 10× higher than n–γ signals.

3. n–γ signals from the hockey puck experiment were used for MCNP/ACCEPT code validation. Also, puck signals served as an *in-situ* GCD calibration source; as a result they provided one method to determine the $D(T,\gamma)/D(T,n)$ branching ratio. Preliminary calculations carried out using four puck materials indicate $D(T,\gamma)/D(T,n)$ ranges from 1×10^{-5} to 4×10^{-5}.

Defect Implosion Experiment (DIME): The Los Alamos DIME campaign involves perturbed spherical implosions, driven by 60 OMEGA beams with uniform, symmetrical illumination (~24 kJ). DT-filled CH-shell targets with equatorial-plane defects are designed to produce a nonspherical neutron burn region. The objectives of the DIME series are to observe the nonspherical burn with the neutron imaging system (NIS) and to successfully simulate the physics of the neutron production. For the first shot day on OMEGA (shots 54135 to 54145), we demonstrated adequate yield for NIS imaging and monitored yield degradation for the presence of defects. The targets had a diameter of 860 μm. All were filled with 5 atm of DT. We used two separate shell thicknesses: 8 μm and 15 μm, thereby testing both exploding pusher and ablative designs. Perfect targets have no defects. Target defect details are shown in Fig. 120.104. For all shots, the groove depth was 2 μm.

The yield compared to perfect capsules was reduced by ~50% for both thick- and thin-walled targets with defects (see Fig. 120.105), although the exploding pusher capsules (thin walls) performed better for total yield. Both the NIS and a gated, x-ray framing camera diagnosed target emission edge-on—in the plane of the defect. In all cases, the NIS obtained neutron images but was not optimal for resolving the defect. This is encouraging because the perturbation was minimal, and additional degradation for larger defects should be less disruptive of yield. Numerical simulations predicted enhanced x-ray emission, as suggested in Fig. 120.106. During the next campaign, experiments will feature larger, deeper channel defects, and the NIS will be more mature.

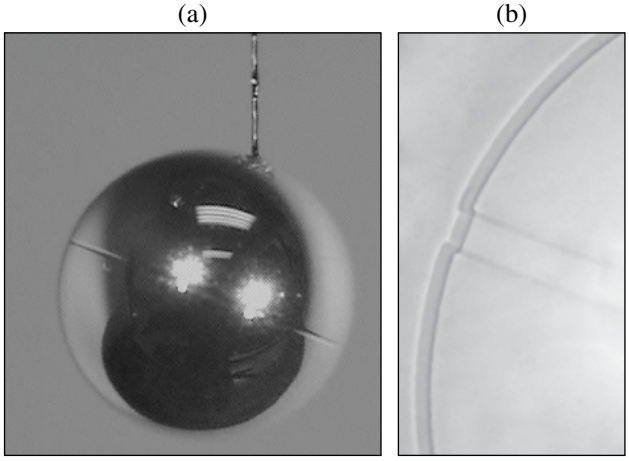

Figure 120.104
(a) LLE photograph of a target with a 20-μm-wide groove defect. (b) A General Atomics radiograph of a 30-μm wide defect with high magnification.

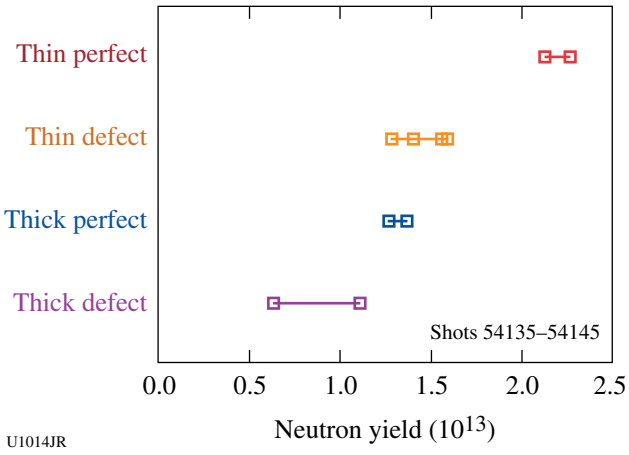

Figure 120.105
Yield for 20-μm-wide, 2-μm-deep groove defects.

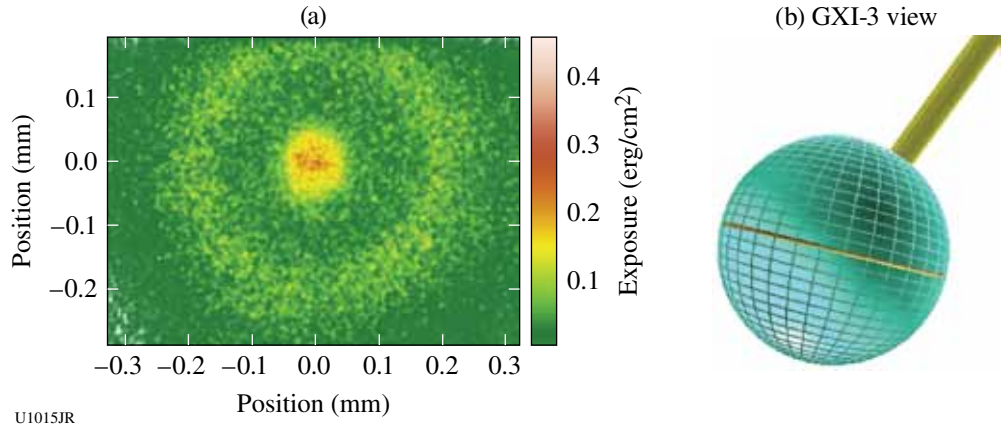

Figure 120.106
(a) A gated, x-ray image (3 to 5 keV) of a defect target implosion suggests enhanced x-ray emission (higher density) in the plane of the defect. (b) The VISRAD view of the GXI-3 x-ray framing camera.

High-Energy Backlighting on OMEGA EP: At the end of January 2009 Los Alamos participated in the first international collaboration on OMEGA EP along with LLE, LLNL, LULI, and NRL. These experiments produced high-quality x-ray images of static gold grids using silver K_α emission produced from 100-ps, 1-kJ laser pulses (Fig. 120.107).

Los Alamos experiments in March 2009 were in collaboration with NRL and were limited to the spectroscopic evaluation of high-energy x-ray backlighters (imaging diagnostics were not available because of requalification). A scan of x-ray yield as a function of pulse duration of silver K_α emission was performed and measured with the NRL diagnostic dual-crystal spectrometer (DCS), which is a high-energy Laue configuration spectrometer. Excellent data were obtained with the spectrometer showing very little change in conversion efficiency with pulse durations ranging from 10 ps to 100 ps.

Neutron Imaging: The Neutron Imaging Campaign made great advances with the NIS to be fielded on the NIF during FY09. Using a staggered approach, different components of the NIF Ia neutron imaging system were tested to ensure that each component functioned properly. The spatial resolution and the DQE of the NIF Ia detector were determined from these experiments. The response and time delay of new paddle detectors were also measured.

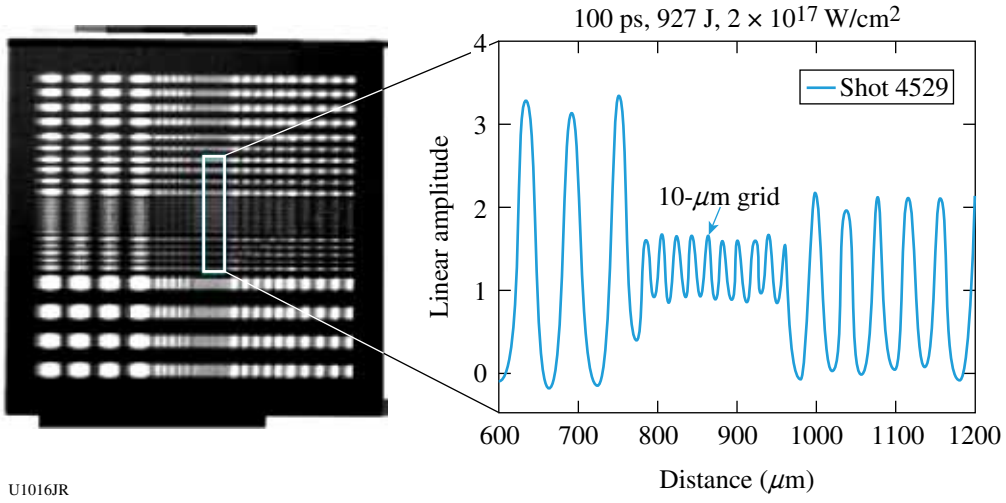

Figure 120.107
(a) A radiographic image of a resolution grid using a silver backlighter. (b) A lineout from the radiograph demonstrating high spatial resolution.

FY09 AWE OMEGA Experimental Programs

AWE-led experiments on OMEGA in FY09 continued to test radiation–hydrodynamic simulations of hohlraum drive and capsule implosion under conditions where a hohlraum target was driven in a deliberately asymmetric manner.

Techniques to achieve uniform, near-spherical symmetry of radiation drive on a capsule in a laser-heated hohlraum have received detailed attention in the context of inertial confinement fusion. Much less attention, however, has been paid to understanding the hohlraum physics and hydrodynamics in cases where the radiation drive departs significantly from spherical symmetry. In work on the OMEGA laser, AWE has carried out a series of experiments to study the implosion dynamics of a capsule irradiated by a deliberately asymmetric x-ray drive. The experimental data provide a sensitive test of radiation transport within the hohlraum enclosure in which drive symmetry was modulated by using variable albedo layers (low-Z coatings on the high-Z hohlraum wall), asymmetric laser-beam timing, and other techniques. In cases where the radiation drive was highly asymmetric, the imploding capsule developed a well-defined polar jet that interacted with the opposite capsule wall. The hydrodynamics of jet formation and interaction were investigated using x-ray backlighting radiography, providing a sensitive test of hydrodynamic modeling in this strongly converging geometry.

A 1.6-mm-diam, 2.7-mm-overall-length hohlraum was used (Fig. 120.108) and driven with up to 30 beams (1.6-ns pulse duration) from the OMEGA laser. Asymmetry was introduced by means of an imbalance of laser energy or timing between the two ends of the hohlraum, or by asymmetry of wall material. In some cases the wall material of one half of the hohlraum cavity was aluminum (low albedo, in comparison with the gold wall material of the other half of the hohlraum); in other cases a thin aluminum coating on the gold hohlraum wall was used to introduce a time-varying albedo (low albedo at early time, followed by increased drive after the laser beams burned through the aluminum layer).

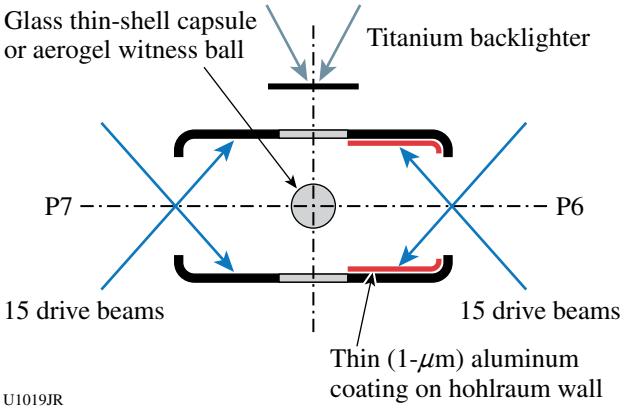

Figure 120.108
Experiment to investigate asymmetric hohlraum drive. The hohlraum was aligned on the P6–P7 axis of the OMEGA target chamber, and asymmetry was introduced by imbalance of laser beam energy and timing from the P6 and P7 directions, and by the use of a low-Z coating on the hohlraum wall.

Both silica aerogel spheres (600-μm diameter, 325-mg cm^{-3} density) and thin-walled glass capsules (600-μm diameter, 3.5-μm wall thickness, 30-μm-thick CH ablator coating) were used as diagnostics of the angular distribution of radiation drive. The position of the ablation front in the aerogel witness spheres[36,37] was used to characterize the angular distribution of the drive, whereas the integral effect of asymmetric drive on the implosion hydrodynamics[38] was observed in the late-time evolution and jet formation of the thin-shell capsules. Both were diagnosed by x-ray backlighting, using a 4.75-keV titanium area backlighter and x-ray framing camera. Hohlraum wall emission was also characterized using the Dante diagnostic, viewing through the laser entry hole of the hohlraum. The experiments were modeled using the AWE Lagrangian radiation–hydrodynamics code NYM, followed by the Eulerian code PETRA to which the simulation was linked after the mesh in the Lagrangian phase of the simulation became sufficiently distorted to limit further progress. The hydrodynamics simulation was post-processed to generate synthetic radiographs for comparison with the experimental data.

The position of the ablation front in the aerogel witness-sphere experiments was characterized by its decomposition into Legendre polynomials. Figure 120.109 shows a comparison between the amplitudes of Legendre moments from both the experimental data and simulation. The simulation was shown to reproduce the experiment rather closely.

The hydrodynamics of the thin-shelled capsules was significantly more sensitive than that of the foam witness balls to the angular distribution of drive. Figure 120.110 compares experimental data with post-processed images for a NYM–PETRA simulation at different times after the onset of the radiation drive. The hydrodynamics is seen to progress somewhat slower in experiment than simulation (as quantified by the equatorial diameter), and although both experiment and simulation show a well-defined polar jet at late time (Fig. 120.111), the density distribution at the hot pole of the capsule was different in the two cases. It seems likely that these differences arose from

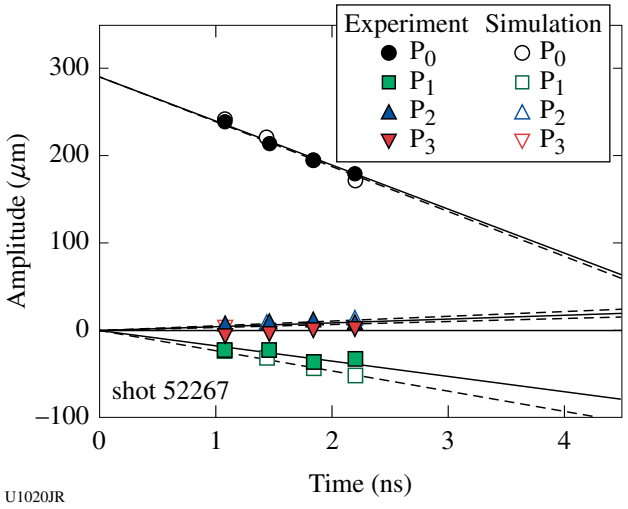

Figure 120.109
Legendre polynomial decomposition of the position of the ablation front in an asymmetrically driven foam witness-ball experiment. The amplitudes of the first four Legendre polynomials (P_0, P_1, P_2, P_3) are shown for both experiment (filled symbols) and simulation (open symbols).

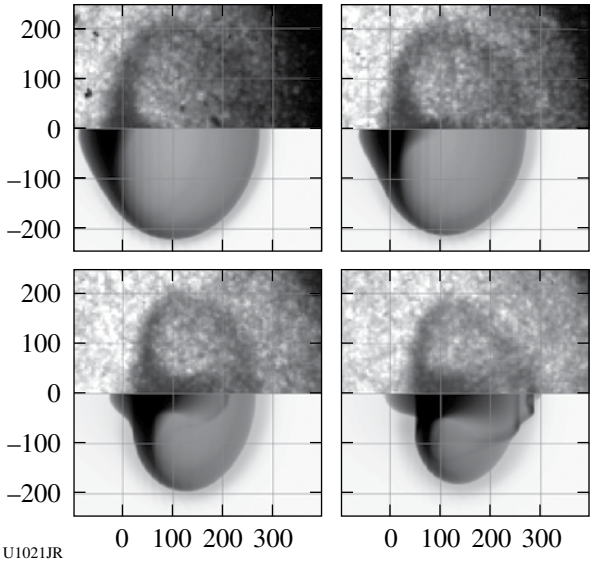

Figure 120.110
Sequence of frames showing experimental data (top) and simulation (bottom) of the implosion of an asymmetrically driven, thin-shell glass capsule. The sequence of times is 2.8, 3.2, 3.6, and 4.0 ns in the experimental data and 2.6, 2.8, 3.0, and 3.4 ns in the simulation. In the simulation, times were chosen to match approximately the experimentally observed equatorial diameter of the capsule. The formation and propagation of the polar jet were reproduced in the simulation, although there are some differences of density distribution at the pole of the capsule. (Units shown are microns.)

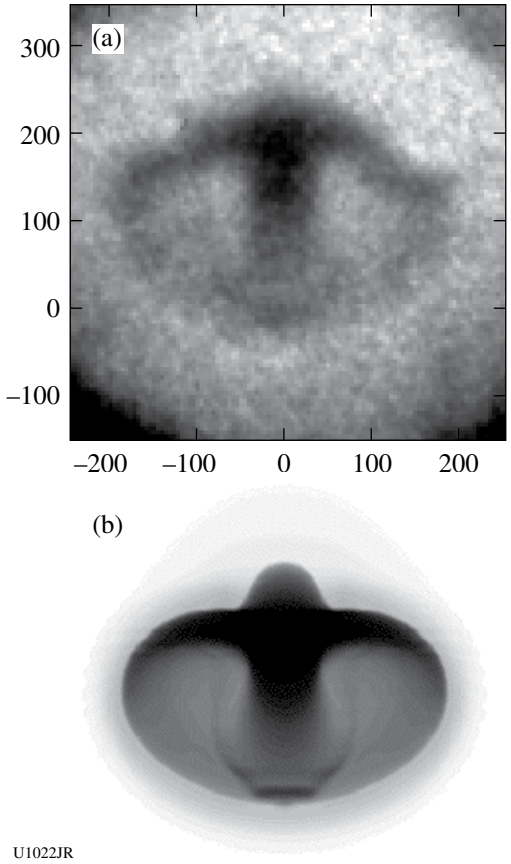

Figure 120.111
The bow shock produced on interaction of the polar jet with the opposite wall of the capsule is clearly seen in (a) experiment (top) and evident also in (b) simulation (bottom).

subtle differences in the laser hot-spot position, or the albedo of the indirectly heated hohlraum wall, and resolving these differences will form the focus for further work during FY10.

FY09 CEA OMEGA Experimental Programs

CEA conducted 56 shots on the Omega Laser Facility in FY09. The CEA efforts included the following:

CEA Copper Activation Diagnostic for Primary DT Neutron-Yield Measurement: The neutron yield is one of the most important parameters used to characterize the performance of inertial confinement fusion experiments. For the Laser Megajoule (LMJ) and National Ignition Facility (NIF), neutron-yield measurements will be performed by an array of neutron time-of-flight (nTOF) detectors composed of scintillation counters and chemical vapor deposition (CVD) diamond detectors. An accuracy of 4% is required to measure neutron yield. All these detectors are calibrated against the nuclear activation diagnostic, which is a valuable measurement technique because of its reaction threshold and its absolute calibration. The copper activation method is used for the 14.1-MeV primary DT neutron-yield measurement. This diagnostic has been used as a reference on many laser facilities (PHEBUS, NOVA, OMEGA) and will now be used on future megajoule-scale lasers. Copper activation will be the first nuclear diagnostic installed on LMJ.

The copper disk to be used for this diagnostic is pure copper (99.99%) and is composed of 69.2% of ^{63}Cu and 30.8% of ^{65}Cu. The ^{63}Cu(n,2n)^{62}Cu reaction has a Q value of 11 MeV. ^{62}Cu decays with a half-life of 9.73 min and emits a positron, resulting in the production of two back-to-back 511-keV gamma rays on annihilation. On the other hand, the ^{65}Cu(n,2n)^{64}Cu reaction produces ^{64}Cu that decays with a half-life of 12.7 h and emits a positron. The CEA activation acquisition system consists of two 7.62-mm-diam, 7.62-mm-thick NaI(Tl) scintillation detectors. Associated electronics allow us to detect 511-keV gammas in coincidence between two detectors. In 2002 the activation diagnostic was calibrated on a Van De Graaff accelerator at CEA Bruyères le Châtel with an accuracy of 4.5%. The main error contribution comes from the reference detector, which measures the neutron yield delivered by the accelerator. The optimum sensitivity is obtained by using a 10-mm-thick copper disk because it is the best compromise between copper activation and 511-keV gamma detection. We use a 7.62-mm-diam copper disk that is similar in dimension to the NaI(Tl) detectors.

To compare CEA and LLE primary DT neutron calibration, a CEA copper activation diagnostic was implemented on OMEGA during direct-drive implosions of DT capsules yielding 10^{13} primary DT neutrons. The tertiary activation diagnostic (TAD) inserter was used to place copper disks at 40 cm and 100 cm from target chamber center (TCC). Immediately after the shot, the TAD inserter was retracted and the activated copper disk was extracted from the target chamber. The disk was then dropped into a plastic container by the Target Bay operators and carried to the acquisition systems to be measured. Data acquisition began about 10 min after the shot, and measurements were made every minute for at least 2 h to properly describe the ^{62}Cu and ^{64}Cu decays (see Fig. 120.112). This acquisition technique allows us to remove the ^{64}Cu decay contribution to evaluate the neutron yield with the ^{62}Cu decay only. Since OMEGA shots are at about 1-h intervals, we used two acquisition systems.

A 10-mm-thick, 7.62-mm-diam copper disk was used during the three first shots performed in February 2009 to test our operating procedure (shots 53590 to 53592). We decided to use this sample geometry because its calibration is well known with an accuracy of 4.5%. However, the high copper activation level produced by a 10^{13} neutron yield results in an acquisition system saturation with a dead time of 40% about 30 min after the shots. Therefore, neutron yield was determined using data below a coincidence count rate of 300 c/s. Counting-station saturation is a crucial problem because it prevents us from determining the primary DT neutron yield from ^{62}Cu decay when the ^{64}Cu contribution is minimum, even if it was previously calibrated. To reduce acquisition system saturation in the later shots taken in May, we used 3-mm-thick copper disks placed at 1 m from TCC.

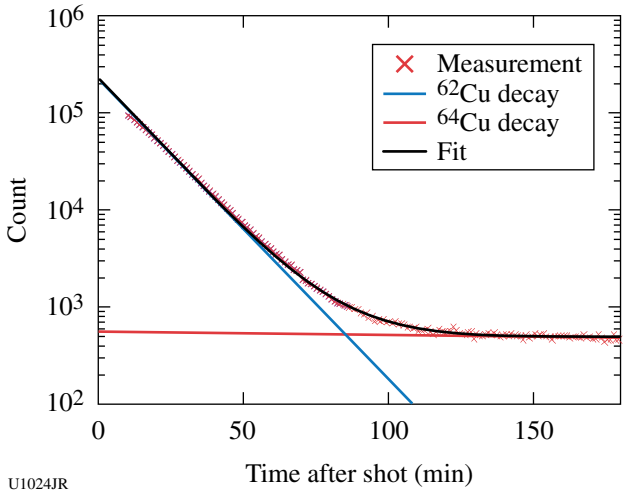

Figure 120.112
^{62}Cu and ^{64}Cu decays measured at 1 m from TCC with a 3-mm-thick disk during shot 54460 yielding 2×10^{13} neutrons.

The primary DT neutron yield was compared to the LLE time-of-flight scintillation counter located at 12 m from the target (12mnTOFh). The CEA copper activation diagnostic was used on 19 DT shots. The neutron yields in these experiments ranged from 8.9×10^{12} to 3×10^{13}. The neutron-yield measurement accuracy was 4.6%. Except for one shot (54471), nTOF measurements were consistent with the CEA copper activation. If we compare shot-to-shot CEA copper activation and LLE nTOF measurements, the dispersion is about 3.6% (rms) and the average difference between primary DT neutron-yield calibrations is only 1.8% (see Fig. 120.113).

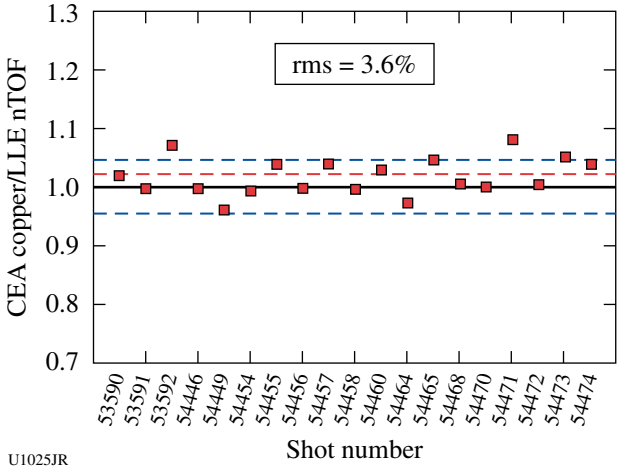

Figure 120.113
Shot-to-shot comparison between CEA copper activation and nTOF neutron-yield measurement. The two independently calibrated neutron-yield diagnostics show a dispersion of 3.6% (dashed blue line) with an average difference of 1.8% (dashed red line).

The 2009 copper-activation measurement campaign confirmed that the CEA and LLE independent neutron-yield calibrations are very close.

It is worth noting that, compared to a 10-mm-thick geometry, the sensitivity of the 3-mm-thick sample was determined with only one calibration measurement at 14.1 MeV. The best way to reduce statistical effects is to perform several measurements with exactly the same sample geometry at the same energy. For this reason, two calibration weeks have been scheduled between 16 and 27 November 2009 on the 4-MV Van de Graaff accelerator at CEA (Bruyères le Châtel). All data acquired on OMEGA will be processed again with this new calibration to determine final results.

MeV Photon X-Ray Sources Produced on OMEGA EP: High-power laser–plasma experiments have been used for several years to study the generation of energetic particles. With chirped-pulse–amplification laser systems, the interaction of a high-intensity laser pulse ($I\lambda^2 > 10^{19}$ W/cm^2 μm^2) with a gas-jet or thin-foil target leads to the generation of relativistic, multi-MeV electrons, accelerated from many physical processes, such as the Brunel effect, ponderomotive or $j \times B$ acceleration, and Wakefield acceleration. If they propagate in a high-Z solid target located behind the interaction area, these relativistic electrons will generate copious high-energy Bremsstrahlung emission. These x-ray photons can be an interesting bright high-energy (>1 MeV) source for radiography, nuclear activation, radiation effects, and radiation safety studies.

Two experiments were carried out using the "backlighter" of the OMEGA EP laser. For the first experiment performed in a high-power regime (CEA/LLE collaboration), the short pulse delivered up to 300 J in τ = 0.6 ps at a wavelength of λ = 1.053 μm. The short pulse was focused at the center of the vacuum chamber, at 45° of the normal to the target. Peak laser intensity was estimated to be $\sim 4 \times 10^{19}$ W/cm^2. Two types of targets were irradiated: 20-μm-thick (500×500 μm^2) and 100-μm-thick (200×200 μm^2) square gold foils.

For the second experiment performed in a high-energy regime (CEA/AWE collaboration), the short pulse delivered up to 1 kJ in τ = 10 ps and was focused at the center of the vacuum chamber, at 18° off the normal to the target. The peak laser intensity was estimated to be $\sim 8 \times 10^{18}$ W/cm^2 and the target was a 2-mm-thick, 2-mm-diam Ta cylinder coated with 10-μm-thick plastic. For some of the shots, a nanosecond heating beam (1 kJ, 1 ns, ϕ = 800 μm) was used to produce a preformed plastic plasma that was intended to increase the short-pulse energy absorption. Since no phase plate was available for the heating beam, a large focal spot was obtained by defocusing the beam.

In these experiments, the ratio $d/(c\tau/2)$, where c is the speed of light in vacuum and roughly corresponds to the speed of the fastest electrons and d is the target thickness, is close to 1 for thin targets (<1 for a 20-μm target and >1 for a 100-μm target) and is well above 1 for a 1-mm-thick target. Electron recirculation in the target is therefore expected to result in greater bremsstrahlung emission and a larger source size in thinner targets.

The high-energy part (>10 MeV) of the x-ray spectrum was studied from ^{63}Cu(γ,n)^{62}Cu and ^{12}C(γ,n)^{11}C photonuclear reaction measurements. Assuming a Maxwellian distribution for the spectrum $S(E) \sim K_h \exp(-E/T_h)$, where K_h is the amplitude

of the spectrum, T_h can be deduced from an activity ratio measurement. The x-ray dose is inferred using x-ray dosimeters and from the radiography of a tower of Hanoi-shaped structure composed of W (tungsten). The x-ray source size is estimated using a penumbral imaging diagnostic (cylindrical 80-mm-thick W pinhole) and also from the radiography of an image quality indicator (IQI). This IQI is made of two 20-mm-diam W hemispheres with internal sinusoidal modulations. The signal is recorded using image plates combined with Ta reinforcement screens that increase the plate sensitivity for high-energy photons.

Figures 120.114(a) and 120.114(b) show spatial profiles of penumbral images obtained during the high-power-regime experiment with 20-μm-thick and 100-μm-thick gold targets, respectively. These profiles can be estimated with an edge response function associated to an x-ray source with either a Bennett or a Gaussian radial profile. The Bennett fit gives a source size of FWHM = 160 μm (resolution ~40 μm) for the 20-μm-thick foil and FWHM = 90 μm (resolution ~30 μm) for the 100-μm-thick foil. Surprisingly, a larger x-ray source size was obtained with the thinnest foil. This may be explained by the electron recirculation in targets of different sizes. Activation measurements show a quite high temperature T_h ~ 10±4 MeV for 100-μm-thick foils and a significantly lower temperature T_h ~ 5±1 MeV for 20-μm-thick foils. The effects of electron circulation on bremsstrahlung emission and x-ray source dimensions will be studied using the PIC numerical code Calder coupled to the Monte Carlo code MCNP.

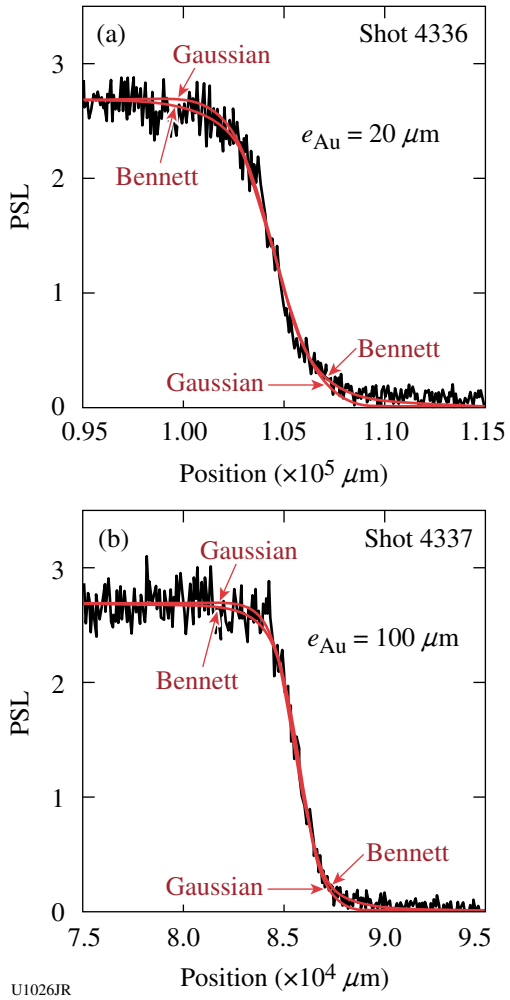

Figure 120.114
Spatial profiles of penumbral images obtained from laser shots on (a) 20-μm-thick and (b) 100-μm-thick gold foils.

Results from the second experiment using a thick Ta target (2 mm) in a high-energy laser regime show a relatively large x-ray source, FWHM = 400 μm (resolution ~130 μm), when the heating beam was combined with the short pulse [Fig. 120.115(a)]. Analysis of the radiographic image of the IQI [Fig. 120.115(b)] indicates that a smaller x-ray source (below 200 μm) was obtained when only the short pulse was focused on target, which is in agreement with past results obtained on other laser facilities. The results also show that the x-ray dose produced with only the short pulse was almost one order of magnitude larger than when the heating beam was combined. Since this long pulse had to be defocused here to produce large preformed plasma, the short pulse probably encountered inhomogeneous plasma with transverse density gradients that can lead to laser refraction. Phase plates should be available in FY2010 for long pulse and will be used for the next experiment.

CEA γ-Background Measurements after High-Neutron-Yield Shots on OMEGA: Knowledge of γ doses produced after high-neutron-yield shots is very important for the nuclear safety of megajoule-class laser facilities (NIF and LMJ). Indeed, neutrons produced during fusion reactions can activate the structural materials in the experimental hall, and γ background levels should be monitored after high-neutron-yield shots (DT implosions). Experiments dedicated to these measurements on OMEGA were initiated in 2005 and were continued in 2008 and 2009. These results will allow us to validate Monte Carlo activation calculations and therefore better predict γ background levels after high-gain shots on LMJ.

<u>γ-Dose-Rate Measurements with a FH40 Dosimeter.</u> During the two first campaigns (2005 and 2008), a FH40 dosimeter (based on a plastic scintillator) was used to perform the measurements [see Fig. 120.116(a)]. This dosimeter can measure the γ-dose rate per second (in μSv/h) in the range of 40 keV to

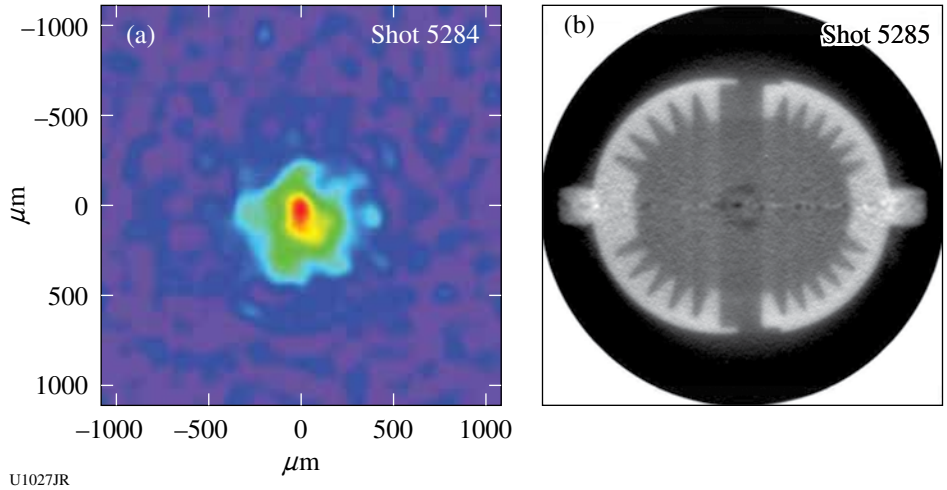

Figure 120.115
Reconstructed image of (a) the x-ray source and (b) radiography of the IQI after tomography obtained during the high-energy laser regime experiment.

1.3 MeV. The dynamic range covers 10 nSv/h up to 100 mSv/h with a 5% uncertainty.

In May 2008, we performed γ-dose-rate measurements at three positions [see Fig. 120.116(b)]:

- at ~8 m from TCC in the Target Bay [near the CEA-neutron imaging system's (NIS) alignment station]
- at ~3 m from TCC in the Target Bay (in the P9 port), and
- in La Cave, just below the target chamber, under the 70-cm concrete slab

Figure 120.117 shows the γ-dose rate measured by the FH40 dosimeter in La Cave before the high-neutron-yield shot campaign. The mean residual background was 0.07±0.02 μSv/h.

Similar results were obtained in the Target Bay. During this high-yield shot campaign (21–22 May 2009), 23 shots were recorded (ten at the NIS position, eight in the P9 port, and five in La Cave), for neutron yields ranging from 2.46×10^{12} to 4.3×10^{13}. A typical signal obtained with the FH40 dosimeter is shown in Fig. 120.118, for the "NIS" position (at ~8 m from TCC).

Similar temporal behavior was observed in all three positions. At least three materials with a high half-life (>1 min) were activated (red lines on the curve of Fig. 120.118). These results have to be compared with calculations and predictions of Monte Carlo simulations.

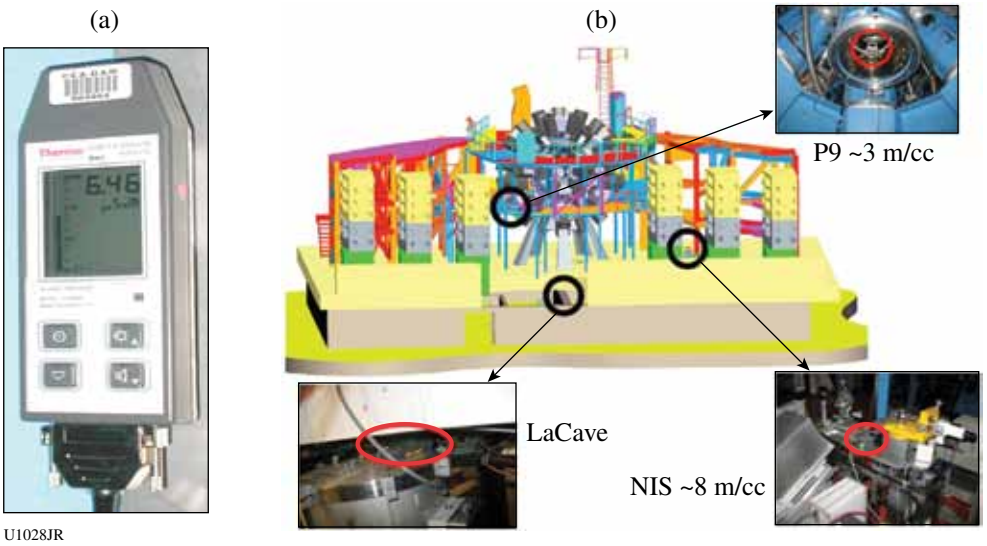

Figure 120.116
(a) The FH40 dosimeter; (b) the three positions for the FH40 dosimeter.

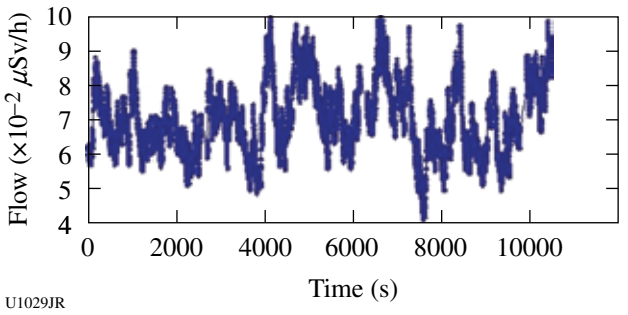

Figure 120.117
Residual γ-dose rate recorded in La Cave before a high-neutron-yield shot with the FH40 dosimeter.

Figure 120.119
Germanium detector with its electronic cryogenic module.

γ Spectroscopy with a Germanium Detector. To obtain more-detailed results on this γ background after high-neutron-yield shots, γ spectroscopy was performed with a germanium detector in May 2009. This detector was an N-type germanium coaxial diode with 85% relative efficiency (see Fig. 120.119). The dimensions of the germanium crystal were 79 mm in diameter and 62 mm in length. The resolution was 2 keV for a 1-MeV γ, and the detectable energy range was 100 keV to 3 MeV. To avoid the use of liquid nitrogen, the crystal was cooled with an electronic cryogenic module.

Monte Carlo activation calculations were performed at CEA for a 5×10^{13} neutron yield on the OMEGA facility. Table 120.XIII shows expected γ rates, 4 m from TCC.

As in the 2008 campaign, the detector was located in three different positions:

- at ~8 m from TCC in the Target Bay (near the CEA-NIS alignment station)
- at ~4 m from TCC in the Target Bay (near the chamber)
- in La Cave, protected by the 70-cm concrete slab

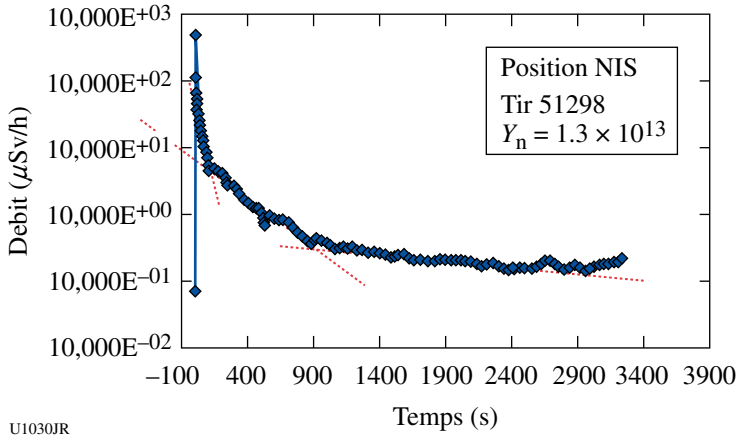

Figure 120.118
γ-dose rates recorded on OMEGA for shot 51298 ("NIS" position) with the FH40 dosimeter.

Table 120.XIII: Gamma-ray rates predicted using a Monte Carlo activation calculation for a 5×10^{13}-neutron-yield OMEGA shot at 4 m from TCC.

Time after shot	Rate (γ/cm^2)	Main radionuclide	Reaction channel	$T_{1/2}$
10 s	5.2×10^2	^{27}Mg	^{27}Al(n,p)^{27}Mg	9.46 min
100 s	2.3×10^2	^{24}Na	^{27}Al(n,α)^{24}Na	14.66 h
1000 s	4.7×10^1	^{24}Na	^{27}Al(n,α)^{24}Na	14.66 h

To protect the electronic device, the detector was inactive during the shot. The high voltage was turned on 2 to 3 min after the shot. To observe the decay time of γ rays, γ spectra were recorded each minute. Figure 120.120 presents a background γ spectrum recorded before the high-neutron-yield shots campaign during a 10-h period. For example, one can clearly see the 1460.8-keV γ ray coming from the ^{40}K nucleus. Other radioactive nuclei present in the environment (concrete, etc.), derived from uranium or thorium, may be identified in the spectrum.

For this campaign (13–14 May 2009), 15 shots were recorded (nine shots in NIS position, four near the aluminum chamber, and two in La Cave). The γ spectrum of Fig. 120.121 was obtained for shot 54446 ($Y_n = 2.58 \times 10^{13}$). The germanium detector was located in the NIS position, at ~8 m from TCC. The spectrum shows all γ rays recorded by the germanium detector during the 64-min period after the shot.

Some reaction channels are clearly identified:

- ^{27}Al (n,p) ^{27}Mg
- ^{27}Al (n,α) ^{24}Na

We also identified neutron activation of iron present in the OMEGA Target Bay structure and also neutron capture on ^{27}Al (because of slow neutrons diffused by the environment).

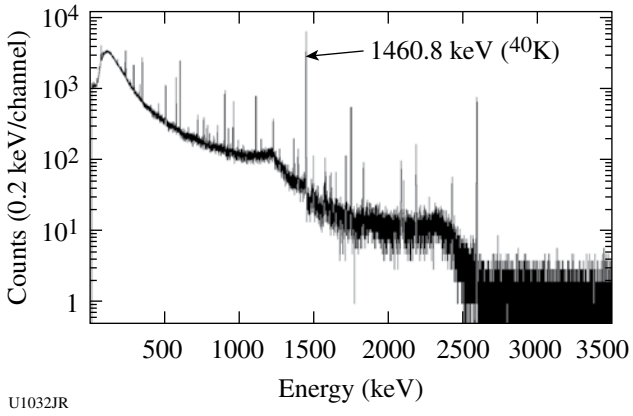

Figure 120.120
γ-background spectrum recorded by the germanium detector during a 10-h period before high-yield shots.

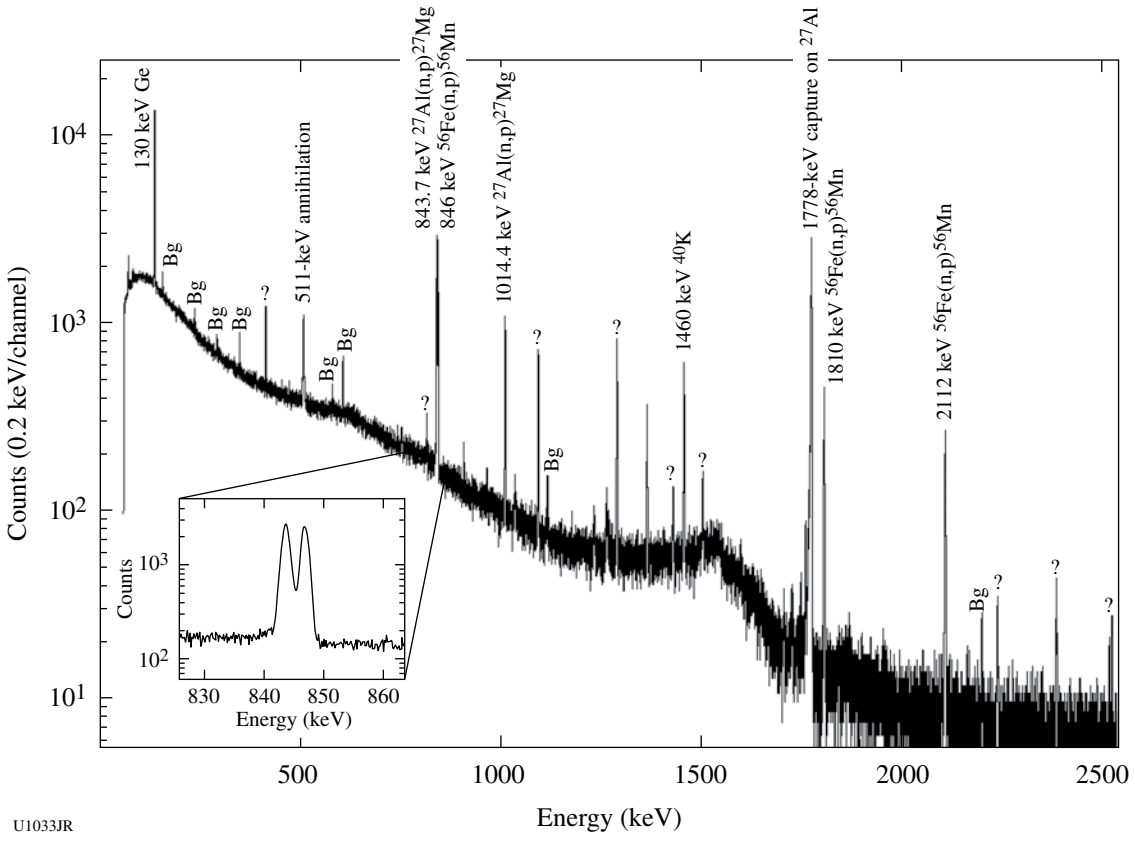

Figure 120.121
γ spectrum recorded by the germanium detector during a 64-min period after shot 54446 (see text for details).

Some γ rays present in the background spectrum were found and labeled "Bg." They were caused only by natural radioactivity and not related to the DT shot. Unknown γ rays were present in the spectrum and have to be identified. Data analysis is still in progress in France. The zoom in Fig. 120.121 shows that we can separate closely spaced γ rays thanks to the high resolution of the germanium detector.

As for the γ-dose-rate measurements, these results will be useful in constraining our simulations. Indeed, not all materials of the environment are well known (exact concrete composition, for example), and data from γ spectroscopy will give us some idea of the main radionuclei responsible of γ background after high-neutron-yield shots.

Two New Neutron-Imaging Systems on OMEGA: Neutron imaging system experiments by CEA have been conducted on OMEGA for many years. For the LMJ nuclear diagnostics development, we have tested several imaging techniques based on the use of thick penumbral apertures. It was shown[39] that design and alignment are essential for measurement quality. We also experimented with several detector designs and configurations using segmented scintillators,[40] or capillary arrays filled with a high-refractive-index liquid scintillator.[41,42] The latter was found to be very efficient and gave a high spatial resolution.

We designed and assembled a large (150-mm entrance diameter) neutron imaging system (LNIS) based on the capillary-filled technique. A large capillary array had to be composed by assembling four arrays of 5-cm length. A large optical-fiber taper reducer (150/75 mm) collected light generated in the scintillator sealed in the capillaries to a fast and large light amplifier (75-mm diameter). This amplifier allows for time gating down to 12 ns with accurate timing precision and therefore makes it possible to select light generated by 14-MeV neutrons interacting with the scintillator material. A second optical fiber taper (75/50 mm) matched the amplifier diameter to a cooled charge-coupled device (CCD) 2084 $\times$ 2084 pixels of 24 μm^2 (see Fig. 120.122). Two rotations were added to the system to allow for detector autocollimation on the neutron line-of-sight (LOS) path.

Our aim was to test this detector on OMEGA during National Ignition Campaign (NIC) shots. Following the OMEGA qualification procedure (starting in February 2008 with a Preliminary Design Review), we were able to implement this camera using a 13-m LOS on the May 2009 NIC campaign. This detector was placed in the La Cave area. Using this LOS, we obtained a good shielding from scattered neutrons and γ rays generated in the Target Bay; also, by using our usual penumbral aperture[43] at this distance, we were able to obtain a larger magnification ratio and, therefore, a smaller resolution (down to 15 μm) with this capillary technique detector. Alignment was performed by using our laser technique (for details see Ref. 44) with the alignment station placed on the Target Bay floor at 8 m.

The detector was characterized on an accelerator-generated 14-MeV neutron source and on a Co^{60} gamma-ray source. The images obtained are shown in Fig. 120.123. We note that the capillary assembly is clearly visible. We also distinguish four black spots that correspond to capillaries destroyed during manufacturing. The top-left part of the image is more intense than the rest of the image by a factor of 2 due to light amplifier

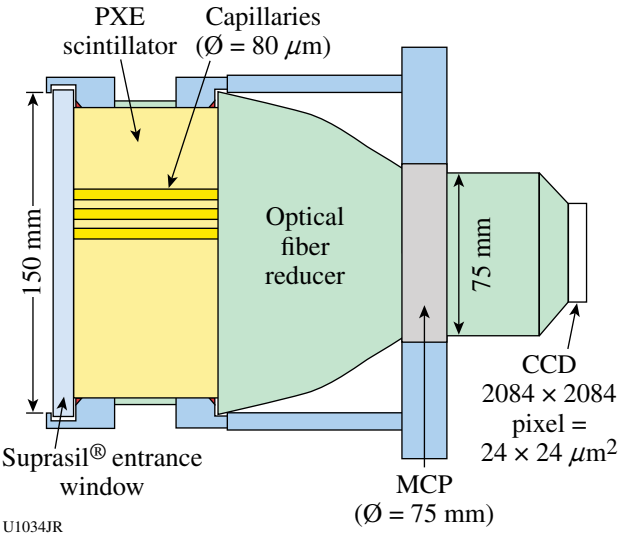

Figure 120.122
LNIS neutron detector scheme.

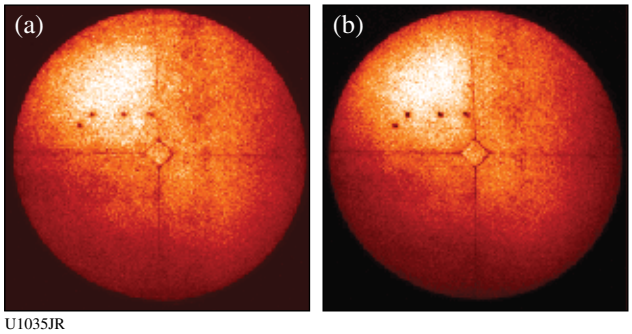

Figure 120.123
(a) Neutron flat-field image yield 8.5 $\times$ 10^3 n/cm^{-2}; (b) Co^{60} γ-rays flat-field image.

inhomogeneity. There is a good agreement between these images, showing that detector response is similar in neutron and γ rays. At low neutron yield (see Fig. 120.124), we were able to register individual proton recoil tracks with a range of about 625 μm, consistent with detector resolution for 14-MeV neutrons.[43]

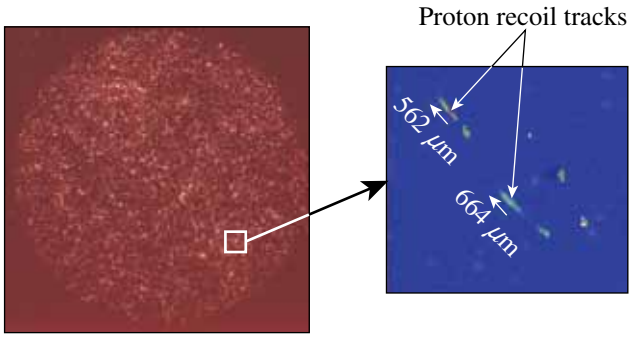

Figure 120.124
14-MeV neutrons image obtained on an accelerator (yield = 53 n/cm^2).

We were able to register ten penumbral images and three flat-field images on the CCD during the two days of target shots. Some shots were dedicated to amplifier time-gating adjustment on DT neutron time of flight. A sample raw penumbral image obtained for shot 54466 at 1.15×10^{13} neutrons is shown in Fig. 120.125(a). In Fig. 120.125(b), one can see that the black spots do not alter image quality since they are not in a region that contains image information. The spots are not visible after flat-fielding the image. The image was then unfolded using our autocorrelation method[45] [see Fig. 120.126(a)]. In that case, the unfolded image was not corrected from optical transport image distortions. In Fig. 120.126(b) we plotted the vertical and horizontal lineout showing that the source diameter was about 50-μm FWHM. Figure 120.127(a) shows an image resulting from the superposition of a 2- to 10-keV x-ray image with a neutron image contour obtained for shot 54466. Figure 120.127(b) is also a superposition of an x-ray image from 7 keV to 9 keV with the same neutron image contour. We see that both images are consistent in shape and size.

A small neutron imaging system (SNIS) was also developed this past year. This system is based on a detector that was specifically designed for low-neutron-yield shots (10^9 to 10^{10} neutrons/4π). This detector was implemented at the rear port of the TIM-6 at 4 m from TCC. As for the previous one, this detector is based on a scintillator-filled capillary array. High sensitivity is obtained primarily by the fact that this camera does not contain any optical-fiber reducer between the capillaries and the light amplifier (see Fig. 120.128). The entrance diameter is 40 mm. This detector was also characterized on an a Co^{60} γ-ray source and measurements showed that efficiency is 4× lower than for the traditional NIS. At this distance, the

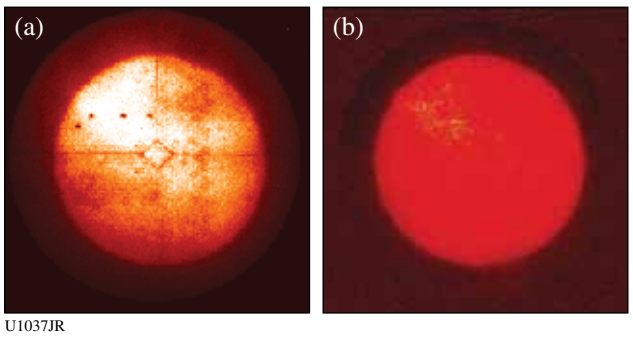

Figure 120.125
(a) Raw image of a DT implosion (shot 54466) yielding 1.15×10^{13} neutrons; (b) flat-fielded image.

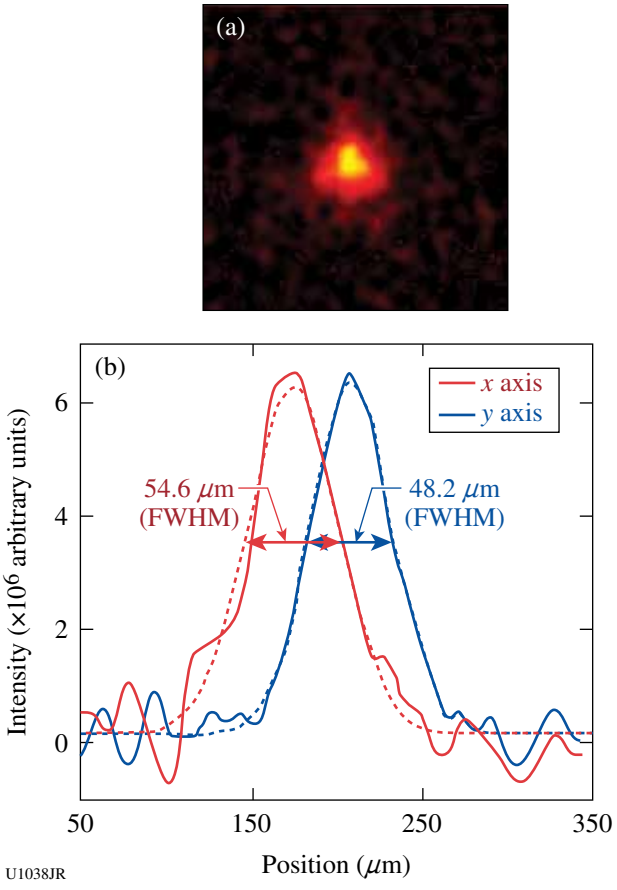

Figure 120.126
(a) Unfolded image using autocorrelation method[42] (SNR = 16); (b) vertical and horizontal lineouts.

magnification ratio is smaller; therefore achievable resolution is larger (43 μm). At 4 m from TCC, the neutron fluence is 4× higher than at 8 m. The aperture type and alignment technique are the same as used for the larger NIS.

This detector was activated on 16 June shots for indirect-drive, deuterium-filled targets. We were able to register an image on shot 54747 with a neutron yield of 1.37×10^{10} neutrons/4π [Fig. 120.129(a)]. In this image, one can see that the statistics are quite low compared to the LNIS image. To reach a reasonable signal-to-noise ratio (SNR) with the autocorrelation technique, the resolution had to be degraded to 54 μm in the unfolded image [Fig. 120.129(b)]. This last image reveals a noncircular shape. This observation is contrary to the circular source (caused by the implosion symmetry) that would be expected along the hohlraum axis. This result could be due to source misalignment in the aperture field of view, or aperture misalignment itself, or

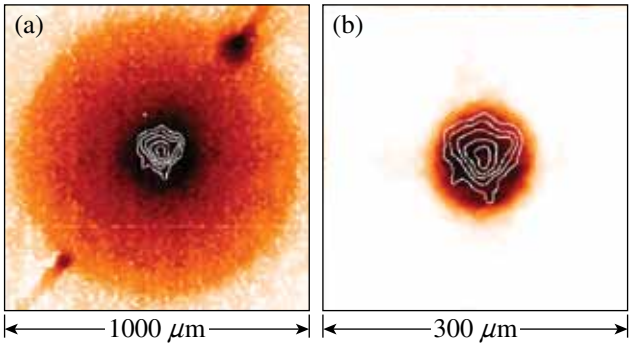

Figure 120.127
(a) Neutron (contours) and x-ray (2- to 10-keV) image superposition; (b) neutron (contours) and x-ray (7- to 9-keV) image superposition.

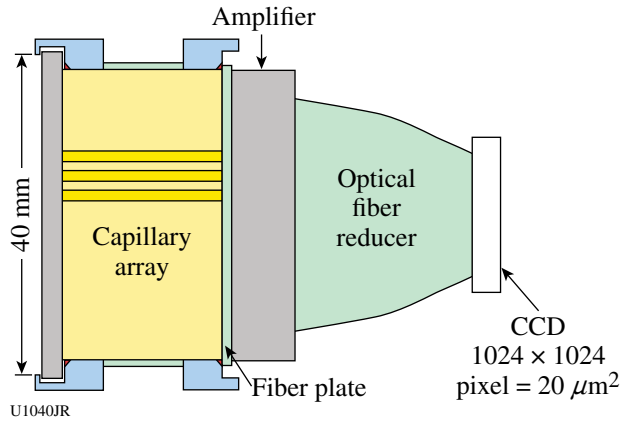

Figure 120.128
SNIS neutron detector scheme.

due to optical coupling between the light amplifier and the fiber plate, which was found imperfect after detector tests. Nevertheless, this camera had demonstrated its particular high sensitivity to low-neutron-yield shots.

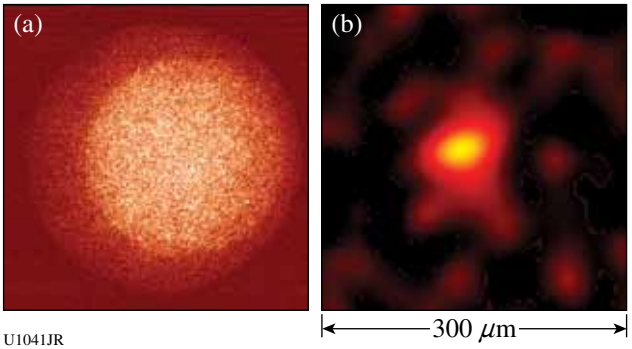

Figure 120.129
(a) Raw image of DD implosion (shot 54747) yielding 1.37×10^{10} neutrons; (b) unfolded image (SNR = 10, resolution = 54 μm).

Neutron-imaging measurements were obtained for the first time with 15-μm resolution on OMEGA during the May 2009 NIC campaign. We successfully tested the first part of the LMJ-NIS detector design. This detector resolution may now help us to discriminate the anisotropy in the neutron source linked to the driver energy balance, but this will require specific dedicated experiments.

The first neutron image on an indirect-drive shot was registered with 54-μm resolution. This last image was a milestone for CEA-NIS, which is now able to register images with resolution from 43 μm to 15 μm and detection threshold from a few 10^9 until the maximum accessible yields on OMEGA.

Next year's experiments will be dedicated to indirect-drive shots and, more particularly, to improving optical coupling between a fiber plate and a light amplifier. This will probably improve light collection and detector sensitivity. Concerning LNIS, a new light amplifier and a new one-block capillary array will be implemented.

Ablative Rayleigh–Taylor Stabilization Mechanisms Experiment: Ablative Rayleigh–Taylor growth measurements in laminated samples were obtained on OMEGA on 17 June 2009. The experimental platform consisted of a gas-filled, 1.2-mm-diam halfraum along with side-on and face-on radiography x-ray sources (Fig. 120.130).

Rayleigh–Taylor growth measurements were obtained using face-on radiography and are in good agreement with 2-D hydrodynamic simulations based on published theoretical and numerical predictions.[46] Different behavior was found for homogeneous and laminated samples (Fig. 120.131), the latter showing a strong reduction of the initial perturbation mode.

Side-on radiography shows the absence of Rayleigh–Taylor spikes in the case of laminated samples (Fig. 120.132), while the acceleration was found to be identical for both kinds of samples.

These first experimental measurements strongly motivate new designs using laminated structures for ignition capsules.

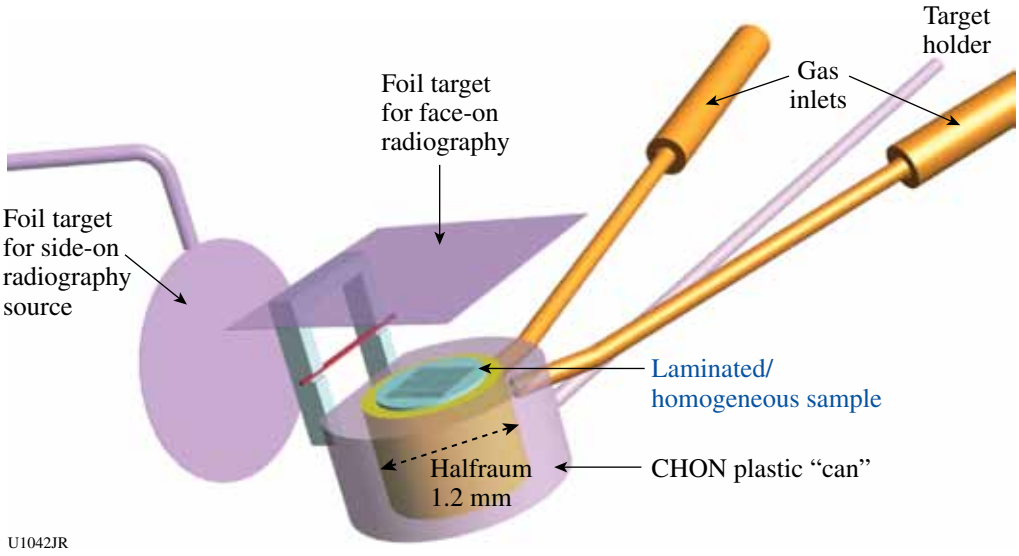

Figure 120.130
Experimental setup.

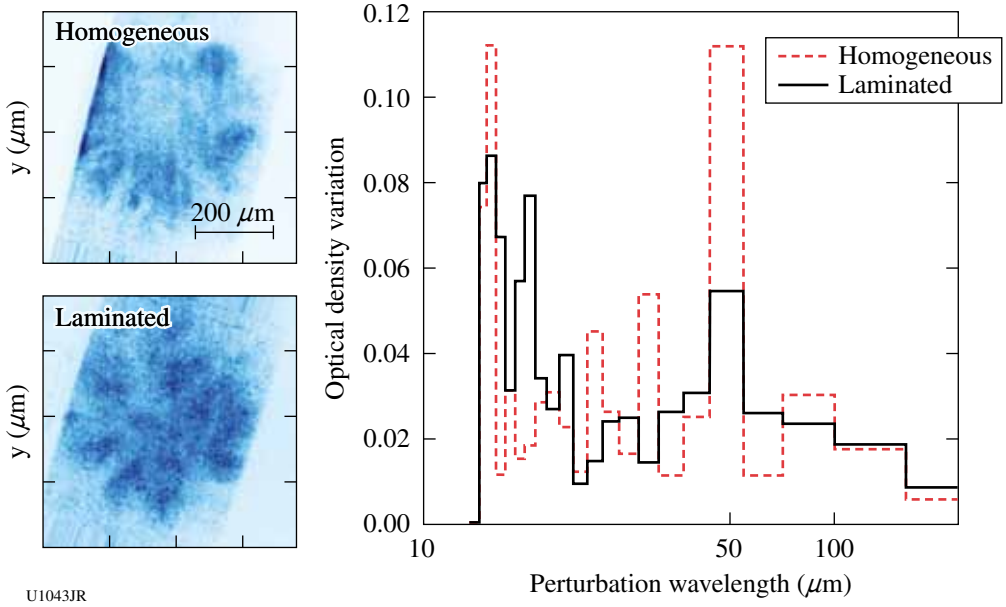

Figure 120.131
Face-on snapshots for homogeneous and laminated samples and corresponding perturbation spectra.

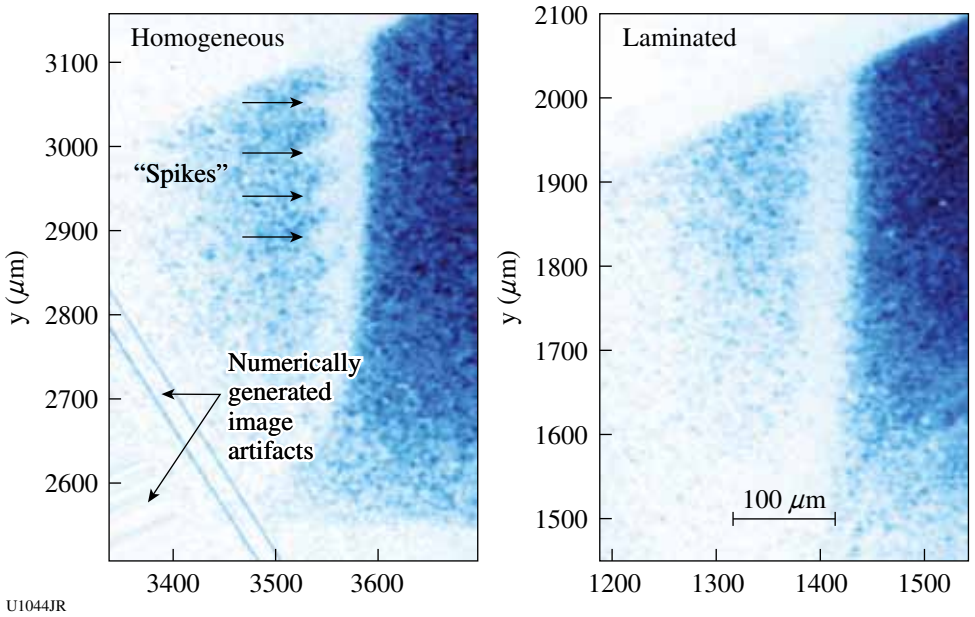

Figure 120.132
Side-on radiographies of (a) homogeneous and (b) laminated samples.

REFERENCES

1. S. H. Glenzer *et al*., Phys. Rev. Lett. **90**, 175002 (2003).
2. H. J. Lee, P. Neumayer, J. Castor, T. Döppner, R. W. Falcone, C. Fortmann, B. A. Hammel, A. L. Kritcher, O. L. Landen, R. W. Lee, D. D. Meyerhofer, D. H. Munro, R. Redmer, S. P. Regan, S. Weber, and S. H. Glenzer, Phys. Rev. Lett. **102** 115001 (2009).
3. L. Willingale *et al*., Phys. Rev. Lett. **96**, 245002 (2006); L. Willingale *et al*., Phys. Rev. Lett. **102**, 125002 (2009).
4. A. L. Lei *et al*., Phys. Plasmas **16**, 056307 (2009).
5. G. Li *et al*., Phys. Rev. Lett. **100**, 125002 (2008).
6. C. K. Li, F. H. Séguin, J. A. Frenje, J. R. Rygg, R. D. Petrasso, R. P. J. Town, P. A. Amendt, S. P. Hatchett, O. L. Landen, A. J. Mackinnon, P. K. Patel, V. A. Smalyuk, T. C. Sangster, and J. P. Knauer, Phys. Rev. Lett. **97**, 135003 (2006).
7. C. K. Li, F. H. Séguin, J. A. Frenje, J. R. Rygg, R. D. Petrasso, R. P. J. Town, P. A. Amendt, S. P. Hatchett, O. L. Landen, A. J. Mackinnon, P. K. Patel, M. Tabak, J. P. Knauer, T. C. Sangster, and V. A. Smalyuk, Phys. Rev. Lett. **99**, 015001 (2007).
8. C. K. Li, F. H. Séguin, J. A. Frenje, J. R. Rygg, R. D. Petrasso, R. P. J. Town, O. L. Landen, J. P. Knauer, and V. A. Smalyuk, Phys. Rev. Lett. **99**, 055001 (2007).
9. C. K. Li, F. H. Séguin, J. R. Rygg, J. A. Frenje, M. Manuel, R. D. Petrasso, R. Betti, J. Delettrez, J. P. Knauer, F. Marshall, D. D. Meyerhofer, D. Shvarts, V. A. Smalyuk, C. Stoeckl, O. L. Landen, R. P. J. Town, C. A. Back, and J. D. Kilkenny, Phys. Rev. Lett. **100**, 225001 (2008).
10. C. K. Li, F. H. Séguin, J. A. Frenje, R. D. Petrasso, P. A. Amendt, R. P. J. Town, O. L. Landen, J. R. Rygg, R. Betti, J. P. Knauer, D. D. Meyerhofer, J. M. Soures, C. A. Back, J. D. Kilkenny, and A. Nikroo, Phys. Rev. Lett. **102**, 205001 (2009).
11. R. D. Petrasso, C. K. Li, F. H. Séguin, J. R. Rygg, J. A. Frenje, R. Betti, J. P. Knauer, D. D. Meyerhofer, P. A. Amendt, D. H. Froula, O. L. Landen, P. K. Patel, J. S. Ross, and R. P. J. Town, Phys. Rev. Lett. **103**, 085001 (2009).
12. J. R. Rygg, F. H. Séguin, C. K. Li, J. A. Frenje, M. J.-E. Manuel, R. D. Petrasso, R. Betti, J. A. Delettrez, O. V. Gotchev, J. P. Knauer, D. D. Meyerhofer, F. J. Marshall, C. Stoeckl, and W. Theobald, Science **319**, 1223 (2008).
13. C. K. Li, F. H. Séguin, J. A. Frenje, J. R. Rygg, R. D. Petrasso, R. P. J. Town, P. A. Amendt, S. P. Hatchett, O. L. Landen, A. J. Mackinnon, P. K. Patel, V. Smalyuk, J. P. Knauer, T. C. Sangster, and C. Stoeckl, presented at the 16th Topical Conference on High-Temperature Plasma Diagnostics, Williamsburg, VA, 7–11 May 2006 (invited).
14. C. K. Li, presented at the Fifth International Conference on Inertial Fusion Sciences and Applications, Kobe, Japan, 9–14 September 2007, Paper ThO4.1 (invited).
15. R. Petrasso, presented at the Program of the 49th Annual Meeting of the Division of Plasma Physics, Orlando, FL, 12–16 November 2007, Paper GI1 4 (invited).
16. C. K. Li, presented at the 50th Annual Meeting of the APS Division of Plasma Physics, Dallas, TX, 17–21 November 2008, Paper BI1 5 (invited).
17. R. D. Petrasso, presented at the 2008 APS April Meeting and HEDP/HEDLA Meeting, St. Louis, MO, 11–15 April 2008, Paper 14HE.00002 (invited).
18. R. D. Petrasso, C. K. Li, F. H. Séguin, J. A. Frenje, M. Manuel, D. Casey, N. Sinenian, M. Rosenberg, H. Rir. Landen, J. R. Rygg, R. P. J. Town, R. Betti, J. Delettrez, J. P. Knauer, F. J. Marshall, D. D. Meyerhofer, V. A. Smalyuk, J. M. Soures, C. A. Back, J. D. Kilkenny, and A. Nikroo,

presented at the Second International Conference on High Energy Density Physics, Austin, TX, 19–22 May 2009 (invited).

19. C. K. Li, presented at The 8th Pacific Rim Conference on Lasers and Electro-Optics (CLEO/Pacific Rim 2009), Shanghai, China, 30 August–3 September 2009 (invited).

20. C. K. Li, presented at The Sixth International Conference on Inertial Fusion Sciences and Applications (IFSA 2009), San Francisco, CA, 6–11 September 2009, Paper 5.2.3 (invited).

21. J. A. Frenje, D. T. Casey, F. H. Séguin, C. K. Li, N. Sinenian, R. D. Petrasso, V. Yu. Glebov, T. C. Sangster, D. D. Meyerhofer, S. Hatchett, S. Haan, C. Cerjan, D. Eder, O. Landen, M. Moran, K. Fletcher, and R. Leeper, presented at the Sixth International Conference on Inertial Fusion Sciences and Applications (IFSA 2009), San Francisco, CA, 6–11 September 2009, Paper 3.6.3 (invited).

22. C. K. Li, F. H. Séguin, J. A. Frenje, J. R. Rygg, R. D. Petrasso, R. P. J. Town, P. A. Amendt, S. P. Hatchett, O. L. Landen, A. J. Mackinnon, P. K. Patel, V. Smalyuk, J. P. Knauer, T. C. Sangster, and C. Stoeckl, Rev. Sci. Instrum. **77**, 10E725 (2006).

23. H. Chen, S. C. Wilks, J. D. Bonlie, E. P. Liang, J. Myatt, D. F. Price, D. D. Meyerhofer, and P. Beiersdorfer, Phys. Rev. Lett. **102**, 105001 (2009).

24. J. Myatt, A. V. Maximov, R. W. Short, and D. D. Meyerhofer, presented at the 49th Annual Meeting of the APS Division of Plasma Physics, Orlando, FL, 12–16 November 2007, Paper CO6 1.

25. W. Theobald, R. Betti, V. A. Smalyuk, K. S. Anderson, J. A. Delettrez, J. A. Frenje, V. Yu. Glebov, F. J. Marshall, D. D. Meyerhofer, J. F. Myatt, R. D. Petrasso, C. Ren, T. C. Sangster, W. Seka, A. A. Solodov, C. Stoeckl, and B. Yaakobi, "Shock-Ignition Experiments on OMEGA and NIF-Relevant Intensities," submitted to Physical Review Letters.

26. W. Theobald, K. S. Anderson, R. Betti, R. S. Craxton, J. A. Delettrez, J. A. Frenje, V. Yu. Glebov, O. V. Gotchev, J. H. Kelly, C. K. Li, A. J. Mackinnon, F. J. Marshall, R. L. McCrory, D. D. Meyerhofer, J. F. Myatt, P. A. Norreys, P. M. Nilson, P. K. Patel, R. D. Petrasso, P. B. Radha, C. Ren, T. C. Sangster, W. Seka, V. A. Smalyuk, A. A. Solodov, R. B. Stephens, C. Stoeckl, and B. Yaakobi, "Advanced-Ignition-Concept Exploration on OMEGA," Plasma Phys. Control. Fusion **51**, 124052 (2009).

27. D. H. Froula, L. Divol, R. L. Berger, R. A. London, N. B. Meezan, D. J. Strozzi, P. Neumayer, J. S. Ross, S. Stagnitto, L. J. Suter, and S. H. Glenzer, Phys. Rev. Lett. **101**, 115002 (2008).

28. D. H. Froula, Phys. Rev. Lett. **103**, 045006 (2009).

29. E. L. Dewald *et al*., Rev. Sci. Instrum. **79**, 10E903 (2008).

30. T. Döppner, O. L. Landen, H. J. Lee, P. Neumayer, S. P. Regan, and S. H. Glenzer, High Energy Density Phys. **5**, 182 (2009).

31. T. Döppner, P. F. Davis, A. L. Kritcher, O. L. Landen, H. J. Lee, S. P. Regan, and S. H. Glenzer, in *Soft X-Ray Lasers and Applications VII*, edited by J. Dunn and G. J. Tallents (SPIE, Bellingham, WA, 2009), Vol. 7451, p. 74510H.

32. *LLE Review Quarterly Report* **116**, 249, Laboratory for Laser Energetics, University of Rochester, Rochester, NY, LLE Document No. DOE/NA/28302-866 (2008).

33. H. W. Herrmann, R. M. Malone, W. Stoeffl, S. E. Caldwell, S. C. Evans, J. M. Mack, P. Sanchez, T. Sedillo, C. S. Young, C. J. Horsfield, D. Drew, E. K. Miller, and V. Yu. Glebov, presented at the 17th Topical Conference on High-Temperature Plasmas Diagnostics, Albuquerque, NM, 11–15 May 2008, Paper D35.

34. H. W. Herrmann, S. C. Evans, J. M. Mack, C. S. Young, C. J. Horsfield, R. M. Malone, E. K. Miller, V. Yu. Glebov, and W. Stoeffl, presented at the 17th Topical Conference on High-Temperature Plasma Diagnostics, Albuquerque, NM, 11–15 May 2008, Paper D34.

35. E. Miller, presented at The Sixth International Conference on Inertial Fusion Sciences and Applications (IFSA 2009), San Francisco, CA, 6–11 September 2009, Poster 3.10.110.

36. P. Amendt *et al*., Rev. Sci. Instrum. **66**, 785 (1995).

37. P. Amendt *et al*., Phys. Rev. Lett. **77**, 3815 (1996).

38. A. A. Hauer *et al*., Phys. Plasmas **2**, 2488 (1995).

39. *LLE Review Quarterly Report* **112**, 270, Laboratory for Laser Energetics, University of Rochester, Rochester, NY, LLE Document No. DOE/SF/19460-790 (2007).

40. L. Disdier, A. Rouyer, D. C. Wilson, A. Fedotoff, C. Stoeckl, J. L. Bourgade, V. Yu. Glebov, J.-P. Garçonnet, and W. Seka, Nucl. Instrum. Methods Phys. Res. A **489**, 496 (2002).

41. L. Disdier, A. Rouyer, A. Fedotoff, J.-L. Bourgade, F. J. Marshall, V. Yu. Glebov, and C. Stoeckl, Rev. Sci. Instrum. **74**, 1832 (2003).

42. L. Disdier, R. A. Lerche, J. L. Bourgade, and V. Yu. Glebov, Rev. Sci. Instrum. **75**, 2134 (2004).

43. L. Disdier, A. Rouyer, I. Lantuéjoul, O. Landoas, J. L. Bourgade, T. C. Sangster, V. Yu. Glebov, and R. A. Lerche, Phys. Plasmas **13**, 056317 (2006).

44. *LLE Review Quarterly Report* **116**, 258, Laboratory for Laser Energetics, University of Rochester, Rochester, NY, LLE Document No. DOE/NA/28302-866 (2008).

45. A. Rouyer, Rev. Sci. Instrum. **74**, 1234 (2003).

46. L. Masse, Phys. Rev. Lett. **98**, 245001 (2007).

Publications and Conference Presentations

Publications

Z. A. Ali, V. Yu. Glebov, M. Cruz, T. Duffy, C. Stoeckl, S. Roberts, T. C. Sangster, R. Tommasini, A. Throop, M. Moran, L. Dauffy, and C. Horsefield, "Tests and Calibration of NIF Neutron Time of Flight Detectors," Rev. Sci. Instrum. **79**, 10E527 (2008).

S.-W. Bahk, J. D. Zuegel, J. R. Fienup, C. C. Widmayer, and J. Heebner, "Spot-Shadowing Optimization to Mitigate Damage Growth in a High-Energy-Laser Amplifier Chain," Appl. Opt. **47**, 6586 (2008).

Z.-M. Bei, T. B. Jones, A. Tucker-Schwartz, and D. R. Harding, "Electric Field Mediated Droplet Centering," Appl. Phys. Lett. **93**, 184101 (2008).

A. Belousov, S. Katrych, J. Jun, J. Zhang, D. Günther, R. Sobolewski, J. Karpinski, and B. Batlogg, "Bulk Single-Crystal Growth of the Ternary $Al_xGa_{1-x}N$ from Solution in Gallium Under High Pressure," J. Cryst. Growth **311**, 3971 (2009).

T. R. Boehly, D. Munro, P. M. Celliers, R. E. Olson, D. G. Hicks, V. N. Goncharov, G. W. Collins, H. F. Robey, S. X. Hu, J. A. Marozas, T. C. Sangster, O. L. Landen, and D. D. Meyerhofer, "Demonstration of the Shock-Timing Technique for Ignition Targets on the National Ignition Facility," Phys. Plasmas **16**, 056302 (2009) (invited).

J. L. Bourgade, P. Troussel, A. Casner, G. Huser, T. C. Sangster, G. Pien, F. J. Marshall, J. Fariaud, C. Remond, D. Gontier, C. Chollet, C. Zuber, C. Reverdin, A. Richard, P. A. Jaanimagi, R. L. Keck, R. E. Bahr, W. J. Armstrong, J. DeWandel, R. Maroni, F. Aubard, B. Angelier, C. Y. Cote, and S. Magnan, "A Versatile High-Resolution X-Ray Imager (HRXI) for Laser-Plasma Experiments on OMEGA," Rev. Sci. Instrum. **79**, 10E904 (2008).

E. Brambrink, H. G. Wei, B. Barbrel, P. Audebert, A. Benuzzi-Mounaix, T. Boehly, T. Endo, C. Gregory, T. Kimura, R. Kodama, N. Ozaki, H.-S. Park, M. Rabec le Gloahec, and M. Koenig, "X-Ray Source Studies for Radiography of Dense Matter," Phys. Plasmas **16**, 033101 (2009).

J. Bromage, S.-W. Bahk, D. Irwin, J. Kwiatkowski, A. Pruyne, M. Millecchia, M. Moore, and J. D. Zuegel, "A Focal-Spot Diagnostic for On-Shot Characterization of High-Energy Petawatt Lasers," Opt. Express **16**, 16,561 (2008).

H. Chen, S. C. Wilks, J. D. Bonlie, E. P. Liang, J. Myatt, D. F. Price, D. D. Meyerhofer, and P. Beiersdorfer, "Relativistic Positron Creation Using Ultraintense Short Pulse Lasers," Phys. Rev. Lett. **102**, 105001 (2009).

B. Ciftcioglu, J. Zhang, L. Zhang, J. R. Marciante, J. D. Zuegel, R. Sobolewski, and H. Wu, "3-GHz Silicon Photodiodes Integrated in a 0.18-μm CMOS Technology," IEEE Photon. Technol. Lett. **20**, 2069 (2008).

B. Ciftcioglu, L. Zhang, J. Zhang, J. R. Marciante, J. Zuegel, R. Sobolewski, and H. Wu, "Integrated Silicon PIN Photodiodes Using Deep N-Well in a Standard 0.18-μm CMOS Technology," J. Lightwave Technol. **27**, 3303 (2009).

X. L. Cross, X. Zheng, P. D. Cunningham, L. M. Hayden, Š. Chromik, M. Sojkova, V. Štrbík, P. Odier, and R. Sobolewski, "Pulsed-THz Characterization of Hg-Based, High-Temperature Superconductors," IEEE Trans. Appl. Supercond. **19**, 3614 (2009).

C. Dorrer, "High-Damage-Threshold Beam Shaping Using Binary Phase Plates," Opt. Lett. **34**, 2330 (2009).

C. Dorrer, "Signal Analyser on an Optical Chip," Nat. Photon. **3**, 136 (2009).

C. Dorrer, "Statistical Analysis of Incoherent Pulse Shaping," Opt. Express **17**, 3341 (2009).

V. Yu. Glebov, M. Moran, C. Stoeckl, T. C. Sangster, and M. Cruz, "Neutron Bang Time Detector Based on a Light Pipe," Rev. Sci. Instrum. **79**, 10E528 (2008).

V. N. Goncharov, "Ablative Richtmyer-Meshkov Instability: Theory and Experimental Results," in *Laser-Plasma Interactions*, Scottish Graduate Series, edited by D. A. Jaroszynski, R. Bingham, and R. A. Cairns (CRC Press, Boca Raton, FL, 2009), pp. 419–427.

V. N. Goncharov, "Direct-Drive Inertial Fusion: Basic Concepts and Ignition Target Designing," in *Laser-Plasma Interactions*, Scottish Graduate Series, edited by D. A. Jaroszynski, R. Bingham, and R. A. Cairns (CRC Press, Boca Raton, FL, 2009), pp. 409–418.

O. V. Gotchev, J. P. Knauer, P. Y. Chang, N. W. Jang, M. J. Shoup III, D. D. Meyerhofer, and R. Betti, "Seeding Magnetic Fields for Laser-Driven Flux Compression in High-Energy-Density Plasmas," Rev. Sci. Instrum. **80**, 043504 (2009).

W. Guan and J. R. Marciante, "Complete Elimination of Self-Pulsations in Dual-Clad Ytterbium-Doped Fiber Lasers at All Pumping Levels," Opt. Lett. **34**, 815 (2009).

G. Guarino, W. R. Donaldson, M. Mikulics, M. Marso, P. Kordoš, and R. Sobolewski, "Finite Element Simulation of Metal–Semiconductor–Metal Photodetector," Solid-State Electron. **53**, 1144 (2009).

E. T. Gumbrell, A. S. Moore, J. A. Lazarus, E. L. Clark, P. M. Nilson, W. J. Garbett, A. J. Comley, J. S. Robinson, M. Hohenberger, R. D. Edwards, R. E. Eagleton, R. J. Clarke, D. R. Symes, and R. A. Smith, "Laser Heating of Large Noble Gas Clusters: From the Resonant to the Relativistic Interaction Regimes," New J. Phys. **10**, 123011 (2008).

D. G. Hicks, T. R. Boehly, P. M. Celliers, D. K. Bradley, J. H. Eggert, R. S. McWilliams, R. Jeanloz, and G. W. Collins, "High Precision Measurements of the Diamond Hugoniot In and Above the Melt Region," Phys. Rev. B **78**, 174102 (2008).

D. G. Hicks, T. R. Boehly, P. M. Celliers, J. H. Eggert, S. J. Moon, D. D. Meyerhofer, and G. W. Collins, "Laser-Driven Single Shock Compression of Fluid Deuterium from 45 to 220 GPa," Phys. Rev. B **79**, 014112 (2009).

S. X. Hu, L. A. Collins, and B. I. Schneider, "Attosecond Photoelectron Microscopy of H_2^+," Phys. Rev. A **80**, 023426 (2009).

I. V. Igumenshchev, "Magnetic Inversion as a Mechanism for the Spectral Transition of Black Hole Binaries," Astrophys. J. **702**, L72 (2009).

I. V. Igumenshchev, F. J. Marshall, J. A. Marozas, V. A. Smalyuk, R. Epstein, V. N. Goncharov, T. J. B. Collins, T. C. Sangster, and S. Skupsky, "The Effects of Target Mounts in Direct-Drive Implosions on OMEGA," Phys. Plasmas **16**, 082701 (2009).

Z. Jiang and J. R. Marciante, "Comments on 'Beam Quality Factor of Higher Order Modes in a Step-Index Fiber,'" J. Lightwave Technol. **27**, 1236 (2009).

A. M. Kaplan, G. P. Agrawal, and D. N. Maywar, "All-Optical Flip-Flop Operations of VCSOA," Electron. Lett. **45**, 127 (2009).

C. Kim, K. L. Marshall, J. U. Wallace, and S. H. Chen, "Photochromic Glassy Liquid Crystals Comprising Mesogenic Pendants to Dithienylethene Cores," J. Mater. Chem. **18**, 5592 (2008).

J. A. King, K. U. Akli, R. R. Freeman, J. Green, S. P. Hatchett, D. Hey, P. Jaanimagi, M. H. Key, J. Koch, K. L. Lancaster, T. Ma, A. J. MacKinnon, A. MacPhee, P. A. Norreys, P. K. Patel, T. Phillips, R. B. Stephens, W. Theobald, R. P. J. Town, L. Van Woerkom, B. Zhang, and F. N. Beg, "Studies of the Transport of High Intensity Laser-Generated Hot Electrons in Cone Coupled Wire Targets," Phys. Plasmas **16**, 020701 (2009).

J. Kitaygorsky, S. Dorenbos, E. Reiger, R. Schouten, V. Zwiller, and R. Sobolewski, "HEMT-Based Readout Technique for Dark- and Photon-Count Studies in NbN Superconducting Single-Photon Detectors," IEEE Trans. Appl. Supercond. **19**, 346 (2009).

C. K. Li, F. H. Séguin, J. A. Frenje, M. Manuel, D. Casey, N. Sinenian, R. D. Petrasso, P. A. Amendt, O. L. Landen, J. R. Rygg, R. P. J. Town, R. Betti, J. Delettrez, J. P. Knauer, F. Marshall, D. D. Meyerhofer, T. C. Sangster, D. Shvarts, V. A. Smalyuk, J. M. Soures, C. A. Back, J. D. Kilkenny, and A. Nikroo, "Proton Radiography of Dynamic Electric and Magnetic Fields in Laser-Produced High-Energy-Density Plasmas," Phys. Plasmas **16**, 056304 (2009).

J. R. Marciante, "Gain Filtering for Single-Spatial-Mode Operation of Large-Mode-Area Fiber Amplifiers," IEEE J. Sel. Top. Quantum Electron. **15**, 30 (2009).

F. J. Marshall, P. W. McKenty, J. A. Delettrez, R. Epstein, J. P. Knauer, V. A. Smalyuk, J. A. Frenje, C. K. Li, R. D. Petrasso, F. H. Séguin, and R. C. Mancini, "Plasma-Density Determination from X-Ray Radiography of Laser-Driven Spherical Implosions," Phys. Rev. Lett. **102**, 185004 (2009).

C. Miao, S. N. Shafrir, J. C. Lambropoulos, J. Mici, and S. D. Jacobs, "Shear Stress in Magnetorheological Finishing for Glasses," Appl. Opt. **48**, 2585 (2009).

E. I. Moses, R. L. McCrory, D. D. Meyerhofer, and C. J. Keane, "A New Era for High-Energy-Density Physics," Opt. Photonics News **20**, 42 (2009).

J. Myatt, J. A. Delettrez, A. V. Maximov, D. D. Meyerhofer, R. W. Short, C. Stoeckl, and M. Storm, "Optimizing Electron-Positron Pair Production on Kilojoule-Class High-Intensity Lasers for the Purpose of Pair-Plasma Creation," Phys. Rev. E **79**, 066409 (2009).

P. M. Nilson, W. Theobald, J. F. Myatt, C. Stoeckl, M. Storm, J. D. Zuegel, R. Betti, D. D. Meyerhofer, and T. C. Sangster, "Bulk Heating of Solid-Density Plasmas During High-Intensity-Laser Plasma Interactions," Phys. Rev. E **79**, 016406 (2009).

A. V. Okishev, D. Westerfeld, L. Shterengas, and G. Belenky, "A Stable Mid-IR, GaSb-Based Diode Laser Source for the Cryogenic Target Layering at the Omega Laser Facility," Opt. Express **17**, 15,760 (2009).

J. B. Oliver, S. Papernov, A. W. Schmid, and J. C. Lambropoulos, "Optimization of Laser-Damage Resistance of Evaporated Hafnia Films at 351 nm," in *Laser-Induced Damage in Optical Materials: 2008*, edited by G. J. Exarhos, D. Ristau, M. J. Soileau, and C. J. Stolz (SPIE, Bellingham, WA, 2008), Vol. 7132, Paper 71320J.

D. Pan, G. P. Pepe, V. Pagliarulo, C. De Lisio, L. Parlato, M. Khafizov, I. Komissarov, and R. Sobolewski, "Layered Ferromagnet/Superconductor Heterostructures: Nonequilibrium Quasiparticle Dynamics and Photodetector Applications," Phys. Rev. B **78**, 174503 (2008).

S. Papernov and A. W. Schmid, "Laser-Induced Surface Damage of Optical Materials: Absorption Sources, Initiation, Growth, and Mitigation," in *Laser-Induced Damage in Optical Materials: 2008*, edited by G. J. Exarhos, D. Ristau, M. J. Soileau, and C. J. Stolz (SPIE, Bellingham, WA, 2008), Vol. 7132, Paper 71321J.

G. P. Pepe, D. Pan, V. Pagliarulo, L. Parlato, N. Marrocco, C. De Lisio, G. Peluso, A. Barone, U. Scotti di Uccio, A. Casaburi, F. Tafuri, M. Khafizov, T. Taneda, and R. Sobolewski, "Ultrafast Photoresponse of Superconductor/Ferromagnet Nano-Layered Hybrids," IEEE Trans. Appl. Supercond. **19**, 376 (2009).

B. Punsly, I. V. Igumenshchev, and S. Hirose, "Three-Dimensional Simulations of Vertical Magnetic Flux in the Immediate Vicinity of Black Holes," Astrophys. J. **704**, 1065 (2009).

J. Sanz, R. Betti, V. A. Smalyuk, M. Olazabal-Loume, V. Drean, V. Tikhonchuk, X. Ribeyre, and J. Feugeas, "Radiation Hydrodynamic Theory of Double Ablation Fronts in Direct-Drive Inertial Confinement Fusion," Phys. Plasmas **16**, 082704 (2009).

H. Sawada, S. P. Regan, P. B. Radha, R. Epstein, D. Li, V. N. Goncharov, S. X. Hu, D. D. Meyerhofer, J. A. Delettrez, P. A. Jaanimagi, V. A. Smalyuk, T. R. Boehly, T. C. Sangster, B. Yaakobi, and R. C. Mancini, "Al 1*s*–2*p* Absorption Spectroscopy of Shock-Wave Heating and Compression in Laser-Driven Planar Foil," Phys. Plasmas **16**, 052702 (2009).

J. E. Schoenly, W. Seka, and P. Rechmann, "Laser Ablation of Dental Calculus at 400 nm Using a Ti:Sapphire Laser," in *Lasers in Dentistry XV*, edited by R. Rechmann and D. Fried (SPIE, Bellingham, WA, 2009), Vol. 7162, Paper 71620E.

W. Seka, D. H. Edgell, J. A. Myatt, A. V. Maximov, R. W. Short, V. N. Goncharov, and H. A. Baldis, "Two-Plasmon-Decay Instability in Direct-Drive Inertial Confinement Fusion Experiments," Phys. Plasmas **16**, 052701 (2009).

S. N. Shafrir, S. D. Jacobs, S. Adar, C. Miao, H. Romanofsky, and J. C. Lambropoulos, "Drag Force and Surface Texture in Material Removal with MRF on Optical Glass and Hard Ceramics," in the *Proceedings of the 12th DoD Electromagnetic Windows Symposium* (U.S. Army Research, Development, and Engineering Center, Redstone Arsenal, AL, 2008), pp. 1–23.

V. A. Smalyuk, R. Betti, T. R. Boehly, R. S. Craxton, J. A. Delettrez, D. H. Edgell, V. Yu. Glebov, V. N. Goncharov, D. R. Harding, S. X. Hu, J. P. Knauer, F. J. Marshall, R. L. McCrory, P. W. McKenty, D. D. Meyerhofer, P. B. Radha, S. P. Regan, T. C. Sangster, W. Seka, R. W. Short, D. Shvarts, S. Skupsky, J. M. Soures, C. Stoeckl, B. Yaakobi, J. A. Frenje, C. K. Li, R. D. Petrasso, and F. H. Séguin, "Cryogenic-Target Perfor-

mance and Implosion Physics Studies on OMEGA," Phys. Plasmas **16**, 056301 (2009) (invited).

V. A. Smalyuk, S. X. Hu, J. D. Hager, J. A. Delettrez, D. D. Meyerhofer, T. C. Sangster, and D. Shvarts, "Rayleigh-Taylor Growth Measurements in the Acceleration Phase of Spherical Implosions on OMEGA," Phys. Rev. Lett. **103**, 105001 (2009).

A. A. Solodov, K. S. Anderson, R. Betti, V. Gotcheva, J. Myatt, J. A. Delettrez, S. Skupsky, W. Theobald, and C. Stoeckl, "Integrated Simulations of Implosion, Electron Transport, and Heating for Direct-Drive Fast-Ignition Targets," Phys. Plasmas **16**, 056309 (2009).

A. A. Solodov, K. S. Anderson, R. Betti, V. Gotcheva, J. Myatt, J. A. Delettrez, S. Skupsky, W. Theobald, and C. Stoeckl, "Simulations of Electron Transport and Ignition for Direct-Drive Fast-Ignition Targets," Phys. Plasmas **15**, 112702 (2008).

C. Stoeckl, K. S. Anderson, R. Betti, T. R. Boehly, J. A. Delettrez, J. A. Frenje, V. N. Goncharov, V. Yu. Glebov, J. H. Kelly, A. J. MacKinnon, R. L. McCrory, D. D. Meyerhofer, S. F. B. Morse, J. F. Myatt, P. A. Norreys, P. M. Nilson, R. D. Petrasso, T. C. Sangster, A. A. Solodov, R. B. Stephens, M. Storm, W. Theobald, B. Yaakobi, L. J. Waxer, and C. D. Zhou, "Fast-Ignition Target Design and Experimental-Concept Validation on OMEGA," Plasma Phys. Control. Fusion **50**, 124044 (2008) (invited).

M. Storm, I. A. Begishev, R. J. Brown, C. Guo, D. D. Meyerhofer, C. Mileham, J. F. Myatt, P. M. Nilson, T. C. Sangster, C. Stoeckl, W. Theobald, and J. D. Zuegel, "A High-Resolution Coherent Transition Radiation Diagnostic for Laser-Produced Electron Transport Studies," Rev. Sci. Instrum. **79**, 10F503 (2008) (invited).

M. Storm, A. A. Solodov, J. F. Myatt, D. D. Meyerhofer, C. Stoeckl, C. Mileham, R. Betti, P. M. Nilson, T. C. Sangster, W. Theobald, and C. Guo, "High-Current, Relativistic Electron-Beam Transport in Metals and the Role of Magnetic Collimation," Phys. Rev. Lett. **102**, 235004 (2009).

L. Sun, S. Jiang, J. D. Zuegel, and J. R. Marciante, "Effective Verdet Constant in a Terbium-Doped-Core Phosphate Fiber," Opt. Lett. **34**, 1699 (2009).

W. Theobald, C. Stoeckl, P. A. Jaanimagi, P. M. Nilson, M. Storm, D. D. Meyerhofer, T. C. Sangster, D. Hey, A. J. MacKinnon, H.-S. Park, P. K. Patel, R. Shepherd, R. A. Snavely, M. H. Key, J. A. King, B. Zhang, R. B. Stephens, K. U. Akli, K. Highbarger, R. L. Daskalova, L. Van Woerkom, R. R. Freeman, J. S. Green, G. Gregori, K. Lancaster, and P. A. Norreys, "A Dual-Channel, Curved-Crystal Spectrograph for Petawatt Laser, X-Ray Backlighter Source Studies," Rev. Sci. Instrum. **80**, 083501 (2009).

A. Trajkovska Petkoska and S. D. Jacobs, "Effect of Different Dopants on Polymer Cholesteric Liquid Crystal Flakes," Mol. Cryst. Liq. Crys. **495**, 334 (2008).

I. A. Walmsley and C. Dorrer, "Characterization of Ultrashort Electromagnetic Pulses," Adv. Opt. Photon. **1**, 308 (2009).

S. K. H. Wei, S. H. Chen, K. Dolgaleva, S. G. Lukishova, and R. W. Boyd, "Robust Organic Lasers Comprising Glassy-Cholesteric Pentafluorene Doped with a Red-Emitting Oligofluorene," Appl. Phys. Lett. **94**, 041111 (2009).

L. Zeng, F. Yan, S. K.-H. Wei, S. W. Culligan, and S. H. Chen, "Synthesis and Processing of Monodisperse Oligo(fluorene-*co*-bithiophene)s into Oriented Films by Thermal and Solvent Annealing," Adv. Funct. Mater. **19**, 1978 (2009).

C. D. Zhou and R. Betti, "A Measurable Lawson Criterion and Hydro-Equivalent Curves for Inertial Confinement Fusion," Phys. Plasmas **15**, 102707 (2008).

Y. Zhu, J. D. Zuegel, J. R. Marciante, and H. Wu, "Distributed Waveform Generator: A New Circuit Technique for Ultra-Wideband Pulse Generation, Shaping and Modulation," IEEE J. Solid-State Circuits **44**, 808 (2009).

J. D. Zuegel, S.-W. Bahk, J. Bromage, C. Dorrer, R. Earley, T. J. Kessler, B. J. Kruschwitz, S. F. B. Morse, D. N. Maywar, J. B. Oliver, J. Qiao, A. L. Rigatti, A. W. Schmid, M. J. Shoup III, L. J. Waxer, and J. H. Kelly, "Novel Laser and Diagnostic Technologies for the OMEGA EP High-Energy Petawatt Laser," Rev. Laser Eng. **37**, 437 (2009).

OMEGA External Users' Publications

P. M. Bellan, M. Livio, Y. Kato, S. V. Lebedev, T. P. Ray, A. Ferrari, P. Hartigan, A. Frank, J. M. Foster, and P. Nicolaï, "Astrophysical Jets: Observations, Numerical Simulations, and Laboratory Experiments," Phys. Plasmas **16**, 041005 (2009).

J. L. Bourgade, A. E. Costley, R. Reichle, E. R. Hodgson, W. Hsing, V. Glebov, M. Decreton, R. Leeper, J. L. Leray, M. Dentan, T. Hutter, A. Moroño, D. Eder, W. Shmayda, B. Brichard, J. Baggio, L. Bertalot, G. Vayakis, M. Moran, T. C. Sangster, L. Vermeeren, C. Stoeckl, S. Girard, and G. Pien, "Diagnostic Components in Harsh Radiation Environments: Possible Overlap in R&D Requirements of Inertial Confinement and Magnetic Fusion Systems," Rev. Sci. Instrum. **79**, 10F304 (2008).

J. L. Bourgade, R. Marmoret, S. Darbon, R. Rosch, P. Troussel, B. Villette, V. Glebov, W. T. Shmayda, J. C. Gomme, Y. Le Tonqueze, F. Aubard, J. Baggio, S. Bazzoli, F. Bonneau, J. Y. Boutin, T. Caillaud, C. Chollet, P. Combis, L. Disdier, J. Gazave, S. Girard, D. Gontier, P. Jaanimagi, H. P. Jacquet, J. P. Jadaud, O. Landoas, J. Legendre, J. L. Leray, R. Maroni, D. D. Meyerhofer, J. L. Miquel, F. J. Marshall, I. Masclet-Gobin, G. Pien, J. Raimbourg, C. Reverdin, A. Richard, D. Rubin de Cervens, C. T. Sangster, J. P. Seaux, G. Soullie, C. Stoeckl, I. Thfoin, L. Videau, and C. Zuber, "Diagnostics Hardening for Harsh Environment in Laser Mégajoule," Rev. Sci. Instrum. **79**, 10F301 (2008) (invited).

D. K. Bradley, J. H. Eggert, R. F. Smith, S. T. Prisbrey, D. G. Hicks, D. G. Braun, J. Biener, A. V. Hamza, R. E. Rudd, and G. W. Collins, "Diamond at 800 GPa," Phys. Rev. Lett. **102**, 075503 (2009).

D. K. Bradley, S. T. Prisbrey, R. H. Page, D. G. Braun, M. J. Edwards, R. Hibbard, K. A. Moreno, M. P. Mauldin, and A. Nikroo, "Measurements of Preheat and Shock Melting in Be Ablators During the First Few Nanoseconds of a National Ignition Facility Ignition Drive Using the Omega Laser," Phys. Plasmas **16**, 042703 (2009).

E. Brambrink, H. G. Wei, B. Barbrel, P. Audebert, A. Benuzzi-Mounaix, T. Boehly, T. Endo, C. Gregory, T. Kimura, R. Kodama, N. Ozaki, H.-S. Park, M. Rabec le Gloahec, and M. Koenig, "X-Ray Source Studies for Radiography of Dense Matter," Phys. Plasmas **16**, 033101 (2009).

G. V. Brown, P. Beiersdorfer, J. Emig, M. Frankel, M. F. Gu, R. F. Heeter, E. Magee, D. B. Thorn, K. Widmann, R. L. Kelley, C. A. Kilbourne, and F. S. Porter, "Rapid, Absolute Calibration of X-Ray Filters Employed by Laser-Produced Plasma Diagnostics," Rev. Sci. Instrum. **79**, 10E309 (2008).

A. Casner, D. Galmiche, G. Huser, J.-P. Jadaud, S. Liberatore, and M. Vandenboomgaerge, "Indirect Drive Ablative Rayleigh–Taylor Experiments with Rugby Hohlraums on OMEGA," Phys. Plasmas **16**, 092701 (2009).

D. Colombant and W. Manheimer, "Krook Model for Non-thermal Electron Energy Transport. III. Spherical Configurations," Phys. Plasmas **16**, 062705 (2009).

J. Colvin, C. Cerjan, R. Hoffman, M. Stoyer, and P. Amendt, "Radiochemical Tracers as a Mix Diagnostic for the Ignition Double-Shell Capsule," Phys. Plasmas **15**, 102704 (2008).

N. D. Delamater, D. C. Wilson, G. A. Kyrala, A. Seifter, N. M. Hoffman, E. Dodd, R. Singleton, V. Glebov, C. Stoeckl, C. K. Li, R. Petrasso, and J. Frenje, "Use of d-^{3}He Proton Spectroscopy as a Diagnostic of Shell ρr in Capsule Implosion Experiments with ~0.2 NIF Scale High Temperature Hohlraums at OMEGA," Rev. Sci. Instrum. **79**, 10E526 (2008).

T. Döppner, P. F. Davis, A. L. Kritcher, O. L. Landen, and H. J. Lee, "Using Collective X-Ray Thomson Scattering to Measure Temperature and Density of Warm Dense Matter," in *Soft X-Ray Lasers and Applications VIII*, edited by J. Dunn and G. J. Tallents (SPIE, Bellingham, WA, 2009), Vol. 7451, Paper 74510H.

R. P. Drake, "Perspectives on High-Energy-Density Physics," Phys. Plasmas **16**, 055501 (2009) (invited).

R. P. Drake, E. C. Harding, and C. C. Kuranz, "Approaches to Turbulence in High-Energy-Density Experiments," Phys. Scr. **T132**, 014022 (2008).

R. P. Drake and J. P. Knauer, "Design of Jet-Driven, Radiative-Blast-Wave Experiments for the 10 kJ Class Lasers," Astrophys. Space Sci. **322**, 97 (2009).

R. P. Drake, C. C. Kuranz, A. R. Miles, H. J. Muthsam, and T. Plewa, "Stellar Explosions, Instabilities, and Turbulence," Phys. Plasmas **16**, 041004 (2009).

J. H. Eggert, P. M. Celliers, D. G. Hicks, J. R. Rygg, G. W. Collins, S. Brygoo, P. Loubeyre, R. S. McWilliams,

D. Spaulding, R. Jeanloz, and T. R. Boehly, "Shock Experiments on Pre-Compressed Fluid Helium," in *Atomic Processes in Plasmas*, edited by K. B. Fournier (American Institute of Physics, New York, 2009), Vol. 1161, pp. 26–31.

R. Florido, T. Nagayama, R. C. Mancini, R. Tommasini, J. A. Delettrez, S. P. Regan, V. A. Smalyuk, R. Rodríguez, and J. M. Gil, "Analysis of Time-Resolved Argon Line Spectra from OMEGA Direct-Drive Implosions," Rev. Sci. Instrum. **79**, 10E310 (2008).

J. J. Fortney, S. H. Glenzer, M. Koenig, B. Militzer, D. Saumon, and D. Valencia, "Frontiers of the Physics of Dense Plasmas and Planetary Interiors: Experiments, Theory, and Applications," Phys. Plasmas **16**, 041003 (2009).

K. B. Fournier, J. H. Satcher, M. J. May, J. F. Poco, C. M. Sorce, J. D. Colvin, S. B. Hansen, S. A. MacLaren, S. J. Moon, J. F. Davis, F. Girard, B. Villette, M. Primout, D. Babonneau, C. A. Coverdale, and D. E. Beutler, "Absolute X-Ray Yields from Laser-Irradiated Germanium-Doped Low-Density Aerogels," Phys. Plasmas **16**, 052703 (2009).

J. A. Frenje, D. T. Casey, C. K. Li, J. R. Rygg, F. H. Séguin, R. D. Petrasso, V. Yu. Glebov, D. D. Meyerhofer, T. C. Sangster, S. Hatchett, S. Haan, C. Cerjan, O. Landen, M. Moran, P. Song, D. C. Wilson, and R. J. Leeper, "First Measurements of the Absolute Neutron Spectrum Using the Magnetic Recoil Spectrometer at OMEGA," Rev. Sci. Instrum. **79**, 10E502 (2008) (invited).

J. A. Frenje, C. K. Li, J. R. Rygg, F. H. Séguin, D. T. Casey, R. D. Petrasso, J. Delettrez, V. Yu. Glebov, T. C. Sangster, O. Landen, and S. Hatchett, "Diagnosing Ablator ρR and ρR Asymmetries in Capsule Implosions Using Charged-Particle Spectrometry at the National Ignition Facility," Phys. Plasmas **16**, 022702 (2009).

J. A. Frenje, C. K. Li, F. H. Séguin, D. T. Casey, R. D. Petrasso, T. C. Sangster, R. Betti, V. Yu. Glebov, and D. D. Meyerhofer, "Diagnosing Fuel ρR and ρR Asymmetries in Cryogenic Deuterium-Tritium Implosions Using Charged-Particle Spectrometry at OMEGA," Phys. Plasmas **16**, 042704 (2009).

D. H. Froula, L. Divol, R. A. London, R. L. Berger, T. Döppner, N. B. Meezan, J. S. Ross, L. J. Suter, C. Sorce, and S. H. Glenzer, "Observation of the Density Threshold Behavior for the Onset of Stimulated Raman Scattering in High-Temperature Hohlraum Plasmas," Phys. Rev. Lett. **103**, 045006 (2009).

F. Girard, M. Primout, B. Villette, Ph. Stemmler, L. Jacquet, D. Babonneau, and K. B. Fournier, "Titanium and Geranium Lined Hohlraums and Halfraums as Multi-keV X-Ray Radiators," Phys. Plasmas **16**, 052704 (2009).

G. P. Grim, J. P. Finch, N. S. P. King, G. L. Morgan, J. A. Oertel, C. H. Wilde, M. D. Wilke, D. C. Wilson, and D. E. Johnson, "A Spatially Resolved Ion Temperature Diagnostic for the National Ignition Facility," Rev. Sci. Instrum. **79**, 10E537 (2008).

M. J. Grosskopf, R. P. Drake, C. C. Kuranz, A. R. Miles, J. F. Hansen, T. Plewa, N. Hearn, D. Arnett, and J. C. Wheeler, "Modeling of Multi-Interface, Diverging, Hydrodynamic Experiments for the National Ignition Facility," Astrophys. Space Sci. **322**, 57 (2009).

E. C. Harding, J. F. Hansen, O. A. Hurricane, R. P. Drake, H. F. Robey, C. C. Kuranz, B. A. Remington, M. J. Bono, M. J. Grosskopf, and R. S. Gillespie, "Observation of a Kelvin-Helmholtz Instability in a High-Energy-Density Plasma on the Omega Laser," Phys. Rev. Lett. **103**, 045005 (2009).

R. F. Heeter, S. G. Anderson, R. Booth, G. V. Brown, J. Emig, S. Fulkerson, T. McCarville, D. Norman, M. B. Schneider, and B. K. F. Young, "OZSPEC-2: An Improved Broadband High-Resolution Elliptical Crystal X-Ray Spectrometer for High-Energy Density Physics Experiments," Rev. Sci. Instrum. **79**, 10E303 (2008) (invited).

H. W. Herrmann, J. R. Langenbrunner, J. M. Mack, J. H. Cooley, D. C. Wilson, S. C. Evans, T. J. Sedillo, G. A. Kyrala, S. E. Caldwell, C. S. Young, A. Nobile, J. Wermer, S. Paglieri, A. M. McEnvoy, Y. Kin, S. H. Batha, C. J. Horsfield, D. Drew, W. Garbett, M. Rubery, V. Yu. Glebov, S. Roberts, and J. A. Frenje, "Anomalous Yield Reduction in Direct-Drive Deuterium/Tritium Implosions Due to ^{3}He Addition," Phys. Plasmas **16**, 056312 (2009) (invited).

O. A. Hurricane, J. F. Hansen, H. F. Robey, B. A. Remington, M. J. Bono, E. C. Harding, R. P. Drake, and C. C. Kuranz, "A High Energy Density Shock Driven Kelvin-Helmholtz Shear Layer Experiment," Phys. Plasmas **16**, 056305 (2009) (invited).

G. Huser, C. Courtois, and M.-C. Monteil, "Wall and Laser Spot Motion in Cylindrical Hohlraums," Phys. Plasmas **16**, 032703 (2009).

R. K. Kirkwood, J. Milovich, D. K. Bradley, M. Schmitt, S. R. Goldman, D. H. Kalantar, D. Meeker, O. S. Jones, S. M.

Pollaine, P. A. Amendt, E. Dewald, J. Edwards, O. L. Landen, and A. Nikroo, "Sensitivity of Ignition Scale Backlit Thin-Shell Implosions to Hohlraum Symmetry in the Foot of the Drive Pulse," Phys. Plasmas **16**, 012702 (2009).

J. A. Koch, B. J. Kozioziemski, J. Salmonson, A. Chernov, L. J. Atherton, E. Dewald, N. Izumi, M. A. Johnson, S. Kucheyev, J. Lugten, E. Mapoles, J. D. Moody, J. W. Pipes, J. D. Sater, and D. Stefanescu, "Optical and X-Ray Characterization of Groove Profiles in D-T Ice Layers," Fusion Sci. Technol. **55**, 244 (2009).

A. L. Kritcher, P. Neumayer, J. Castor, T. Döppner, R. W. Falcone, O. L. Landen, H. J. Lee, R. W. Lee, E. C. Morse, A. Ng, S. Pollaine, D. Price, and S. H. Glenzer, "K-α X-Ray Thomson Scattering from Dense Plasmas," in *Atomic Processes in Plasmas*, edited by K. B. Fournier (American Institute of Physics, New York, 2009), Vol. 1161, pp. 286–292.

C. C. Kuranz, R. P. Drake, M. J. Grosskopf, A. Budde, C. Krauland, D. C. Marion, A. J. Visco, J. R. Ditmar, H. F. Robey, B. A. Remington, A. R. Miles, A. B. R. Cooper, C. Sorce, T. Plewa, N. C. Hearn, K. L. Killebrew, J. P. Knauer, D. Arnett, and T. Donajkowski, "Three-Dimensional Blast-Wave-Driven Rayleigh–Taylor Instability and the Effects of Long-Wavelength Modes," Phys. Plasmas **16**, 056310 (2009) (invited).

C. C. Kuranz, R. P. Drake, M. J. Grosskopf, H. F. Robey, B. A. Remington, J. F. Hansen, B. E. Blue, and J. Knauer, "Image Processing of Radiographs in 3D Rayleigh-Taylor Decelerating Interface Experiments," Astrophys. Space Sci. **322**, 49 (2009).

C. C. Kuranz, R. P. Drake, E. C. Harding, M. J. Grosskopf, H. F. Robey, B. A. Remington, M. J. Edwards, A. R. Miles, T. S. Perry, B. E. Blue, T. Plewa, N. C. Hearn, J. P. Knauer, D. Arnett, and D. R. Leibrandt, "Two-Dimensional Blast-Wave-Driven Rayleigh–Taylor Instability: Experiment and Simulation," Astrophys. J. **696**, 749 (2009).

H. J. Lee, P. Neumayer, J. Castor, T. Döppner, R. W. Falcone, C. Fortmann, B. A. Hammel, A. L. Kritcher, O. L. Landen, R. W. Lee, D. D. Meyerhofer, D. H. Munro, R. Redmer, S. P. Regan, S. Weber, and S. H. Glenzer, "X-Ray Thomson-Scattering Measurements of Density and Temperature in Shock-Compressed Beryllium," Phys. Rev. Lett. **102**, 115001 (2009).

C. K. Li, J. A. Frenje, R. D. Petrasso, F. H. Séguin, P. A. Amendt, O. L. Landen, R. P. J. Town, R. Betti, J. P. Knauer, D. D. Meyerhofer, and J. M. Soures, "Pressure-Driven, Resistive Magnetohydrodynamic Interchange Instabilities in Laser-Produced High-Energy-Density Plasmas," Phys. Rev. E **80**, 016407 (2009).

C. K. Li, F. H. Séguin, J. A. Frenje, M. Manuel, R. D. Petrasso, V. A. Smalyuk, R. Betti, J. Delettrez, J. P. Knauer, F. Marshall, D. D. Meyerhofer, D. Shvarts, C. Stoeckl, W. Theobald, J. R. Rygg, O. L. Landen, R. P. J. Town, P. A. Amendt, C. A. Back, and J. D. Kilkenny, "Study of Direct-Drive Capsule Implosions in Inertial Confinement Fusion with Proton Radiography," Plasma Phys. Control. Fusion **51**, 014003 (2009).

C. K. Li, F. H. Séguin, J. A. Frenje, R. D. Petrasso, P. A. Amendt, R. P. J. Town, O. L. Landen, J. R. Rygg, R. Betti, J. P. Knauer, D. D. Meyerhofer, J. M. Soures, C. A. Back, J. D. Kilkenny, and A. Nikroo, "Observations of Electromagnetic Fields and Plasma Flow in Hohlraums with Proton Radiography," Phys. Rev. Lett. **102**, 205001 (2009).

R. A. London, D. H. Froula, C. M. Sorce, J. D. Moody, L. J. Suter, S. H. Glenzer, O. S. Jones, N. B. Meezan, and M. D. Rosen, "Optical Transmission of Glass for the National Ignition Facility Near Backscatter Imagers Under X-Ray Pressure," Rev. Sci. Instrum. **79**, 10F549 (2008).

A. G. MacPhee, K. U. Akli, F. N. Beg, C. D. Chen, H. Chen, R. Clarke, D. S. Hey, R. R. Freeman, A. J. Kemp. M. H. Key, J. A. King, S. Le Pape, A. Link, T. Y. Ma, H. Nakamura, D. T. Offermann, V. M. Ovchinnikov, P. K. Patel, T. W. Phillips, R. B. Stephens, R. Town, Y. Y. Tsui, M. S. Wei, L. D. Van Woerkom, and A. J. Mackinnon, "Diagnostics for Fast Ignition Science," Rev. Sci. Instrum. **79**, 10E302 (2008) (invited).

C. Michaut, E. Falize, C. Cavet, S. Bouquet, M. Koenig, T. Vinci, A. Reighard, and R. P. Drake, "Classification of and Recent Research Involving Radiative Shocks," Astrophys. Space Sci. **322**, 77 (2009).

J. D. Moody, L. Divol, D. H. Froula, S. H. Glenzer, G. Gregori, R. K. Kirkwood, A. Mackinnon, N. Meezan, C. Niemann, L. J. Suter, R. Bahr, and W. Seka, "Control of 2ω (527 nm) Stimulated Raman Scattering in a Steep Density Gradient Plasma," Phys. Plasmas **16**, 062704 (2009).

E. I. Moses, R. N. Boyd, B. A. Remington, C. J. Keane, and R. Al-Ayat, "The National Ignition Facility: Ushering in a New Age for High Energy Density Science," Phys. Plasmas **16**, 041006 (2009).

T. Nagayama, R. C. Mancini, R. Florido, R. Tommasini, J. A. Koch, J. A. Delettrez, S. P. Regan, V. A. Smalyuk, L. A. Welser-Sherrill, and I. E. Golovkin, "Comparison of Genetic-Algorithm and Emissivity Analyses of Image Data from OMEGA Implosion Cores," Rev. Sci. Instrum. **79**, 10E921 (2008).

P. Neumayer, C. Sorce, D. H. Froula, L. Divol, V. Rekow, K. Loughman, R. Knight, S. H. Glenzer, R. Bahr, and W. Seka, "A Pulsed-Laser Calibration System for the Laser Backscatter Diagnostics at the Omega Laser," Rev. Sci. Instrum. **79**, 10F548 (2009).

L. J. Perkins, R. Betti, K. N. LaFortune, and W. H. Williams, "Shock Ignition: A New Approach to High Gain Inertial Confinement Fusion on the National Ignition Facility," Phys. Rev. Lett. **103**, 045004 (2009).

R. D. Petrasso, C. K. Li, F. H. Seguin, J. R. Rygg, J. A. Frenje, R. Betti, J. P. Knauer, D. D. Meyerhofer, P. A. Amendt, D. H. Froula, O. L. Landen, P. K. Patel, J. S. Ross, and R. P. J. Town, "Lorentz Mapping of Magnetic Fields in Hot Dense Plasmas," Phys. Rev. Lett. **103**, 085001.

H. F. Robey, P. A. Amendt, J. L. Milovich, H.-S. Park, A. V. Hamza, and M. J. Bono, "Hohlraum-Driven Mid-Z (SiO_2) Double-Shell Implosions on the Omega Laser Facility and Their Scaling to NIF," Phys. Rev. Lett. **103**, 145003 (2009).

J. R. Rygg, J. A. Frenje, C. K. Li, F. H. Séguin, R. D. Petrasso, D. D. Meyerhofer, and C. Stoeckl, "Electron-Ion Thermal Equilibration After Spherical Shock Collapse," Phys. Rev. E **80**, 026403 (2009).

D. J. Strozzi, E. A. Williams, D. E. Hinkel, D. H. Froula, R. A. London, and D. A. Callahan, "Ray-Based Calculations of Backscatter in Laser Fusion Targets," Phys. Plasmas **15**, 102703 (2008).

D. C. Swift, R. G. Kraus, E. N. Loomis, D. G. Hicks, J. M. McNaney, and R. P. Johnson, "Shock Formation and the Ideal Shape of Ramp Compression Waves," Phys. Rev. E **78**, 066115 (2008).

T. Tanimoto, H. Habara, R. Kodama, M. Nakatsutsumi, K. A. Tanaka, K. L. Lancaster, J. S. Green, R. H. H. Scott, M. Sherlock, P. A. Norreys, R. G. Evans, M. G. Haines, S. Kar, M. Zepf, J. King, T. Ma, M. S. Wei, T. Yabuuchi, F. N. Beg, M. H. Key, P. Nilson, R. B. Stephens, H. Azechi, K. Nagai, T. Norimatsu, K. Takeda, J. Valente, and J. R. Davies, "Measurements of Fast Electron Scaling Generated by Petawatt Laser Systems," Phys. Plasmas **16**, 062703 (2009).

M. D. Wilke, S. H. Batha, P. A. Bradley, R. D. Day, D. D. Clark, V. E. Fatherly, J. P. Finch, R. A. Gallegos, F. P. Garcia, G. P. Grim, S. A. Jaramillo, A. J. Montoya, M. J. Moran, G. L. Morgan, J. A. Oertel, T. A. Ortiz, J. R. Payton, P. Pazuchanics, D. W. Schmidt, A. C. Valdez, C. H. Wilde, and D. C. Wilson, "The National Ignition Facility Neutron Imaging System," Rev. Sci. Instrum. **79**, 10E529 (2008).

L. Willingale, S. R. Nagel, A. G. R. Thomas, C. Bellei, R. J. Clarke, A. E. Dangor, R. Heathcote, M. C. Kaluza, C. Kamperidis, S. Kneip, K. Krushelnick, N. Lopes, S. P. D. Mangles, W. Nazarov, P. M. Nilson, and Z. Najmudin, "Characterization of High-Intensity Laser Propagation in the Relativistic Transparent Regime through Measurements of Energetic Proton Beams," Phys. Rev. Lett. **102**, 125002 (2009).

D. C. Wilson, P. A. Bradley, C. J. Cerjan, J. D. Salmonson, B. K. Spears, S. P. Hatchett II, H. W. Hermann, and V. Yu. Glebov, "Diagnosing Ignition woth DT Reaction History," Rev. Sci. Instrum. **79**, 10E525 (2008).

Conference Presentations

R. L. McCrory, "Progress in Direct-Drive Inertial Confinement Fusion," 22nd IAEA Fusion Energy Conference, Geneva, Switzerland 13–18 October 2008.

The following presentations were made at Frontiers in Optics 2008, Rochester, NY, 19–23 October 2008:

W. Guan and J. R. Marciante, "Elimination of Self-Pulsations in Dual-Clad, Ytterbium-Doped Fiber Lasers."

W. Guan and J. R. Marciante, "Single-Frequency Hybrid Brillouin/Ytterbium Fiber Lasers."

L. Ji, W. R. Donaldson, and T. Y. Hsiang, "Multi-Wavelength Electro-Optic Pulse Sampling."

Z. Jiang and J. R. Marciante, "Precise Model Decomposition in Multimode Optical Fibers by Maximizing the Sum of Modal Weights."

L. Sun, S. B. Jiang, J. D. Zuegel, and J. R. Marciante, "Measurement of the Verdet Constant in a Terbium-Core–Doped Fiber."

L. J. Waxer, J. H. Kelly, B. E. Kruschwitz, J. Qiao, I. A. Begishev, J. Bromage, C. Dorrer, J. L. Edwards, L. Folnsbee, M. J. Guardalben, S. D. Jacobs, R. Jungquist, T. J. Kessler, R. W. Kidder, S. J. Loucks, J. R. Marciante, D. N. Maywar, R. L. McCrory, D. D. Meyerhofer, S. F. B. Morse, A. V. Okishev, J. B. Oliver, G. Pien, J. Puth, A. L. Rigatti, A. W. Schmid, M. J. Shoup, III, C. Stoeckl, K. A. Thorp, and J. D. Zuegel, "The OMEGA EP High-Energy, Short-Pulse Laser System," Laser Science XXIV, Rochester, NY, 19–23 October 2008 (invited).

The following presentations were made at the Optical Fabrication and Testing Topical Meeting, Rochester, NY, 19–23 October 2008:

J. H. Kelly, R. Jungquist, L. J. Waxer, M. J. Guardalben, B. E. Kruschwitz, J. Qiao, I. A. Begishev, J. Bromage, C. Dorrer, J. L. Edwards, L. Folnsbee, S. D. Jacobs, T. J. Kessler, R. W. Kidder, S. J. Loucks, J. R. Marciante, D. N. Maywar, R. L. McCrory, D. D. Meyerhofer, S. F. B. Morse, A. V. Okishev, J. B. Oliver, G. Pien, J. Puth, A. L. Rigatti, A. W. Schmid, M. J. Shoup, III, K. A. Thorp, and J. D. Zuegel, "Optical Engineering of the OMEGA EP Laser System."

T. J. Kessler, "Surface Artifacts in Manufacturing and Use of Large Imaging Optics" (invited).

C. Miao, S. N. Shafrir, H. Romanofsky, J. Mici, J. C. Lambropoulos, and S. D. Jacobs, "Frictional Investigation for Magnetorheological Finishing (MRF) of Optical Glass and Hard Ceramics."

S. Salzman, H. Romanofsky, S. N. Shafrir, J. C. Lambropoulos, and S. D. Jacobs, "*In-Situ* Drag Force Measurements in MRF of Optical Glasses."

S. N. Shafrir, C. Miao, H. Romanofsky, J. C. Lambropoulos, and S. D. Jacobs, "Surface Texture in Material Removal with MRF on Optical Ceramics."

The following presentations were made at the International Conference on Ultrahigh Intensity Lasers, Shanghai-Tongli, China, 27–31 October 2008:

J. Bromage, S.-W. Bahk, D. Irwin, J. Kwiatkowski, A. Pruyne, M. Millecchia, M. Moore, and J. D. Zuegel, "A Focal-Spot Diagnostic for On-Shot Characterization of OMEGA EP."

J. Bromage, M. Moore, S.-W. Bahk, B. E. Kruschwitz, R. Earley, D. Irwin, D. Canning, R. Jungquist, G. King, J. Kwiatkowski, D. Weiner, M. J. Shoup III, and J. D. Zuegel, "Tools and Techniques for Focusing OMEGA EP."

C. Dorrer, J. Bromage, and J. D. Zuegel, "High-Dynamic-Range, Single-Shot Cross-Correlator Using a Pulse Replicator."

T. J. Kessler and H. Huang, "Spatial Chirp Smoothing Within Temporal Pulse Compression."

J. Qiao, J. H. Kelly, J. Bunkenburg, A. Kalb, D. Canning, and T. Nguyen, "Construction and Activation of Large-Aperture, Tiled-Grating Compressors for High-Energy, Petawatt-Class Chirped-Pulse–Amplification Systems."

J. Qiao, J. H. Kelly, L. J. Waxer, B. E. Kruschwitz, I. A. Begishev, J. Bromage, S.-W. Bahk, C. Dorrer, J. L. Edwards, L. Folnsbee, M. J. Guardalben, S. J. Jacobs, R. Jungquist, T. J. Kessler, R. W. Kidder, S. J. Loucks, J. R. Marciante, D. N. Maywar, R. L. McCrory, D. D. Meyerhofer, S. F. B. Morse, A. V. Okishev, J. B. Oliver, G. Pien, J. Puth, A. L. Rigatti, A. W. Schmid, M. J. Shoup III, C. Stoeckl, K. A. Thorp, and J. D. Zuegel, "Activation of the OMEGA EP High-Energy, Short-Pulse Laser System."

J. D. Zuegel, C. Dorrer, I. A. Begishev, J. Bromage, R. Brown, A. V. Okishev, P. M. Nilson, W. Theobald, V. Ovchinnikov, J. F. Myatt, B. Eichman, S. Ivancic, M. Storm, O. V. Gotchev, C. Stoeckl, T. C. Sangster, R. Betti, and D. D. Meyerhofer,

"High-Temporal-Contrast Target Experiments Using a Hybrid OPCPA-Nd:Glass Multi-Terawatt (MTW) Laser System."

The following presentations were made at IEEE LEOS 2008, Newport Beach, CA, 9–13 November 2008:

W. R. Donaldson, J. R. Marciante, and R. G. Roides, "Single-Shot, Electro-Optic Measurements at 10 GHz with a Dynamic Range of 2400:1."

L. Ji, W. R. Donaldson, and T. Y. Hsiang, "Multi-Wavelength Electro-Optic Pulse Characterization."

S. P. Regan, B. Yaakobi, R. Epstein, J. A. Delettrez, V. N. Goncharov, H. Sawada, D. D. Meyerhofer, P. B. Radha, T. C. Sangster, V. A. Smalyuk, R. C. Mancini, D. A. Haynes, J. A. Koch, and R. Tommasini, "Applied Plasma Spectroscopy I: Laser Fusion Experiments," 13th International Workshop on Radiative Properties of Hot Dense Matter, Santa Barbara, CA, 10–14 November 2008.

The following presentations were made at the 50th Annual Meeting of the APS Division of Plasma Physics, Dallas, TX, 17–21 November 2008:

K. S. Anderson, A. A. Solodov, R. Betti, P. W. McKenty, and W. Theobald, "Parametric Study of Direct-Drive, Fuel-Assembly Simulations of Fast-Ignition, Cone-in-Shell Targets."

M. A. Barrios, D. E. Fratanduono, T. R. Boehly, D. D. Meyerhofer, D. G. Hicks, P. M. Celliers, and J. H. Eggert, "Precision Equation-of-State (EOS) Measurements Using Laser-Driven Shock Waves Using the OMEGA Laser."

T. R. Boehly, D. H. Munro, P. M. Celliers, R. E. Olson, D. G. Hicks, V. N. Goncharov, H. F. Robey, S. X. Hu, J. A. Marozas, T. C. Sangster, O. L. Landen, and D. D. Meyerhofer, "Demonstration of the Shock-Timing Technique for Ignition Targets" (invited).

D. T. Casey, J. A. Frenje, C. K. Li, F. H. Séguin, M. Manuel, R. D. Petrasso, V. Yu. Glebov, D. D. Meyerhofer, S. Roberts, and T. C. Sangster, "Using GEANT4 to Model the Magnetic Recoil Spectrometer (MRS) for Down-Scattered and Primary-Neutron Measurements at OMEGA."

H. Chen, S. C. Wilks, E. Liang, J. F. Myatt, K. Cone, L. Elberson, D. D. Meyerhofer, M. Schneider, R. Shepherd, R. Stafford, R. Tommasini, and P. Beiersdorfer, "Making Positrons Using the Titan Short-Pulse Laser."

T. J. B. Collins, F. J. Marshall, M. J. Bonino, R. Forties, V. N. Goncharov, I. V. Igumenshchev, J. A. Marozas, P. W. McKenty, and V. A. Smalyuk, "3-D Modeling of Planar Target-Mount Perturbation Experiments on OMEGA."

R. S. Craxton, P. W. McKenty, J. A. Marozas, and A. M. Cok, "Simulations of Polar-Drive NIF Targets Optimized for High Neutron Yields."

J. A. Delettrez, V. N. Goncharov, A. V. Maximov, J. F. Myatt, P. B. Radha, T. C. Sangster, W. Seka, V. A. Smalyuk, C. Stoeckl, B. Yaakobi, and J. A. Frenje, "Transport of Energetic Electrons Produced from Two-Plasmon Decay in the 1-D Hydrodynamic Code *LILAC*."

D. H. Edgell, W. Seka, J. A. Delettrez, R. S. Craxton, V. N. Goncharov, I. V. Igumenshchev, J. F. Myatt, A. V. Maximov, R. W. Short, T. C. Sangster, and R. E. Bahr, "Precision Scattered-Laser-Light Spectroscopy in Direct-Drive Implosions."

R. Epstein, J. A. Delettrez, V. N. Goncharov, S. X. Hu, P. W. McKenty, F. J. Marshall, P. B. Radha, V. A. Smalyuk, W. Theobald, and B. Yaakobi, "Simulation and Optimization of Backlit Images of Cryogenic Implosions on OMEGA."

D. E. Fratanduono, M. A. Barrios, T. R. Boehly, D. D. Meyerhofer, D. G. Hicks, P. M. Celliers, S. Wilks, and R. Smith, "Optical Properties of Materials at High Pressure Using 'Sandwich' Targets."

J. A. Frenje, D. T. Casey, C. K. Li, J. R. Rygg, F. H. Séguin, R. D. Petrasso, V. Yu. Glebov, T. C. Sangster, D. D. Meyerhofer, and K. A. Fletcher, "First Measurements of the Down-Scattered and Primary Neutron Spectrum Using the Magnetic Recoil Spectrometer (MRS) at OMEGA."

M. C. Ghilea, T. C. Sangster, D. D. Meyerhofer, D. J. Lonobile, R. A. Lerche, and L. Disdier, "First Tests on OMEGA of a Bubble Chamber for Neutron Detection."

V. N. Goncharov, T. C. Sangster, T. R. Boehly, P. B. Radha, R. L. McCrory, D. D. Meyerhofer, and S. Skupsky, "Multiple-Picket, Direct-Drive Target Designs for OMEGA and the NIF."

O. V. Gotchev, R. Betti, P. Chang, J. P. Knauer, D. D. Meyerhofer, J. A. Frenje, C. K. Li, M. Manuel, R. D. Petrasso, and F. H. Séguin, "Magnetized Hot-Spot Implosions Via Laser-Driven Flux Compression."

J. D. Hager, V. A. Smalyuk, S. X. Hu, D. D. Meyerhofer, and T. C. Sangster, "Rayleigh–Taylor Measurements in Planar Cryogenic D_2 Targets Using X-Ray Radiography on OMEGA."

S. X. Hu, P. B. Radha, J. A. Marozas, R. Betti, T. J. B. Collins, R. S. Craxton, J. A. Delettrez, D. H. Edgell, R. Epstein, V. N. Goncharov, I. V. Igumenshchev, J. P. Knauer, F. J. Marshall, R. L. McCrory, P. W. McKenty, D. D. Meyerhofer, S. P. Regan, T. C. Sangster, W. Seka, S. Skupsky, V. A. Smalyuk, C. Stoeckl, B. Yaakobi, and D. Shvarts, "Two-Dimensional Investigation of Neutron-Yield Performance in Direct-Drive, Low-Adiabat D_2 Implosions on OMEGA."

I. V. Igumenshchev, F. J. Marshall, J. A. Marozas, V. A. Smalyuk, R. Epstein, T. J. B. Collins, M. J. Bonino, V. N. Goncharov, and T. C. Sangster, "Investigation of the Effects of Target Mounting in Direct-Drive Implosions on OMEGA."

J. P. Knauer, V. N. Goncharov, J. A. Delettrez, V. Yu. Glebov, F. J. Marshall, J. A. Frenje, C. K. Li, R. D. Petrasso, and F. H. Séguin, "Optimization of Multiple-Picket, Direct-Drive Laser-Pulse Shapes with Foam Shells."

C. K. Li, "Proton Radiography of Electromagnetic Fields Associated with ICF Implosions and Laser-Irradiated Hohlraums."

D. Li, V. N. Goncharov, A. V. Maximov, I. V. Igumenshchev, and S. Skupsky, "Modeling of Multiple-Ion Heat Transport in ICF Implosions."

G. Li, C. Ren, R. Yan, V. N. Goncharov, T. L. Wang, W. B. Mori, and J. Tonge, "Three-Dimensional Effects in Laser Channeling in Fast-Ignition Targets."

J. A. Marozas, J. D. Zuegel, and T. J. B. Collins, "1.0-MJ CH-Foam Ignition Targets on the NIF Using 1-D Multi-FM SSD with 0.5 THz of Bandwidth."

F. J. Marshall, R. S. Craxton, R. Epstein, V. Yu. Glebov, V. N. Goncharov, J. P. Knauer, P. W. McKenty, D. D. Meyerhofer, P. B. Radha, T. C. Sangster, W. Seka, S. Skupsky, V. A. Smalyuk, J. A. Frenje, C. K. Li, R. D. Petrasso, and F. H. Séguin, "Low-Adiabat Polar-Drive Implosion Experiments on OMEGA."

A. V. Maximov, J. F. Myatt, R. W. Short, W. Seka, C. Stoeckl, and J. A. Delettrez, "Modeling of Two-Plasmon-Decay Instability in OMEGA Plasmas."

D. D. Meyerhofer, J. Bromage, V. Yu. Glebov, J. H. Kelly, B. E. Kruschwitz, S. J. Loucks, R. L. McCrory, S. F. B. Morse, J. F. Myatt, P. M. Nilson, J. Qiao, T. C. Sangster, C. Stoeckl, W. Theobald, R. D. Petrasso, F. H. Séguin, J. A. Frenje, C. K. Li, A. J. MacKinnon, and P. K. Patel, "Initial Experiments Using the OMEGA EP Laser System."

J. F. Myatt, D. H. Edgell, W. Seka, A. V. Maximov, R. W. Short, D. F. DuBois, D. A. Russell, and H. X. Vu, "Two-Plasmon-Decay Hot-Electron Distributions from Anistropic Thick-Target Bremsstrahlung Measurements."

P. M. Nilson, W. Theobald, J. F. Myatt, C. Stoeckl, P. A. Jaanimagi, J. A. Delettrez, M. Storm, R. Betti, D. D. Meyerhofer, T. C. Sangster, J. S. Green, K. L. Lancaster, P. A. Norreys, F. Beg, R. B. Stephens, and M. H. Key, "Fast-Electron-Energy Deposition in Dense Plasma."

O. Polomarov and R. Betti, "MHD Effects in Laser-Produced Plasmas."

P. B. Radha, V. N. Goncharov, T. C. Sangster, R. Betti, J. A. Delettrez, S. X. Hu, D. D. Meyerhofer, S. Skupsky, V. A. Smalyuk, C. Stoeckl, J. A. Frenje, C. K. Li, R. D. Petrasso, and D. Shvarts, "Modeling Observables to Diagnose Areal Density in OMEGA Implosions."

S. P. Regan, T. C. Sangster, D. D. Meyerhofer, W. Seka, R. L. McCrory, C. Stoeckl, V. Yu. Glebov, N. B. Meezan, L. J. Suter, D. J. Strozzi, E. A. Williams, W. L. Kruer, O. S. Jones, D. A. Callahan, M. D. Rosen, O. L. Landen, S. H. Glenzer, C. Sorce, and B. J. MacGowan, "Hohlraum Energetics with a Plastic-Lined Laser Entrance Hole."

T. C. Sangster, V. N. Goncharov, P. B. Radha, J. A. Delettrez, R. Betti, T. R. Boehly, V. Yu. Glebov, S. X. Hu, J. P. Knauer, F. J. Marshall, R. L. McCrory, P. W. McKenty, D. D. Meyerhofer, S. P. Regan, V. A. Smalyuk, W. Seka, S. Skupsky, C. Stoeckl,

B. Yaakobi, J. A. Frenje, C. K. Li, R. D. Petrasso, F. H. Séguin, and D. Shvarts, "Recent Experimental Results from Cryogenic Implosions on OMEGA."

H. Sawada, S. P. Regan, P. B. Radha, R. Epstein, D. Li, V. N. Goncharov, S. X. Hu, D. D. Meyerhofer, J. A. Delettrez, P. A. Jaanimagi, V. A. Smalyuk, T. R. Boehly, T. C. Sangster, B. Yaakobi, and R. C. Mancini, "Experimental Investigation of Thermal-Transport Models in Direct-Drive Targets Using X-Ray Absorption Spectroscopy."

W. Seka, H. A. Baldis, D. H. Edgell, J. F. Myatt, A. V. Maximov, R. S. Craxton, R. W. Short, V. N. Goncharov, A. Simon, and R. E. Bahr, "Two-Plasmon-Decay Instability in Direct-Drive Implosion Experiments."

R. W. Short, "Two-Plasmon Decay Driven by Multiple Obliquely Incident Laser Beams."

A. Shvydky, F. J. Marshall, P. W. McKenty, I. V. Igumenshchev, R. Epstein, J. A. Marozas, R. S. Craxton, T. C. Sangster, S. Skupsky, and R. L. McCrory, "Numerical Investigation of OMEGA Saturn Implosions."

N. Sinenian, J. A. Frenje, C. K. Li, F. H. Séguin, R. D. Petrasso, and J. A. Delettrez, "Measurements of Ablator-Ion Spectra for Preheat and Compression Studies."

S. Skupsky, V. N. Goncharov, and D. Li, "Nonlocal Ion-Heat and Momentum Transport in ICF Implosions."

V. A. Smalyuk, R. Betti, T. R. Boehly, R. S. Craxton, J. A. Delettrez, D. H. Edgell, V. Yu. Glebov, V. N. Goncharov, D. R. Harding, S. X. Hu, J. P. Knauer, F. J. Marshall, R. L. McCrory, P. W. McKenty, D. D. Meyerhofer, P. B. Radha, S.P. Regan, T. C. Sangster, W. Seka, R. W. Short, D. Shvarts, S. Skupsky, J. M. Soures, C. Stoeckl, B. Yaakobi, J. A. Frenje, C. K. Li, R. D. Petrasso, and F. H. Séguin, "Cryogenic Target Performance and Implosion Physics Studies on OMEGA" (invited).

A. A. Solodov, K. S. Anderson, R. Betti, V. Gotcheva, J. F. Myatt, J. A. Delettrez, S. Skupsky, W. Theobald, and C. Stoeckl, "Integrated Simulations of Implosion, Electron Transport, and Ignition for Direct-Drive, Fast-Ignition Targets."

C. Stoeckl, K. S. Anderson, T. R. Boehly, R. Betti, J. A. Delettrez, V. N. Goncharov, V. Yu. Glebov, R. L. McCrory, D. D. Meyerhofer, J. F. Myatt, P. M. Nilson, T. C. Sangster, A. A. Solodov, M. Storm, W. Theobald, B. Yaakobi, C. D. Zhou, J. A. Frenje, R. D. Petrasso, A. J. MacKinnon, P. A. Norreys, and R. B. Stephens, "Advanced Ignition Experiments on OMEGA."

M. Storm, C. Guo, D. D. Meyerhofer, C. Mileham, J. F. Myatt, P. M. Nilson, T. C. Sangster, A. A. Solodov, C. Stoeckl, and W. Theobald, "High-Current Electron Transport Studies Using Coherent Transition Radiation."

W. Theobald, V. Ovchinnikov, B. Eichman, S. Ivancic, P. M. Nilson, C. Stoeckl, J. F. Myatt, J. A. Delettrez, L. Von Woerkom, R. R. Freeman, C. Ren, R. B. Stephens, J. D. Zuegel, and T. C. Sangster, "Intense Laser-to-Fast-Electron Coupling Efficiency in Wedge-Shaped-Cavity Targets."

D. R. Harding, Z. Bei, S. H. Chen, R. Q. Gram, T. Jones, M. Moynihan, and R. Garrell, "Microfluidic Methods for Producing Millimeter-Size Fuel Capsules for Inertial Fusion Energy," 2008 MRS Fall Meeting, Boston, MA, 1–5 December 2008.

J. E. Schoenly, W. Seka, and P. Rechmann, "Laser Ablation of Dental Calculus Around 400 nm Using a Ti:Sapphire Laser," Lasers in Dentistry XV, San Jose, CA, 24–29 January 2009.

C. Stoeckl, K. S. Anderson, R. Betti, J. A. Delettrez, J. A. Frenje, V. N. Goncharov, V. Yu. Glebov, A. J. Mackinnon, R. L. McCrory, D. D. Meyerhofer, J. F. Myatt, P. A. Norreys, P. M. Nilson, R. D. Petrasso, T. C. Sangster, A. A. Solodov, R. B. Stephens, M. Storm, W. Theobald, B. Yaakobi, and C. D. Zhou, "Inertial Fusion Research at the Laboratory for Laser Energetics," 29th International Workshop on Physics of High Energy Density in Matter, Hirschegg, Austria, 1–6 February 2009.

S. P. Regan, P. B. Radha, T. R. Boehly, T. Doeppner, K. Falk, V. N. Goncharov, S. H. Glenzer, G. Gregori, O. L. Landen, D. D. Meyerhofer, P. Neumayer, T. C. Sangster, and V. A. Smalyuk, "Experimental Investigation of Inelastic X-Ray Scattering from Shock-Heated and Compressed Deuterium," International Workshop on Warm Dense Matter, Hakone, Japan, 16–19 March 2009.

P. M. Nilson, W. Theobald, J. F. Myatt, C. Stoeckl, P. A. Jaanimagi, J. A. Delettrez, C. Dorrer, J. D. Zuegel, R. Betti, D. D. Meyerhofer, T. C. Sangster, A. J. Mackinnon, P. K. Patel, and K. U. Akli, "Bulk Heating of Solid-Density Matter Using Kilojoule Pulses on OMEGA EP," 16th International Con-ference on Atomic Processes in Plasmas, Monterey, CA, 22–26 March 2009.

The following presentations were made at OMEGA Laser Facility Users' Group Workshop, Rochester, NY, 29 April–1 May 2009:

M. A. Barrios, D. E. Fratanduono, T. R. Boehly, D. D. Meyerhofer, D. G. Hicks, P. M. Celliers, and J. H. Eggert, "Precision Equation of State (EOS) Measurements Using Laser-Driven Shock Waves on the OMEGA Laser."

D. E. Fratanduono, M. A. Barrios, T. R. Boehly, D. D. Meyerhofer, J. Eggert, R. Smith, D. G. Hicks, and G. Collins, "Measurements of Strain-Induced Refractive Index Changes in Shocked LiF Using Laser-Driven Flyer Plates."

O. V. Gotchev, R. Betti, P. Y. Chang, J. P. Knauer, O. Polomarov, D. D. Meyerhofer, J. A. Frenje, C. K. Li, M. Manuel, R. D. Petrasso, and F. H. Séguin, "Embedding Strong External Magnetic Fields in OMEGA Implosions—An Experimental Reality with Applications to Fusion, Exotic Plasma States, and More. The Designer and Use Perspectives."

J. Hager, V. A. Smalyuk, I. V. Igumenshchev, D. D. Meyerhofer, and T. C. Sangster, "First Rayleigh–Taylor and Richtmyer–Meshkov Instability Measurements in Laser-Driven Planar Targets on the OMEGA EP Laser."

D. R. Harding and M. J. Bonino, "Target Fabrication: Capabilities and the Ordering Process."

S. F. B. Morse, "Omega Facility: Status and Performance."

P. M. Nilson, W. Theobald, J. F. Myatt, C. Stoeckl, P. A. Jaanimagi, J. A. Delettrez, B. Yaakobi, J. D. Zuegel, R. Betti, D. D. Meyerhofer, T. C. Sangster, P. K. Patel, A. J. Mackinnon, and K. Akli, "Characterization and Optimization of Fast-Electron Sources Using Intense, Multi-kJ Pulses on OMEGA EP."

G. Pien, "Engineering Support and Qualification Process for Interfacing New Experiments."

C. Ren, G. Li, R. Yan, J. Tonge, and W. B. Mori, "Simulations of Laser Channeling in Millimeter-Scale Underdense Plasmas for Fast Ignition."

T. C. Sangster, "Diagnostic Status on OMEGA EP."

C. Stoeckl, "Status of OMEGA EP, an Experimentalist's Perspective."

W. Theobald, K. S. Anderson, R. Betti, R. S. Craxton, J. A. Delettrez, J. A. Frenje, V. Yu. Glebov, O. V. Gotchev, A. J. Mackinnon, F. J. Marshall, R. L. McCrory, D. D. Meyerhofer, J. F. Myatt, P. A. Norreys, P. M. Nilson, P. K. Patel, R. D. Petrasso, P. B. Radha, C. Ren, T. C. Sangster, A. A. Solodov, R. B. Stephens, C. Stoeckl, M. Storm, and C. D. Zhou, "Status of Integrated Fast- and Shock-Ignition Experiments on OMEGA."

K. A. Thorp, "OMEGA Properties and Capabilities."

The following presentations were made at the Second International Conference on High Energy Density Physics, Austin, TX, 19–22 May 2009:

V. N. Goncharov, T. C. Sangster, T. R. Boehly, R. L. McCrory, D. D. Meyerhofer, P. B. Radha, V. A. Smalyuk, S. Skupsky, J. A. Frenje, and R. D. Petrasso, "Multiple-Picket, Low-Adiabat Cryogenic Fuel Compression on OMEGA."

W. Theobald, K. S. Anderson, R. Betti, R. S. Craxton, J. A. Delettrez, B. Eichman, V. Yu. Glebov, O. V. Gotchev, S. Ivancic, F. J. Marshall, R. L. McCrory, D. D. Meyerhofer, J. F. Myatt, P. M. Nilson, P. B. Radha, C. Ren, T. C. Sangster, A. A. Solodov, C. Stoeckl, M. Storm, C. D. Zhou, J. D. Zuegel, J. A. Frenje, R. D. Petrasso, P. A. Norreys, V. M. Ovchinnikov, F. F. Freeman, L. Van Woerkom, D. Hey, M. H. Key, A. J. MacKinnon, P. K. Patel, K. Akli, R. B. Stephens, and R. Lauck, "Integrated Fast- and Shock-Ignition Experiments on OMEGA. "

The following presentations were made at CLEO/IQEC 2009, Baltimore, MD, 31 May–5 June 2009:

S.-W. Bahk and J. D. Zuegel, "A High-Resolution Amplitude and Wavefront Control System Based on a Direct Zonal Closed-Loop Approach."

I. A. Begishev, A. V. Okishev, R. G. Roides, and J. D. Zuegel, "All-Fiber Discrete Arbitrary Picket-Pulse Shaping."

J. Bromage, C. Dorrer, M. J. Shoup III, and J. D. Zuegel, "Optimizing Injection into Large-Mode-Area Photonic Crystal-Fiber Amplifiers by Spatially Resolved Spectral Interferometry."

C. Dorrer, "Near-Field Intensity Shaping with Binary Phase Plates."

C. Dorrer, "Statistical Analysis of Incoherent Pulse Shaping."

C. Dorrer and J. Bromage, "Simple High-Sensitivity, Electro-Optic Sagnac Spectral Shearing Interferometry for Short Optical Pulse Characterization."

J. R. Marciante and R. G. Roides, "Mode Control in Large-Mode-Area Fiber Lasers Via Gain Filtering."

W. Yang and C. Dorrer, "Ultrafast Pulse Characterization of Semiconductor Single-Section Fabry–Perot Mode-Locked Lasers."

The following presentations were made at ICOPS/SOFE 2009, San Diego, CA, 31 May–5 June 2009:

D. R. Harding, D. H. Edgell, L. M. Elasky, R. Q. Gram, T. B. Jones, S. J. Verbridge, A. J. Weaver, and M. D. Wittman, "Cryogenic Targets for Inertial Confinement Fusion Experiments and Future Fusion-Energy Applications."

W. T. Shmayda, G. Wainwright, and R. Janezic, "Cryogenic Tritium Operations at OMEGA."

The following presentations were made at the 39th Anomalous Absorption Conference, Bodega Bay, CA, 14–19 June 2009:

D. DuBois, D. Russell, H. Vu, and J. Myatt, "1/2 ω_0 Emission from the Nonlinear Currents Generated by the Two Plasmon Decay Instability."

D. H. Edgell, W. Seka, V. N. Goncharov, I. V. Igumenshchev, R. S. Craxton, J. A. Delettrez, J. F. Myatt, A. V. Maximov, R. W. Short, R. E. Bahr, "Time-Dependent Scattered-Light Spectroscopy in Direct-Drive-Implosion Experiments."

A. V. Maximov, J. F. Myatt, R. W. Short, W. Seka, J. A. Delettrez, and C. Stoeckl, "Modeling of Two-Plasmon-Decay Instability Under Crossed-Beam Irradiation."

J. F. Myatt, A. V. Maximov, R. W. Short, J. A. Delettrez, W. Seka, D. H. Edgell, D. F. DuBois, H. X. Vu, and D. A. Russell, "Extended Zakharov Modeling of the Two-Plasmon-Decay Instability in Inhomogeneous Direct-Drive ICF-Relevant Plasma."

D. Russell, D. DuBois, H. Vu, and J. Myatt, "3/2 ω_0 Emission from the LDI Langmuir Waves Excited in the Nonlinear Saturation of the Two Plasmon Decay Instability."

W. Seka, D. H. Edgell, J. F. Myatt, A. V. Maximov, R. W. Short, V. N. Goncharov, D. F. DuBois, H. X. Vu, D. A. Russell, and H. A. Baldis, "Two-Plasmon-Decay Instability Relevant to Direct-Drive Experiments."

R. W. Short, "Anistropy of Two-Plasmon Decay for Multiple Obliquely Incident Laser Beams."

H. Vu, D. DuBois, D. Russell, and J. Myatt, "Hot Electrons Production from the Two-Plasmon Decay Instability."

The following presentations were made at the 16th APS Topical Conference in Shock Compression of Condensed Matter, Nashville, TN, 28 June–3 July 2009:

M. A. Barrios, D. E. Fratanduono, T. R. Boehly, D. D. Meyerhofer, D. G. Hicks, P. M. Celliers, and J. H. Eggert, "High-Precision Measurements of the Equation of State (EOS) of Polymers at 100 to 1000 GPa Using Laser-Driven Shock Waves."

D. E. Fratanduono, M. A. Barrios, T. R. Boehly, D. D. Meyerhofer, R. Smith, J. H. Eggert, D. G. Hicks, P. M. Celliers, and G. W. Collins, "Measurements of Strain-Induced Refractive-Index Changes in Shocked LiF Using Laser-Driven Flyer Plates."

J. Bromage, C. Dorrer, J. R. Marciante, M. J. Shoup III, and J. D. Zuegel, "Modal Measurement of a Large-Mode-Area

Photonic-Crystal Fiber Amplifier Using Spatially Resolved Spectral Interferometry," 22nd Annual Solid State and Diode Laser Technology Review, Newton, MA, 29 June–1 July 2009.

W. Theobald, K. S. Anderson, R. Betti, R. S. Craxton, J. A. Delettrez, J. A. Frenje, V. Yu. Glebov, O. V. Gotchev, J. H. Kelly, C. K. Li, A. J. Mackinnon, F. J. Marshall, R. L. McCrory, D. D. Meyerhofer, J. F. Myatt, P. A. Norreys, P. M. Nilson, P. K. Patel, R. D. Petrasso, P. B. Radha, C. Ren, T. C. Sangster, W. Seka, V. A. Smalyuk, A. A. Solodov, R. B. Stephens, C. Stoeckl, and B. Yaakobi, "Advanced-Ignition-Concept Exploration on OMEGA," 36th EPS Conference on Plasma Physics, Sofia, Bulgaria, 29 June–3 July 2009.

L. Ji, W. R. Donaldson, and T. Y. Hsiang, "Electro-Optic Sampling Using Two/Multiple Optical Pulses," 14th Opto-Electronics and Communications Conference, Hong Kong, 13–17 July 2009.

The following presentations were made at Optical Manufacturing and Testing VIII, San Diego, CA, 2–6 August 2009:

C. Miao, J. C. Lambropoulos, S. N. Shafrir, H. Romanofsky, and S. D. Jacobs, "Contributions of Nanodiamond Abrasives and Deionized Water in Magnetorheological Finishing of Aluminum Oxynitride."

C. Miao, S. N. Shafrir, J. C. Lambropoulos, and S. D. Jacobs, "Normal Force and Drag Force in Magnetorheological Finishing."

S. N. Shafrir, R. Shen, C. Miao, H. Romanofsky, M. Wang, J. Mici, J. Yang, J. C. Lambropoulos, and S. D. Jacobs, "Zirconia Coated Carbonyl Iron Particle-Based Magnetorheological Fluid for Polishing."

E. Glowacki, C. W. Ching, and K. L. Marshall, "Photoswitchable Gas Permeation Membranes Based on Azobenzene-Doped Liquid Crystals," Optics and Photonics, San Diego, CA, 2–6 August 2009 (invited).

The following presentations were made at the Ultrafast Optics and High Field Short Wavelength Meeting, Arcachon, France, 31 August–4 September 2009:

C. Dorrer, "High-Damage-Threshold Beam Shapers for High-Energy Laser Systems."

C. Dorrer and J. Bromage, "Simple High-Sensitivity, Electro-Optic Sagnac Spectral Shearing Interferometry for Optical Pulse Characterization."

C. Dorrer, J. Bromage, and J. D. Zuegel, "Single-Shot High-Dynamic-Range Cross-Correlator for High-Energy Laser Systems."

The following presentations were made at the Sixth International Conference on Inertial Fusion Sciences and Applications, San Francisco, CA, 6–11 September 2009:

R. Betti, K. S. Anderson, P. Y. Chang, R. Nora, and C. D. Zhou, "A Measurable Lawson Criterion for Inertial Confinement Fusion."

T. R. Boehly, V. N. Goncharov, D. E. Fratanduono, M. A. Barrios, S. X. Hu, T. C. Sangster, D. D. Meyerhofer, D. Munro, P. M. Celliers, D. G. Hicks, H. F. Robey, G. W. Collins, N. Landen, R. E. Olson, and A. Nikroo, "Demonstration of the Shock-Timing Technique for Ignition Targets at the National Ignition Facility."

V. N. Goncharov, T. C. Sangster, T. R. Boehly, R. L. McCrory, D. D. Meyerhofer, P. B. Radha, V. A. Smalyuk, S. Skupsky, J. A. Frenje, and R. D. Petrasso, "Multiple-Picket, Cryogenic Target Designs and Performance for OMEGA and the NIF."

R. L. McCrory, R. Betti, R. S. Craxton, J. A. Delettrez, D. H. Edgell, V. Yu. Glebov, V. N. Goncharov, D. R. Harding, S. X. Hu, J. P. Knauer, F. J. Marshall, P. W. McKenty, D. D. Meyerhofer, P. B. Radha, S. P. Regan, T. C. Sangster, W. Seka, R. W. Short, D. Shvarts, S. Skupsky, V. A. Smalyuk, J. M. Soures, C. Stoeckl, W. Theobald, B. Yaakobi, J. A. Frenje, C. K. Li, R. D. Petrasso, F. H. Séguin, and D. T. Casey, "Progress in Cryogenic Target Implosions on OMEGA."

P. W. McKenty, R. S. Craxton, J. A. Marozas, A. M. Cok, M. J. Bonino, D. R. Harding, D. D. Meyerhofer, R. L. McCrory, J. D.

Kilkenny, A. Nikroo, J. Fooks, M. Hoppe, J. M. Edwards, A. J. MacKinnon, D. H. Munro, and R. J. Wallace, "Design of High-Neutron-Yield Polar-Drive Targets for Diagnostic Activation Experiments on the NIF."

D. D. Meyerhofer, R. Betti, T. R. Boehly, J. Bromage, C. Dorrer, V. Yu. Glebov, J. H. Kelly, B. E. Kruschwitz, S. J. Loucks, R. L. McCrory, S. F. B. Morse, J. F. Myatt, P. M. Nilson, J. Qiao, T. C. Sangster, A. A. Solodov, C. Stoeckl, W. Theobald, J. D. Zuegel, H. S. Park, B. Maddox, A. MacPhee, J. Workman, M. Koenig, E. Brimbrank, C. Szabo, and G. Holland "Performance of and Initial Experimental Results from the Omega EP Laser System."

S. P. Regan, P. B. Radha, T. R. Boehly, T. Doeppner, K. Falk, V. N. Goncharov, S. H. Glenzer, G. Gregori, O. L. Landen, D. D. Meyerhofer, P. Neumayer, T. C. Sangster, and V. A. Smalyuk, "Inferring the Electron Temperature and Density of Shocked Liquid Deuterium Using Inelastic X-Ray Scattering."

T. C. Sangster, L. Ahle, D. Bleuel, D. T. Casey, M. J. Eckart, M. J. Edwards, R. J. Fortner, J. A. Frenje, V. Yu. Glebov, G. P. Grim, H. W. Herrmann, C. J. Horsfield, J. D. Kilkenny, O. Landoas, R. A. Lerche, K. J. Moody, M. J. Moran, R. D. Petrasso, M. Schmitt, D. Schneider, D. A. Shaughnessy, C. Stoeckl, W. Stoeffl, and M. D. Wilke, "The Nuclear Diagnostics Suite for the NIF."

A. A. Solodov, M. Storm, J. F. Myatt, R. Betti, D. D. Meyerhofer, P. M. Nilson, W. Theobald, and C. Stoeckl, "The Role of Resistive Filamentation and Self-Generated Magnetic Fields in Hot-Electron-Beam Transport Through Solid Targets."

A. L. Rigatti, J. B. Oliver, A. Kozlov, and A. W. Schmid, "Comparison of 10-ps In-Air and In-Vacuum Damage Thresholds," Laser Damage 2009, Boulder, CO, 21–23 September 2009.


1850
MELIORA
UNIVERSITY of
ROCHESTER